UNIVERSITÉ DE STRASBOURG

ÉCOLE DOCTORALE physique et chimie-physique (ED 182)

Institut de Physique et Chimie des Matériaux de Strasbourg

THÈSE présentée par :

Jean-Gabriel HARTMANN

soutenue le : **15 novembre 2024**

pour obtenir le grade de : **Docteur de l'université de Strasbourg**

Discipline/ Spécialité : Physique

Hilbert space engineering and optimal control for quantum computing with applications for rare-earth single molecule magnets

THÈSE dirigée par :

M. HERVIEUX Paul-Antoine	Prof., IPCMS UMR-7504 CNRS, Université de Strasbourg
M. RUBEN Mario	Prof., CESQ-ISIS UMR-7006 CNRS, Université de Strasbourg

RAPPORTEURS :

M. SUGNY Dominique	Prof., LICB UMR-6303 CNRS, Université de Bourgogne
M. HUNGER David	Prof., PHI, Institut de Technologie de Karlsruhe

---

AUTRES MEMBRES DU JURY :

M. GENET Cyriaque	Dr., CESQ-ISIS UMR-7006 CNRS, Université de Strasbourg
M. PRIVAT Yannick	Prof., IECL UMR-7502 CNRS, Université de Lorraine
M. BONNEAU Ludovic	Dr., LP2I UMR-5797 CNRS, Université de Bordeaux
Mme. MILMAN Perola	Dr., MPQ UMR-7162 CNRS, Université Paris Cité

UNIVERSITÉ DE STRASBOURG

ÉCOLE DOCTORALE physique et chimie-physique (ED 182)

Institut de Physique et Chimie des Matériaux de Strasbourg

THÈSE

présentée par :

Jean-Gabriel HARTMANN

soutenue le : 15 novembre 2024

pour obtenir le grade de : Docteur de l'université de Strasbourg

Discipline/ Spécialité : Physique

Hilbert space engineering and optimal control for quantum computing with applications for rare-earth single molecule magnets

THÈSE dirigée par :

M. HERVIEUX Paul-Antoine	Prof., IPCMS UMR-7504 CNRS, Université de Strasbourg
M. RUBEN Mario	Prof., CESQ-ISIS UMR-7006 CNRS, Université de Strasbourg

RAPPORTEURS :

M. SUGNY Dominique	Prof., LICB UMR-6303 CNRS, Université de Bourgogne
M. HUNGER David	Prof., PHI, Institut de Technologie de Karlsruhe

---

AUTRES MEMBRES DU JURY :

M. GENET Cyriaque	Dr., CESQ-ISIS UMR-7006 CNRS, Université de Strasbourg
M. PRIVAT Yannick	Prof., IECL UMR-7502 CNRS, Université de Lorraine
M. BONNEAU Ludovic	Dr., LP2I UMR-5797 CNRS, Université de Bordeaux
Mme. MILMAN Perola	Dr., MPQ UMR-7162 CNRS, Université Paris Cité

To my wife Shannon,
for always being by my side, every step of the way.

Acknowledgements

First and foremost, I would like to thank my supervisor, Paul-Antoine Hervieux, for his unwavering guidance, support, and mentorship throughout the years. I will be forever grateful for the opportunity he offered me with this thesis; it really changed my life. His inspiring passion for physics and science in general, and openness of communication, created an exceptional working environment. I would like to extend these thanks to my co-supervisor, Mario Ruben, whose multidisciplinary expertise and scientific rigour helped not only to maintain clarity of perspective, but also to shape the foundation of this thesis: his weekly group meetings fostered a sense of community and scientific collaboration, across disciplines and borders.

My sincere thanks go to all of the jury members for their time and effort spent in evaluating this thesis. I am grateful to Prof. Dr. David Hunger and Prof. Dominique Sugny for agreeing to be examiners and for reviewing this thesis. These extend to Prof. Yannick Privat, Dr. Cyriaque Genet, Dr. Perola Milman and Dr. Ludovic Bonneau for agreeing to be members of the jury, with additional thanks to Dr. Cyriaque Genet for agreeing to serve as president of the jury.

This thesis would not have been possible without significant financial support, and so I wish to acknowledge both the EUCOR QUSTEC and ANR QMat programs, including their affiliated institutions and their scientific and administrative support staff for enabling this training experience as an early-stage researcher.

I am appreciative of the efforts of my supervisors for having provided the mobility and networking opportunities to collaborate with many exceptional researchers throughout the PhD. On the nuclear study, I am deeply appreciative of the work with experts Johann Bartel and Hervé Molique from IPHC, as well as Ludovic Bonneau of LP2I Bordeaux. On the chemical side, I thank Senthil, Sai, Jo and Svetlana of the Ruben Group in KIT, and also Saad, Vincent and Thanasis of ILB Strasbourg for their insightful perspectives. This extends to the experimentalists of PHI KIT: Prof. Philip Wilke, and members of the Wernsdorfer Group, Eufemio Moreno-Pineda and Luca Kosche. On the mathematical side, it was a pleasure working together with Killian Lutz and Emmanuel Franck of IRMA Strasbourg and Yannick Privat of IEC Nancy, who always provided such valuable fundamental insights into our projects.

To the Q-Dyno Group, its leaders Giovanni Manfredi and Paul-Antoine Hervieux, and the Q-Dynosaurs, members past, present and honorary, I will always be thankful for the convivial atmosphere that made working in the lab each day such a pleasure. I cannot express enough gratitude to my “brother in quantum”, my friend, Dr. Denis Janković, the first person I met when I arrived in Strasbourg and whose boundless enthusiasm and

scientific skill made working together every day a privilege. To Dr. Rémi Pasquier, I am constantly in awe of your scientific (and general) knowledge. Dr. Adrien Andoche, your optimistic and positive attitude is inspiring, and I'll miss our coffee break discussions. And speaking of coffee breaks, they were made possible by the generosity of Dr. Vincent Hardel and his well-stocked coffee machines; perhaps he is responsible for at least four theses being finished successfully on time. To the young Q-Dynosaurs, Benjamin Bakri, Pierre Guichard, Paul-Louis Etienney and Andrea Victoria, I hope that your time in the group will be equally memorable. To the past interns, Julian Mayr and Gustavo Kufatty: It was really amazing to tackle together (Denis included) a well-coordinated project, and your efforts really helped to lay the foundations for a lot of our subsequent research projects.

Within the larger DON department (and beyond), thank you to my fellow QUSTECers Dr. Md. Samiul Islam and Patrick Lawes for your friendship throughout the years, as well as to the permanent members Lorry Engel, Damien Cianfarani, and Wilfried Grange for the friendly camaraderie in our corridor. In the IPCMS as a whole, I must thank the support and administrative personnel, particularly Catherine Bonnin and Ratibe Aksoz, and the information services personnel, particularly Christine Tugene, Thien Ho Minh, and Xavier Ledoux, for their kind and friendly assistance in any situation.

Penultimately, I would be remiss if I did not extend my thanks to all of my friends, near and far, old and new, without whom I would not be the person I am today. You are too numerous to all mention by name, but I trust that you know who you are. A special mention must go out to Dr. Dale Annear and Eleesha Annear, fellow scientists who share in the trials and tribulations of life as researchers, and who always seem to be prepared with words of wisdom and encouragement. To my family, my parents Marie-José and Mark, my brother Tristan, and my cousin Lisa, I cannot thank you enough for the endless support throughout the years, for always believing in me and for always being close despite the long distances. To my late grandmother, Faith, I would never have been able to even begin my master's degree without your help, let alone move halfway across the world to pursue a doctorate. You were always my strongest proponent, and I only wish that you could have been here at this milestone.

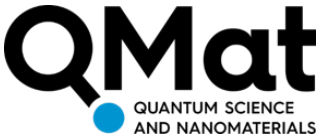
Finally, and most importantly, to my one and only, my wife Shannon: I couldn't have done it without you, and no words can truly express the depth of my gratitude. I love you, forever and always.

Support and Funding



This work was funded through the **EUCOR QUSTEC** project of the European Union's **Horizon 2020** research and innovation program under the **Marie Skłodowska-Curie** Grant Agreement No. 847471.

This work was jointly funded by the **QMat** program of the **French National Research Agency** (ANR) through the **Programme d'Investissement d'Avenir** under contract **ANR-11-LABX-0058_NIE** and **ANR-17-EURE-0024** within the **Investissement d'Avenir** program **ANR-10-IDEX-0002-02**.





The work of this thesis was carried out on the premises and with the resources of the **Institut de Physique et de Chimie de Matériaux de Strasbourg** (IPCMS), UMR-7504 **CNRS**, within the **QDyno** group.



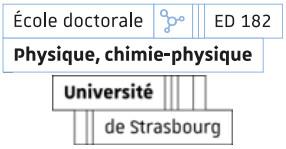






The author would also like to acknowledge the **High Performance Computing Center** of the **University of Strasbourg** for supporting this work by providing scientific support and access to computing resources. Part of the computing resources were funded by the **Equipex Equip@Meso project** (Programme Investissements d'Avenir) and the **CPER Alsacalcul/ Big Data**.

Finally, this research was made possible thanks to the financial and administrative support provided by the **ED182** Doctoral School of the **University of Strasbourg**.



Scientific Outputs

Publications

1. Janković, D., Hartmann, JG., Ruben, M., Hervieux, PA. Noisy qudit vs multiple qubits: conditions on gate efficiency for enhancing fidelity. npj Quantum Inf 10, 59 (2024).

2. Hartmann, J.-G., Janković, D., Pasquier, R., Ruben, M. & Hervieux, P.-A. Nonlinearity of the Fidelity in Open Qudit Systems: Gate and Noise Dependence in High-dimensional Quantum Computing. Quantum 9, 1690 (2025).

3. Hervieux, PA, Hartmann, JG., Janković, D., Bartel, J., Molique, H., Bonneau, L. *Ab initio* Modelling of Lanthanide Nuclei and Study of the Hyperfine Anomaly. [Manuscript in preparation for submission to PRX]

4. Janković, D., Hartmann, JG., Hervieux, PA, Elucidating the Phyiscal and Mathematical Properties of the Prouhet-Thue-Morse Sequence in Quantum Computing. [Submitted to J. Phys. A: Math. Theor.]

5. Hartmann, JG., Janković, D., Ruben, M., Hervieux, PA. Benchmarking Quantum Optimal Control Techniques for Qudit Gate Synthesis [Manuscript in preparation for submission to Comput. Phys. Commun.]

6. Chen, H., Borzi, A., Janković, D., Hartmann, JG., Hervieux, PA. Full- and low-rank exponential Euler integrators for the Lindblad equation [Submitted to SIAM Journal on Scientific Computing]

Dissemination Activities

Presentations

1. **QuantMOCOTE 2023 - Modelling, Optimization and Control of Quantum Systems in Technology and Education**
   06/03/2023 - 08/03/2023
   Institute of Mathematics, Wurzburg, Germany

2. **Optically Addressable Molecular Lanthanide Qubits for Quantum Devices**
   05/10/2023 - 06/10/2023
   Baden-Baden, Germany

3. **Controlling Molecular Qudits: From Pulses to Quantum Gates.**
   Invited by Dr. Saad Yalouz 19/05/2024
   Laboratory for Quantum Chemistry, Strasbourg, France

Posters

1. **NCCR QCQT QUSTEC Summer School 2021**
   14/09/2021 - 17/09/2021
   Engelberg, Switzerland

2. **Ecole Joliot-Curie 2021 - The Interplay Between Atomic Electrons and the Nucleus**
   03/10/2021 - 08/10/2021
   Saint-Pierre d'Oléron, France

3. **ED182 Congrés des Doctorants 2022**
   30/03/2022
   European Doctoral College, Strasbourg, France

4. **EFEQT European Spring School in Quantum Science and Technology 2022**
   10/04/2022 - 14/04/2022
   ISIS, Strasbourg, France

5. **ITI QMat Scientific Day 2022**
   01/06/2022
   IPCMS, Strasbourg, France

6. **molQueST 2022 - Quantum Science Emerging from Atoms and Molecules at Surfaces**
   21/08/2022 - 25/08/2022
   Ascona, Switzerland

7. **ED182 Congrés des Doctorants 2023**
   23/03/2023
   European Doctoral College, Strasbourg, France

8. **quantumBasel 2023 - US-Switzerland Quantum Symposium**
   27/04/2023 - 28/04/2023
   Basel, Switzerland

9. **ITI QMat Scientific Day 2023** ***(Poster Award: 2nd Place)***
   15/06/2023
   IPCMS, Strasbourg, France

10. **EGAS 54 - European Group on Atomic Systems**
    18/06/2023 - 22/06/2023
    Strasbourg, France

11. **KSQM MSCA QUSTEC EUCOR Summer School 2023 - European Summer School in Quantum Science and Technology**
    17/09/2023 - 22/09/2023
    Durbach, Germany

Outreach

1. **Interview - Savoir Magazine**
   10/05/2021
   Strasbourg, France

2. **Student organiser - Machine Learning for Quantum X online pop-up conference**
   05/07/2021 - 09/07/2021
   Strasbourg, France

3. **Co-organiser - European Spring School in Quantum Science and Technology 2022**
   10/04/2021 - 14/04/2022
   Strasbourg, France

Résumé en français

Mais oui, c'est clair!

- Eddy Malou

Contents

Introduction xiii
Modélisation *ab initio* des noyaux de lanthanide xxxi
Anomalies hyperfines dans les ions hydrogènoide de dysprosium xli
Qudit bruyant vs Qubits multiples xlix
Non-linéarité de la fidélité dans les systèmes quantiques ouverts lv
Techniques de contrôle optimal quantique pour la synthèse de portes Qudit lxi
Conclusion lxxi
Références citées dans ce chapitre lxxv

Introduction

Contexte et Motivations

L'histoire de l'informatique classique et celle de l'informatique quantique sont profondément liées, partageant une quête commune pour comprendre et manipuler les principes fondamentaux de l'information. Alors que les efforts mondiaux progressent vers la réalisation d'une informatique quantique universelle et tolérante aux erreurs, les plateformes basées sur les qubits - en particulier les qubits supraconducteurs - se trouvent à l'avant-garde technologiques de la recherche. Cependant, malgré leur développement rapide, des défis techniques subsistent en matière d'évolutivité, de cohérence et de correction d'erreurs [1].

Cette thèse étudie une voie complémentaire à travers l'exploitation des qudits : des systèmes quantiques à plusieurs niveaux qui dépassent le cadre binaire des qubits. En exploitant les états de spin nucléaire d'ions lanthanides intégrés dans des aimants moléculaires, ce travail vise à établir une base théorique pour l'informatique quantique basée sur les qudits, en explorant comment ces systèmes peuvent fonctionner et dans quelles conditions ils pourraient potentiellement défier les plateformes utilisant des qubits. Grâce à de nouveaux modèles théoriques et à des techniques de contrôle optimal, cette recherche vise à faire progresser les capacités de traitement de l'information quantique de ces nouveaux systèmes quantiques de haute dimensionalité.

Traitement de l'information quantique

Pour comprendre le potentiel des qubits, il est essentiel d'explorer d'abord les principes fondamentaux de l'informatique quantique et le rôle que les qubits ont joué dans son développement. Ce développement peut être envisagé sous différents angles. D'une part, les premières propositions de calcul avec des informations quantiques ont été faites au début des années 1980, l'attribution étant généralement faite à Richard Feynman avec son article de 1982 « Simulating physics with computers » [2] et sa citation souvent évoquée (basée sur un exposé de 1981) : « La nature n'est pas classique, bon sang, et si vous voulez faire une simulation de la nature, vous feriez mieux de la faire en mécanique quantique. »

Toutefois, comme l'indique l'article de Nature sur les « 40 ans de l'informatique quantique » [3], la proposition originale d'un ordinateur exploitant les principes de la mécanique quantique (en l'occurrence, l'échelle exponentielle de l'espace de Hilbert) a été faite par Yuri Manin en 1980 [4]. Il convient également de mentionner les premières contributions de Paul Benioff, qui a proposé en 1980 un modèle de mécanique quantique des ordinateurs en tant que machines de Turing dans son article « The computer as a physical system » [5], et de David Deutsch, qui a proposé en 1985 le premier modèle d'ordinateur quantique universel [6].

D'autre part, le développement de l'informatique quantique a été motivé par la nécessité de relever des défis fondamentaux en matière de puissance de calcul (informatique), tels que la factorisation de grands nombres et la simulation de systèmes quantiques. Les travaux fondamentaux de Peter Shor en 1994 sur les algorithmes quantiques pour la factorisation et les logarithmes discrets [7], de Lov Grover en 1996 sur les algorithmes de recherche quantique [8], et de Seth Lloyd en 1996 sur les simulateurs quantiques universels [9] ont joué un rôle déterminant dans l'évolution du domaine. Ces algorithmes ont démontré que les systèmes quantiques pouvaient être plus performants que les ordi-

nateurs classiques pour résoudre des problèmes spécifiques, ce qui a déclenché une vague de recherche sur les algorithmes quantiques, sur la correction quantique des erreurs et sur la théorie quantique de l'information. En effet, en exploitant les principes de superposition, d'intrication et d'interférence, ces travaux fondamentaux ont jeté les bases du développement de l'informatique quantique telle que nous la connaissons aujourd'hui.

En revanche, il convient de noter que la miniaturisation continue des ordinateurs classiques a également joué un rôle moteur dans le développement des technologies de l'informatique quantique. La taille des transistors continuant à s'approcher des limites de ce qui est réalisable dans le cadre de la physique classique, le besoin de nouveaux paradigmes informatiques se fait de plus en plus pressant. En effet, on constate désormais des effets quantiques mesurables au niveau des composants ultra réduits des technologies actuelles. Ce constat nous permets d'avoir une base de travail pour le développement de futurs composants dont le fonctionnement repose sur les principes de l'informatique quantique. Mais en même temps, l'état avancé de la technologie informatique classique peut aussi fournir une plateforme préexistante pour le développement futur des technologies informatiques quantiques [10, 11].

Alors qu'une grande partie des travaux en informatique quantique est restée théorique pendant la majeure partie de ses 40 ans d'histoire, les progrès technologiques des deux dernières décennies ont conduit à une augmentation significative du nombre de plateformes expérimentales développées avec succès. A l'instar de l'informatique classique, l'informatique quantique connait l'essor de nombreux types de plateformes expérimentales. Avant que le MOSFET (transistor à effet de champ métal-oxyde-silicium) ne devienne la technologie dominante, la mise au point des transistors électriques à vu de nombreuses technologies fleurir, comme des relais, des tubes à vide et des commutateurs à semi-conducteurs [12]. De même, de nos jours, les plateformes expérimentales pour l'étude de l'informatique quantique sont nombreuses, comme les circuits supraconducteurs [13], les ions piégés [14, 15], les systèmes photoniques [16, 17], les atomes neutres (Rydberg) [18, 19], les spins nucléaires et électroniques dans les aimants moléculaires [20, 21, 22] et les points quantiques à base de semi-conducteurs [23, 24].

Chacune de ces plateformes a ses propres forces et faiblesses, et chacune a fait des progrès significatifs dans le développement et le contrôle des qubits. Par exemple, les ions piégés ont montré des temps de cohérence longs et une fidélité logique élevée sur des systèmes simples, mais ils ont montré des performances bien moins satisfaisantes pour des circuits logiques plus complexes. Les systèmes photoniques, tout en offrant la possibilité d'un contrôle précis de l'état de l'information à distance, sont des systèmes avec lesquels il est difficile de réaliser des portes quantiques de haute fidélité et des architectures de qubits évolutifs [25]. Les systèmes d'atomes neutres froids utilisant des états excités de Rydberg sont prometteurs, mais nécessitent, comme les systèmes photoniques, l'utilisation de techniques de contrôle sophistiquées. De même, les points quantiques à base de semiconducteurs se sont également révélés prometteurs notamment pour les architectures de qubits évolutives, mais il est difficile d'obtenir des temps de cohérence longs et un contrôle individuel de chaque qubit.

D'autre part, les circuits supraconducteurs sont apparus comme le type de plateforme expérimentale le plus prometteur pour l'informatique quantique [26], avec une évolutivité notable et des systèmes éprouvés allant jusqu'à des centaines de qubits et dans lesquelles ont été alloué des investissements importants à la fois par le milieu universitaire et l'industrie, y compris des entreprises telles que IBM [27] et Google [28]. Ces

systèmes ont franchi des étapes importantes en matière de fidélité en sortie de porte logique, de temps de cohérence et de protocoles de correction d'erreurs, ce qui en fait des candidats de premier plan pour les applications d'informatique quantique à court terme [13, 29]. Cependant, bien qu'ils aient atteint un haut niveau de maturité technologique, les défis liés à la décohérence, de la gestion du bruit et à l'extensibilité générale de ces dispositifs mésoscopiques restent importants.

Aujourd'hui, à ce stade intermédiaire où des plateformes à petite échelle comptant jusqu'à 100 qubits sont mises en œuvre, il est pertinent de parler de mesures de performance telles que la fidélité et les temps de cohérence, leur rapport, le facteur de mérite, et les taux d'erreur par rapport aux seuils de correction d'erreur. Ces mesures sont regroupées dans les critères de DiVincenzo [30], un ensemble de cinq exigences qu'une plateforme de calcul quantique doit remplir pour être considérée comme universelle. Ces critères sont les suivants (i) des qubits physiques évolutifs, (ii) l'initialisation des qubits, (iii) de longs temps de cohérence pertinents, (iv) un ensemble de portes universelles et (v) la lecture des qubits. Il est essentiel de satisfaire ces critères pour atteindre la maturité des technologies de l'informatique quantique.

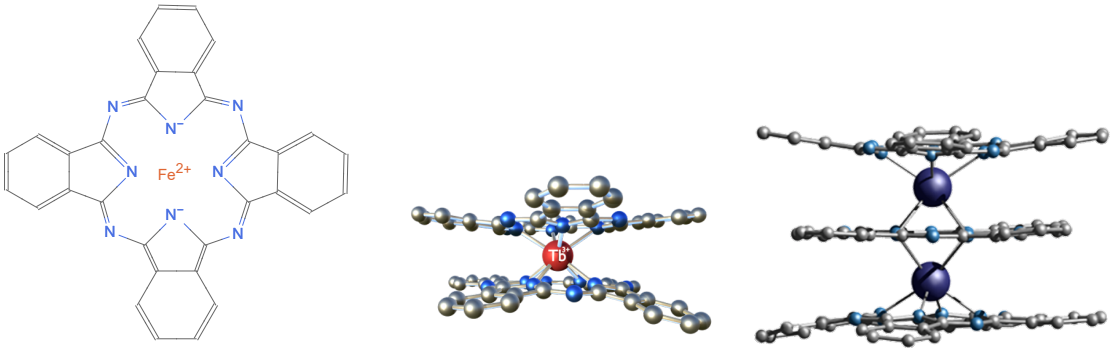
Comme on le voit, l'universalité du calcul, sans parler d'une véritable tolérance aux erreurs, est un défi technique de taille, qui exige que chacun de ces critères soit respecté en même temps que tous les autres. Il ne suffit pas d'avoir un jeu de portes universel si les temps de cohérence sont trop courts, ou d'avoir des qubits physiques évolutifs s'ils ne peuvent pas tous être initialisés de manière cohérente. En effet, des plateformes telles que les qubits supraconducteurs ont clairement satisfait aux critères deux à cinq et ont montré une bonne évolutivité, mais le défi est de maintenir ces performances sur des circuits logiques quantiques plus complexes.

Qudits de spin nucléaire

L'extensibilité étant un tel défi à court terme pour les dispositifs, cela vaut la peine d'explorer d'autres supports d'information quantique qui pourraient potentiellement offrir des propriétés d'extensibilité avantageuses tout en maintenant des fidélités de porte et des temps de cohérence comparables. L'une de ces options sont les systèmes basés sur les qudits, qui exploitent les états excités de plus grande dimension d'un système quantique pour encoder un espace de Hilbert plus large sur moins de sites physiques [31].

Bien que la logique binaire ait été finalement adoptée comme système fondamental pour les ordinateurs classiques une fois que les problèmes d'extensibilité et de correction d'erreurs résolus, on a vu l'apparition de la logique ternaire pour coder l'information et augmenter la capacité de calcul, comme l'ordinateur soviétique Setun [32], et comme les protocoles basiques de correction d'erreurs qui utilisent un système ternaire comme forme de contrôle de la parité.

Cette évolution se reflète dans le domaine de l'informatique quantique, où les qubits ont été le principal objet de recherche en raison de leur simplicité et de leur facilité de manipulation. Cependant, au fur et à mesure du développement de l'amélioration du contrôle des systèmes quantiques individuels, le potentiel des systèmes quantiques de plus haute dimension à offrir des avantages en termes d'évolutivité et d'efficacité de calcul est devenu de plus en plus évident. Ceci est particulièrement pertinent dans le contexte de (i) de la correction quantique des erreurs, où les systèmes de dimensions supérieures peuvent coder des qubits à l'épreuve des erreurs [33], (ii) de la simulation quantique de systèmes de dimensions supérieures [34], et (iii) des algorithmes quantiques, où les



(a) FePc **(b)** $TbPc_2$ **(c)** Tb_2Pc_3

Figure 1 – Complexes moléculaires à base de phtalocyanine. Exemples de complexes moléculaires à base de phtalocyanine, notamment : (a) FePc, (b) $TbPc_2$ et (c) Tb_2Pc_3.

systèmes de dimensions supérieures peuvent réduire le nombre de portes d'intrication à longue portée nécessaires pour effectuer certains calculs [35].

Comme nous le verrons, ce dernier aspect est particulièrement pertinent comme point de départ de cette thèse. On peut dès à présent souligner que les spins nucléaires est un système intéressant pour l'informatique quantique basée sur les qudits, en particulier parce que l'interaction entre les degrés de liberté électronique et nucléaire est à la fois complexe et avantageuse pour le traitement de l'information. Bien entendu, de nombreux systèmes quantiques ont la capacité d'encoder des qudits, comme le moment angulaire orbital des photons dans les systèmes photoniques [36], les états de spin nucléaire d'ions piégés [37], les points quantiques à l'état solide [38] et les états excités supèrieurs de l'oscillateur anharmonique supérieur des transmons supraconducteurs [39, 40]. Cependant, les degrés de liberté du spin nucléaire ont l'avantage d'être naturellement durables, bien isolés de l'environnement et très cohérents, ce qui en fait des candidats attrayants pour les mémoires quantiques de haute dimension [41]. Cette forte isolation, d'un autre côté, peut aussi être un inconvénient, car elle rend les spins nucléaires difficiles à contrôler et à manipuler, ce qui nécessite une conception minutieuse de la plateforme et des techniques de contrôle sophistiquées [42].

En ce qui concerne ce choix minutieux de la plateforme physique pour intégrer les spins nucléaires, les aimants molèculaires (SMM) à base de lanthanide ont démontré leur potentiel prometteur pour l'informatique quantique basée sur le qudit au cours des dernières années. En particulier, le travail de cette thèse sert d'extension théorique aux travaux essentiellement expérimentaux de Clément Godfrin [43] et Stefan Thiele [42] dans le cadre de la collaboration entre les chimistes du groupe de M. Ruben et les physiciens du groupe de W. Wernsdorfer (KIT). Dans leurs travaux, ils ont étudié les états de spin nucléaire des ions lanthanides, en particulier le dysprosium et le terbium, intégrés dans des aimants à molécule unique. Les complexes appelés à "double-decker" à base de phtalocyanine (Pc) avec un seul ion lanthanide ($LnPc_2$) au centre, notamment, ont connu le plus grand succès : $TbPc_2$ (terbium bis-phthalocyanine, voir Fig. 1).

Les phtalocyanines sont devenues un choix populaire pour les aimants moléculaires en raison de leur symétrie élevée, de leur fort champ de ligands et de leur structure électronique bien définie. Synthétisées pour la première fois accidentellement en 1907 par Braun et Tcherniac, puis caractérisées par Linstead en 1934 [44], ce sont de grands ligands macrocycliques avec un anneau central de quatre atomes d'azole qui sont responsables

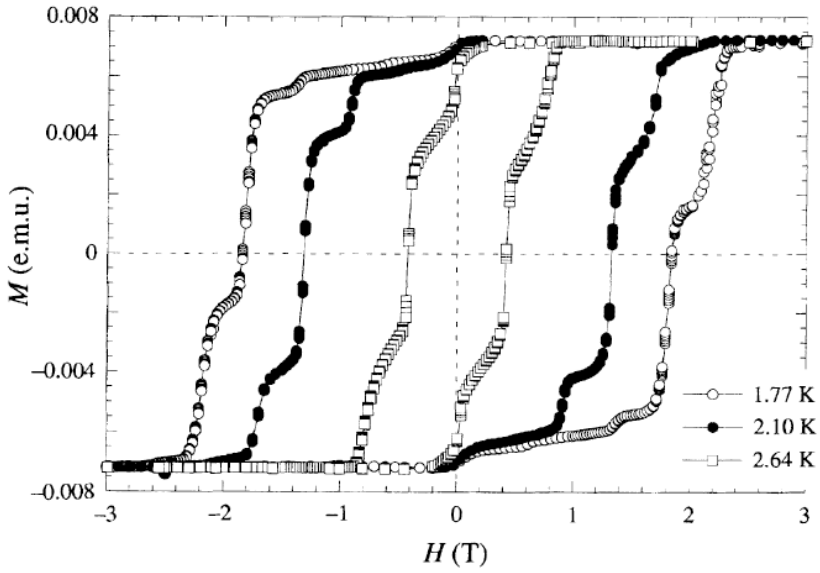


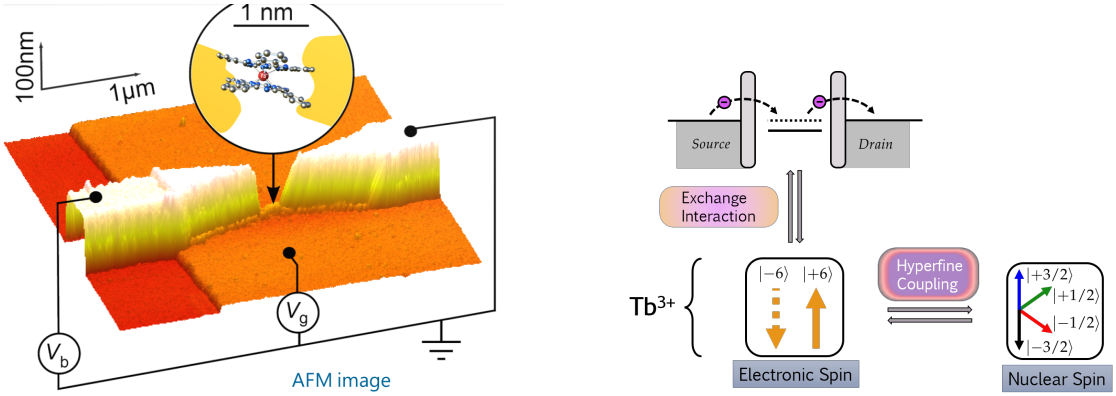
Figure 2 – Boucles d'hystérésis de magnétisation mesurées sur un monocristal de Mn_{12}-ac. Un monocristal de 0,066 mm^3 de Mn_{12}-ac présente des cycles d'hystérésis d'aimantation à basse température mésurés par magnétométrie SQUID. Les transitions QTM sont observées comme des sauts soudains dans l'aimantation lors d'une variation lente du champ magnétique appliqué. Tiré de [49].

de la liaison avec l'atome central de métal unique. Ils sont utilisés depuis longtemps comme colorants et pigments pour leur couleur bleu-vert caractéristique, et ont trouvé une utilisation plus large dans de nombreuses applications industrielles, y compris dans le stockage de données optiques et les écrans solaires [45].

Ce n'est que dans les années 1990 que les premiers complexes métallophtalocyaniques, tels que le MnPc, ont commencé à être étudiés pour leurs propriétés magnétiques [46], et l'intérêt de la recherche n'a cessé de croître à mesure que leur potentiel pour les aimants mmoléculaires et les dispositifs spintroniques devenait évident. Cela a conduit aux travaux d'Ishikawa et de Wernsdorfer, *et. al.* au début et au milieu des années 2000, où ils ont étudié les propriétés magnétiques du $TbPc_2$, observant les propriétés clés de la relaxation magnétique lente et de l'effet tunnel quantique de l'aimantation (QTM) [47, 48].

Observé pour la première fois dans les nano-aimants par Thomas et Sessoli *et. al.* [49], cet effet QTM se présente sous la forme de paliers ou de plateaux abrupts dans la courbe, ailleurs lisse, du changement d'aimantation dans un cycle d'hystérésis magnétique (voir Fig. 2). Ces étapes se produisent lorsque le champ magnétique aligne les énergies des différents états de spin, ce qui permet à l'aimantation de franchir brusquement la barrière d'énergie au lieu de la surmonter lentement par voie thermique. Il en résulte des inversions discrètes et rapides de l'aimantation, créant une série de discontinuités qui reflètent la nature quantique de l'inversion magnétique.

L'une des techniques de mesure les plus populaires pour observer le QTM est celle des magnétomètres à dispositif d'interférence quantique supraconducteur (SQUID), qui peuvent mesurer l'aimantation d'un échantillon avec une sensibilité et une résolution élevées. Avec le développement par Wernsdorfer de nano-SQUIDs en 2009 [51] améliorant les capacités des dispositifs micro-SQUID, la sensibilité accrue a permis la lecture électronique



(a) circuit nano-SQUID **(b)** Couplage nucléaire-électronique

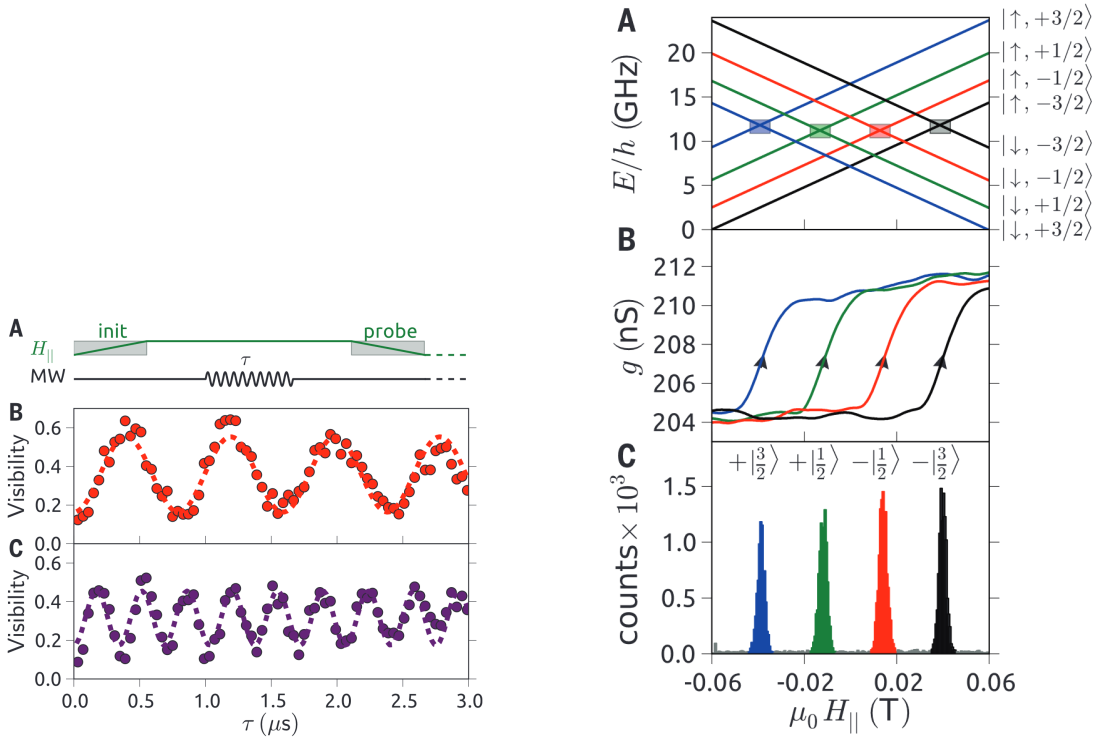
Figure 3 – Illustration schématique du dispositif de lecture de spin du $TbPc_2$. (a) Image AFM colorée d'un SMM $TbPc_2$ connecté à des électrodes de source et de puits en or par des barrières à effet tunnel, à l'intérieur d'une jonction de rupture au sommet d'une couche Au/HfO2. Adapté de [50]. (b) Schéma de la procédure de couplage des états de spin nucléaire aux états de spin électronique du Tb^{3+} via l'interaction hyperfine, puis à l'électron délocalisé du courant tunnel via l'interaction d'échange. Adapté de [42].

directe des états de spin nucléaire individuels de l'ion métallique central Tb^{3+} dans les SMMs $TbPc_2$ [52] (voir Fig. 3).

Après avoir démontré le principe de lecture pour une plateforme potentielle basée sur le qudit et construite sur les états de spin nucléaire du Tb^{3+} dans le $TbPc_2$, les prochaines étapes, en termes de développement d'un dispositif de traitement de l'information quantique en suivant les critères de DiVincenzo, seraient de démontrer une initialisation et une lecture cohérentes de l'état, idéalement avec de longs temps de cohérence maintenus pendant la période intermédiaire. Ce travail a été réalisé peu après par Thiele *et. al.* en 2014, qui a démontré la résonance nucléaire de spin du Tb^{3+} dans le $TbPc_2$ électriquement [42].

Ces travaux ont constitué une étape importante dans le développement de l'informatique quantique basée sur le qudit, car ils ont démontré la capacité de manipuler les états de spin nucléaire du Tb^{3+} avec des champs électriques, ouvrant ainsi la voie à la mise en œuvre de portes et d'algorithmes quantiques sur cette plateforme. Non seulement Thiele a montré qu'une initialisation et une lecture cohérentes des états du qudit par augmentation et diminution du champ magnétique $H_{||}$ étaient possibles, mais il a également obtenu les temps de cohérence caractéristiques des états de spin nucléaire. Ceci lui a permis de jeté les bases de la manipulation de ces états par l'utilisation d'un contrôle cohérent par le biais d'oscillations de Rabi induites par des champs électriques (voir Fig. 4).

Soit dit en passant, ce dernier point - le contrôle cohérent des spins nucléaires par des champs électriques - a soulevé une question théorique importante qui a inspiré une étude détaillée dans les travaux de notre collègue, Denis Janković, que nous mentionnerons brièvement. La question centrale ici est de savoir comment un spin nucléaire, qui est un degré de liberté sensible au champ magnétique, peut être influencé par un champ électrique. En effet, dans le cas d'un atome ou d'un ion libre, le champ électrique n'aurait aucun effet sur le spin nucléaire. Cependant, une fois intégré dans un complexe moléculaire, comme le $TbPc_2$, Janković a découvert que le champ du ligand de la molécule provoque un mélange des états autrement purs qui permet une telle interaction via l'effet



(a) Oscillations de Rabi dans le $TbPc_2$.

(b) Levée de dégénéréscence due à l'effet Zeeman des états de spin nucléaire.

Figure 4 – Initialisation de qudit, contrôle cohérent et lecture dans $TbPc_2$. (a) Le panneau A montre la procédure d'initialisation et de lecture par montée et descente du champ magnétique $H_{||}$, tandis que les panneaux B et C montrent les populations d'états intermédiaires subissant des oscillations de Rabi à deux intensités de champ électrique différentes. (b) Le panneau A montre le diagramme Zeeman de l'état $J = \pm 6$ de l'état fondamental électronique $4f^8$, avec les 4 croisements QTM mis en évidence. Le panneau B montre les sauts de conductance dus à l'inversion magnétique se produisant aux croisements respectifs. Le panneau C montre un histogramme du nombre de renversements magnétiques observés en fonction de l'intensité du champ magnétique. Reproduit de [42].

Stark hyperfin [53].

Maintenant, en poursuivant notre développement d'une plateforme d'informatique quantique basée sur le qudit, le prochain critère serait de démontrer la capacité de réaliser des portes quantiques en utilisant les états de spin nucléaire de l'ion terbium. C'est ce qu'a fait Godfrin *et. al.* en 2017 [43], en démontrant que les temps de cohérence étaient suffisamment longs et les oscillations de Rabi suffisamment cohérentes pour mettre en œuvre la porte de superposition (Hadamard généralisé) et l'algorithme de recherche de Grover sur les états du qudit (voir Fig. 5).

Cette mise en œuvre a été inspirée par les travaux théoriques antérieurs de Leuenberger et Loss qui, dans une série d'articles publiés au début des années 2000, ont proposé des protocoles généraux pour l'informatique quantique avec de grands spins nucléaires et, à titre d'exemple spécifique, une mise en œuvre d'une nouvelle version de l'algorithme de Grover sur un qudit unique en grande dimension [35, 54, 55].

Alors que Godfrin a réalisé des progrès significatifs dans la démonstration d'une plateforme informatique quantique complète basée sur un qudit, la mise en œuvre de l'algorithme

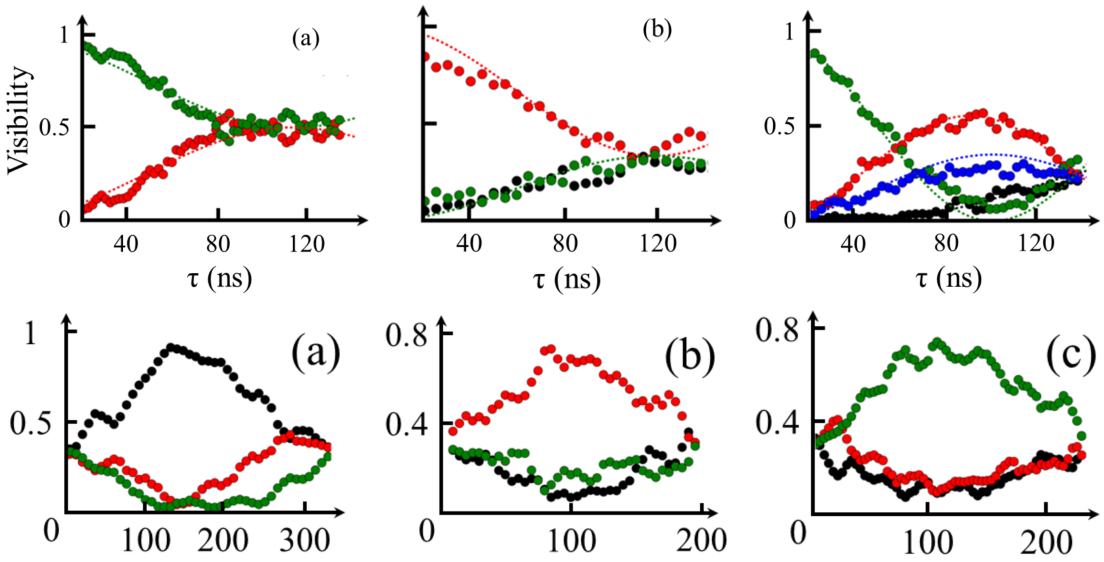
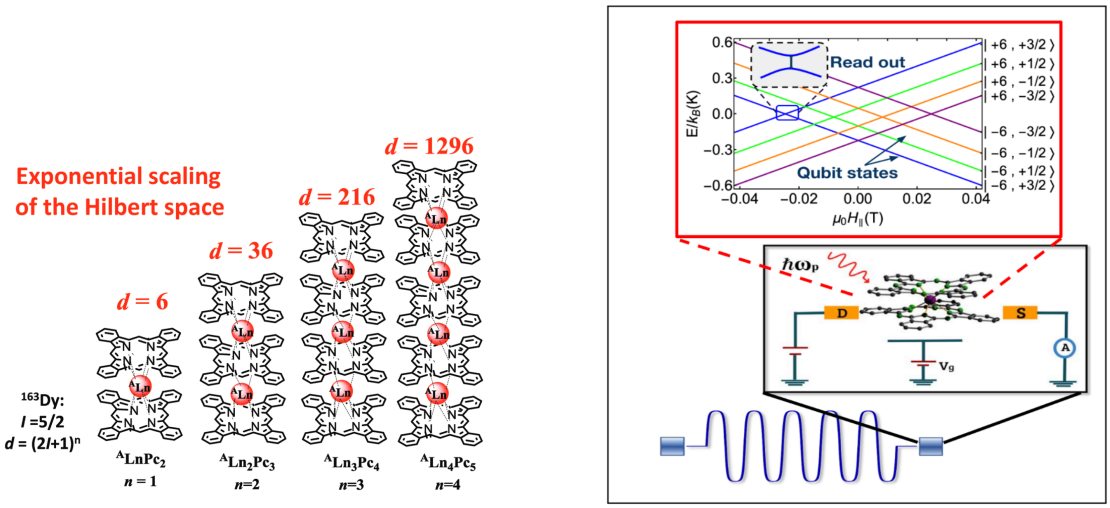


Figure 5 – Réalisation expérimentale de l'algorithme de Grover dans $TbPc_2$. Chaque panneau présente les populations des états de spin nucléaire individuels du $TbPc_2$ (rouge, vert, noir et bleu) en fonction du temps en ns. La ligne supérieure montre l'implémentation de la porte de superposition QFT (Hadamard généralisé) en $d = 4$ sur 2, 3 et tous les 4 niveaux dans les première, deuxième et troisième colonnes, respectivement. La rangée inférieure montre les populations soumises à deux cycles de l'opérateur de diffusion de Grover sur l'état marqué (noir à gauche, rouge au centre, vert à droite), avec une amplification d'amplitude ultérieure atteignant un maximum avant de revenir à l'état de superposition original (pour plus de détails sur l'algorithme de Grover, voir Section 6.4.1). Reproduit de [43].

de Grover a été limitée à trois des quatre états de spin nucléaire du noyau de terbium. Cela a conduit à une autre question théorique sur l'universalité du qudit : les états de spin nucléaire de l'ion terbium pourraient-ils être utilisés pour mettre en œuvre un ensemble universel de portes quantiques, et donc n'importe quel algorithme quantique arbitraire ? Cette question a été l'une des principales motivations du travail de ce travail de thèse thèse, et a été abordée dans Chapter 6.

L'autre préoccupation à prendre en compte dans le développement d'une plateforme de calcul quantique basée sur les qubits est la question de l'évolutivité. Pour faire évoluer une plateforme de calcul quantique, il est nécessaire de pouvoir contrôler et manipuler simultanément un grand nombre de qudits, ainsi que des opérations d'intrication. Une série de propositions consiste à concevoir et à synthétiser des complexes multimétalliques plus grands (voir Fig. 6a), tels que la molécule à triple-decker Tb_2Pc_3 (voir Fig. 1c), qui pourrait potentiellement offrir un espace de Hilbert plus grand pour les applications de calcul quantique [50]. D'autres propositions impliquent le couplage à longue portée de paires de double-decker à chaque extrémité d'un résonateur supraconducteur, de la même manière que les opérations d'intrication sont effectuées dans les systèmes de qubits supraconducteurs par une porte de résonance croisée, mais dans ce cas avec des aimants moléculaires au lieu de transmons à chaque extrémité [57] (voir Fig. 6b). Il s'agit d'un concept prometteur en termes de contrôlabilité du couplage, mais qui présente des défis significatifs, techniquement pour localiser les aimants moléculaires aux extrémités du résonateur, et en termes d'évolutivité avec le couplage de plusieurs qubits ensemble.



(a) Tb_2Pc_3 **(b)** 2 $TbPc_2$ couplés.

Figure 6 – Approches de dimensionnement pour les spins nucléaires couplés. (a) Mise à l'échelle conceptuelle des complexes moléculaires ${}^{A}Ln_nPc_{n+1}$ (extrait de [56]). (b) Couplage à longue portée de complexes $TbPc_2$ via un résonateur supraconducteur (extrait de [57]).

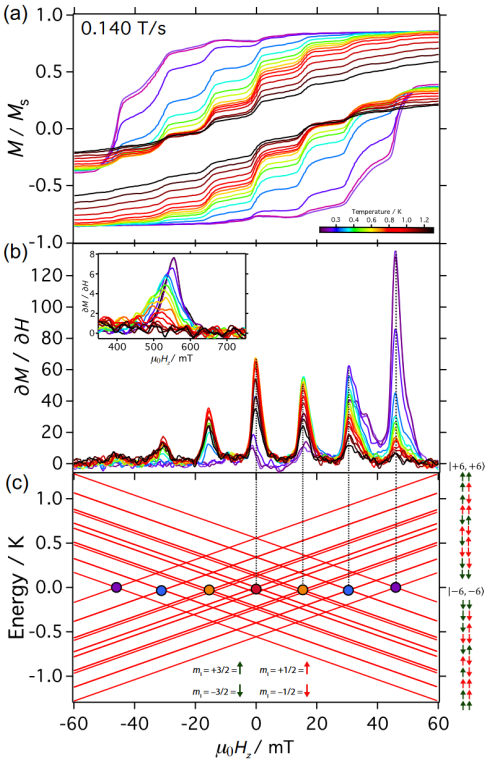
Le rôle du noyau

Dans leurs tentatives d'aborder la question de la mise à l'échelle de l'espace de Hilbert des SMM à base de lanthanides, les groupes de Ruben et Wernsdorfer se sont tournés vers la chimie des isotopologues d'ions lanthanides [56]. Dans cette approche, l'espace de Hilbert (spin nucléaire) d'un double-decker $LnPc_2$ peut être augmenté par synthèse avec des lanthanides de spins nucléaires plus importants, tels que le dysprosium et l'holmium, pour former des $DyPc_2$ et $HoPc_2$ ayant des espaces de Hilbert de $d = 6$ et $d = 8$, respectivement. Ce concept a ensuite été étendu à la synthèse de molécules plus complexes à triple-decker, telles que Tb_2Pc_3 (voir Fig. 1c) [50, 58], où les états de spin nucléaire de deux ions terbium sont couplés par des interactions dipolaires et d'échange pour former un espace de Hilbert plus grand.

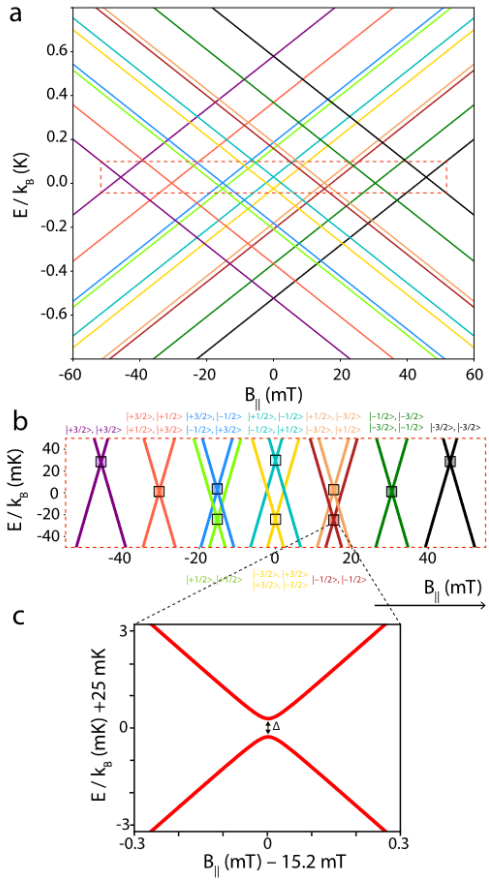
En outre, il convient de noter que cette approche va au-delà du simple choix de l'élément lanthanide, pour étudier (i) les différents comportements liés à la nature isotopique d'un même élément en fonction de leur structure nucléaire fondamentale et (ii) le choix du ligand et des groupes fonctionnels et leur influence sur les états hyperfins par le biais du champ du ligand. Comme exemple de principe (voir Fig. 7), les états couplés de $d = 4$ chacun devraient produire un espace de Hilbert élargi de $d = 16$, cependant, seuls 7 états ont été résolus dans les premières expériences, en raison des dégénérescences des niveaux d'énergie et des transitions QTM qui se chevauchent.

Ces progrès révèlent la possibilité de tirer parti de la chimie des isotopologues de ces molécules pour construire des espaces de Hilbert plus grands et pour explorer de fortes divisions nucléaires dipolaires et quadrupolaires afin d'améliorer le contrôle et la lecture de l'état. Ces progrès s'ajoutent à la recherche d'autres lanthanides ayant des spins nucléaires encore plus grands, comme l'holmium, qui, lorsqu'ils sont éventuellement couplés dans des molécules à triple-decker telles que $DyHoPc_3$, pourraient offrir des espaces de Hilbert considérablement élargis pour des applications informatiques.

Cependant, la précision de ces efforts expérimentaux souligne la nécessité d'une com-



(a) Cycles d'hystérésis pour le Tb_2Pc_3.



(b) Levée de dégénéréscence due à l'effet Zeeman de Tb_2Pc_3.

Figure 7 – Cycles d'hystérésis et levée de dégénéréscence due à l'effet Zeeman de Tb_2Pc_3. (a) Le panneau supérieur, a, montre les cycles d'hystérésis magnétiques en fonction de la température, le panneau central, b, montrant la dérivée première de l'aimantation par rapport au champ magnétique, mettant en évidence les transitions QTM indiquées dans le panneau inférieur, c, sur un diagramme Zeeman. Tiré de [58]. (b) Les panneaux montrent des diagrammes Zeeman simulés basés sur l'hamiltonien théorique de Tb_2Pc_3. Le panneau supérieur, a, montre le levée de dégénéréscence due à l'effet Zeeman de l'état fondamental, avec des zooms dans le panneau central, b, des transitions QTM, y compris les dégénérescences, le panneau inférieur, c, montrant un zoom final d'un anti-croisement individuel. Tiré de [50].

préhension plus complète des propriétés nucléaires intrinsèques, en particulier des moments dipolaires magnétiques et quadripolaires électriques des noyaux de lanthanides concernés. En effet, le fait de disposer d'un nombre beaucoup plus important d'états sans augmentation correspondante de l'espacement entre les niveaux pourrait conduire à un encombrement de fréquence, où les croisements d'inversion de spin magnétique sont trop proches les uns des autres pour être résolus individuellement. Ou, comme nous l'avons vu dans le cas du Tb_2Pc_3, des dégénérescences dans les transitions QTM qui peuvent empêcher la résolution complète de l'espace de Hilbert. Une telle compréhension est cruciale pour optimiser la conception moléculaire et donc améliorer les interactions hyperfines dans ces systèmes, permettant ainsi des plateformes qudit plus robustes avec des temps de cohérence plus longs et des fidélités de porte plus élevées. Pour y parvenir, les modèles nucléaires *ab initio*, tels que l'approche Hartree-Fock-BCS (HFBCS), jouent un rôle essentiel dans la prédiction précise des observables nucléaires qui ont un impact

direct sur le comportement des qudits.

L'exploration des systèmes de spin nucléaire et de leur rôle (moderne) dans l'informatique quantique remonte aux études fondamentales des propriétés atomiques et nucléaires du début du 20e siècle. Le concept de spin nucléaire lui-même est apparu avec la découverte du moment angulaire intrinsèque des protons et des neutrons, qui influence les propriétés magnétiques des atomes. Les premières expériences spectroscopiques menées par Otto Stern et Walther Gerlach dans les années 1920, qui ont révélé la nature quantifiée du moment angulaire, ont jeté les bases de la compréhension du spin des électrons et des noyaux [59]. Ces découvertes ont joué un rôle crucial dans le développement de la mécanique quantique en tant que cadre de description de la structure atomique et des propriétés magnétiques au niveau microscopique.

Le développement de la résonance magnétique nucléaire (RMN) au milieu du 20e siècle par Felix Bloch et Edward Purcell a marqué une avancée significative dans l'étude de la dynamique des spins nucléaires [60]. La RMN a fourni un outil détaillé pour comprendre les états de spin nucléaire et leurs interactions avec les champs magnétiques externes, ouvrant l'étude de la structure hyperfine (HFS) dans les atomes et les molécules. Les états de spin nucléaire étant isolés de la dynamique électronique, ils présentent des temps de cohérence plus longs et une relaxation du spin plus lente, ce qui en fait un candidat précoce pour le stockage d'informations sous forme d'aimants moléculaires, à la suite des travaux pionniers de Sessoli *et. al.* sur le magnétisme moléculaire [61, 62, 63]. Cependant, comme nous l'avons déjà mentionné, cet isolement est également un défi pour la modélisation et pour le contrôle précis des états de spin nucléaire qui est un enjeux central des efforts expérimentaux et théoriques.

L'exploration des interactions hyperfines en tant que lieu entre la structure nucléaire et les applications de l'information quantique est donc une nécessité. Les premières mesures des niveaux hyperfins dans les atomes, par des techniques telles que la spectroscopie par faisceau atomique et, plus tard, la spectroscopie laser, ont révélé l'influence nuancée des distributions de charges nucléaires et des moments dipolaires magnétiques sur les états électroniques. Le formalisme théorique permettant de comprendre ces interactions, développé par Breit, Rosenthal, Bohr et Weisskopf, a permis d'établir des corrections pour la taille finie du noyaux et les distributions de charge et de magnétisation dans les structures hyperfines [64, 65]. Ces corrections, connues sous le nom d'effets Breit-Rosenthal (BR) et Bohr-Weisskopf (BW), ont été essentielles pour affiner les modèles nucléaires afin de prendre en compte des géométries nucléaires et des profils d'aimantation interne réalistes, et seront étudiées en détail dans Chapters 2 and 3.

Le rôle des muons dans l'étude de la structure nucléaire remonte au milieu du 20e siècle, après la découverte du muon par Carl D. Anderson et Seth Neddermeyer en 1936 dans le cadre d'expériences sur les rayons cosmiques [66]. Peu après, on a compris que le muon, cousin plus lourd de l'électron, présenterait des interactions différentes avec les noyaux atomiques. La masse du muon, environ 207 fois supérieure à celle de l'électron, se traduit par un rayon de Bohr beaucoup plus petit pour les atomes muoniques, ce qui permet au muon de sonder plus directement les distributions de charge et de magnétisation nucléaires en raison du chevauchement accru de la fonction d'onde muonique avec le noyau.

Les études expérimentales sur les atomes muoniques ont débuté dans les années 1950 et 1960, avec des travaux pionniers menés par des chercheurs tels que Vernon Hughes et ses collaborateurs, qui ont utilisé des faisceaux de muons pour mesurer les structures

hyperfines et les déplacements isotopiques dans une série d'éléments [67, 68]. L'avènement de la spectroscopie muonique de haute précision a ouvert une fenêtre sans précédent sur les propriétés nucléaires, notamment les rayons de charge et les moments quadripolaires. Cette technique s'est avérée particulièrement puissante pour les noyaux lourds tels que les lanthanides, où le chevauchement nucléaire accru de la fonction d'onde muonique a amplifié les effets dus à la structure nucléaire.

Parallèlement, des modèles théoriques ont été développés pour décrire la sensibilité accrue des atomes muoniques aux propriétés nucléaires. Ces modèles ont étendu le cadre traditionnel de l'interaction hyperfine pour inclure les corrections significatives découlant de la taille du noyau (effet BR) et de la magnétisation interne (effet BW). Ce travail théorique a jeté les bases de l'utilisation des atomes muoniques comme sondes de la structure nucléaire complexe, motivant davantage leur application dans notre étude des noyaux de lanthanide pour les applications de l'information quantique.

Le potentiel des muons en tant que sondes de la structure nucléaire a été revitalisé ces dernières années avec le développement d'installations de faisceaux de muons de nouvelle génération dans des laboratoires tels que le PSI [69] ou le KEK [70], permettant ainsi la réalisation de nouvelles expériences de haute précision. Ces expériences permettent de tester et d'affiner les modèles du noyau, en particulier pour les isotopes ayant des applications dans les technologies quantiques. En offrant un lien direct entre la structure nucléaire et les interactions hyperfines, la spectroscopie muonique continue de jouer un rôle essentiel dans l'avancement de la physique nucléaire et de la science de l'information quantique.

Contrôle optimal quantique

L'étude du contrôle optimal dans les systèmes quantiques est ancrée dans un effort plus large pour parvenir à une manipulation précise des états et opérations quantiques. Initialement motivé par les besoins de la spectroscopie et de la résonance magnétique au milieu du 20e siècle, le développement de séquences d'impulsions pour la résonance magnétique nucléaire (RMN) et la résonance de spin électronique (RSE) a jeté les bases de ce qui allait devenir la théorie du contrôle quantique. Dans le contexte de la RMN, les travaux pionniers d'Erwin Hahn et d'autres ont conduit au développement de techniques de contrôle cohérent telles que l'écho de spin et les impulsions composites, qui ont été utilisées pour corriger les imperfections des champs magnétiques et améliorer la détection du signal [71, 72]. Ces premières avancées ont démontré qu'il était possible de façonner activement des champs de contrôle pour manipuler des systèmes quantiques avec une grande précision, ouvrant ainsi la voie à des applications dans le traitement de l'information quantique.

L'avènement de l'informatique quantique dans les années 1980 et 1990 a fait passer la théorie du contrôle de la simple manipulation d'état à la synthèse de portes quantiques, en suivant les fondements théoriques posés par Rabitz et ses collègues [73, 74]. Étant donné que les portes quantiques doivent être mises en œuvre avec une grande fidélité pour garantir une exécution précise, les techniques de contrôle optimal sont devenues de plus en plus importantes pour surmonter les imperfections du matériel et le bruit ambiant. Ceci est particulièrement important à l'ère actuelle des dispositifs NISQ (Noisy Intermediate-Scale Quantum, inventé par Preskill [75]) dans le cadre de la deuxième révolution quantique (inventée par Dowling et Milburn [76]).

Dans notre contexte de développement de portes quantiques en forme d'impulsion pour

les systèmes quantiques à base de lanthanide, un certain nombre de considérations importantes doivent être abordées. Dans le but de généraliser et d'étendre les travaux de Godfrin *et. al.* [43, 77, 78], il est d'abord nécessaire de comprendre les rôles et les relations entre la contrôlabilité du système physique et l'universalité résultante des portes quantiques qui peuvent être mises en œuvre avec l'ensemble des champs de contrôle autorisés [79, 80]. Nous rappelons qu'il s'agit d'un aspect essentiel des critères de DiVincenzo pour l'informatique quantique, et qu'il s'agit d'une condition nécessaire à la mise en œuvre de tout algorithme quantique arbitraire.

Dans un deuxième temps, nous devons considérer la variété des différentes techniques de contrôle qui peuvent être utilisées pour façonner les impulsions permettant de construire ces portes, et les compromis entre la complexité de l'algorithme de mise en forme des impulsions et la complexité des champs de contrôle calculés. Ceci est particulièrement important dans le contexte de l'informatique quantique basée sur le qudit, où la dimensionnalité accrue de l'espace de Hilbert pose des défis supplémentaires pour l'optimisation du contrôle des séquences d'impulsions multi-chromatiques [81].

Dans une troisième étape, il est essentiel que les techniques de contrôle soient étudiées en ce qui concerne la fidélité des portes en présence de bruit environnemental et d'erreurs de contrôle, en préparation de la mise en œuvre sur du matériel du laboratoire. Il s'agit d'une étape essentielle pour développer des protocoles de correction d'erreurs quantiques robustes et optimiser les impulsions de contrôle afin d'atténuer l'influence du bruit. Les premiers travaux théoriques se sont concentrés sur la caractérisation des différents canaux de bruit, tels que le déphasage, l'amortissement de l'amplitude, la relaxation du spin et les erreurs de retournement des bits, et leurs effets sur les opérations quantiques basées sur les qubits [82], ainsi que des modèles markoviens simples pour modéliser les effets environnementaux dans le formalisme des systèmes quantiques ouverts de Gorini-Kossakowski-Sudarshan-Lindblad (GKSL) [83, 84, 85]. Les extensions modernes comprennent des modèles de bruit non markoviens plus complexes qui modélisent les effets de mémoire et les corrélations dans le temps, comme dans les petits systèmes atomiques où l'hypothèse d'un bain infini peut ne pas être parfaitement valide [86], et le développement de jumeaux numériques complets pour les plateformes de calcul quantique qui fournissent un modèle complet de la pile matérielle et logicielle, y compris l'électronique de contrôle et le processeur quantique lui-même [87, 88].

Dans une quatrième étape, on peut imaginer étendre les méthodes de mise en forme des impulsions pour introduire ensuite des protocoles de correction d'erreurs, tels que le découplage dynamique, ou des codes stabilisateurs et de surface plus complexes, afin d'améliorer encore la robustesse et la fidélité des portes quantiques dans le cadre des efforts déployés en faveur de l'informatique quantique tolérante aux erreurs. Sans entrer dans ce vaste domaine de recherche qui progresse rapidement et qui dépasse le cadre de cette thèse, il convient de rappeler brièvement que les qudits commencent à offrir des avantages potentiels par rapport aux qubits dans certains protocoles de correction d'erreurs, car le plus grand espace d'état permet des encodages intelligents de qubits logiques qui peuvent être plus robustes contre certains types d'erreurs [33, 39, 89, 90, 91, 92].

Le paysage du contrôle quantique est intrinsèquement de haute dimension, caractérisé par un vaste espace de paramètres sur lequel les champs de contrôle doivent être optimisés. Dans les systèmes à qudits, ce paysage devient encore plus complexe que dans les systèmes à qubits en raison du nombre accru de niveaux et de transitions possibles.

Historiquement, cela a posé des défis importants, car la dimensionnalité du problème de contrôle augmente avec la taille de l'espace de Hilbert, ce qui rend difficile la recherche efficace de solutions optimales.

En référence à la théorie classique du contrôle, les concepts de contrôlabilité et d'accessibilité sont particulièrement pertinents dans le contexte des systèmes quantiques. La contrôlabilité fait référence à la capacité de faire passer un système d'un état à un autre à l'aide d'un ensemble de champs de contrôle, tandis que l'accessibilité détermine l'ensemble minimal d'opérations nécessaires pour obtenir un contrôle total sur l'espace d'état [93]. Ces concepts sont essentiels pour comprendre la contrôlabilité des systèmes quantiques et guider la conception des séquences de contrôle pour la mise en œuvre de portes quantiques.

En raison de cette complexité, un véritable zoo (particulièrement approprié compte tenu des conventions de dénomination actuelles, telles que GRAPE, CRAB, GOAT, GECCO) de techniques d'optimisation numérique a été développé pour naviguer dans le paysage du contrôle quantique. Les premières approches reposaient sur la conception manuelle d'impulsions et le réglage heuristique, mais au fur et à mesure de la maturation du domaine, des méthodes plus systématiques ont vu le jour. Koch *et. al.* a fourni des examens complets de ce domaine en plein essor [94, 95], et a mis en évidence la nécessité des techniques d'optimisation numérique pour parvenir à une synthèse de porte quantique de haute fidélité. D'une manière générale, ces techniques peuvent être divisées en plusieurs catégories, notamment : les méthodes numériques et analytiques, l'optimisation basée sur le gradient et sans gradient, l'apprentissage automatique en ligne et hors ligne, le contrôle en boucle ouverte et en boucle fermée basé sur la rétroaction, et bien sûr les techniques hybrides qui combinent des éléments de différentes approches, sans mentionner d'autres techniques de contrôle classiques qui sont utilisées, telles que le principe du maximum de Pontryagin (PMP), la méthode de Krotov et les techniques de linéarisation adaptative. En général, toutes ces méthodes d'optimisation se résument à différentes approches pour résoudre le problème de contrôle général en fonction d'un coût fonctionnel particulier, le plus simple étant la fidélité de la porte mise en œuvre par rapport à la porte cible.

En mentionnant brièvement chaque classe, les méthodes analytiques telles que PMP peuvent être puissantes dans leur généralité, mais doivent toujours être calculées numériquement. L'approche linéaire-algébrique de Brennen *et. al.* nous intéresse particulièrement dans cette thèse [96], et est basée sur la décomposition des rotations de Givens. Les rotations de Givens, qui généralisent le concept de rotations dans les systèmes à deux niveaux aux systèmes à plusieurs niveaux, fournissent un cadre algébrique pour la décomposition des portes de qudit complexes en opérations plus simples, et nous l'étudierons en détail dans Chapter 6.

L'approche basée sur le gradient la plus connue est sans doute l'algorithme GRAPE (Gradient Ascent Pulse Engineering), qui a été introduit pour la première fois par Khaneja *et. al.* en 2005 [97] dans le contexte de la mise en forme de séquences d'impulsions RMN. La flexibilité et l'efficacité de GRAPE l'ont rendu très adaptable à diverses plateformes quantiques, des qubits supraconducteurs aux ions piégés, et ont jeté les bases de l'extension du contrôle optimal à des systèmes plus complexes, tels que les qubits. L'approche itérative consistant à faire varier les champs de contrôle constants par morceaux pour optimiser la fonction de coût a été largement adoptée et facilement mise en œuvre dans les bibliothèques d'optimisation numérique standard (voir Chapter 6).

Le principal avantage de l'optimisation sans gradient est qu'elle ne nécessite pas le calcul

des gradients, qui peut s'avérer coûteux en termes de calcul pour les systèmes à haute dimension. Cependant, cela se fait au prix d'une convergence potentiellement plus lente et d'une exploration moins efficace du paysage de contrôle. Néanmoins, des méthodes sans gradient telles que la stratégie d'évolution de l'adaptation de la matrice de covariance (CMA-ES) ont été appliquées avec succès à des problèmes de contrôle quantique. D'autres méthodes générales comprennent l'algorithme du simplexe de Nelder-Mead, l'algorithme d'optimisation par essaimage de particules (PSO), le recuit simulé (SA) et les algorithmes évolutionnaires et génétiques.

Les techniques d'apprentissage automatique constituent une approche moderne puissante pour l'optimisation non linéaire du problème de contrôle. Les algorithmes d'apprentissage par renforcement, tels que l'apprentissage Q et les réseaux Q profonds (DQN), ont été utilisés pour adapter les champs de contrôle en temps réel en fonction du retour d'information du système, ce qui permet une optimisation dynamique des portes quantiques. Les deux principales sous-catégories de l'apprentissage automatique sont l'apprentissage supervisé et l'apprentissage non supervisé. Si l'apprentissage par renforcement ne nécessite aucune connaissance du problème, ce qui lui confère des capacités de généralisation exceptionnelles, il est également très coûteux en temps de calcul en raison du nombre d'itérations nécessaires pour converger vers une solution. Une alternative récemment développée, les réseaux neuronaux informés par la physique (PINN), exploite la connaissance *a priori* de la physique régissant le problème de contrôle avec les capacités d'approximation de la fonction universelle des réseaux neuronaux pour obtenir une convergence rapide et une grande précision dans l'optimisation du contrôle. Ces techniques ont été récemment développées et nos études préliminaires se sont révélées prometteuses pour la production de champs de contrôle de haute fidélité, en particulier en combinaison avec les méthodes PMP pour l'optimalité temporelle [98, 99, 100, 101, 102, 103].

Enfin, la distinction entre le contrôle en boucle ouverte et le contrôle en boucle fermée est cruciale pour comprendre le rôle de la rétroaction dans le contrôle quantique. Le contrôle en boucle ouverte implique la conception d'impulsions de contrôle basées sur une porte cible et une fonction de coût prédéfinies, sans retour d'information de la part du système. Le contrôle en boucle fermée, quant à lui, utilise des mesures en temps réel du système pour ajuster les champs de contrôle de manière dynamique, ce qui permet une optimisation adaptative des portes quantiques. Alors que les méthodes en boucle ouverte comme GRAPE sont largement utilisées pour la synthèse de portes, les techniques en boucle fermée deviennent de plus en plus importantes pour traiter le bruit et les imperfections dans les systèmes quantiques. En conjonction avec les techniques d'apprentissage automatique en ligne, l'apprentissage de contrôle en boucle fermée d'un réseau d'apprentissage automatique formé sur une plateforme expérimentale serait l'objectif ultime pour le contrôle en temps réel des systèmes quantiques.

Objectifs de cette thèse

Sur la base des discussions menées jusqu'à présent, les objectifs de cette thèse se situent à l'intersection entre la théorie de la structure nucléaire et le traitement quantique de l'information, et visent à explorer la manière dont ces domaines peuvent contribuer au développement de technologies quantiques évolutives, pratiques et efficaces.

Tout d'abord, nous cherchons à modéliser la structure nucléaire des noyaux de lanthanides, à évaluer leurs propriétés magnétiques et électriques et à comprendre comment ces propriétés influencent les interactions hyperfines dans les systèmes électroniques et

muoniques. Cette recherche répond à la nécessité de disposer de modèles nucléaires précis pour éclairer la conception de systèmes quantiques basés sur le spin nucléaire, qui pourraient constituer des alternatives de plus haute dimension aux qubits dans l'informatique quantique.

Deuxièmement, nous effectuons une analyse théorique approfondie de la fidélité des portes quantiques qudit en présence de bruit markovien, dans le but d'identifier les conditions dans lesquelles les qudits sont plus performants que les systèmes à qubits multiples. L'accent mis sur la fidélité des portes est essentiel pour comprendre comment atténuer la décohérence et le bruit et permettre des opérations quantiques plus robustes. Étant donné que les qudits encodent naturellement des espaces de Hilbert plus grands, notre travail aborde directement les défis d'extensibilité des systèmes quantiques, offrant une voie potentielle vers des architectures quantiques de plus grande dimension qui maintiennent l'efficacité de calcul. Nous avons étendu ce cadre du régime presque sans bruit à la limite du couplage fort, où les effets non linéaires des bruits d'ordre supérieur deviennent significatifs, ce qui nécessite un développement perturbatif de l'AGI pour tenir compte de ces effets. À partir de ce développement perturbatif complèt, nous visons à caractériser la transition d'un comportement linéaire à un comportement non linéaire dans les systèmes ouverts qudits et à explorer les implications pour l'informatique quantique basée sur le qudit.

Enfin, nous développons et comparons des techniques de contrôle optimal sur l'impulsion pour la synthèse de portes qudit, en évaluant leur robustesse au bruit environnemental et aux imperfections de contrôle. En développant un cadre pour l'évaluation comparative des méthodes de contrôle optimal sur les systèmes qudit, ce travail vise à améliorer la précision et l'efficacité des opérations de portes quantiques dans les systèmes qudit de haute dimension. Les implications de ce travail sont vastes, car le contrôle optimal est fondamental pour la réalisation d'opérations quantiques de haute fidélité, de circuits quantiques évolutifs et, en fin de compte, d'une informatique quantique tolérante aux erreurs.

Aperçu de la thèse

La thèse est structurée en deux parties principales, chacune se concentrant sur un aspect différent de la science de l'information quantique et de la physique nucléaire, mais liées par le thème général de l'amélioration de l'informatique quantique grâce aux systèmes de spin nucléaire et aux qudits.

La première partie, *Qudits dans les spins nucléaires des complexes moléculaires de lanthanide*, examine la structure nucléaire des isotopes de lanthanide et leurs anomalies hyperfines afin de jeter les bases de la compréhension du rôle des spins nucléaires dans le traitement de l'information quantique.

Chapter 2 explore la structure nucléaire des isotopes ^{161}Dy, ^{163}Dy, ^{159}Tb, et ^{165}Ho en utilisant le modèle HFBCS. Ce chapitre donne un aperçu de la déformation des distributions de nucléons et de leurs implications pour les moments dipolaires magnétiques et quadripolaires électriques. Il valide la précision du modèle HFBCS pour les structures nucléaires fortement déformées et ouvre la voie à des recherches plus approfondies sur les interactions hyperfines.

Chapter 3 s'étend à la structure hyperfine des ions dysprosium semblables à l'hydrogène, en se concentrant sur les corrections découlant de la taille du noyau finie et de la magnéti-

sation - les effets Breit-Rosenthal et Bohr-Weisskopf. Le chapitre analyse ces corrections dans les systèmes électroniques et muoniques, révélant l'impact significatif de la structure nucléaire sur les états hyperfins et fournissant une base pour tirer parti de la spectroscopie muonique dans l'étude des propriétés nucléaires.

La deuxième partie, *Traitement de l'information quantique avec les qudits*, passe à l'exploration de l'informatique quantique basée sur les qudits, en examinant comment ces systèmes fonctionnent dans des conditions bruyantes et comment les techniques de contrôle optimal peuvent être utilisées pour synthétiser efficacement les portes de qudits.

Chapter 4 compare la fidélité des portes quantiques dans les systèmes mono-qudit bruyants aux systèmes multi-qubits équivalents, en établissant des seuils critiques pour les avantages du qudit dans la performance des portes. Le chapitre introduit un cadre théorique pour l'évaluation de l'AGI en relation avec l'intensité du bruit et le temps de la porte, fournissant des repères pratiques pour les systèmes qudit de différentes dimensions.

Chapter 5 étend l'analyse de la fidélité au régime non linéaire, où les corrections de bruit d'ordre supérieur deviennent significatives. Un développement perturbatif de l'AGI est obtenu, et des simulations numériques valident la transition d'un comportement linéaire à un comportement non linéaire dans les systèmes ouverts de type qudit. Le chapitre souligne l'importance des effets de fidélité dépendant de la porte et explore leurs implications pour l'informatique quantique basée sur le qudit.

Chapter 6 étudie les techniques des impulsions de contrôle pour la synthèse des portes de qudit, en comparant spécifiquement les algorithmes GRD (Givens Rotation Decomposition) et GRAPE. Le chapitre examine leur robustesse au bruit et aux erreurs de contrôle, offrant des lignes directrices pratiques pour la génération de portes dans les systèmes qudit et introduisant des approches hybrides pour optimiser la fidélité et l'efficacité des portes.

Tous, ces chapitres contribuent à une meilleure compréhension de la manière dont les qudits à spin nucléaire peuvent être exploités pour le traitement de l'information quantique et comment les méthodes de contrôle optimal peuvent être adaptées pour améliorer l'informatique quantique à haute dimension. En comblant le fossé entre la théorie de la structure nucléaire et la science de l'information quantique, cette thèse vise à faire progresser le domaine des technologies quantiques et à ouvrir la voie à une informatique quantique évolutive et de haute fidélité basée sur les qudits.

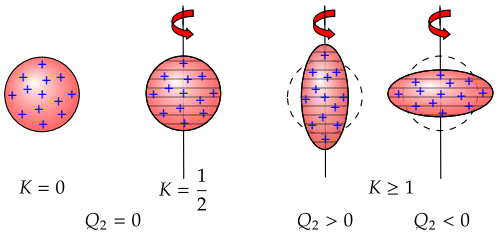


Figure 8 – Illustration schématique de l'effet des déformations nucléaires. Les distributions de charge nucléaire et de courant sont représentées pour différentes formes de noyaux. Pour les noyaux ayant un spin $K \geq 1$, un quadripôle électrique Q est autorisé.

Modélisation *ab initio* des noyaux de lanthanide

Note : Ce chapitre et les résultats qui y sont exposés, ainsi que Chapter 3 et les résultats qui y sont présentés, ont été préparés concomitamment avec un manuscrit à publier sous le titre « The hyperfine interaction as a probe of the microscopic structure of the atomic nucleus », en collaboration avec Johann Bartel, Hervé Molique et Ludovic Bonneau.

Introduction

Dans ce chapitre, nous étudions la structure nucléaire de certains isotopes de lanthanides à l'aide du modèle Hartree-Fock-BCS (HFBCS) afin d'approfondir notre compréhension de leurs propriétés complexes et de leur importance en tant qu'éléments constitutifs de nouvelles plateformes de traitement de l'information quantique. En nous concentrant sur les isotopes du terbium, du dysprosium et de l'holmium, qui présentent une déformation nucléaire et des interactions magnétiques et quadrupolaires notables, nous visons à extraire des observables nucléaires comme les rayons, les moments dipolaires magnétiques et les moments quadrupolaires électriques. Le chapitre présente le contexte des défis théoriques, souligne les objectifs et les contributions de l'étude, et offre une feuille de route à travers les fondements théoriques, les méthodes de calcul, et les résultats clés.

Contexte et motivations

Le paysage nucléaire, composé de 254 isotopes stables et de plus de 3000 isotopes radioactifs connus, constitue un large spectre d'objet pour l'étude des forces fondamentales qui régissent la matière au niveau subatomique. Parmi ces isotopes, les noyaux de lanthanide représentent une région particulièrement intrigante de la carte nucléaire. Connus pour leur grand nombre d'atomes et leurs formes très déformées, les noyaux de lanthanides constituent à la fois un défi et une opportunité pour la théorie nucléaire. Dans ces systèmes, l'interaction entre les forces nucléaires fortes, la répulsion de Coulomb et les effets quantiques donne lieu à des phénomènes complexes tels que la déformation nucléaire (voir Fig. 8), les corrélations d'appariement et, par conséquent, des propriétés magnétiques et électriques significatives.

Dans le contexte de la théorie nucléaire à basse énergie, où l'on cherche à obtenir une description microscopique précise de la structure nucléaire dans le cadre d'un traitement non relativiste (sans incorporer les degrés de liberté mésoniques qui nécessiteraient un traitement relativiste), deux défis fondamentaux se posent : Premièrement, le noyau est un problème à N corps, où N est le nombre de protons et de neutrons dans le noyau. Ce

problème est insoluble pour tous les noyaux, sauf les plus petits, et des approximations doivent être faites pour modéliser les interactions entre de nombreux nucléons [104]. Deuxièmement, la force nucléaire, qui est principalement régie par l'interaction forte, ne trouve qu'une prise en compte partielle dans les approches par premier principe, et doit être approximée à l'aide d'interactions effectives [105]. Par conséquent, des modèles théoriques sophistiqués sont nécessaires pour comprendre et décrire avec précision ces phénomènes dans les grands noyaux complexes.

Dans un premier temps, l'une des approches les plus prometteuses est l'utilisation de fonctionnelles de densité d'énergie (EDF), qui modélisent la force nucléaire par des interactions effectives [106]. Le modèle Skyrme-Hartree-Fock-BCS (HFBCS) est apparu comme un outil puissant pour décrire la structure nucléaire. En incorporant des interactions nucléaires effectives dans une approche de champ moyen contraint et en tenant compte de corrélations d'appariement plus complexes, le modèle HFBCS offre une approche par premier principe pour l'étude des noyaux déformés, en particulier ceux de la région des lanthanides [107]. Cependant, il reste de nombreux défis à relever pour obtenir des prédictions précises et cohérentes sur les nombreuses propriétés nucléaires, y compris les rayons de charge, les moments magnétiques et les moments multipolaires, en particulier lorsqu'il s'agit de traiter la grande variation des complexités de la structure nucléaire dans le paysage des noyaux exotiques, particulièrement ceux de masse impaire [108].

Ce travail est motivé par la nécessité de mieux comprendre les propriétés électriques et magnétiques des noyaux de lanthanide d'un point de vue *ab initio*. Le modèle HFBCS offre un cadre précieux pour l'étude de ces systèmes nucléaires complexes, permettant de comprendre la source de ces propriétés grâce à une description microscopique de leur structure et de leur comportement internes. Cette compréhension est non seulement essentielle pour affiner les théories de la structure nucléaire, mais elle revêt également une importance plus large pour de nombreuses applications, qu'elles soient technologiques, comme les appareils informatiques et les lasers modernes, ou encore les composants des batteries et des moteurs des véhicules électriques [109], aux applications fondamentales, telles que l'étude de la nucléosynthèse astrophysique dans les kilonova (supernovae sous-lumineuses de systèmes binaires compacts, tels que deux étoiles à neutrons) des fusions d'étoiles à neutrons [110].

Dans le contexte de nos travaux, les lanthanides présentent un intérêt pratique significatif en tant que composants fondamentaux des aimants à molécule unique (SMM) lanthanides-organiques, qui ont des cas d'utilisation potentiels dans une variété d'applications en informatique quantique et en technologies de l'information quantique, et qui font l'objet d'un intérêt croissant en matière de recherche, en particulier dans le cadre de notre collaboration [41, 56, 78]. Ces complexes reposent sur la manipulation des états de spin nucléaire via des interactions hyperfines avec les électrons de valence. En outre, les lanthanides présentent des propriétés d'émission optique favorables et une relaxation magnétique lente, ce qui les rend appropriés pour les lasers et les transmetteurs quantiques dans les réseaux de communication quantique, ainsi que pour les mémoires quantiques [111]. Par conséquent, il est essentiel de comprendre comment les propriétés nucléaires, telles que le spin et la déformation, influencent le comportement des électrons dans ces systèmes, tant pour la modélisation théorique que pour les progrès technologiques.

Objectifs et contributions

Cette étude vise à développer une compréhension globale de la structure nucléaire des noyaux de lanthanides à l'aide du modèle HFBCS. Nous nous concentrons plus particulièrement sur les isotopes du terbium ($_{65}$Tb), du dysprosium ($_{66}$Dy) et de l'holmium ($_{67}$Ho), qui présentent des effets de déformation nucléaire non triviaux et des écarts hyperfins magnétiques et quadrupolaires proéminents. Ces éléments nous intéressent particulièrement dans le contexte des complexes moléculaires de lanthanides pour les applications de traitement de l'information quantique, car ils ont été bien étudiés par nos collaborateurs [56]. Sur les 15, 10 et 12 isotopes respectifs du terbium, du dysprosium et de l'holmium ayant une parité de spin non nulle (voir Tables A.1 to A.3 dans Appendix A.1), seuls ^{159}Tb, ^{161}Dy, ^{163}Dy, et ^{165}Ho sont stables. Ces quatre isotopes ont donc été choisis pour notre étude.

Les objectifs sont de calculer et d'analyser les distributions de nucléons, les moments dipolaires magnétiques et les moments quadripolaires électriques de ces noyaux. Un objectif clé est d'étudier le pouvoir prédictif du modèle HFBCS dans la reproduction des observables expérimentaux tels que les rayons nucléaires, les moments magnétiques et les moments quadripolaires électriques.

En plus de prédire les observables nucléaires, cette étude cherche également à répondre à des questions plus profondes sur la structure nucléaire de ces noyaux de lanthanides. Par exemple, elle examine la précision avec laquelle le modèle HFBCS peut décrire les courants de protons et de neutrons et comment ces courants contribuent aux moments dipolaires magnétiques, en particulier dans les noyaux de masse impaire où la symétrie de renversement du temps est brisée, ce qui permet de mieux comprendre le rôle des corrélations d'appariement dans l'élaboration des propriétés magnétiques nucléaires. Un autre objectif important est d'évaluer dans quelle mesure le modèle rend compte de la déformation des noyaux, telle qu'elle se reflète dans leur masse et leurs moments quadrupolaires électriques, et de comparer ces résultats avec d'autres modèles nucléaires tels que le modèle de la charge ponctuelle, le modèle de la coquille sphérique et le modèle paramétrique de Fermi.

Les contributions de ce chapitre sont triples : (i) appliquer le modèle HFBCS aux isotopes de lanthanide pour obtenir des informations sur leurs distributions de nucléons et leurs propriétés magnétiques, en validant les résultats par rapport aux données expérimentales ; (ii) fournir une analyse détaillée des courants de protons et de neutrons, entre leurs contributions de spin et orbitales, et leurs rôles dans la génération de moments dipolaires magnétiques, en mettant l'accent sur les corrélations d'appariement et le comportement des noyaux de masse impaire ; (iii) faire progresser les méthodes de calcul des moments nucléaires en affinant les implémentations HFBCS pour améliorer la précision et la fiabilité de la détermination des moments multipolaires et des distributions de densité radiale. En améliorant les techniques d'intégration numérique pour les distributions de densité radiale et en explorant la précision de différents schémas de calcul de moyenne pour les potentiels monopolaires, cette étude contribue au développement de méthodes plus fiables pour l'analyse de la structure nucléaire.

Aperçu

La structure de ce manuscrit est organisée de manière à fournir une progression claire depuis le fondement théorique du modèle HFBCS jusqu'à son application dans les calculs de structure nucléaire. Dans Section 2.2, le cadre théorique du modèle Skyrme-Hartree-

Fock est discuté en détail, y compris les interactions effectives qui forment la base du modèle. La section couvre également le traitement des corrélations d'appariement et de la brisure de symétrie inversée dans le temps, qui sont toutes deux essentielles pour la modélisation des noyaux de masse impaire. Enfin, la méthode de l'expansion multipolaire est présentée comme un moyen de calculer les moments nucléaires, en se concentrant sur les moments du monopôle électrique, du dipôle magnétique et du quadripôle électrique.

Dans Section 2.3, les techniques de calcul utilisées dans cette étude sont décrites. Cela comprend une discussion sur le code HFBCS et les algorithmes mis en œuvre pour calculer les moments multipolaires à partir des distributions de nucléons générées par le modèle. La section fournit une explication détaillée du processus de calcul, depuis l'obtention des données sur les nucléons jusqu'à l'exécution des intégrations finales des moments multipolaires.

Les résultats de l'étude sont présentés dans Section 2.4. Les distributions de matière des nucléons (neutrons et protons), les courants des protons et des neutrons et les moments multipolaires associés y sont analysés pour chacun des isotopes étudiés. Les résultats sont comparés aux données expérimentales et les points forts et les limites du modèle HFBCS sont discutés. La section se termine par une évaluation de la précision du modèle dans la prédiction des propriétés nucléaires des noyaux de lanthanides déformés.

Discussion des résultats

Sommaire des résultats

Dans cette étude, nous avons utilisé le modèle Skyrme-HFBCS pour étudier la structure nucléaire des noyaux de lanthanides déformés, en nous concentrant sur les isotopes $^{159}_{65}$Tb, $^{161}_{66}$Dy, $^{163}_{66}$Dy, et $^{165}_{67}$Ho. Le modèle HFBCS, qui incorpore des interactions effectives nucléon-nucléon et un blocage auto-cohérent pour décrire les noyaux qui brisent la symétrie de renversement du temps, permet des calculs détaillés des distributions de nucléons et des moments multipolaires pour ces noyaux.

Les distributions de nucléons obtenues révèlent des déformations significatives dans tous les isotopes étudiés, les protons présentant des concentrations distinctes vers les pôles, en particulier pour le dysprosium et l'holmium (voir Figs. 9 and 10). Les distributions de courant correspondantes, décomposées en contributions de spin et d'orbite des protons et des neutrons, sont cohérentes avec les structures de boucle de courant attendues, basées sur la nature paire paire/impaire des isotopes et les harmoniques sphériques correspondantes de l'oscillateur harmonique $3D$ avec les nombres d'occupation associés.

Pour les noyaux pairs-impairs de terbium et d'holmium, avec un seul proton non apparié, les courants de protons ont montré des contributions dominantes au moment magnétique, en particulier de la part des courants de spin (voir Fig. 11). D'autre part, les noyaux pairs-impairs de dysprosium, avec un neutron non apparié chacun, présentent des contributions dominantes des courants de spin du neutron au moment magnétique. Dans les deux cas, les courants non dominants des nucléons semblent être induits par les courants dominants, ayant les mêmes structures de boucle de courant, bien qu'à une échelle plus petite, environ un ordre de grandeur plus faible.

Les moments multipolaires ont été calculés pour chaque isotope. Les moments monopolaires, dérivés des densités de charge des protons à moyenne sphérique, ont fourni des estimations raisonnables des rayons nucléaires, montrant une augmentation par rapport aux valeurs empiriques. Les moments dipolaires magnétiques ont montré quelques écarts

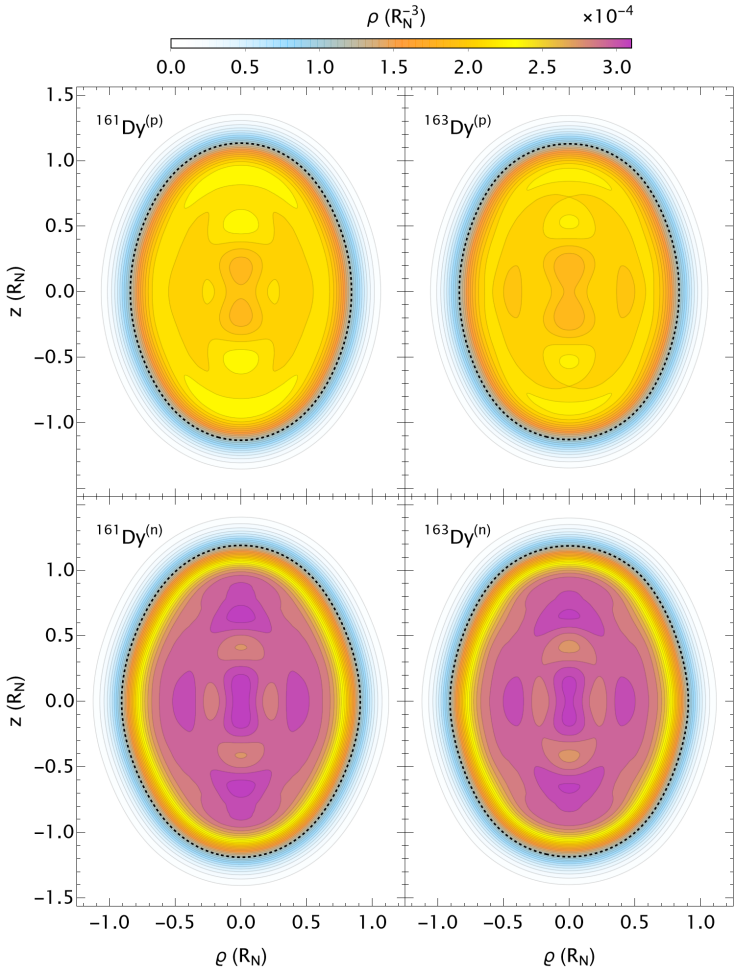
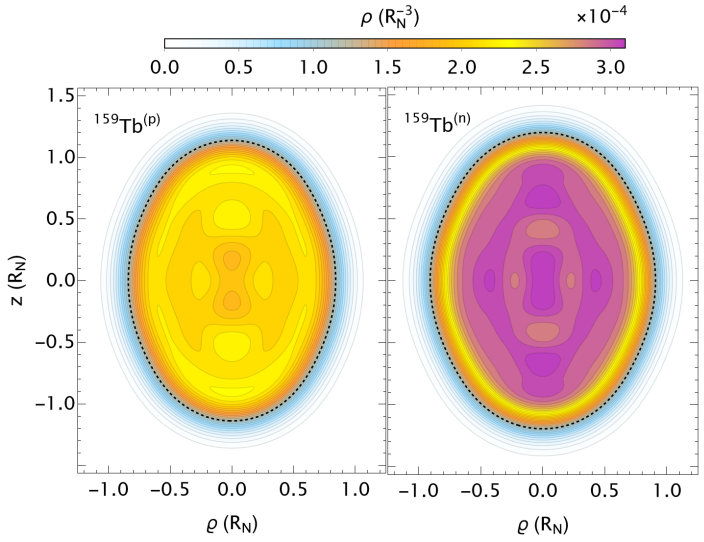


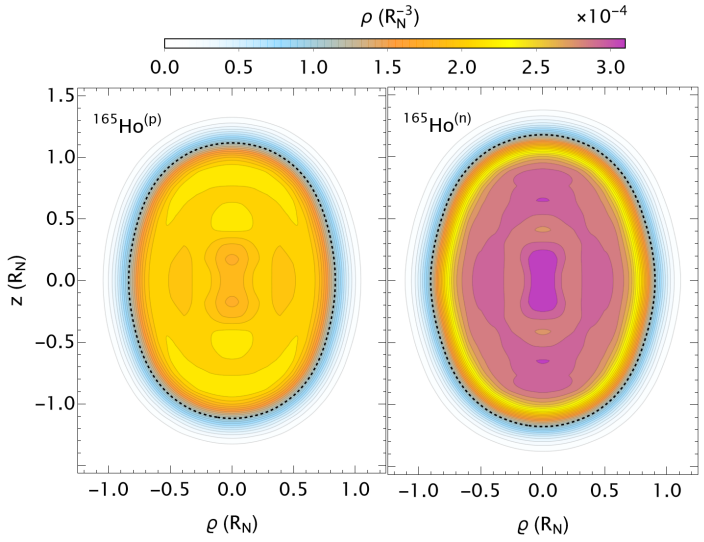
Figure 9 – Distributions de densité de nucléons de ^{161}Dy et ^{163}Dy. Les distributions des densités de protons (p) et de neutrons (n) pour ^{161}Dy et ^{163}Dy sont représentées en coordonnées cylindriques (z, ϱ) sur une tranche plane le long de l'axe z. Les coordonnées spatiales sont exprimé en rayon nucléaire empirique pour chaque isotope, R_N, les densités étant exprimées en unités de R_N^{-3}. Les lignes de contour de la densité équivalente sont espacées logarithmiquement, avec l'échelle indiquée dans la légende. Les enveloppes externes des noyaux sont représentées par la largeur totale à mi-hauteur (FWHM) de la densité de protons de l'isotope correspondant (lignes pointillées).

par rapport aux données expérimentales, mais les tendances générales ont été reproduites par le modèle, en particulier pour le noyau lourd de l'holmium. Les moments quadripolaires ont été reproduits avec un haut degré de précision, avec des erreurs relatives inférieures à 5% pour tous les isotopes, ce qui souligne la capacité du modèle à capturer les effets de déformation nucléaire (voir Table 1).

Si l'on examine de plus près les moments dipolaires magnétiques, il convient de noter que le modèle ne tient pas compte des effets relativistes ni des contributions mésoniques, qui peuvent influencer les interactions neutron-proton et les propriétés magnétiques. Ces effets pourraient être à l'origine des écarts observés dans les moments dipolaires magnétiques, en particulier pour les isotopes tels que ^{161}Dy. L'incorporation de ces effets pourrait améliorer la précision des prédictions du modèle.



(a) ^{159}Tb

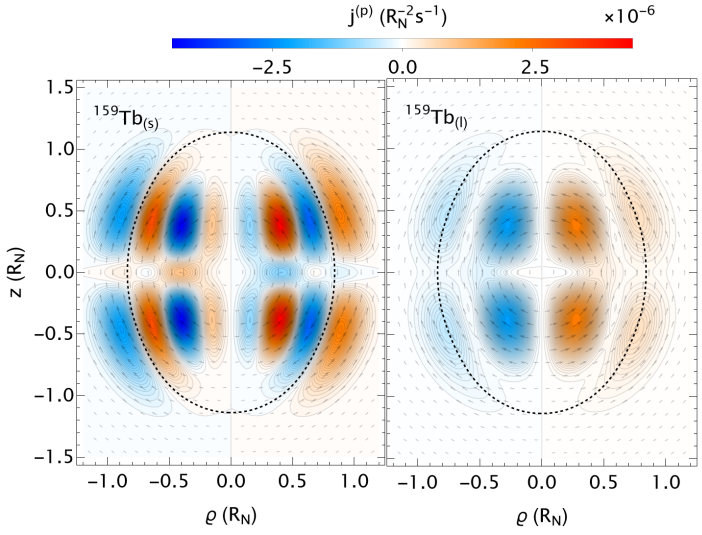


(b) ^{165}Ho

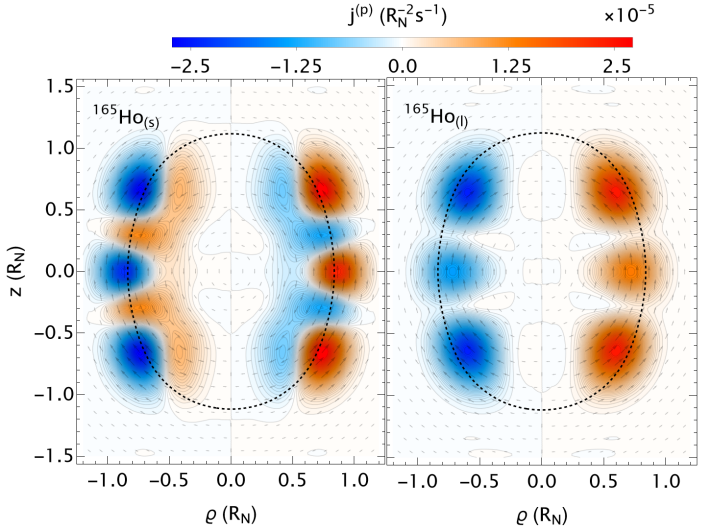
Figure 10 – Distributions de densité de nucléons ^{159}Tb et ^{165}Ho. Les distributions des densités de protons (p) et de neutrons (n) pour (a) ^{159}Tb et (b) ^{165}Ho sont représentées en coordonnées cylindriques (z, ϱ) sur une tranche plane le long de l'axe z. Les coordonnées spatiales sont mises à l'échelle du rayon nucléaire empirique de chaque isotope, R_N, les densités étant exprimées en unités de R_N^{-3}. Les lignes de contour de la densité équivalente sont espacées logarithmiquement, avec l'échelle indiquée dans la légende. Les enveloppes externes des noyaux sont représentées par la FWHM de la densité de protons de l'isotope correspondant (lignes pointillées).

Perspectives d'avenir

Bien que le modèle HFBCS démontre une forte capacité à décrire la structure et les moments nucléaires des noyaux de lanthanides déformés, il reste des domaines à améliorer et à explorer davantage. Les écarts dans les moments dipolaires magnétiques, en particulier pour les isotopes tels que ^{161}Dy, suggèrent qu'il est nécessaire d'affiner le modèle pour mieux prendre en compte les interactions complexes entre les nucléons. L'incorporation d'effets relativistes et de contributions mésoniques, qui influencent les interactions neutron-



(a) ^{159}Tb



(b) ^{165}Ho

Figure 11 – Distribution des courants protoniques du ^{159}Tb et ^{165}Ho. Les contributions de spin (panneaux de gauche) et orbitale (panneaux de droite) aux distributions de courant protoniques $\vec{j}^{(p)}(\vec{R})$ pour ^{159}Tb (a) et ^{165}Ho (b) ont été représentées en coordonnées cylindriques (z, ϱ) sur une tranche plane le long de l'axe z. Les valeurs des contributions sont indiquées par les lignes de contour comme indiqué dans la légende, normalisées par isotope. Les moments dipolaires magnétiques, donnés par $\vec{R} \wedge \frac{1}{2}\left(\vec{j}^{(p)}(\vec{R})\right)$, sont représentés par le champ de vecteurs fléchés. La ligne en pointillé marque la largeur totale à mi-maximum (FWHM) de la densité de protons de l'isotope concerné, indiquant la limite extérieure du noyau.

proton et les propriétés magnétiques, pourrait améliorer la précision de ces prédictions.

Les recherches futures devraient également se concentrer sur l'extension du modèle afin d'inclure un traitement plus complet des corrélations d'appariement, éventuellement par le biais de méthodes HFBCS entièrement autoconsistantes qui intègrent un traitement cohérent à la fois du champ moyen et des champs d'appariement. En outre, le modèle pourrait bénéficier de l'incorporation de moments multipolaires d'ordre supérieur, tels que des termes octupolaires ou hexadécapolaires, qui peuvent être utiles pour décrire

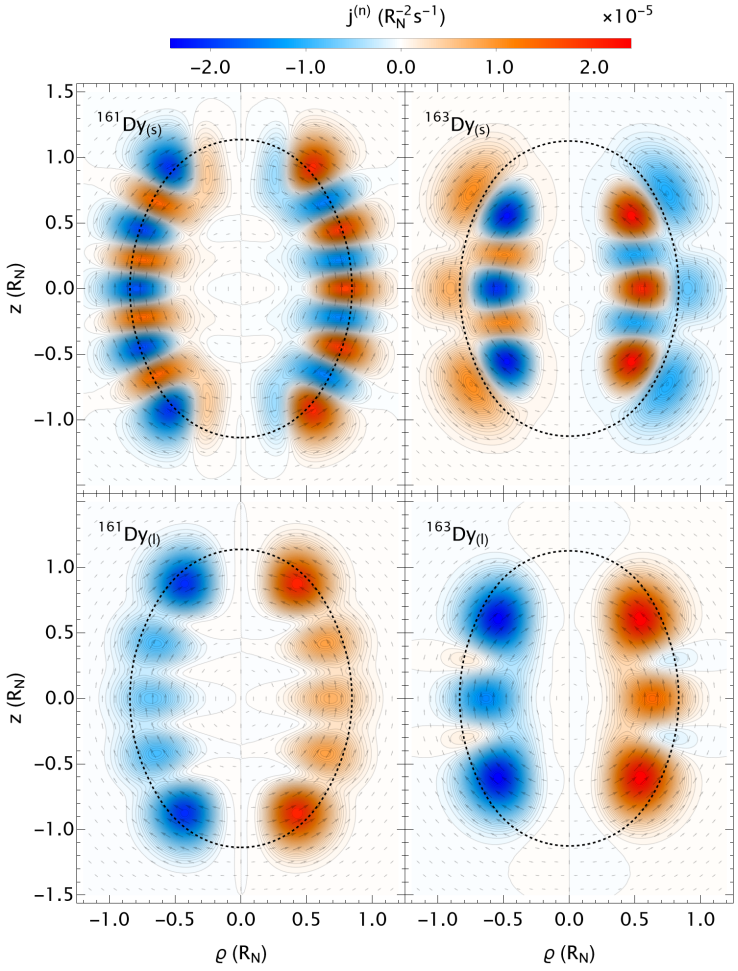


Figure 12 – Distribution des courants neutroniques du ^{161}Dy et ^{163}Dy. Distributions de courant neutronique, $\vec{j}^{(n)}(\vec{R})$ (en haut : contributions de spin, en bas : contributions orbitales), de ^{161}Dy (à gauche) et ^{163}Dy (à droite) avec les moments dipolaires magnétiques associés $\vec{R} \wedge \frac{1}{2}\left(\vec{j}^{(n)}(\vec{R})\right)$ indiqués par les vecteurs fléchés. Les figures sont tracées en coordonnées cylindriques (z, ϱ), sur une tranche plane passant par l'axe $z-$. Les contours représentent les courbes de densité équivalente, avec les valeurs numériques indiquées dans la légende. La courbe en pointillé indique la ligne de contour du FWHM de la densité de protons de l'isotope, représentant l'enveloppe externe du noyau.

Isotope	$\langle Q_2^{(ch)} \rangle_{\text{int}}$ ($e$barn)	$\langle Q_2^{(ch)} \rangle_{\text{spec}}$ ($e$barn)	$\langle Q_2^{(ch)} \rangle_{\text{exp}}$ ($e$barn)	ΔQ_{exp}^{spec} (%)
^{159}Tb	7.27	1.45	1.43	1.40%
^{161}Dy	7.34	2.62	2.51	4.38%
^{163}Dy	7.64	2.73	2.65	3.02%
^{165}Ho	7.70	3.60	3.58	0.56%

Table 1 – Moments quadrupolaires de charge intrinsèques et spectroscopiques. Tableau montrant les moments quadrupolaires (en $e$barn) pour ^{159}Tb, ^{161}Dy, ^{163}Dy et ^{165}Ho comparés aux quantités mesurées expérimentalement [112]. L'erreur relative entre les valeurs spectroscopiques et expérimentales est également indiquée.

les détails fins des formes nucléaires et des excitations collectives dans les noyaux forte-

ment déformés. Nos collaborateurs poursuivent leurs recherches sur l'incorporation de l'approximation HTDA (Higher-Tamm-Dancoff Approximation) pour une meilleure description microscopique des effets de corrélation multiparticulaire, ce qui peut également aider à décrire les phénomènes collectifs.

Enfin, l'extension de l'application de cette approche à un plus grand nombre d'isotopes et de régions de la carte nucléaire permettrait de mieux comprendre comment la structure nucléaire et les moments multipolaires évoluent dans différentes gammes de masse, ce qui pourrait permettre de mieux comprendre la structure des noyaux exotiques riches en neutrons.

Anomalies hyperfines dans les ions hydrogènoide de dysprosium

Note : Ce chapitre et les résultats qui y sont exposés, ainsi que Chapter 2 et les résultats qui y sont présentés, ont été préparés concomitamment avec un manuscrit à publier sous le titre « The hyperfine interaction as a probe of the microscopic structure of the atomic nucleus », en collaboration avec Johann Bartel, Hervé Molique et Ludovic Bonneau.

Introduction

Dans ce chapitre, nous étudions la structure hyperfine (HFS) des ions de type hydrogène, en nous concentrant sur les isotopes ^{161}Dy et ^{163}Dy. La structure hyperfine résulte de l'interaction entre les moments magnétiques et électriques nucléaires et l'électron atomique ou le muon, offrant ainsi une fenêtre sur la structure interne du noyau. En calculant les anomalies hyperfines entre ces isotopes, nous cherchons à comprendre comment les propriétés nucléaires se manifestent dans les phénomènes au niveau atomique. Nous explorons les corrections de Bohr-Weisskopf (BW) et de Breit-Rosenthal (BR) à la HFS, qui tiennent compte de la taille finie et de l'aimantation interne du noyau, respectivement. Ces corrections sont cruciales pour prédire avec précision les interactions hyperfines et améliorer notre compréhension de la structure nucléaire.

Contexte et motivation

L'étude de la structure nucléaire permet de comprendre non seulement les interactions complexes au sein du noyau, mais aussi leur influence profonde sur les systèmes atomiques. Dans Chapter 2, nous avons exploré les propriétés internes des noyaux de lanthanides, en particulier les moments dipolaires et quadripolaires magnétiques, en utilisant le modèle Hartree-Fock-BCS (HFBCS) [107]. Ces propriétés constituent la base des interactions qui s'étendent au-delà du noyau, se manifestant dans la structure hyperfine atomique (HFS). Sur la base de cette étude, nous nous concentrons maintenant sur les implications de ces propriétés nucléaires dans le contexte des ions hydrogenoïdes, où l'interaction entre le noyau et l'électron ou le muon lié fournit un cadre convaincant pour sonder les effets nucléaires au niveau atomique.

La compréhension de la HFS est essentielle car elle englobe l'influence de la distribution de charge nucléaire et de la magnétisation sur le cortége électronique environnant. Étant donné que ce projet fait partie d'un effort plus large visant à explorer le potentiel des complexes moléculaires de lanthanide pour le traitement quantique de l'information avec leurs états de spin nucléaire, la prédiction et la compréhension précises des interactions hyperfines sont essentielles pour concevoir des dispositifs quantiques qui tirent parti des propriétés uniques de ces systèmes [56].

Bien que les niveuax hyperfins soient souvent considérés comme derivait d'une perturbation des niveaux d'énergie atomiques sans structure hyperfin sous-jacente (HFS), ils contiennent une mine d'informations sur la structure nucléaire sous-jacente [113]. Les lanthanides, dont les noyaux sont fortement déformés et magnétisés, présentent des interactions hyperfines prononcées [112] qui sont particulièrement sensibles à la configuration nucléaire interne. Par conséquent, les ions hydrogenoïdes de ces éléments constituent une plateforme idéale pour étudier l'impact de la structure nucléaire sur les observables au niveau atomique [114], offrant un aperçu des effets BR [64] et BW [65], en plus de la

recherche d'une nouvelle physique avec des mesures de haute précision [115]. L'effet BR est dû à la distribution finie de la charge nucléaire, tandis que l'effet BW découle de la distribution magnetique nucléaire. Ensemble, ces corrections à la HFS permettent une compréhension nuancée de la manière dont les caractéristiques nucléaires influencent les états liés électroniques ou muoniques.

En outre, l'étude des interactions hyperfines devient encore plus intrigante lorsque l'on considère les atomes muoniques [116, 117, 118]. La masse nettement plus importante du muon (environ 207 fois celle de l'électron) lui permet d'orbiter beaucoup plus près du noyau, ce qui amplifie la sensibilité de sa fonction d'onde à le description de la structure nucléaire. Cette sensibilité accrue amplifie les effets BR et BW, offrant une fenêtre unique sur la distribution de la charge et de l'aimantation nucléaires. Les atomes muoniques ne sont donc pas seulement convaincants d'un point de vue théorique, mais aussi avantageux d'un point de vue expérimental, car ils permettent de sonder les effets de la structure nucléaire avec une plus grande précision. En effet, des groupes de recherche ont récemment déployé des efforts considérables, par exemple au Laboratoire de spectroscopie de spin des muons du PSI en Suisse et au KEK Muon Science Laboratory au Japon, pour mettre au point des installations à faisceaux de muons de haute précision pouvant être utilisées à cette fin [69, 70].

Le potentiel de mesures nucléaires de haute précision est important, y compris par exemple la détermination des rayons de charge nucléaire [119], la mesure des moments quadripolaires de charge dans les noyaux lourds [120], et même l'observation de structures atomiques plus exotiques au-delà des ions muoniques semblables à l'hydrogène [121]. En étendant notre exploration des systèmes électroniques aux systèmes muoniques, nous pouvons donc approfondir notre compréhension de l'interaction entre les propriétés nucléaires et les spectres atomiques, et offrir de nouvelles prédictions qui peuvent être testées dans des expériences de pointe.

En outre, les anomalies hyperfines entre deux isotopes, tels que ^{161}Dy et ^{163}Dy, offrent une occasion unique d'étudier l'effet des différences de structure nucléaire sur les propriétés atomiques, en isolant l'impact des changements de charge nucléaire et de magnétisation, tout en gardant les autres paramètres atomiques constants. On dispose ainsi d'une base solide pour le développement et l'évaluation comparative de nouvelles méthodes de modélisation des noyaux [115].

Les implications de ces études sont vastes. Qu'il s'agisse de tester la validité de différents modèles nucléaires ou de jeter les bases d'applications dans le domaine du traitement quantique de l'information, l'analyse des HFS des hydrogenoïdes lourds fait le lien entre la théorie nucléaire fondamentale et les avancées technologiques pratiques. Les lanthanides, qui sont déjà reconnus pour leur potentiel dans les dispositifs quantiques en raison de leurs propriétés magnétiques complexes, bénéficieront grandement d'une compréhension détaillée de leurs interactions hyperfines. En fin de compte, ces interactions déterminent comment les propriétés nucléaires influencent les transitions électroniques, les niveaux d'énergie et le comportement général dans les champs externes.

En outre, dans le contexte de cette thèse et des objectifs visant à faire progresser les applications des SMM à base de lanthanides en tant que plateformes pour le QIP, nous devons noter le rôle important joué par les interactions hyperfines pour permettre le contrôle cohérent des états de spin nucléaire des noyaux de lanthanides. Comme indiqué dans Section 1.1.3, une meilleure compréhension de ces interactions et de leur rôle dans la chimie des isotopologues est nécessaire pour améliorer l'évolutivité de ces systèmes

[56].

Objectifs et contributions

Ce chapitre a pour but d'approfondir les connaissances sur la structure nucléaire acquises lors de l'étude précédente des noyaux de lanthanides en examinant comment ces structures se manifestent dans les interactions hyperfines des ions hydrogenoïdes, en particulier pour les isotopes ^{161}Dy et ^{163}Dy. Plus précisément, nous visons à calculer et à analyser les corrections BR et BW de la HFS dans plusieurs modèles de potentiel nucléaire : ponctuel, sphérique, distribué par Fermi et basé sur la HFBCS. En résolvant l'équation de Dirac radiale pour les ions électroniques et muoniques dans le cadre de ces modèles nucléaires, nous voulons élucider l'effet de la distribution de la charge nucléaire et de la magnétisation sur les fonctions d'onde, les niveaux d'énergie et d'autres observables des particules liées.

Un aspect essentiel de cette étude consiste à examiner les variations isotopiques de la structure hyperfine, en quantifiant les anomalies hyperfines entre ^{161}Dy et ^{163}Dy afin de comprendre comment les différences de structure nucléaire se manifestent dans les propriétés atomiques. L'analyse comprend l'évaluation des contributions dipolaires et quadripolaires à la HFS, en explorant leur importance relative, en particulier dans le système muonique où les effets nucléaires sont renforcés. En outre, l'étude cherche à déterminer comment ces corrections varient en fonction du nombre quantique principal et du moment angulaire orbital, révélant ainsi la dépendance complexe des interactions hyperfines par rapport aux caractéristiques atomiques et nucléaires.

En fin de compte, ce chapitre s'efforce de souligner le rôle important des modèles nucléaires réalistes dans la prédiction précise de l'influence de la structure nucléaire microscopique sur les corrections HFS dans les ions hydrogenoïdes. Une telle compréhension est cruciale pour l'interprétation des mesures spectroscopiques, l'amélioration des modèles de théorie nucléaire et l'exploration des applications en physique atomique et moléculaire.

Les contributions de ce chapitre sont doubles : nous développons un cadre de calcul robuste pour résoudre l'équation de Dirac pour les ions de type hydrogène avec différents modèles nucléaires. Cette approche numérique permet un calcul détaillé des corrections BR et BW dans les systèmes électroniques et muoniques. En outre, le travail offre une analyse complète des anomalies hyperfines entre ^{161}Dy et ^{163}Dy, soulignant la sensibilité amplifiée des systèmes muoniques à la structure nucléaire, et révélant le rôle dominant des effets quadrupolaires dans les fractionnements hyperfins muoniques, ce qui en fait des sondes nucléaires prometteuses pour la recherche future. Bien que ces effets soient mineurs pour les états électroniques, ce travail démontre l'importance cruciale d'utiliser des descriptions nucléaires réalistes pour les ions muoniques où les effets nucléaires sont considérablement amplifiés.

Dans l'ensemble, ce chapitre fait le lien entre l'analyse théorique de la structure nucléaire des lanthanides et leurs manifestations au niveau atomique dans les interactions hyperfines. En combinant la théorie nucléaire et atomique dans un cadre unifié, il ouvre la voie à des prédictions plus précises des interactions hyperfines dans des systèmes complexes et met en évidence le potentiel des futures recherches expérimentales, en particulier dans le domaine des atomes muoniques.

Aperçu

Le chapitre est organisé comme suit. Dans Section 3.2, nous fournissons le cadre théorique pour comprendre les interactions hyperfines dans les ions de type hydrogène, en commençant par l'équation de Dirac en présence de divers potentiels nucléaires. La dérivation des effets BR et BW, ainsi que l'expansion multipolaire des potentiels électriques et magnétiques, est présentée afin d'établir une base pour les calculs suivants. Le formalisme des constantes de structure hyperfine, des décalages isotopiques et des anomalies est également passé en revue.

Dans Section 3.3, les méthodes de calcul utilisées pour résoudre l'équation de Dirac radiale et calculer les corrections BR et BW sont détaillées. La discussion porte sur les modules FORTRAN développés pour ces calculs, les techniques numériques pour atteindre la convergence dans les calculs des valeurs propres et de la fonction d'onde, et l'approche pour comparer les résultats entre les différents modèles nucléaires.

Les résultats sont présentés dans Section 3.4, où les fonctions d'onde pour les systèmes électroniques et muoniques sous différents modèles nucléaires sont analysées. Le chapitre discute des déplacements d'énergie et des corrections hyperfines dus aux effets BR et BW, évalue les anomalies hyperfines entre les isotopes et conclut par une évaluation des corrections quadrupolaires à la HFS.

Enfin, Section 3.5 fournit une synthèse des résultats, soulignant leurs implications pour la physique nucléaire, les applications spectroscopiques et les recherches futures. Le chapitre aborde également les améliorations potentielles du cadre de calcul et esquisse des pistes pour une exploration plus approfondie, en particulier dans le contexte des atomes muoniques et de leur sensibilité accrue à la structure nucléaire.

Discussion des résultats

Sommaire des résultats

Dans ce chapitre, nous avons entrepris une analyse complète de la structure hyperfine du dysprosium analogue à l'hydrogène, en nous concentrant particulièrement sur les corrections découlant de la taille et de la structure finies des noyaux de ^{161}Dy et de ^{163}Dy. Les calculs sont centrés sur deux effets principaux : les corrections de BR et de BW, qui ont été étudiées pour les systèmes électroniques et muoniques, en soulignant leur influence sur les interactions hyperfines.

Nos solutions numériques de l'équation de Dirac ont permis d'obtenir les fonctions d'onde radiales pour différents modèles nucléaires, notamment ponctuels, sphériques, de Fermi et HFBCS. Pour les modèles ponctuels, sphériques et de Fermi, les fonctions d'onde ont été obtenues à partir de ces modèles analytiquement définis de distributions de charges nucléaires, tandis que pour le modèle HFBCS, les fonctions d'onde ont été obtenues à partir des distributions nucléaires microscopiques (voir Fig. 13).

Pour les ions électroniques, les fonctions d'onde obtenues à partie des différents modèles nucléaires présentaient des différences minimes en dehors du rayon nucléaire, et des variations plus importantes se produisant dans la region intérieur. Les fonctions d'onde muoniques, cependant, présentaient des différences plus prononcées en raison de la plus grande pénétration du muon dans le noyau, soulignant la sensibilité des atomes muoniques à la structure nucléaire (voir Fig. 14).

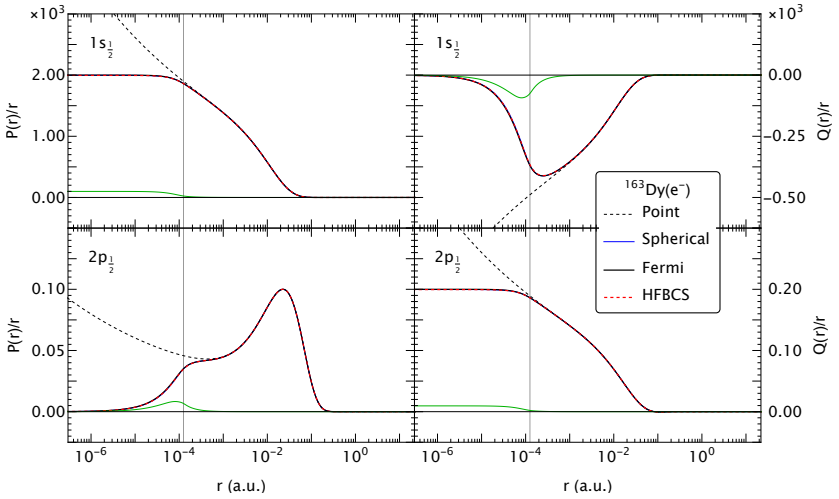


Figure 13 – Fonctions d'onde électroniques de ^{163}Dy de type hydrogène. Les grandes ($P_{n\kappa}$, panneaux de gauche) et petites composantes ($Q_{n\kappa}$, panneaux de droite) des fonctions d'onde radiales pour les orbitales $1s_{1/2}$ (panneaux supérieurs) et $2p_{1/2}$ (panneaux inférieurs) de $^{163}Dy^{65+}$ sont représentées en unités atomiques. Les courbes noires et rouges en pointillés représentent respectivement les modèles ponctuels et HFBCS, tandis que les courbes noires et bleues pleines représentent respectivement les modèles de Fermi et sphérique. La ligne verte continue représente la différence entre les modèles de Fermi et HFBCS multipliée par 20. Les lignes verticales indiquent la position du rayon nucléaire R_N. Les différences étant insignifiantes, les résultats pour $^{161}Dy^{65+}$ sont présentés dans Fig. B.1 dans Appendix B.1.

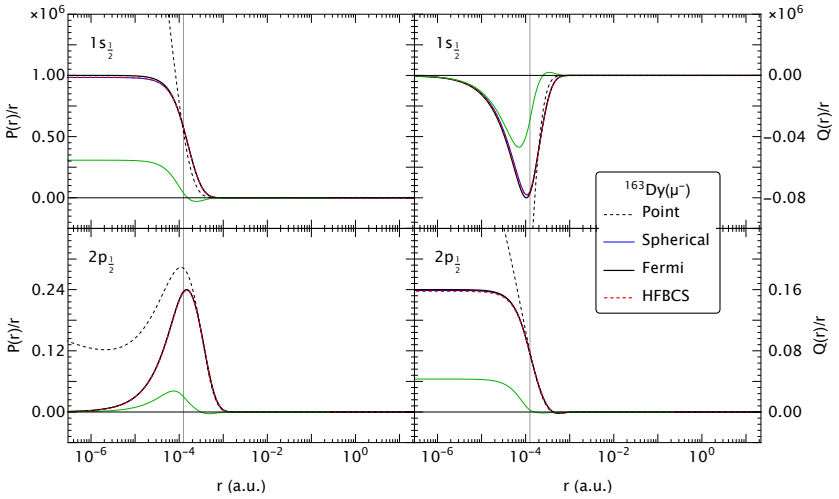


Figure 14 – Fonctions d'onde muoniques de l'hydrogène ^{163}Dy. Identique à Fig. 13 mais pour un atome muonique de type hydrogène présenté en unités atomiques. Les différences entre les résultats pour $^{161}Dy^{65+}$ et $^{163}Dy^{65+}$, étant mineures, sont donnés dans Fig. B.2 dans Appendix B.1.

On a constaté que les corrections BR influencent principalement les orbitales $ns_{1/2}$, leur ampleur diminuant pour les nombres quantiques plus élevés et les orbitales $np_{1/2}$. Ces corrections sont faibles pour les ions électroniques (environ 5%) mais nettement plus importantes pour les systèmes muoniques (jusqu'à 90%), ce qui souligne la sensibilité accrue des muons à la distribution finie de la charge nucléaire. Les comparaisons entre

les modèles de Fermi et HFBCS ont révélé que, bien que le modèle microscopique HFBCS fournisse une description plus précise de la structure nucléaire, son effet sur la division hyperfine est relativement faible par rapport à la distribution de Fermi plus simple pour les ions électroniques et muoniques.

Les corrections BW sont également plus importantes pour les orbitales $ns_{1/2}$ et sont principalement dues à l'aimantation nucléaire des spins de neutrons. Comme les noyaux de ^{161}Dy et ^{163}Dy sont tous deux pairs-impairs, avec un seul neutron non apparié, c'est ce neutron non apparié qui apporte la contribution dominante au moment magnétique par l'intermédiaire des courants de spin neutroniques. L'effet de la correction BW était d'environ 1 à 2% pour les orbitales électroniques, mais atteignait 80% pour les orbitales muoniques, ce qui indique un impact beaucoup plus important du magnétisme nucléaire sur les interactions hyperfines muoniques.

Les anomalies dans les interactions hyperfines entre les isotopes ^{161}Dy et ^{163}Dy ont également été analysées. L'anomalie hyperfine magnétique, caractérisée par l'effet combiné des corrections BR et BW, est de l'ordre de 10^{-4} pour les ions électroniques et jusqu'à 10^{-1} pour les ions muoniques. L'anomalie hyperfine quadripolaire est également beaucoup plus prononcée pour les ions muoniques, de l'ordre de 10^{-3} à 10^{-4}, contre 10^{-7} à 10^{-8} pour les ions électroniques.

Enfin, la correction quadrupolaire de l'interaction hyperfine a été étudiée pour les ions électroniques et muoniques. On a constaté que cette correction est négligeable pour les ions électroniques (environ 10^{-3}%) mais nettement plus importante pour les systèmes muoniques, en particulier pour les états $p_{3/2}$ (environ 50%). La prédominance de l'interaction quadripolaire dans la division hyperfine de l'état muonique $2p_{3/2}$ rend le décalage quadripolaire mesurable, avec des décalages de l'ordre de dizaines de keV, ce qui contraste avec les effets plus subtils dans les ions électroniques.

Perspectives d'avenir

Les résultats de ce chapitre ouvrent plusieurs voies pour la poursuite de la recherche et les applications potentielles. La sensibilité accrue des atomes muoniques à la structure nucléaire offre une occasion unique d'étudier les propriétés nucléaires, telles que la distribution des charges et les champs magnétiques internes, avec une grande précision. Les ions muoniques, avec leurs orbitales profondément liées qui pénètrent de manière significative dans le noyau, offrent un outil pour sonder les détails les plus fins des modèles nucléaires, au-delà des capacités des systèmes électroniques.

Les calculs effectués pour les effets BR et BW indiquent que si une simple distribution de Fermi est souvent suffisante pour estimer les interactions hyperfines électroniques, le modèle HFBCS est nécessaire pour saisir tout l'impact de la structure nucléaire pour les systèmes muoniques. Les travaux futurs pourraient se concentrer sur l'affinement des modèles microscopiques du noyau afin de mieux correspondre aux données expérimentales pour les fractionnements hyperfins muoniques, ce qui pourrait permettre de mieux comprendre l'aimantation nucléaire et son impact sur les systèmes atomiques.

Une application future importante réside dans la mesure expérimentale des anomalies hyperfines dans les systèmes muoniques. L'ampleur relativement importante de ces anomalies suggère qu'elles pourraient être mesurées à l'aide de techniques spectroscopiques actuelles ou proches de l'avenir, ce qui permettrait de tester les modèles nucléaires et les interactions fondamentales régissant la structure atomique. Les différences de com-

portement entre les systèmes électroniques et muoniques pourraient servir de référence pour valider les modèles théoriques d'interactions hyperfines, les systèmes muoniques fournissant un test plus rigoureux en raison de leur plus grande sensibilité.

En outre, l'anomalie hyperfine quadripolaire dans les atomes muoniques, d'une ampleur significative, offre une nouvelle possibilité de vérification expérimentale. Les déplacements d'énergie mesurables de dizaines de keV suggèrent qu'il est possible d'observer directement les contributions quadripolaires à la structure hyperfine, qui ont été traditionnellement difficiles à mesurer dans les systèmes électroniques. Cela pourrait permettre d'améliorer les contraintes sur les modèles de structure nucléaire et de mieux comprendre les interactions quadripolaires dans les éléments lourds.

Les lacunes et les limites du présent travail découlent principalement des défis informatiques posés par la modélisation de structures nucléaires complexes et de la nécessité d'une plus grande précision dans la résolution de l'équation de Dirac pour les états liés. Une amélioration immédiate de la précision des calculs pourrait être obtenue en incorporant les corrections QED dans le code numérique. En général, les techniques de calcul pourraient être optimisées pour les fonctions d'onde nucléaires et atomiques, ainsi que l'exploration de modèles nucléaires supplémentaires au-delà de HFBCS, ce qui pourrait améliorer la précision des calculs futurs. En outre, l'extension de l'analyse aux corrections d'ordre supérieur dans l'interaction hyperfine, telles que les effets de second ordre ou les moments d'ordre supérieur comme les octupoles, permettrait d'obtenir une image plus complète de la structure hyperfine des noyaux de lanthanides bien déformés.

À notre connaissance, cette étude est la première à identifier l'origine microscopique du magnétisme nucléaire qui contribue à l'interaction hyperfine. Pour les isotopes étudiés ici, le magnétisme provenant des protons, qu'il soit orbital ou de spin, est très faible, alors que les courants de spin des neutrons dominent. Il serait intéressant et important d'étendre cette étude à d'autres noyaux et à leurs isotopes afin d'améliorer notre compréhension du magnétisme nucléaire et de sa relation avec les observables atomiques tels que l'interaction hyperfine.

En résumé, l'étude des interactions hyperfines dans les ions hydrogène de type électronique et muonique offre un riche champ d'exploration de l'interaction entre la physique nucléaire et la physique atomique. Les connaissances acquises grâce à ces corrections et anomalies ne font pas seulement progresser notre compréhension de la structure hyperfine, mais ont également des implications plus larges pour la théorie nucléaire, la spectroscopie et le traitement quantique de l'information, où le contrôle précis des états hyperfins est crucial. En améliorant notre compréhension des origines microscopiques du magnétisme nucléaire et de la déformation quadrupolaire, non seulement dans différents éléments mais aussi entre les isotopes d'un même élément, nous pouvons améliorer le processus de sélection des isotopes et des ligands dans la chimie des isotopologues, conduisant ainsi à des complexes SMM avec des états de spin plus nombreux et mieux définis, optimisés pour les applications de l'informatique quantique.

Qudit bruyant vs Qubits multiples : Conditions d'efficacité des portes pour l'amélioration de la fidélité

Note : Ce chapitre présente un résumé de l'étude publiée dans npj Quantum Information sous le titre « Noisy Qudit vs Mutliple Qubits : Conditions on Gate Efficiency for Enhancing Fidelity » (Qudit bruyant et Qubits multiples : conditions sur l'efficacité des portes pour améliorer la fidélité). La citation bibliographique de la publication se trouve dans [122], et le code et les données utilisés dans l'étude ont été rendus publics à [123]. La publication originale est incluse dans Appendix C, avec les informations complémentaires.

Introduction

Dans ce chapitre, nous étudions les performances comparées des qudits et des systèmes multi-qubits dans le contexte d'environnements quantiques bruyants. Les qudits, qui sont des systèmes quantiques à d niveaux, offrent une alternative prometteuse aux qubits dans le traitement de l'information quantique (QIP) en raison de leur potentiel d'augmentation de la densité d'information et de l'efficacité de calcul. Cependant, la dimensionnalité accrue des qubits introduit des canaux d'erreur supplémentaires, qui peuvent avoir un impact sur leur performance dans des environnements bruyants. Cette étude vise à déterminer les conditions dans lesquelles les qubits peuvent surpasser les systèmes multiqubits en termes d'efficacité et de fidélité des portes.

Contexte et motivation

Dans cette étude, nous discutons de l'intérêt émergent pour les systèmes quantiques basés sur les qudits, avec d niveaux, en tant qu'alternative aux qubits conventionnels dans la QIP. Alors que les qubits sont les éléments fondamentaux de la QIP dans la plupart des plateformes modernes, offrant des systèmes quantiques couplés à deux niveaux, nous soulignons comment les qudits peuvent fournir des espaces de calcul de plus grande dimension, offrant potentiellement des avantages dans les systèmes de calcul quantique limités par le bruit. En faisant une analogie avec les jeunes jours de l'informatique classique, nous suggérons que si les bits binaires sont finalement devenus la norme, les qudits peuvent fournir une approche viable à court terme pour relever les défis de l'évolutivité dans les systèmes quantiques.

Nous notons que les qubits supraconducteurs ont permis de progresser dans la mise à l'échelle, les systèmes actuels atteignant des centaines de qubits, mais des défis techniques persistent dans l'augmentation exponentielle de l'espace de Hilbert en utilisant uniquement des qubits [1]. Avec leur mise à l'échelle d^n, les qudits offrent une approche potentiellement plus efficace pour augmenter la capacité de calcul. Nous soutenons que les plateformes de qudits peuvent présenter des avantages pratiques, tels que des taux de décohérence plus faibles, par exemple dans les systèmes de spin nucléaire, une meilleure correction d'erreurs grâce à l'encodage des états logiques sur des niveaux supplémentaires, une plus grande densité d'information par site, moins d'opérations non locales (comme la résonance croisée ou les portes d'intrication) et des mémoires quantiques plus robustes. Les avantages théoriques comprennent également l'extension des capacités de calcul à des groupes plus importants tels que $\bigotimes SU(d)$, ce qui peut simplifier certains algorithmes quantiques, tels que l'algorithme de Grover, et ouvrir la voie à de nouveaux algorithmes quantiques [31, 35, 124].

Cependant, les qudits sont confrontés à leurs propres défis, principalement en raison du nombre accru de canaux d'erreur associés à leur plus grande dimensionnalité. Il est donc essentiel d'évaluer si les avantages potentiels des qudits l'emportent sur les complexités introduites par ces erreurs supplémentaires. La motivation de notre étude est de comparer les qudits aux systèmes multiqubits, en mettant l'accent sur des mesures telles que l'infidélité moyenne des portes (AGI), afin d'identifier les conditions dans lesquelles les qudits pourraient fournir des performances supérieures pour l'informatique quantique pratique.

L'ère actuelle de l'informatique quantique est dominée par les systèmes NISQ (Noisy Intermediate-Scale Quantum), où le bruit et la décohérence sont des facteurs limitatifs importants [75, 125]. Pour parvenir à une informatique quantique tolérante au bruit, il faut progresser soit dans le développement de schémas de correction d'erreurs robustes, soit dans l'amélioration de la résilience au bruit intrinsèque des systèmes quantiques. Les qubits supraconducteurs, les ions piégés et d'autres plateformes basées sur les qubits ont connu des progrès considérables, mais le défi de la mise à l'échelle demeure.

Objectifs et contributions

Dans cette étude, nous avons comparé des systèmes à qudit unique avec des systèmes à qubits multiples dans des conditions presque exemptes de bruit afin de déterminer quand un qudit maintient ou améliore l'efficacité de calcul malgré un plus grand nombre de canaux d'erreur potentiels. L'infidélité moyenne des portes (Average Gate Infidelity, AGI), telle qu'elle a été définie par Nielsen [126], est une mesure clé de cette comparaison. Elle quantifie la perte d'informations de calcul d'une manière indépendante des états d'entrée et qui reste pertinente à toutes les étapes d'un algorithme quantique. L'analyse s'est concentrée sur des systèmes de dimensions d'espace de Hilbert équivalentes subissant des transformations unitaires arbitraires dans des conditions de bruit similaires, en explorant la façon dont l'AGI réagissait aux taux d'erreur et au temps de porte par rapport aux échelles de temps de décohérence.

Nous avons cherché à déterminer comment l'AGI s'échelonnait en fonction du taux d'erreur (γ) et du temps de passage sans dimension (γt), ainsi que la manière dont il variait en fonction de la dimension du qudit d. Cela nous a permis d'évaluer si une plateforme de qudit unique pouvait compenser son plus grand nombre de canaux d'erreur potentiels par des temps de décohérence avantageux et des opérations de porte plus rapides. Les résultats dépendaient des propriétés physiques de la plateforme, notamment le couplage avec l'environnement, la dynamique des impulsions de contrôle et la vitesse d'adressage. Pour des dimensions d'espace de Hilbert équivalentes entre un qudit et un système multiqubit, notre analyse a permis de déterminer si la plateforme qudit atteignait une fidélité de calcul compétitive pour des paramètres de bruit et de temps donnés (γ, t). En outre, en examinant la mise à l'échelle avec d, nous avons fourni des limites supérieures théoriques pour les dimensions du qudit afin de maintenir les avantages en termes de performances sans être submergé par le bruit.

Les objectifs de l'étude étaient triples : (i) établir un cadre théorique pour comparer l'efficacité des portes des qudits et des qubits, en dérivant une courbe critique qui relie la dimension du qudit à sa performance par rapport à un système multiqubit. (ii) Valider les résultats théoriques par des simulations numériques utilisant la bibliothèque QuTiP, en appliquant des modèles de bruit réalistes tels que le déphasage pur et l'amortissement de l'amplitude à diverses plateformes quantiques. (iii) Proposer des lignes directrices

pratiques pour déterminer quand les qudits présentent des avantages en termes de fidélité et d'efficacité par rapport aux qubits, applicables à des systèmes réels tels que les ions piégés, les qubits supraconducteurs et les systèmes de spin nucléaire moléculaire.

Les contributions de ce travail au traitement de l'information quantique sont multiples. Nous avons introduit une formule indépendante de la porte pour la réponse de premier ordre de l'AGI au bruit markovien, fournissant un outil de référence universel pour les comparaisons de l'efficacité de la porte entre les qudits et les qubits. Une expression analytique pour une courbe critique, $(d^2-1)/3\log_2(d)$, a été dérivée pour déterminer les conditions dans lesquelles les qudits surpassent les qubits en termes de fidélité de calcul. Nous avons ensuite validé ces modèles théoriques par des simulations numériques utilisant QuTiP, démontrant que dans des conditions spécifiques de bruit et de temps de cohérence, les qudits pouvaient dépasser les performances des qubits. Enfin, nous avons analysé les plateformes quantiques actuelles, en soulignant les avantages potentiels des systèmes de qudit en matière de calcul dans les environnements d'informatique quantique à court terme.

Aperçu

Dans notre résumé de cette étude, nous discutons des contributions présentées dans le cadre du contexte théorique et des résultats analytiques, de l'approche méthodologique, des résultats numériques et des implications pour la recherche future.

Dans Section 4.2, nous commençons par présenter notre dérivation d'une formule indépendante de la porte pour la réponse du premier ordre de l'AGI au bruit markovien dans le cadre du formalisme de Lindblad, en nous concentrant particulièrement sur son application au régime de quasi-absence d'erreur pertinent pour les systèmes QIP à court terme. Le cadre analytique a dérivé des expressions pour la dépendance linéaire de l'AGI sur le produit sans dimension γt, où γ est le taux d'erreur et t est le temps de porte, et applique ces expressions à des systèmes à qudit unique, multiqubit et multiqudit. Une comparaison critique est faite entre les taux d'augmentation de l'IAG pour un qudit unique et des systèmes multiqubits équivalents, en tenant compte de l'impact d'opérateurs d'effondrement arbitraires.

Après le travail théorique de base, le chapitre comprend ensuite dans Section 4.3 un compte rendu détaillé de la façon dont les simulations numériques ont été effectuées en utilisant le QuTiP Python [127, 128], conçu pour compléter et illustrer les résultats analytiques.

Les résultats numériques sont ensuite discutés dans Section 4.4, où nous examinons l'applicabilité et les limites du formalisme de réponse linéaire pour l'AGI et explorons plusieurs aspects clés : le domaine de validité de γt et sa dépendance à la dimensionnalité du qudit ; l'étendue de l'indépendance de la porte ; l'adaptabilité aux modèles de bruit au-delà du déphasage pur ; et les conditions sur les temps de porte pour lesquels les qudits ou les multiqubits ont un avantage en termes de calcul. Ce dernier aspect est examiné de près en tenant compte de paramètres tels que les taux de décohérence et les temps d'opération des portes, spécifiques aux plateformes quantiques existantes, offrant une comparaison entre les qudits et les qubits dans divers environnements sonores et validant la courbe critique dérivée. Enfin, une discussion explore les implications de ces résultats, en particulier le potentiel des qudits en tant qu'alternatives aux qubits dans l'informatique quantique pratique, et conclut avec une perspective pour la recherche future et les avancées potentielles dans le domaine.

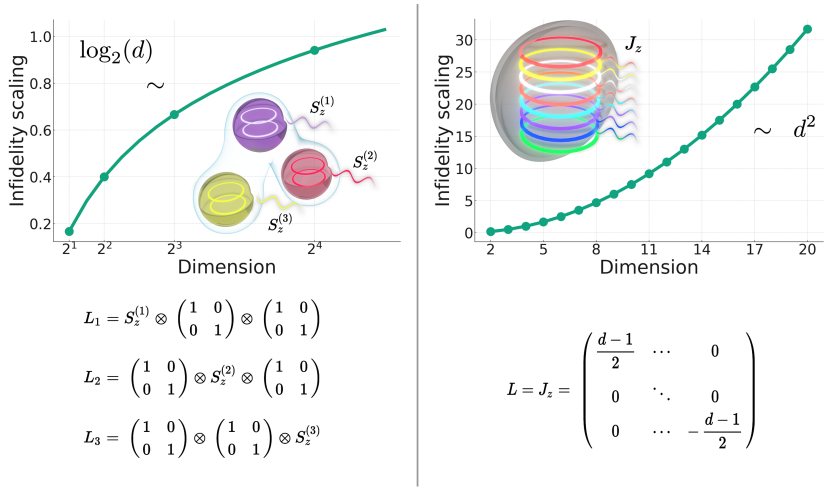


Figure 15 – Synthèse visuelle de l'échelle d'infidélité dans des qubits multiples et un qudit unique. Diagramme récapitulatif illustrant les opérateurs d'effondrement sélectionnés et les échelles d'infidélité attendue analytiques associées en tant que fonctions de la dimension de l'espace de Hilbert, telles que dérivées de Eq. (4.17) et Eq. (4.13). Ceci est illustré pour deux systèmes distincts : des qubits multiples (à gauche), dont l'échelle est $\sim \log_2(d)$ et un qudit unique (à droite) dont l'échelle est $\sim d^2$. Le terme « échelle d'infidélité » se réfère ici aux pentes des AGI du premier ordre dans γt, notées c dans Eq. (4.18).

Discussion des résultats

Sommaire des résultats

Dans cette étude, nous avons effectué une analyse comparative de l'efficacité des portes pour les qudits et les systèmes à qubits multiples, en tenant compte des paramètres physiques qui affectent de manière significative leurs performances, tels que le temps de décohérence et la dimension de l'espace de Hilbert. En tirant parti de calculs analytiques et de simulations numériques, *nous avons dérivé dans Eq. (4.6) une relation de type fluctuation-dissipation pour l'infidélité des portes dans les opérations d'état pur.* Une méthodologie fondée sur la physique a été mise au point pour obtenir l'effet de premier ordre du bruit markovien sur l'infidélité moyenne des portes (AGI), ce qui a facilité le lien avec la formulation initiale indépendante des portes (voir Fig. 15).

Nous avons analysé le taux d'augmentation de l'AGI pour des qudits uniques et l'avons comparé à celui de qubits multiples de dimension d'espace de Hilbert équivalente en cas de déphasage pur. Cette comparaison a conduit à la dérivation d'une courbe critique, qui décrit le rapport de leurs temps de porte en unités de temps de décohérence voir (Fig. 16). Cette courbe établit effectivement un point de référence pour l'efficacité temporelle des opérations de porte, les valeurs situées d'un côté ou de l'autre indiquant que le système - qu'il s'agisse d'un qudit ou d'un multiqubit - présente une fidélité de porte supérieure. Il est important de noter que les résultats montrent que, pour maintenir une fidélité compétitive à mesure que la dimension d augmente, les portes qudit ne doivent pas seulement être plus performantes que les portes multi-qubit par un facteur de $O(d^2/\log_2(d))$, mais par un facteur plus précis de $\frac{d^2-1}{3\log_2(d)}$, en particulier pour les d inférieurs, où la contrainte est moins exigeante.

En outre, nous avons fourni des expressions analytiques générales pour les réponses linéaires applicables à des opérateurs d'effondrement arbitraires et à des systèmes multi-

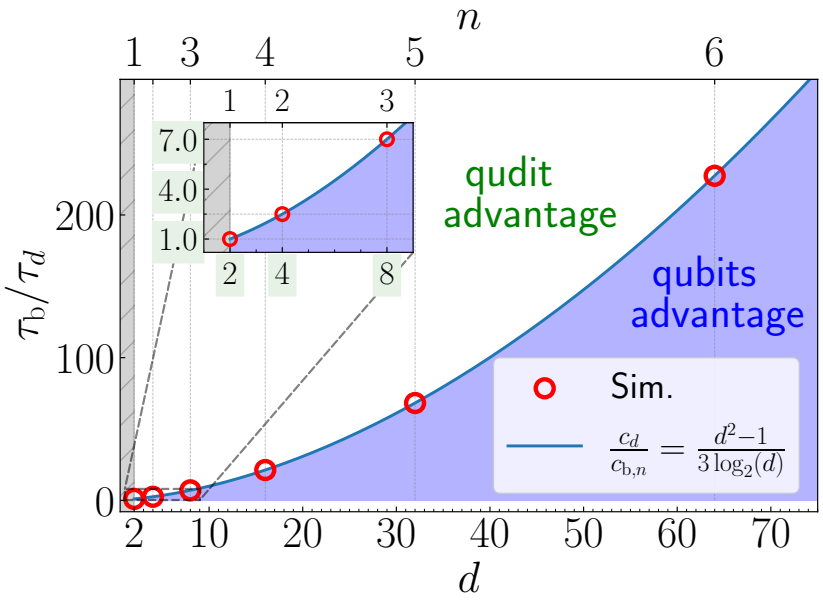


Figure 16 – Plage potentielle pour la facteur de mérite τ_b/τ_d. Les cercles arrondis montrent les valeurs numériques obtenues pour $c_d/c_{b,n}$. La courbe pleine provient de Eq. (4.19) et met en évidence les valeurs critiques théoriques de $T_{2,d}/T_{2,b}$.

qubit. Ces formulations offrent une utilité pratique pour l'évaluation comparative des plateformes qudit en fonction de leur dimensionnalité pratique maximale ou de la facteur de mérite requise pour compenser l'augmentation du bruit par rapport aux contreparties multiqubit.

Les simulations numériques ont corroboré la validité de l'hypothèse de réponse linéaire et délimité ses limites en tenant compte de facteurs tels que la dimension du qudit, les caractéristiques de la porte et la nature du bruit. Il a été observé que la plage de $\gamma t \ll 1$ diminue avec l'augmentation de la dimension du qudit, mais que les écarts relatifs dépendant de la porte diminuent également. Les simulations ont confirmé la courbe critique analytique et nous ont permis d'évaluer les plateformes quantiques actuelles en ce qui concerne leur efficacité en termes de temps de grille. Pour le déphasage pur, certaines plateformes qudit - tirant parti de temps de décohérence favorables et d'opérations de porte rapides - se sont révélées plus performantes que les plateformes multiqubit à dimensions d'espace de Hilbert équivalentes. En particulier, cette performance s'étend aux qudits avec d jusqu'à ~ 40, comme on l'a vu dans le cas des spins nucléaires dans les aimants moléculaires.

Perspectives d'avenir

Bien que certaines plateformes multi-qubits offrent actuellement une évolutivité supérieure en termes de nombre de sous-systèmes, les résultats suggèrent que les systèmes qudit évolutifs peuvent continuer à surpasser les systèmes multi-qubits équivalents en ce qui concerne la fidélité des portes. Il convient d'étudier plus avant la manière dont les temps de porte des systèmes multi-qudit et multi-qubit évoluent en fonction du nombre de sous-systèmes. Cela permettrait de mieux comprendre les compromis entre les deux systèmes et d'éclairer la conception des futures plateformes quantiques.

L'analyse actuelle a été limitée à la réponse de premier ordre du bruit. Toutefois, des

développements récents indiquent que, grâce à des stratégies de correction d'erreurs quantiques appropriées, il est possible d'annuler entièrement la réponse de premier ordre dans les qudits logiques (qu-k-its, $k < d$) encodés dans des qudits physiques (qu-d-its) [33, 90]. Cela a des implications prometteuses pour l'amélioration de la fidélité des calculs en intégrant des opérations logiques résistantes aux erreurs dans des systèmes physiques de plus grande dimension. Par conséquent, en étudiant les réponses au bruit d'ordre supérieur dans les qudits logiques, nous pouvons envisager des encodages résistants au bruit au-delà de la réponse de premier ordre, ce qui pourrait encore améliorer les avantages des qudits en matière de calcul.

La compréhension du comportement dépendant de l'hamiltonien de l'AGI dépendant de la dimension constitue une piste de travail essentielle pour l'avenir. En outre, une étude complète des réponses au bruit d'ordre supérieur dans les qubits logiques par rapport aux qubits physiques est nécessaire pour évaluer la robustesse des avantages de calcul présentés par les qubits, en particulier à la lumière d'une éventuelle mise à l'échelle du système. Une telle étude serait essentielle pour déterminer si les avantages des qudits persistent au-delà de l'ère quantique intermédiaire bruyante (NISQ), contribuant ainsi au développement de plateformes quantiques plus résistantes et évolutives.

Non-linéarité de la fidélité dans les systèmes quantiques ouverts : Dépendance de la porte et du bruit dans l'informatique quantique à haute dimension

Note : Ce chapitre est directement adapté de l'article « Nonlinearity of the Fidelity in Open Qudit Systems : Gate and Noise Dependence in High-dimensional Quantum Computing » soumis pour publication et en révision dans Quantum et téléchargé en tant que manuscrit préimprimé sur arXiv. La citation bibliographique du préprint se trouve dans [129], et tous les codes et données utilisés pour générer les résultats présentés dans cette étude ont été mis à la disposition du public sur Zenodo [130].

Introduction

Dans ce chapitre, nous étendons les travaux de Chapter 2, en nous appuyant sur le cadre théorique développé dans [122] pour étudier la fidélité moyenne des portes (AGF) des systèmes à porte unique soumis à un bruit markovien dans le formalisme de Lindblad. Nous nous concentrons sur l'expansion perturbative de l'Average Gate Infidelity (AGI), permettant le calcul de termes de correction d'ordre supérieur à l'AGF au-delà du régime linéaire, et explorant les implications de la dépendance de la porte sur la robustesse des systèmes quantiques bruyants.

Contexte et motivation

L'informatique quantique à haute dimension a suscité un intérêt scientifique remarquable ces derniers temps, introduisant un changement par rapport aux paradigmes informatiques traditionnels. Alors que les plateformes de traitement de l'information quantique (QIP) basées sur des qubits, en particulier les qubits supraconducteurs, ont la plus grande maturité technologique, elles sont confrontées à des défis techniques à court terme en matière d'évolutivité et de correction d'erreurs [1, 131]. D'autre part, des avancées récentes ont mis en évidence le potentiel des qudits - des systèmes quantiques avec d niveaux - comme puissantes alternatives pour de nouvelles architectures QC [16, 21, 41, 132].

En effet, les qudits offrent plusieurs avantages, notamment (i) des taux de décohérence plus faibles dans certains systèmes physiques [31], (ii) une correction d'erreur quantique améliorée grâce à des niveaux supplémentaires [33, 90, 133] et des codes stabilisateurs [134], ainsi que (iii) une densité d'information plus élevée pour réduire la complexité des circuits et permettre la conception de nouveaux algorithmes [56]. Ils promettent également des mémoires quantiques volantes plus robustes [135, 136].

Si l'informatique classique s'est finalement contentée de bits une fois que l'évolutivité et la tolérance aux erreurs ont été suffisantes, les premières plateformes ont expérimenté des systèmes multiniveaux [32]. De la même manière, on peut affirmer que les débuts de l'informatique quantique pourraient bénéficier de l'exploration de bases à plus haute dimension pour résoudre les problèmes actuels. Dans le cadre de la progression vers un QC universel, l'augmentation de la dimension totale de l'espace de Hilbert des systèmes quantiques est essentielle [137]. Cette dimension est déterminée par d^n, où d est la dimensionnalité et n le nombre de qudits. Malgré des avancées impressionnantes dans les plateformes supraconductrices [26], la mise à l'échelle du nombre de qubits continue de poser des défis importants. Ainsi, les approches basées sur les qudits permettent d'aggrandir l'espace de Hilbert avec moins d'unités physiques [26, 42, 43, 132].

D'autre part, avec l'augmentation du nombre d'états excités utilisés pour mettre en œuvre des états de plus haute dimension dans les systèmes physiques, les qudits peuvent introduire un plus grand nombre de canaux d'erreur par rapport aux qubits. Cela pourrait conduire à une sensibilité accrue au bruit ambiant, affectant les temps de cohérence et compliquant les processus de correction des erreurs [138].

Objectifs et contributions

Dans l'article précédent [122], nous avons étudié ce scénario en détail en comparant les effets du bruit markovien sur les systèmes multi-qubits et à quotient unique de même dimension d'espace de Hilbert. Nous avons développé un modèle théorique des effets de premier ordre du bruit dans le formalisme de Lindblad, démontrant comment le bruit affecte la performance des portes quantiques dans ces différents systèmes, et nous avons étayé ces résultats par des simulations numériques.

Les quantités fondamentales étudiées sont la fidélité moyenne des portes (AGF, $\bar{\mathcal{F}}$) - équivalente à l'infidélité (AGI, $\bar{\mathcal{I}}$) - et le facteur de mérite ($\tau = t_{gate}/T_2$). Comme son nom l'indique, l'AGF est utile en ce sens qu'il intègre toutes les caractéristiques spécifiques dues à un choix particulier de l'état initial. Par conséquent, contrairement à la fidélité de l'état ou à la fidélité du processus, qui calculent les chevauchements cible-sortie des transferts d'états quantiques et des portes unitaires, respectivement, l'AGF est fondamental en tant que mesure de la qualité de l'interaction d'un système avec son environnement, indépendante de la plateforme [126, 139]. De même, le facteur de mérite est important pour quantifier de manière réaliste la profondeur de circuit qui peut être atteinte dans un système, sur la base du temps de porte, t_{gate}, et du temps de décohérence, T_2.

Ces résultats ont montré que dans le régime de quasi-absence d'erreur - couplage faible - la réponse du premier ordre de l'AGI (une fonction linéaire de la force de couplage sans dimension γt_{gate}) était suffisante pour caractériser le comportement du système qudit ou multi-qubit. Cependant, les approximations de premier ordre sont insuffisantes pour comprendre pleinement le comportement des qudits dans des conditions réalistes, à court terme, où l'on s'attend à ce que les effets de bruit d'ordre supérieur deviennent significatifs, soit par un couplage plus fort, soit par des temps de porte plus longs (ou des profondeurs de circuit) approchant la limite de décohérence.

Cette étude vise donc à élargir la compréhension de l'AGF des systèmes à qudit unique dans des conditions de bruit markovien par le biais d'une expansion perturbative générale. En particulier, nous nous concentrons sur les termes de correction d'ordre supérieur et leurs implications sur les performances des portes quantiques dans le régime de couplage fort. En s'appuyant sur nos travaux précédents, nous développons un cadre théorique complet qui inclut ces effets non linéaires, avec une méthode constructive généralisant l'AGF à un ordre arbitraire dans γt. Ceci est soutenu par des simulations numériques détaillées, en mettant l'accent sur les différences entre les termes du premier et du second ordre dans le cas d'un déphasage pur. Ce faisant, nous visons à capturer plus précisément l'impact du bruit sur la fidélité des portes quantiques.

La principale question de recherche abordée dans notre étude est la suivante : comment les termes de correction d'ordre supérieur et la force de couplage du bruit influencent-ils l'AGI des systèmes à qudit unique, et quelles sont les implications pour la sélection et la conception des portes quantiques ? Nos résultats fournissent des indications importantes sur (i) l'établissement de repères et de limites pour la performance des systèmes quan-

tiques bruyants de dimension arbitraire en identifiant les effets dépendant des portes, (ii) les méthodologies pour améliorer la performance en optimisant les portes de base qui ont des caractéristiques de décohérence favorables, et (iii) l'avancement des protocoles de correction d'erreur en permettant l'annulation des effets de bruit d'ordre supérieur.

Aperçu

Le chapitre est structuré comme suit : Nous commençons dans Section 5.2 par un examen du contexte théorique pertinent concernant le formalisme de Lindblad pour les systèmes quantiques ouverts qudit et la représentation du superopérateur des canaux quantiques bruyants, ainsi que les portes quantiques généralisées sur les qudits.

Dans Section 5.4.1, nous présentons notre résultat général pour l'expansion perturbative de l'AGI dans la force du bruit, en dérivant les expressions générales à un ordre arbitraire en γt et en discutant les implications de sa structure.

Section 5.4.2 examine la non-linéarité de l'IAG dans le régime de couplage fort du déphasage pur au moyen de simulations numériques qui élucident les caractéristiques clés de ce comportement et motivent les recherches ultérieures qui établissent le lien avec les résultats théoriques. Ensuite, dans Section 5.4.4, nous explorons la dépendance de l'AGI par rapport à la porte et au bruit, en mettant particulièrement l'accent sur la manière dont le choix de la porte quantique peut influencer les performances du canal quantique.

Enfin, Section 5.4.5 présente une étude analytique et numérique détaillée des termes de correction de premier et de second ordre de l'AGI, étendant les résultats du travail précédent et les plaçant sur une base théorique plus rigoureuse qui servira aux investigations futures.

Discussion des résultats

Sommaire des résultats

Dans ce travail, nous avons effectué une analyse complète de l'AGF pour les systèmes quantiques ouverts à qudit unique couplés à des environnements de bruit markoviens dans le formalisme du superopérateur de Lindblad. Nos principales contributions et conclusions sont les suivantes :

Nous avons étendu l'AGF de manière perturbative en puissances de la constante de couplage sans dimension γt (voir Fig. 17). Nous en avons déduit notre principal résultat dans Eq. (5.30) pour les expressions générales des termes de correction à un ordre arbitraire. Le résultat a été exprimé en termes de commutateurs itérés des superopérateurs de porte et de bruit, $\mathcal{S}$ et $\mathcal{L}$, respectivement, sur la base de l'expansion obtenue dans Eq. (5.27). Il est particulièrement important que ces corrections soient exprimées sous une forme qui peut être directement mise en œuvre dans des calculs numériques. Nous avons constaté que, à chaque ordre supérieur au premier, le terme de correction pouvait être séparé en un terme indépendant de la porte $\mathcal{O}((\gamma t)^m)$ dépendant uniquement de $\mathcal{L}$, et d'autres termes dépendants de la porte contenant $\mathcal{S}$ et des puissances supérieures de t. Le terme de correction du premier ordre, $\mathcal{I}^{(1)}$, est indépendant de la porte et dépend uniquement du superopérateur de bruit $\mathcal{L}$. La dépendance à la porte apparaît pour la première fois à $\gamma^2 t^4$, dans le terme de correction de second ordre $\mathcal{I}^{(2)}$, soulignant le rôle important de l'interaction entre l'hamiltonien de contrôle $\mathcal{S}$ et l'opérateur de bruit $\mathcal{L}$.

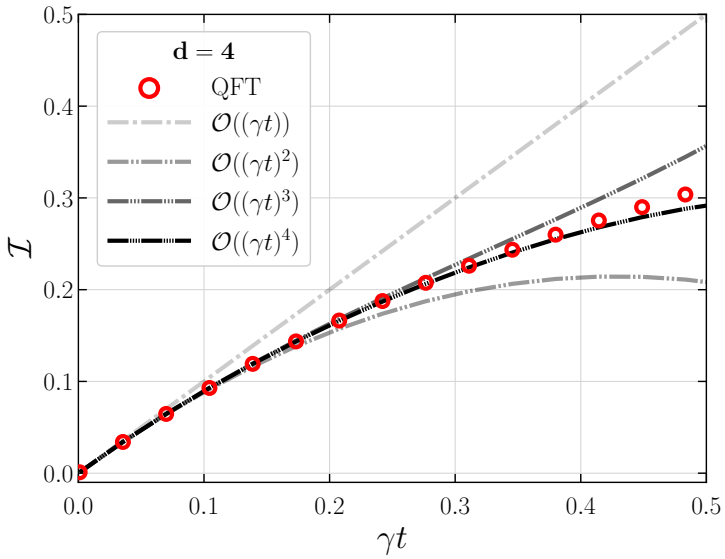


Figure 17 – Comparaison des quatre premiers termes de correction de l'AGI avec les simulations numériques. AGIs pour la porte QFT appliquée à un qudit $d = 4$ subissant un déphasage pur ($L = J_z$) aux couplages $\gamma t \in [0, 0.5]$. Les points discrets (en rouge) représentent les valeurs AGI simulées, tandis que les lignes pointillées successives représentent les termes de correction du premier au quatrième ordre.

Des expressions explicites pour les termes de correction de premier et de second ordre dans la représentation de l'opérateur ont également été dérivées.

Nos simulations numériques sous un bruit de déphasage pur ont révélé une transition claire d'un comportement linéaire à un comportement non linéaire dans l'AGI lorsque la force de couplage du bruit γt augmente. Pour $\gamma t \sim 1$, l'AGI s'écarte de manière significative de l'approximation linéaire et atteint finalement un plateau à une valeur stable (voir Fig. 18). Les valeurs de plateau, $\mathcal{I}^*$, ainsi que leurs points de saturation correspondants, $\gamma t)^*$, se sont avérés dépendre non seulement de la dimension de qudit d mais aussi de la porte quantique spécifique mise en œuvre.

En effet, en utilisant notre cadre théorique, nous avons pu dériver dans Eq. (5.57) un résultat significatif pour les limites universelles supérieures et inférieures des valeurs du plateau de l'AGI dans le régime de couplage fort, dépendant uniquement de la dimensionnalité du système. En outre, nous avons pu identifier des portes spécifiques qui saturent ces limites : La porte de l'identité ($\mathbb{1}_d$) et le NOT généralisé (X) atteignent respectivement les limites inférieure et supérieure, tandis que la porte QFT (F_d) plafonne à la valeur moyenne de l'AGI de la mesure de Haar. En outre, nous avons introduit les portes interpolées X^η pour démontrer la gamme des valeurs AGI entre ces limites. Les points de saturation de ces portes interpolées ont été étudiés numériquement et ont été bien décrits par un modèle de loi de puissance de $(\gamma t)^*$ en fonction de d.

Nous avons analysé la convergence du terme de correction de second ordre, identifiant qu'environ 50 itérations sont suffisantes pour un calcul précis jusqu'à $d < 64$ dans une tolérance absolue de $\varepsilon < 1 \times 10^{-8}$. Le nombre d'itérations jusqu'à la convergence est logarithmique avec la dimension du système d, et linéaire avec le temps de porte t.

Les simulations numériques ont confirmé les prédictions analytiques, démontrant que l'erreur relative de l'AGI est significativement réduite lorsque l'on inclut le terme de

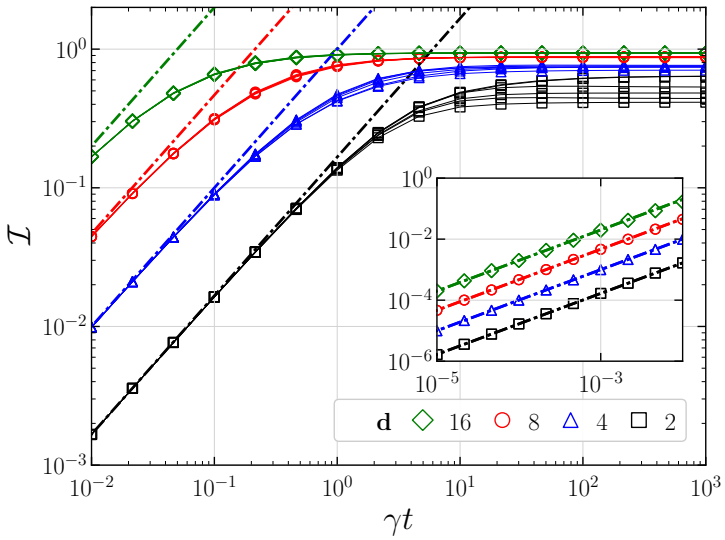


Figure 18 – Écart par rapport à la linéarité des AGI pour les qubits soumis à un fort déphasage. Les simulations de l'AGI en fonction de la force du déphasage pur ($L = J_z$) sont représentées sur des axes log-log sur γt *dans* $\left[10^{-2}, 10^{3}\right]$. Les simulations ont été effectuées sur un ensemble de dimensions de qudit, $d \in \{2, 4, 8, 16\}$ chacun pour 100 portes quantiques aléatoires de Haar. Les lignes en pointillé représentent le régime linéaire donné par la correction de premier ordre de l'IAG à chaque dimension. L'encadré montre le régime linéaire pour des valeurs plus petites de γt *dans* $\left[10^{-5}, 10^{-2}\right]$.

correction de second ordre. Pour $d = 4$, l'erreur est réduite à l'ordre de 1%, et pour $d = 2$, elle est réduite à 0.01%, indiquant la nécessité de corrections d'ordre supérieur pour une modélisation précise de la fidélité, en particulier lorsque la dimension du système augmente.

Perspectives d'avenir

Les informations obtenues grâce à cette étude ont plusieurs applications et implications importantes dans le domaine de l'informatique quantique, en particulier compte tenu de l'intérêt croissant pour les qudits. La compréhension du comportement de l'AGI et de sa dépendance à l'égard du type de porte quantique et du bruit ambiant facilite l'optimisation de la conception des portes quantiques. Notre approche fournit une méthodologie pour identifier les portes quantiques qui ont des fidélités favorables. Ainsi, par un choix ou une conception appropriés des portes de base, il peut être possible d'améliorer les performances des circuits quantiques. Cela pourrait conduire à des améliorations significatives pour optimiser la robustesse des algorithmes quantiques sur les plateformes bruyantes à court terme.

Les résultats soulignent l'importance d'incorporer des corrections d'ordre supérieur dans les protocoles de correction d'erreur. Ceci est particulièrement pertinent pour les qubits de dimensions supérieures, où les effets du bruit sont plus prononcés. Nous envisageons que les expansions perturbatives fournies dans ce travail puissent être exploitées pour développer des techniques avancées de correction d'erreur, par exemple en incorporant les termes de correction d'ordre supérieur dans la fonction de coût des méthodes de contrôle optimal. En particulier, nos termes de correction peuvent être utilisés pour quantifier et atténuer l'erreur dans les protocoles d'intégration de qubits logiques jusqu'à un ordre arbitraire. Des recherches futures sont nécessaires pour montrer comment cela

pourrait aboutir à une protection contre de telles erreurs au-delà du premier ordre, et comment cela pourrait intégrer les dépendances de porte identifiées.

Les limites dérivées et les comportements de l'AGI pour différentes portes et dimensions servent également de repères pour l'évaluation des performances des systèmes quantiques. Ces repères peuvent guider les expérimentateurs dans l'évaluation et l'amélioration de leur matériel quantique et de leurs implémentations de portes. En effet, d'autres études sont nécessaires pour étendre ces résultats de l'hamiltonien idéalisé à une seule impulsion (indépendante du temps) à des techniques réalistes de contrôle optimal basées sur les impulsions pour la génération de portes.

Alors que cette étude s'est principalement concentrée sur le déphasage pur et les erreurs de retournement de bits, les recherches futures devraient explorer davantage l'impact d'autres modèles de bruit, tels que l'amortissement de l'amplitude et le bruit dépolarisant. Comprendre comment les différents types de bruit affectent l'AGI fournira un cadre plus complet pour la conception de systèmes quantiques résistants au bruit.

Il est nécessaire d'étendre ce cadre aux systèmes multi-qudits. Ceux-ci introduisent une complexité supplémentaire due aux interactions inter-qudit et aux effets de bruit corrélés. L'étude de ces facteurs sera cruciale pour l'évolution des architectures basées sur les qubits, mais pourrait s'avérer fructueuse pour réduire la complexité des circuits des opérations d'intrication à longue portée.

Enfin, il serait utile de procéder à une vérification expérimentale de ces prédictions. Tester les termes de correction dérivés et les points de transition dans des systèmes quantiques réels permettra de valider et d'affiner les modèles présentés.

En conclusion, cette étude fournit une base théorique détaillée pour comprendre la fidélité des portes quantiques dans des environnements bruyants. Les résultats contribuent aux efforts en cours pour développer des opérations quantiques robustes et de haute fidélité, ouvrant la voie à une informatique quantique pratique et évolutive.

Techniques de contrôle optimal quantique pour la synthèse de portes Qudit

Note : Les résultats présentés dans ce chapitre font actuellement l'objet d'un manuscrit pour publication, intitulé « Quantum Optimal Control Techniques for Qudit Gate Synthesis », et seront mis à la disposition du public dès leur soumission. L'ensemble du code et des données utilisés pour générer les résultats présentés seront également mis à la disposition du public.

Introduction

Dans ce chapitre, nous étudions le problème des techniques de contrôle au niveau des impulsions pour les systèmes quantiques à qubit unique, en nous concentrant sur la mise en œuvre de différentes méthodes de synthèse de portes et en comparant leur robustesse au bruit et aux erreurs de contrôle. L'objectif est d'étendre les capacités des méthodes de contrôle quantique développées pour les systèmes de qubits à des qubits de dimension supérieure, en mettant l'accent sur leur potentiel pour le traitement de l'information quantique. Les systèmes de qubits offrent des avantages par rapport aux qubits en permettant un encodage plus compact de l'information et une mise en œuvre potentiellement plus rapide de certains algorithmes quantiques en réduisant le nombre d'opérations d'intrication nécessaires. Cependant, comme nous l'avons déjà vu, ils présentent également des défis importants en termes de contrôle des portes et de gestion du bruit. Dans cette introduction, nous fournissons le contexte nécessaire, soulignons la motivation et les objectifs de cette étude, résumons les principales contributions et décrivons l'organisation de ce chapitre.

Contexte et motivation

Le contrôle optimal quantique est devenu un domaine de recherche essentiel dans la quête de la construction d'ordinateurs quantiques évolutifs et tolérants aux erreurs. Au cœur du contrôle quantique se trouve le problème de la synthèse de portes quantiques à l'aide de champs de contrôle dépendant du temps. Une grande partie de la recherche s'est concentrée jusqu'à présent sur le contrôle des systèmes de qubits, où les méthodes de synthèse de portes quantiques telles que l'algorithme GRAPE et d'autres techniques de mise en forme des impulsions se sont avérées très efficaces lorsqu'elles étaient adaptées à des plateformes matérielles spécifiques. Cependant, avec l'intérêt croissant pour les systèmes qudit, il est nécessaire d'étendre ces techniques de contrôle à des dimensions plus élevées et d'étudier leurs performances.

Les systèmes quantiques ont fait l'objet d'études approfondies en raison de leur capacité à accroître la puissance de calcul des systèmes quantiques. En particulier, les systèmes de qudit permettent un encodage plus efficace de l'information quantique, réduisant la complexité de certains algorithmes quantiques tels que l'algorithme de Grover [31, 54, 55]. En outre, les systèmes multi-qudit peuvent présenter une robustesse accrue au bruit et, avec des encodages appropriés, peuvent offrir de nouvelles voies pour l'informatique quantique tolérante aux pannes [33, 90, 91, 133]. Toutefois, pour exploiter pleinement le potentiel des systèmes quantiques, il est essentiel de développer des méthodes efficaces et évolutives pour contrôler le grand nombre de canaux de contrôle requis.

Avec l'essor des systèmes quantiques multiniveaux, il est de plus en plus nécessaire de mettre au point des méthodes fiables et évolutives pour contrôler les portes qudit, en

particulier face au bruit ambiant et aux imperfections du matériel.

Des progrès considérables ont été réalisés dans le développement de techniques de synthèse de portes quantiques, et certaines méthodes, telles que la décomposition par rotation de Givens (GRD) [96], offrent une approche algébrique de la génération de portes quantiques par rotations séquentielles qui s'étend naturellement à des systèmes de dimensions supérieures, ce qui les rend efficaces sur le plan du calcul pour des types de portes spécifiques. Cependant, la comparaison entre les méthodes d'optimisation numérique, telles que GRAPE, et les méthodes algébriques, telles que GRD, dans le contexte du contrôle optimal pour les systèmes quantiques reste sous-explorée par rapport aux systèmes de qubits [140].

En outre, le bruit et les erreurs de contrôle restent des obstacles importants à l'obtention de portes de haute fidélité. Alors qu'une grande attention a été accordée à la compréhension des effets du bruit environnemental et des erreurs de contrôle pour un matériel spécifique sur les systèmes à base de qubits, on en sait moins sur l'impact de ce bruit et de ces erreurs sur les systèmes à base de qubits. Jusqu'à présent, nous avons étudié les effets des environnements markoviens sur des portes qubit idéales, à impulsion unique, dans les régimes linéaire et non linéaire, respectivement. L'étude de ces effets sur les contrôles au niveau de l'impulsion est cruciale pour le développement futur des technologies quantiques qui exploitent tout le potentiel des qudits.

Objectifs et contributions

L'objectif de cette étude est de faire progresser les techniques de contrôle au niveau des impulsions pour les systèmes quantiques qudit, en se concentrant sur la synthèse des portes par le biais de l'algorithme GRD et de l'algorithme GRAPE. En comparant ces méthodes, nous étudions leurs avantages et leurs limites respectifs dans la réalisation d'un contrôle de porte qudit efficace. En outre, nous analysons l'impact du bruit markovien, y compris le déphasage, le bit-flip et la relaxation de spin, ainsi que les erreurs de contrôle telles que les fluctuations d'amplitude et de phase et l'asymétrie de l'horloge, afin de comprendre leur influence sur la fidélité de la porte.

Pour faciliter cette exploration, nous développons un cadre de simulation modulaire et flexible, fournissant une base pour la recherche future sur les techniques de contrôle, les modèles de bruit et les scénarios d'erreur plus réalistes, ainsi que pour l'extension aux systèmes multi-quotidiens. En outre, des approches hybrides de la synthèse de portes sont explorées en combinant la technique algébrique GRD avec l'optimisation numérique via GRAPE, dans le but d'améliorer l'efficacité de calcul et la fidélité des portes.

Les contributions de ce travail comprennent une analyse comparative de la GRD et de GRAPE pour la synthèse de portes à quotient unique, offrant des aperçus de leur efficacité en termes de calcul et de portes. Nous examinons la robustesse de ces méthodes de synthèse de portes dans diverses conditions de bruit et d'erreurs de contrôle, fournissant des conseils pour atténuer les effets du bruit dans les systèmes qudit reéls.

Le cadre de simulation que nous avons développé est polyvalent, il permet de générer et d'analyser la fidélité des portes qudit dans différentes conditions et facilite les futures études comparatives des techniques de contrôle quantique. L'introduction d'approches de synthèse hybrides exploite les forces des méthodes algébriques et numériques, optimisant les performances des portes et suggérant de nouvelles directions pour le développement de protocoles de contrôle quantique robustes.

Aperçu

Le chapitre est organisé comme suit : Dans le Section 6.2, nous fournissons une description détaillée du contexte théorique sous-jacent à la synthèse de portes de qudit, y compris l'algorithme GRD et GRAPE. Dans Section 6.3, nous décrivons le cadre de simulation et les modèles de bruit utilisés dans cette étude. Section 6.4 est divisé en deux parties : premièrement, une discussion des méthodes de synthèse de portes et de leurs performances dans des conditions sans bruit dans Section 6.4.1 ; deuxièmement, une analyse des effets du bruit et des erreurs de contrôle sur la fidélité des portes dans Section 6.4.2. Nous y présentons également les approches hybrides et discutons de leur impact sur l'efficacité des portes. Enfin, dans Section 6.5, nous examinons les principales conclusions, les implications de nos résultats et les orientations futures de la recherche.

Discussion des résultats

Sommaire des résultats

Dans ce chapitre, nous avons présenté une étude détaillée des méthodes de synthèse au niveau de l'impulsion des portes quantiques à quotient unique. Après avoir établi dans Section 6.2 les fondements théoriques de la modélisation de ces systèmes, nos principales contributions et résultats sont les suivants :

Section 6.2 a examiné les conditions de contrôlabilité et d'universalité des portes dans les systèmes qudit de dimensionnalité arbitraire. Étant donné un ensemble d'hamiltoniens de contrôle, on dit que le système est contrôlable si l'algèbre de Lie des hamiltoniens de contrôle anti-Hermitiens génère le groupe de Lie complet des opérateurs unitaires dans l'espace de Hilbert du système. En effet, il suffit de montrer que le système présente une universalité si le graphe de transition du système est connecté. En d'autres termes, il existe une séquence d'hamiltoniens de contrôle (chemin) qui peut conduire le système de n'importe quel état initial à n'importe quel état final. Dans cette optique, nous avons choisi de restreindre notre étude au cas minimal des systèmes qudit, avec seulement xy-impulsions de contrôle (dans l'image de l'interaction) entre les états adjacents.

La méthode GRD a été introduite comme une approche algébrique linéaire pour générer des portes quantiques en décomposant les opérations unitaires en une séquence de rotations de Givens plus simples, chacune agissant sur un sous-espace bidimensionnel de l'espace de Hilbert complet. Cette méthode est pratique à la fois sur le plan conceptuel et sur le plan de la mise en œuvre, car chaque rotation peut être dérivée analytiquement et, dans le cas d'impulsions idéales dans un système quantique fermé, elle est exacte. En outre, les rotations peuvent être appliquées au système comme une impulsion bang-bang unique en utilisant notre ensemble d'hamiltoniens de contrôle, et sont faciles à visualiser comme des rotations autour d'un axe sur le plan xy de la sphère de Bloch du sous-espace.

L'algorithme GRAPE a été présenté comme une méthode basée sur l'optimisation numérique pour générer des portes quantiques par le biais d'une séquence d'impulsions multichromatiques constantes par morceaux. À partir d'une estimation initiale de la séquence d'impulsions, l'algorithme optimise de manière itérative les paramètres des impulsions afin de minimiser une fonction de coût pour atteindre l'opération unitaire cible. Cette méthode est très flexible et peut être configurée avec une variété de fonctions de coût de type Mayer, Lagrange ou Bolza, ainsi qu'avec des contraintes pour optimiser la séquence d'impulsions pour différents scénarios. Dans ce travail, nous avons considéré la fonction de coût standard basée sur la fidélité, qui minimise l'infidélité entre la cible et les

opérations unitaires réalisées.

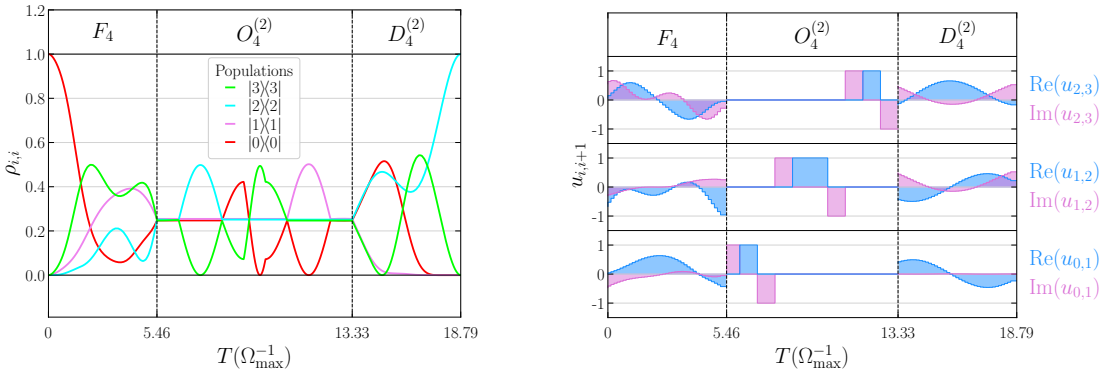
Dans Section 6.3, nous avons présenté notre développement d'un cadre de simulation extensible conçu pour simuler le contrôle au niveau des impulsions des systèmes quantiques quantiques. La base de code sur la bibliothèque QuTiP dans Python, et étend la fonctionnalité de la bibliothèque pour inclure des classes pour la simulation de portes quantiques sur des systèmes quantiques dans des environnements bruyants.

La classe `Qudit` représente le système quantique, avec des états de base et des opérateurs, et fournit la base pour effectuer des opérations quantiques avec des hamiltoniens de contrôle dans l'image d'interaction en utilisant l'approximation des ondes tournantes (RWA). Les classes `Pulse`, `ComplexPulse` et `MultiPulse` sont responsables de la coordination des séquences d'impulsions générées par l'algorithme GRAPE et les classes GRD, et fournissent une interface flexible qui facilite l'intégration de futures méthodes de génération de portes. La classe `NoiseGenerator` configure le bruit environnemental et les erreurs de contrôle mises en œuvre lors de l'évolution temporelle et des calculs de fidélité. Elle comprend actuellement des opérateurs d'effondrement de spin pour le déphasage, le retournement de bit et le bruit de relaxation, et peut être étendue pour inclure d'autres sources de bruit. Les erreurs de contrôle mises en œuvre dans cette étude comprennent des erreurs de décalage d'amplitude et de phase, ainsi que des erreurs de décalage d'horloge, qui peuvent être appliquées aux canaux d'impulsions des portes.

Une classe `QuditGate` a également été ajoutée pour faciliter la sélection et la génération de portes quantiques et d'algorithmes particuliers ainsi que de portes quantiques aléatoires à partir d'une variété de méthodes de génération. En outre, un ensemble de classes de soutien, telles que `ConfigManager` et `DatabaseManager`, ont été mises en œuvre pour faciliter la configuration initiale du simulateur et le stockage des résultats de simulation dans une base de données en vue d'une analyse ultérieure, respectivement. Les simulations de bruit sont basées sur le solveur d'équation maîtresse GKS-Lindblad de QuTiP `mesolve`, qui décrit la dynamique des systèmes quantiques ouverts. Dans l'ensemble, ce code modifié fournit un cadre complet pour la simulation et l'analyse des techniques de contrôle au niveau des impulsions dans les systèmes quantiques ouverts qudit, permettant une approche modulaire pour l'étude de différentes techniques dans une grande variété de conditions, ce qui le rend adaptable à différents scénarios d'informatique quantique.

En utilisant ce cadre, nos résultats dans Section 6.4 ont été séparés en deux parties : dans Section 6.4.1 nous avons montré quelques exemples d'application des différentes méthodes de génération de portes pour différentes portes quantiques, et dans Section 6.4.2 nous avons effectué une comparaison détaillée de la performance des algorithmes GRAPE et GRD.

Nous avons testé les méthodes de génération de portes sur la porte QFT et l'algorithme de recherche de Grover, et nous avons constaté que les deux méthodes étaient capables de synthétiser les portes avec précision dans le cas sans bruit. La seule exception concerne l'opérateur Oracle de l'algorithme de Grover, pour lequel l'algorithme GRAPE n'a pas trouvé de solution acceptable, probablement parce que l'opération d'inversion de phase est une porte diagonale qui n'affecte pas la dynamique des populations. Dans ce cas, nous avons pu utiliser notre cadre pour simuler l'algorithme par une approche hybride GRAPE-GRD où l'Oracle a été implémenté par des rotations de Givens et les opérateurs QFT et de diffusion par GRAPE (voir Fig. 19). Il s'agit d'une nouvelle approche, qui met en évidence la flexibilité de notre cadre pour combiner différentes méthodes de génération de portes afin d'obtenir le résultat souhaité. D'autre part, nous avons montré que le GRD



(a) Populations $\rho_{i,i}$.

(b) Pulses $u_{i,i+1}(t)$.

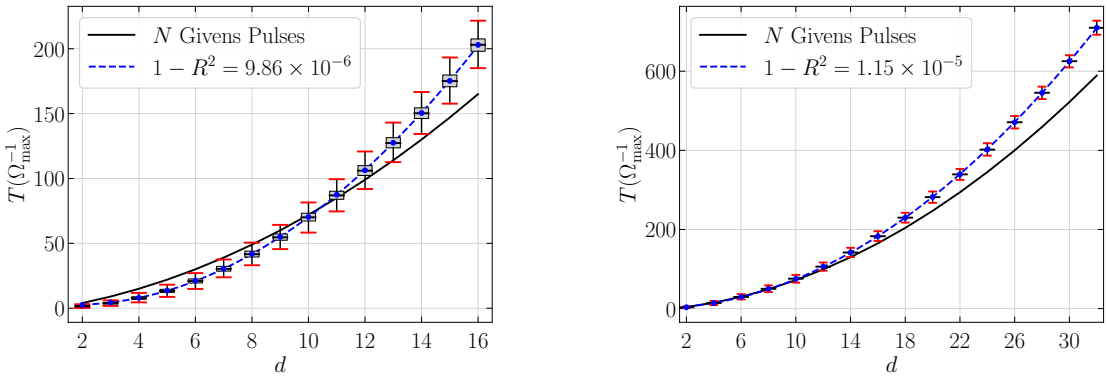
Figure 19 – Mise en œuvre de l'algorithme hybride GRD-GRAPE de l'algorithme probabiliste de Grover. L'algorithme GRAPE a été appliqué à un système qudit de dimension $d = 4$ pour générer la QFT et les portes de diffusion, tandis que l'inversion de phase Oracle a été mise en œuvre par des rotations de Givens. Le qudit a été initialisé dans l'état fondamental $\rho(0) = |0\rangle\langle 0|$ et l'état $|2\rangle\langle 2|$ a été marqué comme état de recherche. Les états $\rho_{i,i}$ indiqués en (a) ont été modifiés par les séquences d'impulsions complexes normalisées comme indiqué en (b), ce qui a permis d'obtenir l'état final après une itération de Grover.

était capable de synthétiser suffisamment bien tous les opérateurs de Grover. À l'aide d'un bloc-notes Mathematica interactif conçu sur mesure pour visualiser les simulations de portes de qudit, nous avons étendu les simulations de la version probabiliste à un protocole déterministe à deux paramètres plus récent, capable de localiser l'état cible avec certitude. Cette variante déterministe est très prometteuse en principe, mais au prix d'une complexité accrue et d'un plus grand nombre d'itérations, ce qui a pour effet d'allonger considérablement les temps d'accès à l'algorithme complet.

Dans Section 6.4.2, nous avons comparé l'algorithme GRAPE et GRD en termes de : (i) coût de calcul, (ii) durée de la porte, (iii) fidélité de la porte en cas de bruit markovien, et (iv) robustesse aux erreurs de contrôle.

En ce qui concerne le coût de calcul, nous avons constaté que l'utilisation en mémoire des deux méthodes est approximativement égale à d^4. Cependant, la GRD nécessite beaucoup moins de mémoire que GRAPE en raison d'un préfacteur beaucoup plus petit, ce qui la rend plus adaptée aux systèmes de haute dimension. GRAPE a également un coût de traitement plus élevé en raison de la nature itérative de la routine d'optimisation L-BFGS-B, tandis que le GRD offre un traitement plus rapide en raison de son approche linéaire-algébrique, le temps de traitement s'échelonnant de manière similaire à l'utilisation de la mémoire pour les deux portes en raison de la croissance du nombre de calculs matriciels s'échelonnant avec la dimensionnalité du système. Le GRD est donc plus adapté aux grands systèmes où les ressources de calcul et le temps de génération sont critiques, tandis que GRAPE est compétitif pour les dimensions inférieures.

Le temps de porte est une mesure de performance critique dans les systèmes quantiques bruyants, et afin d'analyser avec précision les temps de porte entre les deux méthodes, les amplitudes d'impulsion de chaque méthode ont été normalisées à $\Omega_{max} = 1$, et des tests ont été effectués sur de grands ensembles de portes aléatoires de Haar. Les simulations ont été effectuées sur des dimensions de qudit allant de $d = 2$ à $d = 32$ pour le GRD et jusqu'à $d = 16$ pour GRAPE en raison de contraintes informatiques. Dans les deux cas, l'analyse des moindres carrés a montré que les temps de porte s'échelonnaient de la



(a) GRAPE algorithm **(b)** GRD

Figure 20 – Temps de porte des algorithmes GRD et GRAPE pour les portes aléatoires de Haar. Les méthodes GRAPE (a) et GRD (b) ont été utilisées pour générer des impulsions pour un ensemble de 1 000 portes unitaires aléatoires de Haar pour des qudits uniques sur les dimensions $d \in [2, 16]$ et $d \in [2, 32]$, respectivement. Les temps de porte ont été comparés à l'échelle du nombre d'impulsions requises par dimension pour la GRD, $\frac{1}{2}d(d-1)+3(d-1)$. Les données pour chaque dimension sont représentées dans des diagrammes en boîte et en pointillé, montrant la moyenne (cercle bleu), la médiane (ligne noire), les quartiles (boîte grise) et l'étendue (lignes rouges). Des ajustements polynomiaux de second ordre ont été appliqués aux moyennes de chaque ensemble de données.

manière la plus appropriée en fonction de d^2.

En y regardant de plus près, nous avons constaté que l'algorithme GRAPE produisait des impulsions significativement plus rapides et plus optimisées dans les dimensions inférieures à $d \leq 12$, mais qu'en raison d'une mise à l'échelle plus abrupte, il produisait des temps de porte plus longs que GRD pour les dimensions supérieures à $d \geq 12$. En examinant les diagrammes en boîte et en moustache pour chaque méthode (voir Fig. 20), il est raisonnable de penser que cette moins bonne mise à l'échelle de GRAPE est due à la complexité accrue de l'espace de recherche pour les dimensions plus élevées, ce qui entraîne des temps plus longs et des solutions potentiellement sous-optimales. En revanche, le GRD présente une évolution plus prévisible en fonction de la dimensionnalité et est capable de maintenir des performances cohérentes dans toutes les dimensions.

L'impact du bruit markovien par déphasage, retournement de bits et bruit de relaxation sur la fidélité moyenne de la porte (AGF) a été étudié pour les deux méthodes. Les tests ont été effectués de manière analogue à ceux présentés dans Section 5.4, où les AGI ont été calculés sur des ensembles de portes aléatoires de Haar pour une gamme de dimensions de qudit, ainsi que pour les portes QFT et les portes généralisées-X pour $d = 4$. Une différence par rapport aux résultats présentés dans Chapter 5 est qu'il a été nécessaire de tenir compte de la variation des temps de porte dans le paramètre de force de couplage sans dimension $\gamma_z t_g$ afin de comparer de manière cohérente les performances entre les différentes portes, les méthodes de génération et les dimensions.

Dans l'ensemble, il y avait peu de différences significatives sur le plan statistique entre les algorithmes GRAPE et GRD lorsque l'on tenait compte de la variation des temps de porte et que l'on calculait la moyenne sur un ensemble de portes aléatoires de Haar. En effet, les IAG moyens des deux méthodes se sont révélés conformes aux prévisions théoriques du comportement idéal de l'IAG dans le régime linéaire à faible couplage, tel qu'il a été identifié dans Chapter 4. Dans le régime non linéaire à fort couplage, les deux

méthodes ont montré le même comportement en plateau dans les limites universelles identifiées dans Chapter 5, ainsi que le phénomène de concentration du mésure attendu pour l'augmentation de la dimensionnalité.

Une différence notable entre les deux méthodes est la variance des IAG, GRAPE présentant un éventail de valeurs plus large que GRD à chaque niveau de bruit. Cette différence est particulièrement évidente dans la limite de couplage faible pour les dimensions inférieures. Cela suggère que, bien que le GRAPE puisse être plus performant pour certaines portes, le GRD fournit une performance plus fiable et plus cohérente dans différentes conditions de bruit. Cela peut être particulièrement important pour les applications pratiques où la fidélité de la porte est critique et où les conditions environnementales ne sont pas connues avec précision.

Enfin, nous avons étudié les effets des erreurs de contrôle sur les performances des portes synthétisées par l'algorithme GRAPE et le GRD. Dans cette étude, nous avons considéré des erreurs constantes de décalage d'amplitude, de déphasage et d'asymétrie d'horloge sur les impulsions de commande, et étudié la robustesse des portes à ces erreurs par le biais de la largeur maximale à mi-hauteur (FWHM) de la courbe AGI moyenne par rapport à la condition de bruit zéro. Pour les décalages d'amplitude et de phase, nous avons considéré deux cas d'erreurs absolues et relatives, tandis que pour les erreurs de décalage d'horloge, seuls les décalages absolus dans la chronologie des impulsions ont été considérés comme physiquement pertinents. Les méthodes ont été comparées sur un ensemble de portes aléatoires de Haar, avec des erreurs introduites individuellement dans chaque canal d'impulsion pour chaque porte.

Les résultats ont montré que le GRD est plus résistant que le GRAPE aux erreurs de décalage d'amplitude absolue dues aux effets de la normalisation de l'amplitude sur les séquences d'impulsions monochromatiques et multichromatiques, respectivement. D'autre part, le GRAPE est plus résistant aux erreurs d'amplitude relative en raison de ses profils d'impulsions plus lisses sur les rotations bang-bang du GRD. Ce même effet se reflète dans les erreurs de phase relatives, où GRAPE a un léger avantage en raison de sa structure d'impulsion continue. Le GRAPE présente également une plus grande robustesse aux erreurs de synchronisation (décalage d'horloge), alors que le GRD souffre gravement de sa dépendance à l'égard de la synchronisation précise des impulsions dans la séquence monochromatique.

En outre, il était intéressant d'observer la dépendance des courbes AGI par rapport au choix de la transition modulée, ainsi que l'asymétrie entre les valeurs d'erreur positives et négatives. Cela suggère que la robustesse des portes aux erreurs de contrôle n'est pas uniforme dans l'espace de Hilbert et que les canaux d'impulsions contrôlant les transitions des états centraux sont significativement plus sensibles à toutes les erreurs de contrôle que les états périphériques (état fondamental et état le plus excité).

Dans l'ensemble, ce chapitre propose une analyse complète de deux techniques connues de synthèse de portes pour les systèmes qudit : les algorithmes GRD et GRAPE. Chaque méthode présente des forces et des faiblesses en fonction de la dimensionnalité du système, des contraintes de calcul et de la nature du bruit et des erreurs de contrôle. Le GRD est efficace sur le plan des calculs, ce qui le rend idéal pour les grands systèmes de quantification où l'évolutivité est essentielle. Il donne également de bons résultats dans les scénarios où les ressources sont limitées et offre des performances constantes dans diverses conditions de bruit et pour différentes tailles de systèmes. L'algorithme GRAPE, bien que coûteux en termes de calcul, excelle dans les systèmes de petite à moyenne taille

nécessitant un contrôle précis et optimisé, en particulier lorsque des temps d'accès rapides et des contrôles robustes sont essentiels.

Perspectives d'avenir

Les résultats présentés dans ce chapitre offrent un cadre complet pour comprendre et mettre en œuvre le contrôle optimal au niveau des impulsions des systèmes quantiques quantiques. La comparaison entre les algorithmes GRD et GRAPE dans la synthèse de portes fournit des indications précieuses sur leurs applications pratiques et leurs limites. Pour aller de l'avant, plusieurs applications potentielles, extensions et domaines d'amélioration peuvent être explorés sur la base de ces résultats. En outre, il existe d'importantes lacunes dans nos connaissances que la recherche future peut combler pour faire progresser la mise en œuvre pratique des portes quantiques dans les systèmes basés sur le qudit.

Les systèmes à qubits, avec leur dimensionnalité plus élevée, offrent un espace d'état plus riche que les systèmes à qubits, ce qui permet un encodage plus compact de l'information quantique. Cette étude jette les bases de la construction et du contrôle de portes quantiques avec une grande fidélité, qui peuvent être directement appliquées à des tâches telles que les protocoles de communication quantique, la distribution de clés quantiques et certains codes de correction d'erreurs quantiques qui nécessitent des systèmes multiniveaux pour une plus grande efficacité et une meilleure sécurité. Elle est également intéressante pour les tâches de simulation quantique qui modélisent des systèmes physiques avec des espaces d'état naturellement de plus grande dimension, tels que les particules avec un spin supérieur à 1/2 ou les systèmes décrits par des symétries SU(d).

Bien que cette étude constitue une base solide pour la synthèse de portes qudit, plusieurs extensions et améliorations pourraient accroître la portée et l'applicabilité de ce travail :

L'algorithme GRAPE s'est avéré très efficace pour les systèmes de dimension petite à moyenne, mais il souffre de problèmes d'extensibilité et du risque d'être piégé dans des minima locaux. Une première étape consisterait à explorer plus en détail l'optimisation des hyperparamètres de l'algorithme GRAPE, tels que le nombre d'itérations, le choix de la fonctionnelle de coût et la supposition de l'impulsion initiale. En outre, l'algorithme pourrait être parallélisé pour tirer parti des ressources informatiques modernes à haute performance, ce qui permettrait une convergence plus rapide et des solutions plus robustes pour les systèmes de qudit plus importants.

Les travaux futurs pourraient explorer d'autres algorithmes d'optimisation numérique basés sur le gradient ou des techniques d'optimisation sans gradient telles que l'optimisation par essaims de particules et les algorithmes génétiques. Ces méthodes pourraient offrir de meilleures propriétés de convergence et de meilleurs temps d'accès, une meilleure évolutivité pour les systèmes qudit à haute dimension ou une meilleure robustesse au bruit. À cet égard, nous avons déjà entamé des travaux exploratoires sur les approches basées sur l'apprentissage automatique. [141] : L'approche aveugle de l'apprentissage par renforcement (RL) profond est conceptuellement intéressante mais s'est avérée difficile à entraîner sur des systèmes quantiques complexes, tandis que nous avons découvert que l'approche du réseau neuronal informé par la physique (PINN) est une technique puissante pour générer des portes de haute fidélité avec des temps de porte très rapides. En outre, les réseaux neuronaux peuvent être facilement entraînés sur des données bruyantes et avec des contraintes et des fonctions de coût arbitraires, ce qui en fait un outil potentiellement puissant pour générer des impulsions robustes aux différentes sources de bruit

et aux erreurs de contrôle.

Cette étude a également introduit une approche hybride, utilisant GRAPE pour la synthèse de portes complexes et le GRD pour d'autres opérations telles que les inversions de phase dans l'opérateur Grover Oracle. En développant ce concept, les travaux futurs pourraient étudier des méthodes hybrides plus sophistiquées qui exploitent les points forts de chaque technique. Par exemple, la GRD pourrait être utilisée pour générer une approximation grossière d'une porte, qui serait ensuite affinée par GRAPE ou par un modèle d'apprentissage automatique formé sur les impulsions de la GRD. Cette stratégie hybride pourrait améliorer l'efficacité et les performances de calcul pour les systèmes de quantification à grande échelle ou bruyants.

Cette étude s'est principalement concentrée sur les modèles de bruit markoviens, où les effets de l'environnement sur le système quantique sont sans mémoire. Cependant, de nombreux systèmes quantiques réalistes, en particulier dans les plateformes solides et moléculaires, présentent un comportement non markovien, où les corrélations environnementales persistent dans le temps. L'extension du cadre pour inclure le bruit non markovien fournirait un modèle plus précis pour les systèmes quantiques, améliorant la robustesse des séquences d'impulsions contre les sources de bruit du monde réel. Des techniques telles que les équations maîtresses sans évolution temporelle ou les modèles hamiltoniens stochastiques pourraient être incorporées pour simuler une telle dynamique.

Les erreurs de contrôle étudiées dans ce travail se limitaient à des erreurs de décalage d'amplitude et de phase constantes et à des erreurs de décalage d'horloge. Les recherches futures pourraient explorer d'autres erreurs de contrôle plus réalistes sur le plan physique, notamment le bruit stochastique dû au bruit thermique et environnemental sur le matériel de contrôle, la bruit entre les canaux d'impulsion, les distorsions de la forme de l'impulsion dues aux limitations de la largeur de bande dans les filtres, la gigue temporelle et l'interaction entre la fréquence et l'amplitude du signal dans les générateurs d'impulsions. Ces erreurs sont courantes dans les systèmes quantiques expérimentaux et peuvent avoir un impact significatif sur la fidélité de la porte. En intégrant ces erreurs dans le cadre de simulation, les chercheurs peuvent développer des séquences d'impulsions plus robustes qui résistent à un plus grand nombre d'imperfections expérimentales.

Malgré les progrès réalisés dans cette étude, il reste plusieurs lacunes que les recherches futures devront combler pour rapprocher l'informatique quantique basée sur le qudit d'une mise en œuvre pratique. Dans l'informatique quantique pratique, les erreurs de porte et la décohérence sont inévitables. Bien que cette étude analyse les effets du bruit et des erreurs de contrôle sur la fidélité de la porte, il sera nécessaire d'explorer des stratégies d'atténuation des erreurs en temps réel. Il s'agit notamment de techniques telles que le découplage dynamique, le contrôle par rétroaction en temps réel et la correction d'erreurs quantiques, qui pourraient être intégrées dans le cadre de contrôle au niveau des impulsions. Ces méthodes permettraient de maintenir une grande fidélité de la porte en présence de bruit environnemental et de contrôles imparfaits.

Cette étude s'est concentrée exclusivement sur la synthèse de portes pour les systèmes à quotient unique. Cependant, pour progresser vers une informatique quantique pratique basée sur les qudits, il faut s'intéresser aux systèmes multi-qudit, dans lesquels les interactions entre les qudits introduisent des complexités supplémentaires. Il est essentiel, dans une prochaine étape, d'étendre le cadre de simulation pour inclure des portes d'intrication multiqudit, telles que des généralisations des portes CNOT, SWAP ou à incrément contrôlé (CINC) à des systèmes de plus haute dimension. En effet, nous avons commencé

à étudier les travaux complémentaires de Brennen *et. al.* qui généralisent l'approche linéaire-algébrique de la décomposition QR en utilisant les réflexions de Householder pour synthétiser la porte d'intrication CINC sur les systèmes à 2 qubits, ne nécessitant qu'un terme de couplage dipolaire à mettre en œuvre. La possibilité de simuler des opérations d'intrication permettrait de concevoir des circuits et des algorithmes quantiques plus complexes dans des architectures basées sur le qudit, et faciliterait une étude beaucoup plus approfondie des différences de performance entre les systèmes multi-qudit et muti-qubit.

Enfin, bien que les résultats théoriques et de simulation présentés ici fournissent des indications précieuses sur la synthèse de portes qudit, une validation expérimentale est nécessaire pour confirmer ces résultats. Nous envisageons ici une collaboration avec un groupe expérimental de la Faculté de chimie de l'Université de Strasbourg, spécialisé dans les techniques de résonance paramagnétique électronique (RPE) pulsée pour les SMM. Cela nous permettrait, dans un premier temps, de tester la mise en œuvre des séquences d'impulsions générées sur des systèmes quantiques réels liés à nos complexes moléculaires lanthanide-organique. Cela nous fournirait un retour d'information crucial sur les défis pratiques de la mise en œuvre des portes quantiques, tels que les sources de bruit spécifiques au système et les limitations de contrôle.

Alors que le matériel quantique continue de se développer, il est de plus en plus nécessaire d'adapter les méthodes de contrôle du niveau d'impulsion à des plateformes spécifiques, telles que les ions piégés, les circuits supraconducteurs ou les systèmes photoniques. Chaque plateforme matérielle présente des contraintes uniques, telles que les limitations de la bande passante, les temps de cohérence du qudit et la résolution du contrôle. Les travaux futurs pourraient consister à optimiser les méthodes de synthèse de portes présentées ici pour des architectures matérielles spécifiques, en veillant à ce que les avantages théoriques se traduisent effectivement par des réalisations expérimentales.

Cette étude constitue une étape cruciale vers la réalisation pratique de l'informatique quantique basée sur le qudit, en offrant un aperçu du contrôle au niveau de l'impulsion, de la synthèse de porte et des effets du bruit et des erreurs de contrôle. En s'appuyant sur cette base, les recherches futures pourront étendre et améliorer les méthodes présentées ici, ce qui nous rapprochera des systèmes quantiques évolutifs et de haute dimension capables de surpasser les ordinateurs classiques. Les défis à relever - évolutivité, résistance au bruit et optimisation du matériel - sont importants, mais les bénéfices potentiels, en particulier dans des domaines tels que le traitement de l'information quantique, la cryptographie et la simulation, en font un domaine de recherche prometteur et passionnant.

Conclusion

Synthèse de la thèse

Cette thèse a entrepris une exploration multidisciplinaire reliant la science de l'information quantique et la théorie de la structure nucléaire, dans le but de faire progresser notre compréhension des interactions hyperfines dans les complexes moléculaires de lanthanide et la fidélité des opérations quantiques dans les systèmes quantiques de haute dimension. Organisée en deux parties principales, la recherche a traversé les domaines de la modélisation de la structure nucléaire et du traitement quantique de l'information avec des qudits, convergeant vers le thème général de l'exploitation des propriétés du spin nucléaire pour les progrès de l'informatique quantique.

Dans Part I, nous nous sommes concentrés sur la structure nucléaire et les anomalies hyperfines des ions lanthanides, établissant une base théorique pour les systèmes de qudits basés sur le spin nucléaire.

Dans Chapter 2, nous avons utilisé le modèle Skyrme-Hartree-Fock-Bardeen-Cooper-Schrieffer (HFBCS) pour élucider la structure nucléaire des isotopes $^{159}_{65}$Tb, $^{161}_{66}$Dy, $^{163}_{66}$Dy, et $^{165}_{67}$Ho. L'approche HFBCS, intégrant les interactions effectives et le blocage auto-cohérent, a permis d'identifier des déformations prononcées dans les distributions de nucléons, en particulier pour les noyaux de dysprosium et d'holmium. Ces déformations ont des implications significatives pour leurs moments magnétiques et quadrupolaires. Alors que les moments quadripolaires ont été prédits avec précision, avec des erreurs relatives inférieures à 5% pour tous les isotopes, les moments dipolaires magnétiques ont montré des déviations, en particulier pour ^{161}Dy, mettant en évidence les domaines dans lesquels le modèle pourrait être affiné. Ces résultats ont validé l'applicabilité du modèle à des structures nucléaires hautement déformées et ont souligné l'importance d'incorporer des corrections relativistes et mésoniques pour améliorer la précision prédictive des fractionnements hyperfins dans les systèmes de spin nucléaire pertinents pour les applications du crédit.

Dans Chapter 3, la structure hyperfine des ions dysprosium de type hydrogène a été disséquée, en mettant l'accent sur les corrections Breit-Rosenthal (BR) et Bohr-Weisskopf (BW), représentant les effets de la taille du noyau et de l'aimantation sur les interactions hyperfines. Des comparaisons détaillées entre les modèles nucléaires, y compris les distributions ponctuelles, sphériques, de Fermi et HFBCS, ont démontré la sensibilité unique des fonctions d'onde muoniques aux structures nucléaires. L'étude des ions électroniques par rapport aux ions muoniques a révélé la sensibilité accrue des systèmes muoniques à la structure nucléaire, avec des corrections BR atteignant jusqu'à 90% dans les atomes muoniques, contre environ 5% dans les systèmes électroniques. De même, les corrections BW ont eu un impact marqué sur la division hyperfine des ions muoniques, atteignant environ 80%, ce qui ouvre une fenêtre unique sur le magnétisme nucléaire. Les anomalies hyperfines calculées entre les isotopes ^{161}Dy et ^{163}Dy ont fourni des indications essentielles sur l'interaction entre la physique nucléaire et la physique atomique, en révélant des différences qui étaient de plusieurs ordres de grandeur plus importantes dans les ions muoniques que dans les ions électroniques. Ces résultats soulignent le potentiel de la spectroscopie muonique pour sonder les propriétés nucléaires avec une précision sans précédent, suggérant que les ions muoniques pourraient servir d'outils essentiels pour affiner les modèles nucléaires et explorer expérimentalement les anomalies hyperfines, en particulier dans le contexte du traitement de l'information quantique.

Part II a fait la transition vers le domaine de l'informatique quantique basée sur le qudit, en explorant la théorie et les applications pratiques des systèmes à haute dimension.

Dans Chapter 4, nous avons analysé l'efficacité et la fidélité des portes dans les systèmes à qudit unique bruyants par rapport aux systèmes à qubits multiples de dimensions d'espace de Hilbert équivalentes. En dérivant une relation de type fluctuation-dissipation pour l'infidélité des portes et en comparant l'efficacité opérationnelle des qudits à celle des qubits, nous avons établi une courbe critique délimitant l'efficacité nécessaire pour les portes de qudit, à savoir $(d^2-1)/3\log_2(d)$. Cette courbe a servi de référence pour déterminer les conditions dans lesquelles les qudits conservent leurs avantages en termes de fidélité au fur et à mesure que la dimension augmente. L'étude a démontré que les systèmes de qudits pouvaient s'étendre jusqu'à des dimensions de l'ordre de $d \approx 40$ dans les plateformes de spin nucléaire tout en conservant des avantages opérationnels. Ces expressions analytiques ont offert des repères essentiels pour optimiser les plateformes qudit en termes de fidélité, en indiquant quand les qudits surpassent les qubits et en fournissant des lignes directrices pratiques pour les architectures de calcul quantique basées sur les qudits.

Dans Chapter 5, nous avons étendu l'analyse de la fidélité au régime non linéaire, en nous concentrant sur la fidélité moyenne des portes (AGF) dans les systèmes quantiques ouverts couplés à un bruit markovien. Les expansions perturbatives théoriques de l'AGF en termes de la constante de couplage sans dimension γt ont fourni des limites universelles et des termes de correction explicites pour des opérateurs d'effondrement arbitraires, étendant le champ d'application de l'analyse du bruit. Les simulations numériques ont confirmé le passage d'un comportement linéaire à un comportement non linéaire dans l'AGF à mesure que l'intensité du bruit augmente, avec des plateaux indiquant des valeurs d'infidélité stables dépendant à la fois du type de porte et de la dimension du qudit. Les limites dérivées ont établi que des portes spécifiques saturaient ces limites : l'identité atteignant les limites inférieures et la porte NOT généralisée atteignant les limites supérieures, la porte de la transformée de Fourier quantique (QFT) atteignant un plateau aux valeurs moyennes de l'AGI telles que définies par la mesure de Haar. La possibilité de séparer les termes dépendants et indépendants de la porte dans les corrections d'ordre supérieur a permis une compréhension plus nuancée de l'impact du bruit sur les différentes portes et dimensions. Cette analyse complète a souligné la nécessité d'inclure des corrections d'ordre supérieur dans la fidélité de la modélisation pour les qudits de haute dimension et a suggéré que la conception de portes dépendantes du bruit pourrait encore améliorer la performance des qudits.

Dans Chapter 6, nous avons examiné la synthèse au niveau de l'impulsion des portes qudit par la décomposition de la rotation de Givens et l'algorithme GRAPE (Gradient Ascent Pulse Engineering). Le développement d'un cadre de simulation modulaire utilisant Python et QuTiP a facilité les comparaisons de ces méthodes en présence de bruit et d'erreurs de contrôle. Les simulations ont révélé que GRAPE excellait dans la génération d'impulsions précises et optimisées pour les systèmes de faible dimension ($d \leq 12$), tandis que Givens offrait une approche efficace en termes de calcul et cohérente pour des dimensions plus importantes ($d \geq 12$). L'approche de Givens, qui est linéaire algébrique, offre une évolutivité et une performance cohérente à travers les dimensions, en particulier pour les systèmes à haute dimension. L'étude de ces méthodes a mis en évidence des compromis importants : GRAPE a fourni des portes plus rapides pour les dimensions inférieures mais a souffert de problèmes d'extensibilité de calcul dans les dimensions supérieures, tandis que Givens, bien que moins flexible, a maintenu

une extensibilité prévisible avec la taille du système. Une approche hybride combinant l'efficacité de Givens et la précision de GRAPE s'est avérée avantageuse, en particulier dans des scénarios complexes tels que la synthèse de la QFT et l'algorithme de recherche de Grover. L'analyse du bruit a confirmé la cohérence des deux méthodes avec les limites universelles dérivées dans Chapter 5, et a mis en évidence les variations distinctes dans la fidélité de la porte, offrant des aperçus clés pour le contrôle du niveau d'impulsion dans l'informatique quantique pratique basée sur le qudit.

Orientations futures de la recherche

La modélisation complète de la structure nucléaire des lanthanides dans Chapter 2 pose une base théorique solide pour comprendre les interactions hyperfines dans les plateformes potentielles de vérification. Cependant, il est essentiel d'affiner le modèle HFBCS pour saisir toute la complexité des interactions entre nucléons, en particulier pour les moments dipolaires magnétiques. L'incorporation de corrections relativistes et de contributions mésoniques pour tenir compte de la dynamique neutron-proton pourrait améliorer de manière significative la précision des prédictions de division hyperfine. L'extension du modèle à des traitements Hartree-Fock-Bogoliubov (HFB) autoconsistants et l'exploration de moments multipolaires d'ordre supérieur, tels que l'octupole ou l'hexadécapole, permettraient de saisir des détails plus fins de la forme nucléaire et des excitations collectives, en particulier dans les noyaux fortement déformés. Ces développements permettraient non seulement de faire progresser la théorie de la structure nucléaire, mais aussi de fournir une base solide pour les plateformes de quantification dans lesquelles les états de spin nucléaire jouent un rôle essentiel.

L'exploration par Chapter 3 des corrections BR et BW dans les ions dysprosium semblables à l'hydrogène souligne le potentiel des systèmes muoniques en tant que sondes précises de la structure nucléaire. Les travaux futurs devraient se concentrer sur l'exploitation de cette sensibilité accrue pour affiner les modèles nucléaires, en corrélant les prédictions théoriques avec les données expérimentales de la spectroscopie muonique et électronique. Les anomalies hyperfines substantielles dans les systèmes muoniques offrent la possibilité d'effectuer des mesures expérimentales directes, qui permettraient de tester rigoureusement les modèles nucléaires et d'obtenir des informations cruciales sur l'interaction entre l'aimantation nucléaire et les interactions hyperfines, ce qui aurait un impact direct sur les applications de l'information quantique basées sur le qudit.

La courbe critique dérivée dans Chapter 4 offre un cadre pour évaluer quand les qudits peuvent surpasser les qubits dans des environnements bruyants. L'extension de cette analyse aux systèmes multi-qudit, en tenant compte des interactions inter-qudit et des effets de bruit corrélés, est cruciale pour déterminer l'extensibilité et la robustesse des architectures qudit. L'étude des effets dépendant de l'hamiltonien sur l'infidélité moyenne des portes (AGI), ainsi que des intégrations logiques de qudit résistantes au bruit, révélera si les avantages des qudits en matière de fidélité persistent lorsque les systèmes s'étendent, et informera la conception d'opérations de qudit résistantes au bruit, en particulier pour l'informatique quantique tolérante aux fautes au-delà de l'ère NISQ.

Dans Chapter 5, les expansions perturbatives détaillées de l'AGF jettent les bases d'une analyse avancée du bruit et de l'optimisation des portes. Les recherches futures devraient intégrer ces termes de correction d'ordre supérieur dans les stratégies d'atténuation des erreurs, les protocoles de contrôle optimal et les intégrations logiques de qudit, en étendant le champ d'application de la synthèse de porte aux opérations d'intrication de qudit

multiples. L'exploration de différents modèles de bruit au-delà du déphasage pur, tels que l'amortissement de l'amplitude et le bruit dépolarisant, améliorera l'applicabilité du cadre sur diverses plateformes quantiques et affinera notre compréhension des impacts du bruit sur les systèmes de haute dimension.

La comparaison des techniques de synthèse de portes dans Chapter 6 met en évidence les compromis entre la décomposition de Givens et GRAPE dans le contrôle du qudit. Pour affiner encore ces méthodes, les travaux futurs devraient explorer l'optimisation des hyperparamètres de GRAPE et étudier des techniques d'optimisation alternatives, y compris des approches sans gradient comme l'optimisation par essaims de particules ou des stratégies basées sur l'apprentissage automatique comme les réseaux neuronaux informés par la physique (PINN). Une extension significative consisterait à intégrer ces techniques à des protocoles de correction d'erreur, à un contrôle par rétroaction en temps réel et à la conception d'impulsions adaptées au bruit. Le potentiel des stratégies de contrôle hybrides, combinant l'efficacité de Givens et la précision de GRAPE, offre une direction prometteuse pour les systèmes quantiques à grande échelle, où l'équilibre entre l'efficacité de calcul et la précision de contrôle est critique. L'extension du cadre pour prendre en compte le bruit non markovien, les erreurs de contrôle complexes et les interactions entre les qubits sera essentielle pour développer des circuits quantiques évolutifs, robustes et basés sur les qubits.

Des avancées récentes ont démontré que les systèmes qudit peuvent être manipulés à l'aide d'interactions à deux photons assistées par Raman, ce qui permet le contrôle précis d'états de haute dimension dans des circuits supraconducteurs. Ces circuits agissent comme des oscillateurs harmoniques non linéaires, permettant le codage de plusieurs états dans un seul qudit et la création d'états squeezed et les états du chat de Schrödinger. Ce contrôle à haute dimension fournit non seulement une plateforme pour la mise à l'échelle des dispositifs quantiques, mais augmente également la résistance au bruit, un facteur critique pour l'informatique quantique tolérante aux pannes. Les développements dans les processeurs qudit programmables, tels que la mise en œuvre d'unités de traitement à deux qu-4-its ($d = 4$) basées sur la photonique intégrée, soulignent les progrès rapides réalisés dans ce domaine et ouvrent de nouvelles opportunités pour la réalisation de circuits quantiques pratiques et évolutifs basés sur le qudit.

Dans l'ensemble, cette thèse apporte des contributions significatives à la compréhension et au développement de l'informatique quantique basée sur le qudit, en fournissant des bases théoriques pour la structure nucléaire dans les interactions hyperfines, une analyse détaillée du bruit pour l'optimisation de la fidélité, et des lignes directrices pratiques pour la synthèse des portes. L'approche multidisciplinaire, qui fait le lien entre la physique nucléaire et de l'information quantique, fait non seulement progresser la théorie des interactions hyperfines et l'analyse du bruit, mais fournit également une base solide pour le développement d'opérations quantiques évolutives et de haute fidélité. Les futurs travaux expérimentaux, en particulier dans les plateformes de qudit basées sur le spin nucléaire et leurs techniques de contrôle associées, seront déterminants pour valider et développer les connaissances théoriques acquises ici, ouvrant ainsi la voie à des systèmes de calcul quantique pratiques et de haute dimension.

Références citées dans ce chapitre

[1] O. Ezratty. "Perspective on superconducting qubit quantum computing". In: *The European Physical Journal A* 59.5 (May 2, 2023), p. 94. DOI: 10.1140/epja/s10050-023-01006-7.

[2] R. P. Feynman. "Simulating physics with computers". In: *International Journal of Theoretical Physics* 21.6 (June 1982), pp. 467–488. DOI: 10.1007/BF02650179.

[3] "40 years of quantum computing". In: *Nature Reviews Physics* 4.1 (Jan. 10, 2022), pp. 1–1. DOI: 10.1038/s42254-021-00410-6.

[4] J. I. Manin. "Mathematics as Metaphor: Selected Essays of Yuri I. Manin". In: *Philosophia Mathematica* 17.1 (Apr. 1, 2008), pp. 122–123. DOI: 10.1093/philmat/nkn013.

[5] P. Benioff. "The computer as a physical system: A microscopic quantum mechanical Hamiltonian model of computers as represented by Turing machines". In: *Journal of Statistical Physics* 22.5 (May 1980), pp. 563–591. DOI: 10.1007/BF01011339.

[6] D. Deutsch. "Quantum theory, the Church–Turing principle and the universal quantum computer". In: *Proceedings of the Royal Society of London. A. Mathematical and Physical Sciences* 400.1818 (July 8, 1985), pp. 97–117. DOI: 10.1098/rspa.1985.0070.

[7] P. W. Shor. "Polynomial-Time Algorithms for Prime Factorization and Discrete Logarithms on a Quantum Computer". In: *SIAM Journal on Computing* 26.5 (Oct. 1997), pp. 1484–1509. DOI: 10.1137/S0097539795293172.

[8] L. K. Grover. "A fast quantum mechanical algorithm for database search". In: *Proceedings of the twenty-eighth annual ACM symposium on Theory of computing - STOC '96*. Philadelphia, Pennsylvania, United States: ACM Press, 1996, pp. 212–219. DOI: 10.1145/237814.237866.

[9] S. Lloyd. "Universal Quantum Simulators". In: *Science* 273.5278 (Aug. 23, 1996), pp. 1073–1078. DOI: 10.1126/science.273.5278.1073.

[10] M. Veldhorst, H. G. J. Eenink, et al. "Silicon CMOS architecture for a spin-based quantum computer". In: *Nature Communications* 8.1 (Dec. 15, 2017), p. 1766. DOI: 10.1038/s41467-017-01905-6.

[11] M. F. Gonzalez-Zalba, S. De Franceschi, et al. "Scaling silicon-based quantum computing using CMOS technology". In: *Nature Electronics* 4.12 (Dec. 20, 2021), pp. 872–884. DOI: 10.1038/s41928-021-00681-y.

[12] D. Spicer. "The First Computers: History and Architectures (review)". In: *Technology and Culture* 42.3 (July 2001), pp. 615–617. DOI: 10.1353/tech.2001.0140.

[13] M. Kjaergaard, M. E. Schwartz, et al. *Programming a quantum computer with quantum instructions*. Dec. 28, 2020. DOI: https://doi.org/10.48550/arXiv.2001.08838.

[14] I. Pogorelov et al. "Compact Ion-Trap Quantum Computing Demonstrator". In: *PRX Quantum* 2.2 (June 2021), p. 020343. DOI: 10.1103/PRXQuantum.2.020343.

[15] C. D. Bruzewicz, J. Chiaverini, et al. "Trapped-ion quantum computing: Progress and challenges". In: *Applied Physics Reviews* 6.2 (June 1, 2019), p. 021314. DOI: 10.1063/1.5088164.

[16] Y. Chi, J. Huang, et al. "A programmable qudit-based quantum processor". In: *Nature Communications* 13.1 (Mar. 4, 2022), p. 1166. DOI: 10.1038/s41467-022-28767-x.

[17] S. Slussarenko and G. J. Pryde. "Photonic quantum information processing: A concise review". In: *Applied Physics Reviews* 6.4 (Dec. 1, 2019), p. 041303. DOI: 10.1063/1.5115814.

[18] M. Morgado and S. Whitlock. "Quantum simulation and computing with Rydberg-interacting qubits". In: *AVS Quantum Science* 3.2 (June 1, 2021), p. 023501. DOI: 10.1116/5.0036562.

[19] I. S. Madjarov et al. "High-fidelity entanglement and detection of alkaline-earth Rydberg atoms". In: *Nature Physics* 16.8 (Aug. 2020), pp. 857–861. DOI: 10.1038/s41567-020-0903-z.

[20] A. Chiesa et al. "Blueprint for a molecular-spin quantum processor". In: *Physical Review Applied* 19 (June 2023). Publisher: American Physical Society, p. 064060. DOI: 10.1103/PhysRevApplied.19.064060.

[21] E. Moreno-Pineda, C. Godfrin, et al. "Molecular Spin Qudits for Quantum Algorithms". In: *Chemical Society Reviews* 47.2 (2018), pp. 501–513. DOI: 10.1039/c5cs00933b.

[22] Alejandro Gaita-Ariño, Fernando Luis, et al. "Molecular spins for quantum computation." In: *Nature Chemistry* 11.4 (Apr. 1, 2019). MAG ID: 2924254540, pp. 301–309. DOI: 10.1038/s41557-019-0232-y.

[23] G. Burkard, T. D. Ladd, et al. "Semiconductor spin qubits". In: *Reviews of Modern Physics* 95.2 (June 14, 2023), p. 025003. DOI: 10.1103/RevModPhys.95.025003.

[24] X. Zhang, H.-O. Li, et al. "Semiconductor quantum computation". In: *National Science Review* 6.1 (Jan. 1, 2019), pp. 32–54. DOI: 10.1093/nsr/nwy153.

[25] F. Flamini, N. Spagnolo, et al. "Photonic quantum information processing: a review". In: *Reports on Progress in Physics* 82.1 (Jan. 1, 2019), p. 016001. DOI: 10.1088/1361-6633/aad5b2.

[26] F. Arute, K. Arya, et al. "Quantum supremacy using a programmable superconducting processor". In: *Nature* 574.7779 (Oct. 24, 2019), pp. 505–510. DOI: 10.1038/s41586-019-1666-5.

[27] *First IBM Quantum Data Center in Europe Opens; Will Include IBM's Most Performant Quantum Systems*. IBM Newsroom. URL: https://newsroom.ibm.com/2024-10-01-first-ibm-quantum-data-center-in-europe-opens-will-include-ibms-most-performant-quantum-systems (visited on 10/02/2024).

[28] D. Castelvecchi. "Quantum computers ready to leap out of the lab in 2017". In: *Nature* 541.7635 (Jan. 2017), pp. 9–10. DOI: 10.1038/541009a.

[29] S. Krinner et al. "Realizing repeated quantum error correction in a distance-three surface code". In: *Nature* 605.7911 (May 2022), pp. 669–674. DOI: 10.1038/s41586-022-04566-8.

[30] D. P. DiVincenzo. "The Physical Implementation of Quantum Computation". In: *Fortschritte der Physik* 48.9 (Sept. 2000), pp. 771–783. DOI: 10.1002/1521-3978(200009)48:9/11<771::AID-PROP771>3.0.CO;2-E.

[31] Y. Wang, Z. Hu, et al. "Qudits and High-Dimensional Quantum Computing". In: *Frontiers in Physics* 8 (Nov. 10, 2020), p. 589504. DOI: 10.3389/fphy.2020.589504.

[32] N. P. Brusentsov and J. Ramil Alvarez. "Ternary Computers: The Setun and the Setun 70". In: *Perspectives on Soviet and Russian Computing*. Ed. by J. Impagliazzo and E. Proydakov. Vol. 357. IFIP Advances in Information and Communication Technology. Berlin, Heidelberg: Springer Berlin Heidelberg, 2011, pp. 74–80. DOI: 10.1007/978-3-642-22816-2_10.

[33] A. Chiesa, F. Petiziol, et al. “Embedded quantum-error correction and controlled-phase gate for molecular spin qubits”. In: *AIP Advances* 11.2 (Feb. 1, 2021), p. 025134. DOI: 10.1063/9.0000166.

[34] N. P. D. Sawaya, T. Menke, et al. “Resource-efficient digital quantum simulation of d-level systems for photonic, vibrational, and spin-s Hamiltonians”. In: *npj Quantum Information* 6.1 (June 2, 2020), p. 49. DOI: 10.1038/s41534-020-0278-0.

[35] M. N. Leuenberger and D. Loss. “Grover algorithm for large nuclear spins in semiconductors”. In: *Physical Review B* 68.16 (Oct. 16, 2003), p. 165317. DOI: 10.1103/PhysRevB.68.165317.

[36] A. Mair, A. Vaziri, et al. “Entanglement of the orbital angular momentum states of photons”. In: *Nature* 412.6844 (July 2001), pp. 313–316. DOI: 10.1038/35085529.

[37] F. A. An, A. Ransford, et al. “High Fidelity State Preparation and Measurement of Ion Hyperfine Qubits with I $>$ 1 2”. In: *Physical Review Letters* 129.13 (Sept. 19, 2022), p. 130501. DOI: 10.1103/PhysRevLett.129.130501.

[38] C. Adambukulam, B. C. Johnson, et al. “Hyperfine Spectroscopy and Fast, All-Optical Arbitrary State Initialization and Readout of a Single, Ten-Level Ge 73 Vacancy Nuclear Spin Qudit in Diamond”. In: *Physical Review Letters* 132.6 (Feb. 9, 2024), p. 060603. DOI: 10.1103/PhysRevLett.132.060603.

[39] B. L. Brock, S. Singh, et al. *Quantum Error Correction of Qudits Beyond Break-even*. Sept. 23, 2024. DOI: https://doi.org/10.48550/arXiv.2409.15065.

[40] L. E. Fischer, D. Miller, et al. “Ancilla-free implementation of generalized measurements for qubits embedded in a qudit space”. In: *Physical Review Research* 4.3 (July 11, 2022), p. 033027. DOI: 10.1103/PhysRevResearch.4.033027.

[41] E. Moreno-Pineda and W. Wernsdorfer. “Measuring molecular magnets for quantum technologies”. In: *Nature Reviews Physics* 3.9 (Sept. 2021), pp. 645–659. DOI: 10.1038/s42254-021-00340-3.

[42] S. Thiele, F. Balestro, et al. “Electrically driven nuclear spin resonance in single-molecule magnets”. In: *Science* 344.6188 (June 6, 2014), pp. 1135–1138. DOI: 10.1126/science.1249802.

[43] C. Godfrin, A. Ferhat, et al. “Operating Quantum States in Single Magnetic Molecules: Implementation of Grover’s Quantum Algorithm”. In: *Physical Review Letters* 119.18 (Nov. 2, 2017), p. 187702. DOI: 10.1103/PhysRevLett.119.187702.

[44] A. L. Thomas. *Phthalocyanine Research and Applications*. 1st ed. Boca Raton: CRC Press, Sept. 25, 2024. DOI: 10.1201/9781003574231.

[45] P. Gregory. “Industrial applications of phthalocyanines”. In: *Journal of Porphyrins and Phthalocyanines* 04.4 (June 2000). Publisher: World Scientific Publishing Co., pp. 432–437. DOI: 10.1002/(SICI)1099-1409(200006/07)4:4<432::AID-JPP254>3.0.CO;2-N.

[46] B. E. Williamson, T. C. VanCott, et al. “Determination of the ground state of manganese phthalocyanine in an argon matrix using magnetic circular dichroism and absorption spectroscopy”. In: *Journal of the American Chemical Society* 114.7 (Mar. 1992), pp. 2412–2419. DOI: 10.1021/ja00033a016.

[47] Naoto Ishikawa, Miki Sugita, et al. “Lanthanide Double-Decker Complexes Functioning as Magnets at the Single-Molecular Level”. In: *Journal of the American Chemical Society* 125.29 (June 25, 2003), pp. 8694–8695. DOI: 10.1021/ja029629n.

[48] N. Ishikawa, M. Sugita, et al. "Quantum Tunneling of Magnetization in Lanthanide Single-Molecule Magnets". In: *Angewandte Chemie International Edition* 44.19 (May 6, 2005), pp. 2931–2935. DOI: 10.1002/anie.200462638.

[49] L. Thomas, F. Lionti, et al. "Macroscopic quantum tunnelling of magnetization in a single crystal of nanomagnets". In: *Nature* 383.6596 (Sept. 1996), pp. 145–147. DOI: 10.1038/383145a0.

[50] H. Biard, E. Moreno-Pineda, et al. "Increasing the Hilbert space dimension using a single coupled molecular spin". In: *Nature Communications* 12.1 (Dec. 2021), p. 4443. DOI: 10.1038/s41467-021-24693-6.

[51] W. Wernsdorfer. "From micro- to nano-SQUIDs: applications to nanomagnetism". In: *Superconductor Science and Technology* 22.6 (June 1, 2009), p. 064013. DOI: 10.1088/0953-2048/22/6/064013.

[52] Romain Vincent, Svetlana Klyatskaya, et al. "Electronic read-out of a single nuclear spin using a molecular spin transistor". In: *Nature* 488.7411 (Aug. 16, 2012), pp. 357–360. DOI: 10.1038/nature11341.

[53] J. Angel and P. Sandars. "The hyperfine structure Stark effect I. Theory". In: *Proceedings of the Royal Society of London. Series A. Mathematical and Physical Sciences* 305.1480 (May 21, 1968), pp. 125–138. DOI: 10.1098/rspa.1968.0109.

[54] M. N. Leuenberger and D. Loss. "Quantum computing in molecular magnets". In: *Nature* 410.6830 (Apr. 2001), pp. 789–793. DOI: 10.1038/35071024.

[55] M. N. Leuenberger, D. Loss, et al. "Quantum Information Processing with Large Nuclear Spins in GaAs Semiconductors". In: *Physical Review Letters* 89.20 (Oct. 28, 2002), p. 207601. DOI: 10.1103/PhysRevLett.89.207601.

[56] W. Wernsdorfer and M. Ruben. "Synthetic Hilbert Space Engineering of Molecular Qu *d* its: Isotopologue Chemistry". In: *Advanced Materials* 31.26 (June 2019), p. 1806687. DOI: 10.1002/adma.201806687.

[57] K. Najafi, A. L. Wysocki, et al. "Toward Long-Range Entanglement between Electrically Driven Single-Molecule Magnets". In: *The Journal of Physical Chemistry Letters* 10.23 (Dec. 5, 2019), pp. 7347–7355. DOI: 10.1021/acs.jpclett.9b03131.

[58] E. Moreno-Pineda, S. Klyatskaya, et al. "Observation of Cooperative Electronic Quantum Tunneling: Increasing Accessible Nuclear States in a Molecular Qudit". In: *Inorganic Chemistry* 57.16 (Aug. 20, 2018), pp. 9873–9879. DOI: 10.1021/acs.inorgchem.8b00823.

[59] W. Gerlach and O. Stern. "Der experimentelle Nachweis der Richtungsquantelung im Magnetfeld". In: *Zeitschrift für Physik* 9.1 (Dec. 1, 1922), pp. 349–352. DOI: 10.1007/BF01326983.

[60] E. M. Purcell, H. C. Torrey, et al. "Resonance Absorption by Nuclear Magnetic Moments in a Solid". In: *Physical Review* 69.1 (Jan. 1, 1946), pp. 37–38. DOI: 10.1103/PhysRev.69.37.

[61] A. Caneschi, D. Gatteschi, et al. "Toward molecular magnets: the metal-radical approach". In: *Accounts of Chemical Research* 22.11 (Nov. 1, 1989), pp. 392–398. DOI: 10.1021/ar00167a004.

[62] G. Christou, D. Gatteschi, et al. "Single-Molecule Magnets". In: *MRS Bulletin* 25.11 (Nov. 2000), pp. 66–71. DOI: 10.1557/mrs2000.226.

[63] D. Gatteschi, R. Sessoli, et al. *Molecular Nanomagnets*. Oxford University Press, Mar. 2, 2006. DOI: 10.1093/acprof:oso/9780198567530.001.0001.

[64] J. E. Rosenthal and G. Breit. "The Isotope Shift in Hyperfine Structure". In: *Physical Review* 41.4 (Aug. 15, 1932), pp. 459–470. DOI: 10.1103/PhysRev.41.459.

[65] A. Bohr and V. F. Weisskopf. "The Influence of Nuclear Structure on the Hyperfine Structure of Heavy Elements". In: *Physical Review* 77.1 (Jan. 1, 1950), pp. 94–98. DOI: 10.1103/PhysRev.77.94.

[66] C. D. Anderson and S. H. Neddermeyer. "Cloud Chamber Observations of Cosmic Rays at 4300 Meters Elevation and Near Sea-Level". In: *Physical Review* 50.4 (Aug. 15, 1936), pp. 263–271. DOI: 10.1103/PhysRev.50.263.

[67] V. W. Hughes, D. W. McColm, et al. "Formation of Muonium and Observation of its Larmor Precession". In: *Physical Review Letters* 5.2 (July 15, 1960), pp. 63–65. DOI: 10.1103/PhysRevLett.5.63.

[68] K. P. Jungmann. "Past, Present and Future of Muonium". In: *In Memory of Vernon Willard Hughes*. Proceedings of the Memorial Symposium in Honor of Vernon Willard Hughes. Yale University, USA: World Scientific, Dec. 2004, pp. 134–153. DOI: 10.1142/9789812702425_0009.

[69] G. Lospalluto, A. Antognini, et al. "Towards muon cooling at the Paul Scherrer Institute". In: *Proceedings of Muon4Future Workshop — PoS(Muon4Future2023)*. Muon4Future Workshop. Istituto Veneto di Lettere, Scienze ed Arti - Palazzo Franchetti, Venezia, Italy: Sissa Medialab, Mar. 15, 2024, p. 009. DOI: 10.22323/1.452.0009.

[70] K. Shimomura, A. Koda, et al. "Pulsed muon facility of J-PARC MUSE". In: *Interactions* 245.1 (Mar. 5, 2024), p. 31. DOI: 10.1007/s10751-024-01863-8.

[71] E. L. Hahn. "Spin Echoes". In: *Physical Review* 80.4 (Nov. 15, 1950), pp. 580–594. DOI: 10.1103/PhysRev.80.580.

[72] M. H. Levitt. "Composite pulses". In: *Progress in Nuclear Magnetic Resonance Spectroscopy* 18.2 (Jan. 1986), pp. 61–122. DOI: 10.1016/0079-6565(86)80005-X.

[73] A. P. Peirce, M. A. Dahleh, et al. "Optimal control of quantum-mechanical systems: Existence, numerical approximation, and applications". In: *Physical Review A* 37.12 (June 1, 1988), pp. 4950–4964. DOI: 10.1103/PhysRevA.37.4950.

[74] C. Brif, R. Chakrabarti, et al. "Control of quantum phenomena: past, present and future". In: *New Journal of Physics* 12.7 (July 1, 2010), p. 075008. DOI: 10.1088/1367-2630/12/7/075008.

[75] J. Preskill. "Quantum Computing in the NISQ era and beyond". In: *Quantum* 2 (Aug. 6, 2018), p. 79. DOI: 10.22331/q-2018-08-06-79.

[76] J. P. Dowling and G. J. Milburn. "Quantum technology: the second quantum revolution". In: *Philosophical Transactions of the Royal Society of London. Series A: Mathematical, Physical and Engineering Sciences* 361.1809 (Aug. 15, 2003). Ed. by A. G. J. MacFarlane, pp. 1655–1674. DOI: 10.1098/rsta.2003.1227.

[77] Clément Godfrin, Stefan Thiele, et al. "Electrical Read-Out of a Single Spin Using an Exchange-Coupled Quantum Dot". In: *ACS Nano* 11.4 (Apr. 14, 2017). MAG ID: 2606235355, pp. 3984–3989. DOI: 10.1021/acsnano.7b00451.

[78] C. Godfrin, R. Ballou, et al. "Generalized Ramsey interferometry explored with a single nuclear spin qudit". In: *npj Quantum Information* 4.1 (Dec. 2018), p. 53. DOI: 10.1038/s41534-018-0101-3.

[79] M. James. "Optimal Quantum Control Theory". In: *Annual Review of Control, Robotics, and Autonomous Systems* 4.1 (May 3, 2021), pp. 343–367. DOI: 10.1146/annurev-control-061520-010444.

[80] D. D'Alessandro. *Introduction to quantum control and dynamics*. 2nd edition. Advances in mathematics series. Boca Raton: CRC Press, 2021.

[81] I. R. Sola, B. Y. Chang, et al. "Quantum Control in Multilevel Systems". In: *Advances In Atomic, Molecular, and Optical Physics*. Vol. 67. Elsevier, 2018, pp. 151–256. DOI: 10.1016/bs.aamop.2018.02.003.

[82] M. A. Nielsen and I. L. Chuang. *Quantum Computation and Quantum Information: 10th Anniversary Edition*. Cambridge: Cambridge University Press, 2010. DOI: 10.1017/CBO9780511976667.

[83] V. Gorini, A. Kossakowski, et al. "Completely positive dynamical semigroups of N -level systems". In: *Journal of Mathematical Physics* 17.5 (May 1, 1976), pp. 821–825. DOI: 10.1063/1.522979.

[84] G. Lindblad. "On the generators of quantum dynamical semigroups". In: *Communications in Mathematical Physics* 48.2 (June 1976), pp. 119–130. DOI: 10.1007/BF01608499.

[85] D. Manzano. "A short introduction to the Lindblad master equation". In: *AIP Advances* 10.2 (Feb. 1, 2020), p. 025106. DOI: 10.1063/1.5115323.

[86] H.-P. Breuer, E.-M. Laine, et al. "*Colloquium* : Non-Markovian dynamics in open quantum systems". In: *Reviews of Modern Physics* 88.2 (Apr. 19, 2016), p. 021002. DOI: 10.1103/RevModPhys.88.021002.

[87] C. G. Almudever, L. Lao, et al. "The engineering challenges in quantum computing". In: *Design, Automation & Test in Europe Conference & Exhibition (DATE), 2017*. 2017 Design, Automation & Test in Europe Conference & Exhibition (DATE). Lausanne, Switzerland: IEEE, Mar. 2017, pp. 836–845. DOI: 10.23919/DATE.2017.7927104.

[88] C. G. Almudever and E. Alarcon. "Structured Optimized Architecting of Full-Stack Quantum Systems in the NISQ era". In: *2021 Design, Automation & Test in Europe Conference & Exhibition (DATE)*. 2021 Design, Automation & Test in Europe Conference & Exhibition (DATE). Grenoble, France: IEEE, Feb. 1, 2021, pp. 762–767. DOI: 10.23919/DATE51398.2021.9474197.

[89] M. Grassl, L. Kong, et al. "Quantum Error-Correcting Codes for Qudit Amplitude Damping". In: *IEEE Transactions on Information Theory* 64.6 (June 2018), pp. 4674–4685. DOI: 10.1109/TIT.2018.2790423.

[90] F. Petiziol, A. Chiesa, et al. "Counteracting dephasing in Molecular Nanomagnets by optimized qudit encodings". In: *npj Quantum Information* 7.1 (Aug. 26, 2021), p. 133. DOI: 10.1038/s41534-021-00466-3.

[91] A. Chiesa, E. Macaluso, et al. "Molecular Nanomagnets as Qubits with Embedded Quantum-Error Correction". In: *The Journal of Physical Chemistry Letters* 11.20 (Oct. 15, 2020), pp. 8610–8615. DOI: 10.1021/acs.jpclett.0c02213.

[92] R. F. Uy and D. A. Gangloff. *Qudit-based quantum error-correcting codes from irreducible representations of SU(d)*. Oct. 3, 2024. DOI: 10.48550/arXiv.2410.02407.

[93] E. D. Sontag. *Mathematical Control Theory*. Red. by J. E. Marsden, L. Sirovich, et al. Vol. 6. Texts in Applied Mathematics. New York, NY: Springer New York, 1998. DOI: 10.1007/978-1-4612-0577-7.

[94] C. P. Koch, U. Boscain, et al. "Quantum optimal control in quantum technologies. Strategic report on current status, visions and goals for research in Europe". In: *EPJ Quantum Technology* 9.1 (Dec. 2022), p. 19. DOI: 10.1140/epjqt/s40507-022-00138-x.

[95] S. J. Glaser, U. Boscain, et al. "Training Schrödinger's cat: quantum optimal control: Strategic report on current status, visions and goals for research in Europe".

In: *The European Physical Journal D* 69.12 (Dec. 2015), p. 279. DOI: 10.1140/epjd/e2015-60464-1.

[96] G. Brennen, D. O'Leary, et al. "Criteria for exact qudit universality". In: *Physical Review A* 71.5 (May 16, 2005), p. 052318. DOI: 10.1103/PhysRevA.71.052318.

[97] N. Khaneja, T. Reiss, et al. "Optimal control of coupled spin dynamics: design of NMR pulse sequences by gradient ascent algorithms". In: *Journal of Magnetic Resonance* 172.2 (Feb. 2005), pp. 296–305. DOI: 10.1016/j.jmr.2004.11.004.

[98] G. E. Karniadakis, I. G. Kevrekidis, et al. "Physics-informed machine learning". In: *Nature Reviews Physics* 3.6 (May 24, 2021), pp. 422–440. DOI: 10.1038/s42254-021-00314-5.

[99] M. Raissi, P. Perdikaris, et al. "Physics-informed neural networks: A deep learning framework for solving forward and inverse problems involving nonlinear partial differential equations". In: *Journal of Computational Physics* 378 (Feb. 2019), pp. 686–707. DOI: 10.1016/j.jcp.2018.10.045.

[100] S. Mowlavi and S. Nabi. "Optimal control of PDEs using physics-informed neural networks". In: *Journal of Computational Physics* 473 (Jan. 2023), p. 111731. DOI: 10.1016/j.jcp.2022.111731.

[101] A. D. Jagtap, K. Kawaguchi, et al. "Adaptive activation functions accelerate convergence in deep and physics-informed neural networks". In: *Journal of Computational Physics* 404 (Mar. 2020), p. 109136. DOI: 10.1016/j.jcp.2019.109136.

[102] A. Norambuena, M. Mattheakis, et al. "Physics-Informed Neural Networks for Quantum Control". In: *Physical Review Letters* 132.1 (Jan. 3, 2024), p. 010801. DOI: 10.1103/PhysRevLett.132.010801.

[103] N. B. Dehaghani and A. P. Aguiar. *An Application of Pontryagin Neural Networks to Solve Optimal Quantum Control Problems*. Feb. 1, 2023. DOI: https://doi.org/10.48550/arXiv.2302.09143.

[104] P. Ring and P. Schuck. *The nuclear many body problem*. 1. ed., 3. print., study ed. Texts and monographs in physics. Berlin Heidelberg: Springer, 2004. 716 pp.

[105] J. Stone and P.-G. Reinhard. "The Skyrme interaction in finite nuclei and nuclear matter". In: *Progress in Particle and Nuclear Physics* 58.2 (Apr. 2007), pp. 587–657. DOI: 10.1016/j.ppnp.2006.07.001.

[106] M. Bender, P.-H. Heenen, et al. "Self-consistent mean-field models for nuclear structure". In: *Reviews of Modern Physics* 75.1 (Jan. 23, 2003), pp. 121–180. DOI: 10.1103/RevModPhys.75.121.

[107] L. Bonneau, N. Minkov, et al. "Effect of core polarization on magnetic dipole moments in deformed odd-mass nuclei". In: *Physical Review C* 91.5 (May 11, 2015), p. 054307. DOI: 10.1103/PhysRevC.91.054307.

[108] N. Minkov, A. Pálffy, et al. "Skyrme-Hartree-Fock-BCS approach to Th 229 m and neighboring nuclei". In: *Physical Review C* 110.3 (Sept. 26, 2024), p. 034327. DOI: 10.1103/PhysRevC.110.034327.

[109] G. Tessitore, G. A. Mandl, et al. "The role of lanthanide luminescence in advancing technology". In: *RSC Advances* 13.26 (2023), pp. 17787–17811. DOI: 10.1039/D3RA00991B.

[110] H. Carvajal Gallego, J. Deprince, et al. "Overview of the contributions from all lanthanide elements to kilonova opacity in the temperature range from 25 000 to 40 000 K". In: *Astronomy & Astrophysics* 685 (May 2024), A91. DOI: 10.1051/0004-6361/202347723.

[111] D. Serrano, S. K. Kuppusamy, et al. "Ultra-narrow optical linewidths in rare-earth molecular crystals". In: *Nature* 603.7900 (Mar. 10, 2022), pp. 241–246. DOI: 10.1038/s41586-021-04316-2.

[112] N. Stone. "Table of nuclear magnetic dipole and electric quadrupole moments". In: *Atomic Data and Nuclear Data Tables* 90.1 (May 2005), pp. 75–176. DOI: 10.1016/j.adt.2005.04.001.

[113] C. Schwartz. "Theory of Hyperfine Structure". In: *Physical Review* 97.2 (Jan. 15, 1955), pp. 380–395. DOI: 10.1103/PhysRev.97.380.

[114] J. Persson. *Muonic Hyperfine Structure and the Bohr-Weisskopf Effect*. Aug. 11, 2023. DOI: 10.20944/preprints202308.0903.v1.

[115] B. M. Roberts and J. S. M. Ginges. "Hyperfine anomaly in heavy atoms and its role in precision atomic searches for new physics". In: *Physical Review A* 104.2 (Aug. 27, 2021), p. 022823. DOI: 10.1103/PhysRevA.104.022823.

[116] A. Knecht, A. Skawran, et al. "Study of nuclear properties with muonic atoms". In: *The European Physical Journal Plus* 135.10 (Oct. 2020), p. 777. DOI: 10.1140/epjp/s13360-020-00777-y.

[117] A. Skawran, A. Adamczak, et al. "Towards nuclear structure with radioactive muonic atoms". In: *Il Nuovo Cimento C* 42.203 (Sept. 20, 2019), pp. 1–4. DOI: 10.1393/ncc/i2019-19125-7.

[118] P. Strasser, A. Taniguchi, et al. "Muon spectroscopy with trace alkaline-earth and rare-earth isotopes implanted in solid D2". In: *Hyperfine Interactions* 193.1 (Sept. 2009), pp. 121–127. DOI: 10.1007/s10751-009-0055-0.

[119] T. Y. Saito, M. Niikura, et al. *Muonic X-Ray Measurement for the Nuclear Charge Distribution: the Case of Stable Palladium Isotopes*. Apr. 7, 2022.

[120] A. Antognini, N. Berger, et al. "Measurement of the quadrupole moment of Re 185 and Re 187 from the hyperfine structure of muonic X rays". In: *Physical Review C* 101.5 (May 22, 2020), p. 054313. DOI: 10.1103/PhysRevC.101.054313.

[121] T. Okumura, T. Azuma, et al. *Few-electron highly charged muonic Ar atoms verified by electronic K x rays*. July 10, 2024.

[122] D. Janković, J.-G. Hartmann, et al. "Noisy qudit vs multiple qubits: conditions on gate efficiency for enhancing fidelity". In: *npj Quantum Information* 10.1 (June 10, 2024), p. 59. DOI: 10.1038/s41534-024-00829-6.

[123] D. Jankovic. *Source Code for data generation and pulses data for Noisy Qudit vs Multiple Qubits*. In collab. with D. Jankovic. 2024. DOI: 10.35097/1953.

[124] A. S. Nikolaeva, E. O. Kiktenko, et al. "Efficient realization of quantum algorithms with qudits". In: *EPJ Quantum Technology* 11.1 (Dec. 2024), p. 43. DOI: 10.1140/epjqt/s40507-024-00250-0.

[125] N. Cao, J. Lin, et al. "NISQ: Error Correction, Mitigation, and Noise Simulation". In: (Nov. 3, 2021). DOI: 10.48550/arXiv.2111.02345.

[126] M. A. Nielsen. "A simple formula for the average gate fidelity of a quantum dynamical operation". In: *Physics Letters A* 303.4 (Oct. 2002), pp. 249–252. DOI: 10.1016/S0375-9601(02)01272-0.

[127] J. R. Johansson, P. D. Nation, et al. "QuTiP: An open-source Python framework for the dynamics of open quantum systems". In: *Computer Physics Communications* 183.8 (Aug. 2012), pp. 1760–1772. DOI: 10.1016/j.cpc.2012.02.021.

[128] J. R. Johansson, P. D. Nation, et al. "QuTiP 2: A Python framework for the dynamics of open quantum systems". In: *Computer Physics Communications* 184.4 (Apr. 2013), pp. 1234–1240. DOI: 10.1016/j.cpc.2012.11.019.

[129] J.-G. Hartmann, D. Janković, et al. “Nonlinearity of the Fidelity in Open Qudit Systems: Gate and Noise Dependence in High-dimensional Quantum Computing”. In: *Quantum* 9 (Apr. 7, 2025), p. 1690. DOI: 10.22331/q-2025-04-07-1690.

[130] J.-G. Hartmann, D. Janković, et al. *Code and Data for "Nonlinearity of the Fidelity in Open Qudit Systems: Gate and Noise Dependence in High-dimensional Quantum Computing"*. Zenodo, Mar. 19, 2025. DOI: 10.5281/ZENODO.13618284.

[131] N. P. De Leon, K. M. Itoh, et al. “Materials challenges and opportunities for quantum computing hardware”. In: *Science* 372.6539 (Apr. 16, 2021), eabb2823. DOI: 10.1126/science.abb2823.

[132] M. Ringbauer, M. Meth, et al. “A universal qudit quantum processor with trapped ions”. In: *Nature Physics* 18.9 (Sept. 2022), pp. 1053–1057. DOI: 10.1038/s41567-022-01658-0.

[133] H. Miyahara, Y. Chen, et al. “Decoherence mitigation by embedding a logical qubit in a qudit”. In: *Quantum Information Processing* 22.7 (July 11, 2023), p. 278. DOI: 10.1007/s11128-023-04035-9.

[134] L. G. Gunderman. “Local-dimension-invariant qudit stabilizer codes”. In: *Physical Review A* 101.5 (May 28, 2020), p. 052343. DOI: 10.1103/PhysRevA.101.052343.

[135] Y. Zheng, H. Sharma, et al. “Entanglement Distribution with Minimal Memory Requirements Using Time-Bin Photonic Qudits”. In: *PRX Quantum* 3.4 (Nov. 16, 2022), p. 040319. DOI: 10.1103/PRXQuantum.3.040319.

[136] F. Bouchard, R. Fickler, et al. “High-dimensional quantum cloning and applications to quantum hacking”. In: *Science Advances* 3.2 (Feb. 3, 2017), e1601915. DOI: 10.1126/sciadv.1601915.

[137] S. Boixo, S. V. Isakov, et al. “Characterizing quantum supremacy in near-term devices”. In: *Nature Physics* 14.6 (June 2018), pp. 595–600. DOI: 10.1038/s41567-018-0124-x.

[138] M. Otten, K. Kapoor, et al. “Impacts of noise and structure on quantum information encoded in a quantum memory”. In: *Physical Review A* 104.1 (July 16, 2021), p. 012605. DOI: 10.1103/PhysRevA.104.012605.

[139] M. A. Nielsen and I. L. Chuang. *Quantum computation and quantum information*. Cambridge, NY: Cambridge University Press, 2000. 676 pp. DOI: 10.1017/CBO9780511976667.

[140] S. Machnes, U. Sander, et al. “Comparing, optimizing, and benchmarking quantum-control algorithms in a unifying programming framework”. In: *Physical Review A* 84.2 (Aug. 3, 2011), p. 022305. DOI: 10.1103/PhysRevA.84.022305.

[141] Initié par Julian Mayr (Université de Heidelberg) pendant son stage de MSc. Physique sur ce projet.

Contents

Dedication i

Acknowledgements iii

Support and Funding v

Scientific Outputs vii
Publications . . . vii
Dissemination Activities . . . vii

Résumé en français xi
Introduction . . . xiii
Modélisation *ab initio* des noyaux de lanthanide . . . xxxi
Anomalies hyperfines dans les ions hydrogènoide de dysprosium . . . xli
Qudit bruyant vs Qubits multiples . . . xlix
Non-linéarité de la fidélité dans les systèmes quantiques ouverts . . . lv
Techniques de contrôle optimal quantique pour la synthèse de portes Qudit lxi
Conclusion . . . lxxi
Références citées dans ce chapitre . . . lxxv

1 Introduction 1
1.1 Background and Motivation . . . 3
1.1.1 Processing Quantum Information . . . 3
1.1.2 Nuclear Spin Qudits . . . 5
1.1.3 The Role of the Nucleus . . . 10
1.1.4 Quantum Optimal Control . . . 13
1.2 Research Objectives . . . 16
1.3 Thesis Overview . . . 17
References Cited in this Chapter . . . 19

I Qudits in Nuclear Spins of Lanthanide-Molecular Complexes 27

2 *Ab initio* Modelling of Lanthanide Nuclei 31
2.1 Introduction . . . 33
2.1.1 Background and Motivation . . . 33
2.1.2 Objectives and Contributions . . . 34
2.1.3 Overview . . . 35

2.2 Theory . . . 35
2.2.1 Skyrme-Hartree-Fock Model . . . 36
2.2.2 Multipole Moments . . . 40
2.3 Methods . . . 44
2.3.1 Skyrme-HFBCS Code . . . 45
2.3.2 Calculation of the Moments and Potentials . . . 45
2.4 Results . . . 46
2.4.1 Nucleon Distributions . . . 46
2.4.2 Multipole Distributions . . . 53
2.5 Discussion . . . 60
2.5.1 Summary . . . 60
2.5.2 Outlook . . . 61
References Cited in this Chapter . . . 62

3 Hyperfine Anomalies in Hydrogen-like Dysprosium Ions 65
3.1 Introduction . . . 67
3.1.1 Background and Motivation . . . 67
3.1.2 Objectives and Contributions . . . 68
3.1.3 Overview . . . 69
3.2 Theory . . . 70
3.2.1 Multipole Expansions . . . 71
3.2.2 Hyperfine Interactions . . . 74
3.2.3 Isotope Shifts . . . 77
3.3 Methods . . . 81
3.4 Results . . . 82
3.4.1 Hydrogen-like Wavefunctions . . . 82
3.4.2 Charge Corrections . . . 84
3.4.3 Magnetic Corrections . . . 90
3.4.4 Hyperfine Anomaly . . . 92
3.4.5 Quadrupole Corrections . . . 93
3.5 Discussion . . . 95
3.5.1 Summary . . . 95
3.5.2 Outlook . . . 96
References Cited in this Chapter . . . 98

II Quantum Information Processing with Qudits 101

4 Noisy Qudit vs Multiple Qubits 105
4.1 Introduction . . . 107
4.1.1 Background and Motivation . . . 107
4.1.2 Objectives and Contributions . . . 108
4.1.3 Overview . . . 109
4.2 Theory . . . 109
4.2.1 Lindblad Formalism and Noise-Perturbed States . . . 109
4.2.2 Average Gate Infidelity . . . 110
4.3 Methods . . . 111
4.3.1 Numerical Noisy Qudit/ multi-qubit Simulation . . . 111
4.3.2 Random Gate and Pulse Hamiltonian Generation . . . 112
4.4 Results . . . 113

4.4.1 AGI of Qudits vs Qubits . . . 113
4.4.2 Fit and Deviation from Linear Behaviour . . . 114
4.4.3 Gate Dependence . . . 115
4.4.4 Single Qudit vs Ensemble of Qubits . . . 116
4.5 Discussion . . . 118
4.5.1 Summary . . . 118
4.5.2 Outlook . . . 119
References Cited in this Chapter . . . 120

5 Nonlinearity of the Fidelity in Open Qudit Systems 123
5.1 Introduction . . . 125
5.1.1 Background and Motivation . . . 125
5.1.2 Objectives and Contributions . . . 126
5.1.3 Overview . . . 126
5.2 Theory . . . 127
5.2.1 Mathematical Foundations of the Average Gate Fidelity . . . 127
5.2.2 Generalised Operators on Qudits . . . 129
5.3 Methods . . . 131
5.3.1 Numerical Tools . . . 131
5.3.2 Simulation Configuration . . . 132
5.4 Results . . . 134
5.4.1 Perturbative Expansion of the Average Gate Infidelity . . . 134
5.4.2 Nonlinearity of the AGI in the Strong Coupling Regime . . . 137
5.4.3 Distribution of the AGI for Random Qudit Gates . . . 139
5.4.4 Gate- and Noise-Dependence of the Fidelity . . . 147
5.4.5 First- and Second-Order Correction Terms to the AGI . . . 152
5.5 Discussion . . . 158
5.5.1 Summary . . . 158
5.5.2 Outlook . . . 159
References Cited in this Chapter . . . 161

6 Quantum Optimal Control Techniques for Qudit Gate Synthesis 165
6.1 Introduction . . . 167
6.1.1 Background . . . 167
6.1.2 Objectives and Contributions . . . 168
6.1.3 Organisation . . . 168
6.2 Theory . . . 169
6.2.1 Modelling and Control of Single-qudit Systems . . . 169
6.2.2 Gate Generation Techniques . . . 180
6.3 Methods . . . 186
6.3.1 Numerical Tools . . . 186
6.3.2 Simulation Framework . . . 187
6.4 Results . . . 188
6.4.1 Gate Synthesis . . . 189
6.4.2 Comparison of the Different Gate Synthesis Methods . . . 196
6.5 Discussion . . . 210
6.5.1 Summary . . . 210
6.5.2 Outlook . . . 214
References Cited in this Chapter . . . 217

Conclusions **221**

7 Summary and Perspectives **223**
7.1 Thesis Summary . . . 224
7.2 Future Directions . . . 225

Appendices **229**

A Appendices to Chapter 2 **231**
A.1 Lanthanide Isotopes . . . 232
A.2 Numerical Methods . . . 234
A.2.1 Dipole Moments . . . 234
A.2.2 Quadrupole Moments . . . 236
A.3 Additional Results . . . 237
References Cited in this Appendix . . . 240

B Appendices to Chapter 3 **241**
B.1 Additional Results . . . 242

C Appendices to Chapter 4 **247**
C.1 Published Article . . . 248
C.2 Supplementary Information . . . 259

D Appendices to Chapter 5 **265**
D.1 Numerical Packages . . . 266
D.2 Complementary Derivations . . . 266
D.2.1 Integration of the m-th Order Solution to the Master Equation . . . 266
D.2.2 Perturbative Expansion of the AGI . . . 267
D.2.3 Integral over the Fubini-Study Measure . . . 268
D.2.4 Boundedness of the AGI . . . 270
D.2.5 Gate-Independent Correction Terms . . . 272
D.2.6 Second-order Gate-Dependent Correction Term . . . 273
D.2.7 Tracelessness of the Odd-Order Iterated Commutator . . . 277
References Cited in this Appendix . . . 277

E Appendices to Chapter 6 **279**
E.1 Numerical Methods . . . 280

Bibliography **283**

List of Figures

1 Complexes moléculaires à base de phtalocyanine. xvi
2 Boucles d'hystérésis de magnétisation mesurées sur un monocristal de Mn_{12}-ac. xvii
3 Illustration schématique du dispositif de lecture de spin du $TbPc_2$. xviii
4 Initialisation de qudit, contrôle cohérent et lecture dans $TbPc_2$. xix
5 Réalisation expérimentale de l'algorithme de Grover dans $TbPc_2$. xx
6 Approches de dimensionnement pour les spins nucléaires couplés. xxi
7 Cycles d'hystérésis et levée de dégénéréscence due à l'effet Zeeman de Tb_2Pc_3. xxii
8 Illustration schématique de l'effet des déformations nucléaires. xxxi
9 Distributions de densité de nucléons de ^{161}Dy et ^{163}Dy. xxxv
10 Distributions de densité de nucléons ^{159}Tb et ^{165}Ho. xxxvi
11 Distribution des courants protoniques du ^{159}Tb et ^{165}Ho. xxxvii
12 Distribution des courants neutroniques du ^{161}Dy et ^{163}Dy. xxxviii
13 Fonctions d'onde électroniques de ^{163}Dy de type hydrogène. xlv
14 Fonctions d'onde muoniques de l'hydrogène ^{163}Dy. xlv
15 q visuelle de l'échelle d'infidélité dans des qubits multiples et un qudit unique. lii
16 Plage potentielle pour la facteur de mérite τ_b/τ_d. liii
17 Comparaison des quatre premiers termes de correction de l'AGI avec les simulations numériques. lviii
18 Écart par rapport à la linéarité des AGI pour les qubits soumis à un fort déphasage. lix
19 Mise en œuvre de l'algorithme hybride GRD-GRAPE de l'algorithme probabiliste de Grover. lxv
20 Temps de porte des algorithmes GRD et GRAPE pour les portes aléatoires de Haar. lxvi

1.1 Phthalocyanine-based molecular complexes. 6
1.2 Magnetisation hysteresis loops measured on a Mn_{12}-ac single crystal. . . . 7
1.3 Schematic illustration of the $TbPc_2$ spin readout setup. 7
1.4 Qudit initialisation, coherent control and readout in $TbPc_2$. 8
1.5 Experimental realisation of Grover's algorithm in $TbPc_2$. 9
1.6 Scalability approaches for coupled nuclear spins. 10
1.7 Hysteresis loops and Zeeman splittings of Tb_2Pc_3. 11

2.1 Schematic illustration of the effect of nuclear deformations. 38
2.2 Binding energy of the ^{162}Dy nucleus as a function of deformation parameters. 39

2.3 Nucleon density distributions of ^{161}Dy and ^{163}Dy. . . . 47
2.4 Nucleon density distributions of ^{159}Tb and ^{165}Ho. . . . 48
2.5 Proton current distributions of ^{161}Dy and ^{163}Dy. . . . 49
2.6 Proton current distributions of ^{159}Tb and ^{165}Ho. . . . 50
2.7 Neutron current distributions of ^{161}Dy and ^{163}Dy. . . . 51
2.8 Neutron current distributions of ^{159}Tb and ^{165}Ho. . . . 52
2.9 Normalised current distribution for the $3D$ spherical harmonic oscillator. . 53
2.10 Single-particle spectra for the ^{162}Dy nucleons near the Fermi level. . . . 54
2.11 Monopole potentials and densities of ^{159}Tb. . . . 56
2.12 Monopole potential and density of ^{161}Dy. . . . 57
2.13 Dipole densities of ^{161}Dy, ^{163}Dy, ^{159}Tb and ^{165}Ho. . . . 58
2.14 Quadrupole densities of ^{159}Tb, ^{161}Dy, ^{163}Dy and ^{165}Ho. . . . 59

3.1 Electronic wavefunctions of hydrogen-like ^{163}Dy. . . . 83
3.2 Mounic wavefunctions of hydrogen-like ^{163}Dy. . . . 84
3.3 Rescaled wavefunctions of the electronic and muonic hydrogen-like ^{163}Dy. 85
3.4 Monopolar shifts in the energy levels of orbitals of ^{163}Dy^{65+}. . . . 87
3.5 Breit-Rosenthal correction $\varepsilon_{\mathrm{BR}}$ for ^{163}Dy^{65+}. . . . 88
3.6 Bohr-Weisskopf correction $\varepsilon_{\mathrm{BW}}$. . . . 91
3.7 Trends of the Breit-Rosenthal and Bohr-Weisskopf corrections 92
3.8 Hyperfine anomalies of ^{161}Dy^{65+} and ^{163}Dy^{65+}. . . . 93
3.9 Quadrupole shifts for ^{163}Dy^{65+}. . . . 94
3.10 Quadrupole hyperfine anomalies between ^{161}Dy^{65+} and ^{163}Dy^{65+}. . . . 95

4.1 Visual synthesis of the infidelity scaling in multiple qubits and a single qudit. . . . 114
4.2 Average gate infidelities as a function of γt for $H = \mathbb{O}_d$. . . . 115
4.3 Potential range for the figure of merits τ_{b}/τ_d. . . . 117

5.1 Comparison of the first four correction terms of the AGI to numerical simulations. . . . 135
5.2 Deviation from linearity of the AGIs for qudits under strong dephasing. . . 137
5.3 Large-γt behaviour of the AGIs for Haar-random qubit gates under pure dephasing. . . . 138
5.4 Eigenvalue distributions of method QuTiP.`rand_unitary_haar` (and equivalently Cirq.`rand_unitary`). . . . 141
5.5 Eigenvalue distributions of method QuTiP.`rand_unitary` (and equivalently QuTiP.`rand_herm`). . . . 142
5.6 Eigenvalue distributions for method Bristol.`gen_cue`. . . . 143
5.7 Eigenvalue distributions for method Cirq.`rand_special_unitary`. . . . 144
5.8 Probability distributions of the AGI plateaus for different gate generation methods. . . . 145
5.9 Probability distributions of the AGI plateaus. . . . 146
5.10 Gate-dependence of the AGIs and qudit state evolution as functions of noise strength. . . . 149
5.11 Saturation points ($(\gamma t)^*$) of the AGIs for interpolated X^η gates as functions of qudit dimension. . . . 150
5.12 Fitted power-law model parameters as functions of η for the saturation points $(\gamma t)^*$ of the X^η gates. . . . 151
5.13 Effect of bit-flip errors on the AGI. . . . 152

5.14 Relative error of the first-order correction to the AGI, and gate-dependent deviation from linearity. . . . 154
5.15 Iteration-dependent convergence of the second-order AGI correction against qudit dimension. . . . 155
5.16 Time dependence of the convergence of the second-order AGI correction over qudit dimension. . . . 156
5.17 Relative error of the AGI up to second-order. . . . 157

6.1 Sources of control errors in arbitrary waveform generators. . . . 178
6.2 Qubit-based circuit diagram for Grover's search algorithm. . . . 189
6.3 Deterministic 2-parameter (D2p) Grover search algorithm on the Bloch sphere. . . . 191
6.4 Givens rotation pulses and populations for the QFT gate. . . . 194
6.5 GRD of the probabilistic and deterministic Grover's algorithms. . . . 195
6.6 GRAPE algorithm implementation of the qu-4-it QFT gate. . . . 196
6.7 Hybrid GRD-GRAPE algorithm implementation of the probabilistic Grover's algorithm. . . . 197
6.8 Memory usage and processing times for simulating single-qudits with `mesolve`. 198
6.9 Memory usage and processing times for the GRAPE and GRD methods. . 199
6.10 Gate times of the GRD and GRAPE algorithms for the QFT gate. . . . 200
6.11 Gate times of the GRD and GRAPE algorithms for Haar random gates. . 202
6.12 Comparison of gate times between the GRAPE and GRD algorithms for $d = 4$. . . . 203
6.13 GRD of the probabilistic and deterministic Grover's algorithms under Markovian dephasing noise. . . . 204
6.14 Comparison of Markovian error types on Grover's algorithm with GRAPE. 204
6.15 AGIs of the GRAPE and GRD for Haar random gates under pure dephasing. 205
6.16 AGIs of the GRAPE and GRD for qubits under pure dephasing. . . . 206
6.17 Comparison of the AGIs of the GRAPE and GRD algorithms for different Markovian noise types. . . . 207
6.18 AGIs vs amplitude offset errors for qu-8-its. . . . 208
6.19 AGIs vs phase shift errors for qu-8-its. . . . 210
6.20 AGIs vs absolute clock skew for qu-8-its. . . . 211

A.1 Monopole potentials and densities of ^{161}Dy, ^{163}Dy. . . . 238
A.2 Monopole potentials and densities of ^{159}Tb and ^{165}Ho. . . . 239

B.1 Electronic wavefunctions of hydrogen-like ^{161}Dy. . . . 242
B.2 Mounic wavefunctions of hydrogen-like ^{161}Dy. . . . 243
B.3 Rescaled wavefunctions of the electronic and muonic hydrogen-like ^{161}Dy. 244
B.4 Monopolar shifts in the energy levels of orbitals of $^{161}Dy^{65+}$. . . . 245
B.5 Breit-Rosenthal correction ε_{BR} for $^{161}Dy^{65+}$. . . . 245
B.6 Quadrupole corrections for $^{161}Dy^{65+}$. . . . 246

List of Tables

1 Moments quadrupolaires de charge intrinsèques et spectroscopiques. . . . xxxviii

2.1 The Landé g factors for protons and neutrons. 43
2.2 Example tabulated values for the protons of ^{159}Tb. 45
2.3 Table of nuclear radii for ^{159}Tb, ^{161}Dy, ^{163}Dy and ^{165}Ho. 55
2.4 Comparison of the *ab initio* and experimental magnetic moments. 59
2.5 Intrinsic and spectroscopic charge quadrupole moments. 60

3.1 Summary of the corrections to the hyperfine constants. 78
3.2 Binding energies of hydrogen-like ^{163}Dy. 86
3.3 Binding energies of hydrogen-like ^{163}Dy with R_{rms} normalisation. 89
3.4 Plateau values of the BR and BW effects for ^{163}Dy^{65+}. 91
3.5 Hyperfine anomaly plateau values (in %) for different orbitals. 93

4.1 Decoherence times (T_2) and gate times (t_n) of different qubit/qudit platforms. 116
4.2 Ratios of gate times in units of decoherence times between qubits and qudits. 118

5.1 Proportions of random gates with and without turning points. 147

6.1 Table of results for the GRD of the qutrit QFT gate. 201

A.1 Table listing the isotopes of terbium ($_{65}$Tb) with experimentally observed ground-states and non-zero spin-parities. 232
A.2 Table listing the isotopes of dysprosium ($_{66}$Dy) with experimentally observed ground-states and non-zero spin-parities. 233
A.3 Table listing the isotopes of holmium ($_{67}$Ho) with experimentally observed ground-states and non-zero spin-parities. 233

CHAPTER 1

INTRODUCTION

'The time has come,' the Walrus said,
'To talk of many things:
Of shoes — and ships — and sealing-wax —
Of cabbages — and kings —
And why the sea is boiling hot —
And whether pigs have wings.'

The Walrus and the Carpenter in "Through the Looking-Glass, and What Alice Found There" - Lewis Carroll

Contents

1.1 Background and Motivation 3
1.1.1 Processing Quantum Information 3
1.1.1.1 Qubit platforms 4
1.1.1.2 Criteria for universal quantum computing 4
1.1.2 Nuclear Spin Qudits 5
1.1.2.1 Lanthanide-based molecular complexes 5
1.1.2.2 Computing with qudits 7
1.1.3 The Role of the Nucleus 10
1.1.3.1 Muons as probes of nuclear structure 12
1.1.4 Quantum Optimal Control 13
1.1.4.1 Landscape of quantum control techniques 14
1.2 Research Objectives 16
1.3 Thesis Overview 17
References Cited in this Chapter 19

1.1 Background and Motivation

The histories of classical and quantum computing are deeply intertwined, sharing a common quest to understand and manipulate the fundamental principles of information. As global efforts advance toward achieving universal and fault-tolerant quantum computation, qubit-based platforms — particularly superconducting qubits — stand at the forefront of technological readiness and research focus. Yet, despite their rapid development, technical challenges remain in scalability, coherence, and error correction [1].

This thesis investigates a complementary path through the exploration of qudits: multilevel quantum systems that extend beyond the binary framework of qubits. By leveraging the unique nuclear spin states of lanthanide ions embedded in single-molecule magnets, this work aims to establish a theoretical foundation for qudit-based quantum computing, exploring how these systems can perform and under what conditions they could potentially challenge qubit-based platforms. Through new theoretical models and optimal control techniques, this research aims to advance the quantum information processing capabilities of these novel, high-dimensional systems.

1.1.1 Processing Quantum Information

To understand the potential of qudits, it is essential to first explore the foundational principles of quantum computing and the role that qubits have played in its development. This development can be considered from a number of different perspectives. On the one hand, the initial proposals for computing with quantum information were made in the early 1980's, with the attribution commonly being made to Feynman in his 1982 paper "Simulating physics with computers" [2] and the oft-cited quotation (based on the 1981 talk): "Nature isn't classical, dammit, and if you want to make a simulation of nature, you'd better make it quantum mechanical."

However, as noted in the Nature editorial marking "40 years of quantum computing" [3], the original proposal for a computer harnessing the principles of quantum mechanics (in this case, the exponential scaling of the Hilbert space) was made by Yuri Manin in 1980 [4]. It is also worth mentioning the early contributions of Paul Benioff, who in 1980 proposed a quantum mechanical model of computers as Turing machines in his article "The computer as a physical system" [5], and David Deutsch, who in 1985 proposed the first model for a universal quantum computer [6].

On the other hand, the development of quantum computing has been driven by the need to address fundamental challenges in computational complexity, such as factoring large numbers and simulating quantum systems. The seminal works of Peter Shor in 1994 on quantum algorithms for factoring and discrete logarithms [7], Lov Grover in 1996 on quantum search algorithms [8], and Seth Lloyd in 1996 on universal quantum simulators [9] have been instrumental in shaping the field of quantum computing. These algorithms demonstrated the potential for quantum systems to outperform classical computers in solving specific problems, sparking a wave of research into quantum algorithms, quantum error correction, and quantum information theory. Indeed, by harnessing the principles of superposition, entanglement, and interference, these foundational works laid the groundwork for the development of quantum computing as we know it today.

In contrast with this, it is also worth noting that the continuing miniaturisation of classical computers has also been a driver in the development of quantum computing technologies. As transistor sizes continue to approach the limits of classical physics, the need

for new computational paradigms has become increasingly urgent as the lines become increasingly blurred. In this case, there is the concern that quantum effects may begin to have measurable effects on the operation of classical computers, but at the same time that the advanced state of classical computing technology may provide a pre-existing platform for the future development of quantum computing technologies [10, 11].

1.1.1.1 Qubit platforms

While much research on quantum computing has remained in the realm of the theoretical for the majority of the field's 40-year history, technological advances over the last two decades have led to a significant increase in the number of experimental platforms that have seen successful development. Just as with classical computing where the early developmental stages saw a wide variety of different experimental approaches to building electrical transistors (including relays, vacuum tubes and solid-state switches) before settling on the silicon-based MOSFET (metal-oxide-silicon-field-effect-transistor) as the dominant technology [12], quantum computing has seen a similar proliferation of different experimental platforms, including: superconducting circuits [13], trapped ions [14, 15], photonic systems [16, 17], neutral (Rydberg) atoms [18, 19], nuclear and electronic spins in molecular magnets [20, 21, 22] and semiconductor-based quantum dots [23, 24].

Each of these platforms has its own strengths and weaknesses, and each has made significant strides in developing and controlling their qubits. For example, trapped ions have demonstrated long coherence times and high gate fidelities, but face challenges in scaling up to larger systems. Photonic systems, while offering the potential for long-distance quantum communication, have faced challenges in achieving high-fidelity quantum gates and scalable qubit architectures [25]. Cold neutral atom systems using Rydberg excited states are promising, but also require sophisticated control techniques. Similarly, semiconductor-based quantum dots have shown promise for scalable qubit architectures but face challenges in achieving long coherence times and individual controllability over each qubit.

On the other hand, superconducting qubits have emerged as one of the most promising platforms for quantum computing [26], with notable scalability and demonstrated systems of up to hundreds of qubits with significant investment by both academia and industry, including companies such as IBM [27] and Google [28]. These systems have achieved significant milestones in single-gate fidelities, coherence times, and error correction protocols, making them a leading candidate for near-term quantum computing applications [13, 29]. However, despite having the highest level of technological readiness, the challenges of decoherence, noise management, and general scalability in these mesoscopic devices remain prominent.

1.1.1.2 Criteria for universal quantum computing

Now, in this intermediate stage where small-scale platforms of up to 100 qubits are being implemented, it is relevant to speak about performance metrics like gate fidelities and coherence times, their ratio the figure-of-merit, and error rates to error correction thresholds. These metrics are encapsulated in the DiVincenzo criteria [30], a set of five requirements that a quantum computing platform must meet to be considered universal. These criteria include: (i) scalable physical qubits, (ii) qubit initialization, (iii) long relevant coherence times, (iv) a universal gate set, and (v) qubit readout. Meeting these criteria is essential.

As we can see, universality of computation, never mind true fault-tolerance, is a significant technical challenge, requiring each one of these criteria to be upheld along with all the others. It is not enough to have a universal gate set if the coherence times are too short, or to have scalable physical qubits if they cannot all be initialised consistently. Indeed, platforms such as superconducting qubits have clearly met criteria two through five, and have shown good scalability, but the challenges lie in maintaining coherence times and gate fidelities while scaling up to larger systems.

1.1.2 Nuclear Spin Qudits

Since scalability is such a challenge in near-term devices, it has been worth exploring alternative quantum information carriers that could potentially offer advantageous scalability properties while maintaining comparable gate fidelities and coherence times. One such option is qudit-based architectures, which leverage higher-dimensional excited states of a quantum system to encode a larger Hilbert space in fewer physical sites [31].

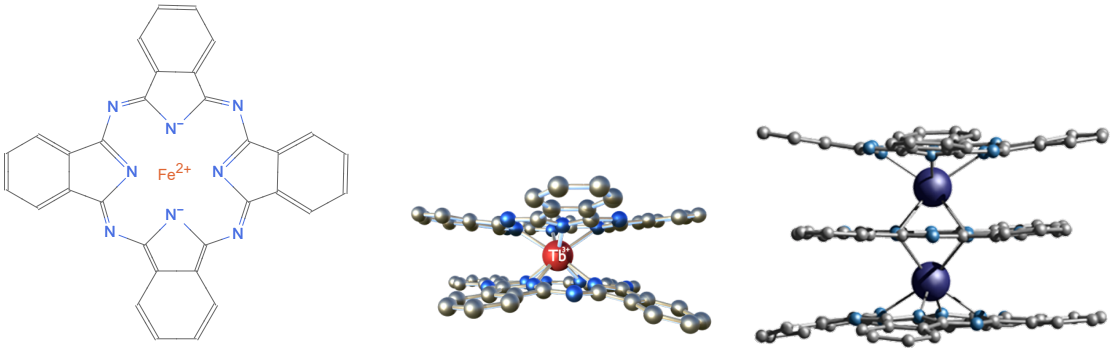
Although classical computers eventually settled on the two-level bit as the fundamental unit of information once scalability and error-correction issues were solved, there were some early platforms that made use of ternary logic to encode information and scale up the computational capacity, such as the Soviet Setun computer [32], while early error-correction protocols made use of a third auxiliary level as a form of parity check.

This development is mirrored in the field of quantum computing, where qubits have been the primary focus of research due to their simplicity and ease of manipulation. However, as the field has developed, and technological control over individual quantum systems has improved, the potential for higher-dimensional quantum systems to offer advantages in terms of computational scalability and efficiency has become increasingly apparent. This is particularly relevant in the context of: (i) quantum error correction, where higher-dimensional systems can encode error-robust qubits [33], (ii) quantum simulation of high-dimensional systems [34], and (iii) quantum algorithms, where higher-dimensional systems can reduce the number of long-range entangling gates required to perform certain computations [35].

As we shall see, this last point is particularly relevant as the starting point of this thesis. In the meantime, let us remark that nuclear spins present an intriguing candidate for qudit-based quantum computing, particularly since the interplay between electronic and nuclear degrees of freedom is both complex and advantageous for quantum information processing. Of course, many quantum systems have some capability for encoding qudits, such as the orbital angular momentum of photons in photonic systems [36], the nuclear spin states of trapped ions [37], solid-state quantum dots [38] and the higher anharmonic oscillator excited states of superconducting transmons [39, 40]. However, the nuclear spin degrees of freedom have the advantage of being naturally long-lived, well-isolated from the environment, and highly coherent, making them attractive candidates for high-dimensional quantum memories [41]. This strong isolation, on the other hand, can also be a disadvantage, as it makes the nuclear spins difficult to control and manipulate, requiring careful platform design and sophisticated control techniques [42].

1.1.2.1 Lanthanide-based molecular complexes

Concerning this careful choice of physical platform for embedding the nuclear spins, lanthanide-based single-molecule magnets (SMMs) have demonstrated promising potential for qudit-based quantum computing in recent years. In particular, the work of this



(a) FePc **(b)** $TbPc_2$ **(c)** Tb_2Pc_3

Figure 1.1 – Phthalocyanine-based molecular complexes. Examples of phthalocyanine-based molecular complexes, including: (a) FePc, (b) $TbPc_2$ and (c) Tb_2Pc_3.

thesis serves as a theoretical extension of the work of Godfrin [43] and Thiele [42] in the collaboration between the chemists of the Ruben Group and physicists of the Wernsdorfer Group (KIT). In their work, they studied the nuclear spin states of lanthanide ions, specifically dysprosium and terbium, embedded in single-molecule magnets. The most successful of these have been the phthalocyanine-based (Pc) double-decker complexes with a single lanthanide ion ($LnPc_2$) at the center, most notably: $TbPc_2$ (terbium bis-phthalocyanine, see Fig. 1.1 for visual examples).

Phthalocyanines have become a popular choice for molecular magnets due to their high symmetry, strong ligand field, and well-defined electronic structure. First synthesised (accidentally) in 1907 by Braun and Tcherniac and later characterised by Linstead in 1934 [44], they are large macrocyclic ligands with a central ring of (four) nitrogens that are responsible for bonding with the single metal atom. They have long been used as dyes and pigments for their distinctive blue-green colour, and have found wider use in a variety of related industrial applications, including in optical data storage and solar screen devices [45].

It was not until the 1990s that early metallophthalocyanine complexes, such as MnPc, began to be studied for their magnetic properties [46], and research interest has continued to grow as their potential for single-molecule magnets and spintronic devices has become apparent. This led on to the work of Ishikawa and Wernsdorfer, *et. al.* in the early-mid 2000s, where they studied the magnetic properties of $TbPc_2$, observing the key properties of slow magnetic relaxation and quantum tunnelling of the magnetisation (QTM) [47, 48].

First observed in nanomagnets by Thomas and Sessoli *et. al.* [49], this QTM effect appears as sharp steps or plateaus in the otherwise smooth curve of magnetisation change in a magnetic hysteresis loop (see Fig. 1.2). These steps occur when the magnetic field aligns the energies of different spin states, allowing the magnetisation to tunnel abruptly through the energy barrier instead of slowly overcoming it thermally. This results in discrete, rapid flips of magnetisation, creating a series of discontinuities that reflect the quantum nature of the magnetic reversal.

One of the most popular measurement techniques for observing the QTM is with superconducting quantum interference device (SQUID) magnetometers, which can measure the magnetisation of a sample with high sensitivity and resolution. With Wernsdorfer's

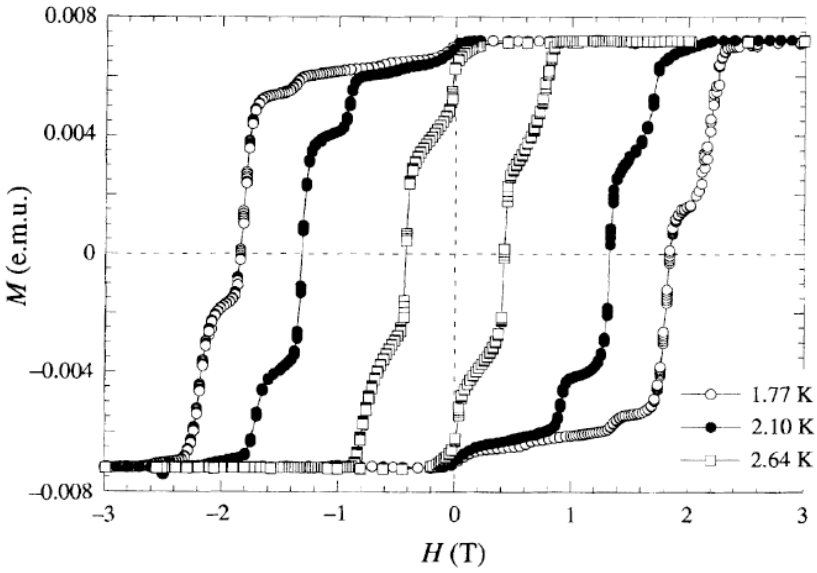
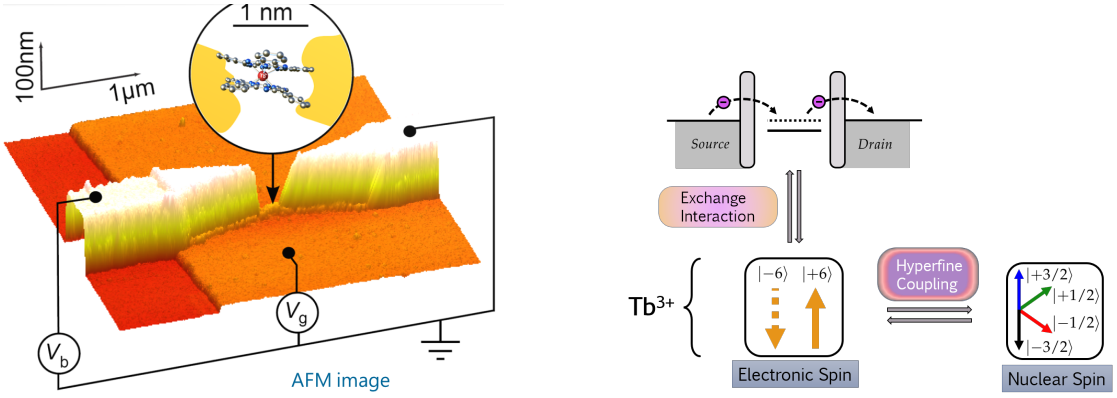


Figure 1.2 – Magnetisation hysteresis loops measured on a Mn_{12}-ac single crystal. A 0.066 mm3 single crystal of Mn_{12}-ac shows magnetisation hysteresis loops at low temperatures by SQUID magnetometry. QTM transitions are observed as sudden jumps in the magnetisation under slow variation in the applied magnetic field. Taken from [49].



(a) nano-SQUID circuit

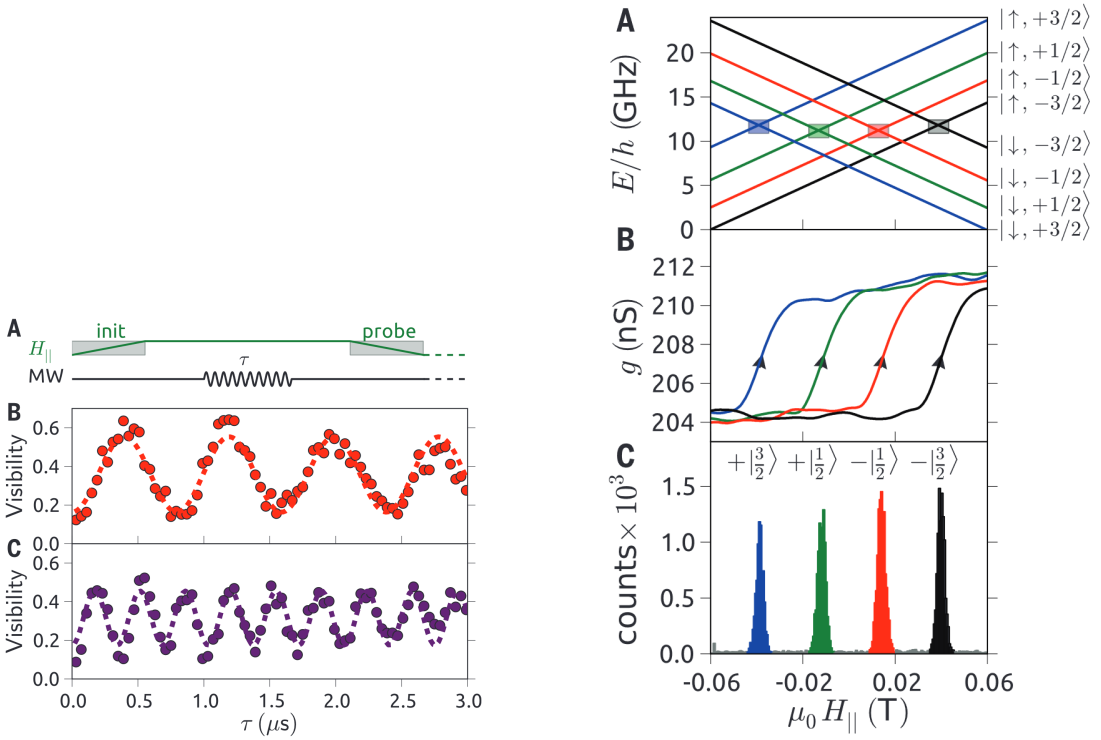
(b) Nuclear-electronic coupling

Figure 1.3 – Schematic illustration of the $TbPc_2$ spin readout setup. (a) AFM coloured image of a $TbPc_2$ SMM connected to gold source and drain electrodes through tunnelling barriers, within a break junction on top of an Au/HfO2 layer. Adapted from [50]. (b) Schematic of the coupling procedure from the nuclear to the electronic spin states of Tb^{3+} via the hyperfine interaction, then to the delocalised electron of the tunnelling current via exchange interaction. Adapted from [42].

development of nano-SQUIDs in 2009 [51] refining the capabilities of the micro-SQUID devices, the increased sensitivity enabled the direct electronic readout of the individual nuclear spin states of the central Tb^{3+} metal ion in $TbPc_2$ SMMs [52] (see Fig. 1.3).

1.1.2.2 Computing with qudits

Having demonstrated the readout principle for a potential qudit-based platform built on the nuclear spin states of Tb^{3+} in $TbPc_2$, the next steps, in terms of developing a quantum information processing device by following the DiVincenzo Criteria, would be



(a) Rabi oscillations in $TbPc_2$.

(b) Zeeman splitting of nuclear spin states.

Figure 1.4 – Qudit initialisation, coherent control and readout in $TbPc_2$. (a) Panel A shows the initialisation and readout procedure by ramp-up and ramp-down of the magnetic field $H_{||}$, while panels B and C show the intermediate state populations undergoing Rabi oscillations at two different electric field strengths. (b) Panel A shows the Zeeman diagram of the $J = \pm 6$ state of the $4f^8$ electronic ground state, with the 4 QTM anticrossings highlighted. Panel B shows the conductance jumps due to the magnetic reversal occurring at the respective anticrossings. Panel C shows a histogram of the counts of observed magnetic reversals occurring as a function of magnetic field strength. Reproduced from [42].

to demonstrate consistent state initialisation and readout, ideally with long coherence times maintained during the intermediate period. This work was achieved soon after, by Thiele *et. al.* in 2014, who demonstrated the electrically-driven nuclear spin resonance of Tb^{3+} in $TbPc_2$ [42].

This work was a significant milestone in the development of qudit-based quantum computing, as it demonstrated the ability to manipulate the nuclear spin states of Tb^{3+} with electrical fields, paving the way for the implementation of quantum gates and algorithms on this platform. Note only did Thiele show consistent qudit initialisation and readout by ramp-up and ramp-down of the magnetic field $H_{||}$, but he also elucidated the characteristically long coherence times of nuclear spin states, and furthermore laid the groundwork for their manipulation by demonstrating coherent control by way of Rabi oscillations induced by electric fields (see Fig. 1.4).

As an aside, this final point - the coherent control of nuclear spins through electric fields - raised an important theoretical question that inspired a detailed study in the work of our colleague, Denis Janković, which we shall briefly mention. The central question here concerns how a nuclear spin, being a magnetic degree of freedom, can be influenced by an electric field. Indeed, for the case of a free atom or ion, the electric field would have

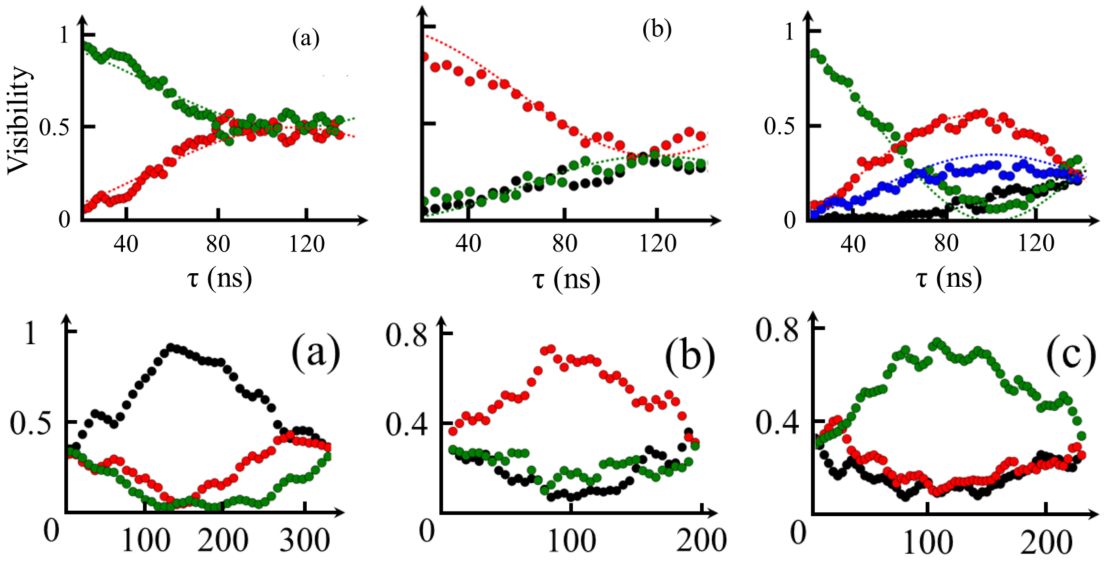


Figure 1.5 – Experimental realisation of Grover's algorithm in $TbPc_2$. Each panel presents the populations of the individual nuclear spin states of $TbPc_2$ (red, green, black and blue) as a function of time in ns. The upper row demonstrates the implementation of the QFT superposition (generalised-Hadamard) gate in $d = 4$ on 2, 3, and all 4 levels in the first, second and third columns, respectively. The lower row shows the populations undergoing two cycles of the Grover diffusion operator on the marked state (black on left, red in center, green on right), with subsequent amplitude amplification reaching a maximum before returning to the original superposition state (For more details on Grover's algorithm, see Section 6.4.1). Reproduced from [43].

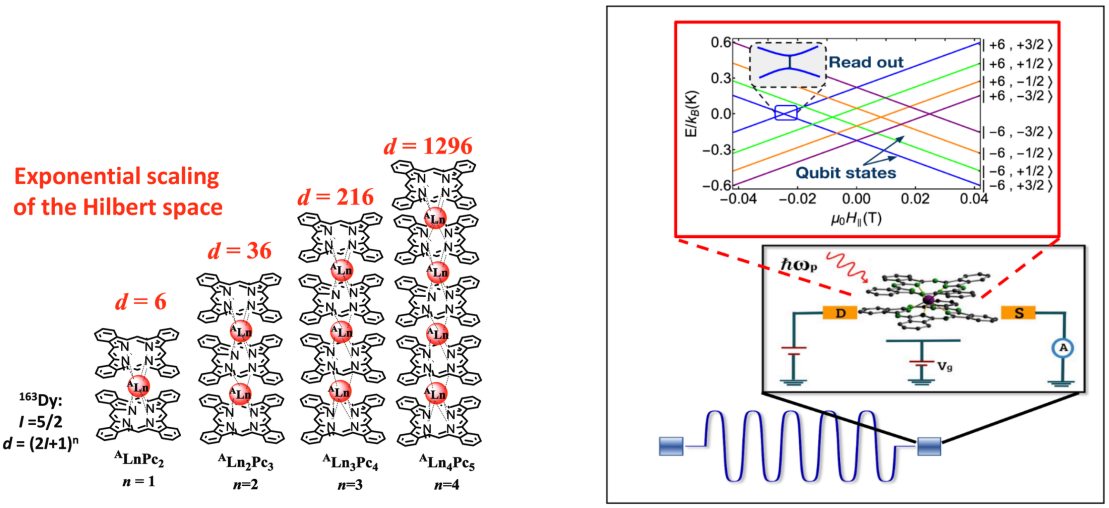
no effect on the nuclear spin. However, once embedded within a molecular complex, like $TbPc_2$, Janković found that the ligand field of the molecule causes a mixing of the otherwise pure states that enables such an interaction via the hyperfine Stark effect [53].

Now, continuing with our development of a qudit-based quantum computing platform, the next criterion would be to demonstrate the ability to perform quantum gates using the nuclear spin states of the terbium ion. This was achieved by Godfrin *et. al.* in 2017 [43], where he demonstrated that the coherence times were long enough, and Rabi oscillations coherent enough, to implement the superposition (generalised-Hadamard) gate, and Grover's search algorithm on the qudit states (see Fig. 1.5).

This implementation itself was inspired by the earlier theoretical work of Leuenberger and Loss, who in a series of papers in the early 2000s proposed general protocols for quantum computing with large nuclear spins, and as a specific example an implementation of a novel version of Grover's algorithm on a single, large, qudit [35, 54, 55].

While Godfrin made significant progress towards demonstrating a full qudit-based quantum computing platform, the implementation of Grover's algorithm was limited to three out of the four nuclear spin states of the terbium nucleus. This led to another theoretical question of qudit universality: whether the nuclear spin states of the terbium ion could be used to implement a universal set of quantum gates, and hence any arbitrary quantum algorithm. This question was one of the main motivations for the work of this thesis, and addressed in Chapter 6.

The other concern to be addressed in the development of a qudit-based quantum comput-



(a) Tb_2Pc_3 (b) Coupled $TbPc_2$s

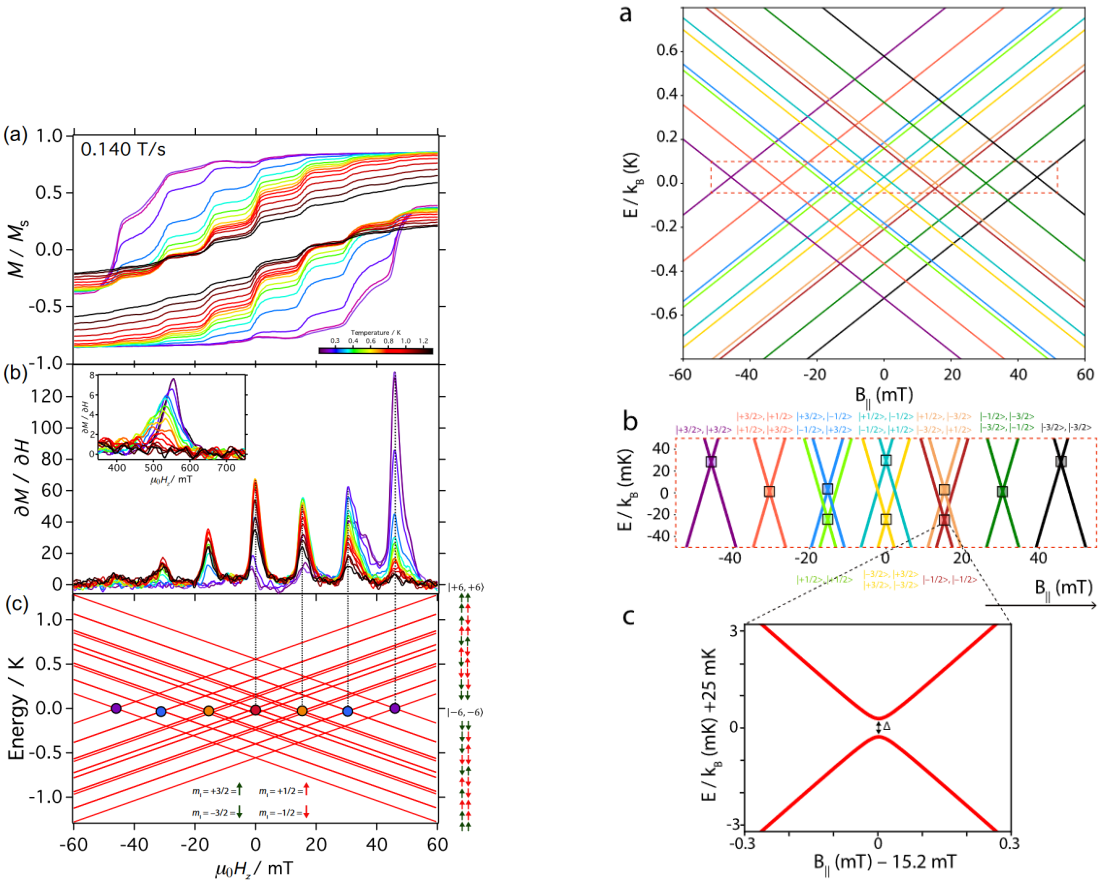
Figure 1.6 – Scalability approaches for coupled nuclear spins. (a) Conceptual scaling of ${}^{A}Ln_nPc_{n+1}$ molecular complexes (taken from [56]). (b) Long-range coupling of $TbPc_2$ complexes via superconducting resonator (taken from [57]).

ing platform is the issue of scalability. To scale up a quantum computing platform, it is necessary to be able to control and manipulate a large number of qudits simultaneously, together with entangling operations. One set of proposals is to engineer and synthesise larger, multi-metallic complexes (see Fig. 1.6a), such as the triple-decker molecule Tb_2Pc_3 (see Fig. 1.1c), which could potentially offer a larger Hilbert space for quantum computing applications [50]. Other proposals involve the long-range coupling of pairs of double-deckers at either end of a superconducting resonator, much in the same way that entangling operations are performed in superconducting qubit systems by a cross-resonance gate, but in this case with molecular magnets instead of transmons at either end [57] (see Fig. 1.6b). This is a promising concept in terms of controllability of the coupling, but presents significant challenges, technically in locating the molecular magnets at the ends of the resonator, and in terms of scalability wtih coupling multiple qudits together.

1.1.3 The Role of the Nucleus

In their attempts to address the issue of scaling the Hilbert space of the lanthanide-based SMMs, the groups of Ruben and Wernsdorfer have turned to the isotopologue chemistry of the lanthanide ions [56]. In this approach, the (nuclear spin) Hilbert space of a $LnPc_2$ double-decker can be increased by synthesis with lanthanides of larger nuclear spins, such as dysprosium and holmium, to form $DyPc_2$ and $HoPc_2$ having Hilbert spaces of $d = 6$ and $d = 8$, respectively. This concept was then extended to the synthesis of more complex, triple-decker molecules, such as Tb_2Pc_3 (see Fig. 1.1c) [50, 58], where the nuclear spin states of two terbium ions are coupled by dipolar and exchange interactions to form a larger Hilbert space.

Moreover, it is worth noting that this approach extends beyond simply the choice of lanthanide element, to investigating (i) the different behaviours of individual isotopes of the same element based on their fundamental nuclear structure and (ii) the choice of ligand and functional groups and their influence on the hyperfine splittings through the



(a) Tb_2Pc_3 Hysteresis loops.

(b) Tb_2Pc_3 Zeeman splittings.

Figure 1.7 – Hysteresis loops and Zeeman splittings of Tb_2Pc_3. (a) The upper panel, a, shows the magnetic hysteresis loops as a function of temperature, with the central panel, b, showing the first derivative of the magnetisation with respect to the magnetic field, highlighting the QTM transitions shown in the lower panel, c, on a Zeeman diagram. Taken from [58]. (b) The panels show simulated Zeeman diagrams based on the theoretical Hamiltonian of Tb_2Pc_3. The upper panel, a, shows the ground state Zeeman splittings, with zooms in the central panel, b, of the QTM transitions including degeneracies, with the lower panel, c, showing a final zoom of an individual anti-crossing. Taken from [50].

ligand field. As an in principle example (see Fig. 1.7), the coupled states of $d = 4$ each should produce an enlarged Hilbert space of $d = 16$, however, only 7 states were resolved in the first experiments, due to degeneracies in the energy levels and overlapping QTM transitions.

This progress reveals the potential for leveraging the isotopologue chemistry of these molecules to build larger Hilbert spaces and to explore strong nuclear dipolar and quadrupolar splittings for improved state control and readout. This is in addition to the search for additional lanthanides with even larger nuclear spins, such as holmium, which, when (possibly) paired in for example triple-decker molecules such as $DyHoPc_3$, could offer significantly enlarged Hilbert spaces for computing applications.

However, the precision of these experimental efforts highlights the need for a more comprehensive understanding of the intrinsic nuclear properties — specifically, the magnetic dipole and electric quadrupole moments of the lanthanide nuclei involved. Since, for

example having a much larger number of states without a consummate increase in the spacings between levels could lead to frequency crowding, where the magnetic spin reversal crossings are too close together to be individually resolved. Or, as we have seen for the case of Tb_2Pc_3, degeneracies in the QTM transitions may prevent the complete resolution of the full Hilbert space. Such understanding is crucial for optimising the molecular design and thus enhancing the hyperfine interactions in these systems, thereby enabling more robust qudit platforms with longer coherence times and higher gate fidelities. To achieve this, *ab initio* nuclear models, such as the Hartree-Fock-BCS (HFBCS) approach, play a vital role in accurately predicting the nuclear observables that directly impact the behaviour of qudits.

Now, the exploration of nuclear spin systems and their (modern) role in quantum computing traces back to foundational studies of atomic and nuclear properties in the early 20th century. The concept of nuclear spin itself emerged with the discovery of the intrinsic angular momentum of protons and neutrons, influencing the magnetic properties of atoms. Early spectroscopic experiments by Otto Stern and Walther Gerlach in the 1920s, which revealed the quantised nature of angular momentum, laid the groundwork for the understanding of spin in both electrons and nuclei [59]. These findings were crucial in developing quantum mechanics as a framework for describing both atomic structure and magnetic properties at a microscopic level.

The development of nuclear magnetic resonance (NMR) in the mid-20th century by Felix Bloch and Edward Purcell marked a significant advancement in probing nuclear spin dynamics [60]. NMR provided a detailed tool for understanding nuclear spin states and their interactions with external magnetic fields, opening up the study of hyperfine structure (HFS) in atoms and molecules. Since nuclear spin states are isolated from electronic dynamics, they exhibit longer coherence times and slower spin relaxation, making them an early candidate for storing information in the form of molecular magnets, following the pioneering work of Sessoli *et. al.* on molecular magnetism [61, 62, 63]. However, as we have mentioned already, this same isolation also makes the challenge of accurately modeling and controlling the nuclear spin states a focus point for both experimental and theoretical efforts.

The exploration of hyperfine interactions as a bridge between nuclear structure and quantum information applications is therefore a necessity. Early measurements of hyperfine splittings in atoms, through techniques like atomic beam spectroscopy and later laser spectroscopy, revealed the nuanced influence of nuclear charge distributions and magnetic dipole moments on electronic states. The theoretical formalism for understanding these interactions, developed by Breit, Rosenthal, Bohr, and Weisskopf, established corrections for finite nuclear size and charge and magnetisation distributions in hyperfine structures [64, 65]. These corrections, known as the Breit-Rosenthal (BR) and Bohr-Weisskopf (BW) effects, were critical for refining nuclear models to account for realistic nuclear geometries and internal magnetisation profiles, and will be studied in detail in Chapters 2 and 3.

1.1.3.1 Muons as probes of nuclear structure

The role of muons in probing nuclear structure has its origins in the mid-20th century, following the discovery of the muon in cosmic ray experiments by Carl D. Anderson and Seth Neddermeyer in 1936 [66]. Soon after, it was understood that the muon, being a heavier cousin of the electron, would exhibit different interactions with atomic nuclei.

The mass of the muon, approximately 207 times that of the electron, results in a much smaller Bohr radius for muonic atoms, enabling the muon to probe the nuclear charge and magnetisation distributions more directly due to the enhanced overlap of the muonic wavefunction with the nucleus.

Experimental studies of muonic atoms began in the 1950s and 1960s, with pioneering work conducted by researchers such as Vernon Hughes and his collaborators, who used muon beams to measure hyperfine structures and isotope shifts in a range of elements [67, 68]. The advent of high-precision muon spectroscopy provided an unprecedented window into nuclear properties, including charge radii and quadrupole moments. This technique was particularly powerful for heavy nuclei like lanthanides, where the enhanced nuclear overlap of the muonic wavefunction amplified the effects of nuclear structure.

In parallel, theoretical models were developed to describe the enhanced sensitivity of muonic atoms to nuclear properties. These models extended the traditional hyperfine interaction framework to include the significant corrections arising from nuclear size (BR effect) and internal magnetisation (BW effect). This theoretical groundwork laid the foundation for using muonic atoms as probes of complex nuclear structure, further motivating their application in our study of lanthanide nuclei for quantum information applications.

The potential of muons as probes of nuclear structure has been revitalised in recent years with the development of next-generation muon beam facilities at institutions like PSI [69] and KEK [70], enabling new high-precision experiments. These experiments provide an opportunity to test and refine nuclear models, particularly for isotopes with applications in quantum technologies. By offering a direct link between nuclear structure and hyperfine interactions, muonic spectroscopy continues to play a pivotal role in advancing both nuclear physics and quantum information science.

1.1.4 Quantum Optimal Control

The study of optimal control in quantum systems is rooted in a broader effort to achieve precise manipulation of quantum states and operations. Initially driven by the requirements of spectroscopy and magnetic resonance in the mid-20th century, the development of pulse sequences for nuclear magnetic resonance (NMR) and electron spin resonance (ESR) laid the foundation for what would become quantum control theory. In the context of NMR, pioneering work by Erwin Hahn and others led to the development of coherent control techniques such as the spin echo and composite pulses, which were used to correct imperfections in magnetic fields and enhance signal detection [71, 72]. These early advances demonstrated the potential for actively shaping control fields to manipulate quantum systems with high precision, setting the stage for applications in processing quantum information.

The advent of quantum computing in the 1980s and 1990s shifted the focus of control theory from mere state manipulation to the synthesis of quantum gates, following the theoretical foundations laid by Rabitz and colleagues [73, 74]. Since quantum gates must be implemented with high fidelity to ensure accurate execution, optimal control techniques have become increasingly important for overcoming hardware imperfections and environmental noise. This is of particular importance in the present-day era of NISQ devices (Noisy Intermediate-Scale Quantum, coined by Preskill [75]) within the second quantum revolution (coined by Dowling and Milburn [76]).

Within our context of developing pulse-shaped quantum gates for lanthanide-based qudit systems, a number of important considerations need to be addressed. With the goal of generalising and extending the work of Godfrin *et. al.* [43, 77, 78], it is necessary to first understand the roles and relationships between controllability of the physical system, and the consequent universality of the quantum gates that can be implemented with the set of allowed control fields [79, 80]. We recall that this is a key aspect of the DiVincenzo Criteria for quantum computing, and is a necessary condition for the implementation of any arbitrary quantum algorithm.

In a second step, we must consider the variety of different control techniques that may be used to shape the pulses implementing these gates, and the trade-offs between the complexity of the pulse-shaping algorithm and the complexity of the computed control fields. This is particularly important in the context of qudit-based quantum computing, where the increased dimensionality of the Hilbert space poses additional challenges for control optimisation of multi-chromatic pulse sequences [81].

In the third step, it is vital that the control techniques be studied with respect to the fidelity of the gates in the presence of environmental noise and control errors, in preparation for the implementation on real-world hardware. This is a critical step towards developing robust quantum error correction protocols and optimising control pulses to mitigate the influence of noise. Early theoretical work focused on characterising different noise channels, such as dephasing, amplitude damping, spin-relaxation and bit-flip errors, and their effects on qubit-based quantum operations [82], as well as simple Markovian models for capturing environmental effects in open quantum systems formalism of Gorini-Kossakowski-Sudarshan-Lindblad (GKSL) [83, 84, 85]. Modern extensions include more complex non-Markovian noise models that capture memory effects and correlations over time, such as in small atomic systems where the assumption of an infinite bath may not be perfectly valid [86], and the development of full-stack digital-twins for quantum computing platforms that provide a comprehensive model of the hardware and software stack, including the control electronics and the quantum processor itself [87, 88].

In a fourth step, one can imagine extending the pulse-shaping methods to then introduce error correction protocols, such as dynamical decoupling, or more complex stabiliser and surface codes, to further enhance the robustness and fidelity of the quantum gates in the efforts towards fault-tolerant quantum computing. Without getting into this vast and rapidly progressing field of research, which is beyond the scope of this thesis, it is worth briefly reiterating that qudits are beginning to offer potential advantages over qubits in some error correction protocols, as the larger state space allows for smart encodings of logical qubits that can be more robust against certain types of errors [33, 39, 89, 90, 91, 92].

1.1.4.1 Landscape of quantum control techniques

The landscape of quantum control is inherently high-dimensional, characterised by a vast parameter space over which control fields must be optimised. In qudit systems, this landscape becomes even more complex than in qubit systems due to the increased number of levels and possible transitions. Historically, this has posed significant challenges, as the dimensionality of the control problem scales with the Hilbert space size, making it difficult to find optimal solutions efficiently.

With reference to classical control theory, the concepts of controllability and reachability are particularly relevant in the context of quantum systems. Controllability refers to the

ability to drive a system from one state to another using a set of control fields, while reachability determines the minimal set of operations required to achieve full control over the state space [93]. These concepts are essential for understanding the controllability of qudit systems and guiding the design of control sequences for implementing quantum gates.

Due to this complexity, a veritable zoo (particularly appropriate given the current naming conventions, such as GRAPE, CRAB, GOAT, GECCO) of numerical optimisation techniques have been developed to navigate the quantum control landscape. Early approaches relied on manual pulse design and heuristic tuning, but as the field has continued to mature, more systematic methods have emerged. Koch *et. al.* have provided comprehensive reviews of this burgeoning field [94, 95], and have highlighted the necessity of numerical optimisation techniques for achieving high-fidelity quantum gate synthesis. Broadly speaking, these techniques can be divided into several categories, including: numerical and analytical methods, gradient-based and gradient-free optimisation, online and offline machine learning, and open-loop and feedback-based closed-loop control, and of course hybrid techniques that combine elements of different approaches, without mentioning other classical control techniques that find usage such as Pontryagin's Maximum Principle, the Krotov method and adaptive linearisation techniques. In general of course, all of these optimisation methods boil down to different approaches for solving the general control problem given a particular cost functional, the simplest being the fidelity of the implemented gate to the target gate.

Giving a brief mention of each class, analytical methods such as PMP may be powerful in their generality, but still must be computed numerically. Of particular interest to us in this thesis is the linear-algebraic approach of Brennen *et. al.* [96] of the Givens Rotation Decomposition. Givens rotations, which generalise the concept of rotations in two-level systems to multi-level systems, provide an algebraic framework for decomposing complex qudit gates into simpler operations, and we shall study it in detail in Chapter 6.

The most widely known gradient-based approach is arguably the Gradient Ascent Pulse Engineering (GRAPE) algorithm, which was first introduced by Khaneja *et. al.* in 2005 [97] in the context of shaping NMR pulse sequences. The flexibility and efficiency of GRAPE made it highly adaptable to various quantum platforms, from superconducting qubits to trapped ions, and laid the groundwork for extending optimal control to more complex systems, such as qudits. The iterative approach on varying the piecewise-constant control fields to optimise the cost functional has been widely adopted and easily implemented in standard numerical optimisation libraries (see Chapter 6).

As for gradient-free optimisation, the main advantage is that it does not require the calculation of gradients, which can be computationally expensive for high-dimensional systems. However, this comes at the cost of potentially slower convergence and less efficient exploration of the control landscape. Nevertheless, gradient-free methods like the Covariance Matrix Adaptation Evolution Strategy (CMA-ES) have been successfully applied to quantum control problems. Other general methods include the Nelder-Mead simplex algorithm, the Particle Swarm Optimisation (PSO) algorithm, Simulated Annealing (SA), and evolutionary and genetic algorithms.

Machine learning techniques are a powerful modern approach for nonlinear optimisation of the control problem. Reinforcement learning algorithms, such as Q-learning and Deep Q Networks (DQN), have been used to adapt control fields in real-time based on feedback from the system, enabling dynamic optimisation of quantum gates. Two primary

subcategories of machine learning are supervised and unsupervised learning. While reinforcement learning requires no *a priori* knowledge of the problem, giving it exceptional generalisation capabilities, it is also highly computationally expensive in terms of the number of iterations required to converge to a solution. A recently developed alternative, Physics-Informed Neural Networks (PINNs), leverage *a priori* knowledge of the physics governing the control problem with the universal function approximation capabilities of neural networks to achieve fast convergence and high accuracy in control optimisation. These techniques have been recently developed and our preliminary investigations have shown promise in producing high-fidelity control fields particularly in combination with PMP methods for time-optimality [98, 99, 100, 101, 102, 103].

Finally, the distinction between open-loop and closed-loop control is crucial for understanding the role of feedback in quantum control. Open-loop control involves designing control pulses based on a predefined target gate and cost function, without feedback from the system. Closed-loop control, on the other hand, uses real-time measurements of the system to adjust control fields dynamically, enabling adaptive optimisation of quantum gates. While open-loop methods like GRAPE are widely used for gate synthesis, closed-loop techniques are becoming increasingly important for addressing noise and imperfections in quantum systems. In conjuction with online machine learning techniques, closed-loop control learning of a machine learning network trained on an existing hardware stack would be the ultimate goal for real-time control of quantum systems.

1.2 Research Objectives

Based on the discussion thus far, the objectives of this thesis lie at the intersection of nuclear structure theory and quantum information processing, aiming to explore how these domains can contribute to the development of scalable, practical and efficient quantum technologies.

Firstly, we seek to model the nuclear structure of lanthanide nuclei, elucidating their magnetic and electric properties and understanding how these properties impact hyperfine interactions in both electronic and muonic systems. This research addresses the need for accurate nuclear models to inform the design of nuclear spin-based qudit systems, which could provide higher-dimensional alternatives to qubits in quantum computing.

Secondly, we perform an in-depth theoretical analysis of the fidelity of qudit quantum gates in the presence of Markovian noise, with the goal of identifying conditions under which qudits outperform multi-qubit systems. This focus on gate fidelity is critical for understanding how to mitigate decoherence and noise, enabling more robust quantum operations. Given that qudits naturally encode larger Hilbert spaces, our work directly addresses the scalability challenges of quantum systems, offering a potential path to higher-dimensional quantum architectures that maintain computational efficiency. We extended this framework from the nearly noise-free regime to the strong-coupling limit, where the nonlinear effects of the higher-order noise effects become significant, requiring a perturbative expansion of the AGI to capture these effects. From this full perturbative expansion, we aim to characterise the transition from linear to nonlinear behaviour in open qudit systems, and explore the implications for qudit-based quantum computing.

Finally, we develop and compare pulse-level optimal control techniques for qudit gate synthesis, assessing their robustness to environmental noise and control imperfections. By developing a framework for benchmarking optimal control methods on qudit systems,

this work aims to enhance the precision and efficiency of quantum gate operations in high-dimensional qudit systems. The implications of this work are broad, as optimal control is fundamental to the realisation of high-fidelity quantum operations, scalable quantum circuits, and ultimately fault-tolerant quantum computing.

1.3 Thesis Overview

The thesis is structured in two main parts, each focusing on a different aspect of quantum information science and nuclear physics, yet tied together by the overarching theme of enhancing quantum computing through nuclear spin systems and qudits.

The first part, *Qudits in Nuclear Spins of Lanthanide-Molecular Complexes*, examines the nuclear structure of lanthanide isotopes and their hyperfine anomalies to lay the groundwork for understanding the role of nuclear spins in quantum information processing.

Chapter 2 explores the nuclear structure of isotopes ^{161}Dy, ^{163}Dy, ^{159}Tb, and ^{165}Ho using the HFBCS model. The chapter provides insights into the deformation of nucleon distributions and their implications for magnetic dipole and electric quadrupole moments. It validates the HFBCS model's accuracy for highly deformed nuclear structures and sets the stage for further investigations into hyperfine interactions.

Chapter 3 extends to the hyperfine structure of hydrogen-like dysprosium ions, focusing on the corrections arising from finite nuclear size and magnetisation—the Breit-Rosenthal and Bohr-Weisskopf effects. The chapter analyses these corrections in both electronic and muonic systems, revealing the significant impact of nuclear structure on hyperfine splittings and providing a basis for leveraging muonic spectroscopy in probing nuclear properties.

The second part, *Quantum Information Processing with Qudits*, transitions to the exploration of qudit-based quantum computing, examining how these systems perform under noisy conditions and how optimal control techniques can be utilised to synthesise qudit gates effectively.

Chapter 4 compares the fidelity of quantum gates in noisy single-qudit systems against equivalent multi-qubit systems, establishing critical thresholds for qudit advantages in gate performance. The chapter introduces a theoretical framework for evaluating the AGI in relation to noise strength and gate time, providing practical benchmarks for qudit systems across different dimensions.

Chapter 5 extends the fidelity analysis to the nonlinear regime, where higher-order noise corrections become significant. A perturbative expansion of the AGI is derived, and numerical simulations validate the transition from linear to nonlinear behavior in open qudit systems. The chapter emphasises the importance of gate-dependent fidelity effects and explores their implications for qudit-based quantum computing.

Chapter 6 investigates pulse-level control techniques for qudit gate synthesis, specifically comparing the Givens Rotation Decomposition (GRD) and GRAPE algorithms. The chapter examines their robustness to noise and control errors, offering practical guidelines for gate generation in qudit systems and introducing hybrid approaches to optimise gate fidelity and efficiency.

Together, these chapters contribute to a deeper understanding of how nuclear spin qudits can be harnessed for quantum information processing and how optimal control methods

can be tailored to enhance high-dimensional quantum computing. By bridging the gap between nuclear structure theory and quantum information science, this thesis aims to advance the field of quantum technologies and pave the way for scalable, high-fidelity qudit-based quantum computing.

References Cited in this Chapter

[1] O. Ezratty. "Perspective on superconducting qubit quantum computing". In: *The European Physical Journal A* 59.5 (May 2, 2023), p. 94. DOI: 10.1140/epja/s10050-023-01006-7.

[2] R. P. Feynman. "Simulating physics with computers". In: *International Journal of Theoretical Physics* 21.6 (June 1982), pp. 467–488. DOI: 10.1007/BF02650179.

[3] "40 years of quantum computing". In: *Nature Reviews Physics* 4.1 (Jan. 10, 2022), pp. 1–1. DOI: 10.1038/s42254-021-00410-6.

[4] J. I. Manin. "Mathematics as Metaphor: Selected Essays of Yuri I. Manin". In: *Philosophia Mathematica* 17.1 (Apr. 1, 2008), pp. 122–123. DOI: 10.1093/philmat/nkn013.

[5] P. Benioff. "The computer as a physical system: A microscopic quantum mechanical Hamiltonian model of computers as represented by Turing machines". In: *Journal of Statistical Physics* 22.5 (May 1980), pp. 563–591. DOI: 10.1007/BF01011339.

[6] D. Deutsch. "Quantum theory, the Church–Turing principle and the universal quantum computer". In: *Proceedings of the Royal Society of London. A. Mathematical and Physical Sciences* 400.1818 (July 8, 1985), pp. 97–117. DOI: 10.1098/rspa.1985.0070.

[7] P. W. Shor. "Polynomial-Time Algorithms for Prime Factorization and Discrete Logarithms on a Quantum Computer". In: *SIAM Journal on Computing* 26.5 (Oct. 1997), pp. 1484–1509. DOI: 10.1137/S0097539795293172.

[8] L. K. Grover. "A fast quantum mechanical algorithm for database search". In: *Proceedings of the twenty-eighth annual ACM symposium on Theory of computing - STOC '96*. Philadelphia, Pennsylvania, United States: ACM Press, 1996, pp. 212–219. DOI: 10.1145/237814.237866.

[9] S. Lloyd. "Universal Quantum Simulators". In: *Science* 273.5278 (Aug. 23, 1996), pp. 1073–1078. DOI: 10.1126/science.273.5278.1073.

[10] M. Veldhorst, H. G. J. Eenink, et al. "Silicon CMOS architecture for a spin-based quantum computer". In: *Nature Communications* 8.1 (Dec. 15, 2017), p. 1766. DOI: 10.1038/s41467-017-01905-6.

[11] M. F. Gonzalez-Zalba, S. De Franceschi, et al. "Scaling silicon-based quantum computing using CMOS technology". In: *Nature Electronics* 4.12 (Dec. 20, 2021), pp. 872–884. DOI: 10.1038/s41928-021-00681-y.

[12] D. Spicer. "The First Computers: History and Architectures (review)". In: *Technology and Culture* 42.3 (July 2001), pp. 615–617. DOI: 10.1353/tech.2001.0140.

[13] M. Kjaergaard, M. E. Schwartz, et al. *Programming a quantum computer with quantum instructions*. Dec. 28, 2020. DOI: https://doi.org/10.48550/arXiv.2001.08838.

[14] I. Pogorelov et al. "Compact Ion-Trap Quantum Computing Demonstrator". In: *PRX Quantum* 2.2 (June 2021), p. 020343. DOI: 10.1103/PRXQuantum.2.020343.

[15] C. D. Bruzewicz, J. Chiaverini, et al. "Trapped-ion quantum computing: Progress and challenges". In: *Applied Physics Reviews* 6.2 (June 1, 2019), p. 021314. DOI: 10.1063/1.5088164.

[16] Y. Chi, J. Huang, et al. "A programmable qudit-based quantum processor". In: *Nature Communications* 13.1 (Mar. 4, 2022), p. 1166. DOI: 10.1038/s41467-022-28767-x.

[17] S. Slussarenko and G. J. Pryde. "Photonic quantum information processing: A concise review". In: *Applied Physics Reviews* 6.4 (Dec. 1, 2019), p. 041303. DOI: 10.1063/1.5115814.

[18] M. Morgado and S. Whitlock. "Quantum simulation and computing with Rydberg-interacting qubits". In: *AVS Quantum Science* 3.2 (June 1, 2021), p. 023501. DOI: 10.1116/5.0036562.

[19] I. S. Madjarov et al. "High-fidelity entanglement and detection of alkaline-earth Rydberg atoms". In: *Nature Physics* 16.8 (Aug. 2020), pp. 857–861. DOI: 10.1038/s41567-020-0903-z.

[20] A. Chiesa et al. "Blueprint for a molecular-spin quantum processor". In: *Physical Review Applied* 19 (June 2023). Publisher: American Physical Society, p. 064060. DOI: 10.1103/PhysRevApplied.19.064060.

[21] E. Moreno-Pineda, C. Godfrin, et al. "Molecular Spin Qudits for Quantum Algorithms". In: *Chemical Society Reviews* 47.2 (2018), pp. 501–513. DOI: 10.1039/c5cs00933b.

[22] Alejandro Gaita-Ariño, Fernando Luis, et al. "Molecular spins for quantum computation." In: *Nature Chemistry* 11.4 (Apr. 1, 2019). MAG ID: 2924254540, pp. 301–309. DOI: 10.1038/s41557-019-0232-y.

[23] G. Burkard, T. D. Ladd, et al. "Semiconductor spin qubits". In: *Reviews of Modern Physics* 95.2 (June 14, 2023), p. 025003. DOI: 10.1103/RevModPhys.95.025003.

[24] X. Zhang, H.-O. Li, et al. "Semiconductor quantum computation". In: *National Science Review* 6.1 (Jan. 1, 2019), pp. 32–54. DOI: 10.1093/nsr/nwy153.

[25] F. Flamini, N. Spagnolo, et al. "Photonic quantum information processing: a review". In: *Reports on Progress in Physics* 82.1 (Jan. 1, 2019), p. 016001. DOI: 10.1088/1361-6633/aad5b2.

[26] F. Arute, K. Arya, et al. "Quantum supremacy using a programmable superconducting processor". In: *Nature* 574.7779 (Oct. 24, 2019), pp. 505–510. DOI: 10.1038/s41586-019-1666-5.

[27] *First IBM Quantum Data Center in Europe Opens; Will Include IBM's Most Performant Quantum Systems*. IBM Newsroom. URL: https://newsroom.ibm.com/2024-10-01-first-ibm-quantum-data-center-in-europe-opens-will-include-ibms-most-performant-quantum-systems (visited on 10/02/2024).

[28] D. Castelvecchi. "Quantum computers ready to leap out of the lab in 2017". In: *Nature* 541.7635 (Jan. 2017), pp. 9–10. DOI: 10.1038/541009a.

[29] S. Krinner et al. "Realizing repeated quantum error correction in a distance-three surface code". In: *Nature* 605.7911 (May 2022), pp. 669–674. DOI: 10.1038/s41586-022-04566-8.

[30] D. P. DiVincenzo. "The Physical Implementation of Quantum Computation". In: *Fortschritte der Physik* 48.9 (Sept. 2000), pp. 771–783. DOI: 10.1002/1521-3978(200009)48:9/11<771::AID-PROP771>3.0.CO;2-E.

[31] Y. Wang, Z. Hu, et al. "Qudits and High-Dimensional Quantum Computing". In: *Frontiers in Physics* 8 (Nov. 10, 2020), p. 589504. DOI: 10.3389/fphy.2020.589504.

[32] N. P. Brusentsov and J. Ramil Alvarez. "Ternary Computers: The Setun and the Setun 70". In: *Perspectives on Soviet and Russian Computing*. Ed. by J. Impagliazzo and E. Proydakov. Vol. 357. IFIP Advances in Information and Communication Technology. Berlin, Heidelberg: Springer Berlin Heidelberg, 2011, pp. 74–80. DOI: 10.1007/978-3-642-22816-2_10.

[33] A. Chiesa, F. Petiziol, et al. "Embedded quantum-error correction and controlled-phase gate for molecular spin qubits". In: *AIP Advances* 11.2 (Feb. 1, 2021), p. 025134. DOI: 10.1063/9.0000166.

[34] N. P. D. Sawaya, T. Menke, et al. "Resource-efficient digital quantum simulation of d-level systems for photonic, vibrational, and spin-s Hamiltonians". In: *npj Quantum Information* 6.1 (June 2, 2020), p. 49. DOI: 10.1038/s41534-020-0278-0.

[35] M. N. Leuenberger and D. Loss. "Grover algorithm for large nuclear spins in semiconductors". In: *Physical Review B* 68.16 (Oct. 16, 2003), p. 165317. DOI: 10.1103/PhysRevB.68.165317.

[36] A. Mair, A. Vaziri, et al. "Entanglement of the orbital angular momentum states of photons". In: *Nature* 412.6844 (July 2001), pp. 313–316. DOI: 10.1038/35085529.

[37] F. A. An, A. Ransford, et al. "High Fidelity State Preparation and Measurement of Ion Hyperfine Qubits with I $>$ 1 2". In: *Physical Review Letters* 129.13 (Sept. 19, 2022), p. 130501. DOI: 10.1103/PhysRevLett.129.130501.

[38] C. Adambukulam, B. C. Johnson, et al. "Hyperfine Spectroscopy and Fast, All-Optical Arbitrary State Initialization and Readout of a Single, Ten-Level Ge 73 Vacancy Nuclear Spin Qudit in Diamond". In: *Physical Review Letters* 132.6 (Feb. 9, 2024), p. 060603. DOI: 10.1103/PhysRevLett.132.060603.

[39] B. L. Brock, S. Singh, et al. *Quantum Error Correction of Qudits Beyond Break-even*. Sept. 23, 2024. DOI: https://doi.org/10.48550/arXiv.2409.15065.

[40] L. E. Fischer, D. Miller, et al. "Ancilla-free implementation of generalized measurements for qubits embedded in a qudit space". In: *Physical Review Research* 4.3 (July 11, 2022), p. 033027. DOI: 10.1103/PhysRevResearch.4.033027.

[41] E. Moreno-Pineda and W. Wernsdorfer. "Measuring molecular magnets for quantum technologies". In: *Nature Reviews Physics* 3.9 (Sept. 2021), pp. 645–659. DOI: 10.1038/s42254-021-00340-3.

[42] S. Thiele, F. Balestro, et al. "Electrically driven nuclear spin resonance in single-molecule magnets". In: *Science* 344.6188 (June 6, 2014), pp. 1135–1138. DOI: 10.1126/science.1249802.

[43] C. Godfrin, A. Ferhat, et al. "Operating Quantum States in Single Magnetic Molecules: Implementation of Grover's Quantum Algorithm". In: *Physical Review Letters* 119.18 (Nov. 2, 2017), p. 187702. DOI: 10.1103/PhysRevLett.119.187702.

[44] A. L. Thomas. *Phthalocyanine Research and Applications*. 1st ed. Boca Raton: CRC Press, Sept. 25, 2024. DOI: 10.1201/9781003574231.

[45] P. Gregory. "Industrial applications of phthalocyanines". In: *Journal of Porphyrins and Phthalocyanines* 04.4 (June 2000). Publisher: World Scientific Publishing Co., pp. 432–437. DOI: 10.1002/(SICI)1099-1409(200006/07)4:4<432::AID-JPP254>3.0.CO;2-N.

[46] B. E. Williamson, T. C. VanCott, et al. "Determination of the ground state of manganese phthalocyanine in an argon matrix using magnetic circular dichroism and absorption spectroscopy". In: *Journal of the American Chemical Society* 114.7 (Mar. 1992), pp. 2412–2419. DOI: 10.1021/ja00033a016.

[47] Naoto Ishikawa, Miki Sugita, et al. "Lanthanide Double-Decker Complexes Functioning as Magnets at the Single-Molecular Level". In: *Journal of the American Chemical Society* 125.29 (June 25, 2003), pp. 8694–8695. DOI: 10.1021/ja029629n.

[48] N. Ishikawa, M. Sugita, et al. "Quantum Tunneling of Magnetization in Lanthanide Single-Molecule Magnets". In: *Angewandte Chemie International Edition* 44.19 (May 6, 2005), pp. 2931–2935. DOI: 10.1002/anie.200462638.

[49] L. Thomas, F. Lionti, et al. "Macroscopic quantum tunnelling of magnetization in a single crystal of nanomagnets". In: *Nature* 383.6596 (Sept. 1996), pp. 145–147. DOI: 10.1038/383145a0.

[50] H. Biard, E. Moreno-Pineda, et al. "Increasing the Hilbert space dimension using a single coupled molecular spin". In: *Nature Communications* 12.1 (Dec. 2021), p. 4443. DOI: 10.1038/s41467-021-24693-6.

[51] W. Wernsdorfer. "From micro- to nano-SQUIDs: applications to nanomagnetism". In: *Superconductor Science and Technology* 22.6 (June 1, 2009), p. 064013. DOI: 10.1088/0953-2048/22/6/064013.

[52] Romain Vincent, Svetlana Klyatskaya, et al. "Electronic read-out of a single nuclear spin using a molecular spin transistor". In: *Nature* 488.7411 (Aug. 16, 2012), pp. 357–360. DOI: 10.1038/nature11341.

[53] J. Angel and P. Sandars. "The hyperfine structure Stark effect I. Theory". In: *Proceedings of the Royal Society of London. Series A. Mathematical and Physical Sciences* 305.1480 (May 21, 1968), pp. 125–138. DOI: 10.1098/rspa.1968.0109.

[54] M. N. Leuenberger and D. Loss. "Quantum computing in molecular magnets". In: *Nature* 410.6830 (Apr. 2001), pp. 789–793. DOI: 10.1038/35071024.

[55] M. N. Leuenberger, D. Loss, et al. "Quantum Information Processing with Large Nuclear Spins in GaAs Semiconductors". In: *Physical Review Letters* 89.20 (Oct. 28, 2002), p. 207601. DOI: 10.1103/PhysRevLett.89.207601.

[56] W. Wernsdorfer and M. Ruben. "Synthetic Hilbert Space Engineering of Molecular Qu *d* its: Isotopologue Chemistry". In: *Advanced Materials* 31.26 (June 2019), p. 1806687. DOI: 10.1002/adma.201806687.

[57] K. Najafi, A. L. Wysocki, et al. "Toward Long-Range Entanglement between Electrically Driven Single-Molecule Magnets". In: *The Journal of Physical Chemistry Letters* 10.23 (Dec. 5, 2019), pp. 7347–7355. DOI: 10.1021/acs.jpclett.9b03131.

[58] E. Moreno-Pineda, S. Klyatskaya, et al. "Observation of Cooperative Electronic Quantum Tunneling: Increasing Accessible Nuclear States in a Molecular Qudit". In: *Inorganic Chemistry* 57.16 (Aug. 20, 2018), pp. 9873–9879. DOI: 10.1021/acs.inorgchem.8b00823.

[59] W. Gerlach and O. Stern. "Der experimentelle Nachweis der Richtungsquantelung im Magnetfeld". In: *Zeitschrift für Physik* 9.1 (Dec. 1, 1922), pp. 349–352. DOI: 10.1007/BF01326983.

[60] E. M. Purcell, H. C. Torrey, et al. "Resonance Absorption by Nuclear Magnetic Moments in a Solid". In: *Physical Review* 69.1 (Jan. 1, 1946), pp. 37–38. DOI: 10.1103/PhysRev.69.37.

[61] A. Caneschi, D. Gatteschi, et al. "Toward molecular magnets: the metal-radical approach". In: *Accounts of Chemical Research* 22.11 (Nov. 1, 1989), pp. 392–398. DOI: 10.1021/ar00167a004.

[62] G. Christou, D. Gatteschi, et al. "Single-Molecule Magnets". In: *MRS Bulletin* 25.11 (Nov. 2000), pp. 66–71. DOI: 10.1557/mrs2000.226.

[63] D. Gatteschi, R. Sessoli, et al. *Molecular Nanomagnets*. Oxford University Press, Mar. 2, 2006. DOI: 10.1093/acprof:oso/9780198567530.001.0001.

[64] J. E. Rosenthal and G. Breit. "The Isotope Shift in Hyperfine Structure". In: *Physical Review* 41.4 (Aug. 15, 1932), pp. 459–470. DOI: 10.1103/PhysRev.41.459.

[65] A. Bohr and V. F. Weisskopf. "The Influence of Nuclear Structure on the Hyperfine Structure of Heavy Elements". In: *Physical Review* 77.1 (Jan. 1, 1950), pp. 94–98. DOI: 10.1103/PhysRev.77.94.

[66] C. D. Anderson and S. H. Neddermeyer. "Cloud Chamber Observations of Cosmic Rays at 4300 Meters Elevation and Near Sea-Level". In: *Physical Review* 50.4 (Aug. 15, 1936), pp. 263–271. DOI: 10.1103/PhysRev.50.263.

[67] V. W. Hughes, D. W. McColm, et al. "Formation of Muonium and Observation of its Larmor Precession". In: *Physical Review Letters* 5.2 (July 15, 1960), pp. 63–65. DOI: 10.1103/PhysRevLett.5.63.

[68] K. P. Jungmann. "Past, Present and Future of Muonium". In: *In Memory of Vernon Willard Hughes*. Proceedings of the Memorial Symposium in Honor of Vernon Willard Hughes. Yale University, USA: World Scientific, Dec. 2004, pp. 134–153. DOI: 10.1142/9789812702425_0009.

[69] G. Lospalluto, A. Antognini, et al. "Towards muon cooling at the Paul Scherrer Institute". In: *Proceedings of Muon4Future Workshop — PoS(Muon4Future2023)*. Muon4Future Workshop. Istituto Veneto di Lettere, Scienze ed Arti - Palazzo Franchetti, Venezia, Italy: Sissa Medialab, Mar. 15, 2024, p. 009. DOI: 10.22323/1.452.0009.

[70] K. Shimomura, A. Koda, et al. "Pulsed muon facility of J-PARC MUSE". In: *Interactions* 245.1 (Mar. 5, 2024), p. 31. DOI: 10.1007/s10751-024-01863-8.

[71] E. L. Hahn. "Spin Echoes". In: *Physical Review* 80.4 (Nov. 15, 1950), pp. 580–594. DOI: 10.1103/PhysRev.80.580.

[72] M. H. Levitt. "Composite pulses". In: *Progress in Nuclear Magnetic Resonance Spectroscopy* 18.2 (Jan. 1986), pp. 61–122. DOI: 10.1016/0079-6565(86)80005-X.

[73] A. P. Peirce, M. A. Dahleh, et al. "Optimal control of quantum-mechanical systems: Existence, numerical approximation, and applications". In: *Physical Review A* 37.12 (June 1, 1988), pp. 4950–4964. DOI: 10.1103/PhysRevA.37.4950.

[74] C. Brif, R. Chakrabarti, et al. "Control of quantum phenomena: past, present and future". In: *New Journal of Physics* 12.7 (July 1, 2010), p. 075008. DOI: 10.1088/1367-2630/12/7/075008.

[75] J. Preskill. "Quantum Computing in the NISQ era and beyond". In: *Quantum* 2 (Aug. 6, 2018), p. 79. DOI: 10.22331/q-2018-08-06-79.

[76] J. P. Dowling and G. J. Milburn. "Quantum technology: the second quantum revolution". In: *Philosophical Transactions of the Royal Society of London. Series A: Mathematical, Physical and Engineering Sciences* 361.1809 (Aug. 15, 2003). Ed. by A. G. J. MacFarlane, pp. 1655–1674. DOI: 10.1098/rsta.2003.1227.

[77] Clément Godfrin, Stefan Thiele, et al. "Electrical Read-Out of a Single Spin Using an Exchange-Coupled Quantum Dot". In: *ACS Nano* 11.4 (Apr. 14, 2017). MAG ID: 2606235355, pp. 3984–3989. DOI: 10.1021/acsnano.7b00451.

[78] C. Godfrin, R. Ballou, et al. "Generalized Ramsey interferometry explored with a single nuclear spin qudit". In: *npj Quantum Information* 4.1 (Dec. 2018), p. 53. DOI: 10.1038/s41534-018-0101-3.

[79] M. James. "Optimal Quantum Control Theory". In: *Annual Review of Control, Robotics, and Autonomous Systems* 4.1 (May 3, 2021), pp. 343–367. DOI: 10.1146/annurev-control-061520-010444.

[80] D. D'Alessandro. *Introduction to quantum control and dynamics*. 2nd edition. Advances in mathematics series. Boca Raton: CRC Press, 2021.

[81] I. R. Sola, B. Y. Chang, et al. "Quantum Control in Multilevel Systems". In: *Advances In Atomic, Molecular, and Optical Physics*. Vol. 67. Elsevier, 2018, pp. 151–256. DOI: 10.1016/bs.aamop.2018.02.003.

[82] M. A. Nielsen and I. L. Chuang. *Quantum Computation and Quantum Information: 10th Anniversary Edition*. Cambridge: Cambridge University Press, 2010. DOI: 10.1017/CBO9780511976667.

[83] V. Gorini, A. Kossakowski, et al. "Completely positive dynamical semigroups of N -level systems". In: *Journal of Mathematical Physics* 17.5 (May 1, 1976), pp. 821–825. DOI: 10.1063/1.522979.

[84] G. Lindblad. "On the generators of quantum dynamical semigroups". In: *Communications in Mathematical Physics* 48.2 (June 1976), pp. 119–130. DOI: 10.1007/BF01608499.

[85] D. Manzano. "A short introduction to the Lindblad master equation". In: *AIP Advances* 10.2 (Feb. 1, 2020), p. 025106. DOI: 10.1063/1.5115323.

[86] H.-P. Breuer, E.-M. Laine, et al. "*Colloquium* : Non-Markovian dynamics in open quantum systems". In: *Reviews of Modern Physics* 88.2 (Apr. 19, 2016), p. 021002. DOI: 10.1103/RevModPhys.88.021002.

[87] C. G. Almudever, L. Lao, et al. "The engineering challenges in quantum computing". In: *Design, Automation & Test in Europe Conference & Exhibition (DATE), 2017*. 2017 Design, Automation & Test in Europe Conference & Exhibition (DATE). Lausanne, Switzerland: IEEE, Mar. 2017, pp. 836–845. DOI: 10.23919/DATE.2017.7927104.

[88] C. G. Almudever and E. Alarcon. "Structured Optimized Architecting of Full-Stack Quantum Systems in the NISQ era". In: *2021 Design, Automation & Test in Europe Conference & Exhibition (DATE)*. 2021 Design, Automation & Test in Europe Conference & Exhibition (DATE). Grenoble, France: IEEE, Feb. 1, 2021, pp. 762–767. DOI: 10.23919/DATE51398.2021.9474197.

[89] M. Grassl, L. Kong, et al. "Quantum Error-Correcting Codes for Qudit Amplitude Damping". In: *IEEE Transactions on Information Theory* 64.6 (June 2018), pp. 4674–4685. DOI: 10.1109/TIT.2018.2790423.

[90] F. Petiziol, A. Chiesa, et al. "Counteracting dephasing in Molecular Nanomagnets by optimized qudit encodings". In: *npj Quantum Information* 7.1 (Aug. 26, 2021), p. 133. DOI: 10.1038/s41534-021-00466-3.

[91] A. Chiesa, E. Macaluso, et al. "Molecular Nanomagnets as Qubits with Embedded Quantum-Error Correction". In: *The Journal of Physical Chemistry Letters* 11.20 (Oct. 15, 2020), pp. 8610–8615. DOI: 10.1021/acs.jpclett.0c02213.

[92] R. F. Uy and D. A. Gangloff. *Qudit-based quantum error-correcting codes from irreducible representations of SU(d)*. Oct. 3, 2024. DOI: 10.48550/arXiv.2410.02407.

[93] E. D. Sontag. *Mathematical Control Theory*. Red. by J. E. Marsden, L. Sirovich, et al. Vol. 6. Texts in Applied Mathematics. New York, NY: Springer New York, 1998. DOI: 10.1007/978-1-4612-0577-7.

[94] C. P. Koch, U. Boscain, et al. "Quantum optimal control in quantum technologies. Strategic report on current status, visions and goals for research in Europe". In: *EPJ Quantum Technology* 9.1 (Dec. 2022), p. 19. DOI: 10.1140/epjqt/s40507-022-00138-x.

[95] S. J. Glaser, U. Boscain, et al. "Training Schrödinger's cat: quantum optimal control: Strategic report on current status, visions and goals for research in Europe".

In: *The European Physical Journal D* 69.12 (Dec. 2015), p. 279. DOI: 10.1140/epjd/e2015-60464-1.

[96] G. Brennen, D. O'Leary, et al. "Criteria for exact qudit universality". In: *Physical Review A* 71.5 (May 16, 2005), p. 052318. DOI: 10.1103/PhysRevA.71.052318.

[97] N. Khaneja, T. Reiss, et al. "Optimal control of coupled spin dynamics: design of NMR pulse sequences by gradient ascent algorithms". In: *Journal of Magnetic Resonance* 172.2 (Feb. 2005), pp. 296–305. DOI: 10.1016/j.jmr.2004.11.004.

[98] G. E. Karniadakis, I. G. Kevrekidis, et al. "Physics-informed machine learning". In: *Nature Reviews Physics* 3.6 (May 24, 2021), pp. 422–440. DOI: 10.1038/s42254-021-00314-5.

[99] M. Raissi, P. Perdikaris, et al. "Physics-informed neural networks: A deep learning framework for solving forward and inverse problems involving nonlinear partial differential equations". In: *Journal of Computational Physics* 378 (Feb. 2019), pp. 686–707. DOI: 10.1016/j.jcp.2018.10.045.

[100] S. Mowlavi and S. Nabi. "Optimal control of PDEs using physics-informed neural networks". In: *Journal of Computational Physics* 473 (Jan. 2023), p. 111731. DOI: 10.1016/j.jcp.2022.111731.

[101] A. D. Jagtap, K. Kawaguchi, et al. "Adaptive activation functions accelerate convergence in deep and physics-informed neural networks". In: *Journal of Computational Physics* 404 (Mar. 2020), p. 109136. DOI: 10.1016/j.jcp.2019.109136.

[102] A. Norambuena, M. Mattheakis, et al. "Physics-Informed Neural Networks for Quantum Control". In: *Physical Review Letters* 132.1 (Jan. 3, 2024), p. 010801. DOI: 10.1103/PhysRevLett.132.010801.

[103] N. B. Dehaghani and A. P. Aguiar. *An Application of Pontryagin Neural Networks to Solve Optimal Quantum Control Problems*. Feb. 1, 2023. DOI: https://doi.org/10.48550/arXiv.2302.09143.

PART I

QUDITS IN NUCLEAR SPINS OF LANTHANIDE-MOLECULAR COMPLEXES

Qudits in Nuclear Spins of Lanthanide-Molecular Complexes

The investigation of highly charged hydrogen-like lanthanide ions, both electronic and muonic, offers a compelling approach to explore the internal structure of their atomic nuclei. In this work, we employ nuclear structure simulations to precisely calculate the hyperfine splitting of such ions, with a particular focus on the inclusion of finite-volume effects, such as the Bohr-Weisskopf and Breit-Rosenthal corrections. These arise from the penetration of the electron and muon wavefunctions into the nuclear charge and magnetic dipole distributions. Incorporating these corrections is crucial for enhancing our understanding of nuclear magnetic and electric moments. Our simulations utilise a modified Skyrme-Hartree-Fock model, incorporating BCS pairing corrections and self-consistent blocking, which is well suited for describing highly deformed nuclei. Special attention is given to the nuclear properties of ^{159}Tb, ^{161}Dy, ^{163}Dy and ^{165}Ho, and the hydrogen-like atomic properties of $^{161}Dy^{65+}$ and $^{163}Dy^{65+}$, and the model's applicability is extended to multi-electron ions by analysing the hyperfine anomaly between different isotopes.

CHAPTER 2

Ab initio MODELLING OF LANTHANIDE NUCLEI

Does the walker choose the path, or the path the walker?

Sabriel in "Sabriel" - Garth Nix

Contents

2.1 Introduction . . . 33
2.1.1 Background and Motivation . . . 33
2.1.2 Objectives and Contributions . . . 34
2.1.3 Overview . . . 35
2.2 Theory . . . 35
2.2.1 Skyrme-Hartree-Fock Model . . . 36
2.2.1.1 Effective interaction . . . 36
2.2.1.2 Skyrme Hartree-Fock equations . . . 37
2.2.1.3 Spherical symmetry and nuclear deformation . . . 38
2.2.1.4 Nucleon pairing and self-consistent blocking . . . 39
2.2.1.5 Time-reversal symmetry breaking . . . 40
2.2.2 Multipole Moments . . . 40
2.2.2.1 Electric monopole moment . . . 42
2.2.2.2 Magnetic dipole moment . . . 42
2.2.2.3 Electric quadrupole moment . . . 44
2.3 Methods . . . 44
2.3.1 Skyrme-HFBCS Code . . . 45
2.3.2 Calculation of the Moments and Potentials . . . 45
2.4 Results . . . 46
2.4.1 Nucleon Distributions . . . 46
2.4.1.1 Nucleon densities . . . 46
2.4.1.2 Proton currents . . . 46
2.4.1.3 Neutron currents . . . 49
2.4.2 Multipole Distributions . . . 53
2.4.2.1 Monopoles . . . 54
2.4.2.2 Dipoles . . . 57
2.4.2.3 Quadrupoles . . . 59
2.5 Discussion . . . 60
2.5.1 Summary . . . 60
2.5.2 Outlook . . . 61
References Cited in this Chapter . . . 62

Note: This chapter and the results presented herein, together with Chapter 3 and the results presented therein, have been prepared concurrently with a manuscript to be published under the working title "The hyperfine interaction as a probe of the microscopic structure of the atomic nucleus" together with our collaborators Johann Bartel, Hervé Molique and Ludovic Bonneau

2.1 Introduction

In this chapter, we study the nuclear structure of select lanthanide isotopes using the Hartree-Fock-BCS (HFBCS) model to deepen our understanding of their complex properties and significance as building blocks of novel quantum information processing platforms. By focusing on isotopes of terbium, dysprosium, and holmium, which exhibit notable nuclear deformation and magnetic and quadrupolar interactions, and from which we aim to extract nuclear observables like radii, magnetic dipole moments, and quadrupole moments. The chapter provides background on the theoretical challenges, outlines the objectives and contributions of the study, and offers a roadmap through the theoretical foundations, computational methods, and key results.

2.1.1 Background and Motivation

The nuclear landscape, comprising 254 stable, and over 3000 known radioactive, isotopes, provides a rich tapestry for studying the fundamental forces that govern matter at the subatomic level. Among these isotopes, the lanthanide nuclei represent a particularly intriguing region of the nuclear chart. Known for their large atomic numbers and highly deformed shapes, lanthanide nuclei pose both a challenge and an opportunity for nuclear theory. In such systems, the interplay between strong nuclear forces, Coulomb repulsion, and quantum effects gives rise to complex phenomena such as nuclear deformation, pairing correlations, and consequently significant magnetic and electric properties.

Within the context of low-energy nuclear theory, where one seeks to obtain a precise microscopic description of nuclear structure within a non-relativistic treatment (without incorporating mesonic degrees of freedom that would require a relativistic treatment), there are two fundamental challenges that arise: Firstly, the nucleus is an N-body problem, where N is the number of protons and neutrons in the nucleus. This problem is intractable for all but the smallest nuclei, and approximations must be made to model the interactions between many nucleons [104]. Secondly, the nuclear force, which is predominantly governed by the strong interaction, is not fully understood from a first-principles approach and must be approximated using effective interactions [105]. Therefore, in order to understand and accurately describe these phenomena in large complex nuclei, sophisticated theoretical models are required.

As a first step, one of the most promising approaches is the use of energy-density functionals (EDFs), which model the nuclear force through effective interactions [106]. Going further, the Skyrme-Hartree-Fock-BCS (HFBCS) model has emerged as a powerful tool for describing nuclear structure. By incorporating effective nuclear interactions into a constrained mean-field approach and also accounting for more complex pairing correlations, the HFBCS model offers a first-principles approach for studying deformed nuclei, particularly those in the lanthanide region [107]. However, many challenges remain in achieving accurate predictions consistently across the many nuclear properties including charge radii, magnetic moments, and multipole moments, especially when dealing with

the large variation in complexities of nuclear structure across the landscape of exotic, specifically odd-mass, nuclei [108].

The motivation for this work stems from the need to better understand the electric and magnetic properties of lanthanide nuclei from an *ab initio* perspective. The HFBCS model offers a valuable framework for investigating these complex nuclear systems, providing insights into the source of these properties through a microscopic description of their internal structure and behaviour. Understanding this is not only essential for refining nuclear structure theories but also holds broader significance for many applications ranging from the technological, including modern computing devices and lasers as well as battery and motor components in electric vehicles [109], to the fundamental, such as in the study of astrophysical nucleosynthesis in the kilonova (underluminous supernovae of compact binary systems, such as two neutron stars) of neutron star mergers [110].

In the context of our work, the lanthanides hold significant practical relevance as the fundamental components of lanthanide-organic single molecule magnets (SMMs), which have potential use cases in a variety of applications in quantum computing and quantum information technologies, and are the focus of increasing research interest, particularly within our collaboration [41, 56, 78]. These complexes rely on the manipulation of nuclear spin states via hyperfine interactions with valence electrons. Moreover, lanthanides exhibit favorable optical emission properties and slow magnetic relaxation, making them suitable for lasers and quantum transmitters in quantum communication networks as well as quantum memories [111]. Therefore, understanding how nuclear properties, such as spin and deformation, influence the behavior of electrons in these systems is crucial for both theoretical modeling and technological advancement.

From a nuclear physics perspective, lanthanide nuclei also serve as a useful benchmark for testing the accuracy and limitations of current nuclear models, such as the HFBCS approach. By studying the structure of these complex nuclei, we aim to refine our understanding of nuclear interactions and improve the predictive power of our models, particularly in relation to nucleon distributions, magnetic dipole moments, and electric quadrupole moments, and provide an ideal testing ground for advancing these models and applying them to real-world problems in both nuclear physics and material science.

2.1.2 Objectives and Contributions

This study aims to develop a comprehensive understanding of the nuclear structure of lanthanide nuclei using the HFBCS model. Specifically, our focus is on the isotopes of terbium ($_{65}$Tb), dysprosium ($_{66}$Dy) and holmium ($_{67}$Ho), exhibiting non-trivial nuclear deformation effects and prominent magnetic and quadrupolar hyperfine splittings. These elements are of particular interest for us in the context of lanthanide molecular complexes for quantum information processing applications, as they have been well-studied by our collaborators [56]. Of the 15, 10 and 12 respective isotopes of terbium, dysprosium and holmium having non-zero spin parity (see Tables A.1 to A.3 in Appendix A.1), only ^{159}Tb, ^{161}Dy, ^{163}Dy, and ^{165}Ho are stable. Hence, these four isotopes were chosen for our study.

The objectives are to compute and analyse the nucleon distributions, magnetic dipole moments, and electric quadrupole moments of these nuclei. A key objective is to investigate the predictive power of the HFBCS model in reproducing experimental observables such as nuclear radii, magnetic moments, and quadrupole moments.

In addition, to predict nuclear observables, this study also seeks to address deeper questions about the nuclear structure of these lanthanide nuclei. For example, it examines how accurately the HFBCS model can describe proton and neutron currents and how these currents contribute to the magnetic dipole moments, particularly in odd-mass nuclei where time-reversal symmetry is broken, offering a deeper understanding of the role of pairing correlations in shaping the nuclear magnetic properties. Another important objective is to assess how well the model captures the deformation of the nuclei, as reflected in their mass and electric quadrupole moments, and to compare these results with alternative nuclear models such as the point-charge, spherical shell models and the parametric Fermi model.

The contributions of this chapter are threefold: (1) applying the HFBCS model to lanthanide isotopes to yield insights into their nucleon distributions and magnetic properties, validating results against experimental data; (2) providing a detailed analysis of proton and neutron currents, between their spin and orbital contributions, and their roles in generating magnetic dipole moments, with an emphasis on pairing correlations and the behaviour of odd-mass nuclei; (3) advancing computational methods in nuclear moment calculations by refining HFBCS implementations for enhanced accuracy and reliability in determining multipole moments and radial density distributions. By improving the numerical integration techniques for the radial density distributions and exploring the accuracy of different averaging schemes for the monopole potentials, this study contributes to the development of more reliable methods for analysing nuclear structure.

2.1.3 Overview

The structure of this manuscript is organized to provide a clear progression from the theoretical foundation of the HFBCS model to its application in nuclear structure calculations. In Section 2.2, the theoretical framework of the Skyrme-Hartree-Fock model is discussed in detail, including the effective interactions that form the basis of the model. The section also covers the treatment of pairing correlations and time-reversal symmetry breaking, both of which are critical for modeling odd-mass nuclei. Finally, the method of multipole expansion is introduced as a means of calculating nuclear moments, focusing on the electric monopole, magnetic dipole, and electric quadrupole moments.

In Section 2.3, the computational techniques used in this study are described. This includes a discussion of the HFBCS code and the algorithms implemented to calculate the multipole moments from the nucleon distributions generated by the model. The section provides a detailed explanation of the computational workflow, from obtaining the nucleon data to performing the final multipole moment integrations.

The results of the study are presented in Section 2.4. Here, the nucleon (neutron and proton) matter distributions, proton and neutron currents, and the associated multipole moments are analysed for each of the isotopes studied. The results are compared with experimental data, and the strengths and limitations of the HFBCS model are discussed. The section concludes with an assessment of the model's accuracy in predicting the nuclear properties of deformed lanthanide nuclei.

2.2 Theory

In this section we present the theoretical framework for modelling the nuclear structure of deformed lanthanide nuclei using the Skyrme-Hartree-Fock model, and the subsequent

calculation of the nuclear moments by the multipole expansion method.

2.2.1 Skyrme-Hartree-Fock Model

Describing from first principles the finite distribution of the nucleons within a nucleus is fundamentally challenging for two main reasons: Firstly, even the simple two-body interaction between two bare nucleons requires quantum chromodynamics (QCD) and is not yet fully understood when one considers the full many-body system of quarks interacting via the strong force. Secondly, the interactions between larger numbers of protons and neutrons is itself an N-body problem, which is not solvable analytically and moreover computationally intractable [142].

2.2.1.1 Effective interaction

To address this first challenge, it is necessary to make some simplifying approximations and consider an effective interaction that captures the fundamental features of the nuclear force in the absence of a full first-principles approach.

The Skyrme-effective interaction provides a practical model for approximating the nuclear force and can be used to calculate the nuclear charge densities. This phenomenological approach has been remarkably successful in low-energy nuclear physics where one is interested in describing the structure and behaviour of nuclei in or near the nuclear ground-state.

The Skyrme interaction is a local effective interaction incorporating terms that each represent different parts of the nuclear force. These include the short-range nature that vanishes at distances larger than 2 fm, is attractive below this limit, and becomes strongly repulsive at very short distances. In the original form proposed by Skyrme [143] and implemented by Vautherin and Brink [144], the interaction is written as a sum of a two-body and three-body potential terms,

$$\mathcal{V}_{Sk} = \mathcal{V}_{Sk,2} + \mathcal{V}_{Sk,3}, \tag{2.1}$$

given by

$$\begin{aligned}\mathcal{V}_{Sk,2}(\vec{R}_i, \vec{R}_j) = t_0 \left[1 + x_0 P_\sigma\right] \delta(\vec{R}_{ij}) + \frac{1}{2} t_1 \left[1 + x_1 P_\sigma\right] \left[\delta(\vec{R}_{ij})\, k^2 + k'^2\, \delta(\vec{R}_{ij})\right] \\ + t_2 \left[1 + x_2 P_\sigma\right] \vec{k}' \cdot \delta(\vec{R}_{ij}) \vec{k} + i W_0 (\sigma_i + \sigma_j) \cdot \left[\vec{k}' \times \delta(\vec{R}_{ij}) \vec{k}\right] ,\end{aligned} \tag{2.2}$$

and

$$\mathcal{V}_{Sk,3}(\vec{R}_i, \vec{R}_j, \vec{R}_k) = t_3 \left[1 + x_3 P_\sigma\right] \delta(\vec{R}_{ij}) \delta(\vec{R}_{jk}) , \tag{2.3}$$

where the interaction is parameterised by Dirac delta distributions on the relative distances $\vec{R}_{ij} = \vec{R}_i - \vec{R}_j$ between nucleons, the P_σ in the first term represents the spin-exchange operator of the σ Pauli matrices, and the $\vec{k}$ and $\vec{k}'$ are the momentum operators of the nucleons and the W_0 is the spin-orbit coupling strength. The t_i and x_i are the Skyrme parameters that are fitted to experimental data, like nuclear ground-state properties, but also to those of nuclear matter (being a fictitious system of $N = 2$ interacting nucleons in the absence of the Coulomb interaction).

Note that in the case of even-even nuclei (with time-reversal symmetry, as we shall see later), the three-body term can itself be expressed as a density-dependent two-body term,

$$\mathcal{V}_{Sk,3}(\vec{R}_i, \vec{R}_j, \rho) = \frac{1}{6} t_3 \left[1 + x_3 P_\sigma\right] \delta(\vec{R}_{ij}) \rho(\vec{\mathcal{R}}_{ij}) , \tag{2.4}$$

where $\vec{\mathcal{R}}_{ij} = (\vec{R}_i + \vec{R}_j)/2$ is the center-of-mass vector of the interacting nucleons and ρ is the total nucleon density $\rho = \rho_n + \rho_p$ of protons (p) and neutrons (n). Discussion of this density-dependent term leads naturally on to the many refinements and extensions of the Skyrme-type parameterisations that have been studied since the original proposal.

Without going into detail on this deep field of research, we will note one particular generalisation of the density-dependent term to one that is not necessarily linear in ρ but can be a general function of the density and also generalised to odd-even and odd-odd nuclei (with broken time-reversal symmetry). This leads to the family of Skyrme-type energy-density functionals (EDFs). Within this family of methods, the Skyrme SIII parametrisation [145] is widely used due to its success in describing nuclear spectroscopic properties, and is the one used in this study.

2.2.1.2 Skyrme Hartree-Fock equations

To now address the second challenge, we must consider the many-body problem of the nucleons interacting via the Skyrme-effective interaction. The Hartree-Fock (HF) method provides a framework for solving this problem by treating the nucleons as independent particles moving in an averaged field generated by the other nucleons. This mean-field approach is a common approximation in quantum many-body systems, and the incorporation of the Skyrme potential enables the further modelling of interactions between nearby nucleons.

Given the Hamiltonian of the system as

$$\mathcal{H} = T + \mathcal{V}_{Sk} + \mathcal{V}_{\text{Coul}} \tag{2.5}$$

with T the kinetic energy operator, $\mathcal{V}_{Sk}$ the Skyrme interaction, and $\mathcal{V}_{\text{Coul}}$ the Coulomb interaction, the expectation value with respect to a nucleus with ground-state $|\Phi\rangle$ a Slater determinant of the single-particle (s.p.) states φ_j is given by

$$\langle\Phi|\mathcal{H}|\Phi\rangle = \int H(\vec{R})\, d^3R. \tag{2.6}$$

Then, the Skyrme-Hartree-Fock equations can be obtained by requiring that the total energy is minimised with respect to the s.p. wavefunctions $\varphi_{q,j}(\vec{R})$, leading to the Schrödinger-like equations

$$\left[-\vec{\nabla}\cdot\frac{\hbar^2}{2m_q^*(\vec{R})}\vec{\nabla} + U_q(\vec{R}) - i\vec{W}_q(\vec{R})\cdot\left(\vec{\nabla}\times\vec{\sigma}\right)\right]\varphi_{q,j}(\vec{R}) = \varepsilon_{q,j}\varphi_{q,j}(\vec{R})\,, \tag{2.7}$$

that the $\varphi_{q,j}(\vec{R}\,)$ need to satisfy under the normalisation constraints

$$\frac{\delta}{\delta\varphi_{q,j}}\left[E - \sum_j \varepsilon_{q,j}\int|\varphi_{q,j}(\vec{R})|^2 d^3R\right] = 0\,. \tag{2.8}$$

Here, $m_q^*(\vec{R})$ is an effective mass term, $U_q(\vec{R})$ is the mean-field potential, $\varepsilon_{q,j}$ are the corresponding energies of the s.p. states $\varphi_{q,j}$ for $q \in n, p$ protons and neutrons, and $\vec{W}_q(\vec{R})$ the spin-orbit form factor.

This leads to an iterative procedure for solving the Skyrme-Hartree-Fock equations. Beginning with an initial guess for the fields entering the Schrödinger-like equations in

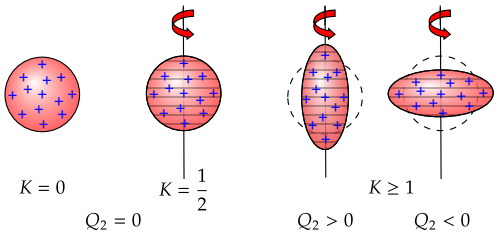


Figure 2.1 – Schematic illustration of the effect of nuclear deformations. The nuclear charge and current distributions are shown for different nuclear shapes. For nuclei with a spin $K \geq 1$, an electric quadrupole Q is allowed.

Eq. (2.7), the s.p. wavefunctions for the protons and neutrons, $\varphi_{p,j}(\vec{R})$ and $\varphi_{n,j}(\vec{R})$, are obtained by solution of the equation. These wavefunctions are in turn used to calculate the new densities of the Skyrme interaction, updating the fields entering the Schrödinger-like equations. This process is repeated until convergence is reached and the resulting local densities are obtained from the final wavefunctions.

2.2.1.3 Spherical symmetry and nuclear deformation

In our work on modelling the nuclear structure of lanthanide nuclei, we must consider the deformations of the nuclei away from sphericity, as it is well known that these nuclei exhibit prolate or oblate deformations. As an illustrative example, see Fig. 2.1.

This leads to a new challenge for solving the Skyrme-Hartree-Fock equations, as the spherical symmetry assumption is no longer valid and the equations cannot be easily resolved in configuration space. Indeed, for the rare earth nuclei we are interested in (and more particularly the lanthanides, whose atoms have interesting magnetic properties), all the nuclei show some well-developed prolate deformation, and axial symmetry can be reasonably assumed. Provided that the simple axial symmetry is dominant, and we can neglect more complex triaxial deformations (see Fig. 2.2), we can maintain the assumption of axial symmetry and truncate our multipolar expansions of the nuclear scalar and vector potentials (see Section 2.2.2) at the quadrupole moment, considering higher-order terms, such as the octupole moment, as negligible.

In order to resolve the Skyrme-Hartree-Fock equations for a deformed nucleus, one approach is to expand the nucleon wavefunctions in a truncated basis of an axially deformed harmonic oscillator (HO) [146, 147]. Then, the oscillator frequencies ω_z and $\omega_\perp$ are used to define the nuclear deformation parameter β. This parameter describes whether the nucleus is prolate ($\beta > 0$) or oblate ($\beta < 0$), and is used to characterise the nuclear shape. This leads to an additional optimisation step in the Skyrme-Hartree-Fock iterations, as the deformation parameter must also be determined self-consistently by minimising the total energy of the nucleus.

As a further refinement, the constrained Hartree-Fock (CHF) method can be used to study the deformation energy of the nucleus as a function of β [149]. Here, the constraint is applied to the mass quadrupole moment of the nucleus, which gives an accurate representation of the nuclear shape away from sphericity. As an example of this method in action, we can consider the nucleus ^{162}Dy, as shown in Fig. 2.2, where the deformation energy is calculated as a function of β to illustrate the transition between prolate and oblate shapes.

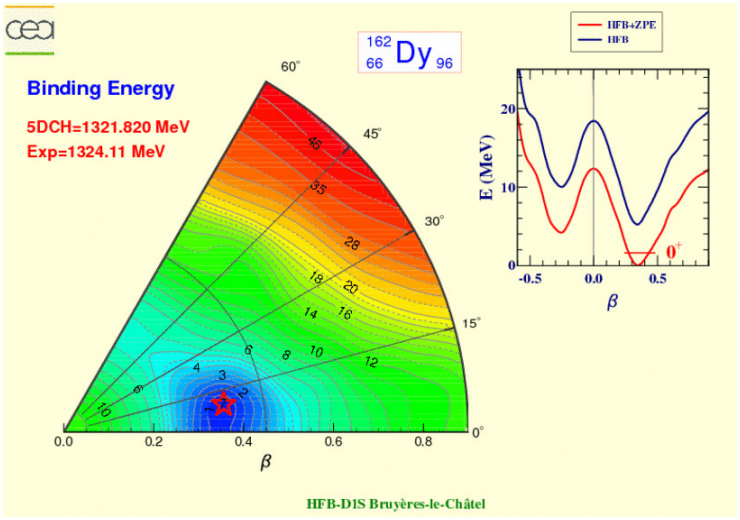


Figure 2.2 – Binding energy of the ^{162}Dy nucleus as a function of deformation parameters. The central panel shows the energy of the nucleus ^{162}Dy in the $\beta\gamma$-plane to explore possible triaxial (three-dimensional) deformation. The top-right panel shows the deformation energy of the nucleus ^{162}Dy as a function of the quadrupole deformation parameter β. Taken from [148].

2.2.1.4 Nucleon pairing and self-consistent blocking

Pairing correlations between nucleons play a significant role in the nuclear structure of most nuclei, with the exception of those near magic numbers having closed shells. This pairing effect is similar in principle to that of electron Cooper pairs in superconductors.

Ideally, these correlations are incorporated through Hartree-Fock-Bogoliubov (HFB) calculations, where both the mean field and pairing field are treated consistently and simultaneously, and derived from the same interaction [104]. One commonly used method here is for example the Gogny D1S force for such mean-field calculations [150].

However, the Skyrme energy-density functionals (EDFs) generally do not treat pairing correlations using the same interaction. Therefore in these cases, pairing is instead addressed separately by performing BCS (Bardeen-Cooper-Schrieffer) calculations during each iterative cycle, after solving the Skyrme-Hartree-Fock equations, and before beginning the next iteration. This is slightly different to, but not entirely unlike, the approach of some post-Hartree-Fock methods in atomic physics and quantum chemistry, such as configuration interaction (CI), where the residual electronic correlations are treated after the full set of mean-field iterations has been completed [151]. This is important, since it means that the nuclear fields still feel the effect of the pairing correlations, and the pairing strength is adjusted self-consistently with the mean-field potential.

These BCS calculations, based on the aforementioned theory of electronic Cooper pairs in superconductors [152], offer a simple and effective way to include pairing correlations in the Skyrme-Hartree-Fock model, where the pairing strength G_q is optimised using the formula:

$$G_q = \frac{G_q^{(\mathrm{o})}}{N_q + 11} \ , \quad q \in \{n, p\} \ , \tag{2.9}$$

where N_q refers to neutron or proton numbers, and controls how strongly nucleons are likely to pair up. This method ensures that the pairing strength is appropriately adjusted

to match experimental observations.

2.2.1.5 Time-reversal symmetry breaking

As a final consideration in the development of our model, we must remark that the standard BCS pairing correlations treatment relies on time-reversed pairs of nucleons, where each single-particle state $|k\rangle$ has a time-reversed partner $\left|\bar{k}\right\rangle = \mathcal{T}\,|k\rangle$, with both states having the same energy due to Kramer's degeneracy. This symmetry holds in systems where both proton and neutron numbers are even.

However, when this symmetry is broken, as in odd-even or odd-odd nuclei, the Kramer degeneracy no longer applies. In such cases, the unpaired nucleon (the odd particle) breaks the time-reversal symmetry across the system, leading to the absence of a true time-reversed partner for all nucleons. Since the time-reversal symmetry breaking caused by the odd particle leads to a core polarisation that affects all the particles of the nuclear system, the BCS method must then be modified to account for the unpaired nucleon, but also for the other nucleons, generally referred to as the core. In these cases, the BCS method must be modified to account for the unpaired nucleon(s), in addition to the nucleons of the core. Therefore, the concept of a pseudo pair is introduced [107, 153], where for each single-particle state $|k\rangle$, a conjugate partner $\left|\widetilde{k}\right\rangle$ is found that has the largest overlap $\left\langle\widetilde{k}\middle|\bar{k}\right\rangle$ with the time-reversed state $\left|\bar{k}\right\rangle$. It turns out that there is no ambiguity in finding such a conjugate partner, but that rather the overlap of a given single-particle state $|k\rangle$ with its conjugate partner $\left|\widetilde{k}\right\rangle$, what was formerly its Cooper-pair partner, is generally of the order of 99% or better. This allows the BCS pairing approach to be extended to odd-even and odd-odd nuclei, ensuring that pairing correlations can still be included.

The presence of an unpaired nucleon in odd-even nuclei, such as in the neighbouring nucleus of an even-even core, causes polarisation effects in the core. This polarisation, induced by the unpaired nucleon, is crucial in reproducing experimentally observed quantities such as the magnetic dipole moments. The computational technique used to handle these cases is known as self-consistent blocking. In this method, the relevant s.p. state associated with the unpaired nucleon is considered to be fully occupied, meaning that it is blocked from participating in pairing. Its conjugate partner, with opposite quantum numbers, is also blocked with zero occupation probability, ensuring that the pair does not contribute to pair excitations. This approach allows for a consistent treatment of nuclear systems with broken time-reversal symmetry.

2.2.2 Multipole Moments

From the aforementioned Skyrme-HBFCS model with self-consistent blocking (HFBCS), it becomes possible to obtain explicitly the nuclear charge densities and current distri-

butions, given by:

$$\rho_q(\vec{R}) = \sum_j \sum_\nu v_{q,\nu}^2 \left|\varphi_{j,\nu}(\vec{R})\right|^2 , \tag{2.10}$$

$$\vec{j}_q^{(l)}(\vec{R}) = i\mu_N \sum_\nu v_{q,\nu}^2 g_q^{(l)} \left[\psi_{q,\nu}(\vec{R})\vec{\nabla}\psi_{q,\nu}^*(\vec{R}) - \psi_{q,\nu}^*(\vec{R})\vec{\nabla}\psi_{q,\nu}(\vec{R})\right] , \tag{2.11}$$

$$\vec{j}_q^{(s)}(\vec{R}) = \mu_N \sum_\nu v_{q,\nu}^2 g_q^{(s)} \vec{\nabla} \wedge \left[\psi_{q,\nu}^*(\vec{R})\vec{s}\psi_{q,\nu}(\vec{R})\right] , \tag{2.12}$$

where, for each nucleon q (proton or neutron), the $g_q^{(l)}$ and $g_q^{(s)}$ are the Landé g factors for the orbital and spin angular momenta, respectively, the μ_N is the nuclear magneton and the $v_{q,\nu}$ are the occupation amplitudes of the associated eigenstates $|\psi_{q,\nu}\rangle$ of the Hartree-Fock Hamiltonian. We therefore expect that, for example, the integral of the convection current density $\vec{j}_q^{(l)}(\vec{R})$ in Eq. (2.10) will give the orbital contributions to the magnetic moment, and likewise the integral of the spin current density $\vec{j}_q^{(s)}(\vec{R})$ in Eq. (2.12) will give the spin contributions.

Therefore, the next step is to detail how these equations can be used to obtain the experimentally observable nuclear moments through the multipolar expansion. For details of the equations summarised here, see for example the standard reference text of Jackson [154]. Let us first consider a generic expansion of the potential $\phi(\vec{r})$ of the nuclear charge distribution $\rho(\vec{R})$ to an electron at a point $\vec{r}$.

The electric potential $\phi(\vec{r})$ that satisfies the Poisson equation,

$$\nabla^2\phi = -\frac{\rho}{\varepsilon_0}, \tag{2.13}$$

is given by

$$\phi(\vec{r}) = \int d^3R \frac{\rho(\vec{R})}{\left|\vec{r} - \vec{R}\right|}, \tag{2.14}$$

where the $\frac{1}{|\vec{r}-\vec{R}|}$ can be expanded in terms of spherical harmonics as

$$\frac{1}{\left|\vec{r} - \vec{R}\right|} = \sum_{\ell=0}^{\infty} \sum_{m=-\ell}^{\ell} \frac{r_<^\ell}{r_>^{\ell+1}} C_m^{(\ell)}(\theta_1, \phi_1) C_m^{(\ell)*}(\theta_2, \phi_2). \tag{2.15}$$

Here, $r_<$ and $r_>$ are the smaller and larger of r and R, respectively, and the $C_m^{(\ell)}(\theta, \phi)$ are the normalised spherical harmonics,

$$C_m^{(\ell)}(\theta, \phi) = \sqrt{\frac{4\pi}{2\ell + 1}} Y_m^{(\ell)}(\theta, \phi), \tag{2.16}$$

forming an orthonormal basis set on the sphere. The $Y_m^{(\ell)}(\theta, \phi)$ are the non-normalised spherical harmonics,

$$Y_m^{(\ell)}(\theta, \phi) = \sqrt{\frac{2\ell + 1}{4\pi}} \sqrt{\frac{(\ell - m)!}{(\ell + m)!}} P^{(\ell)}(\cos\theta) e^{im\phi}, \tag{2.17}$$

with ℓ the degree of the harmonic, $-\ell \leq m \leq \ell$, θ and ϕ the electronic polar and azimuthal angles, and $P^{(\ell)}$ the Legendre polynomial of degree ℓ.

Therefore, the multipole moments of the nucleus can be written as

$$\phi_q^{(k)}(\vec{r}) = \frac{1}{4\pi\epsilon_0}\int_{R=0}^{+\infty}\rho(\vec{R})\frac{\min(r,R)^k}{\max(r,R)^{k+1}}C_q^{(k)}(\Theta,\Phi)d^3\vec{R} \tag{2.18}$$

$$= \frac{1}{4\pi\epsilon_0 r^{k+1}}\int_{R=0}^{r}\rho(\vec{R})R^k C_q^{(k)}(\Theta,\Phi)d^3\vec{R} + \frac{r^k}{4\pi\epsilon_0}\int_{R=r}^{+\infty}\frac{\rho(\vec{R})}{R^{k+1}}C_q^{(k)}(\Theta,\Phi)d^3\vec{R}. \tag{2.19}$$

with Θ and Φ the nuclear polar and azimuthal angles, and with the integral split into the two regions, $r < R$ and $r > R$, inside and outside the nucleus, respectively.

2.2.2.1 Electric monopole moment

The electric monopole is the first term in the multipole expansion, corresponding to $k = 0$ and $C_0^{(0)} = 1$, which reduces Eq. (2.18) to

$$\phi_{0,0}(r) \equiv \phi_0^{(0)}(\vec{r}) = {}^{\text{in}}\phi_0^{(0)}(\vec{r}) + {}^{\text{ex}}\phi_0^{(0)}(\vec{r}) \tag{2.20}$$

$$= \frac{{}^{\text{in}}Q^{(0)}(r)}{4\pi\epsilon_0 r} + \frac{{}^{\text{ex}}Q^{(0)}(r)}{4\pi\epsilon_0}. \tag{2.21}$$

As an illustrative example, when the electron is considered to not penetrate the nucleus, the external charge density for $r > R$ is zero, and the electric monopole moment is given by

$$\phi_{0,0}(r) = \frac{Ze}{4\pi\epsilon_0 r}, \tag{2.22}$$

recovering the proton number of the nucleus. Furthermore, since the monopole is spherically symmetric, we can easily recover the spherically averaged charge density,

$$\rho_{0,0}(R) = \frac{1}{4\pi R^2}\int_{\theta=0}^{\pi}\int_{\phi=0}^{2\pi}\rho(\vec{R})\sin(\theta)d\theta d\phi. \tag{2.23}$$

2.2.2.2 Magnetic dipole moment

Unlike the electric monopole and quadrupole moments, which originate from the charge distribution of the nucleus, the magnetic dipole moment arises from the motion of the protons and neutrons within the nucleus. Therefore, given a finite current density distribution $\vec{j}(\vec{R})$ within the nucleus, the multipole expansion is performed on the vector potential (in the Coulomb gauge $\nabla\cdot\vec{A} = 0$) of the magnetic field $\vec{B} = \nabla\times\vec{A}$,

$$\vec{A}(\vec{r}) = \frac{\mu_0}{4\pi}\int\frac{\vec{j}(\vec{R})}{|\vec{r}-\vec{R}|}d^3\vec{R}. \tag{2.24}$$

The first non-zero term in the expansion corresponds to $k = 1$, producing

$$\vec{A}(\vec{r}) = \frac{\mu_0}{4\pi}\frac{{}^{in}\vec{M}^{(1)}(r)\wedge\vec{r}}{r^3} + \frac{\mu_0}{4\pi}\left({}^{ex}\vec{M}^{(1)}(r)\wedge\vec{r}\right), \tag{2.25}$$

N	$g_q^{(\ell)}$	$\langle \ell_z \rangle_q$	$g_q^{(s)}$	$\langle s_z \rangle_q$
n	0	2.238199	-3.8262	0.261801
p	1	-0.018104	5.58658	0.018104

Table 2.1 – The Landé g factors for protons and neutrons. The g factors were used to calculate the magnetic moments expectation values of the protons in Eq. (2.32).

where the interior and exterior dipole moments are given by

$$ {}^{in}\vec{M}^{(1)}(r) = \frac{1}{2}\int_{R=0}^{r} \vec{R} \wedge \vec{j}(\vec{R}) d^3\vec{R} \ , \text{ and} \tag{2.26} $$

$$ {}^{ex}\vec{M}^{(1)}(r) = \frac{1}{2}\int_{R=r}^{+\infty} \frac{\vec{R} \wedge \vec{j}(\vec{R})}{R^3} d^3\vec{R}. \tag{2.27} $$

By defining the spherically averaged magnetic dipole density as

$$ \vec{\rho}_1(R) \equiv \frac{1}{4\pi R^2}\int_{\Omega} \frac{1}{2}\vec{R} \wedge \vec{j}(\vec{R}) d\Omega, \tag{2.28} $$

this leads to the following expression for the magnetic dipole moment of the nucleus:

$$ \vec{M}^{(1)} = {}^{in}\vec{M}^{(1)}(r \to \infty) = \int 4\pi R^2 \vec{\rho_1}(R) dR. \tag{2.29} $$

For the case of an axially-symmetric charge distribution, the magnetic dipole moment is aligned with the symmetry axis of the nucleus, and the expectation value of the magnetic dipole moment operator is given by

$$ M_z^{(1)} = \int 4\pi R^2 \rho_{1,0}(R) dR \ , \tag{2.30} $$

To compute the total magnetic dipole moment of a nucleus in the nuclear numerical model, we consider contributions from both intrinsic motions of the protons and neutrons. Indeed, we account for the impact of the spin and orbital motion of protons and neutrons. The expression is given, in units of the nuclear magneton,

$$ \mu_N = \frac{e\hbar}{2m}, \tag{2.31} $$

by

$$ \langle \mu_z \rangle_q = g_q^{(\ell)} \langle \ell_z \rangle_q + g_q^{(s)} \langle s_z \rangle_q \tag{2.32} $$

where $\langle \ell_z \rangle_q$ and $\langle s_z \rangle_q$ represent the expectation values of the orbital and spin angular momentum operators, respectively, for $q \in \{n, p\}$ protons and neutrons. The Landé g factors $g_q^{(\ell)}$ and $g_q^{(s)}$ are the proportionality constants between the magnetic moment and the angular momentum for the protons and neutrons, and their values are summarised in Table 2.1. Hence, we find the total magnetic dipole moment to be the sum of the spin and orbital contributions for both protons and neutrons

$$ M_z^{(1)} = \sum_{q \in \{n,p\}} \langle \mu_z \rangle_q \tag{2.33} $$

We must keep in mind that the $\langle \mu_z \rangle$ represents the intrinsic dipole moment of the nucleus. To obtain the spectroscopic moment experienced by the electron, we must consider the total angular momentum of the nucleus, and its projection on the symmetry axis of the nucleus, K. The conversion factor between the intrinsic and spectroscopic moments is given by $\mathcal{I}^M_{lab} = \frac{K}{K+1}$, such that

$$\mu_{\text{spec}} = \mathcal{I}^M_{lab} \langle \Psi | \mu_z | \Psi \rangle . \tag{2.34}$$

$$= \frac{K}{K+1} \langle \Psi | \hat{\mu}_z | \Psi \rangle . \tag{2.35}$$

For the case of free atoms and nuclei, particularly those exhibiting axial symmetry, we can consider the projection K equal to the total I.

2.2.2.3 Electric quadrupole moment

The electric quadrupole potential is given by $k = 2$ in the multipole expansion in Eq. (2.18),

$$\phi_{\text{quad}}(\vec{r}) = \sum_{q=-2}^{2} (-1)^q \phi^{(2)}_{-q}(r) C^{(2)}_q(\theta, \phi), \tag{2.36}$$

with $\phi^{(2)}_q(\vec{r})$ separated into interior and exterior components,

$$\phi^{(2)}_q(\vec{r}) = \frac{{}^{\text{in}}Q^{(2)}_q(r)}{4\pi\epsilon_0 r^3} + \frac{{}^{\text{ex}}Q^{(2)}_q(r) r^2}{4\pi\epsilon_0} \tag{2.37}$$

given by the integrals

$${}^{\text{in}}Q^{(2)}_q(r) \equiv \int_{R=0}^{r} \rho(\vec{R}) R^2 C^{(2)}_q(\Theta, \Phi) d^3\vec{R}, \tag{2.38}$$

$${}^{\text{ex}}Q^{(2)}_q(r) \equiv \int_{R=r}^{+\infty} \frac{\rho(\vec{R})}{R^3} C^{(2)}_q(\Theta, \Phi) d^3\vec{R}. \tag{2.39}$$

The mean-field method that is used in the HFBCS model produces the intrinsic radial quadrupole moment $Q^{(\text{int})}_{20}$ through the finite distribution of nuclear charge (protons) away from spherical symmetry. This quantity must then be converted into the experimentally observable spectroscopic quadrupole moment, $Q^{(\text{spec})}_{20}$ by the conversion factor

$$Q^{(\text{spec})}_{20} = \frac{3K^2 - J(J+1)}{(J+1)(2J+3)} Q^{(\text{int})}_{20}, \tag{2.40}$$

where K is the projection of the total angular momentum J on the symmetry axis of the nucleus.

2.3 Methods

In this section we describe the computational methods used to calculate the multipole moments based on the nucleon distributions obtained from the Skyrme-Hartree-Fock model implemented in what we shall refer to as the HFBCS code.

z	ϱ	ρ_p	$(\vec{j}_p)_z$	$(\vec{j}_p)_\varrho$	$(\vec{j}_p)_\phi$	$(\vec{\nabla}\wedge\vec{s}_p)_z$	$(\vec{\nabla}\wedge\vec{s}_p)_\varrho$	$(\vec{\nabla}\wedge\vec{s}_p)_\phi$
				⋮				
3.191	0.346	0.065	0.000	0.000	0.001	0.000	0.000	-0.001
3.191	0.795	0.064	0.000	0.000	0.002	0.000	0.000	-0.002
3.191	1.246	0.062	0.000	0.000	0.002	0.000	0.000	-0.001
3.191	1.698	0.060	0.000	0.000	0.002	0.000	0.000	0.001
3.191	2.150	0.059	0.000	0.000	0.002	0.000	0.000	0.003
				⋮				

Table 2.2 – Example tabulated values for the protons of ^{159}Tb. The table shows example output data from the HFBCS code with columns for: cylindrical spatial coordinates z and ϱ in fm, proton density ρ_p in fm^{-3}, components of the current $((\vec{j}_p)_z$, $(\vec{j}_p)_\varrho$, $(\vec{j}_p)_\phi)$, and components of the curl of spin $((\vec{\nabla}\wedge\vec{s}_p)_z$, $(\vec{\nabla}\wedge\vec{s}_p)_\varrho$, $(\vec{\nabla}\wedge\vec{s}_p)_\phi)$ both in units of fm^{-2}s^{-1}.

2.3.1 Skyrme-HFBCS Code

The HFBCS code is a computational tool that solves the Skyrme-Hartree-Fock equations with BCS self-consistent blocking for nuclear structure calculations. The details of the code are beyond the scope of this work, and so we refer the interested reader to the work of our collaborators responsible for its implementation and from which they provided us the resulting data of the nucleon charge and current distributions [107].

Table 2.2 provides an example of the values obtained from the HFBCS code for the protons of ^{159}Tb, with columns for the cylindrical spatial coordinates z and ϱ in the upper right quadrant of a plane through the z-axis, with corresponding values for the proton densities ρ_p, and components of the orbital currents $(\vec{j}_p)_z$, $(\vec{j}_p)_\varrho$ and $(\vec{j}_p)_\phi$, as well as the components of the curl of the spin $(\vec{\nabla}\wedge\vec{s}_p)_z$, $(\vec{\nabla}\wedge\vec{s}_p)_\varrho$ and $(\vec{\nabla}\wedge\vec{s}_p)_\phi$. The values for the neutrons are similarly tabulated.

2.3.2 Calculation of the Moments and Potentials

From the tables of data for each isotope, a Fortran code was written to perform the integrals of the multipole moments and potentials (see Appendix A.2 for additional details). As a further step, the data tables and resulting multipole calculations were passed to a Mathematica notebook for final analysis and visualisation as presented in Section 2.4.

The main dipole Fortran routines include `m_dipole`, `mu_component`, and `m_dipole_potential` for the magnetic dipole moments, the individual components of the magnetic moments, and the magnetic dipole potential, respectively, and they use integration over spatial meshes to compute internal and external contributions to the magnetic moments for both protons and neutrons. The `m_dipole` subroutine computes the magnetic dipole moments by calling the `mu_component` subroutine for each relevant component (orbital and spin for protons and neutrons). Then, the `m_dipole_potential` subroutine computes the magnetic dipole constants (`a_wp` and `a_np`) by integrating over the mesh, considering both internal and external contributions.

The main quadrupole Fortran routines include `e_quadrupole` and `e_quadrupole_potential`. The `e_quadrupole` subroutine calculates the intrinsic and spectroscopic quadrupole moments for a nucleus using the density data. Then, the `e_quadrupole_potential` sub-

routine computes the quadrupole potential for both the electric field and charge density, by integrating over the mesh points.

2.4 Results

The Skyrme-Hartree-Fock model (referred to as the HFBCS model), incorporating effective interactions and self-consistent blocking, provides a framework for analysing nuclear structure and properties. By simplifying nucleon interactions, it effectively describes nuclear phenomena such as shapes, pairing effects, and magnetic moments. This section presents HFBCS model results for isotopes ^{161}Dy, ^{163}Dy, ^{159}Tb, and ^{165}Ho, focusing on nucleon and multipole distributions. The findings are discussed in relation to the nuclear structure of these isotopes and compared with other nuclear models, including the point-charge, spherical shell, and Fermi-function models.

2.4.1 Nucleon Distributions

We analyse the obtained nucleon distributions for the isotopes ^{161}Dy, ^{163}Dy, ^{159}Tb, and ^{165}Ho, characterised by proton and neutron densities and currents, decomposed into spin and orbital contributions. These distributions are visualised in cylindrical coordinates (z, ϱ) on a planar slice along the z-axis, with spatial units normalised by the empirical nuclear radius, R_N. The densities are given in units of R_N^{-3}, with contour lines showing equivalent density values. Here, R_N is derived as $R_N = \sqrt{\frac{5}{3}R_{\text{rms}}^2}$ fm, where R_{rms}, the root mean square (RMS) charge radius, follows the empirical formula [155],

$$R_{\text{rms}}^{(\text{empirical})} = (0.836A^{1/3} + 0.57)\ \text{fm}. \tag{2.41}$$

The dashed curve represents the full-width at half-maximum (FWHM) of the proton densities, indicating the outer shells of the respective nuclei.

2.4.1.1 Nucleon densities

The obtained nuclear charge distributions for ^{161}Dy and ^{163}Dy can be seen in Fig. 2.3, and those for ^{159}Tb and ^{165}Ho in Fig. 2.4, representing the spatial distributions of the protons and neutrons within the nuclei.

It is interesting to note the differences in the distributions, not only between the neighbouring elements, but also between the two isotopes of dysprosium. The deformations away from sphericity of each prolate ellipsoidal nucleus are noteworthy, and we shall investigate further how these deformations manifest in the and multipole distributions, particularly the electric quadrupole moments. Indeed, notice how the protons appear to be most concentrated toward the poles of the nucleus, with decreased density toward the center, whereas the neutrons are more uniformly distributed but with slightly higher densities at the poles and equator.

2.4.1.2 Proton currents

Moving on from the nucleon densities, we now show the distributions of the currents of the protons for ^{161}Dy and ^{163}Dy Fig. 2.5 and for ^{159}Tb and ^{165}Ho in Fig. 2.6.

These distributions are decomposed into spin and orbital contributions, where the spin components arise from the intrinsic nucleon spins, while the orbital components stem

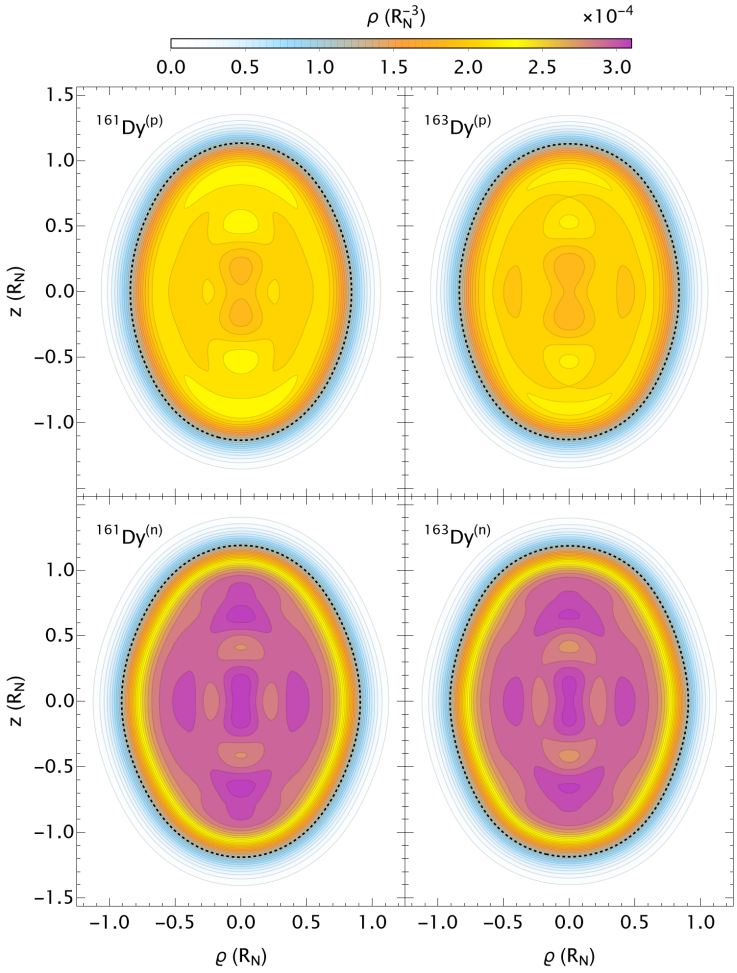
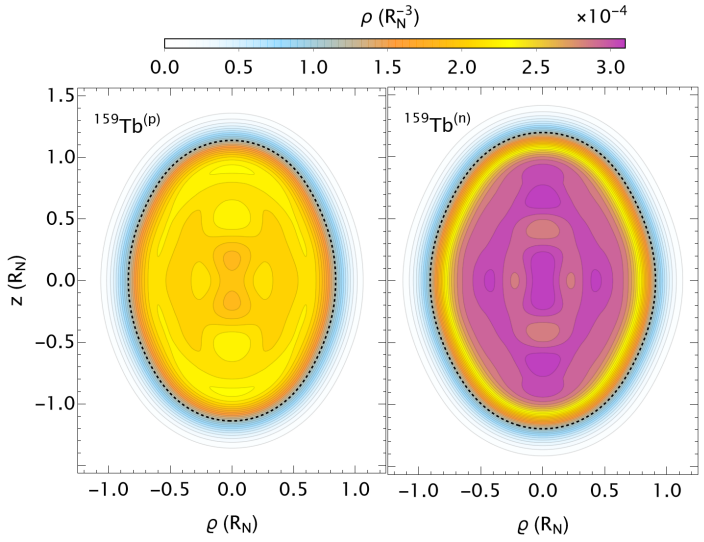


Figure 2.3 – Nucleon density distributions of ^{161}Dy and ^{163}Dy. The proton (p) and neutron (n) density distributions for ^{161}Dy and ^{163}Dy are shown in cylindrical coordinates (z, ϱ) on a planar slice along the z-axis. The spatial coordinates are scaled by each isotope's empirical nuclear radius, R_N, with the densities expressed in units of R_N^{-3}. The contour lines of equivalent density are logarithmically spaced, with scale as shown in the legend. The outer shells of the nuclei are depicted by the full-width at half-maximum (FWHM) of the proton density of the respective isotope (dashed lines).

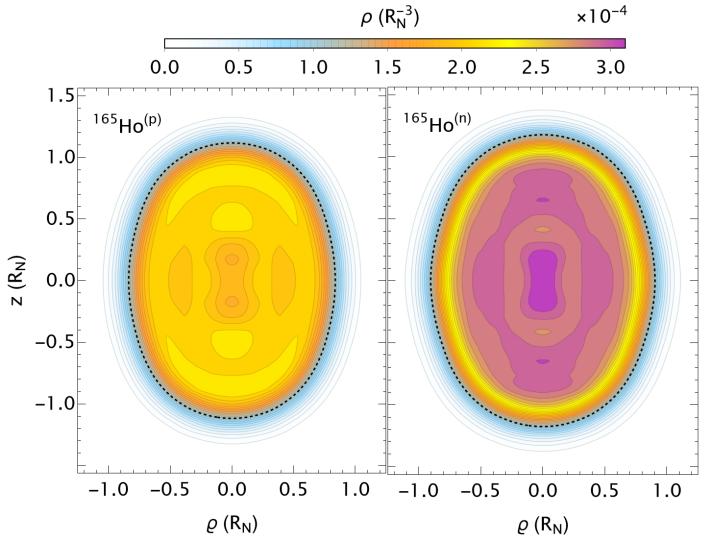
from their motion within the nucleus. Overlaid, we show the magnetic dipole moments as a vector field with arrows indicating the direction and magnitude of the moments. As for the nucleon densities, the dashed contour line of the proton density FWHM indicates the same outer shell of the nucleus.

We make the following observations and remarks concerning these current distributions. Firstly, note the alternating nature of the red and blue nodes, indicating the counter-rotating nature neighbouring current loops.

Secondly, in contrast with the nucleon density distributions, the current distributions appear to be more concentrated away from the center and poles of the nuclei, with the current loops generally found close to or around the FHWM outer shell of the respective nuclei. This indicates that, particularly for dysprosium and holmium, the nucleons in the densely packed core and polar regions have little to no mobility, while those near the surface are free to move and contribute to the currents that generate the magnetic



(a) ^{159}Tb



(b) ^{165}Ho

Figure 2.4 – Nucleon density distributions of ^{159}Tb and ^{165}Ho. The proton (p) and neutron (n) density distributions for (a) ^{159}Tb and (b) ^{165}Ho are shown in cylindrical coordinates (z, ϱ) on a planar slice along the z-axis. The spatial coordinates are scaled by each isotope's empirical nuclear radius, R_N, with the densities expressed in units of R_N^{-3}. The contour lines of equivalent density are logarithmically spaced, with scale as shown in the legend. The outer shells of the nuclei are depicted by the full-width at half-maximum (FWHM) of the proton density of the respective isotope (dashed lines).

dipole moments. As a minor exception, note that the (lighter) terbium nucleus exhibits additional current loops closer to the center.

Thirdly, from the relative scales we see that the spin currents for ^{161}Dy, ^{163}Dy and ^{159}Tb are the dominant contributors towards the magnetic dipole moments, with the orbital currents playing a smaller role. For ^{165}Ho, this effect remains but is less pronounced.

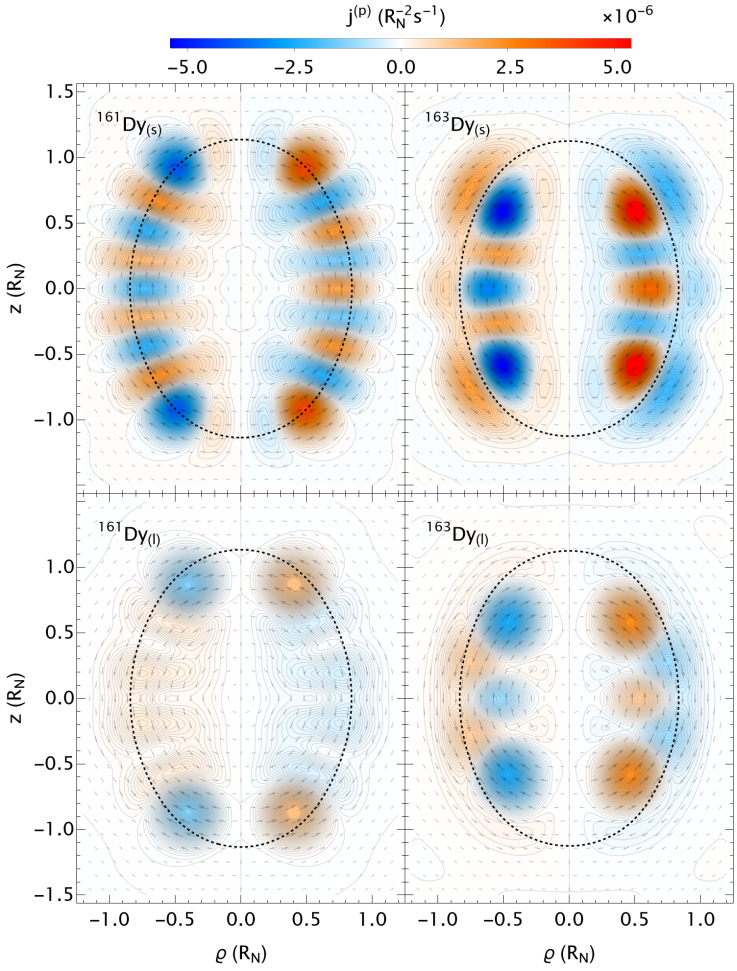


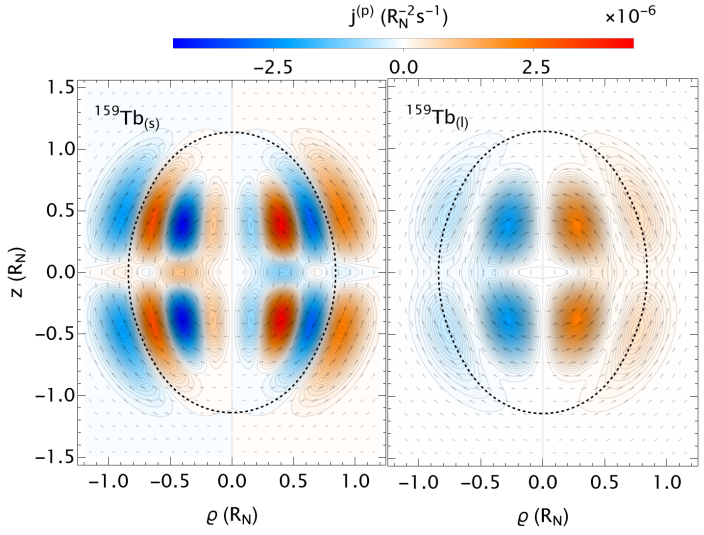
Figure 2.5 – Proton current distributions of ^{161}Dy and ^{163}Dy. Spin (upper) and orbital (lower) contributions of the $\vec{j}^{(p)}(\vec{R})$ proton current distributions for ^{161}Dy (left) and ^{163}Dy (right) were plotted in cylindrical coordinates (z, ϱ) on a planar slice along the z-axis. The values of the contributions are indicated by the contour lines as shown in the legend, with all panels normalised to the same scale. The magnetic dipole moments, given by $\vec{R} \wedge \frac{1}{2}\left(\vec{j}^{(p)}(\vec{R})\right)$, are shown by the field of arrow vectors. The dashed line marks the full-width at half-maximum (FWHM) of the proton density of the respective isotope, indicating the outer boundary of the nucleus.

2.4.1.3 Neutron currents

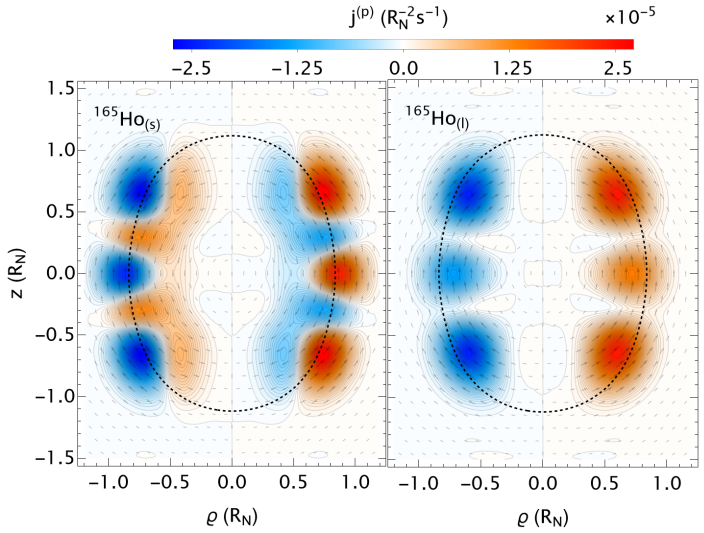
Finally, we present the neutron current distributions for ^{161}Dy and ^{163}Dy in Fig. 2.7 and for ^{159}Tb and ^{165}Ho in Fig. 2.8. These results are presented in the same manner as for the proton currents in Section 2.4.1.2, being shown as spin and orbital current distributions on logarithmic contour plots in cylindrical coordinates representing a planar slice through the nucleus.

Looking closer at this behaviour for the proton and neutron currents of holmium in the Fig. 2.8b and Fig. 2.6b, the neutron currents appear to penetrate deeper into the nucleus, while the proton currents are more concentrated near the surface. A possible factor contributing to this behaviour could be the Coulomb repulsion between the outer protons and the core.

In combination with the discussion of the proton currents in Section 2.4.1.2, let us also



(a) ^{159}Tb



(b) ^{165}Ho

Figure 2.6 – Proton current distributions of ^{159}Tb and ^{165}Ho. Spin (left panels) and orbital (right panels) contributions of the $\vec{j}^{(p)}(\vec{R})$ proton current distributions for ^{159}Tb (a) and ^{165}Ho (b) were plotted in cylindrical coordinates (z, ϱ) on a planar slice along the z-axis. The values of the contributions are indicated by the contour lines as shown in the legend, normalised by isotope. The magnetic dipole moments, given by $\vec{R} \wedge \frac{1}{2}\left(\vec{j}^{(p)}(\vec{R})\right)$, are shown by the field of arrow vectors. The dashed line marks the full-width at half-maximum (FWHM) of the proton density of the respective isotope, indicating the outer boundary of the nucleus.

note the following: Firstly, the node-current-loop structural pattern of the neutrons mostly matches that of the protons for each isotope. This indicates common current loop regions in which the nucleons move.

Secondly, comparing the relative scales of the currents, we see that for the dysprosium isotopes the neutron currents are the dominant contributors to the magnetic dipole moments (noting that the orbital neutron currents do not contribute to the magnetic moment due to the lack of charge), whereas for terbium and holmium the neutron currents are roughly one order of magnitude smaller than for the protons, producing a much smaller

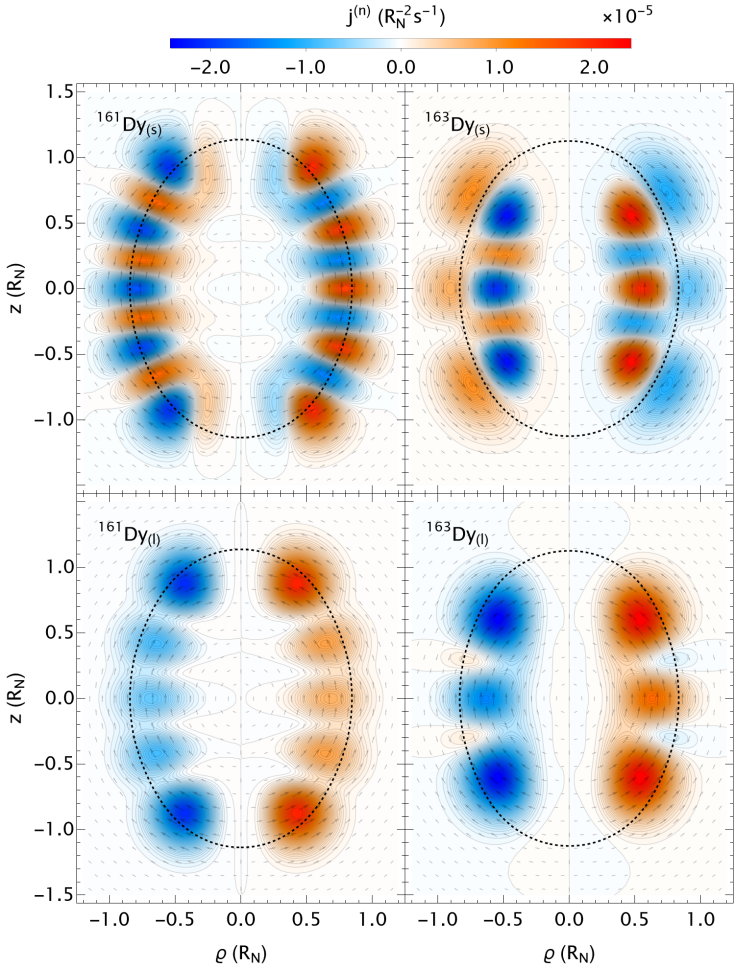
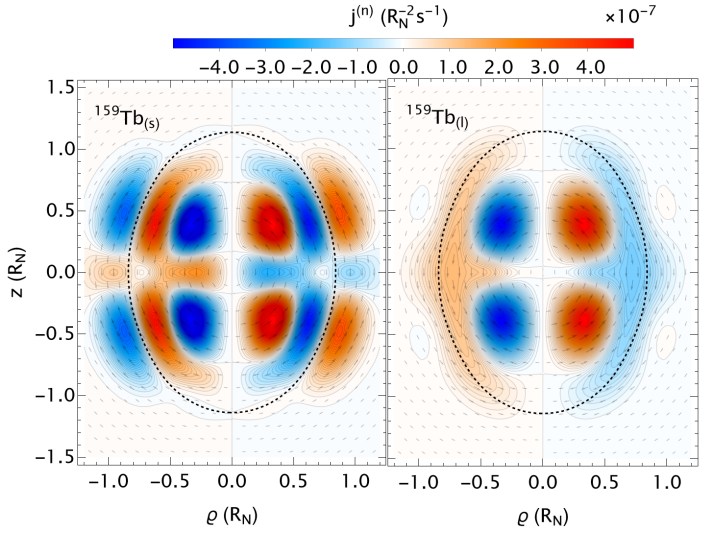


Figure 2.7 – Neutron current distributions of ^{161}Dy and ^{163}Dy.. Neutron current distributions, $\vec{j}^{(n)}(\vec{R})$ (upper : spin contributions, lower: orbital contributions), of ^{161}Dy (left) and ^{163}Dy (right) with associated magnetic dipole moments $\vec{R} \wedge \frac{1}{2}\left(\vec{j}^{(n)}(\vec{R})\right)$ indicated by the arrow vectors. The figures are plotted in cylindrical coordinates (z, ϱ), on a planar slice through the $z-$axis. The contours represent curves of equivalent density, with numerical values as indicated by the legend. The dashed curve indicates the contour line of the FWHM of the isotope's proton density, representing the outer shell of the nucleus.

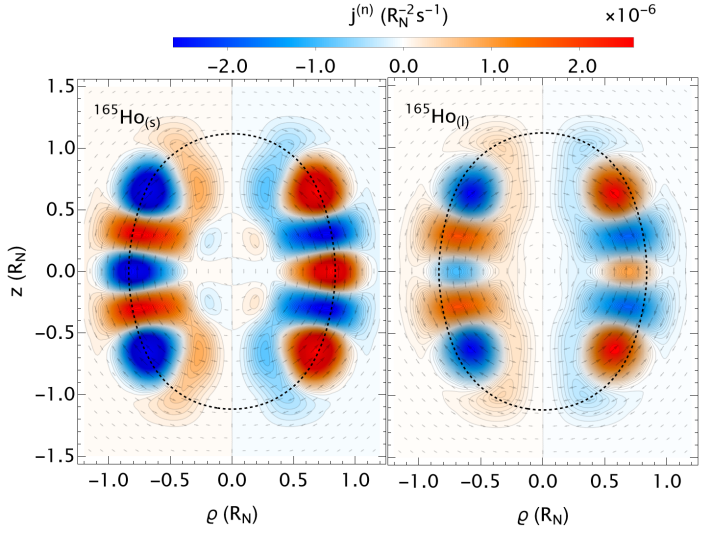
relative contribution.

We may remark that a physical reason explaining both of these observations (common current loop regions and dysprosium having stronger neutron than currents while terbium and holmium have stronger proton than neutron currents) is due to the differences in pairings of the protons and neutrons in the nucleus of each isotope. Terbium and holmium are both odd-even isotopes, with an unpaired proton, while the dysprosium isotopes are both even-odd isotopes, with an unpaired neutron. As noted in Section 2.2.1.5 it is the unpaired nucleon that, through its current motion in the nucleus induces core polarisation and is thus principally responsible for the magnetic dipole moment. Moreover this suggests that, in dysprosium, the unpaired neutron currents induce a weaker current in the protons within the current loop, while in terbium and holmium, the unpaired proton currents induce a weaker current in the neutrons.

Finally, let us discuss the number of observed current loops due to the respective un-



(a) ^{159}Tb



(b) ^{165}Ho

Figure 2.8 – Neutron current distributions of ^{159}Tb and ^{165}Ho. Nucleon current distributions, $\vec{j}^{(n)}(\vec{R})$ (upper : spin contributions, lower: orbital contributions), of (a) ^{159}Tb and (b) ^{165}Ho, with associated magnetic dipole moments $\vec{R} \wedge \frac{1}{2}\left(\vec{j}^{(n)}(\vec{R})\right)$ indicated by the arrow vectors. The figures are plotted in cylindrical coordinates (z, ϱ), on a planar slice through the $z-$axis. The contours represent curves of equivalent density, with numerical values as indicated by the legend. The dashed curve indicates the contour line of the FWHM of the isotope's proton density, representing the outer shell of the nucleus.

paired nucleon. While the single-particle model does not fully capture the intricate interactions among nucleons and their resulting current distributions within the nucleus, it nevertheless provides an instructional framework for understanding the structure of these distributions.

Considering for example ^{163}Dy, having 97 neutrons, simple predictions based on the nuclear shell model indicate that the unpaired neutron occupies the $1h_{9/2}$ state [156]. Furthermore, experimental evidence shows that the ground state of ^{163}Dy corresponds to a $K^\pi = 5/2^-$ band as given in [112] (see Table A.2 in Appendix A.1).

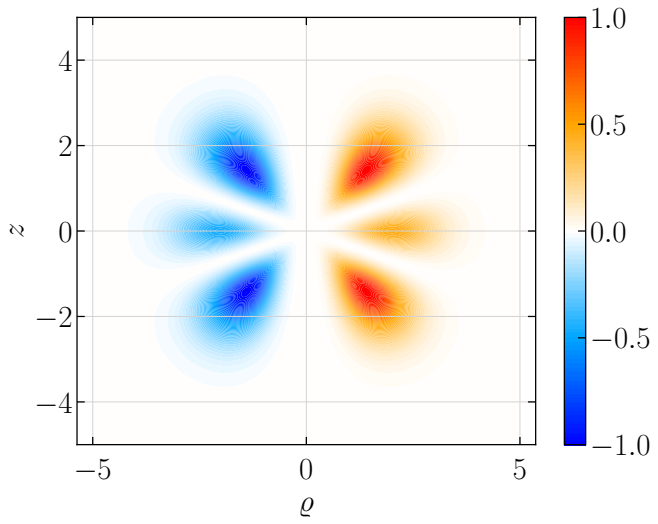


Figure 2.9 – Normalised current distribution for the $3D$ spherical harmonic oscillator. This figure illustrates the eigenstate associated with the quantum state $|1h_{9/2},\ m_j = -5/2\rangle$, which forms part of the single-particle ground state of ^{163}Dy as described by the shell model. The contours are presented in cylindrical coordinates (z, ϱ), on a plane intersecting the z-axis, depicting curves of constant density, with their numerical values specified in the legend.

Figure 2.9 presents the normalised current distributions $(i\left(\psi^*_{n,\ell}\nabla\psi_{n,\ell} - \psi_{n,\ell}\nabla\psi^*_{n,\ell}\right))$, derived from the $3D$ spherical harmonic oscillator eigenstate, which corresponds to the quantum state $|n\ell_j,\ m_j = -5/2\rangle$. This state can be expressed as a superposition of orbital (m_l) and spin (m_s) components:

$$|n\ell_j,\ m_j = -5/2\rangle = \frac{1}{\sqrt{11}}\Big(\sqrt{3}\,|n\ell,\ m_l = -2,\ m_s = -1/2\rangle \tag{2.42}$$

$$-2\sqrt{2}\,|n\ell,\ m_l = -3,\ m_s = +1/2\rangle\Big). \tag{2.43}$$

Here, $n = 6$ and $\ell = 5$, which correspond to the $1h$ orbital state. The Clebsch-Gordan coefficients in the equation determine the relative contributions of the two specific combinations of orbital angular momentum (m_l) and spin angular momentum (m_s) that form the total angular momentum state $m_j = -5/2$.

If we compare these spherical harmonics in Fig. 2.9 with the calculated neutron current distribution in Fig. 2.7 for ^{163}Dy, the resemblance is indeed clear. Comparable qualitative insights can be extended to the other isotopes and elements analysed in this study, although in some instances, one must consider configuration mixing and other complex effects. As an example of this potential configuration mixing, we see in Fig. 2.10 the single-particle energy spectra for the ^{162}Dy nucleus near the Fermi level. The occupation probabilities of each state are given as percentages, with the Nilsson quantum numbers in square brackets indicating the corresponding harmonic oscillator states.

2.4.2 Multipole Distributions

With the distributions of the protons and neutrons for our isotopes in hand, we can now use them to investigate the multipole moments of these simulated nuclei from the *ab initio* perspective of the HFBCS model. We will focus on the electric monopole and

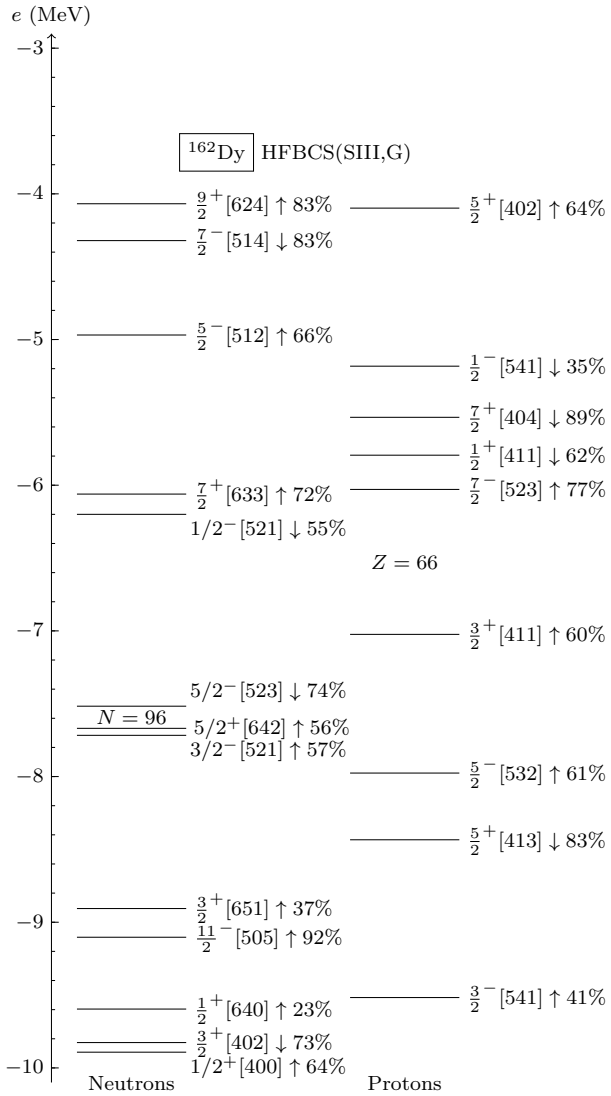


Figure 2.10 – Single-particle spectra for the ^{162}Dy nucleons near the Fermi level. Derived from HFBCS calculations, this figure shows the proton and neutron single-particle energy spectra for the ^{162}Dy nucleus near the Fermi level. The quantum numbers K^π label each level with the projection of the total angular momentum along the symmetry axis K and parity π. The corresponding harmonic oscillator states are shown by the Nilsson quantum numbers in square brackets, with the percentages indicating the occupation probabilities of these states.

quadrupole moments, as well as the magnetic dipole moment, and compare our model against the point-charge, spherical shell, and Fermi-function models.

2.4.2.1 Monopoles

We begin by examining the monopole potentials and charge densities of the isotopes ^{159}Tb, ^{161}Dy, ^{163}Dy, and ^{165}Ho. The monopole densities were obtained by spherically averaging the proton charge densities, normalising by Z the total charge of the nucleus and plotting in units of R_N the nuclear radius of the respective isotopes. The monopole potentials reflect the electric potentials experienced by an electron in the vicinity r of

Isotope	$R^{(\text{emp})}$	$R^{(\text{HFBCS})}$	$R^{(\text{exp})}$
^{159}Tb	6.583	6.704	6.532
^{161}Dy	6.607	6.730	6.708
^{163}Dy	6.631	6.754	6.727
^{165}Ho	6.655	6.781	6.726

Table 2.3 – Table of nuclear radii for ^{159}Tb, ^{161}Dy, ^{163}Dy and ^{165}Ho Comparison of the nuclear radii R_N of the isotopes ^{159}Tb, ^{161}Dy, ^{163}Dy and ^{165}Ho calculated from the empirical Eq. (2.41), the HFBCS model Eq. (2.44) and experimentally obtained results [157] in units of fm.

the nucleus. This was repeated for the spherical and Fermi models, and compared with a Coulomb potential generated by a point-charge.

As an alternative approach to the empirical nuclear radius of Eq. (2.41), we can also calculate the nuclear radii R_N from the monopole charge densities of the HFBCS model,

$$R_{\text{rms}}^{(\text{HFBCS})} = \sqrt{4\pi \int_0^\infty R^2 \rho_{0,0} R^2 \text{dR}}, \tag{2.44}$$

where the 4π factor is due to the spherical averaging, and $\rho_{0,0}$ is the monopole density of the nucleus

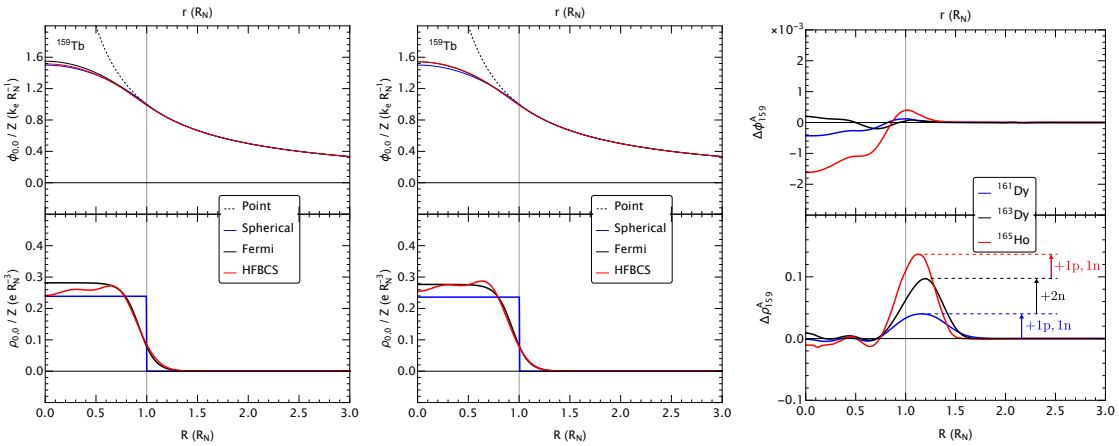
$$\rho_{0,0}(R) = \frac{1}{4\pi} \int \int \rho(\vec{R}) d\vec{R}. \tag{2.45}$$

These calculated values are compared in Table 2.3 against the empirical radii given in Eq. (2.41) and experimentally obtained results [157] of the R_{rms}.

We see in Table 2.3 that the HFBCS-derived radii are consistently larger than the empirical radii, with the difference increasing with the mass number. This is expected, as the HFBCS model accounts for the spatial distribution of the nucleons, which is not necessarily spherically symmetric. While our HFBCS model does match closely with the experimentally obtained radii for ^{161}Dy, ^{163}Dy and ^{165}Ho, we note that for ^{159}Tb the empirical radius is closer.

In Fig. 2.11, we show the monopole potentials and charge densities for ^{159}Tb after normalising by Z the total charge of the nucleus. The monopole potentials are plotted in units of R_N, where in Fig. 2.11a the empirical nuclear radius was used, and in Fig. 2.11b the HFBCS-derived radius was used. Therefore, the x-axes of these two figures are not to scale. The monopole charge densities are shown in the lower panels, with the monopole potentials in the upper panels.

The HFBCS model results are compared with the uniform sphere, Fermi-function, and point-charge Coulomb potentials. We can observe that after normalising by the HFBCS-derived radius, the monopole potential, and the charge density at the nuclear surface are in better agreement with the Fermi-function model. In Fig. 2.11c, we show the relative



(a) ^{159}Tb with $R_{\rm rms}^{\rm (empirical)}$. **(b)** ^{159}Tb with $R_{\rm rms}^{\rm (HFBCS)}$. **(c)** Differences relative to ^{159}Tb.

Figure 2.11 – Monopole potentials and densities of ^{159}Tb. Z-normalised proton monopole charge densities (lower panels) and monopole potentials experienced by the electrons (upper panels) obtained for ^{159}Tb with R normalised to (a) the empirical radius, and (b) the HFBCS-derived radius. The HFBCS type (red) calculations were compared with: a uniform sphere (blue), a Fermi-function (black) and a point-charge Coulomb potential (dotted). $k_e \equiv \frac{e}{4\pi\epsilon_0}$ is the Coulomb constant. In (c) the differences relative to ^{159}Tb are shown for ^{161}Dy (blue), ^{163}Dy (black) and ^{165}Ho (red).

differences of the monopole for ^{161}Dy, ^{163}Dy, and ^{165}Ho with respect to ^{159}Tb, taking,

$$\Delta\rho^{A}_{159} = \frac{\rho^{(A)}_{0,0} - \rho^{(159)}_{0,0}}{\rho^{(159)}_{0,0}}, \tag{2.46}$$

$$\text{and } \Delta\phi^{\rm A}_{159} = \frac{\phi^{(A)}_{0,0} - \phi^{(159)}_{0,0}}{\phi^{(159)}_{0,0}}. \tag{2.47}$$

From this plot of the relative differences, we remark that as A increases from 159 to 165, the relative differences in the charge densities increases at the nuclear surface with each additional pair of nucleons. It is worth speculating that for these heavy nuclei, with the densely packed cores not differing as significantly as the outer shells, the additional nucleons appear to be bound near the surface instead.

As a final example, we show the monopole potentials and charge densities for ^{161}Dy in Fig. 2.12. In green, we show the absolute differences between ^{161}Dy and ^{163}Dy for the HFBCS model. Note the small differences in the charge densities between the two isotopes. Indeed, the absolute differences across all four isotopes are very small to notice on the normalised scale (see Figs. A.1 and A.2 in Appendix A for explicit plots of each isotope.).

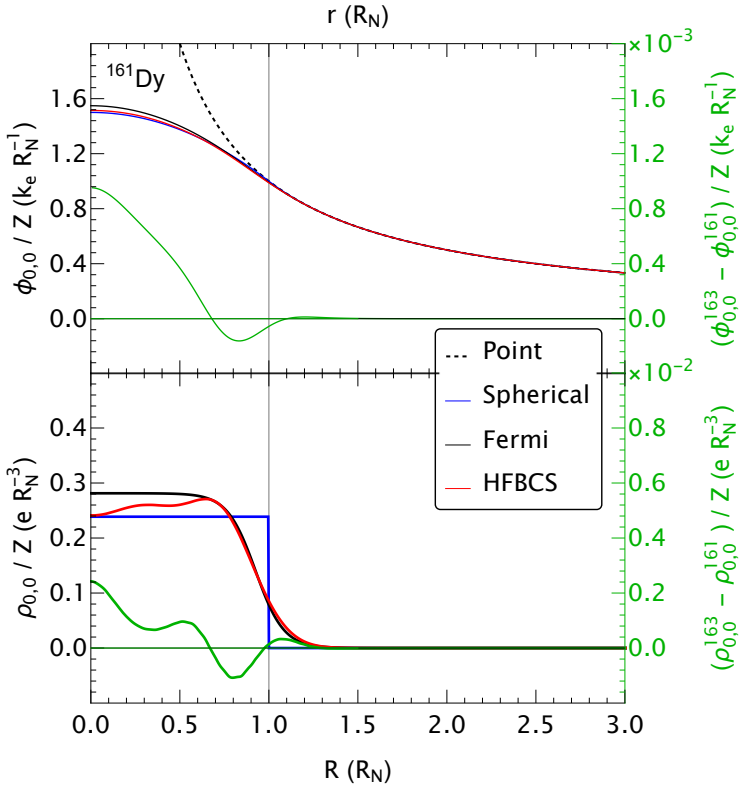


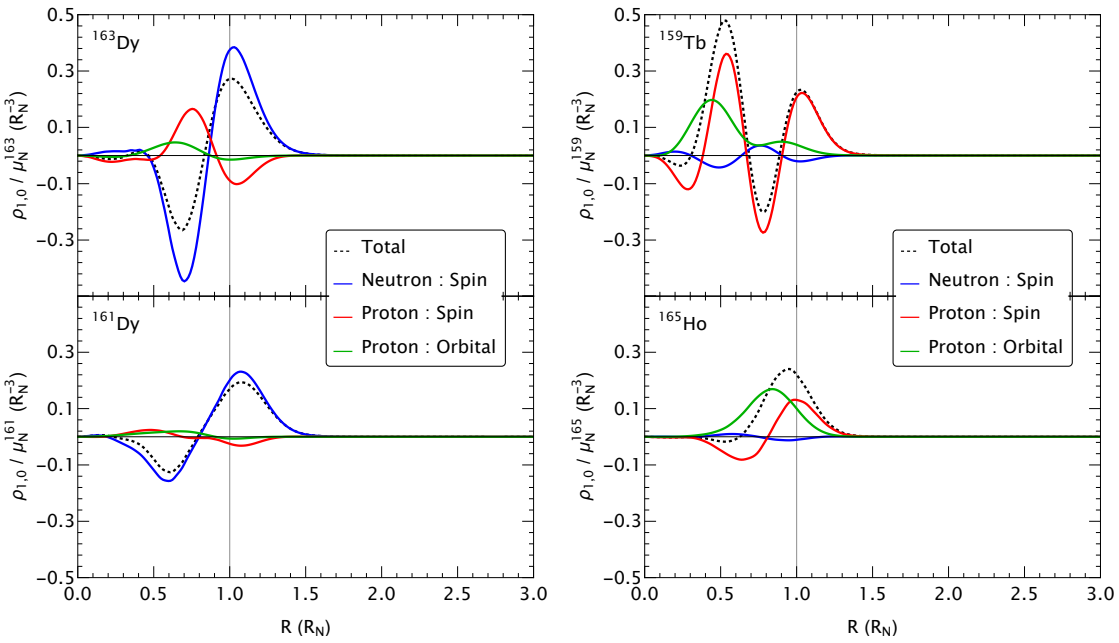
Figure 2.12 – Monopole potential and density of ^{161}Dy. Z-normalised proton monopole charge densities (lower panels) and monopole potentials experienced by the electrons (upper panels) obtained for ^{161}Dy with R normalised to the empirical radius. The HFBCS type (red) calculations were compared with: a uniform sphere (blue), a Fermi-function (black) and a point-charge Coulomb potential (dotted). $k_e \equiv \frac{e}{4\pi\epsilon_0}$ is the Coulomb constant. The absolute differences between ^{161}Dy and ^{163}Dy (green) for the HFBCS model are shown with scale on the right-hand y-axis.

2.4.2.2 Dipoles

We now turn our attention to the magnetic dipole moments of the isotopes ^{161}Dy, ^{163}Dy, ^{159}Tb, and ^{165}Ho. The magnetic dipole moments were obtained by integrating the magnetic dipole densities $\rho_{1,0}(R)$ over the volume of the nucleus as in Eq. (2.30). The magnetic dipole density contributions are given by the sum of the proton and neutron spin densities and the proton orbital current density. The neutron orbital current density does not contribute since its Landé g factor is zero.

In Fig. 2.13, we show the magnetic dipole densities for each isotope. The radial part of the dipole density is plotted in units of R_N^{-3}, with the distributions of the magnetic dipolar radial density contributions normalised by the total magnetic moment of the respective isotope μ_N^{A} as obtained from the HFBCS model. Observe that the neutron (spin) currents are the dominant contribution for dysprosium, while for terbium and holium it is the proton spin and orbital currents that dominate. This is consistent with the fact that the dysprosium nuclei are even-odd (in Z and N), while the terbium and holmium nuclei are odd-even, and so it is the currents of the unpaired nucleons that contribute most to the magnetic dipole moment.

In Table 2.4, we summarise the results of our calculations for the magnetic dipole mo-



(a) ^{161}Dy and ^{163}Dy (b) ^{159}Tb and ^{165}Ho

Figure 2.13 – Dipole densities of ^{161}Dy, ^{163}Dy, ^{159}Tb and ^{165}Ho. The distributions of the magnetic dipolar radial density contributions, normalized by the total magnetic moment of the isotope(μ_N^{iso}), $\rho_{1,0}(R)$ within the nuclei of isotopes ^{163}Dy (a, upper), ^{161}Dy (a, lower), ^{159}Tb (b, upper) and ^{165}Ho (b, lower). R is used in units of the nuclear radius, R_N, thus giving the dipole in units of R_N^{-3}. The vertical line represents the surface of the nucleus at $R = 1 \times R_N$, to which the other curves are normalised. Each curve describes a different contribution to the dipole density distribution: (dashed) the total dipole density, (blue) the neutron spins, (red) the proton spins, and (green) the proton orbital currents.

ments of the isotopes ^{159}Tb, ^{161}Dy, ^{163}Dy, and ^{165}Ho using their respective spin and orbital current distributions obtained with the HFBCS model. We also show the relative error between the total magnetic moment μ_{tot} and the experimental values μ_{exp} [112], calculated by

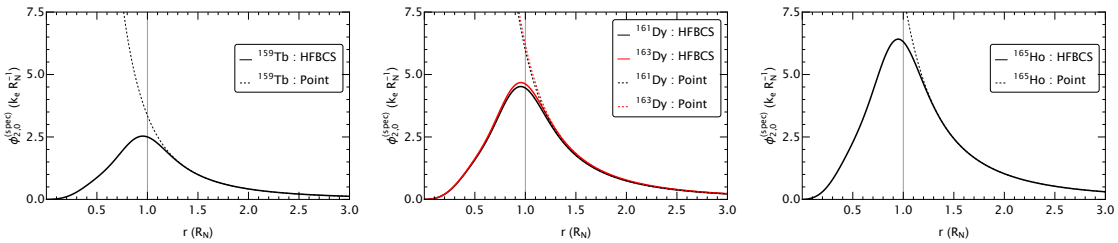
$$\Delta\mu_{\text{exp}}^{\text{spec}} = \frac{\mu_{\text{spec}} - \mu_{\text{exp}}}{\mu_{\text{exp}}} \times 100\%. \tag{2.48}$$

While the general behaviour of the magnetic moments obtained from the model is consistent, there are still some inaccuracies when compared with the experimental data. Indeed, while the model is specialised in the description of nuclei deformed from sphericity (as we shall see for the case of the quadrupole moments in Section 2.4.2.3), further refinements are necessary to better understand the complex interactions producing the magnetic moments from the spherically symmetric dipolar terms.

Pragmatically, these results are quite reasonable when one considers other, more detailed, comparisons with experimental data from this type of mean-field calculation with self-consistent blocking [158]. Moreover, it is important to keep in mind that this non-relativistic model of the nucleonic interactions does not account for the full complexity of the nuclear interactions, including for example the mesonic degrees of freedom that contribute to the nuclear magnetic properties through charged virtual meson currents affecting the neutron-proton interactions [107].

Isotope	$M_z^{(1)}$	μ_{spec}	μ_{exp}	$\Delta\mu_{\text{exp}}^{\text{spec}}$ (%)
^{159}Tb	3.145	1.887	2.014	−6.31%
^{161}Dy	−0.919	−0.656	−0.480	36.67%
^{163}Dy	0.928	0.663	0.673	−1.49%
^{165}Ho	5.071	3.944	4.17	−5.42%

Table 2.4 – Comparison of the *ab initio* and experimental magnetic moments. The table shows the comparisons of magnetic moments between ^{159}Tb, ^{161}Dy, ^{163}Dy, and ^{165}Ho with experimental values in [112]. The relative error between μ_{spec} and μ_{exp} is also shown.



(a) ^{159}Tb. **(b)** ^{161}Dy and ^{163}Dy. **(c)** ^{165}Ho.

Figure 2.14 – Quadrupole densities of ^{159}Tb, ^{161}Dy, ^{163}Dy and ^{165}Ho. The radial part of the spectroscopic quadrupole contribution to the nuclear electric potential for (a) ^{159}Tb (black), (b) ^{161}Dy (black) and ^{163}Dy (red) and (c) ^{165}Ho (black), as obtained from our HFBCS calculations, compared with the corresponding potentials obtained for the point-quadrupole nuclei (dashed). $k_e \equiv \frac{e}{4\pi\epsilon_0}$ is the Coulomb constant.

2.4.2.3 Quadrupoles

Finally, we investigate the electric quadrupole moments of our isotopes of interest. The quadrupole moments were obtained by integrating the quadrupole densities $\rho_{2,0}(R)$ over the volume of the nucleus. These densities were in turn derived from the quadrupole potentials $\phi_{2,0}(r)$ as calculated from the proton distributions obtained from the HFBCS model discussed in Section 2.4.1.

Figure 2.14 shows the spectroscopic quadrupole potentials $\phi_{2,0}(r)$ obtained from the HFBCS simulations after converting from the intrinsic potential via Eq. (2.40), and compared with a point-quadrupole potential, $\frac{Q_0^{(2)}}{r^3}$, shown by the dashed curves. The radial part of the spectroscopic quadrupole contribution to the nuclear electric potential is plotted in units of $\frac{e}{4\pi\epsilon_0}R_N^{-1}$, and plotted on the same axes scales for each isotope.

As for the preceding analysis, the vertical line represents the surface of the nucleus at $R = R_N$, to which the other curves are normalised. Besides the differences in magnitude between isotopes in each figure, note in particular the slightly higher maximum for ^{163}Dy (red) compared to ^{161}Dy (black) in Fig. 2.14b, despite both having the same number of protons. This is due to the different spatial distributions and more pronounced deformation of the proton distribution.

In Table 2.5, we summarise the resulting intrinsic and spectroscopic quadrupole moments as compared with the experimentally measured quantities given in [112]. The relative

Isotope	$\langle Q_2^{(ch)} \rangle_{\text{int}}$ (*e*barn)	$\langle Q_2^{(ch)} \rangle_{\text{spec}}$ (*e*barn)	$\langle Q_2^{(ch)} \rangle_{\text{exp}}$ (*e*barn)	ΔQ_{exp}^{spec} (%)
^{159}Tb	7.27	1.45	1.43	1.40%
^{161}Dy	7.34	2.62	2.51	4.38%
^{163}Dy	7.64	2.73	2.65	3.02%
^{165}Ho	7.70	3.60	3.58	0.56%

Table 2.5 – Intrinsic and spectroscopic charge quadrupole moments. Table showing the quadrupole moments (in *e*barn) for ^{159}Tb, ^{161}Dy, ^{163}Dy and ^{165}Ho compared with the experimentally measured quantities [112]. The relative error between the spectroscopic and experimental values is also shown.

error between the spectroscopic and experimental values is also shown, given by

$$\Delta Q_{\text{exp}}^{\text{spec}} = \frac{\langle Q_2^{(ch)} \rangle_{\text{spec}} - \langle Q_2^{(ch)} \rangle_{\text{exp}}}{\langle Q_2^{(ch)} \rangle_{\text{exp}}} \times 100\%. \tag{2.49}$$

These results show that the HFBCS model is able to reproduce the experimental quadrupole moments with a good degree of accuracy, with the relative errors being less than 5% for all isotopes presented. This is a good indication that the model is able to capture the deformation of the nuclei, which is a key feature of the HFBCS model.

2.5 Discussion

2.5.1 Summary

In this study, we have employed the Skyrme-Hartree-Fock-Bardeen-Cooper-Schrieffer (HFBCS) model to investigate the nuclear structure of deformed lanthanide nuclei, focusing on the isotopes $^{159}_{65}$Tb, $^{161}_{66}$Dy, $^{163}_{66}$Dy, and $^{165}_{67}$Ho. The HFBCS model, incorporating effective nucleon-nucelon interactions and self-consistent blocking to describe nuclei that break time-reversal symmetry, allows for detailed calculations of nucleon distributions and multipole moments for these nuclei.

The nucleon distributions obtained reveal significant deformations in all isotopes studied, with protons showing distinct concentrations towards the poles, especially for dysprosium and holmium. The corresponding current distributions, decomposed into proton and neutron spin and orbital contributions, were consistent with expected current loop structures based on the odd-even/ even-odd nature of the isotopes and the corresponding spherical harmonics of the $3D$ harmonic oscillator with associated occupation numbers.

For the odd-even nuclei of terbium and holmium, with a single unpaired proton, the proton currents showed the dominant contributions towards the magnetic moment, particularly from the spin currents. On the other hand, the even-odd nuclei of dysprosium, with an unpaired neutron each, exhibit dominant contributions from the neutron spin currents towards the magnetic moment. In both cases, the non-dominant nucleon currents appear to be induced by the dominant currents, having the same current loop structures, albeit at a smaller scale, roughly one order of magnitude weaker.

Multipole moments were calculated for each isotope. The monopole moments, derived from the spherically averaged proton charge densities, provided reasonable estimates for nuclear radii, showing an increase relative to empirical values. The magnetic dipole moments displayed some deviations from experimental data, but the general trends were

reproduced by the model, especially for the heavy holmium nucleus. Quadrupole moments were reproduced with a high degree of accuracy, with relative errors below 5% across all isotopes, highlighting the model's ability to capture nuclear deformation effects.

Looking closer at the magnetic dipole moments, it is worth noting that the model does not account for relativistic effects or mesonic contributions, which can influence neutron-proton interactions and magnetic properties. These effects could be responsible for the deviations observed in the magnetic dipole moments, particularly for isotopes such as ^{161}Dy. Incorporating these effects could enhance the accuracy of the model's predictions.

2.5.2 Outlook

While the HFBCS model demonstrates a strong capacity to describe nuclear structure and moments of deformed lanthanide nuclei, there remain areas for improvement and further exploration. The deviations in the magnetic dipole moments, particularly for isotopes such as ^{161}Dy, suggest that refinements to the model are necessary to better account for the complex nucleon interactions. Incorporating relativistic effects and mesonic contributions, which influence neutron-proton interactions and magnetic properties, could enhance the accuracy of these predictions.

Future research should also focus on extending the model to include a more comprehensive treatment of pairing correlations, possibly through fully self-consistent Hartree-Fock-BCS (HFBCS) methods that incorporate consistent treatment of both mean field and pairing fields. Additionally, the model could benefit from incorporating higher-order multipole moments, such as octupole or hexadecapole terms, which may be relevant for describing the fine details of nuclear shapes and collective excitations in highly deformed nuclei. Further investigations are being made by our collaborators regarding incorporation of the Higher-Tamm-Dancoff Approximation (HTDA) for an improved microscopic description of the multiparticle correlation effects, which may also aid in describing collective phenomena.

Finally, expanding the application of this approach to a broader set of isotopes and regions of the nuclear chart would provide a more complete understanding of how the nuclear structure and multipole moments evolve across different mass ranges, potentially offering deeper insight into the structure of exotic, neutron-rich nuclei.

References Cited in this Chapter

[41] E. Moreno-Pineda and W. Wernsdorfer. "Measuring molecular magnets for quantum technologies". In: *Nature Reviews Physics* 3.9 (Sept. 2021), pp. 645–659. DOI: 10.1038/s42254-021-00340-3.

[56] W. Wernsdorfer and M. Ruben. "Synthetic Hilbert Space Engineering of Molecular Qu *d* its: Isotopologue Chemistry". In: *Advanced Materials* 31.26 (June 2019), p. 1806687. DOI: 10.1002/adma.201806687.

[78] C. Godfrin, R. Ballou, et al. "Generalized Ramsey interferometry explored with a single nuclear spin qudit". In: *npj Quantum Information* 4.1 (Dec. 2018), p. 53. DOI: 10.1038/s41534-018-0101-3.

[104] P. Ring and P. Schuck. *The nuclear many body problem*. 1. ed., 3. print., study ed. Texts and monographs in physics. Berlin Heidelberg: Springer, 2004. 716 pp.

[105] J. Stone and P.-G. Reinhard. "The Skyrme interaction in finite nuclei and nuclear matter". In: *Progress in Particle and Nuclear Physics* 58.2 (Apr. 2007), pp. 587–657. DOI: 10.1016/j.ppnp.2006.07.001.

[106] M. Bender, P.-H. Heenen, et al. "Self-consistent mean-field models for nuclear structure". In: *Reviews of Modern Physics* 75.1 (Jan. 23, 2003), pp. 121–180. DOI: 10.1103/RevModPhys.75.121.

[107] L. Bonneau, N. Minkov, et al. "Effect of core polarization on magnetic dipole moments in deformed odd-mass nuclei". In: *Physical Review C* 91.5 (May 11, 2015), p. 054307. DOI: 10.1103/PhysRevC.91.054307.

[108] N. Minkov, A. Pálffy, et al. "Skyrme-Hartree-Fock-BCS approach to Th 229 m and neighboring nuclei". In: *Physical Review C* 110.3 (Sept. 26, 2024), p. 034327. DOI: 10.1103/PhysRevC.110.034327.

[109] G. Tessitore, G. A. Mandl, et al. "The role of lanthanide luminescence in advancing technology". In: *RSC Advances* 13.26 (2023), pp. 17787–17811. DOI: 10.1039/D3RA00991B.

[110] H. Carvajal Gallego, J. Deprince, et al. "Overview of the contributions from all lanthanide elements to kilonova opacity in the temperature range from 25 000 to 40 000 K". In: *Astronomy & Astrophysics* 685 (May 2024), A91. DOI: 10.1051/0004-6361/202347723.

[111] D. Serrano, S. K. Kuppusamy, et al. "Ultra-narrow optical linewidths in rare-earth molecular crystals". In: *Nature* 603.7900 (Mar. 10, 2022), pp. 241–246. DOI: 10.1038/s41586-021-04316-2.

[112] N. Stone. "Table of nuclear magnetic dipole and electric quadrupole moments". In: *Atomic Data and Nuclear Data Tables* 90.1 (May 2005), pp. 75–176. DOI: 10.1016/j.adt.2005.04.001.

[142] In this discussion of the effective mean-field model used in this work, we must acknowledge the work of our collaborators on this project, Johann Bartel and Hervé Molique. They provided the necessary nuclear charge distribution data and helped to refine our understanding of the techniques used in the effective model. Further information on the computational techniques and theoretical framework can be found in the publication resulting from our collaboration.

[143] T. Skyrme. "The effective nuclear potential". In: *Nuclear Physics* 9.4 (Jan. 1958), pp. 615–634. DOI: 10.1016/0029-5582(58)90345-6.

[144] D. Vautherin and D. M. Brink. "Hartree-Fock Calculations with Skyrme's Interaction. I. Spherical Nuclei". In: *Physical Review C* 5.3 (Mar. 1, 1972), pp. 626–647. DOI: 10.1103/PhysRevC.5.626.

[145] M. Beiner, H. Flocard, et al. "Nuclear ground-state properties and self-consistent calculations with the skyrme interaction". In: *Nuclear Physics A* 238.1 (Jan. 1975), pp. 29–69. DOI: 10.1016/0375-9474(75)90338-3.

[146] J. Damgaard, H. Pauli, et al. "A method for solving the independent-particle Schrödinger equation with a deformed average field". In: *Nuclear Physics A* 135.2 (Oct. 1969), pp. 432–444. DOI: 10.1016/0375-9474(69)90174-2.

[147] D. Vautherin. "Hartree-Fock Calculations with Skyrme's Interaction. II. Axially Deformed Nuclei". In: *Physical Review C* 7.1 (Jan. 1, 1973), pp. 296–316. DOI: 10.1103/PhysRevC.7.296.

[148] *Hartree-Fock-Bogoliubov results based on the Gogny force*. URL: https://www-phynu.cea.fr/science_en_ligne/carte_potentiels_microscopiques/carte_potentiel_nucleaire_eng.htm (visited on 09/24/2024).

[149] H. Flocard, P. Quentin, et al. "Nuclear deformation energy curves with the constrained Hartree-Fock method". In: *Nuclear Physics A* 203.3 (Mar. 1973), pp. 433–472. DOI: 10.1016/0375-9474(73)90357-6.

[150] J. Dechargé and D. Gogny. "Hartree-Fock-Bogolyubov calculations with the D 1 effective interaction on spherical nuclei". In: *Physical Review C* 21.4 (Apr. 1, 1980), pp. 1568–1593. DOI: 10.1103/PhysRevC.21.1568.

[151] V. Magnasco. *Methods of molecular quantum mechanics: an introduction to electronic molecular structure*. OCLC: 501193479. Chichester, U.K.: Wiley, 2009.

[152] J. Bardeen, L. N. Cooper, et al. "Theory of Superconductivity". In: *Physical Review* 108.5 (Dec. 1, 1957), pp. 1175–1204. DOI: 10.1103/PhysRev.108.1175.

[153] J. W. Negele. "The mean-field theory of nuclear structure and dynamics". In: *Reviews of Modern Physics* 54.4 (Oct. 1, 1982), pp. 913–1015. DOI: 10.1103/RevModPhys.54.913.

[154] J. D. Jackson. *Classical electrodynamics*. 3. ed., [Nachdr.] Hoboken, NY: Wiley, 2009. 808 pp.

[155] A. Pálffy. "Nuclear effects in atomic transitions". In: *Contemporary Physics* 51.6 (Nov. 2010), pp. 471–496. DOI: 10.1080/00107514.2010.493325.

[156] R. P. de Groote and G. Neyens. "Spins and electromagnetic moments of nuclei". In: *Handbook of nuclear physics*. Ed. by I. Tanihata, H. Toki, et al. Singapore: Springer Nature, 2020, pp. 1–36. DOI: 10.1007/978-981-15-8818-1_42-1.

[157] G. Fricke and H. Schopper, eds. *Numerical data and functional relationships in science and technology. Bd. 20: Gruppe 1: Kern- und Teilchenphysik = Group 1: @Nuclear and particle physics Nuclear charge radii / ed.: H. Schopper. Authors: G. Fricke*. Vol. 20. Berlin Heidelberg: Springer, 2004. 385 pp.

[158] M. Chemtob. "Two-body interaction currents and nuclear magnetic moments". In: *Nuclear Physics A* 123.2 (Jan. 1969), pp. 449–470. DOI: 10.1016/0375-9474(69)90513-2.

CHAPTER 3

HYPERFINE ANOMALIES IN HYDROGEN-LIKE DYSPROSIUM IONS

We demand rigidly defined areas of doubt and uncertainty.

Vroomfondel in "The Hitchhiker's Guide to the Galaxy" - Douglas Adams

Contents

3.1 Introduction . . . 67
3.1.1 Background and Motivation . . . 67
3.1.2 Objectives and Contributions . . . 68
3.1.3 Overview . . . 69
3.2 Theory . . . 70
3.2.1 Multipole Expansions . . . 71
3.2.1.1 Electric monopole and quadrupole potentials . . . 71
3.2.1.2 Magnetic dipole potential . . . 73
3.2.2 Hyperfine Interactions . . . 74
3.2.2.1 Magnetic dipole hyperfine structure constant . . . 74
3.2.2.2 Electric quadrupole hyperfine structure Constant . . . 76
3.2.3 Isotope Shifts . . . 77
3.2.3.1 Breit-Rosenthal correction . . . 77
3.2.3.2 Bohr-Weisskopf correction . . . 77
3.2.3.3 Web of hyperfine anomalies . . . 77
3.2.3.4 Magnetic dipole hyperfine anomaly . . . 78
3.2.3.5 Electric quadrupole hyperfine anomaly . . . 80
3.2.3.6 Additional contributions . . . 81
3.3 Methods . . . 81
3.4 Results . . . 82
3.4.1 Hydrogen-like Wavefunctions . . . 82
3.4.2 Charge Corrections . . . 84
3.4.3 Magnetic Corrections . . . 90
3.4.4 Hyperfine Anomaly . . . 92
3.4.5 Quadrupole Corrections . . . 93
3.5 Discussion . . . 95
3.5.1 Summary . . . 95
3.5.2 Outlook . . . 96
References Cited in this Chapter . . . 98

Note: This chapter and the results presented herein, together with Chapter 2 and the results presented therein, have been prepared concurrently with a manuscript to be published under the working title "The hyperfine interaction as a probe of the microscopic structure of the atomic nucleus" together with our collaborators Johann Bartel, Hervé Molique and Ludovic Bonneau.

3.1 Introduction

In this chapter, we investigate the hyperfine structure (HFS) of hydrogen-like ions, focusing on the isotopes ^{161}Dy and ^{163}Dy. The HFS arises from the interaction between the nuclear magnetic and electric moments and the atomic electron or muon, providing a window into the internal structure of the nucleus. By calculating the hyperfine anomalies between these isotopes, we aim to understand how nuclear properties manifest in atomic-level phenomena. We explore the Bohr-Weisskopf (BW) and Breit-Rosenthal (BR) corrections to the HFS, which account for the finite size and internal magnetisation of the nucleus, respectively. These corrections are crucial for accurately predicting hyperfine interactions and enhancing our understanding of nuclear structure.

3.1.1 Background and Motivation

The study of nuclear structure provides a gateway to understanding not only the complex interactions within the nucleus but also their profound influence on atomic systems. In Chapter 2, we explored the internal properties of lanthanide nuclei, particularly the magnetic dipole and quadrupole moments, using the Hartree-Fock-BCS (HFBCS) model [107]. These properties form the foundation for interactions that extend beyond the nucleus, manifesting in the atomic hyperfine structure (HFS). Building upon that investigation, we now shift our focus to the implications of these nuclear properties in the context of hydrogen-like ions, where the interplay between the nucleus and the bound electron or muon provides a compelling framework to probe nuclear effects at the atomic level.

Understanding the HFS is critical because it encapsulates the influence of nuclear charge distribution and magnetisation on the surrounding electronic cloud. Considering that this project is part of a broader effort to explore the potential of lanthanide-molecular complexes for quantum information processing with their nuclear spin states, the accurate prediction and understanding of hyperfine interactions is essential for designing quantum devices that leverage the unique properties of these systems [56].

While hyperfine splittings are often considered as small perturbations to atomic energy levels in the absence of nuclear hyperfine structure (HFS), they carry a wealth of information about the underlying nuclear structure [113]. The lanthanides, with their highly deformed and magnetised nuclei, exhibit pronounced hyperfine interactions [112] that are particularly sensitive to the internal nuclear configuration. Consequently, hydrogen-like ions of these elements serve as an ideal platform to investigate the impact of nuclear structure on atomic-level observables [114], offering insights into the Breit-Rosenthal (BR) [64] and Bohr-Weisskopf (BW) [65] effects, in addition to the search for new physics with high-precision measurements [115]. The BR effect arises due to the finite distribution of nuclear charge, while the BW effect stems from the distribution of nuclear magnetisation. Together, these corrections to the HFS provide a nuanced understanding of how nuclear characteristics influence electronic or muonic bound states.

Moreover, the study of hyperfine interactions becomes even more intriguing when considering muonic atoms [116, 117, 118]. The significantly larger mass of the muon (approximately 207 times that of the electron) causes it to orbit much closer to the nucleus, amplifying the sensitivity of its wavefunction to nuclear structure details. This enhanced sensitivity magnifies the BR and BW effects, providing a unique window into the distribution of nuclear charge and magnetisation. Muonic atoms are thus not only theoretically compelling but also experimentally advantageous, as they allow for the probing of nuclear structure effects with greater precision. Indeed, there are significant recent efforts by research groups at, for example, the PSI Laboratory for Muon Spin Spectroscopy in Switzerland and the KEK Muon Science Laboratory in Japan to develop high-precision muon-beam facilities that can be applied to this purpose [69, 70].

The potential here for high-precision nuclear measurements is significant, including for example the determination of nuclear charge radii [119], the measurement of charge quadrupole moments in heavy nuclei [120], and even observation of more exotic atomic structures beyond hydrogen-like muonic ions [121]. By extending our exploration from electronic to muonic systems, we can therefore deepen our understanding of the interplay between nuclear properties and atomic spectra, and offer new predictions that can be tested in cutting-edge experiments.

Furthermore, the hyperfine anomalies between two isotopes, such as ^{161}Dy and ^{163}Dy, provide a unique opportunity to study the effect of nuclear structure differences on atomic properties, by isolating the impact of changes in nuclear charge and magnetisation, while keeping other atomic parameters constant. Thus providing a strong foundation for the development and benchmarking of new methods for modelling of nuclei [115].

The implications of these studies are vast. From testing the validity of different nuclear models to providing a foundation for applications in quantum information processing, the analysis of HFS in heavy hydrogen-like ions connects fundamental nuclear theory with practical technological advancements. The lanthanides, which are already recognised for their potential in quantum devices due to their complex magnetic properties, stand to benefit greatly from a detailed understanding of their hyperfine interactions. Ultimately, these interactions determine how nuclear properties influence electronic transitions, energy levels, and overall behaviour in external fields.

Moreover, in the context of this thesis and the goals of advancing the applications of lanthanide-based SMMs as platforms for QIP, we must note the important role played by the hyperfine interactions in enabling the coherent control of the nuclear spin states of the lanthanide nuclei. As discussed in Section 1.1.3, developing an improved understanding of these interactions and their role in isotopologue chemistry is necessary for improving the scalability of these systems [56].

3.1.2 Objectives and Contributions

This chapter aims to build on the nuclear structure insights gained in the previous study of lanthanide nuclei by examining how these structures manifest in the hyperfine interactions of hydrogen-like ions, particularly for the hydrogen-like dysprosium ions, focusing on the isotopes ^{161}Dy and ^{163}Dy. Specifically, we aim to calculate and analyse the BR and BW corrections to the HFS across multiple nuclear potential models: point-like, spherical, Fermi-distributed, and HFBCS-based. By solving the radial Dirac equation for both electronic and muonic ions under these nuclear models, we intend to elucidate

the effect of nuclear charge distribution and magnetisation on the wavefunctions, energy levels, and other observables of the bound particles.

A critical aspect of this study is to examine the isotopic variations in hyperfine structure, quantifying the hyperfine anomalies between ^{161}Dy and ^{163}Dy to understand how differences in nuclear structure manifest in atomic properties. The analysis includes evaluating both dipole and quadrupole contributions to the HFS, exploring their relative significance, especially in the muonic system where nuclear effects are enhanced. Additionally, the study seeks to determine how these corrections vary with principal quantum number and orbital angular momentum, thereby revealing the intricate dependence of hyperfine interactions on both atomic and nuclear characteristics.

Ultimately, this chapter endeavours to underscore the important role of realisitic nuclear models in accurately predicting how the microscopic nuclear structure influences the HFS corrections in hydrogen-like ions. Such an understanding is crucial for interpreting spectroscopic measurements, improving nuclear theory models, and exploring applications in atomic and molecular physics.

The contributions of this chapter are twofold: we develop a robust computational framework for solving the Dirac equation for hydrogen-like ions with various nuclear models. This numerical approach provides a detailed computation of the BR and BW corrections in both electronic and muonic systems. Furthermore, the work offers a comprehensive analysis of the hyperfine anomalies between ^{161}Dy and ^{163}Dy, highlighting the amplified sensitivity of muonic systems to nuclear structure, and revealing the dominant role of quadrupole effects in muonic hyperfine splittings, making them promising nuclear probes for future research. While these effects are found to be minor for electronic states, this work demonstrates the critical importance of using realistic nuclear descriptions for muonic ions where the nuclear effects are significantly amplified.

Overall, this chapter bridges the theoretical nuclear structure analysis of lanthanides with their atomic-level manifestations in hyperfine interactions. By combining nuclear and atomic theory through a unified framework, it paves the way for more accurate predictions of HFS in complex systems and highlights the potential for future experimental investigations, especially in the realm of muonic atoms.

3.1.3 Overview

The chapter is organised as follows. In Section 3.2, we provide the theoretical framework for understanding hyperfine interactions in hydrogen-like ions, starting with the Dirac equation in the presence of various nuclear potentials. The derivation of the BR and BW effects, along with the multipole expansion of electric and magnetic potentials, is presented to establish a foundation for the subsequent calculations. The formalism for hyperfine structure constants, isotope shifts, and anomalies is also reviewed.

In Section 3.3, the computational methods used to solve the radial Dirac equation and calculate the BR and BW corrections are detailed. The discussion includes the Fortran modules developed for these calculations, the numerical techniques for achieving convergence in eigenvalue and wavefunction computations, and the approach for comparing results across different nuclear models.

The results are presented in Section 3.4, where the wavefunctions for both electronic and muonic systems under different nuclear models are analysed. The chapter discusses

the resulting energy shifts and hyperfine corrections due to BR and BW effects, evaluates the hyperfine anomalies between isotopes, and concludes with an assessment of the quadrupole corrections to the HFS.

Finally, Section 3.5 provides a synthesis of the findings, highlighting their implications for nuclear theory, spectroscopic applications, and future research. The chapter also discusses potential improvements to the computational framework and outlines avenues for further exploration, particularly in the context of muonic atoms and their enhanced sensitivity to nuclear structure.

3.2 Theory

The $(\vec{j}, \rho)$ nuclear source terms are responsible for the connection between the nucleus and the atomic electrons via the so-called hyperfine interaction. As discussed in Chapter 2, we have implemented a realistic, ab-initio model that enables us to compute these quantities at the microscopic level. As we will explore later, the magnetic and electric potentials $(\vec{A}, \phi)$, which influence the electrons in the atom, can be derived from $(\vec{j}, \rho)$ and the Maxwell equations.

In this work, we will focus only on hydrogen-like ions with a single electron, or muonic ions being atomic hydrogen-like bound states formed with a negatively charged muon of mass $m_\mu \approx 207 m_e$. Since the net charge of the dysprosium nucleus with $Z = 66$ is large, we need to solve the stationary Dirac equation for a single electron (or muon) in the presence of external electric $\phi(\vec{r})$ and magnetic $\vec{A}(\vec{r})$ potentials due to the nucleus, which is written as [159],

$$
\begin{aligned}
{}^{a}H\psi &= W\psi && (3.1)\\
&= \left(c\vec{\alpha}\cdot(\vec{p} + e\vec{A}(\vec{r})) - e\phi(\vec{r})\mathbb{1} + mc^2\beta\right)\psi && (3.2)\\
&= (T + V + mc^2\beta)\psi\ , && (3.3)
\end{aligned}
$$

where $\psi(\vec{r}) = (u(\vec{r}), v(\vec{r}))$ is a four-component bispinor with u and v two-component spinors, $V \equiv -e\phi\mathbb{1}$ with $e > 0$, and $T \equiv c\vec{\alpha}\cdot(\vec{p} + e\vec{A})$ is the kinetic energy. $\vec{\alpha}$ and β are the Dirac matrices [159], and $\mathbb{1}$ is the identity matrix. In the following, ${}^{a}H$ refers to the electronic or atomic Hamiltonian. In this form, the Dirac equation can be solved separably for the radial and angular parts of the wavefunction,

$$
\begin{aligned}
u_{n\kappa}(\vec{r}) &= g_{n\kappa}(r)\chi_{\kappa}^{m_j}(\Omega) && (3.4)\\
v_{n\kappa}(\vec{r}) &= i f_{n\kappa}(r)\chi_{-\kappa}^{m_j}(\Omega)\ , && (3.5)
\end{aligned}
$$

where χ are the spin spherical harmonic solutions to the angular part of the Dirac equation, and the large and small component radial wavefunctions, $P_{n\kappa} \equiv r g_{n\kappa}$ and $Q_{n\kappa} \equiv r f_{n\kappa}$ are the solutions of the coupled radial differential equations,

$$
\begin{aligned}
\frac{dg_{n\kappa}}{dr} &= -\frac{\kappa+1}{r}g_{n\kappa} + \frac{1}{c\hbar}\left(W - V + mc^2\right) f_{n\kappa}\ , && (3.6)\\
\frac{df_{n\kappa}}{dr} &= +\frac{\kappa-1}{r}f_{n\kappa} - \frac{1}{c\hbar}\left(W - V - mc^2\right) g_{n\kappa}\ , && (3.7)
\end{aligned}
$$

with the following normalisation conditions:

$$
\int_0^\infty \left(P_{n\kappa}^2(r) + Q_{n\kappa}^2(r)\right) dr = 1\ , \tag{3.8}
$$

on the radial part, and

$$\int \chi_{\kappa}^{m_j *}(\Omega)\chi_{\kappa'}^{m_{j'}}(\Omega)d\Omega = \delta_{\kappa\kappa'}\delta_{m_j m_{j'}} \,, \tag{3.9}$$

on the spherical part, over the quantum numbers n and κ, where n is the principal quantum number, and

$$\kappa = \begin{cases} j+1/2 & \text{for } j = \ell - 1/2 \,, \\ -(j+1/2) & \text{for } j = \ell + 1/2 \,, \end{cases} \tag{3.10}$$

where $j = \ell \pm \frac{1}{2}$ is the total angular momentum from $\vec{j} = \vec{\ell} + \vec{s}$, with $\vec{\ell}$ the orbital angular momentum, $\vec{s}$ the spin and the quantum number m_j the projection of the total angular momentum on the z-axis.

3.2.1 Multipole Expansions

Let us briefly recall the multipolar expansions of the electric and magnetic potentials as summarised in Section 2.2.2 from [154, 160]. Here, we will denote $\vec{R} = (R, \theta, \phi)$ and $\vec{r} = (r, \theta, \phi)$ as the spherical coordinates of the nucleus and the electron respectively, where $\Omega \equiv (\theta, \phi)$. The normalised spherical harmonics are defined by $C_q^{(k)}(\theta, \phi) \equiv \sqrt{\frac{4\pi}{(2k+1)}} Y_{k,q}$.

3.2.1.1 Electric monopole and quadrupole potentials

The electric potential generated by the nucleus through its charge density ($\rho(\vec{R}) = e\rho^{(p)}(\vec{R})$ with $\rho^{(p)}$ the proton density), in which the electron moves, has the following form

$$\phi(\vec{r}) = \frac{1}{4\pi\epsilon_0} \int \frac{\rho(\vec{R})}{|\vec{r} - \vec{R}|} d^3R \,, \tag{3.11}$$

and ϕ is solution of the Poisson equation $\Delta\phi = -\frac{\rho}{\epsilon_0}$. By using the usual multipolar expansion

$$\frac{1}{\left|\vec{r} - \vec{R}\right|} = \sum_{k=0}^{\infty} \frac{r_<^k}{r_>^{k+1}} \sum_{q=-k}^{k} (-1)^q C_{-q}^{(k)}(\Theta, \Phi) C_q^{(k)}(\theta, \phi) \,, \tag{3.12}$$

the electric potential takes the form

$$\phi(\vec{r}) = \frac{1}{4\pi\epsilon_0} \sum_{k=0}^{\infty} \frac{1}{r^{k+1}} \sum_{q=-k}^{k} (-1)^q C_q^{(k)}(\theta, \phi)\, {}^{in}Q_q^{(k)}(r) \tag{3.13}$$

$$+ \frac{1}{4\pi\epsilon_0} \sum_{k=0}^{\infty} r^k \sum_{q=-k}^{k} (-1)^q C_q^{(k)}(\theta, \phi)\, {}^{ex}Q_q^{(k)}(r) \tag{3.14}$$

$$= \sum_{k=0}^{\infty} \sum_{q=-k}^{k} \phi_{k,q}(r) C_q^{(k)}(\theta, \phi) \tag{3.15}$$

$$= \sum_{k=0}^{\infty} \phi_k(\vec{r}) \,, \tag{3.16}$$

where we have defined

$${}^{in}Q_q^{(k)}(r) \equiv \int_{R=0}^{r} \rho(\vec{R}) R^k C_q^{(k)}(\Theta, \Phi) d^3R \tag{3.17}$$

and

$$ {}^{ex}Q_q^{(k)}(r) \equiv \int_{R=r}^{\infty} \frac{\rho(\vec{R})}{R^{k+1}} C_q^{(k)}(\Theta,\Phi) d^3R \,. \tag{3.18}$$

Let us recall the usual definition of the multipole electric moment

$$ Q_q^{(k)} \equiv \int_{R=0}^{\infty} \rho(\vec{R}) R^k C_q^{(k)}(\Theta,\Phi) d^3R \,. \tag{3.19}$$

It is worthy of note that if the electronic wave function does not penetrate the nucleus (i.e. $R \ll r$) one has ${}^{in}Q_q^{(k)}(r) = Q_q^{(k)} \ \forall \ r$ since $Q_q^{(k)} = \lim_{r\to+\infty} {}^{in}Q_q^{(k)}(r)$.

The spherically symmetric electric monopole term takes the form

$$ \phi_0(\vec{r}) = \phi_0(r) = \phi_{0,0}(r) = \frac{1}{4\pi\epsilon_0} C_0^{(0)}(\theta,\phi) \left(\frac{{}^{in}Q_0^{(0)}(r)}{r} + {}^{ex}Q_0^{(0)}(r) \right) \tag{3.20}$$

$$ = \frac{1}{4\pi\epsilon_0} \left(\frac{{}^{in}Q_0^{(0)}(r)}{r} + {}^{ex}Q_0^{(0)}(r) \right) \,. \tag{3.21}$$

In the non-penetrating case we would have had

$$ \phi_0(\vec{r}) = \phi_0(r) = \phi_{0,0}(r) = \frac{1}{4\pi\epsilon_0} \frac{Q_0^{(0)}}{r} \,, \tag{3.22}$$

where $Q_0^{(0)}$ is simply the total charge Ze of the nucleus.

To assess the impact of a microscopic calculation of the nuclear charge density on hyperfine interactions, we will compare the results obtained with those derived from a semi-empirical description of the density, which is the well-known Fermi distribution. The latter is computed as follows

$$ \rho(R) = \frac{\rho_0}{1 + \exp\left(\frac{R-\tilde{c}}{a}\right)} \,, \tag{3.23}$$

with

$$ \rho_0 = \frac{3}{4\pi\tilde{c}^3 \left(1 + \left(\frac{\pi a}{\tilde{c}}\right)^2\right)} \,. \tag{3.24}$$

The parameters a, $\tilde{c}$ have been taken from [155].

Due to the symmetry of the nucleus (where, based on our discussions in Chapter 2 of the deformations of the lanthanide nuclei from spherical to prolate or oblate spheroidal, we can assume axial symmetry) the only non-zero component of the quadrupole tensors is $q = 0$, and thus the electric quadrupole term of the electric potential is

$$ \phi_2(\vec{r}) = \frac{1}{4\pi\epsilon_0} C_0^{(2)}(\theta,\phi) \left(\frac{{}^{in}Q_0^{(2)}(r)}{r^3} + r^2 \, {}^{ex}Q_0^{(2)}(r) \right) \,. \tag{3.25}$$

Again, without penetration we have the no longer spherically symmetric potential

$$ \phi_2(\vec{r}) = \frac{C_0^{(2)}(\theta,\phi)}{4\pi\epsilon_0} \frac{Q_0^{(2)}}{r^3} \tag{3.26}$$

$$ = \phi_{2,0}(r) C_0^{(2)}(\theta,\phi) \,. \tag{3.27}$$

3.2.1.2 Magnetic dipole potential

The magnetic field produced by the nucleus and acting on the electrons of the atom via the potential vector $\vec{A}(\vec{r})$ in the Dirac equation Eq. (3.3) is characterised by the current density $\vec{j}(\vec{R})$. Summarising in an analogous way to the electric case, we have the expression for the magnetic field from the Biot and Savart Law for $\vec{B}$ as a function of the current density $\vec{j}$, and using the definition of the vector potential $\vec{B} = \vec{\nabla} \wedge \vec{A}$ in the Coulomb gauge ($\vec{\nabla} \cdot \vec{A} = 0$), we obtain the magnetic equivalent of Eq. (3.11),

$$\vec{A}(\vec{r}) = \frac{\mu_0}{4\pi} \int \frac{\vec{j}(\vec{R})}{|\vec{r} - \vec{R}|} d^3R \,. \tag{3.28}$$

As with the scalar potential, we can perform a multipole expansion of $\vec{A}$ which is expressed as

$$\vec{A}(\vec{r}) = \frac{\mu_0}{4\pi} \sum_{k=0}^{\infty} \sum_{q=-k}^{k} (-1)^q \frac{(-i)}{\hbar k} \left[\vec{L} C_q^{(k)}(\theta, \phi)\right] \frac{{}^{in}M_{-q}^{(k)}(r)}{r^{k+1}} \tag{3.29}$$

$$+ \frac{\mu_0}{4\pi} \sum_{k=0}^{\infty} \sum_{q=-k}^{k} (-1)^q \frac{(-i)}{\hbar k} \left[\vec{L} C_q^{(k)}(\theta, \phi)\right] {}^{ex}M_{-q}^{(k)}(r)\, r^k \,, \tag{3.30}$$

with the interior and exterior magnetic multipole moments defined as

$${}^{in}M_q^{(k)}(r) \equiv -\frac{i}{\hbar(k+1)} \int_{R=0}^{r} \left[\vec{L} C_q^{(k)}(\Theta, \Phi)\right] \cdot \vec{j}(\vec{R}) R^k d^3R \,, \tag{3.31}$$

$${}^{ex}M_q^{(k)}(r) \equiv -\frac{i}{\hbar(k+1)} \int_{R=r}^{\infty} \left[\vec{L} C_q^{(k)}(\Theta, \Phi)\right] \cdot \vec{j}(\vec{R}) \frac{1}{R^{k+1}} d^3R \,. \tag{3.32}$$

Here, $\vec{L} \equiv -i\hbar \vec{R} \wedge \vec{\nabla}$, and the usual definition of the magnetic multipole moments is as follows

$$M_q^{(k)} \equiv -\frac{i}{\hbar(k+1)} \int_{R=0}^{\infty} \left[\vec{L} C_q^{(k)}(\Theta, \Phi)\right] \cdot \vec{j}(\vec{R}) R^k d^3R = {}^{in}M_q^{(k)}(r \to \infty) \,, \tag{3.33}$$

which corresponds to the case without penetration for $R \ll r$. This results in the following expressions for the dipole term:

$$\vec{A}(\vec{r}) = \frac{\mu_0}{4\pi} \frac{{}^{in}\vec{M}^{(1)}(r) \wedge \vec{r}}{r^3} + \frac{\mu_0}{4\pi} \left({}^{ex}\vec{M}^{(1)}(r) \wedge \vec{r}\right) \,, \tag{3.34}$$

where

$${}^{in}\vec{M}^{(1)}(r) = \frac{1}{2} \int_{R=0}^{r} \vec{R} \wedge \vec{j}(\vec{R}) d^3R, \tag{3.35}$$

and

$${}^{ex}\vec{M}^{(1)}(r) = \frac{1}{2} \int_{R=r}^{\infty} \frac{\vec{R} \wedge \vec{j}(\vec{R})}{R^3} d^3R \,. \tag{3.36}$$

3.2.2 Hyperfine Interactions

We begin with a brief overview of the hyperfine structure of hydrogen-like ions, which is a direct consequence of the interaction between the nuclear magnetic and electric moments and the atomic electron or muon.

Following the multipolar expansions, if we consider that the quadrupole term of the scalar potential and the dipole term of the vector potential contribute minimally compared to the spherically symmetric monopole term of the scalar potential in Eq. (3.21), we can address the hyperfine interaction using first-order stationary perturbation theory on the unperturbed electron Hamiltonian from the monopole.

The perturbed Hamiltonian is expressed as

$$
\begin{aligned}
{}^{a}H_{hf} &= -e\phi_2(\vec{r}) + ec\vec{\alpha}\cdot\vec{A}(\vec{r}) && (3.37)\\
&\equiv {}^{a}H_{hf,quad} + {}^{a}H_{hf,dip}\ . && (3.38)
\end{aligned}
$$

Note that the total angular momentum of the nucleus is typically represented by the nuclear spin I. For electrons in atoms, we differentiate between the electron spin $\vec{S}$ and the electron orbital moment $\vec{L}$, which combine to form the total angular momentum $\vec{J}$. However, nuclei tend to behave as a unified body with their own angular momentum $\vec{I}$. Each nuclear spin has a corresponding nuclear magnetic moment, resulting in magnetic interactions with its environment, which give rise to the magnetic hyperfine interaction. For an atom or ion with nuclear spin I and total electronic angular momentum J, the value of the splitting in the electronic energy level, characterised by the quantum numbers $n\kappa$, is determined by the expression

$$
\begin{aligned}
W_F &= \langle n\kappa F M_F|^{a} H_{hf} |n\kappa F M_F\rangle && (3.39)\\
&= \langle n\kappa F M_F|^{a} H_{hf,dip} |n\kappa F M_F\rangle + \langle n\kappa F M_F|^{a} H_{hf,quad} |n\kappa F M_F\rangle && (3.40)\\
&= \frac{1}{2}aK + b\frac{\frac{3}{2}K(K+1) - 2I(I+1)J(J+1)}{2I(2I-1)2J(2J-1)}\ , && (3.41)
\end{aligned}
$$

where $K = F(F+1) - I(I+1) - J(J+1)$, with total angular momentum $\vec{F} = \vec{I} + \vec{J}$. The magnetic dipole and electric quadrupole structure constants are given by a and b, respectively.

3.2.2.1 Magnetic dipole hyperfine structure constant

We are now in a position to obtain explicitly the magnetic dipole hyperfine structure constant a, the first term in Eq. (3.41). Introducing this effect, by way of the dipolar term of the perturbed Hamiltonian, leads to an evenly spaced splitting of the atomic energy levels into a hyperfine multiplet labeled by F. For a relatively weak interaction in the absence of additional terms, the energy difference between adjacent F sub-levels is given by the Landé interval rule, $E_F - E_{F-1} = aF$. However, as we will discuss later, the inclusion of the quadrupole term alters this property.

Following the multipole expansion of the magnetic vector potential from the nucleus and its effect on the electrons, the magnetic dipole hyperfine constant a for electrons with

quantum numbers n and κ is given by [160]:

$$a(\vec{j},\rho) = \mathcal{T}(\kappa,j)\int_0^\infty \left(\frac{1}{r^2}\int_{R=0}^{r}\left[\vec{R}\wedge\vec{j}(\vec{R})\right]_z d^3R + r\int_{R=r}^{\infty}\frac{\left[\vec{R}\wedge\vec{j}(\vec{R})\right]_z}{R^3}d^3R\right)P_{n\kappa}(r)Q_{n\kappa}(r)dr, \tag{3.42}$$

where $\vec{R}$ are the coordinates of the nuclear current and charge distribution, and r is the radial coordinate of the electron. $P_{n\kappa}(r)$ and $Q_{n\kappa}(r)$ represent the large and small radial components, respectively, of the electron's Dirac wavefunction. $\vec{j}(\vec{R})$ is the nuclear current distribution, which we recall is given by

$$\vec{j}(\vec{R}) = \vec{j}_l^{(p)}(\vec{R}) + \vec{j}_l^{(n)}(\vec{R}) + \vec{j}_s^{(p)}(\vec{R}) + \vec{j}_s^{(n)}(\vec{R})\ , \tag{3.43}$$

based on a microscopic description of the nucleus (as discussed in Chapter 2), where $\vec{j}_{l,s}^{(p,n)}$ denote the convection (orbital) and spin currents of protons and neutrons, respectively. The prefactor $\mathcal{T}(\kappa,j)$ is a multiplicative factor that depends on the angular part of the wavefunction, and for configurations with more than two electrons, its computation involves group theoretical tools. For single-electron or single-muon systems, we have that

$$\mathcal{T}(\kappa,j) = \frac{\alpha\kappa}{j(j+1)}\ , \tag{3.44}$$

where $\alpha = -\frac{e}{4\pi\varepsilon_0}\frac{1}{c}\frac{\mu_N}{a_0^2}$ in atomic units. Note that, for the remainder of this study, unless specified, we shall consider only hydrogen-like systems using this definition of $\mathcal{T}(\kappa,j)$.

The dependence of a on the charge distribution ρ is indirect, through the calculation of $P_{n\kappa}$ and $Q_{n\kappa}$, which are solutions to the Dirac equation containing the electric monopole potential created by ρ. We remark that the accuracy of the value of a depends on the quality of the nuclear model used to evaluate $\vec{j}$ and ρ.

In the simplifying assumption of a point-like magnetic dipole model, denoted by the subscript pd, with no penetration into the nucleus from the single electron or single muon, Eq. (3.42) simplifies to

$$a_{pd} = -\frac{e}{4\pi\varepsilon_0}\frac{1}{c}\frac{\mu_N}{a_0^2}\frac{\kappa}{j(j+1)}\frac{\mathcal{I}_{lab}^M M_z^{(1)}}{I}\left[\int_0^\infty \frac{P_{n\kappa}(r)Q_{n\kappa}(r)}{r^2}dr\right]\ , \tag{3.45}$$

where we have written the explicit form of $\mathcal{T}(\kappa,j)$, $M_z^{(1)}$ is in units of μ_N, the integral over the wavefunctions $\left[\int_0^\infty \frac{P_{n\kappa}(r)Q_{n\kappa}(r)}{r^2}dr\right]$ is in units of a_0^{-2}, I is the nuclear spin and $\mathcal{I}_{lab}^M = \frac{K}{K+1}$ is the conversion factor from the intrinsic to spectroscopic magnetic moment as defined in Eq. (2.34).

Let us remark here that $M_z^{(1)}$ is the intrinsic total magnetic dipole moment, and the product $\mathcal{I}_{lab}^M M_z^{(1)} = M_z^{(1,\mathrm{spec})}$ is the spectroscopic total magnetic dipole moment. The total moment may be calculated from the integrals of the individual contributions as defined in Eqs. (2.30), (2.32) and (2.33), while the spectroscopic moment may be obtained from the experimentally determined nuclear gyromagnetic factor g for a nucleus with nuclear spin I by

$$M_z^{(1,\mathrm{spec})} = gI\mu_N\ , \tag{3.46}$$

where we recall that a summary of these comparative values is given in Table 2.4 (using the notation $\mu_{\text{spec}} = M_z^{(1,\text{spec})}$ from Chapter 2) for the simulated isotopes ^{159}Tb, ^{161}Dy, ^{163}Dy, and ^{165}Ho.

Finally, such a point-like dipole will induce modifications to the radial wavefunctions from a finite-size nucleus. The point-like components we denote by $P_{n\kappa}^{(0)}$ and $Q_{n\kappa}^{(0)}$, which result in the following dipole constant:

$$a_{point} = -\frac{e}{4\pi\varepsilon_0}\frac{1}{c}\frac{\mu_N}{a_0^2}\frac{\kappa}{j(j+1)}\frac{\mathcal{I}_{lab}^M M_z^{(1)}}{I}\int_0^\infty \frac{P_{n\kappa}^0(r)Q_{n\kappa}^0(r)}{r^2}dr\ . \tag{3.47}$$

3.2.2.2 Electric quadrupole hyperfine structure Constant

The second term in Eq. (3.41) arises from the matrix element

$$\langle n\kappa F M_F|\, H_{hf,quad}\, |n\kappa F M_F\rangle\ . \tag{3.48}$$

Similarly to that of the magnetic dipole hyperfine constant, it can be shown that the electric quadrupole hyperfine structure constant b takes the form [160]

$$b = 2\mathcal{I}_{lab}^E\frac{e}{4\pi\epsilon_0}\left(\frac{2j-1}{2j+2}\right)\int_0^\infty\left(\frac{1}{r^3}\int_{R=0}^{r}\rho(\vec{R})R^2C_0^{(2)}(\Theta,\Phi)d^3R\right. \tag{3.49}$$

$$\left. + r^2\int_{R=r}^{\infty}\frac{\rho(\vec{R})}{R^3}C_0^{(2)}(\Theta,\Phi)d^3R\right)\left(P_{n\kappa}^2(r)+Q_{n\kappa}^2(r)\right)dr\ , \tag{3.50}$$

where $\mathcal{I}_{lab}^E$ is the conversion factor from the intrinsic nuclear quadrupole moment to the laboratory-measured spectroscopic nuclear quadrupole moment (see Section 2.2.2).

In the case of a point electric quadrupole with no nuclear penetration, denoted by the subscript pq, this simplifies to

$$b_{pq} = 2\mathcal{I}_{lab}^E\frac{e}{4\pi\epsilon_0}\left(\frac{2j-1}{2j+2}\right)\int_{R=0}^{\infty}\rho(\vec{R})R^2C_0^{(2)}(\Theta,\Phi)d^3R\int_0^\infty\frac{\left(P_{n\kappa}^2(r)+Q_{n\kappa}^2(r)\right)}{r^3}dr \tag{3.51}$$

$$= \mathcal{I}_{lab}^E Q\left(\frac{2j-1}{2j+2}\right)\left[\int_0^\infty\frac{\left(P_{n\kappa}^2(r)+Q_{n\kappa}^2(r)\right)}{r^3}dr\right]\times 234.965\text{ MHz}\ , \tag{3.52}$$

where the quadrupole moment Q is defined as $Q \equiv 2\int_{R=0}^{\infty}\rho(\vec{R})R^2C_0^{(2)}(\Theta,\Phi)d^3R = 2Q_0^{(2)}$, expressed in units of $|e|\times$ barn, and the term $\left[\int_0^\infty\frac{\left(P_{n\kappa}^2(r)+Q_{n\kappa}^2(r)\right)}{r^3}dr\right]$ is in units of a_0^{-3}.

Let us make the following remarks: as we shall see later, this term vanishes for orbitals with $j=\frac{1}{2}$, such as $ns_{\frac{1}{2}}$ and $n'p_{\frac{1}{2}}$, for $n>0$ and $n'>1$, and comparing the constants to those for the dipole constant indicates that the quadrupole correction is significantly smaller than the dipole correction. Furthermore it also leads to an *uneven splitting of the energy levels of the hyperfine multiplet over the dipolar splitting*, which will be particularly relevant for quantum information processing applications where it becomes necessary to address and control the individual hyperfine levels. As discussed in Section 1.1.2, a large, uneven splitting of these levels is vital for quantum computing, since if this were not the case and all levels had very similar energies then it would not be possible to selectively excite each transition independently.

3.2.3 Isotope Shifts

Building on the hyperfine structure of hydrogen-like ions and our results for the models of point-like versus finite-size nuclei, let us consider the effect that the neutron number may have between two isotopes of the same element.

It is clear from our results for the ^{161}Dy and ^{163}Dy isotopes of dysprosium in Section 2.4 that varying the neutron number influences both the charge distribution and magnetisation within the nucleus. These variations are significant when considering a finite nuclear model, but are absent in a point-like model. This becomes particularly relevant when one considers that the $1s_{1/2}$ and $2p_{1/2}$ electronic states penetrate the nucleus with non-zero probability. The implication of this is that those wavefunctions are thereby able to probe the internal structure of the nucleus.

Consequently, two effects arise in a finite model, which can be represented as correction factors to the point-like model: (1) the Breit-Rosenthal (BR) effect [64], stemming from the extended distribution of the nuclear charge, and (2) the Bohr-Weisskopf (BW) effect [65], which is associated with the finite distribution of the nuclear magnetisation.

3.2.3.1 Breit-Rosenthal correction

The first study on the influence of the finite charge distribution within the nucleus on the electronic wavefunctions was conducted by Breit and Rosenthal [64]. It was found that this finite distribution of charge affects the wavefunctions, leading to a shift in the hyperfine interaction energy when compared with a point-charge model, referred to as the Breit-Rosenthal (BR) effect. The correction factor arising from the BR effect can be expressed analytically as

$$a_{pd} = a_{point}(1 + \varepsilon_{\mathrm{BR}}) \,, \tag{3.53}$$

where a_{pd} is the hyperfine constant for a nucleus with a finite charge distribution but point-like magnetisation, a_{point} is the hyperfine constant for a point-charge nucleus, and $\varepsilon_{\mathrm{BR}}$ represents the BR correction factor.

3.2.3.2 Bohr-Weisskopf correction

In an analogous manner to the BR effect, the finite distribution of nuclear magnetisation also affects the electronic wavefunctions. This shift of the magnetic dipole constant from a point-dipole model was investigated by Bohr and Weisskopf [65]. The correction factor is written as [161]

$$a = a_{pd}(1 + \varepsilon_{\mathrm{BW}}) \,, \tag{3.54}$$

where a is the hyperfine constant for a finite nucleus, a_{pd} is the hyperfine constant for a point-dipole nucleus, and $\varepsilon_{\mathrm{BW}}$ is the BW correction factor.

3.2.3.3 Web of hyperfine anomalies

Recall that the factors $\varepsilon_{\mathrm{BR}}$ and $\varepsilon_{\mathrm{BW}}$ represent the shifts in the hyperfine constant due to transitioning from a point-like to a non-point-like model of the nuclear charge and magnetisation distributions, respectively. By extension, we can consider the difference in these shifts between two isotopes, labeled as (1) and (2). These differences, known as isotope shifts, are denoted by:

$$^{1}\Delta^{2}_{\mathrm{BR}} = {}^{(1)}\varepsilon_{\mathrm{BR}} - {}^{(2)}\varepsilon_{\mathrm{BR}} \,, \tag{3.55}$$

$\vec{j}(\vec{R})$ \ $\rho(\vec{R})$	**Point charge**	**Charge distribution model**
Point dipole	1 →	$(1-\epsilon_{\mathrm{BR}}^{\mathrm{model}})$
Current distribution model	N/A	$(1-\epsilon_{\mathrm{BR}}^{\mathrm{model}})(1-\epsilon_{\mathrm{BW}})$ ↓

Table 3.1 – Summary of the corrections to the hyperfine constants. This table shows the corrections obtained by successively including the finite charge distribution of the nucleus and then the finite current distribution of the nucleus.

and

$$ {}^{1}\Delta^{2}_{\mathrm{BW}} = {}^{(1)}\varepsilon_{\mathrm{BW}} - {}^{(2)}\varepsilon_{\mathrm{BW}} \, . \tag{3.56} $$

Now, these generic shifts may be applied to any non-point-like model. The point-like model is uniquely defined with respect to the effect of the nucleus on the electronic $M_z^{(1)}$, $P^0_{n\kappa}(r)$, and $Q^0_{n\kappa}(r)$. However, non-point-like distributions are not unique. By utilising the general form of the electric current distribution given in Eq. (3.43), one can explore a variety of models, each associated with distinct correction factors and isotope shifts. Given the potentially infinite set of possible models, we consider grouping them into finite subsets for simplicity. Specifically, we analyse models where the terms in Eq. (3.43) are derived either from (*i*) analytical functions, or (*ii*) numerical (realistic) data. These considerations are summarised in Table 3.1.

3.2.3.4 Magnetic dipole hyperfine anomaly

Having defined the shifts in the magnetic hyperfine interaction energies due to various nuclear charge and magnetisation distribution models, we can combine these two effects by substituting Eq. (3.53) into Eq. (3.54), yielding

$$ a = a_{point}(1+\varepsilon_{\mathrm{BR}})(1+\varepsilon_{\mathrm{BW}}) \, . \tag{3.57} $$

Now, let us consider obtaining a from a realistic nuclear model, either through experimental measurement or numerical simulation. Generally, this is infeasible for complex atoms due to the difficulty in achieving sufficient accuracy in calculating the electronic radial wavefunctions [161]. In practice, one might determine a experimentally (or computationally), but the uncertainties in a_{point} are too large to reliably produce correction factors. Therefore, we consider the difference in these effects between two isotopes of the same atom, known as the hyperfine anomaly. This approach effectively cancels out the uncertainties associated with a_{point}. Specifically, we evaluate Eq. (3.57) for isotopes ${}^{(1)}a$ and ${}^{(2)}a$:

$$ {}^{(1)}a = {}^{(1)}a_{point}(1+{}^{(1)}\varepsilon_{\mathrm{BR}})(1+{}^{(1)}\varepsilon_{\mathrm{BW}}) \tag{3.58} $$

$$ {}^{(2)}a = {}^{(2)}a_{point}(1+{}^{(2)}\varepsilon_{\mathrm{BR}})(1+{}^{(2)}\varepsilon_{\mathrm{BW}}) \, . \tag{3.59} $$

By taking the ratio of these expressions, we obtain:

$$ \frac{{}^{(1)}a}{{}^{(2)}a} = \frac{{}^{(1)}a_{point}(1+{}^{(1)}\varepsilon_{\mathrm{BR}})(1+{}^{(1)}\varepsilon_{\mathrm{BW}})}{{}^{(2)}a_{point}(1+{}^{(2)}\varepsilon_{\mathrm{BR}})(1+{}^{(2)}\varepsilon_{\mathrm{BW}})} \, . \tag{3.60} $$

Now, recall that ${}^{(i)}a_{point}$ is calculated as follows:

$$
\begin{aligned}
{}^{(i)}a_{point} &= \frac{{}^{(i)}M_z^{(1)}}{{}^{(i)}I}\mathcal{T}(\kappa, j)\int_0^\infty \frac{P^0_{n\kappa}(r)Q^0_{n\kappa}(r)}{r^2}dr && (3.61)\\
&= {}^{(i)}g\mu_N\mathcal{T}(\kappa, j)\int_0^\infty \frac{P^0_{n\kappa}(r)Q^0_{n\kappa}(r)}{r^2}dr\ , && (3.62)
\end{aligned}
$$

where ${}^{(i)}M_z^{(1)} = {}^{(i)}g^{(i)}I\mu_N$, μ_N is the nuclear magneton, and ${}^{(i)}g$ is the gyromagnetic factor of the nucleus (i) with spin ${}^{(i)}I$. Since $P^0_{n\kappa}(r)$ and $Q^0_{n\kappa}(r)$ are wavefunctions computed using a point nucleus model, they are identical for both isotopes. Additionally, since $\mathcal{T}(\kappa, j)$ depends only on the electronic configuration, it is also the same for both isotopes. Substituting Eq. (3.62) into Eq. (3.60) gives:

$$
\frac{{}^{(1)}a}{{}^{(2)}a} = \frac{{}^{(1)}g(1+{}^{(1)}\varepsilon_{\mathrm{BR}})(1+{}^{(1)}\varepsilon_{\mathrm{BW}})}{{}^{(2)}g(1+{}^{(2)}\varepsilon_{\mathrm{BR}})(1+{}^{(2)}\varepsilon_{\mathrm{BW}})}\ . \tag{3.63}
$$

We define the hyperfine splitting of the state with maximal projection as (see Eq. (3.41))

$$
\begin{aligned}
W_F^{(i)} &\equiv \left\langle {}^{(i)}I^{(i)}IJJ\right| H_{hf,dip} \left|{}^{(i)}I^{(i)}IJJ\right\rangle && (3.64)\\
&= W_{F={}^{(i)}I+J} && (3.65)\\
&= {}^{(i)}\ a_{point}{}^{(i)}IJ\ , && (3.66)
\end{aligned}
$$

and thus, under the point nucleus approximation, the difference in hyperfine splitting $W_F^{(i)}$ between two isotopes is given by

$$
\begin{aligned}
\frac{{}^{(1)}W_F}{{}^{(2)}W_F} &= \frac{{}^{(1)}a_{point}{}^{(1)}IJ}{{}^{(2)}a_{point}{}^{(2)}IJ} && (3.67)\\
&= \frac{{}^{(1)}g^{(1)}I}{{}^{(2)}g^{(2)}I} && (3.68)\\
&= \frac{{}^{(1)}M_z^{(1)}}{{}^{(2)}M_z^{(1)}}\ . && (3.69)
\end{aligned}
$$

From here, we define the hyperfine anomaly as:

$$
{}^1\Delta^2 = \frac{{}^{(1)}W_F}{{}^{(2)}W_F}\frac{{}^{(2)}M_z^{(1)}}{{}^{(1)}M_z^{(1)}} - 1 = 0\ , \tag{3.70}
$$

which is identically zero in the point nucleus model. However, for a non-point nucleus model, we have:

$$
\begin{aligned}
\frac{{}^{(1)}W_F}{{}^{(2)}W_F} &= \frac{{}^{(1)}a^{(1)}IJ}{{}^{(2)}a^{(2)}IJ} && (3.71)\\
&= \frac{a^{(1)}_{point}{}^{(1)}IJ}{a^{(2)}_{point}{}^{(2)}IJ} \times \frac{(1+{}^{(1)}\varepsilon_{\mathrm{BR}})(1+{}^{(1)}\varepsilon_{\mathrm{BW}})}{(1+{}^{(2)}\varepsilon_{\mathrm{BR}})(1+{}^{(2)}\varepsilon_{\mathrm{BW}})} && (3.72)\\
&= \frac{{}^{(1)}M_z^{(1)}}{{}^{(2)}M_z^{(1)}} \times \frac{(1+{}^{(1)}\varepsilon_{\mathrm{BR}})(1+{}^{(1)}\varepsilon_{\mathrm{BW}})}{(1+{}^{(2)}\varepsilon_{\mathrm{BR}})(1+{}^{(2)}\varepsilon_{\mathrm{BW}})}\ . && (3.73)
\end{aligned}
$$

Therefore, the full hyperfine anomaly can be expressed as:

$$ {}^1\Delta^2 = \frac{{}^{(1)}W_F}{{}^{(2)}W_F}\frac{{}^{(2)}M_z^{(1)}}{{}^{(1)}M_z^{(1)}} - 1 \tag{3.74} $$

$$ = \frac{(1+{}^{(1)}\varepsilon_{\mathrm{BR}})(1+{}^{(1)}\varepsilon_{\mathrm{BW}})}{(1+{}^{(2)}\varepsilon_{\mathrm{BR}})(1+{}^{(2)}\varepsilon_{\mathrm{BW}})} - 1\,, \tag{3.75} $$

and, to a first-order approximation, this reduces to

$$ {}^1\Delta^2 = (1+{}^{(1)}\varepsilon_{\mathrm{BR}} - {}^{(2)}\varepsilon_{\mathrm{BR}})(1+{}^{(1)}\varepsilon_{\mathrm{BW}} - {}^{(2)}\varepsilon_{\mathrm{BW}}) - 1 \tag{3.76} $$

$$ = (1+{}^1\Delta^2{}_{\mathrm{BR}})(1+{}^1\Delta^2{}_{\mathrm{BW}}) - 1 \tag{3.77} $$

where we recall that ${}^1\Delta^2_E = {}^{(1)}\varepsilon_E - {}^{(2)}\varepsilon_E$ for $E \in \{\mathrm{BR}, \mathrm{BW}\}$.

3.2.3.5 Electric quadrupole hyperfine anomaly

Analogously to the magnetic case, we can analyse the influence of the finite nuclear structure on the quadrupole correction of the hyperfine interaction. For this purpose, we introduce the quantity

$$ \Delta B^{\mathrm{m}} \equiv \frac{b^{\mathrm{pt}}_{\mathrm{np}} - b^{\mathrm{m}}_{\mathrm{wp}}}{b^{\mathrm{pt}}_{\mathrm{np}}}\,, \tag{3.78} $$

where $\mathrm{m} \in \{\mathrm{pt}, \mathrm{sp}, \mathrm{fm}, \mathrm{hf}\}$. This expression provides insight into the corrections arising from the nuclear penetration across different structural models, from the simplest (point model, pt) to the most advanced (HFBCS, hf). The term $b^{\mathrm{m}}_{\mathrm{n}}$ in this expression indicates that the quadrupole constant is derived from the radial wavefunctions $P_{n\kappa}, Q_{n\kappa}$, which are calculated based on the spherically symmetric monopole potential Eq. (3.21) produced by the nuclear charge distribution corresponding to one of the following models: point charge Eq. (3.22) ($\mathrm{m} = \mathrm{pt}$), spherical distribution ($\mathrm{m} = \mathrm{sp}$), Fermi distribution ($\mathrm{m} = \mathrm{fm}$), and HFBCS ($\mathrm{m} = \mathrm{hf}$). Additionally, the label n specifies whether nuclear penetration is considered: $\mathrm{n} = \mathrm{wp}$ if penetration is allowed (using the formula Eq. (3.50) to calculate b), or $\mathrm{n} = \mathrm{np}$ if penetration is not considered (where $b = b_{pq}$ is calculated using the form in Eq. (3.51)).

To quantify the effect of the finite size of the nucleus on the quadrupole hyperfine correction, we also define:

$$ \Delta B^{\mathrm{wp,m}}_{\mathrm{np}} \equiv \frac{b^{\mathrm{m}}_{\mathrm{np}} - b^{\mathrm{m}}_{\mathrm{wp}}}{b^{\mathrm{m}}_{\mathrm{np}}}\,. \tag{3.79} $$

This parameter measures the influence of the nuclear charge distribution model (through the radial wavefunctions) on the quadrupole moment correction due to nuclear penetration. Note that $\Delta B^{\mathrm{pt}} = \Delta B^{\mathrm{wp,pt}}_{\mathrm{np}}$.

To assess the impact of a fully microscopic nuclear description (HFBCS) compared to the Fermi model, the most accurate of the non-microscopic models, we define:

$$ \Delta B \equiv \frac{b^{\mathrm{fm}}_{\mathrm{wp}} - b^{\mathrm{hf}}_{\mathrm{wp}}}{b^{\mathrm{fm}}_{\mathrm{wp}}}\,. \tag{3.80} $$

Lastly, the isotopic variation in b is characterised by evaluating:

$$ \Delta B^{163}_{161} \equiv \frac{b^{\mathrm{hf}}_{\mathrm{wp}}(163) - b^{\mathrm{hf}}_{\mathrm{wp}}(161)}{b^{\mathrm{hf}}_{\mathrm{wp}}(161)}\,. \tag{3.81} $$

3.2.3.6 Additional contributions

Referring specifically to the work of Büttgenbach [161], let us consider the hyperfine anomaly from an experimental standpoint. Up to this point, we have adopted a theoretical approach: deriving ${}^1\Delta^2$ based on the electronic wavefunctions $P_{n\kappa}(r)$ and $Q_{n\kappa}(r)$, as well as the nuclear charge and current distributions, $\vec{j}(\vec{R})$. However, these quantities are not directly measurable in experiments. In practice, the objective is to probe the nuclear current distributions via (spectroscopic) measurements of the hyperfine constant. The results can then be compared against existing models to infer details about the nuclear structure. Consequently, the hyperfine anomaly provides a means to investigate isotopic effects on nuclear structure, allowing for the testing and validation of theoretical models of nuclear structure. Additionally, recall that only electrons in s and $p_{1/2}$ orbitals have wavefunctions with a non-zero probability amplitude within the nucleus. These are the sole contact terms contributing to the BW Effect, and hence, the hyperfine anomaly can be employed to distinguish between contact and non-contact contributions to the hyperfine interaction.

In practice, however, the experimentally observed hyperfine anomaly, ${}^1\Delta^2_{exp}$, encompasses more than just the BR and BW Effects.

Other isotopic variations predominantly arise from mass corrections, related to the finite mass of the nucleus. (Note that relativistic corrections are already included within the relativistic electronic wavefunctions, $P_{n\kappa}(r)$ and $Q_{n\kappa}(r)$.) Considering the motion of the electron-nucleus system about their shared center of mass introduces reduced mass corrections to: (i) the electronic wavefunctions, scaled by $(1 + m_e/m_N)^{-3}$, and (ii) the electronic orbital g-factor. It is important to recognise that the magnitude of these mass-related effects decreases with increasing nuclear mass. As a result, these effects can often be neglected for heavy elements, such as the Lanthanides. On the other hand, for such highly-charged hydrogen-like ions with large highly-charged nuclei, incorporating quantum electrodynamics (QED) corrections becomes important, and even more so when we begin to consider multi-electronic states due to the interactions between electrons [162].

Lastly, additional contributions stem from higher-order corrections to the magnetic hyperfine interaction energy. The energy correction presented in (3.41) is only a first-order approximation (assuming that J is a good quantum number). In reality, higher-order terms exist due to off-diagonal elements in the hyperfine interaction Hamiltonian, which correspond to effective hyperfine interactions between different fine structure levels through the nucleus. These interactions imply that J is not strictly a good quantum number, necessitating the use of second-order perturbation theory to accurately account for this effect.

3.3 Methods

The calculation of the Breit-Rosenthal (BR) and Bohr-Weisskopf (BW) effects begins with solving the radial Dirac equations for hydrogen-like ions, which allows for the determination of eigenvalues (energy levels) and eigenfunctions (radial wavefunctions) of the bound electron or muon. We implemented a set of Fortran modules and routines that extend the nuclear moments calculations detailed in Section 2.3 to compute these effects by defining different nuclear potential models that describe the distribution of charge and magnetisation within the nucleus. These potential models: point-like, spherical,

Fermi-distributed, and Hartree-Fock-BCS are used as inputs to solve the radial eigenvalue problem of the Dirac equation under relativistic conditions. The module `reigen` contains the core numerical subroutine, `solve_radial_eigenproblem`, which uses a combination of outward and inward integration of the differential equations. Bisection and perturbation methods are employed to ensure that the energy eigenvalues converge within a specified tolerance. The subroutine iterates over the principal quantum number (`n`), the orbital quantum number (`l`), and the relativistic parameter (`relat`) to compute the radial solutions for each potential model and determine the appropriate wavefunctions.

Once the radial wavefunctions are obtained for the various potential models, they are used to evaluate the effects of the finite size and structure of the nucleus on the hyperfine splitting (HFS) of the energy levels. To quantify these effects, the wavefunctions are used to calculate the magnetic dipole constants (`a_wp` and `a_np`) over the radial grid. The discrepancies in energy between different potential models reflect the corrections due to the finite charge and magnetic structure of the nucleus, thereby providing a measure of the BR and BW effects.

The final step in the numerical procedure is to compare the calculated energies and wavefunctions for the different nuclear models to extract the relative differences associated with the BR and BW corrections. Specifically, the energies obtained from solving the radial eigenproblem are used to compute the relative discrepancies (`e_BR` and `e_BW`) for each model. These discrepancies indicate the influence of the finite nuclear charge distribution (BR effect) and the magnetic dipole distribution (BW effect) on the hyperfine splitting. The results are then output for each quantum state (`n`, `l`), and these calculations are repeated for different hydrogen-like ions, including both electronic and muonic systems. By comparing the hyperfine structure splitting across different potential models and relativistic conditions, the scripts provide a comprehensive analysis of how nuclear structure affects the hyperfine interactions in these ions. This approach allows for an accurate estimation of the BR and BW effects, which are crucial for matching theoretical predictions with experimental spectral data.

3.4 Results

Let us now present the results of our calculations for the hyperfine structure of hydrogen-like ions, focusing on the Breit-Rosenthal (BR) and Bohr-Weisskopf (BW) effects. The results are presented in atomic units $m_e = e = 4\pi\epsilon_0 = \hbar = 1$.

3.4.1 Hydrogen-like Wavefunctions

By numerically solving the radial Dirac equation in Eqs. (3.6) and (3.7) with the potential $V = -e\phi_0$ and the spherically symmetric electric monopole potential in Eq. (3.21) for an electron or muon bound to a nucleus, we can obtain the large and small components of the radial wavefunctions, $P_{n\kappa}(r)$ and $Q_{n\kappa}(r)$, respectively. This can be done for a variety of different nuclear models, as we have already discussed, including point-like, spherical, Fermi-distributed, and the HFBCS models.

The radial components of the relativistic Dirac wavefunctions for the $1s_{1/2}$ and $2p_{1/2}$ orbitals of hydrogen-like electronic and muonic $^{163}Dy^{65+}$ are shown in Figs. 3.1 and 3.2 respectively, which highlight the behaviour of both large $P_{n\kappa}$ and small $Q_{n\kappa}$ components. These wavefunctions have been computed using different nuclear monopole potential

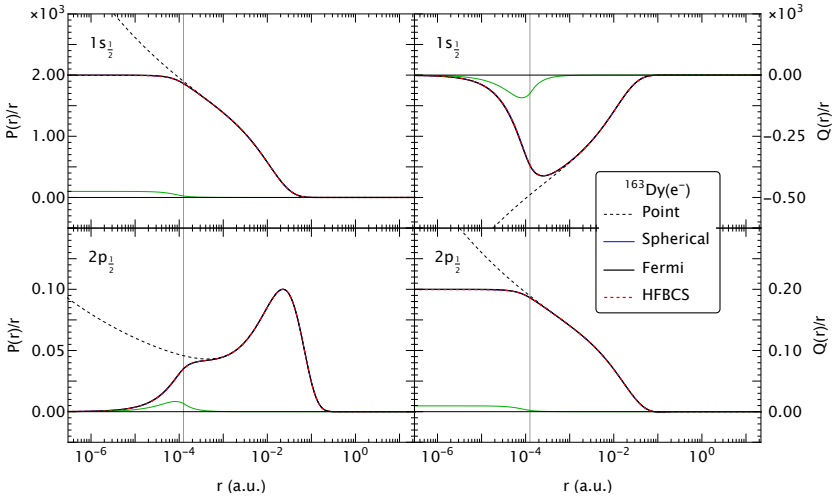


Figure 3.1 – Electronic wavefunctions of hydrogen-like ^{163}Dy. The large ($P_{n\kappa}$, left panels) and small components ($Q_{n\kappa}$, right panels) of the radial wave functions for the $1s_{1/2}$ (upper panels) and $2p_{1/2}$ (lower panels) orbitals of $^{163}Dy^{65+}$ are shown in atomic units. The dashed black and red curves represent the point and HFBCS models respectively, while the solid black and blue curves represent the Fermi and spherical models respectively. The solid green line represents the difference between the Fermi and HFBCS models multiplied by 20. Vertical lines indicate the position of the nuclear radius R_N. Since the differences are insignificant, the results for $^{161}Dy^{65+}$ are shown in Fig. B.1 in Appendix B.1.

models: the point charge, a spherical distribution, a Fermi distribution, and a microscopic model based on the HFBCS method.

For both figures, the comparison between the point charge model and the finite size distributions (Spherical, Fermi, and HFBCS) reveals significant deviations within the nucleus, marked by a vertical line at the nuclear radius R_N. Outside this radius, the wavefunctions from the three finite-size models are very similar, and the influence of nuclear structure is negligible. This behaviour is well-described by the electrostatic shielding effect of Gauss's theorem. Within the nucleus, however, the point charge model significantly overestimates the amplitude of the wavefunctions due to the neglect of nuclear finite size effects. Differences between the microscopic HFBCS model and the commonly used Fermi distribution are very small and are primarily confined to the nuclear interior, as demonstrated by the green curves where the difference is amplified by a factor of 20.

A distinct perspective arises when considering the muon as the orbiting particle instead of the electron, as shown in Fig. 3.2. Due to the increased mass of the muon ($m_\mu \approx 207 m_e$), the corresponding wavefunctions are significantly rescaled and exhibit greater penetration into the nucleus. This increased presence within the nuclear radius amplifies the differences between the Fermi and HFBCS models, which are more pronounced for the muon than for the electron. As a result, muonic atoms provide a sensitive probe for the microscopic properties and structure of the nucleus, potentially allowing the investigation of both charge distribution and internal magnetic fields.

The scaling behaviour of the wavefunctions in the point charge model can be described by the Dirac equation's scaling law, where $P_{n\kappa}(r) = a_0^{-3/2} P_{n\kappa}(a_0^{-1} r)$ and $Q_{n\kappa}(r) = a_0^{-3/2} Q_{n\kappa}(a_0^{-1} r)$, with the Bohr radius a_0 given by $a_0 = \frac{4\pi\varepsilon_0\hbar^2}{me^2}$. For a muon, this reduces to $a_0 \approx 1/207$ in atomic units, indicating a contraction of the wavefunctions. Figure 3.3

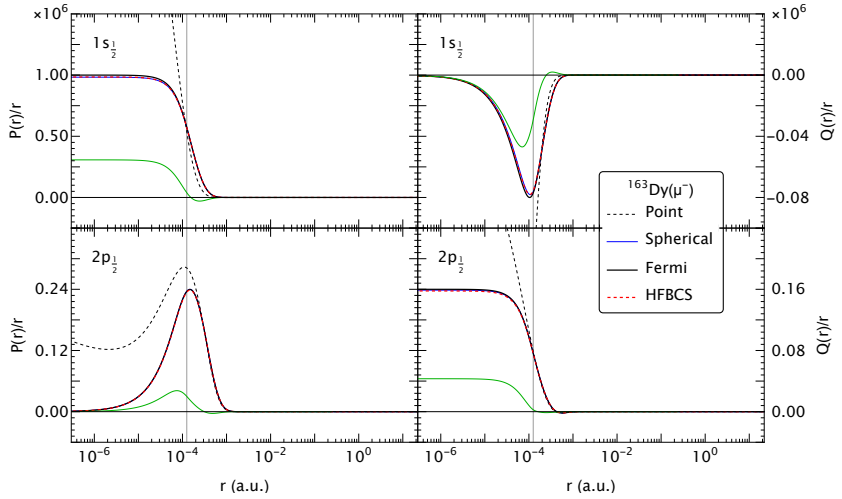


Figure 3.2 – Muonic wavefunctions of hydrogen-like ^{163}Dy. Same as Fig. 3.1 but for a muonic hydrogen-like atom presented in atomic units. Since the differences are insignificant, the results for $^{161}Dy^{65+}$ are given in Fig. B.2 in Appendix B.1.

verifies that this scaling law is accurately fulfilled for both electron and muon wavefunctions under the point charge model but is no longer valid when considering finite-size nuclear models.

Overall, the comparison between electronic and muonic wavefunctions underscores the importance of nuclear structure in heavy ion systems, particularly in muonic atoms where the stronger penetration into the nucleus enhances sensitivity to the choice of nuclear model. The finite size of the nucleus generally leads to a reduction in wavefunction amplitude at the nuclear center, which is more pronounced for muons, and the differences between the Fermi and HFBCS models are accentuated within the nuclear region. Thus, muonic ions serve as a valuable tool for probing nuclear charge distributions and understanding the interplay between atomic and nuclear physics.

3.4.2 Charge Corrections

Given the resulting wavefunctions in Section 3.4.1, they can be used to obtain numerous observables, which can be compared across the selected models (pt=point-like, sp=spherical, fm=Fermi, hf=HFBCS) and also to experimental data. As a first step, let us consider the shifts in the energy levels of the electronic and muonic states due to the finite size of the nucleus.

As an example, Tables 3.2a and 3.2b show the electronic and muonic binding energies, respectively, of $^{163}Dy^{65+}$ in the different excited states from $1s_{1/2}$ to $4f_{7/2}$ in atomic units. Note the rescaling in the muonic binding energies due to the increased mass.

The relative shifts are then quantified by the monopolar corrections, which are defined as the relative differences in energy levels between the point charge model and the finite-size models, or more generally models m_1 and m_2:

$$\Delta E^{\mathrm{m_2}}_{\mathrm{m_1}}(n\ell j) = \frac{(E^{\mathrm{m_2}}(n\ell j) - E^{\mathrm{m_1}}(n\ell j))}{E^{\mathrm{m_1}}(n\ell j)} \,, \tag{3.82}$$

where $E^{\mathrm{model}}(n\ell j)$ is the energy of the $n\ell j$ state with a chosen monopole charge distri-

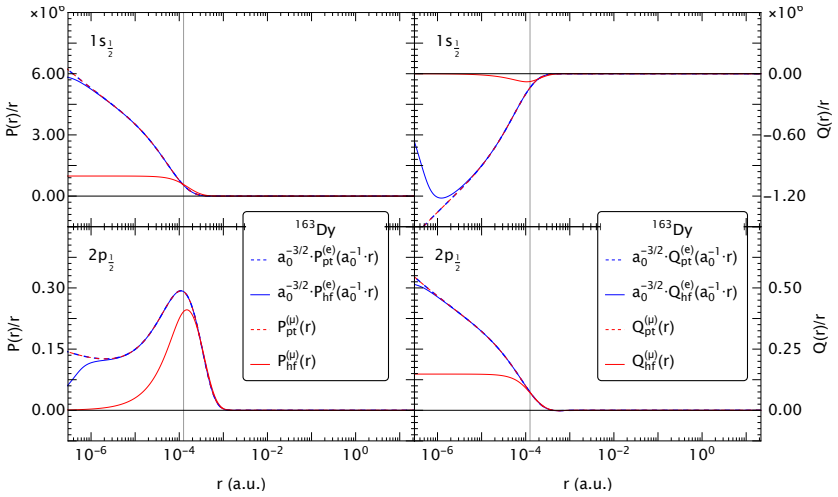


Figure 3.3 – Rescaled wavefunctions of the electronic and muonic hydrogen-like ^{163}Dy. The rescaled large ($P_{n\kappa}$, left panels) and small components ($Q_{n\kappa}$, right panels) of the radial wave functions for the $1s_{1/2}$ (upper panels) and $2p_{1/2}$ (lower panels) orbitals of $^{163}Dy^{65+}$ are shown in atomic units. The figures show the comparison between the electronic (blue) and muonic (red) states for point (dashed lines) and HFBCS (solid lines) models. The results for the electron are rescaled using the Bohr radius for the muon ($a_0 = 1/207$ a.u). The vertical lines indicate the position of the nuclear radius R_N. For the point model, we note that $a_0^{-3/2} P_{\mathrm{pt}}^{(e)}(a_0^{-1}r)$ and $P_{\mathrm{pt}}^{(\mu)}(r)$ are identical. The same is true for $a_0^{-3/2} Q_{\mathrm{pt}}^{(e)}(a_0^{-1}r)$ and $Q_{\mathrm{pt}}^{(\mu)}(r)$. Since the differences are insignificant, the results for $^{161}Dy^{65+}$ are shown in Fig. B.3 in Appendix B.1.

bution model.

The effect of different nuclear models on the orbital energies of $^{163}Dy^{65+}$ is illustrated in Fig. 3.4, where the monopolar shifts for electronic states from $1s_{1/2}$ to $4f_{7/2}$ are shown in (a) (Fig. 3.4a). For each charge distribution considered, the relative energy shift between these models is given by Eq. (3.82), where $n\ell j$ indexes the orbitals, and m_1, m_2 denote different models. The top panel of the figure shows that the relative energy differences compared to the point-charge model are very small (on the order of 0.01%), predominantly affecting the s states, with the effect decreasing for larger principal quantum number n. This is due to the greater penetration of the s orbitals within the nucleus, where deviations from the point-charge model are more pronounced. The p orbitals exhibit negligible shifts, consistent with their reduced overlap with the nucleus.

The lower panel of Fig. 3.4a highlights the impact of the microscopic HFBCS model relative to the Fermi model. Here, $\Delta E_{\mathrm{fm},i}^{\mathrm{hf}} = \frac{E_i^{\mathrm{hf}} - E_i^{\mathrm{fm}}}{E_i^{\mathrm{fm}}}$ is presented, showing that the relative differences are minimal (less than 0.001%). This reinforces the observation that a detailed microscopic nuclear description has only a minor effect on orbital energies. Additionally, the isotopic energy shifts, quantified by $\Delta E_{161,i}^{163}$, are extremely small ($< 0.0001\%$), further supporting the minimal influence of nuclear model variations on electronic orbital energies.

The situation changes significantly in the case of a muonic ion, as shown in Fig. 3.4b. Due to the muon's greater mass, the penetration into the nucleus is deeper, leading to larger monopolar energy shifts. The relative differences $\Delta E_{\mathrm{pt},i}^{\mathrm{m}_2}$ for $\mathrm{m}_2 = \mathrm{sp}, \mathrm{fm}, \mathrm{hf}$ reach up to 40% for the $1s_{1/2}$ orbital and are around 10% for other orbitals. Additionally, the differences between the HFBCS and Fermi models ($\Delta E_{\mathrm{fm},i}^{\mathrm{hf}}$) are now non-negligible, up to

nl_j	E^{sp}	E^{fm}	E^{hf}
$1s_{1/2}$	-2321.038	-2321.039	-2321.024
$2s_{1/2}$	-589.5601	-589.5603	-589.5580
$2p_{1/2}$	-589.6269	-589.6269	-589.6268
$2p_{3/2}$	-552.6315	-552.6315	-552.6315
$3s_{1/2}$	-257.8184	-257.8184	-257.8177
$3p_{1/2}$	-257.8382	-257.8382	-257.8381
$3p_{3/2}$	-246.8293	-246.8293	-246.8293
$3d_{3/2}$	-246.8293	-246.8293	-246.8293
$3d_{5/2}$	-243.5797	-243.5797	-243.5797
$4s_{1/2}$	-143.2802	-143.2802	-143.2799
$4p_{1/2}$	-143.2884	-143.2884	-143.2884
$4p_{3/2}$	-138.6699	-138.6699	-138.6699
$4d_{3/2}$	-138.6699	-138.6699	-138.6699
$4d_{5/2}$	-137.2922	-137.2922	-137.2922
$4f_{5/2}$	-137.2922	-137.2922	-137.2922
$4f_{7/2}$	-136.6220	-136.6220	-136.6220

(a) Electronic

nl_j	E^{sp}	E^{fm}	E^{hf}
$1s_{1/2}$	-285823	-286916	-284560
$2s_{1/2}$	-90810.8	-91087.4	-90671.6
$2p_{1/2}$	-115503	-115443	-115250
$2p_{3/2}$	-111674	-111596	-111468
$3s_{1/2}$	-43553.2	-43650.9	-43513.4
$3p_{1/2}$	-51122.5	-51106.6	-51042.3
$3p_{3/2}$	-50101.0	-50076.4	-50032.1
$3d_{3/2}$	-50980.2	-50978.1	-50976.4
$3d_{5/2}$	-50322.2	-50320.8	-50319.9
$4s_{1/2}$	-25412.2	-25456.7	-25395.6
$4p_{1/2}$	-28664.8	-28658.5	-28630.5
$4p_{3/2}$	-28250.6	-28240.1	-28220.4
$4d_{3/2}$	-28640.1	-28638.8	-28637.8
$4d_{5/2}$	-28363.4	-28362.6	-28362.1
$4f_{5/2}$	-28368.1	-28368.1	-28368.1
$4f_{7/2}$	-28229.6	-28229.6	-28229.6

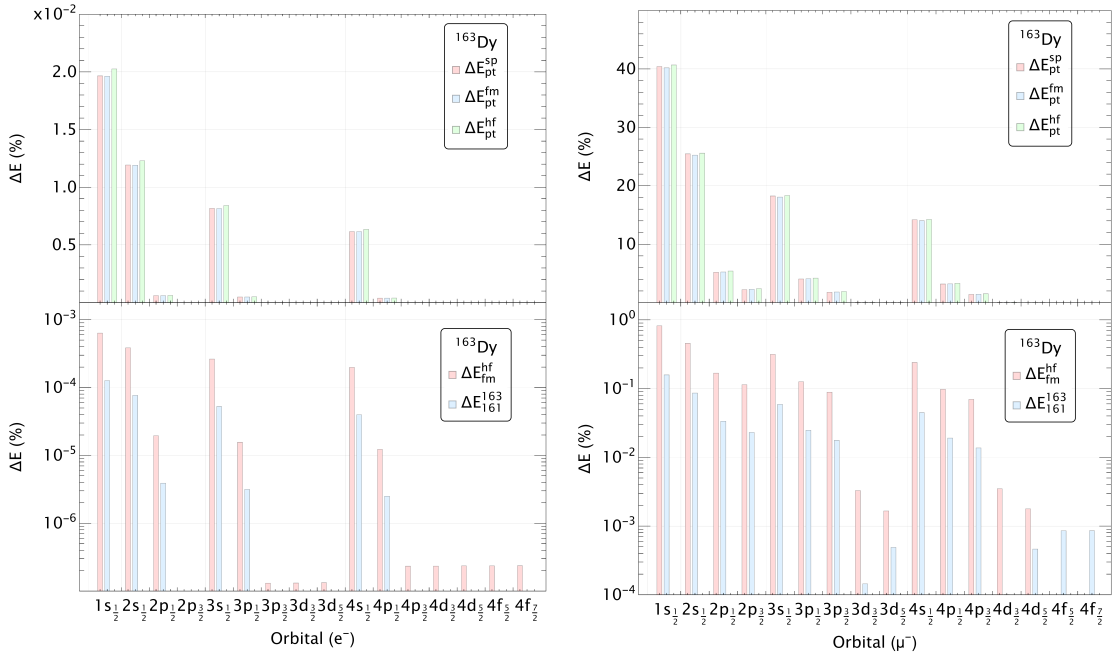
(b) Muonic

Table 3.2 – Binding energies of hydrogen-like ^{163}Dy. This table presents the binding energies in Hartrees for the $n\ell_j$ states of the (a) electronic, and (b) muonic, $^{163}\text{Dy}^{65+}$ ion. The relativistic energy values E^{m} (excluding the rest mass) are obtained by solving the Dirac equation for three nuclear models: the spherical distribution (m=sp), the Fermi distribution (m=fm), and the spherically averaged HFBCS realistic model (m=hf).

1%, suggesting that muonic systems can more effectively discriminate between nuclear charge distributions. The isotopic shift $\Delta E^{163}_{161,i}$ also increases to approximately 0.1%, indicating an observable sensitivity to the nuclear composition.

The Breit-Rosenthal correction, defined by ε_{BR} in Eq. (3.53), is explored in Fig. 3.5 for the nuclear models. For the electronic ions in Fig. 3.5a, this correction is most significant for $ns_{1/2}$ orbitals (approximately 5%) and diminishes for $np_{1/2}$ and higher orbitals, becoming negligible for $np_{3/2}$ and others. The correction remains almost constant as a function of n. The lower panels of the figures show $\Delta\varepsilon^{\text{hf}}_{\text{fm}}$, which quantifies the difference in the BR correction between the HFBCS and Fermi models. The magnitude of this correction is around 1% for most orbitals, with a notable exception for $np_{3/2}$ orbitals, where it exceeds 5%. The isotopic influence on the BR correction is given by $\Delta\varepsilon^{163}_{161}$, revealing that only a microscopic nuclear model can capture the small but non-zero isotopic effects ($\approx 0.2\%$ for most orbitals and up to 1% for $np_{3/2}$). This provides further evidence for muonic ions being more sensitive to nuclear structure effects than electronic ions.

Now, as discussed in Section 2.4.2.1, it is important to remark that both the spherical and Fermi charge distributions can be rescaled to match the root-mean-square radius ($R_{\text{rms}} = \sqrt{\langle R^2\rangle}$) of the HFBCS model with the nuclear radius $R_N = \sqrt{\frac{5}{3}R^2_{\text{rms}}}$ being modified to align with the new R_{rms}. The thusly recalculated binding energies for both the electronic and muonic ions are provided in Table 3.3, allowing for comparison with the original results in Table 3.2.



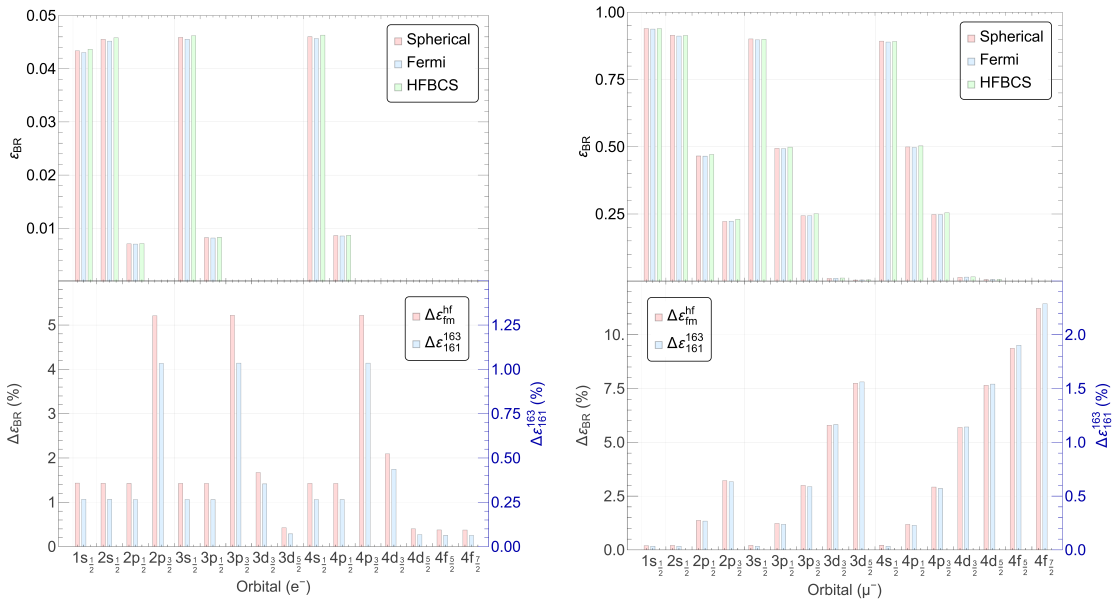
(a) Electronic **(b)** Muonic

Figure 3.4 – Monopolar shifts in the energy levels of orbitals of $^{163}Dy^{65+}$. Shown are the relative shifts in energy of the (a) electronic and (b) muonic states from $1s_{1/2}$ to $4f_{7/2}$ for different nuclear models: point (pt), spherical (sp), Fermi (fm) and HFBCS (hf). We have defined, $\Delta E^{\mathrm{m}_2}_{\mathrm{m}_1,i} \equiv \frac{E^{\mathrm{m}_2}_i - E^{\mathrm{m}_1}_i}{E^{\mathrm{m}_1}_i}$ with $\mathrm{m}_2 = \mathrm{sp}, \mathrm{fm}, \mathrm{hf}$ and $\mathrm{m}_1 = \mathrm{pt}, \mathrm{fm}$ and $\Delta E^{163}_{161,i} \equiv \frac{E^{163}_i - E^{161}_i}{E^{161}_i}$ with i running from $1s_{1/2}$ to $4f_{7/2}$. Since the differences are insignificant, the results for $^{161}Dy^{65+}$ are given in Fig. B.4 in Appendix B.1.

After performing this normalisation, it becomes evident that the energy shifts between the Fermi distribution and the HFBCS model for the electronic ion are on the order of 10^{-6}%, which corresponds to energy differences of a few hundred μeV. This indicates that the primary factor influencing the energy levels of electronic ions is R_{rms}, as discussed in [155]. *As a result, a computationally efficient approach may be to use the HFBCS model to determine the nuclear R_{rms} and then employ a Fermi distribution adjusted to this same R_{rms} to compute the energy levels accurately and with reduced computational demands.*

For the muonic ion, however, the energy shifts between the Fermi and HFBCS models are more substantial, around 10^{-3}%, equating to differences in the range of hundreds of eV. *This signifies that for muonic ions, the R_{rms} alone is insufficient to fully characterise the energy levels, and the binding energies retain a critical role in differentiating between various nuclear models.*

Additionally, when comparing isotopic energy shifts between ^{161}Dy and ^{163}Dy, the shifts for the electronic ion are on the order of 10^{-5} to 10^{-4}% for $s_{1/2}$ states and approximately 10^{-6}% for $p_{1/2}$ states, leading to changes in the range of meV. In contrast, for the muonic ion, these shifts are much larger, ranging from 10^{-2} to 10^{-1}%, with corresponding energy differences of several hundred eV. This highlights that isotopic shifts in muonic atoms can be an effective tool for distinguishing between isotopes of the same element.



(a) Electronic **(b)** Muonic

Figure 3.5 – Breit-Rosenthal correction ε_{BR} for $^{163}Dy^{65+}$. Shown are the BR effects for the (a) electronic and (b) muonic states for the different nuclear models: spherical, Fermi and HFBCS. We have defined $\Delta\varepsilon_{fm}^{hf} \equiv \frac{\varepsilon_{BR}^{hf}-\varepsilon_{BR}^{fm}}{\varepsilon_{BR}^{fm}}$ (left axis) and $\Delta\varepsilon_{161}^{163} \equiv \frac{\varepsilon_{BR}^{hf}(163)-\varepsilon_{BR}^{hf}(161)}{\varepsilon_{BR}^{hf}(161)}$ (right axis). The results for $^{161}Dy^{65+}$ are given in Fig. B.5 in Appendix B.1.

nl_j	E^{sp}	E^{fm}	E^{hf}
$1s_{1/2}$	-2321.024	-2321.024	-2321.024
$2s_{1/2}$	-589.5579	-589.5581	-589.5580
$2p_{1/2}$	-589.6268	-589.6268	-589.6268
$2p_{3/2}$	-552.6315	-552.6315	-552.6315
$3s_{1/2}$	-257.8177	-257.8178	-257.8177
$3p_{1/2}$	-257.8381	-257.8381	-257.8381
$3p_{3/2}$	-246.8293	-246.8293	-246.8293
$3d_{3/2}$	-246.8293	-246.8293	-246.8293
$3d_{5/2}$	-243.5797	-243.5797	-243.5797
$4s_{1/2}$	-143.2799	-143.2799	-143.2799
$4p_{1/2}$	-143.2884	-143.2884	-143.2884
$4p_{3/2}$	-138.6699	-138.6699	-138.6699
$4d_{3/2}$	-138.6699	-138.6699	-138.6699
$4d_{5/2}$	-137.2922	-137.2922	-137.2922
$4f_{5/2}$	-137.2922	-137.2922	-137.2922
$4f_{7/2}$	-136.6220	-136.6220	-136.6220

(a) Electronic

nl_j	E^{sp}	E^{fm}	E^{hf}
$1s_{1/2}$	-283536	-284602	-284560
$2s_{1/2}$	-90405.7	-90677.2	-90671.6
$2p_{1/2}$	-115315	-115256	-115250
$2p_{3/2}$	-111551	-111473	-111468
$3s_{1/2}$	-43419.0	-43515.2	-43513.4
$3p_{1/2}$	-51060.0	-51044.4	-51042.3
$3p_{3/2}$	-50058.0	-50033.7	-50032.1
$3d_{3/2}$	-50978.7	-50976.5	-50976.4
$3d_{5/2}$	-50321.5	-50320.0	-50319.9
$4s_{1/2}$	-25352.5	-25396.3	-25395.6
$4p_{1/2}$	-28637.6	-28631.4	-28630.5
$4p_{3/2}$	-28231.5	-28221.1	-28220.4
$4d_{3/2}$	-28639.2	-28637.9	-28637.8
$4d_{5/2}$	-28363.0	-28362.1	-28362.1
$4f_{5/2}$	-28368.1	-28368.1	-28368.1
$4f_{7/2}$	-28229.6	-28229.6	-28229.6

(b) Muonic

Table 3.3 – Binding energies of hydrogen-like ^{163}Dy with R_{rms} normalisation. This table shows the binding energies in Hartrees for various $n\ell_j$ states of the (a) electronic, and (b) muonic, $^{163}Dy^{65+}$ ion. The energies are calculated using both spherical and Fermi charge distributions, normalised to have the same root-mean-square (RMS) radius, R_{rms}, as the HF model, ensuring a consistent comparison across all models.

3.4.3 Magnetic Corrections

Following the charge corrections, we now turn our attention to the magnetic corrections, which is described by the Bohr-Weisskopf (BW) effect.

The Bohr-Weisskopf (BW) corrections, as defined in Eq. (3.54), are evaluated for the hyperfine structure of the electronic orbitals in $^{161}Dy^{65+}$ and $^{163}Dy^{65+}$, ranging from $1s_{\frac{1}{2}}$ to $4f_{\frac{7}{2}}$. In Figure 3.6, the individual contributions of the orbital and spin currents for protons and neutrons ($j_l^{(p)}$, $j_l^{(n)}$, $j_s^{(p)}$, and $j_s^{(n)}$) to the BW correction $\varepsilon_{\mathrm{BW}}$ are shown for both isotopes with either an electron (Fig. 3.6a) or a muon (Fig. 3.6b).

For the electronic case, *the most dominant contribution across all orbitals and for both isotopes is the neutron spin current*, which is almost entirely responsible for the positive correction observed. We remark that, with reference to the discussion of the proton and neutron currents in Section 2.4.1.3, where the neutron currents of the even-odd nuclei of ^{163}Dy and ^{163}Dy were roughly one order of magnitude larger than those of the protons, this dominance is due to the unpaired nucleon being a neutron. We may therefore speculate that, repeating this same analysis for the odd-even nuclei of ^{159}Tb and ^{165}Ho, we would expect the magnetic moments to be dominated by the proton currents.

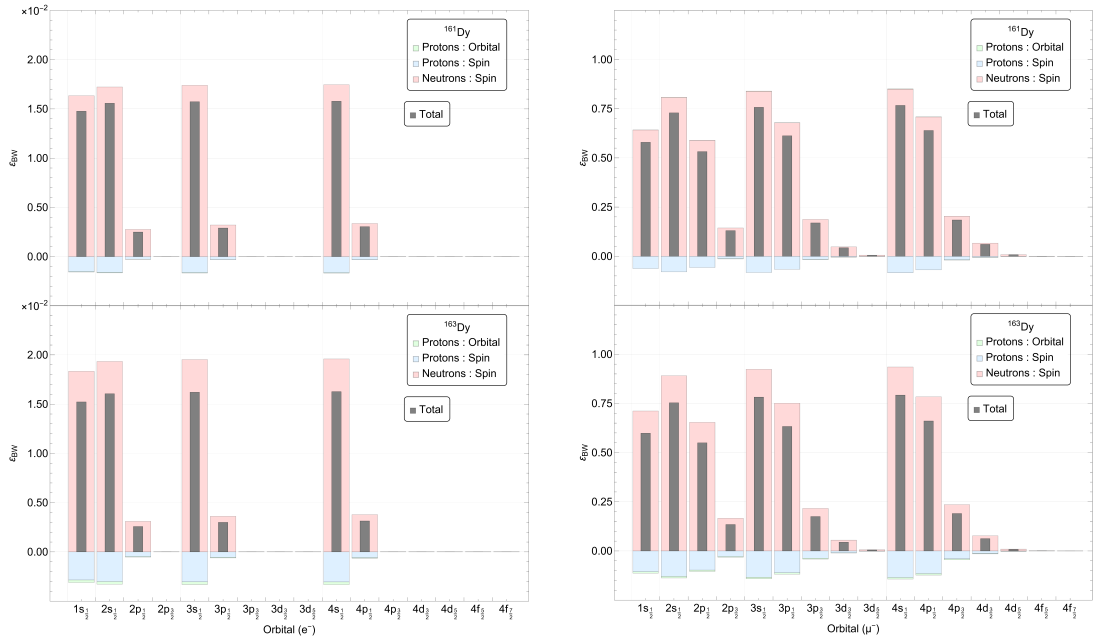
Additionally, the proton spin and orbital currents of ^{163}Dy and ^{163}Dy here in Fig. 3.6 contribute negatively, with the orbital current's effect being minimal. This dominance of the spin contribution suggests that nuclear magnetism, primarily from nucleon spins, plays a key role in the hyperfine interaction. The correction is most pronounced for the s orbitals, due to their greater penetration into the nucleus, reaching around 2%. Moreover, a notable feature between the isotopes is the increased magnitude of the spin contributions for both protons and neutrons in ^{163}Dy compared to ^{161}Dy, but with opposite signs, leaving the overall correction almost unchanged.

The case for muonic orbitals is presented in Fig. 3.6b. As expected, due to the deeper penetration of muonic wavefunctions into the nucleus, the magnitude of the BW correction is significantly higher, by a factor of approximately 50 compared to the electronic case. This brings the correction to nearly 100%, comparable to the uncorrected value. Additionally, unlike in the electronic case, the $np_{\frac{1}{2}}$ orbitals exhibit corrections similar to the $ns_{\frac{1}{2}}$ orbitals. Consistent with the electronic case, nuclear magnetism originating from the nucleon spins is the primary driver of the hyperfine interaction with the muons.

Figure 3.7 compares both the BW and BR corrections for the $s_{\frac{1}{2}}$, $p_{\frac{1}{2}}$, and $p_{\frac{3}{2}}$ orbitals as a function of the principal quantum number n, for both isotopes. For the electronic ions in Fig. 3.7a the isotopic effects are minimal and can be observed predominantly in the BW correction for the $s_{\frac{1}{2}}$ and $p_{\frac{1}{2}}$ orbitals. Both corrections, $\varepsilon_{\mathrm{BR}}$ and $\varepsilon_{\mathrm{BW}}$, remain approximately constant for $n \geq 2$.

For muonic ions, as shown in Fig. 3.7b, the isotopic effects are more pronounced than in the electronic case, influencing even the $p_{\frac{1}{2}}$ orbitals. Moreover, the values of the BR and BW corrections are nearly equal across the $s_{\frac{1}{2}}$, $p_{\frac{1}{2}}$, and $p_{\frac{3}{2}}$ orbitals, which contrasts with the electronic case where BR corrections typically dominated over BW corrections. Additionally, the trend as a function of n exhibits greater variability than for the electron, particularly for lower n values.

In both electronic and muonic cases, the s and p orbitals experience the greatest influence from the finite nuclear size, consistent with the non-relativistic limit where the Fermi



(a) Electronic **(b)** Muonic

Figure 3.6 – Bohr-Weisskopf correction $\varepsilon_{\mathrm{BW}}$. The BW corrections for (a) electronic and (b) muonic $^{161}\mathrm{Dy}^{65+}$ (upper panels) and $^{163}\mathrm{Dy}^{65+}$ (lower panels) are shown for the HFBCS model. The various magnetic contributions, proton (red) and neutron (blue) spins and proton orbital motion (green) are shown, together with the total correction (grey).

Orbital	BR	BW
$s_{1/2}$	4.7	1.6
$p_{1/2}$	0.9	0.4
$p_{3/2}$	0	0

(a) Electronic

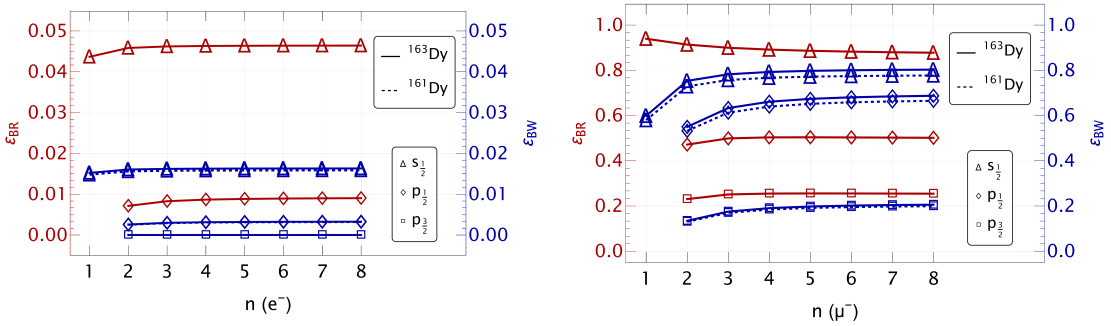
Orbital	BR	BW
$s_{1/2}$	90	80
$p_{1/2}$	50	65
$p_{3/2}$	25	20

(b) Muonic

Table 3.4 – Plateau values of the BR and BW effects for $^{163}\mathrm{Dy}^{65+}$. This table shows the approximate plateau values of the Breit-Rosenthal and Bohr-Weisskopf corrections (in %) for the (a) electronic and (b) muonic orbitals of $^{163}\mathrm{Dy}^{65+}$ and $^{161}\mathrm{Dy}^{65+}$.

contact term is dominant. The dependence of the corrections on the principal quantum number n is examined in Fig. 3.7, showing that for electronic orbitals, these corrections are mostly constant beyond $n = 2$, with minor deviations for the $1s_{1/2}$ and $2p_{1/2}$ orbitals. Approximate values for these corrections are summarsed in Table 3.4a.

In contrast, Fig. 3.7b highlights the greater variability of the corrections with respect to n for the muonic orbitals, particularly for the BW correction which shows a pronounced dip for the $1s_{1/2}$ orbital. Despite this variability, the corrections tend to plateau for higher values of n, with these plateau values detailed in Table 3.4b.



(a) Electronic **(b)** Muonic

Figure 3.7 – Trends of the Breit-Rosenthal and Bohr-Weisskopf corrections. The BR (in red and reading on the left axis) and BW (in blue and reading on the left axis) corrections for (a) electronic and (b) muonic ^{163}Dy (solid line) and ^{161}Dy (dashed line) are plotted as a function of quantum number n for the orbitals $ns_{1/2}$ (triangle), $np_{1/2}$ (diamond) and $np_{3/2}$ (square). Note that, except for the BW correction for the $s_{1/2}$ and $p_{1/2}$ orbitals, where there is a slight difference for ^{161}Dy^{65+} and ^{163}Dy^{65+}, the other curves are superimposed for both isotopes. For $p_{3/2}$, as the corrections are very small, the straight line with square symbols actually corresponds to four superimposed curves including the two corrections and the two isotopes.

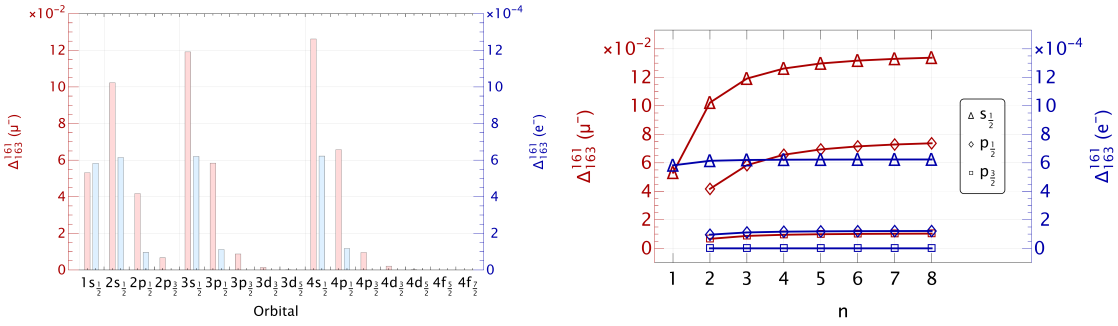
3.4.4 Hyperfine Anomaly

We are finally in a position to investigate the hyperfine anomaly of ^{161}Dy^{65+} and ^{163}Dy^{65+}, using the BR and BW effect calculations.

The hyperfine anomaly between isotopes ^{161}Dy and ^{163}Dy, was calculated for both electronic and muonic ions. Figure 3.8a shows these anomalies, with results for both cases presented on the same graph. The orders of magnitude are around 10^{-4} and up to 10^{-1}, respectively, and both sets of results appearing consistent with known values [114, 163, 164]. The states that exhibit the largest anomalies are the $j = 1/2$ states ($s_{1/2}$ and $p_{1/2}$), with $p_{3/2}$ states also showing notable effects. This trend mirrors the behaviour seen in the BR and BW corrections.

To understand how this anomaly varies with the principal quantum number n, Figure 3.8b illustrates its behaviour as n increases. For electronic atoms, the anomaly remains approximately constant across all n. However, for muonic atoms, Δ^{161}_{163} grows with increasing n and eventually reaches a plateau for $n > 7$. These approximate anomaly values are detailed in Table 3.5.

Overall, our analysis highlights the significantly enhanced hyperfine anomalies in muonic atoms compared to their electronic counterparts, especially in s orbitals and for higher n.



(a) Bar chart **(b)** Trend

Figure 3.8 – Hyperfine anomalies of ^{161}Dy^{65+} and ^{163}Dy^{65+}. The quantity $\Delta^{161}_{163} \equiv \frac{[(1+\varepsilon_{\mathrm{BR}})\times(1+\varepsilon_{\mathrm{BW}})]^{161}}{[(1+\varepsilon_{\mathrm{BR}})\times(1+\varepsilon_{\mathrm{BW}})]^{163}} - 1$ is depicted for muonic (red, left axis) and electronic (blue, right axis) states as (a) bar charts of the orbitals from $1s_{1/2}$ to $4f_{7/2}$, and (b) trends for the $ns_{1/2}$ (triangle), $np_{1/2}$ (diamond) and $np_{3/2}$ (square) orbitals.

Orbital	Anomaly
$s_{1/2}$	0.065
$p_{1/2}$	0.01
$p_{3/2}$	0

(a) Electronic

Orbital	Anomaly
$s_{1/2}$	13.5
$p_{1/2}$	7.5
$p_{3/2}$	1

(b) Muonic

Table 3.5 – Hyperfine anomaly plateau values (in %) for different orbitals.

3.4.5 Quadrupole Corrections

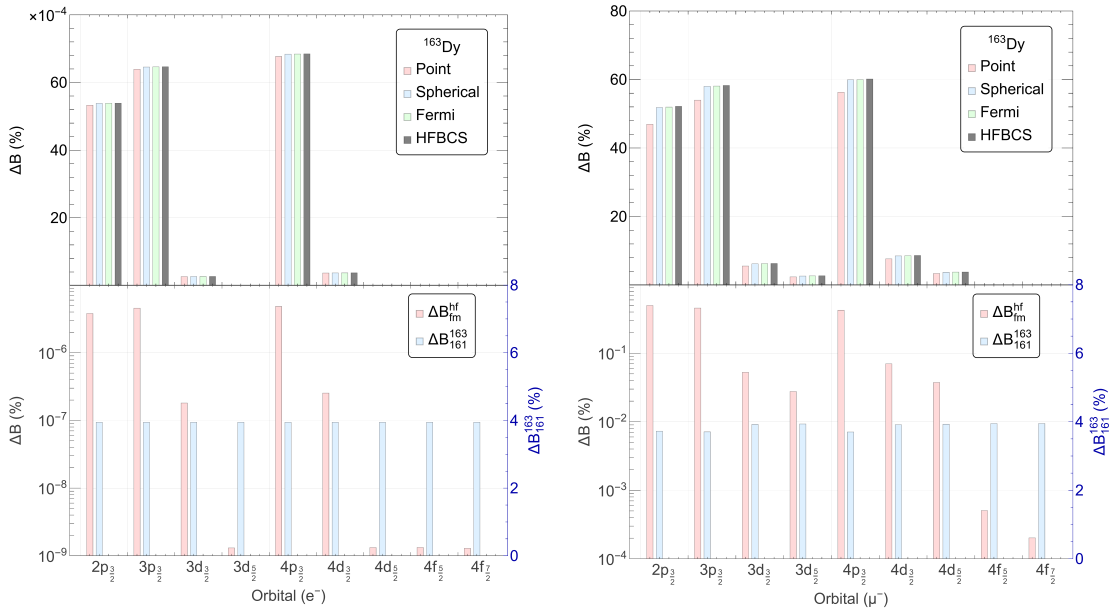
We can repeat our analysis for the quadrupole correction, as defined in Eq. (3.50) and Eq. (3.51). Figure 3.9 displays three key quantities, focusing on the quadrupole shifts and their dependence on nuclear models for the electronic states in Fig. 3.9a and the muonic states in Fig. 3.9b. Recall that the quadrupole hyperfine constant is zero for the $s_{1/2}$ and $p_{1/2}$ states, and thus the quadrupole shifts are not defined for these orbitals.

We can make the following remarks based on the calculation of the quantity ΔB^{m} for the different nuclear models: (i) all four nuclear models yield nearly identical results, (ii) the $np_{3/2}$ orbitals contribute most significantly to the quadrupole shifts, and (iii) in the point-charge model (m = pt), ΔB^{pt} quantifies the impact of nuclear penetration on the quadrupole moment, which is very small (about 0.006% for $np_{3/2}$ orbitals).

Comparing the HFBCS model with the Fermi distribution (ΔB) in the lower panel, shows the relative deviation is on the order of 10^{-6}%. Thus, for practical purposes, the Fermi model provides a suitable approximation. Furthermore, ΔB^{163}_{161} quantifies the isotopic effect on the quadrupole correction, derived using the HFBCS model.

For electronic ions, the quadrupole shifts are approximately 10^{-3}% for $p_{3/2}$ states, which is considerably larger than the hyperfine corrections for the same states. The quadrupole contribution to the hyperfine splitting of the $2p_{3/2}$ state (transition $F = 4 \to F = 3$) in ^{163}Dy^{65+} is around 24 meV, nearly eight times larger than the dipole contribution (≈ 3 meV). Nonetheless, the quadrupole shift is still about 10^{-3}% of the total transition energy, rendering it difficult to measure for electronic ions.

In contrast, the quadrupole shifts for the muonic orbitals of ^{163}Dy$^{65+}(\mu^-)$, as seen in



(a) Electronic **(b)** Muonic

Figure 3.9 – Quadrupole shifts for ^{163}Dy^{65+}. The relative shifts in the quadrupole moment of the (a) electronic and (b) muonic states from $1s_{1/2}$ to $4f_{7/2}$ for different nuclear models: point (pt), spherical (sp), Fermi (fm) and HFBCS (hf). We have defined in the upper panels $\Delta B^{\mathrm{m}} \equiv \frac{b^{\mathrm{pt}}_{\mathrm{np}} - b^{\mathrm{m}}_{\mathrm{wp}}}{b^{\mathrm{pt}}_{\mathrm{np}}}$ with $\mathrm{m} \in \{\mathrm{pt}, \mathrm{sp}, \mathrm{fm}, \mathrm{hf}\}$. The lower indices np and wp represent no penetration and with penetration respectively (see text for explanation). In the lower panels, the two quantities are depicted $\Delta B \equiv \frac{b^{\mathrm{fm}}_{\mathrm{wp}} - b^{\mathrm{hf}}_{\mathrm{wp}}}{B^{\mathrm{fm}}_{\mathrm{wp}}}$ for ^{163}Dy^{65+} (red, left axis) and $\Delta B^{163}_{161} \equiv \frac{b^{\mathrm{hf}}_{\mathrm{wp}}(163) - b^{\mathrm{hf}}_{\mathrm{wp}}(161)}{b^{\mathrm{hf}}_{\mathrm{wp}}(161)}$ (blue, right axis). The results for ^{161}Dy^{65+} are given in Fig. B.6 in Appendix B.1.

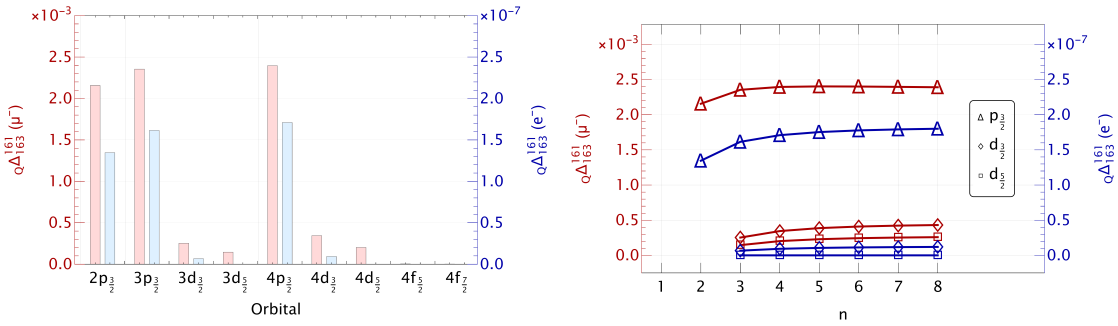
Fig. 3.9b, are much larger: around 50% for $p_{3/2}$ states, $5-10\%$ for $d_{3/2}$ states, and 5% for $d_{5/2}$ states. These values can be compared to the magnetic hyperfine corrections for the same states, which are around $1-2\%$. Here, the quadrupole contribution to the hyperfine splitting of the $2p_{3/2}$ state in the muonic ion is about 100 keV, significantly higher than the dipole contribution (≈ 100 eV), also consistent with recent results [114]. Therefore we may note that the quadrupole interaction is the dominant factor in the hyperfine splitting of the muonic $2p_{3/2}$ state, making the quadrupole shift measurable with an energy shift on the order of tens of keV.

The quadrupole hyperfine anomaly is further calculated for both electronic and muonic ions, as defined by

$$ {}_{Q}\Delta^{A}_{B} \equiv \frac{{}^{(A)}b}{{}^{(B)}b} \frac{{}^{(B)}Q_0^{2,\,\mathrm{spec}}}{{}^{(A)}Q_0^{2,\,\mathrm{spec}}} - 1, \tag{3.83} $$

where ${}^{(A)}b$ and ${}^{(B)}b$ are the quadrupole hyperfine constants for isotopes A and B, ${}^{(A)}Q_0^{2,\,\mathrm{spec}}$ and ${}^{(B)}Q_0^{2,\,\mathrm{spec}}$ are their respective nuclear quadrupole moments. This anomaly is computed similarly to the magnetic hyperfine anomaly.

Unlike other hyperfine anomalies, this can be determined purely experimentally by comparing two isotopes, without relying on theoretical calculations. As displayed in Fig. 3.10, our results suggest that the anomaly is of the order of 10^{-7} to 10^{-8} for the electronic ion and 10^{-3} to 10^{-4} for the muonic ion. Coupled with the much larger quadrupole



(a) Bar Chart **(b)** Trend

Figure 3.10 – Quadrupole hyperfine anomalies between ^{161}Dy^{65+} and ^{163}Dy^{65+}. (a) Bar charts, and (b) trends of the ratio by isotope of the shift in quadrupole moment from the simplest (np, pt) to most complex (wp, hf) model, as defined by: $_{Q}\Delta^{161}_{163} = \frac{\Delta B(161)}{\Delta B(163)} - 1$ where $\Delta B(A) \equiv \frac{^{(A)}b^{\mathrm{hf}}_{\mathrm{wp}}}{^{(A)}b^{\mathrm{pt}}_{\mathrm{np}}}$. Results for the electron and muon are shown in blue and red, with readings on the right and left axes respectively. Note that the $ns_{1/2}$ and $np_{1/2}$ contributions are zero.

hyperfine interaction in the muonic case, this makes the quadrupole hyperfine anomaly observable for the muonic ion but not for the electronic ion.

The dependence on the principal quantum number n for $p_{3/2}$ and $d_{5/2}$ states is illustrated in Fig. 3.10b. Similar to the magnetic hyperfine anomaly, the quadrupole anomaly is fairly constant with n, with a slight dip for the $2p_{3/2}$ state. The behaviour is consistent across both electronic and muonic ions, aside from the four orders of magnitude difference in magnitude.

3.5 Discussion

3.5.1 Summary

In this chapter, we have undertaken a comprehensive analysis of the hyperfine structure of hydrogen-like dysprosium, focusing particularly on the corrections arising from the finite size and structure of the nuclei of ^{161}Dy and ^{163}Dy. The calculations centered on two primary effects: the Breit-Rosenthal (BR) and Bohr-Weisskopf (BW) corrections, which were investigated for both electronic and muonic systems, highlighting their influence on hyperfine interactions.

Our numerical solutions of the Dirac equation yielded the radial wavefunctions for various nuclear models, including point-like, spherical, Fermi, and HFBCS. For the point-like, spherical and Fermi models, the wavefunctions were obtained from these analytically defined models of nuclear charge distributions, while for the HFBCS model the wavefunctions were obtained from the microscopic nuclear distributions.

For electronic ions, the wavefunctions from the different nuclear models exhibited minimal differences outside the nuclear radius, with more significant deviations occurring within. Muonic wavefunctions, however, displayed more pronounced differences due to the greater penetration of the muon into the nucleus, emphasising the sensitivity of muonic atoms to nuclear structure.

The BR corrections were found to predominantly influence the $ns_{1/2}$ orbitals, reducing in

magnitude for higher quantum numbers and $np_{1/2}$ orbitals. These corrections were small for electronic ions (around 5%) but significantly larger for muonic systems (up to 90%), emphasising the enhanced sensitivity of muons to the finite nuclear charge distribution. Comparisons between the Fermi and HFBCS models revealed that, although the microscopic HFBCS model provides a more accurate description of the nuclear structure, its effect on the hyperfine splitting is relatively small compared to the simpler Fermi distribution for both electronic and muonic ions.

The BW corrections were similarly most significant for $ns_{1/2}$ orbitals and were primarily driven by the nuclear magnetisation from neutron spins. Since the nuclei of ^{161}Dy and ^{163}Dy are both even-odd, having a single unpaired neutron, it is this unpaired neutron that presented the dominant contribution towards the magnetic moment through the neutron spin currents. The effect of the BW correction was approximately $1 - 2\%$ for electronic orbitals but reached as high as 80% for muonic orbitals, indicating a much larger impact of nuclear magnetism on muonic hyperfine interactions.

The anomalies in hyperfine interactions between isotopes ^{161}Dy and ^{163}Dy were also analysed. The magnetic hyperfine anomaly, characterised by the combined effect of BR and BW corrections, was shown to be of the order of 10^{-4} for electronic ions and up to 10^{-1} for muonic ions. The quadrupole hyperfine anomaly was similarly much more pronounced for muonic ions, being around 10^{-3} to 10^{-4}, compared to 10^{-7} to 10^{-8} for electronic ions.

Finally, the quadrupole correction to the hyperfine interaction was explored for both electronic and muonic ions. It was found that this correction is negligible for electronic ions (around $10^{-3}\%$) but significantly larger for muonic systems, particularly for the $p_{3/2}$ states (around 50%). The dominance of the quadrupole interaction in the hyperfine splitting of the muonic $2p_{3/2}$ state makes the quadrupole shift measurable, with shifts on the order of tens of keV, a contrast to the more subtle effects in electronic ions.

3.5.2 Outlook

The results of this chapter open several pathways for further research and potential applications. The enhanced sensitivity of muonic atoms to the nuclear structure presents a unique opportunity to study nuclear properties, such as the charge distribution and internal magnetic fields, with high precision. Muonic ions, with their deeply bound orbitals that significantly penetrate the nucleus, offer a tool for probing finer details of nuclear models, beyond the capabilities of electronic systems.

The calculations performed for BR and BW effects indicate that while a simple Fermi distribution is often sufficient to estimate electronic hyperfine interactions, the HFBCS model is necessary to capture the full impact of nuclear structure for muonic systems. Future work could focus on refining microscopic models of the nucleus to better match experimental data for muonic hyperfine splittings, potentially providing a deeper understanding of the nuclear magnetisation and its impact on atomic systems.

An important future application lies in the experimental measurement of hyperfine anomalies in muonic systems. The relatively large magnitude of these anomalies suggests that they could be measured with current or near-future spectroscopic techniques, providing a valuable test framework of nuclear models and the fundamental interactions governing atomic structure. The differences in behaviour between electronic and muonic systems could serve as a benchmark for validating theoretical models of hyperfine in-

teractions, with muonic systems providing a more stringent test due to their greater sensitivity.

Additionally, the quadrupole hyperfine anomaly in muonic atoms, being of significant magnitude, provides a new avenue for experimental verification. The measurable energy shifts of tens of keV suggest that it is feasible to directly observe the quadrupole contributions to hyperfine structure, which have traditionally been difficult to measure in electronic systems. This could lead to improved constraints on nuclear structure models and a better understanding of quadrupole interactions in heavy elements.

The shortcomings and limitations of the present work primarily stem from the computational challenges of modelling complex nuclear structures and the need for higher precision in solving the Dirac equation for bound states. An immediate improvement in the accuracy of the calculations could be improved by incorporating the QED corrections into the numerical code. In general, the low-level computational techniques could be optimised for both the nuclear and atomic wavefunctions, as well as exploring additional nuclear models beyond HFBCS, which could enhance the accuracy of future calculations. Moreover, extending the analysis to higher-order corrections in the hyperfine interaction, such as second-order effects, or higher-order moments like octupoles, would provide a more complete picture of the hyperfine structure of the well-deformed lanthanide nuclei.

To our knowledge, this is the first study to identify the microscopic origin of the nuclear magnetism that contributes to the hyperfine interaction. For the isotopes studied here, the magnetism coming from the protons, whether orbital or spin related, is very weak, while the neutron spin currents dominate. It would be interesting and important to extend this study to other nuclei and their isotopes in order to improve our understanding of nuclear magnetism and its relationship with atomic observables such as the hyperfine interaction.

In summary, the study of hyperfine interactions in both electronic and muonic hydrogen-like ions offers a rich field for exploring the interplay between nuclear and atomic physics. The insights gained from these corrections and anomalies not only advance our understanding of hyperfine structure but also have broader implications for nuclear theory, spectroscopy, and quantum information processing, where precise control over hyperfine states is crucial. By improving our understanding of the microscopic origins of the nuclear magnetism and quadrupolar deformation, not only in different elements but between isotopes of the same element, we can improve the process of isotope and ligand selection in isotopologue chemistry, thereby leading to SMM complexes with more, and more well-defined, spin states optimised for quantum computing applications.

References Cited in this Chapter

[56] W. Wernsdorfer and M. Ruben. "Synthetic Hilbert Space Engineering of Molecular Qu *d* its: Isotopologue Chemistry". In: *Advanced Materials* 31.26 (June 2019), p. 1806687. DOI: 10.1002/adma.201806687.

[64] J. E. Rosenthal and G. Breit. "The Isotope Shift in Hyperfine Structure". In: *Physical Review* 41.4 (Aug. 15, 1932), pp. 459–470. DOI: 10.1103/PhysRev.41.459.

[65] A. Bohr and V. F. Weisskopf. "The Influence of Nuclear Structure on the Hyperfine Structure of Heavy Elements". In: *Physical Review* 77.1 (Jan. 1, 1950), pp. 94–98. DOI: 10.1103/PhysRev.77.94.

[69] G. Lospalluto, A. Antognini, et al. "Towards muon cooling at the Paul Scherrer Institute". In: *Proceedings of Muon4Future Workshop — PoS(Muon4Future2023)*. Muon4Future Workshop. Istituto Veneto di Lettere, Scienze ed Arti - Palazzo Franchetti, Venezia, Italy: Sissa Medialab, Mar. 15, 2024, p. 009. DOI: 10.22323/1.452.0009.

[70] K. Shimomura, A. Koda, et al. "Pulsed muon facility of J-PARC MUSE". In: *Interactions* 245.1 (Mar. 5, 2024), p. 31. DOI: 10.1007/s10751-024-01863-8.

[107] L. Bonneau, N. Minkov, et al. "Effect of core polarization on magnetic dipole moments in deformed odd-mass nuclei". In: *Physical Review C* 91.5 (May 11, 2015), p. 054307. DOI: 10.1103/PhysRevC.91.054307.

[112] N. Stone. "Table of nuclear magnetic dipole and electric quadrupole moments". In: *Atomic Data and Nuclear Data Tables* 90.1 (May 2005), pp. 75–176. DOI: 10.1016/j.adt.2005.04.001.

[113] C. Schwartz. "Theory of Hyperfine Structure". In: *Physical Review* 97.2 (Jan. 15, 1955), pp. 380–395. DOI: 10.1103/PhysRev.97.380.

[114] J. Persson. *Muonic Hyperfine Structure and the Bohr-Weisskopf Effect*. Aug. 11, 2023. DOI: 10.20944/preprints202308.0903.v1.

[115] B. M. Roberts and J. S. M. Ginges. "Hyperfine anomaly in heavy atoms and its role in precision atomic searches for new physics". In: *Physical Review A* 104.2 (Aug. 27, 2021), p. 022823. DOI: 10.1103/PhysRevA.104.022823.

[116] A. Knecht, A. Skawran, et al. "Study of nuclear properties with muonic atoms". In: *The European Physical Journal Plus* 135.10 (Oct. 2020), p. 777. DOI: 10.1140/epjp/s13360-020-00777-y.

[117] A. Skawran, A. Adamczak, et al. "Towards nuclear structure with radioactive muonic atoms". In: *Il Nuovo Cimento C* 42.203 (Sept. 20, 2019), pp. 1–4. DOI: 10.1393/ncc/i2019-19125-7.

[118] P. Strasser, A. Taniguchi, et al. "Muon spectroscopy with trace alkaline-earth and rare-earth isotopes implanted in solid D2". In: *Hyperfine Interactions* 193.1 (Sept. 2009), pp. 121–127. DOI: 10.1007/s10751-009-0055-0.

[119] T. Y. Saito, M. Niikura, et al. *Muonic X-Ray Measurement for the Nuclear Charge Distribution: the Case of Stable Palladium Isotopes*. Apr. 7, 2022.

[120] A. Antognini, N. Berger, et al. "Measurement of the quadrupole moment of Re 185 and Re 187 from the hyperfine structure of muonic X rays". In: *Physical Review C* 101.5 (May 22, 2020), p. 054313. DOI: 10.1103/PhysRevC.101.054313.

[121] T. Okumura, T. Azuma, et al. *Few-electron highly charged muonic Ar atoms verified by electronic K x rays*. July 10, 2024.

[154] J. D. Jackson. *Classical electrodynamics*. 3. ed., [Nachdr.] Hoboken, NY: Wiley, 2009. 808 pp.

[155] A. Pálffy. "Nuclear effects in atomic transitions". In: *Contemporary Physics* 51.6 (Nov. 2010), pp. 471–496. DOI: 10.1080/00107514.2010.493325.

[159] P. Strange. *Relativistic quantum mechanics: With applications in condensed matter and atomic physics*. Cambridge: Cambridge University Press, 1998. DOI: 10.1017/CBO9780511622755.

[160] W. R. Johnson. *Atomic structure theory*. Berlin, Heidelberg: Springer, 2007. DOI: 10.1007/978-3-540-68013-0.

[161] S. Büttgenbach. "Magnetic hyperfine anomalies". In: *Hyperfine Interactions* 20.1 (July 1984), pp. 1–64. DOI: 10.1007/BF02043319.

[162] S. Boucard. "Calcul de haute precision d'energies de transitions dans les atomes exotiques et les lithiumoides : corrections relativistes, corrections radiatives, structure hyperfine et interaction avec le cortege electronique residuel". These de doctorat. Paris 6, Jan. 1, 1998.

[163] J. Persson. "Table of hyperfine anomaly in atomic systems — 2023". In: *Atomic Data and Nuclear Data Tables* 154 (Nov. 2023), p. 101589. DOI: 10.1016/j.adt.2023.101589.

[164] J. Persson. "Table of hyperfine anomaly in atomic systems". In: *Atomic Data and Nuclear Data Tables* 99.1 (Jan. 2013), pp. 62–68. DOI: 10.1016/j.adt.2012.04.002.

PART II

QUANTUM INFORMATION PROCESSING WITH QUDITS

Quantum Information Processing with Qudits

Qudit-based quantum computing, which generalises the traditional qubit approach to d-level systems, offers a promising pathway to address scalability and error correction challenges in quantum information processing (QIP). This part provides a comprehensive analysis of qudit systems, examining their operational efficiency, robustness to noise, and optimal control methods. We first compare the infidelity scalings of single-qudit and multi-qubit systems within identical Hilbert space dimensions under noisy environments in the Lindblad formalism. An analytically derived critical curve, $(d^2-1)/3\log_2(d)$, benchmarks the operational time efficiency of qudits relative to qubits, revealing scenarios where qudits outperform in terms of gate efficiencies. Further, we deepen our study of the Average Gate Fidelity (AGF) of single-qudit systems under Markovian noise, extending the previous work by deriving a comprehensive theoretical framework for calculating higher-order correction terms. Through this framework, we explore the transition from linear to nonlinear behaviour in gate infidelities in the strong coupling regime, providing critical insights into the impact of qudit dimensionality, noise strength and gate dependence on the performance of quantum gates. This theoretical investigation is complemented by extensive numerical simulations, which validate the derived universal bounds for the Average Gate Infidelity (AGI) and offer practical implications for enhancing near-term qudit architectures. In the final chapter, we investigate pulse-level optimal control techniques for quantum gates in qudit systems using the Givens Rotation Decomposition (GRD) and the GRAPE algorithm. These methods are evaluated using benchmark gates including the Quantum Fourier Transform (QFT) and Grover's Search Algorithm, with a focus on their performance under environmental noise and control errors. A custom simulation framework was developed to analyse these gates, demonstrating that the GRD method is more efficient for high-dimensional systems, while GRAPE provides faster and more precise control in lower dimensions. The study also assesses the robustness of each method to noise and control errors, revealing that GRAPE is more resilient to phase and timing errors, whereas the GRD is less affected by amplitude offsets. This chapter not only advances our understanding of qudit systems in high-dimensional quantum computing but also provides a robust foundation for future research. It highlights the potential of qudits in offering competitive gate efficiencies, informs optimal gate design and error correction protocols, and suggests pathways for extending these methods to multi-qudit systems and specific hardware platforms. This work lays the groundwork for realising scalable, high-fidelity qudit-based quantum gates.

CHAPTER 4

NOISY QUDIT VS MULTIPLE QUBITS: CONDITIONS ON GATE EFFICIENCY FOR ENHANCING FIDELITY

Who are You, Who are so Wise in the ways of Science?

- Sir Bedivere to Denis Janković in "Conversations with God"

Contents

4.1 Introduction . . . 107
4.1.1 Background and Motivation . . . 107
4.1.2 Objectives and Contributions . . . 108
4.1.3 Overview . . . 109
4.2 Theory . . . 109
4.2.1 Lindblad Formalism and Noise-Perturbed States . . . 109
4.2.2 Average Gate Infidelity . . . 110
4.3 Methods . . . 111
4.3.1 Numerical Noisy Qudit/ multi-qubit Simulation . . . 111
4.3.1.1 Standard packages . . . 111
4.3.1.2 Parameters . . . 112
4.3.1.3 Time evolution . . . 112
4.3.1.4 Fidelity calculation . . . 112
4.3.1.5 Curve fitting . . . 112
4.3.2 Random Gate and Pulse Hamiltonian Generation . . . 112
4.3.2.1 Gate generation . . . 112
4.3.2.2 Pulse generation . . . 112
4.3.2.3 Choice of Hamiltonian . . . 113
4.4 Results . . . 113
4.4.1 AGI of Qudits vs Qubits . . . 113
4.4.2 Fit and Deviation from Linear Behaviour . . . 114
4.4.3 Gate Dependence . . . 115
4.4.4 Single Qudit vs Ensemble of Qubits . . . 116
4.5 Discussion . . . 118
4.5.1 Summary . . . 118
4.5.2 Outlook . . . 119
References Cited in this Chapter . . . 120

Note: This Chapter presents a summary of the study that was published in npj Quantum Information under the title "Noisy Qudit vs Mutliple Qubits: Conditions on Gate Efficiency for Enhancing Fidelity". The bibliographical citation of the publication can be found in [122], and the code and data used in the study have been made publicly available at [123]. The original publication is included in Appendix C, along with the supplementary information.

4.1 Introduction

In this chapter, we investigate the comparative performance of qudits and multi-qubit systems in the context of noisy quantum environments. Qudits, which are d-level quantum systems, offer a promising alternative to qubits in quantum information processing (QIP) due to their potential for increased information density and computational efficiency. However, the increased dimensionality of qudits introduces additional error channels, which can impact their performance in noisy environments. This study aims to determine the conditions under which qudits may outperform multi-qubit systems in terms of gate efficiency and fidelity.

4.1.1 Background and Motivation

In this study, we discuss the emerging interest in qudit-based quantum systems, with d levels, as an alternative to the conventional qubits in QIP. While qubits serve as the foundational building blocks of QIP in most modern platforms, offering coupled two-level quantum systems, we highlight how qudits can provide higher-dimensional computational spaces, potentially offering advantages in noise-limited quantum computing systems. Drawing an analogy to the early days of classical computing, we suggest that while binary bits eventually became the standard, qudits may provide a viable near-term approach to address the challenges of scalability in quantum systems.

We note that superconducting qubits have led progress in scaling, with current systems reaching hundreds of qubits, yet technical challenges persist in exponentially increasing the Hilbert space using qubits alone [1]. With their d^n scaling, qudits offer a potentially more efficient approach to expanding computational capacity. We argue that qudit platforms may present practical benefits, such as lower decoherence rates in, for example nuclear spin systems, enhanced error correction through encoding of logical states over additional levels, greater information density per site, fewer nonlocal operations (like cross-resonance or entangling gates), and more robust quantum memories. Theoretical advantages also include extended computational capabilities to larger groups like $\bigotimes SU(d)$, which can simplify certain quantum algorithms, such as Grover's algorithm, and pave the way for novel quantum algorithms [31, 35, 124].

However, qudits face their own challenges, primarily due to an increased number of error channels associated with their higher dimensionality. It is therefore critical to assess whether the potential benefits of qudits outweigh the complexities introduced by these additional errors. The motivation behind our study is to benchmark qudits against multi-qubit systems, with a focus on metrics like Average Gate Infidelity (AGI), to identify the conditions under which qudits could provide superior performance in practical quantum computing.

The current era of quantum computing is dominated by NISQ (Noisy Intermediate-Scale Quantum) systems, where noise and decoherence are significant limiting factors [75,

125]. Achieving fault-tolerant quantum computing requires progress in either developing robust error correction schemes or enhancing the intrinsic noise resilience of quantum systems. Superconducting qubits, trapped ions, and other qubit-based platforms have seen considerable progress, but the challenge of scaling remains.

4.1.2 Objectives and Contributions

In this study, we compared single qudit systems with multi-qubit systems under near noise-free conditions to determine when a qudit maintains or improves computational efficiency despite having more potential error channels. A key metric in this comparison was the Average Gate Infidelity (AGI), as defined by Nielsen [126], which quantified the loss of computational information in a way that was independent of input states and remained relevant throughout any stage of a quantum algorithm. The analysis focused on systems with equivalent Hilbert space dimensions undergoing arbitrary unitary transformations under similar noisy conditions, exploring how AGI responded to error rates and gate time relative to decoherence timescales.

We aimed to investigate how the AGI scaled with respect to both the error rate (γ) and the dimensionless gate time (γt), as well as how it varied with the qudit's dimension d. This allowed us to benchmark whether a single-qudit platform could offset its larger number of potential error channels through advantageous decoherence times and faster gate operations. The outcomes depended on the physical properties of the platform, including environmental coupling, control pulse dynamics, and addressing speed. For equivalent Hilbert space dimensions between a qudit and a multi-qubit system, our analysis identified whether the qudit platform achieved competitive computational fidelity for given noise and time parameters (γ, t). Additionally, by examining the scaling with d, we provided theoretical upper bounds for qudit dimensions to maintain performance benefits without being overwhelmed by noise.

The objectives of the study were threefold: (1) To establish a theoretical framework for comparing the gate efficiency of qudits and qubits, deriving a critical curve that related the qudit's dimensionality to its performance relative to a multi-qubit system. (2) To validate the theoretical findings with numerical simulations using the QuTiP package, applying realistic noise models like pure dephasing and amplitude damping to various quantum platforms. (3) To offer practical guidelines for determining when qudits had fidelity and efficiency advantages over qubits, applicable to real-world systems such as trapped ions, superconducting qubits, and molecular nuclear spin systems.

The contributions of this work to quantum information processing were multifaceted. We introduced a gate-independent formula for the first-order response of AGI to Markovian noise, providing a universal benchmarking tool for gate efficiency comparisons between qudits and qubits. An analytical expression for a critical curve, $(d^2-1)/3\log_2(d)$, was derived to determine the conditions under which qudits outperform qubits in terms of computational fidelity. We further validated these theoretical models through numerical simulations using QuTiP, demonstrating that under specific noise and coherence time conditions, qudits could exceed the performance of qubits. Finally, we analysed current quantum platforms, highlighting the potential computational advantages of qudit systems in near-term quantum computing environments.

4.1.3 Overview

In our summary of this study, we discuss the contributions presented therein in the framework of the theoretical background and analytical findings, methodological approach, numerical results, and implications for future research.

In Section 4.2 we begin by presenting our derivation of a gate-independent formula for the first-order response of the AGI to Markovian noise within the Lindblad formalism, particularly focusing on its application to the quasi-errorless regime relevant to near-term QIP systems. The analytical framework derived expressions for the linear dependence of the AGI on the dimensionless product γt, where γ is the error rate and t is the gate time, and applies these expressions to single-qudit, multi-qubit, and multi-qudit systems. A critical comparison is made between the rates of increase in AGI for a single qudit versus equivalent multi-qubit systems, considering the impact of arbitrary collapse operators.

Following the theoretical groundwork, the chapter then includes in Section 4.3 a detailed account of how the numerical simulations were performed using the QuTiP Python package [127, 128], designed to complement and illustrate the analytical results.

The numerical results are then discussed in Section 4.4, where we examine the applicability and limitations of the linear response formalism for AGI and explore several key aspects: the range of validity of γt and its dependence on qudit dimensionality; the extent of gate-independence; the adaptability to noise models beyond pure dephasing; and conditions on gate times for which either qudits or multi-qubits have a computational advantage. This final aspect is examined closely by factoring in parameters such as decoherence rates and gate operation times, specific to existing quantum platforms, offering a comparison between qudits and qubits across various noise environments and validating the derived critical curve. Finally, a discussion explores the implications of these results, particularly the potential of qudits as alternatives to qubits in practical quantum computing, and concludes with an outlook for future research and potential advancements in the field.

4.2 Theory

The theoretical framework of this study revolved around quantifying noise-induced errors in quantum systems using the Average Gate Infidelity (AGI). The AGI provides a state- and gate-independent measure of how closely a noisy quantum channel approximates its ideal operation, thereby serving as a benchmark for comparing single-qudit systems and multi-qubit systems under realistic noise conditions. This analysis was grounded in the Lindblad formalism, which is commonly used to describe the dynamics of open quantum systems under Markovian noise.

4.2.1 Lindblad Formalism and Noise-Perturbed States

The dynamical evolution of a quantum system's density matrix $\rho(t)$ under noise can be described by the Lindblad master equation [85]:

$$\frac{d\rho(t)}{dt} = -\frac{i}{\hbar}[H, \rho(t)] + \mathcal{L}[\rho(t)], \tag{4.1}$$

where H is the Hamiltonian of the system, and $\mathcal{L}[\rho(t)]$ is the Lindbladian, representing the effect of noise and decoherence on the system. The Lindbladian is given by

$$\mathcal{L}[\rho(t)] = \sum_k \left(L_k \rho(t) L_k^\dagger - \frac{1}{2}\{L_k^\dagger L_k, \rho(t)\} \right), \tag{4.2}$$

where $\{A, B\} = AB + BA$ is the anticommutator, and L_k are the Lindblad operators (also called collapse operators), which model different types of environmental interactions.

To describe various noise processes, we can choose different forms for the Lindblad operators L_k. Some common noise models are:

- **Pure Dephasing**: Described by $L_k = \sqrt{\gamma}\sigma_z$, where γ is the dephasing rate. This process leads to phase damping without energy loss.
- **Amplitude Damping**: Described by $L_k = \sqrt{\gamma}\sigma_-$, where $\sigma_- = \frac{1}{2}(\sigma_x - i\sigma_y)$ and γ is the damping rate. This noise model accounts for spontaneous emission or energy relaxation to the environment.
- **Bit-flip** (or depolarising noise): Described by $L_k = \sqrt{\gamma}\sigma_x$, where σ_x is the Pauli-X operator. This noise operator models random bit-flip errors induced in the system.

If we now consider the perturbation due to a single weak collapse operator acting on short timescales, $\gamma t \ll 1$, we can assume an ansatz for the density matrix $\rho(t)$,

$$\rho(t) = \rho^* - \gamma t M + \mathcal{O}((\gamma t)^2) \,, \tag{4.3}$$

with perturbation matrix

$$M = \frac{1}{2}\left\{L^\dagger L, \rho^*\right\} - L\rho^* L^\dagger. \tag{4.4}$$

Applying this ansatz to the state fidelity between the perturbed and unperturbed states, we have [165]

$$\mathcal{F}(\rho(t), \rho^*) \equiv \left[\mathrm{Tr}\left(\sqrt{\sqrt{\rho(t)}\rho^*\sqrt{\rho(t)}} \right) \right]^2 . \tag{4.5}$$

Expanding this, and writing for the infidelity $\mathscr{E} \equiv 1 - \mathcal{F}$,

$$\mathscr{E}(\rho^*) = \gamma t \Delta_* L + \mathcal{O}((\gamma t)^2) \,, \tag{4.6}$$

where

$$\Delta_* L = \langle L^\dagger L \rangle_* - \langle L^\dagger \rangle_* \langle L \rangle_* \,, \tag{4.7}$$

with

$$\langle L^\dagger L \rangle_* \equiv \mathrm{Tr}\left(\rho^* L^\dagger L \right). \tag{4.8}$$

4.2.2 Average Gate Infidelity

Extending this state-dependent result to the more general case of the Average Gate Infidelity (AGI), we can define the AGI as the average deviation of a noisy quantum

channel $\mathcal{E}$ from an ideal unitary gate U over all possible input states. The AGI is then given by

$$\overline{\mathcal{I}}(U,\mathcal{E}) = 1 - \int d\rho_0 \, \mathrm{F}\left(\rho(t), \rho^*\right) \ , \tag{4.9}$$

$$= 1 - \int d\rho_0 \left\langle \mathcal{U}^\dagger \circ \mathcal{E}[\rho_0] \right\rangle_0 \ , \tag{4.10}$$

where the integral is taken over the Haar-measure induced by the Fubini-Study metric.

By writing the density matrix in the Kraus representation, $\rho(t) = \sum_k E_k \rho^* E_k^\dagger$, we have the following expression [126, 166]:

$$\bar{\mathcal{F}}(\mathcal{E},U) = \frac{d + \sum_k \left|\mathrm{Tr}\left(\tilde{E}_k U^\dagger\right)\right|^2}{d(d+1)} = \frac{d + \sum_k \left|\mathrm{Tr}\left(E_k\right)\right|^2}{d(d+1)} \ . \tag{4.11}$$

This leads to the following expression for the AGI to first-order in γt, for an arbitrary quantum channel $\mathcal{X}$ with collapse operator L

$$\overline{\mathscr{E}}(\mathcal{X}) = \frac{\gamma t}{d+1}\left(\mathrm{Tr}\left(L^\dagger L\right) - \frac{1}{d}\left|\mathrm{Tr}(L)\right|^2\right) + \mathcal{O}((\gamma t)^2). \tag{4.12}$$

For the case of pure dephasing, where $L = \sqrt{\gamma} J_z$, this reduces to

$$\overline{\mathscr{E}}(\mathcal{E}_z) = \frac{\gamma t}{12} d(d-1) + \mathcal{O}((\gamma t)^2). \tag{4.13}$$

For small noise levels, the AGI is often approximated by the first-order term in γt, where γ is the noise rate and t is the gate time. This linear response regime is particularly relevant for near-term quantum information processing systems, which operate in a quasi-errorless regime.

4.3 Methods

4.3.1 Numerical Noisy Qudit/ multi-qubit Simulation

The data and source code used to generate the results in this paper are publicly available on the RADAR4KIT Repository [123]. All simulations were conducted using the Python package QuTiP [127] version 4.7, along with SciPy version 1.7.3 and NumPy version 1.21.5. In this section, we describe the process of obtaining the numerical results: In particular, the AGIs $\overline{\mathscr{E}}$ as presented in Figures 3 and 4 of the published article, and the AGI slopes c, displayed in the remaining figures.

4.3.1.1 Standard packages

To simulate the quantum dynamics and fit the resulting data curves, we utilised essential functions provided by QuTiP, including the calculation of propagators in superoperator form (`qt.propagator`) and the evaluation of gate fidelities (`average_gate_fidelity` from `qutip.metrics`). Curve fitting was performed using the `curve_fit` function from `scipy.optimise`.

4.3.1.2 Parameters

The main parameters for each simulation were the system's dimension d, the noise decay rate γ, and the collapse operators $\{L_k\}$, each represented as a `QObj` in the canonical basis. Additionally, we defined a list of time points to simulate the system's evolution. Given that the primary quantity of interest was γt, the error rate γ was set to a fixed value, and the range of γt was derived from the span of the selected time points.

4.3.1.3 Time evolution

The evolution of the quantum system over time was simulated by calculating the propagator using the system's Hamiltonian, the list of time points, and the collapse operators scaled by $\sqrt{\gamma}$. This generated a series of `QObj` superoperators for various values of γt. While a more detailed discussion of the Hamiltonian is provided in a subsequent subsection, it should be noted that, except in Figure 5 of the published article (which examines gate- and Hamiltonian-dependence), we performed simulations with a vanishing Hamiltonian $H = \mathbb{0}_d$, as the quantities studied were assumed to be independent of the Hamiltonian.

4.3.1.4 Fidelity calculation

For each value of γt, we calculated the average gate fidelity relative to a target gate. In cases where $H = \mathbb{0}_d$, the target gate was the identity matrix. The calculated fidelities for these scenarios are shown in Figures 3 and 4 of the published article.

4.3.1.5 Curve fitting

To analyse the relationship between AGI and γt, we fitted a linear curve using `curve_fit`, following the functional form $1 - c\gamma t$. The parameter c represents the slope of the AGI, and the extracted slopes $c(\{L_k\})$ are presented in Figures 2, 5, 6, 7 and 8 of the published article. Furthermore, the least-square fit parameter R from the fitting functions is the value reported in this paper.

4.3.2 Random Gate and Pulse Hamiltonian Generation

4.3.2.1 Gate generation

In our study examining deviations from the gate-independent analytical results, we randomly generated a set of $N_g = 5000$ quantum gates for each dimension d using the Bristol package [167] in Python. These gates were drawn from the circular unitary ensemble, ensuring a uniform distribution over the Haar measure. To find an associated set of control pulses for each gate, we used the `optimize_pulse_unitary` function from QuTiP's pulse optimisation module (`control.pulse_optim`).

4.3.2.2 Pulse generation

Control pulses were generated using gradient-ascent methods via the `GRAPE` algorithm [97]. To expedite this process, the optimisations were executed in parallel on a high-performance computing cluster, using the L-BFGS-B optimiser. The control Hamiltonian $H_c(t)$, expressed as

$$H_c(t) = \sum_{k=0}^{N} u_k(t) H_k, \tag{4.14}$$

consists of a basis set of controls $\{H_k\}$ and corresponding time-dependent amplitudes $u_k(t)$. The optimisation aimed to find the optimal set of amplitudes $\{u_k(t)\}$ to best approximate the target gate.

4.3.2.3 Choice of Hamiltonian

For the simulations in this paper, we modeled qudits as ladder systems, assigning one control pulse to each transition between adjacent levels, similar to experiments on single-molecule magnets (e.g., $TbPc_2$, with $d = 4$) by Godfrin *et al.* [43]. The $d-1$ transitions were represented by pairs of control Hamiltonians in the interaction picture, specifically choosing a basis set of controls as $|k\rangle\langle k+1| + |k+1\rangle\langle k|$ and $i(|k\rangle\langle k+1| - |k+1\rangle\langle k|)$ for $k = 1, \ldots, d-1$. The free-evolution Hamiltonian H_0 was set to zero as we considered the interaction frame.

4.4 Results

4.4.1 AGI of Qudits vs Qubits

We applied the techniques described in the previous section to a different system: an ensemble of n identical dephasing qubits with a total Hilbert space dimension of $d = 2^n$. To enable a fair comparison with the qudit analysis, we assumed that each individual qubit decohered at the same rate through its spin operator S_z, in a similar manner to the dephasing of a qudit with $d = 2$. Considering only this type of environmental coupling provided a best-case scenario for the multi-qubit implementation since any additional inter-qubit interactions would likely introduce further decoherence. Under these conditions, the system evolves according to the master equation:

$$\frac{\mathrm{d}\rho}{\mathrm{d}t} = -i\,[H,\rho] + \sum_{k=1}^{n} L_k \rho L_k^\dagger - \frac{1}{2}\sum_{k=1}^{n}\left\{L_k^\dagger L_k, \rho\right\}\ , \tag{4.15}$$

where the Lindblad operators L_k are given by the tensor product of identity operators and the S_z operator at the k-th qubit, and leading to the $n+1$ Kraus operators. The AGI for this system was then calculated using the same methodology as for the qudit case,

$$\overline{\mathscr{E}}(\mathcal{E}_z) = \frac{\gamma t}{4}\frac{n2^n}{2^n+1} + \mathcal{O}((\gamma t)^2) \tag{4.16}$$

$$= \frac{\gamma t}{4}\frac{\log_2(d)d}{d+1} + \mathcal{O}((\gamma t)^2)\ , \tag{4.17}$$

which reproduces the result found by Abad *et al.* [168] for identically dephasing qubits without energy relaxation.

The analytical expressions in Eqs. (4.13) and (4.17) formed one of the key outcomes of this work. Specifically, for a single qudit, the average gate infidelity (AGI) was found to scale as d^2, while for an ensemble of n qubits, it was found to scale as $\log_2(d)$. Assuming a qudit dephasing time $T_{2,d}$ that matches the $T_{2,\mathrm{b}}$ dephasing time of a single qubit, $\frac{1}{T_2} = \frac{\gamma}{2}$ holds in both cases.

Taking now the ratio between the AGIs for qudits and n-qubit systems, for gate durations t_d and $t_{\mathrm{b},n}$ respectively, we found

$$\frac{\overline{\mathscr{E}_d}(\mathcal{E}_z)}{\overline{\mathscr{E}_{\mathrm{b},n}}(\mathcal{E}_z)} = \frac{c_d t_d/T_{2,d}}{c_{\mathrm{b},n} t_{\mathrm{b},n}/T_{2,\mathrm{b}}}. \tag{4.18}$$

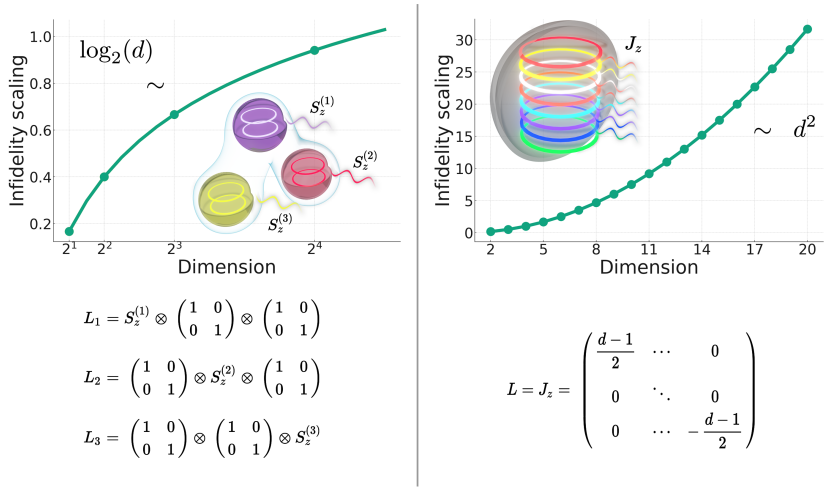


Figure 4.1 – Visual synthesis of the infidelity scaling in multiple qubits and a single qudit. Summary diagram illustrating the selected collapse operators and the associated analytically derived expected infidelity scalings as functions of the Hilbert Space dimension, as derived from Eqs. (4.13) and (4.17). This is depicted for two distinct systems: multiple qubits (left), scaling as $\sim \log_2(d)$ and a single qudit (right) scaling as $\sim d^2$. The term infidelity scaling here refers to the slopes of the first-order-in-γt AGIs, denoted as c in Eq. (4.18).

Thus, for a single qudit ($d = 2^n$) to outperform an ensemble of n qubits in terms of resilience to noise, the following inequality must hold:

$$\frac{t_{\mathrm{b},n}/T_{2,\mathrm{b}}}{t_d/T_{2,d}} > \frac{c_d}{c_{\mathrm{b},n}} = \frac{d^2-1}{3\log_2(d)} = \frac{4^n-1}{3n}. \tag{4.19}$$

This expression provides a precise condition for the gate time to decoherence time ratio, $\tau_d = t_d/T_{2,d}$ relative to $\tau_{\mathrm{b},n} = t_{\mathrm{b},n}/T_{2,\mathrm{b}}$, required for qudits to outperform qubits in terms of fidelity. It also confirms that matching T_2 times is insufficient for qudits to exhibit superior noise resilience, as the scaling in γt differs between the systems.

The relationship in Eq. (4.19) is a key result of this work, and summarised visually in Fig. 4.1. Furthermore, the calculations were shown to be extended to an ensemble of N qudits undergoing pure dephasing:

$$\overline{\mathscr{E}_{d,N}}(\mathcal{E}_z) = \frac{\gamma t}{12}\frac{N d^N}{d^N+1}(d^2-1) + \mathcal{O}((\gamma t)^2), \tag{4.20}$$

and more generally for an ensemble of N qudits with arbitrary collapse operators. This generalised formula can be applied to qudit systems with arbitrary collapse operators, thus extending the results to a wide range of physical implementations beyond those considered in this paper.

4.4.2 Fit and Deviation from Linear Behaviour

Using the previously described numerical methods, we simulated single-qudits with dimension d under pure dephasing, considering a Hamiltonian $H = \mathbb{0}_d$ and small values of the dimensionless parameter $\gamma t \in [5\times10^{-4}, 1\times10^{-2}]$. This range of γt is typical in certain nuclear spin systems, such as those studied in molecular magnets by Godfrin *et al.* [43], where $\gamma \sim 10^{-4}$. Simulations were performed for even dimensions $d \in \{2, 4, 8, 16, 32\}$.

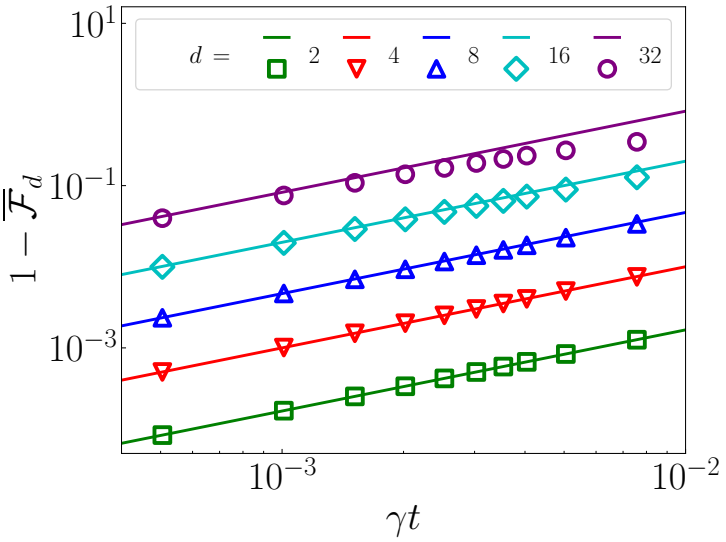


Figure 4.2 – Average gate infidelities as a function of γt for $H = \mathbb{O}_d$. The data points show the computed values. The solid lines represent the linear theoretical behaviour from Eq. (4.13). Each colour/marker pair corresponds to a different value of d.

The resulting AGIs were computed and presented in Fig. 4.2, together with the theoretically expected linear behavior of infidelity derived in Eq. (4.13).

This analysis revealed that the AGIs for the qudit systems closely followed the theoretically predicted linear behavior for small values of γt. The deviations from linearity were minimal, with the AGIs exhibiting a near-linear response to the noise rate γ and gate time t. Howwever, for larger values of γt, the AGIs began to deviate from the linear regime, as shown in Fig. 4.2. This deviation was more pronounced for higher-dimensional qudits, indicating that the linear approximation is more sensitive to noise for larger systems. Assuming that the prefactor of the $(\gamma t)^2$ term in the AGI series expansion scales as d^4, we estimate that the deviation from linearity becomes negligible when $\gamma t \ll \frac{1}{d^2}$, thereby providing a criterion for the validity of the linear approximation. Indeed, this nonlinear behaviour forms the basis of the subsequent study in Chapter 5.

4.4.3 Gate Dependence

While the AGI's linear behaviour does not scale favourably with d, as shown in Fig. 4.2, Eq. (4.13) possesses another key characteristic worth exploring: the gate independence of the AGI. To investigate this property, we examined a large number of random gates for a fixed dimension d. Specifically, random unitary gates from the group $U(d)$ were sampled from the circular unitary ensemble, which represents a uniform distribution over unitary square matrices of dimension d, known as the Haar measure on $U(d)$. These gates were then implemented on a qudit via a Hamiltonian derived using gradient-ascent methods.

We modelled qudits as ladder systems, with a pulse for each transition between adjacent levels, similar to the experimental setup by Godfrin *et al.* [43], who considered single-molecule magnets such as $TbPc_2$ with $d = 4$. In this setup, the $d - 1$ transitions were represented by independent control Hamiltonians within the interaction picture. It is important to note that multiple parameters can influence the results under consideration, such as the form of the free-evolution Hamiltonian and the matrix structure of the control pulses, both of which depend on the physical implementation. As such, other possible

	d	n	T_2	t_n	τ_n	ref.	platform
qubits	2	2	~ 10 μs	60 ns	$\sim 10^{-2}$	[13] (2020)	superconducting
	2	2	~ 2 μs	51 ns	$\sim 10^{-2}$	[19] (2020)	Rydberg atoms
	2	17	~ 30 μs	~ 100 ns	$\sim 10^{-3}$	[29] (2022)	superconducting
	2	24	~ 100 ms	~ 200 μs	$\sim 10^{-3}$	[14] (2021)	trapped ions
	2	1	~ 1 ms	~ 1 μs	$\sim 10^{-3}$	[20] (2023)	e^- SMM spins
qudits	4	1	0.32 ms	~ 100 ns	$\sim 10^{-4}$	[21] (2018)	nuc. SMM spins
	4	1	~ 100 μs	~ 150 ns	$\sim 10^{-3}$	[169] (2023)	superconducting
	3	2	~ 100 ms	~ 100 μs	$\sim 10^{-3}$	[132] (2022)	trapped ions
	4	2	$\infty^{(1)}$	–	0	[16] (2022)	photonic qudits
	52	1	–	~ 100 ns$^{(2)}$	–	[170] (2020)	Rydberg atoms

(1) considered unlimited by the source authors

(2) no universal gates for the moment, only specific quantum operations implemented

Table 4.1 – Decoherence times (T_2) and gate times (t_n) of different qubit/qudit platforms. d and n are the maximum dimension and number of qudits an operation was applied to, while $\tau_n = t_n/T_2$ is the figure of merit. Note that in the platform column: (i) superconducting refers to superconducting qubits, (ii) e^- SMM spins refers to electronic spins in molecular magnets, and (iii) nuc. SMM spins refers to nuclear spins in molecular magnets.

physical realisations and pulse reference frames were considered, and the deviations they introduce from linear behavior required detailed examination.

To this end, we computed the AGIs over a range of $\gamma t \in [10^{-5}, 10^{-3}]$, which aligns with the typical values seen in current quantum platforms, as summarised in Table 4.1. Without going into the details of this analysis here, we may remark that the AGI may only be considered gate-independent when $\gamma t \ll 1$ and $\gamma t \ll \dfrac{1}{||H||t}$. Indeed, the detailed study of the gate dependence of the AGI is the subject of Chapter 5.

4.4.4 Single Qudit vs Ensemble of Qubits

An ensemble of n qubits was simulated under identical pure dephasing conditions, with the Hamiltonian set to zero, $H = \mathbb{0}_{2^n}$, and using small values for $\gamma t \in [0, 10^{-4}]$. The simulations were carried out for qubit numbers ranging from $n = 1$ to $n = 7$. By fitting the AGI, $\overline{\mathscr{E}_{\mathrm{b},n}}(\mathcal{E}_z) = c_{\mathrm{b},n}\gamma t$, as a function of γt, the slopes $c_{\mathrm{b},n}$ were obtained.

The same simulations were performed on single-qudits of equivalent dimension $d = 2^n$. Figure 4.3 presents the key results of this study. The data points show the ratios $\frac{c_d}{c_{\mathrm{b},n}}$ for $n \in \{1, 6\}$ and d up to 64, along with the theoretical curve provided by Eq. (4.19).

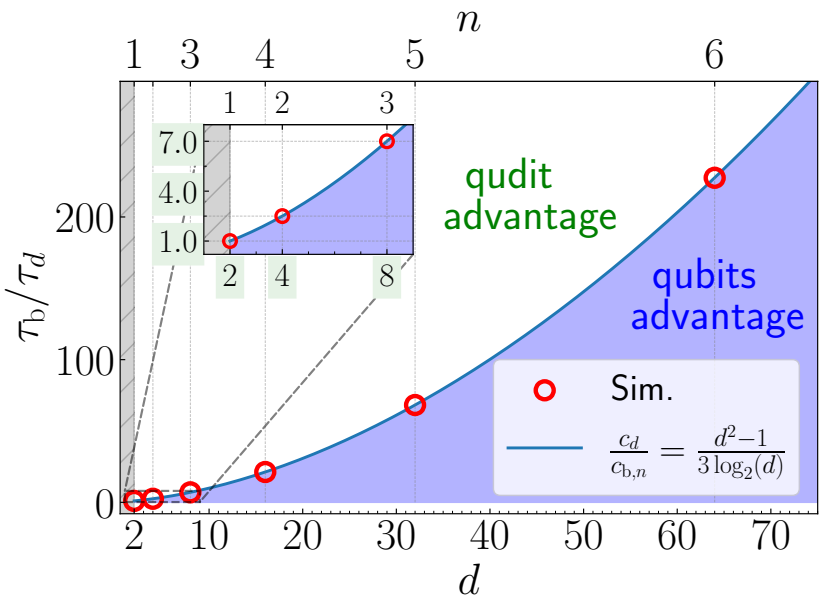


Figure 4.3 – Potential range for the figure of merits τ_b/τ_d. The rounded circles show the numerical values obtained for $c_d/c_{b,n}$. The solid curve comes from Eq. (4.19) and highlights the theoretical critical values of $T_{2,d}/T_{2,b}$.

This curve indicates the critical values of the figure of merit τ_b/τ_d, where $\tau_k = t_k/T_{2,k} = \gamma_k t_k/2$, thus providing a benchmark for qudit versus multi-qubit advantages in terms of the growth rate of the AGI. Table 4.2 summarises some values of interest, for instance, to achieve computational fidelity, a qudit with $d = 8$, a qu-8-it, must have a coherence time at least seven times longer than that of an equivalent three-qubit system for a fixed gate time. Note that a simpler scaling model of $\frac{d^2}{\log_2(d)}$ would predict a significantly higher threshold of 21.5.

Furthermore, Table 4.1 compares different state-of-the-art qudit platforms. For instance, single-qudit platforms such as trapped ions, as demonstrated in [132], exhibit coherence times on the order of 100 ms for qudits with $d = 7$, which are several orders of magnitude longer than those for superconducting qubits [13, 171, 172, 173]. Trapped ions achieve $\gamma t \approx 10^{-3}$, while superconducting qubits have $\gamma t \approx 10^{-2}$, leading to a ratio of 10, which suggests that qudits with $d \lesssim 10$ can be advantageous. Specifically, a single qu-7-it would maintain a higher average gate fidelity over a single gate acting on the entire Hilbert space compared to a multi-qubit system.

Finally, using the generalised results for N qudits, we were able to infer the conditions under which N qudits could outperform $N\log_2(d)$ qubits. In particular, if a single qudit outperforms $\log_2(d)$ qubits, this advantage is conserved as long as the gate time for multi-qudits scales more slowly from 1 to N qudits than it does from $\log_2(d)$ to $N\log_2(d)$ qubits.

Number n of qubits	Dimension d of the qudit	Critical τ_b/τ_d
1	2	1
2	4	2.5
3	8	7
6	64	227.5

Table 4.2 – Ratios of gate times in units of decoherence times between qubits and qudits. For specific values of n and d, (τ_b/τ_d needs to be larger than the critical values in order for a single qudit to be advantageous vs an equivalent ensemble of n qubits).

4.5 Discussion

4.5.1 Summary

In this study, we conducted a comparative analysis of gate efficiency for qudits and multi-qubit systems, taking into account the physical parameters that significantly affect their performance, such as decoherence time and Hilbert space dimension. By leveraging both analytical calculations and numerical simulations, *we derived in Eq. (4.6) a fluctuation-dissipation-like relation for gate infidelity in pure state operations.* A physically-informed methodology was developed to obtain the first-order effect of Markovian noise on the Average Gate Infidelity (AGI), which facilitated a connection to the initial gate-independent formulation.

We analysed the rate of increase of the AGI for single qudits and compared it against that of multiple qubits of equivalent Hilbert space dimension under pure dephasing. This comparison led to the derivation of a critical curve, which describes the ratio of their gate times in units of decoherence time. This curve effectively sets a benchmark for time-efficiency in gate operations, with values on either side indicating the system — qudit or multi-qubit — with superior gate fidelity. Importantly, the results show that, to maintain competitive fidelity as the dimension d increases, qudit gates must not only outperform multi-qubit gates by a factor of $O(d^2/\log_2(d))$ but by a more precise factor of $\frac{d^2-1}{3\log_2(d)}$, especially for lower d, where the constraint is less demanding.

Furthermore, we provided general analytical expressions for linear responses applicable to arbitrary collapse operators and multi-qudit systems. These formulations offer practical utility for benchmarking qudit platforms based on their maximal practical dimensionality or required figure of merit to compensate for increased noise when compared with multi-qubit counterparts.

The numerical simulations corroborated the validity of the linear response assumption and delineated its limitations by considering factors like qudit dimension, gate characteristics, and the nature of the noise. It was observed that the range of $\gamma t \ll 1$ decreases with increasing qudit dimension, yet the relative gate-dependent deviations also diminish. The simulations supported the analytical critical curve and allowed us to evaluate current quantum platforms with respect to their gate time efficiencies. For pure dephasing, certain qudit platforms—leveraging favorable decoherence times and rapid gate oper-

ations—were found to outperform multi-qubit platforms with equivalent Hilbert space dimensions. In particular, this performance extends to qudits with d up to ~ 40, as seen in the case of nuclear spins in molecular magnets.

4.5.2 Outlook

Although certain multi-qubit platforms currently offer superior scalability in the number of subsystems, the results suggest that scalable qudit systems may continue to outperform equivalent multi-qubit systems regarding gate fidelity. Further investigation into how gate times for multi-qudit and multi-qubit systems scale with subsystem count is warranted. This would provide a more comprehensive understanding of the trade-offs between the two systems and could inform the design of future quantum platforms.

The current analysis was restricted to the first-order response of noise. However, recent developments indicate that through appropriate quantum error correction strategies, it is possible to entirely nullify the first-order response in logical qudits (qu-k-its, $k < d$) encoded within physical qudits (qu-d-its) [33, 90]. This has promising implications for enhancing computational fidelity by embedding error-resilient logical operations within higher-dimensional physical systems. Therefore, by studying the higher-order noise responses in logical qudits, we can consider noise-robust encodings beyond the first-order response, which could further enhance the computational advantages of qudits.

A key avenue for future work lies in understanding the Hamiltonian-dependent behavior of the dimension-dependent AGI. Moreover, a comprehensive study of higher-order noise responses in logical qudits versus physical qubits is necessary to evaluate the robustness of the computational advantages presented by qudits, particularly in light of possible system scaling. Such an investigation would be critical to determine whether qudit advantages persist beyond the Noisy Intermediate-Scale Quantum (NISQ) era, contributing to the development of more resilient and scalable quantum platforms.

References Cited in this Chapter

[1] O. Ezratty. "Perspective on superconducting qubit quantum computing". In: *The European Physical Journal A* 59.5 (May 2, 2023), p. 94. DOI: 10.1140/epja/s10050-023-01006-7.

[13] M. Kjaergaard, M. E. Schwartz, et al. *Programming a quantum computer with quantum instructions*. Dec. 28, 2020. DOI: https://doi.org/10.48550/arXiv.2001.08838.

[14] I. Pogorelov et al. "Compact Ion-Trap Quantum Computing Demonstrator". In: *PRX Quantum* 2.2 (June 2021), p. 020343. DOI: 10.1103/PRXQuantum.2.020343.

[16] Y. Chi, J. Huang, et al. "A programmable qudit-based quantum processor". In: *Nature Communications* 13.1 (Mar. 4, 2022), p. 1166. DOI: 10.1038/s41467-022-28767-x.

[19] I. S. Madjarov et al. "High-fidelity entanglement and detection of alkaline-earth Rydberg atoms". In: *Nature Physics* 16.8 (Aug. 2020), pp. 857–861. DOI: 10.1038/s41567-020-0903-z.

[20] A. Chiesa et al. "Blueprint for a molecular-spin quantum processor". In: *Physical Review Applied* 19 (June 2023). Publisher: American Physical Society, p. 064060. DOI: 10.1103/PhysRevApplied.19.064060.

[21] E. Moreno-Pineda, C. Godfrin, et al. "Molecular Spin Qudits for Quantum Algorithms". In: *Chemical Society Reviews* 47.2 (2018), pp. 501–513. DOI: 10.1039/c5cs00933b.

[29] S. Krinner et al. "Realizing repeated quantum error correction in a distance-three surface code". In: *Nature* 605.7911 (May 2022), pp. 669–674. DOI: 10.1038/s41586-022-04566-8.

[31] Y. Wang, Z. Hu, et al. "Qudits and High-Dimensional Quantum Computing". In: *Frontiers in Physics* 8 (Nov. 10, 2020), p. 589504. DOI: 10.3389/fphy.2020.589504.

[33] A. Chiesa, F. Petiziol, et al. "Embedded quantum-error correction and controlled-phase gate for molecular spin qubits". In: *AIP Advances* 11.2 (Feb. 1, 2021), p. 025134. DOI: 10.1063/9.0000166.

[35] M. N. Leuenberger and D. Loss. "Grover algorithm for large nuclear spins in semiconductors". In: *Physical Review B* 68.16 (Oct. 16, 2003), p. 165317. DOI: 10.1103/PhysRevB.68.165317.

[43] C. Godfrin, A. Ferhat, et al. "Operating Quantum States in Single Magnetic Molecules: Implementation of Grover's Quantum Algorithm". In: *Physical Review Letters* 119.18 (Nov. 2, 2017), p. 187702. DOI: 10.1103/PhysRevLett.119.187702.

[75] J. Preskill. "Quantum Computing in the NISQ era and beyond". In: *Quantum* 2 (Aug. 6, 2018), p. 79. DOI: 10.22331/q-2018-08-06-79.

[85] D. Manzano. "A short introduction to the Lindblad master equation". In: *AIP Advances* 10.2 (Feb. 1, 2020), p. 025106. DOI: 10.1063/1.5115323.

[90] F. Petiziol, A. Chiesa, et al. "Counteracting dephasing in Molecular Nanomagnets by optimized qudit encodings". In: *npj Quantum Information* 7.1 (Aug. 26, 2021), p. 133. DOI: 10.1038/s41534-021-00466-3.

[97] N. Khaneja, T. Reiss, et al. "Optimal control of coupled spin dynamics: design of NMR pulse sequences by gradient ascent algorithms". In: *Journal of Magnetic Resonance* 172.2 (Feb. 2005), pp. 296–305. DOI: 10.1016/j.jmr.2004.11.004.

[122] D. Janković, J.-G. Hartmann, et al. "Noisy qudit vs multiple qubits: conditions on gate efficiency for enhancing fidelity". In: *npj Quantum Information* 10.1 (June 10, 2024), p. 59. DOI: 10.1038/s41534-024-00829-6.

[123] D. Jankovic. *Source Code for data generation and pulses data for Noisy Qudit vs Multiple Qubits*. In collab. with D. Jankovic. 2024. DOI: 10.35097/1953.

[124] A. S. Nikolaeva, E. O. Kiktenko, et al. "Efficient realization of quantum algorithms with qudits". In: *EPJ Quantum Technology* 11.1 (Dec. 2024), p. 43. DOI: 10.1140/epjqt/s40507-024-00250-0.

[125] N. Cao, J. Lin, et al. "NISQ: Error Correction, Mitigation, and Noise Simulation". In: (Nov. 3, 2021). DOI: 10.48550/arXiv.2111.02345.

[126] M. A. Nielsen. "A simple formula for the average gate fidelity of a quantum dynamical operation". In: *Physics Letters A* 303.4 (Oct. 2002), pp. 249–252. DOI: 10.1016/S0375-9601(02)01272-0.

[127] J. R. Johansson, P. D. Nation, et al. "QuTiP: An open-source Python framework for the dynamics of open quantum systems". In: *Computer Physics Communications* 183.8 (Aug. 2012), pp. 1760–1772. DOI: 10.1016/j.cpc.2012.02.021.

[128] J. R. Johansson, P. D. Nation, et al. "QuTiP 2: A Python framework for the dynamics of open quantum systems". In: *Computer Physics Communications* 184.4 (Apr. 2013), pp. 1234–1240. DOI: 10.1016/j.cpc.2012.11.019.

[132] M. Ringbauer, M. Meth, et al. "A universal qudit quantum processor with trapped ions". In: *Nature Physics* 18.9 (Sept. 2022), pp. 1053–1057. DOI: 10.1038/s41567-022-01658-0.

[165] R. Jozsa. "Fidelity for Mixed Quantum States". In: *Journal of Modern Optics* 41.12 (Dec. 1994), pp. 2315–2323. DOI: 10.1080/09500349414552171.

[166] N. Johnston and D. W. Kribs. "Quantum gate fidelity in terms of Choi matrices". In: *Journal of Physics A: Mathematical and Theoretical* 44.49 (Dec. 9, 2011), p. 495303. DOI: 10.1088/1751-8113/44/49/495303.

[167] M. Suezen, C. Weber, et al. *Spectral Ergodicity In Deep Learning Architectures Via Surrogate Random Matrices*. July 3, 2017. DOI: 10.5281/zenodo.822410.

[168] T. Abad, J. Fernández-Pendás, et al. "Universal Fidelity Reduction of Quantum Operations from Weak Dissipation". In: *Physical Review Letters* 129.15 (Oct. 7, 2022), p. 150504. DOI: 10.1103/PhysRevLett.129.150504.

[169] S. Cao, M. Bakr, et al. "Emulating two qubits with a four-level transmon qudit for variational quantum algorithms". In: *Quantum Science and Technology* 9.3 (July 1, 2024), p. 035003. DOI: 10.1088/2058-9565/ad37d4.

[170] A. Larrouy et al. "Fast Navigation in a Large Hilbert Space Using Quantum Optimal Control". In: *Physical Review X* 10.2 (June 2020), p. 021058. DOI: 10.1103/PhysRevX.10.021058.

[171] A. Ozaeta and P. L. McMahon. "Decoherence of up to 8-qubit entangled states in a 16-qubit superconducting quantum processor". In: *Quantum Science and Technology* 4.2 (Apr. 2019), p. 025015. DOI: 10.1088/2058-9565/ab13e5.

[172] Y. Chen et al. "Qubit Architecture with High Coherence and Fast Tunable Coupling". In: *Physical Review Letters* 113.22 (Nov. 2014), p. 220502. DOI: 10.1103/PhysRevLett.113.220502.

[173] S. Rosenblum et al. "A CNOT gate between multiphoton qubits encoded in two cavities". In: *Nature Communications* 9.1 (Feb. 2018), p. 652. DOI: 10.1038/s41467-018-03059-5.

CHAPTER 5

NONLINEARITY OF THE FIDELITY IN OPEN QUDIT SYSTEMS: GATE AND NOISE DEPENDENCE IN HIGH-DIMENSIONAL QUANTUM COMPUTING

In Hilbert space, no one can hear you scream.

- Yakir Aharonov

Contents

5.1 Introduction . . . 125
5.1.1 Background and Motivation . . . 125
5.1.2 Objectives and Contributions . . . 126
5.1.3 Overview . . . 126
5.2 Theory . . . 127
5.2.1 Mathematical Foundations of the Average Gate Fidelity . . . 127
5.2.2 Generalised Operators on Qudits . . . 129
5.3 Methods . . . 131
5.3.1 Numerical Tools . . . 131
5.3.2 Simulation Configuration . . . 132
5.4 Results . . . 134
5.4.1 Perturbative Expansion of the Average Gate Infidelity . . . 134
5.4.2 Nonlinearity of the AGI in the Strong Coupling Regime . . . 137
5.4.3 Distribution of the AGI for Random Qudit Gates . . . 139
5.4.4 Gate- and Noise-Dependence of the Fidelity . . . 147
5.4.5 First- and Second-Order Correction Terms to the AGI . . . 152
5.5 Discussion . . . 158
5.5.1 Summary . . . 158
5.5.2 Outlook . . . 159
References Cited in this Chapter . . . 161

Note: This Chapter is directly adapted from a paper of the same title published in Quantum and also uploaded as a preprint manuscript to the arXiv. The bibliographical citation of the article can be found in [129], and all code and data used to generate the results presented in this study have been made publicly available on Zenodo [130].

5.1 Introduction

In this chapter, we extend the work of Chapter 2, building upond the theoretical framework developed in [122] to investigate the Average Gate Fidelity (AGF) of single qudit systems under Markovian noise in the Lindblad formalism. We focus on the perturbative expansion of the Average Gate Infidelity (AGI), enabling the calculation of higher-order correction terms to the AGF beyond the linear regime, and exploring the implications of gate dependence on the robustness of noisy quantum systems.

5.1.1 Background and Motivation

High-dimensional quantum computing (QC) has generated remarkable scientific interest of late, introducing a shift from traditional computing paradigms. While qubit-based quantum information processing (QIP) platforms, particularly superconducting qubits, have the highest technological maturity, they are faced with near-term technical challenges of scalability and error correction [1, 131]. On the other hand, recent advancements have highlighted the potential of qudits — quantum systems with d levels — as powerful alternatives for novel QC architectures [16, 21, 41, 132].

Indeed, qudits offer several advantages, including (i) lower decoherence rates in certain physical systems [31], (ii) enhanced quantum error correction through additional levels [33, 90, 133] and stabiliser codes [134], as well as (iii) higher information density for reducing circuit complexity and enabling novel algorithm design [56]. They also promise more robust flying quantum memories [135, 136].

While classical computing ultimately settled on bits once sufficient scalability and fault-tolerance were achieved, early platforms did experiment with multi-level systems [32]. Analogously, it can be argued that quantum computing's infancy stage could benefit from exploring higher-dimensional bases to address these current issues. In the push towards universal QC, increasing the total Hilbert space dimension of quantum systems is critical [137]. This dimension is determined by d^n, where d is the dimensionality and n the number of qudits. Despite impressive advancements in superconducting platforms [26], scaling the number of qubits continues to pose significant challenges. Thus, qudit-based approaches may provide an avenue for increasing the Hilbert space with fewer physical units [26, 42, 43, 132].

On the other hand, with the increased number of excited states utilised to implement higher-dimensional states in physical systems, qudits may introduce a greater number of error channels compared to qubits. This could lead to increased sensitivity to environmental noise, affecting coherence times and complicating error correction processes [138].

5.1.2 Objectives and Contributions

In a previous paper [122], we studied this scenario in detail by comparing the effects of Markovian noise on multi-qubit and single-qudit systems of equal Hilbert space dimension. We developed a theoretical model of the first-order effects of the noise in the Lindblad formalism, demonstrating how the noise impacts the performance of quantum gates in these different systems, and supported these results with numerical simulations.

The fundamental quantities investigated were the average gate fidelity (AGF, $\bar{\mathcal{F}}$) - equivalently infidelity (AGI, $\bar{\mathcal{I}}$) - and the figure-of-merit ($\tau = t_{gate}/T_2$). As the name suggests, the AGF is useful in that it integrates out any specific features due to a particular choice of initial state. Therefore, unlike the state fidelity or process fidelity, which compute the target-to-output overlaps of quantum state transfers and unitary gates, respectively, the AGF is fundamental as a platform-agnostic measure of the quality of a system's interaction with its environment [126, 139]. Similarly, the figure-of-merit is important for quantifying realistically the circuit depth that can be achieved in a system, based on the gate time, t_{gate}, and decoherence time, T_2.

Those results showed that in the quasi-error-free - weak coupling - regime, the first-order response of the AGI (a linear function of the dimensionless coupling strength γt_{gate}) was sufficient to characterise the behaviour of the qudit or multi-qubit system. However, first-order approximations are insufficient for fully understanding the behaviour of qudits under realistic, near-term, conditions where higher-order noise effects are expected to become significant, either through stronger coupling or longer gate times (or circuit depths) approaching the decoherence limit.

Thus, this study aims to extend the understanding of the AGF of single qudit systems under Markovian noise conditions through a general perturbative expansion. Specifically, we focus on higher-order correction terms and their implications on quantum gate performance in the strong coupling regime. Building upon our previous work, we develop a comprehensive theoretical framework that includes these nonlinear effects, with a constructive method generalising the AGF to arbitrary order in γt. This is supported by detailed numerical simulations, with an emphasis on the differences between the first and second order terms in the case of pure dephasing. By doing so, we aim to capture the nuanced impact of noise on the fidelity of quantum gates more precisely.

The key research question addressed in our study is: How do higher-order correction terms and noise coupling strength influence the AGI of single qudit systems, and what implications do these have for the selection and design of quantum gates? Our findings provide important insights on: (i) setting benchmarks, as well as limits, for the performance of noisy quantum systems of arbitrary dimension by identifying gate-dependent effects, (ii) methodologies for improving performance through optimising basis gates that have favourable decoherence characteristics, and (iii) advancing error correction protocols by enabling the cancellation of higher-order noise effects.

5.1.3 Overview

The chapter is structured as follows: We begin in Section 5.2 with a review of the relevant theoretical background concerning the Lindblad formalism for qudit open quantum systems and the superoperator representation of noisy quantum channels, as well as generalised quantum gates on qudits.

In Section 5.4.1, we present our general result for the perturbative expansion of the AGI

in noise strength, deriving the general expressions to arbitrary order in γt and discussing the implications of its structure.

Section 5.4.2 examines the nonlinearity of the AGI in the strong coupling regime of pure dephasing through numerical simulations that elucidate key characteristics of this behaviour and motivate the proceeding investigations that make the link with the theoretical results. Subsequently, in Section 5.4.4 we explore the gate- and noise-dependence of the AGI, with particular emphasis on how the choice of quantum gate can influence the performance of the quantum channel.

Finally, Section 5.4.5 presents a detailed analytical and numerical study of the first- and second-order correction terms to the AGI, extending the results of the previous work and placing them on a more rigorous theoretical foundation that serves future investigations.

5.2 Theory

5.2.1 Mathematical Foundations of the Average Gate Fidelity

5.2.1.1 Lindblad formalism for open qudit systems

We begin with the study of a single qudit, of arbitrary dimension d, whose state is represented by a $d \times d$ density matrix $\rho(t)$, and evolves according to the Gorini-Kossakowski-Sudarshan-Lindblad (GKSL) master equation [83, 84], which may be expressed in superoperator form as [174]

$$\partial_t \rho = \mathcal{S}[\rho] + \mathcal{D}[\rho]. \tag{5.1}$$

Here, setting $\hbar = 1$, the Liouvillian superoperator $\mathcal{S}$ represents the unitary evolution operator of the von Neumann equation, and $\mathcal{D}$ the dissipation superoperator coupling the qudit to the environment,

$$\mathcal{S}[\rho] = -i[H, \rho], \tag{5.2}$$

$$\mathcal{D}[\rho] = \sum_{k=1}^{K} \gamma_k \mathcal{L}_k[\rho] \tag{5.3}$$

$$= \sum_{k=1}^{K} \gamma_k \left(L_k \rho L_k^\dagger - \frac{1}{2} \left\{ L_k^\dagger L_k, \rho \right\} \right), \tag{5.4}$$

where H is the time-independent interaction Hamiltonian, and L_k one of K possible collapse operators characterising the Markovian noise with coupling coefficient γ_k and $\mathcal{L}_k$ the matrix superoperator form [85].

The solution to the master equation for $\rho(0) = \rho_0$ is therefore given by the completely-positive and trace-preserving (CPTP) quantum channel $\mathcal{E}$ as [175]

$$\rho(t) = \mathcal{E}[\rho_0] \tag{5.5}$$

$$= e^{(\mathcal{S}+\mathcal{D})t} \rho_0. \tag{5.6}$$

5.2.1.2 Superoperator representation of noisy quantum channels

Considering the application of a quantum gate $\mathcal{U}[\rho] = U\rho U^\dagger$ to the system then corresponds to a composition operation, that in the matrix superoperator representation reduces to the matrix product, from which we may express the AGF, $\bar{\mathcal{F}}(\mathcal{E},\mathcal{U})$, of implementing a unitary operator over the quantum channel in the presence of a noisy environment [126]:

$$\bar{\mathcal{F}}(\mathcal{E},\mathcal{U}) = \int_{\mathscr{H}} \left\langle U^\dagger \mathcal{E}[\rho_0] U \right\rangle_0 d\rho_0, \tag{5.7}$$

$$1 - \bar{\mathcal{I}}(\mathcal{E},\mathcal{U}) = \int_{\mathscr{H}} \left\langle \left(\mathcal{U}^\dagger \circ \mathcal{E}\right)[\rho_0] \right\rangle_0 d\rho_0. \tag{5.8}$$

The integral is taken uniformly over the Haar measure $\mathscr{H}$ of the state space, with the expectation value $\langle \mathcal{A} \rangle_0 = \mathrm{Tr}\{\mathcal{A}\rho_0\}$ representing the average over all initial states. For convenience, we shall use $\bar{\mathcal{F}}$ and $\mathcal{F}$ interchangeably for the AGF, and likewise for the AGI.

In this study we shall consider pure initial states, $\mathrm{Tr}\{\rho_0^2\} = 1$. Then the state space is reduced to the complex-projective space $\mathbb{C}\mathbf{P}^{d-1}$ such that the Haar measure (over all ρ_0) then induces the Fubini-Study measure, the integral of which is normalised, $\int_{\mathscr{H}} d\rho_0 = 1$, [176] and may be calculated analytically (see Appendix D.2.1). Furthermore, unless specified, we shall also assume that: (i) the dissipator term is dominated by a single noise channel, such that $\mathcal{D} = \gamma\mathcal{L}$, (ii) the associated superoperators $\mathcal{S}$ and $\mathcal{L}$ are time-independent and (iii) we are working in the interaction picture, such that the free evolution Hamiltonian $H_0 = \mathbb{0}_d$, and therefore $\mathcal{S}_0 = \mathbb{0}_{d\times d}$ such that the unitary evolution simplifies to $\mathcal{U} = e^{(\mathcal{S}_0+\mathcal{S}_c)t} = e^{\mathcal{S}t}$ with $\mathcal{S} = \mathcal{S}_c$ corresponding to only the control (driving) Hamiltonian $H = H_c$ implementing the quantum gate. This allows us to rewrite Eqs. (5.5) and (5.6) as

$$\mathcal{E}[\rho_0] = e^{(\mathcal{S}+\gamma\mathcal{L})t}\rho_0. \tag{5.9}$$

We note that the $(d \times d) \times (d \times d)$ superoperators acting on the $\mathcal{H} \otimes \mathcal{H}$ Hilbert space of the quantum dynamical semigroup (QDS) may be written explicitly in Liouville matrix form in terms of the standard operator form as [177]:

$$\mathcal{U}[\cdot] = (U^* \otimes U)\,\mathrm{vec}(\cdot), \tag{5.10}$$

$$\mathcal{S}[\cdot] = -i\left(\mathbb{1}_d \otimes H - H^T \otimes \mathbb{1}_d\right)\mathrm{vec}(\cdot), \tag{5.11}$$

$$\mathcal{L}[\cdot] = \left(L^* \otimes L - \frac{1}{2}\left(L^\dagger L \otimes \mathbb{1}_d + \left(\mathbb{1}_d \otimes L^\dagger L\right)^T\right)\right)\mathrm{vec}(\cdot), \tag{5.12}$$

where we identify the adjoint ($\dagger$), complex-conjugate ($*$) and transpose (T) operations, $\mathbb{1}_d$ the $d \times d$ identity matrix, $\otimes$ the tensor, or equivalently here for linear maps, the Kronecker product, and $\mathrm{vec}(\cdot)$ the vectorisation operation that, when applied to a $d \times d$ density matrix ρ, produces a $1 \times d^2$ column vector by stacking vertically each column of the matrix from left to right. This corresponds to the explicit mapping

$$\mathrm{vec}(\rho) \;:\; \sum_{i,j} \rho_{ij}\,|i\rangle\langle j| \;\rightarrow\; \sum_{i,j} \rho_{ij}\,|j\rangle \otimes |i\rangle, \tag{5.13}$$

of the quantum state from the Hilbert to the Fock-Liouville space [85]. Furthermore, the quantum gate U_g and associated control Hamiltonian H_c (and their respective superoperator representations $\mathcal{U}$ and $\mathcal{S}$) are related by the matrix exponent (and, inversely)

logarithm operations. Therefore, given some quantum gate, it may be implemented by the control term,

$$H_c t_g = i \log U_g, \tag{5.14}$$

where the now time-independent H_c represents a single, ideal control pulse that implements the gate in time t_g, which can be modulated by the absolute amplitude of the pulse $\|H_c\|$. Existence and uniqueness of the matrix logarithm map are well established under the conditions that U_g is unitary and $-\pi < H_c t_g \leq \pi$ [178]. This is an idealisation that necessitates simultaneous control over all pulse amplitudes, phases and detunings on each possible transition between all d states. Platform-dependent physical constraints on the control pulses may preclude experimental realisation of such a control term. Nevertheless it allows for a time-optimal multi-chromatic pulse for studying the robustness of quantum gates that is independent of constraints imposed by the physical platform or pulse control technique [179].

5.2.2 Generalised Operators on Qudits

5.2.2.1 Quantum gates

We now precisely define the gate and collapse operators that will be of interest in this study. We begin with the following set of single-qudit quantum gates $U_g \in \{\mathbb{1}, X, Z, F\}$ that generalise the single-qubit identity, Pauli-x, Pauli-z and Hadamard gates to d dimensions, and generate the d-dimensional generalised Clifford algebra (GCA) [180]

$$\mathbb{1}_d = \sum_{j=0}^{d-1} |j\rangle\langle j| , \tag{5.15}$$

$$X_d = \sum_{j=0}^{d-1} |(j+1) \bmod d\rangle\langle j| , \tag{5.16}$$

$$Z_d = \sum_{j=0}^{d-1} \omega^j |j\rangle\langle j| , \tag{5.17}$$

$$F_d = \frac{1}{\sqrt{d}} \sum_{j=0}^{d-1} \sum_{k=0}^{d-1} \omega^{jk} |j\rangle\langle k| , \tag{5.18}$$

where $\omega = e^{\frac{2\pi i}{d}}$ is the d-th root of unity. The subscript d is used to specify the dimension of the operator, and may be omitted in cases where it is clear from context or when referring to the general operator. The X, Z and F gates retain unitarity (and tracelessness for X and Z) as well as the relations $X^d = Z^d = \mathbb{1}_d$ and $X = FZF^\dagger$ of involution and change-of-basis, respectively. However, it is worth noting that they are no longer Hermitian for $d > 2$. Furthermore, in the generalised forms, it can be observed that (i) X is extended from a bit-flip (NOT) gate to a cyclic permutation (INC/ SHIFT) gate that increments the qudit state, (ii) Z is extended from a phase-flip to a phase-shift (CLOCK) gate of each state over the d roots of unity, and (iii) the Walsh-Hadamard gate is extended to the matrix form of the Quantum Fourier Transform (QFT) (equivalently referred to as the Discrete Fourier Transform, Sylvester or Chrestenson matrix).

Given this set of single-qudit gates $U_g \in \{\mathbb{1}_d, X, Z, F\}$, we present them in matrix form to illustrate their structure. The identity matrix in d dimensions is trivial, and generated

by a null control Hamiltonian $H_c = \mathbb{0}_d$, corresponding to no action on the qudit state. The generalised Pauli-X or SHIFT gate $X = \Sigma_x$ is defined as

$$X = \begin{bmatrix} 0 & 1 & 0 & 0 & \cdots & 0 \\ 0 & 0 & 1 & 0 & \cdots & 0 \\ 0 & 0 & 0 & 1 & \cdots & 0 \\ \vdots & \vdots & \vdots & \vdots & \ddots & \vdots \\ 0 & 0 & 0 & 0 & \cdots & 1 \\ 1 & 0 & 0 & 0 & \cdots & 0 \end{bmatrix},$$

which cyclically permutes the basis states, incrementing them all by 1 level. An equivalent formulation is given by the transpose X^T, which cyclically permutes the states downwards,

$$X^T = \begin{bmatrix} 0 & 0 & 0 & \cdots & 0 & 1 \\ 1 & 0 & 0 & \cdots & 0 & 0 \\ 0 & 1 & 0 & \cdots & 0 & 0 \\ 0 & 0 & 1 & \cdots & 0 & 0 \\ \vdots & \vdots & \vdots & \ddots & \vdots & \vdots \\ 0 & 0 & 0 & \cdots & 1 & 0 \end{bmatrix}.$$

The generalised Pauli-Z or CLOCK gate $Z = \Sigma_z$ is defined as

$$Z = \begin{bmatrix} 1 & 0 & 0 & \cdots & 0 \\ 0 & \omega & 0 & \cdots & 0 \\ 0 & 0 & \omega^2 & \cdots & 0 \\ \vdots & \vdots & \vdots & \ddots & \vdots \\ 0 & 0 & \cdots & 0 & \omega^{d-1} \end{bmatrix},$$

where the d-th roots of unity, ω, are also used to define the matrix form of the Quantum Fourier Transform in d dimensions, being the generalisation of the Walsh-Hadamard (superposition) gate,

$$F = \frac{1}{\sqrt{d}} \begin{bmatrix} 1 & 1 & 1 & 1 & \cdots & 1 \\ 1 & \omega & \omega^2 & \omega^3 & \cdots & \omega^{d-1} \\ 1 & \omega^2 & \omega^4 & \omega^6 & \cdots & \omega^{2(d-1)} \\ 1 & \omega^3 & \omega^6 & \omega^9 & \cdots & \omega^{3(d-1)} \\ \vdots & \vdots & \vdots & \vdots & \ddots & \vdots \\ 1 & \omega^{d-1} & \omega^{2(d-1)} & \omega^{3(d-1)} & \ldots & \omega^{(d-1)(d-1)} \end{bmatrix}.$$

Now, we introduce the interpolated X (SHIFT) and Z CLOCK gates, where we raise the X and Z gates to the power $\eta \in [0, 1]$, which allows us to smoothly interpolate the action of the gate(s) between the identity ($\eta = 0$) and the original gate ($\eta = 1$). As an example, consider $\eta = \frac{3d-2}{4d}$ for $d = 2$:

$$X^{0.5} = \frac{1}{\sqrt{2}} \begin{bmatrix} e^{i\frac{\pi}{4}} & e^{-i\frac{\pi}{4}} \\ e^{-i\frac{\pi}{4}} & e^{i\frac{\pi}{4}} \end{bmatrix}.$$

5.2.2.2 Collapse operators

Regarding the choice of collapse operators $L \in \{J_z, J_x\}$ representing the coupling of the qudit to the environment in the master equation, we shall primarily consider the effect of pure dephasing by the operator J_z, and of secondary consideration is the bit-flip error effected by the operator J_x. These higher-order spin operators from spin-$\frac{1}{2}$ to spin-$\frac{d-1}{2}$ can be obtained through the generalised Gell-Mann matrices, and written as

$$J_z = \sum_{j=1}^{d} \frac{1}{2}(d+1-2j)\,|j\rangle\langle j| \tag{5.19}$$

$$J_x = \sum_{j=1}^{d-1} \frac{1}{2}\sqrt{j(d-j)}\,(|j+1\rangle\langle j| + |j\rangle\langle j+1|) \tag{5.20}$$

We present a brief example for the collapse operators of pure dephasing and bit-flip. In $d = 4$, these are precisely the generalised spin operators J_z and J_x for spin-$\frac{3}{2}$ systems, given by

$$J_z = \frac{1}{2}\begin{bmatrix} 3 & 0 & 0 & 0 \\ 0 & 1 & 0 & 0 \\ 0 & 0 & -1 & 0 \\ 0 & 0 & 0 & -3 \end{bmatrix},$$

and

$$J_x = \frac{1}{2}\begin{bmatrix} 0 & \sqrt{3} & 0 & 0 \\ \sqrt{3} & 0 & 2 & 0 \\ 0 & 2 & 0 & \sqrt{3} \\ 0 & 0 & \sqrt{3} & 0 \end{bmatrix}.$$

5.3 Methods

In this section, we describe in detail the numerical methods used to simulate the AGI of single qudit systems under Markovian noise and to generate the results presented in the following sections. All data and source code used for generating the results are publicly available on Zenodo [130].

5.3.1 Numerical Tools

All numerical simulations were performed using the Python programming language version 3.9.5. We categorise the libraries used into three groups: standard, external, and custom libraries. Standard libraries are built-in libraries that come with the Python distribution, external libraries are third-party libraries that are freely available for download, and custom libraries are those developed specifically for this or other studies.

The following built-in libraries were used in the simulations: The `pickle` library was used for serialising and deserialising Python objects to save and load simulation result data files. The `joblib` library, specifically the `Parallel` function, was used to parallelise the simulations across multiple CPU cores. Additional libraries included `os`, `time`, `math`, `sys`, amongst others.

See Appendix D.1 for a detailed list of all the third-party libraries used and their respective versions.

QuTiP is an open-source quantum computing library for Python that provides a wide range of tools for simulating quantum systems, including the Lindblad master equation solver used in this study. The library is well-documented and has a large user base, making it an ideal choice for our numerical simulations. QuTiP version 4.7.1 was used for all simulations. The following functions are of particular note: `mesolve` and `propagator` for solving the master equation and calculating the time evolution propagator, and `to_super`, `spre`, `spost` and `sprepost` for computing the superoperator representation of quantum operators. Furthermore, random unitary gates were generated using the functions `rand_unitary_haar` and `rand_unitary`. Regarding the calculation of the fidelity, we implemented the updated `process_fidelity` function introduced in version 5.0.0 of QuTiP, from which we calculated the AGI.

NumPy is a fundamental library for scientific computing in Python that provides support for large multi-dimensional arrays and matrices. We used NumPy version 1.24.3 for various tasks, such as generating random numbers, performing matrix operations, and calculating the trace of matrices. In particular, the `linalg` sub-package was used for studying the eigenvalue distributions of random unitary matrices in Section 5.4.3.

SciPy version 1.14.0 was used for numerical integration and optimisation tasks. Sub-package `linalg` was used for matrix operations, `interpolate` for spline interpolation with function `CubicSpline`, `stats` for statistical functions and curve fitting with function `linregress`. Numerical optimisation was done with the `optimize` sub-package using functions `root_scalar`, `curve_fit`, `minimize_scalar` and `fsolve`.

Matplotlib version 3.7.1 was used for creating plots and visualising the simulation results. The `pyplot` module was used to generate line plots, histograms, and heatmaps, and the `cm` module was used to access the colour maps for the plots.

Additional statistical modelling was performed using StatsModels library version 0.14.1 and Scikit-learn library version 1.4.1.

Cirq version 1.2.0 was also used for additional methods for generating unitary quantum gates with functions `random_unitary` and `random_special_unitary` in sub-package `testing.lin_alg_utils`.

The Bristol library version 0.2.14 [167] was used for sampling unitary matrices from the Circular Unitary Ensemble using `Circular.gen_cue`. A custom library was developed for generating the generalised single-qudit gates and collapse operators, encapsulated the `Qudit` class for simulation of qudit systems of arbitrary dimension. A custom function, `compute_matrix_logarithm` was also implemented for computing the matrix logarithm of a given unitary gate in order to implement the idealised control Hamiltonian, based on [178]. This was necessitated by observations of numerical instability and inaccuracies in the SciPy.`linalg.logm` function for certain unitary matrices.

5.3.2 Simulation Configuration

We now describe the configuration of the simulations used to generate the results presented in the following sections. We divide the configuration into two parts: internal parameters and input parameters. Internal parameters are constants that are fixed during the simulations, and do not necessarily reflect the physical system being studied.

Input parameters, on the other hand, are variables that can be adjusted to explore different aspects or systems.

Each individual simulation and calculation of an AGI quantity is uniquely specified by the following parameters: the dimension of the qudit d, the coupling strength γ of the choice of collapse operator L, and the gate time t_{gate} of the particular quantum gate U_g. Furthmore, for the purposes of the simulations presented in Section 5.4, depending on the particular investigation, we extend the calculations through parallelisation to compute the AGIs for a large number of unique configurations. For example, for a set of N randomly generated gates, or for a range of gate times or coupling strengths or even covering a set of different qudit dimensions. The particular values of these parameters are detailed in the respective sections of the results and associated figure captions.

Also important to note are the internal parameters that specify auxiliary settings for the simulations. The choice of quantum gate, specific to the particular test, is selected from the set of generalised single-qudit gates $U_g \in \{\mathbb{1}_d, X, Z, F\}$, X^η. The random gates were all generated by the QuTiP function `rand_unitary_haar`.

Except for Fig. 5.13 simulating bit-flip errors due to the action of the $L = J_x$ collapse operator, all simulations were performed for qudits under the effect of pure dephasing noise due to $L = J_z$. Regarding the Hamiltonian evolution, as noted in Eq. (5.14), the control Hamiltonian H_c was implemented by the matrix logarithm of the quantum gate U_g to implement the gate in time t_{gate}. Apart from Fig. 5.16, the gate time for all gates was normalised to 1, such that the dimensionless noise-time product γt_{gate} is modulated only by γ.

The final specification of the time evolution operations through the `propagator` function were the options for the numerical solver. Here, we used the implicit backwards-differentiation `bdf` solver for stiff systems due to the appearance of multiple timescales in the master equation due to the noise effects in the strong coupling regime. The tolerances were set to 1×10^{-8} for the absolute and relative tolerances, and the maximum number of iterations was set to 10^6 with a maximum step size of 10^{-3}. This was sufficient for most simulations, though for qudit dimensions $d > 12$ at very large coupling strengths, the solver required additional iterations and smaller step sizes to converge, 10^8 and 10^{-4} being sufficient up to $d = 16$, respectively.

Additional parameters used post-AGI computation included the number of bins for the histogram plots, calculated by Sturges' formula, and the tolerances and error thresholds for the curve fitting, statistical analyses, calculation of the AGI saturation points and the convergence of the second-order iterated commutators in the perturbative expansion.

Finally, for each test, once the total number of configurations was decided, the number of cores used was set to the maximum available on the machine, and the batch sizes calculated to ensure that each core was assigned an equal computational load.

5.4 Results

5.4.1 Perturbative Expansion of the Average Gate Infidelity

5.4.1.1 General case

Given the simplified expression for the time-evolution of the quantum channel $\mathcal{E}$ in (5.9), we want to study the effects on the AGF, not only from the choice of $\mathcal{S}$ or $\mathcal{L}$, but also from the coupling strength γ. Therefore, performing a Taylor series expansion of the AGF in powers of γ,

$$\bar{\mathcal{F}}(\mathcal{E},\mathcal{U}) = 1 - \sum_{m=1}^{\infty} \gamma^m F^{(m)}(t). \tag{5.21}$$

To calculate explicitly the correction terms $F^{(m)}$, we begin by expanding the solution to the master equation,

$$\rho(t) = \rho^{(0)} + \sum_{m=1}^{\infty} \gamma^m \rho^{(m)}, \tag{5.22}$$

where the m-th order correction to the non-perturbed solution of the master equation can be written as [181, 182]

$$\rho^{(m)} = e^{\mathcal{S}t} \left(\int_0^t \int_0^{t_1} \cdots \int_0^{t_{m-1}} \left(\prod_{i=1}^{m} e^{-\mathcal{S}t_i} \mathcal{L} e^{\mathcal{S}t_i} \right) dt_m \cdots dt_2 dt_1 \right) \rho_0, \tag{5.23}$$

and we separate the zero order term $\rho^{(0)}$ from the summation, since it corresponds to only unitary evolution through the von Neumann equation in the abscence of environmental coupling.

We may then define a new quantity $\tilde{M}^{(m)}(t)$ containing the integral terms, such that $\rho^{(m)} := e^{\mathcal{S}t} \left(\tilde{M}^{(m)}(t) \right) \rho_0$, and therefore the m-th order of the solution to the master equation in terms of the quantum channel reduces to $\mathcal{E}^{(m)} = \mathcal{U} \circ M^{(m)}(t)$. Now, in order to render this term $\tilde{M}^{(m)}(t)$ into a more computationally tractable form, we make use of the eponymous lemma of Campbell resulting from the Baker-Campbell-Hausdorff (BCH) Formula [183, 184],

$$e^X Y e^{-X} = \sum_{n=0}^{\infty} \frac{[(X)^n, Y]}{n!}, \tag{5.24}$$

utilising the iterated commutator defined by the recursion relation

$$[(X)^n, Y] = \left[X, \left[(X)^{n-1}, Y\right]\right] \tag{5.25}$$

with the halting condition $\left[(X)^0, Y\right] = Y$. With $\mathcal{S}$ and $\mathcal{L}$ time-independent, $\tilde{M}^{(m)}(t)$ simplifies to (see Appendix D.2.1)

$$\tilde{M}^{(m)}(t) = t^m \sum_{n_1=0}^{\infty} \sum_{n_2=0}^{\infty} \cdots \sum_{n_m=0}^{\infty} \left(\prod_{i=1}^{m} \frac{(-t)^{n_i} [(\mathcal{S})^{n_i}, \mathcal{L}]}{n_i! \sum_{j=i}^{m} (n_j + 1)} \right) \tag{5.26}$$

$$= t^m \frac{\mathcal{L}^m}{m!} + t^m \sum_{n_1=1}^{\infty} \sum_{n_2=1}^{\infty} \cdots \sum_{n_m=1}^{\infty} \left(\prod_{i=1}^{m} \frac{(-t)^{n_i} [(\mathcal{S})^{n_i}, \mathcal{L}]}{n_i! \sum_{j=i}^{m} (n_j + 1)} \right). \tag{5.27}$$

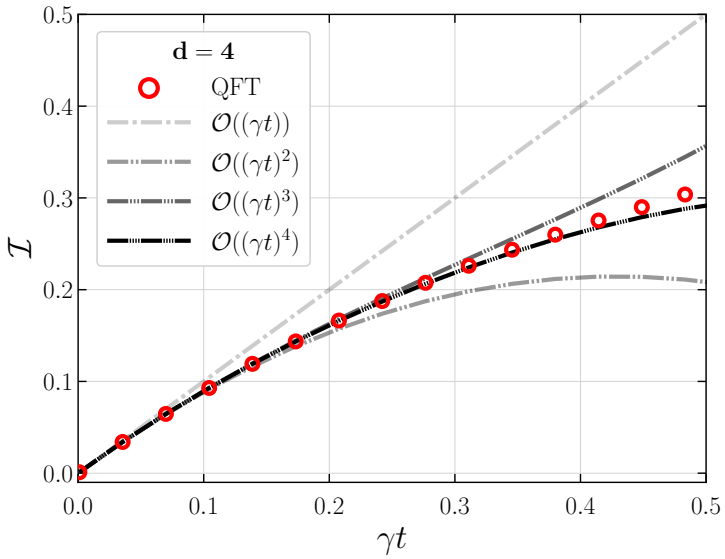


Figure 5.1 – Comparison of the first four correction terms of the AGI to numerical simulations. AGIs for the QFT gate applied to a $d = 4$ qudit undergoing pure dephasing ($L = J_z$) at couplings $\gamma t \in [0, 0.5]$. The discrete points (red) represent the simulated AGI values, while the successive dashed-dotted lines represent the correction terms from first to fourth order.

For the sake of future convenience, we define the new quantity $\tilde{M}^{(m)}(t) := t^m M^{(m)}(t)$, from which we obtain the following general form for the correction terms of the AGF in Eq. (5.21) in terms of Eq. (5.9) (see Appendix D.2.2):

$$F^{(m)}(t) = -\int_{\mathscr{H}} \left\langle \mathcal{U}^\dagger \circ \mathcal{U} \circ \left(t^m M^{(m)}(t)\right)[\rho_0] \right\rangle_0 d\rho_0 \tag{5.28}$$

$$= -t^m \int_{\mathscr{H}} \mathrm{Tr}\left\{ M^{(m)}[\rho_0]\, \rho_0 \right\} d\rho_0. \tag{5.29}$$

This integral over the Fubini-Study measure of pure initial states may now be evaluated using results from Weingarten calculus [185] (see Appendix D.2.3). From here we obtain our main result for the general perturbative expansion of the AGI, $\mathcal{I} = 1 - \mathcal{F} = \sum_{m=1}^{\infty} \mathcal{I}^{(m)}$:

$$\mathcal{I} = \frac{-1}{d(d+1)} \sum_{m=1}^{\infty} (\gamma t)^m \,\mathrm{Tr}\left\{ M^{(m)}(t) \right\}, \tag{5.30}$$

where d is the dimensionality of the qudit system, and the powers of (γt) have been grouped to form a single, dimensionless quantity.

As an illustrative example of the utility of this expression, in Fig. 5.1 we present the cumulative correction terms up to fourth order in γt for the QFT gate F_4 acting on a qudit of $d = 4$. With $t = 1$ normalised by the amplitude of the control Hamiltonian H_c, the pure dephasing operator $L = J_z$ was applied over the couplings $\gamma t \in [0, 0.5]$. While the first-order approximation shows good agreement with the simulated AGI for small $\gamma t \ll 1$, the deviation becomes significant as the coupling grows large, necessitating the addition of the higher-order corrections.

5.4.1.2 Gate-independent case

Looking closer at this general result for $\mathcal{I}$, let us consider the case of no coherent driving. This is implemented through a zero control Hamiltonian, $H = \mathbb{0}_d$, giving $\mathcal{S} = \mathbb{0}_{d\times d}$ and corresponding to evolution by the identity gate $U_g = \mathbb{1}_d$. Then, the system evolves only through decay due to the collapse operator $\mathcal{L}$, since only the iterated commutator terms $[(\mathcal{S})^{n_i}, \mathcal{L}]$ for $n_i = 0$ in $M^{(m)}(t)$ survive, resulting in

$$\mathcal{I}_0^{(m)} = \frac{-(\gamma t)^m}{d(d+1)} \frac{\mathrm{Tr}\{\mathcal{L}^m\}}{m!}, \tag{5.31}$$

which is precisely the first term in Eq. (5.27), with the subscript 0 used to refer to the gate-independent correction term. Therefore, generalising to nonzero $\mathcal{S}$, it is clear that the m-th order correction can always be separated into the sum of two parts as in Eq. (5.27): These gate-independent terms $\mathcal{O}((\gamma t)^m)$ (when all $n_i = 0$) and the product of the gate-dependent iterated commutators $\mathcal{O}((\gamma t)^m \prod_{i=1}^m t^{n_i})$.

Combining the summation over m in Eq. (5.30) and the m-th order expression in Eq. (5.31) allows us to rewrite the gate-independent part as a Taylor expansion,

$$\mathcal{I}_0 = \frac{\mathrm{Tr}\{\mathbb{1}_{d\times d} - e^{\gamma t\mathcal{L}}\}}{d(d+1)}. \tag{5.32}$$

Furthermore, as long as the collapse operator is real and symmetric, obeying $L = L^* = L^T = L^\dagger$, (as for J_z, for example), it is possible to use a multinomial expansion on the operator form of $\mathcal{L}$ in Eq. (5.12) to obtain explicit expressions to arbitrary order $(\gamma t)^m$ for the gate-independent correction in Eq. (5.31):

$$\mathrm{Tr}\{\mathcal{L}^m\} = \mathrm{Tr}\left\{\left(L^* \otimes L - \frac{1}{2}L^\dagger L \otimes \mathbb{1} - \frac{1}{2}\mathbb{1} \otimes L^\dagger L\right)^m\right\} \tag{5.33}$$

$$= m! \sum_{k_1+k_2+k_3=m} \frac{\mathrm{Tr}\{L^{k_1+2k_2}\}\,\mathrm{Tr}\{L^{k_1+2k_3}\}}{k_1!k_2!k_3!(-2)^{k_2+k_3}}. \tag{5.34}$$

In the case of a pure (spin) dephasing channel $L = J_z$, considering that $\mathrm{Tr}\{J_z^m\} \sim d^{m+1}$, it can be easily seen that this expression for the m-th-order correction scales as

$$\mathcal{O}\left(\mathrm{Tr}\{\mathcal{L}^m\}\right) \sim d^{2(m+1)} \tag{5.35}$$

$$\implies \mathcal{O}\left(\mathcal{I}_0^{(m)}\right) \sim (\gamma t)^m d^{2m}. \tag{5.36}$$

Now, given this scaling of the gate-independent AGI, let us refer to the work of Chiesa *et al.* [91], where the authors proposed the use of a physical qudit to encode a logical qubit. Using their binomial encoding and error-correction protocol would result in a logical qubit robust to pure dephasing up to order $(\gamma t)^m$ where $2m + 1 = d$. Effectively, the AGI of such a logical qubit would be of the same order as $\mathcal{I}_0^{(m)}$. In turn, to maintain $\mathcal{I}_0 \ll 1$, this sets a limit on the maximum dimension (equivalently, order m of noise correction), such that $d < \frac{1}{\sqrt{\gamma t}}$. Such investigations for protecting against decoherence have already been studied with alternative logical qubit encodings and a discrete error evolution protocol in the work of Miyahara *et al.* [133].

In what follows in the remainder of this study, we shall focus on the first- and second-order correction terms to the AGF. We note that the preceding analytical approach provides

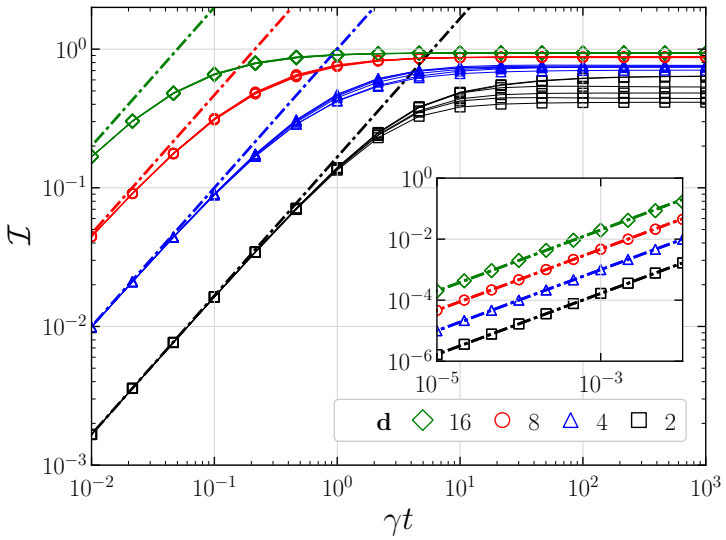


Figure 5.2 – Deviation from linearity of the AGIs for qudits under strong dephasing. Simulations of the AGI against the strength of pure dephasing ($L = J_z$) are plotted on log-log axes over $\gamma t \in [10^{-2}, 10^{3}]$. The simulations were performed on a set of qudit dimensions, $d \in \{2, 4, 8, 16\}$ each for 100 Haar-random quantum gates. The dashed lines represent the linear regime given by the first-order correction to the AGI at each dimension. The inset shows the linear regime for smaller values of $\gamma t \in [10^{-5}, 10^{-2}]$.

a framework for computing any correction term to arbitrary order. However, explicit calculations up to second-order serve as an extension of our prior work [122], in which the first-order correction to the AGF was investigated. Thus, we study in detail the effects due to the second-order correction terms as they relate to our particular system of interest, particularly with regard to the choice of quantum gate and collapse operator.

5.4.2 Nonlinearity of the AGI in the Strong Coupling Regime

Let us now motivate our investigation into the AGI in the regime of strong coupling between the qudit and the environment. As identified in Fig. 5.1, the linear first-order approximation may be sufficient in the weak coupling regime, but nonlinear effects become significant above $\gamma t \sim 10^{-1}$. It is therefore necessary to identify a clear transition or separation between these two regimes, and how the AGI behaves in the limit of strong coupling.

To investigate, we perform calculations of the AGI over a large range of scales for γt. Therefore, in Fig. 5.2, we show numerical simulations of the AGIs for qudits under pure dephasing ($L = J_z$) where the coupling strengths varied logarithmically in $\gamma t \in [10^{-5}, 10^{3}]$. Evolutions were repeated on qudits with dimensions $d \in \{2, 4, 8, 16\}$ for 100 Haar-random quantum gates, with the inset showing the linear regime for small $\gamma t \in [10^{-5}, 10^{-2}]$ and the main figure showing the transition region and strong-coupling regime. The dashed-dotted straight lines give the first-order correction terms at each qudit dimension, defined by the linear function [122]

$$\mathcal{I}^{(1)} = \frac{d(d-1)}{12}\gamma t, \tag{5.37}$$

showing the d-dependence in the weak coupling regime.

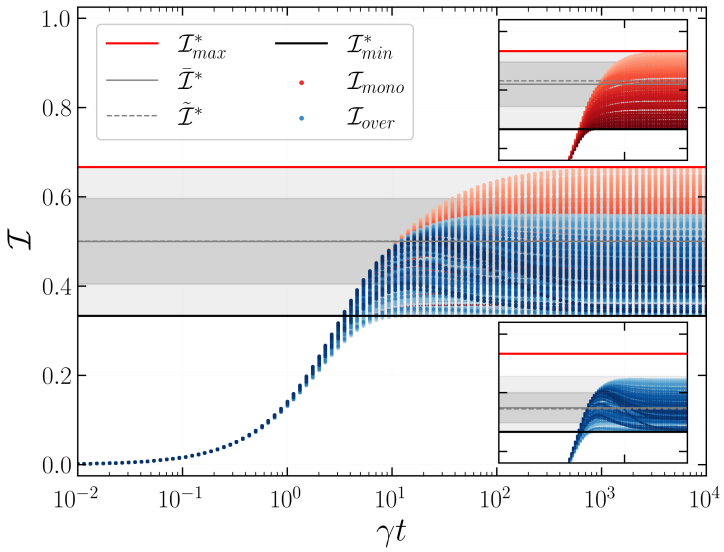


Figure 5.3 – Large-γt behaviour of the AGIs for Haar-random qubit gates under pure dephasing. Simulations of the AGI were performed for a sample of one million (300 displayed) Haar-random qubit ($d = 2$) gates under pure dephasing ($L = J_z$) for $\gamma t \in \left[10^{-2}, 10^4\right]$. For each gate, the AGI curves fall into one of two groups, exhibiting different behaviour near their respective saturation points ($(\gamma t)^*$). The curves in red ($\mathcal{I}_{mono}$) approach their plateau values monotonically from below. The blue curves ($\mathcal{I}_{over}$) rapidly approach their plateau values, before overshooting once with a single turning point, and then converging monotonically from above. The degree of blue shading for each curve indicates the degree of overshoot above the plateau value. All sampled gates converged to their $\mathcal{I}^*$ plateau values within the range $[\mathcal{I}^*_{min}, \mathcal{I}^*_{max}]$ indicated by the black and red horizontal lines.

Further effects of the system dimension on the AGI are notable for larger couplings: The start of deviation from linearity, the plateau values $\mathcal{I}^*$ that the AGI curves converge to in the large γt limit, and the associated saturation points $(\gamma t)^*$ (both denoted by the superscript $*$) at which the curves reach their respective plateau values. Each of these effects confirms an overall decrease in robustness as the system dimension increases: Compared to the behaviour for qubits, the AGIs (for arbitrary gates) of higher-dimensional qudits begin to deviate from the linear regime, and reach the higher plateau limits, at lower noise thresholds. These quantities shall be studied in more detail in Section 5.4.4.

Finally, it is interesting to note the gate dependence of the $\mathcal{I}^*$ and $(\gamma t)^*$, which is more pronounced for smaller d. Given the sample size of 100 gates, it is apparent that, at each dimension, there exists an upper and lower bound to the AGI plateau values, with all the sampled gates converging within this range. It is also noticeable (particularly so for $d = 2$) that the $(\gamma t)^*$ and $\mathcal{I}^*$ are positively correlated, as curves with lower plateau infidelity appear to reach their plateau values at lower $(\gamma t)^*$ than those with higher plateau infidelities.

Studying these effects of the large-γt behaviour in more detail, in Fig. 5.3 we present simulations of a sample of 1 million Haar-random qubit ($d = 2$) gates over $\gamma t \in \left[10^{-2}, 10^4\right]$. This larger sample size provides stronger evidence that the $\mathcal{I}^*$ are indeed bounded above and below, as shown by the red and black horizontal lines, respectively. It was observed that the randomly generated quantum gates fall into one of two groups, indicated by the red and blue shaded curves. The red shaded curves ($\mathcal{I}_{mono}$) approach their plateau values monotonically from below. The blue shaded curves ($\mathcal{I}_{over}$) all experience an overshoot

above their plateau value, with a single turning point, before settling to $\mathcal{I}^*$ monotonically from above. From the full sample, approximately 73% of all gates fell in the red, monotonic group, and the remaining 27% in the blue, overshoot group. The degree of blue shading represents the amount of overshoot, defined by the difference $\mathcal{I}_{max} - \mathcal{I}^*$ between the height of the peak and the plateau value. Furthermore, there appears to be some correlation between this quantity and the saturation point; the larger the overshoot the longer the curve takes to settle. Gates that experience this overshoot may therefore perform worse at intermediate noise strengths over the strong coupling limit.

The insets show each category plotted separately, from which it may be seen that, unlike the blue curves, the red curves span the range between the upper and lower bounds, indicated by the lightly-shaded regions. The darker shaded regions, show the standard deviation about the mean, $\bar{\mathcal{I}}^*$, with the dashed line being the median value, $\tilde{\mathcal{I}}^*$. We can see from these quantities that, despite spanning the range, the red curves are not distributed uniformly, but instead weighted upwards towards the upper bound, while the blue curves are weighted towards the lower bound. Both groups have significant numbers of outliers at either extreme, shifting the medians away from the means. In fact, it is only when averaging over the combined samples that the distribution becomes centered about the mean of $\bar{\mathcal{I}}^* = 0.5$.

The presence of these two distinct groups of AGI curves, and the fact that the average AGI converges to the expected mean value of 0.5, suggests that the AGI is not only bounded in the strong coupling regime, but also that the distribution of AGIs for Haar-random gates is bimodal. This bimodality is a consequence of the gate-dependence of the AGI, which we shall investigate further in the following sections.

5.4.3 Distribution of the AGI for Random Qudit Gates

Given the bimodal distribution of AGIs for Haar-random qubit gates, we now extend our study to higher-dimensional qudits.

5.4.3.1 Uniformity of the CUE for Haar-random unitaries

As noted in Section 5.4.2, the ability to generate ensembles of well-distributed random matrices for arbitrary qudit dimensions is of fundamental importance to the study of the statistical behaviour of the AGI, particularly regarding the aspect of gate-dependence. Given a qudit of dimension d, we identify the space of all possible quantum gates with the unitary group $\mathbf{U}(d)$ of $d \times d$ unitary matrices, associated to skew-Hamiltonian control terms generated through the matrix exponential map of the Lie algebra $\mathfrak{u}(d)$. Therefore, the aim is to sample from a uniform distribution over this group.

Since $\mathbf{U}$ is a compact, connected Lie group, it has a unique (up to positive scalar multiplication) and operation-invariant measure, referred to as the Haar measure [186]. When normalised to one, it produces a uniform probability measure on $\mathbf{U}$, with the associated probability space referred to by the name Circular Unitary Ensemble (CUE), as originally introduced by Dyson [187]. Elements of the CUE are thus typically referred to as Haar-random unitary matrices. The properties of these random matrices have been well-studied, particularly in the standard reference text on random matrix theory by Mehta [188], to which we shall refer. For the specific case of the generation of random unitary matrices, we shall refer to the work of Mezzadri [186].

The spectral statistics form the foundation for the study of random matrices, and in

particular we shall concern ourselves with the two primary quantities: (1) the eigenvalue distribution (level density), and (2) the nearest-neighbour eigenvalue (n-level, for $n = 1$) spacing distribution.

Since we are studying unitary matrices whose eigenvalues all lie on the unit circle in the complex plane, $\lambda_j = e^{i\theta_j}$, the eigenvalue distribution is thus the distribution of the complex phases θ_j of the d eigenvalues:

$$-\pi \leq \theta_j < \pi \quad \forall \quad 1 \leq j \leq d. \tag{5.38}$$

In the large matrix limit where $d \to \infty$ the eigenvalue phases will tend towards a uniform distribution on the domain $[-\pi, \pi)$ with probability density $\rho(\theta) = \frac{1}{2\pi}$.

Next, the nearest-neighbour eigenvalue spacing distribution $p(s)$ is obtained by: (1) sorting the spectrum of phases θ_j from smallest to largest, (2) unfolding this spectrum by the factor $\frac{d}{2\pi}$ to normalise the mean spacing to 1, and then (3) taking their successive differences $s_j = \frac{d}{2\pi}(\theta_{j+1} - \theta_j)$, resulting in a list of $d - 1$ elements. This distribution for the unitary ensembles is well approximated by the Wigner Surmise $p_w(s)$,

$$p_w(s) = \frac{32s^2}{\pi^2} e^{\frac{-4s^2}{\pi}}, \tag{5.39}$$

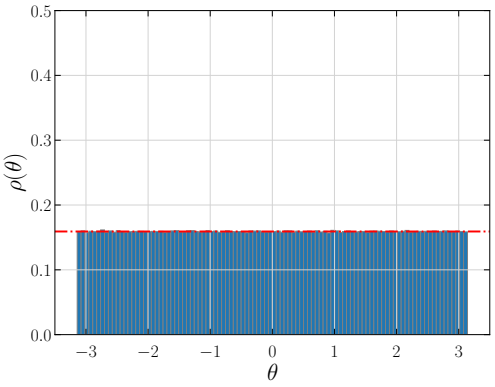
where s is taken in the continuous limit of s_j. In the original work of Wigner [189] on the Gaussian Unitary Ensemble (GUE) of random Hamiltonian (Hermitian) matrices, this is the exact analytical form for the case of 2×2 matrices, which applies to very good approximation for large d. Additionally since the GUE and CUE are related functionally, these two distributions become equivalent for both ensembles for large d.

Given our requirements of sampling random matrices uniformly from the unitary group, we note that there exist numerous (Python-based) packages with methods for generating unitary matrices. Some common, but non-exhaustive, examples include: QuTiP [127, 128] (`rand_unitary`, `rand_unitary_haar`, `rand_herm`), Cirq [190] (`rand_unitary`, `rand_special_unitary`), and Bristol [167] (`gen_cue`).

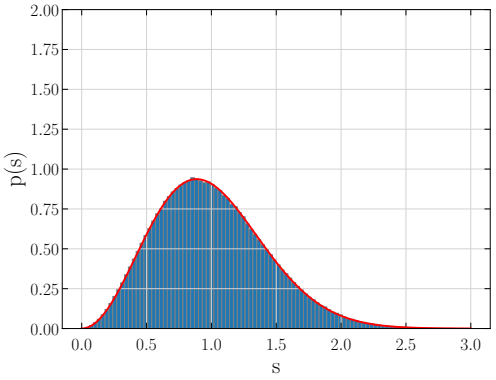
Both QuTiP's `rand_unitary_haar` and Cirq's `rand_unitary` methods implement precisely the algorithm provided by Mezzadri in [186]. The Cirq.`rand_special_unitary` method augments the original `rand_unitary` method by normalising the determinant of the randomly generated matrix to 1. The QuTiP.`rand_unitary` method uses the `rand_herm` method to generate a random Hermitian matrix and then computes its unitary equivalent by matrix exponentiation.

We tested each of these different methods by sampling one million eigenvalues in each of 2 matrix size configurations, $d =\in \{2, 100\}$ for each method. These two values were chosen to represent the two regimes of large and small matrix dimensions. The number of eigenvalues was chosen such that, for the algorithm of Mezzadri the standard deviation of the mean for the level density of the eigenvalue phases of the $d = 100$ matrices fell below the threshold of 0.001. The number of eigenvalues was kept constant at 10^6 for each dimension by varying the number of quantum gates generated, specifically 500000 and 10000 gates for $d = 2$ and $d = 100$ respectively.

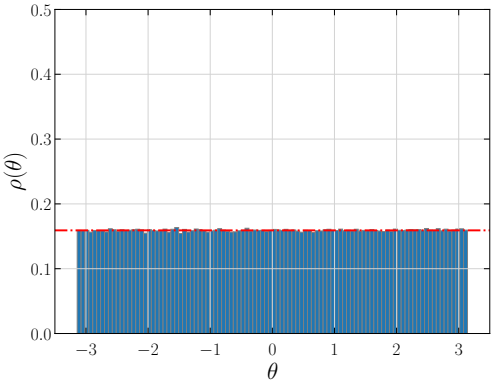
In Figs. 5.4 to 5.7, the simulated data of eigenvalue and spacing distributions (blue) are compared to their analytically expected results (red). We can see that the method of Mezzadri in Fig. 5.4 performs the best for generating uniformly distributed Haar-random gates. Hence this is our method of choice. However, even for this method the spacing



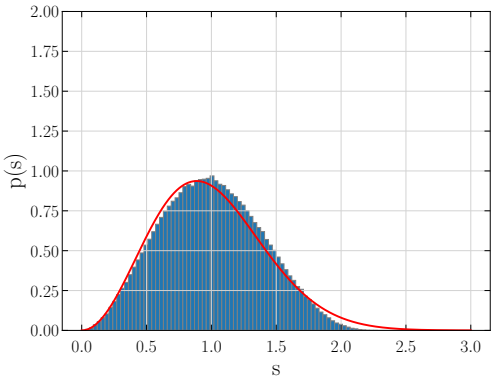
(a) $d = 100$ level density



(b) $d = 100$ spacings



(c) $d = 2$ level density



(d) $d = 2$ spacings

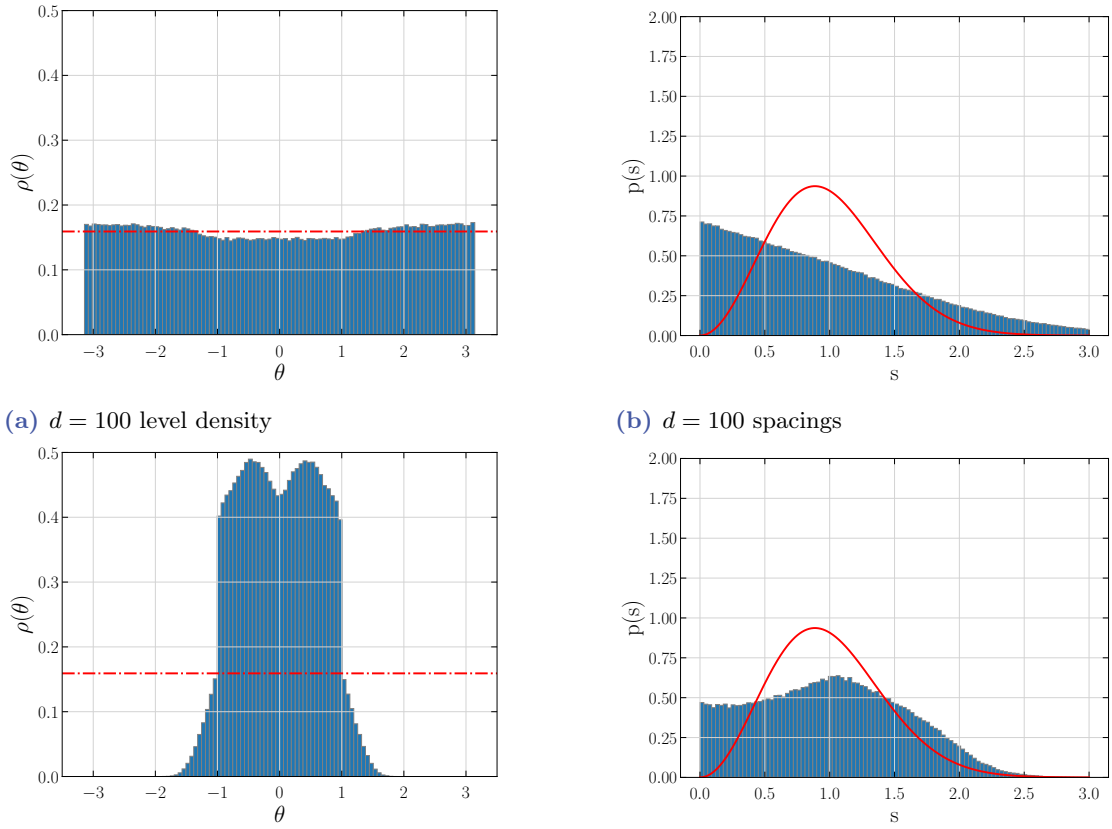
Figure 5.4 – Eigenvalue distributions of method QuTiP.rand_unitary_haar (and equivalently Cirq.rand_unitary). (a) Level density of eigenvalue phases for 10000 randomly generated $d = 100$ qudit gates. (b) Nearest-neighbour spacing distribution of eigenvalue phases for 10000 randomly generated $d = 100$ qudit gates. (c) Level density of eigenvalue phases for 500000 randomly generated $d = 2$ qubit gates. (d) Nearest-neighbour spacing distribution of eigenvalue phases for 500000 randomly generated $d = 2$ qubit gates. Based on [186].

distribution does show reduced accuracy for lower dimensions, despite the level densities remaining uniform. This could be attributed to the fact that the Wigner Surmise is exact for 2×2 Hermitian matrices (but still very accurate for large d), but it is only in the large d limit that the distributions for the CUE are identical to that of the GUE [188]. Thus some deviation is to be expected for small unitary matrices.

The QuTiP.`rand_unitary` and QuTiP.`rand_herm` methods in Fig. 5.5 do not appear suitable for sampling uniformly from the CUE. Indeed, inspection of the sampled matrices showed that approximately 50% of the generated unitary matrices were diagonal. On the other hand, the Bristol.`gen_cue` in Fig. 5.6 is well optimised for high-dimensional systems but is unsuitable for small dimensions. Finally, it is interesting to note that the special unitary matrices of Cirq.`rand_special_unitary` in Fig. 5.7 are similarly distributed for large dimension, but show singular behaviour for small d.

5.4.3.2 Distribution of the asymptotic AGIs

We continue our investigations on the different Python methods for generating random unitary gates.



(a) $d = 100$ level density

(b) $d = 100$ spacings

(c) $d = 2$ level density

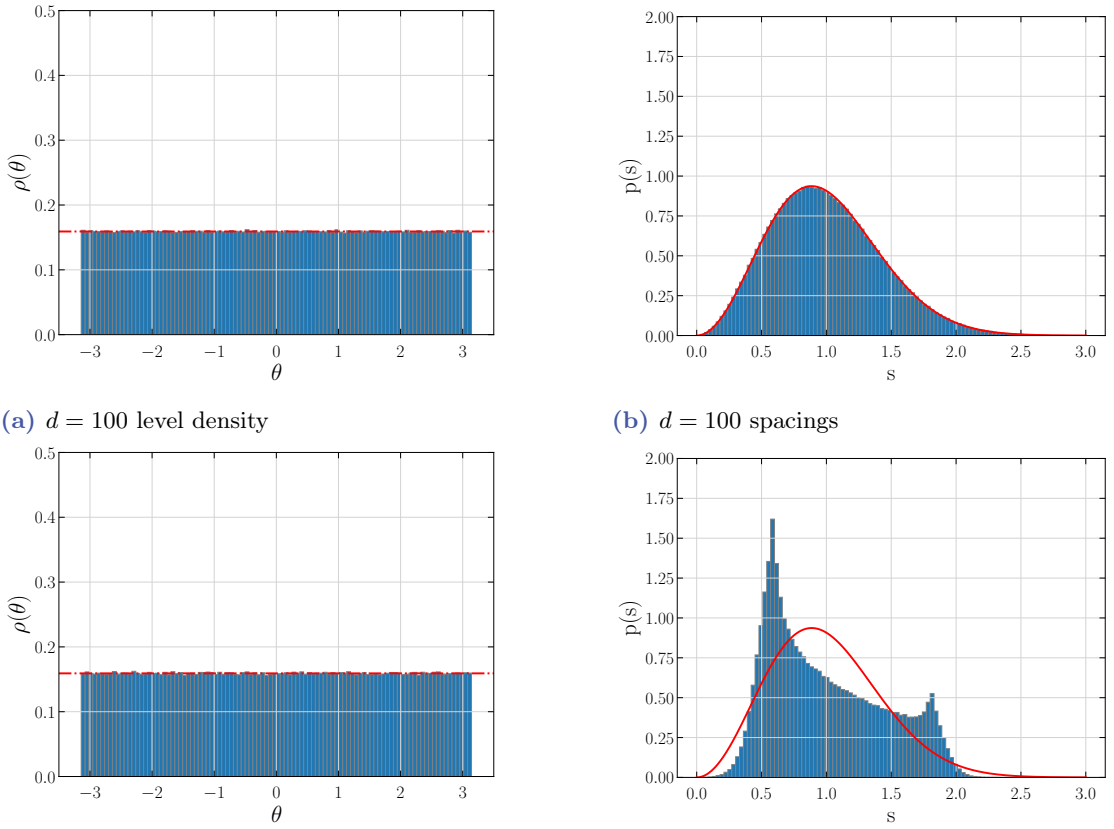
(d) $d = 2$ spacings

Figure 5.5 – Eigenvalue distributions of method QuTiP.`rand_unitary` (and equivalently QuTiP.`rand_herm`). (a) Level density of eigenvalue phases for 10000 randomly generated $d = 100$ qudit gates. (b) Nearest-neighbour spacing distribution of eigenvalue phases for 10000 randomly generated $d = 100$ qudit gates. (c) Level density of eigenvalue phases for 500000 randomly generated $d = 2$ qubit gates. (d) Nearest-neighbour spacing distribution of eigenvalue phases for 500000 randomly generated $d = 2$ qubit gates.

In Fig. 5.3 we discussed the distribution of the plateau values $\mathcal{I}^*$ of the AGI in the large-γt regime. Recall that we refer to these plateau values $\mathcal{I}^*$ at the large-γt limit, $\lim_{\gamma t \gg 1} \mathcal{I} \to \mathcal{I}^*$. We showed that they must be bounded above and below for all gates by Eq. (5.57). We also observed the appearance of two distinct behaviours ($\mathcal{I}^*_{mono}$ and $\mathcal{I}^*_{over}$) in the sampled Haar-random gates: (1) Monotonic growth of the AGI towards $\mathcal{I}^*$, and (2) overshoot with a single turning point above $\mathcal{I}^*$.

We note that, as for all the numerical results, the QuTiP.`rand_unitary_haar` method was used to generate the data shown in Fig. 5.3. We complement this work by repeating these simulations using the remaining methods (for $d = 2$) and also with QuTiP's `rand_unitary_haar` for $d \in \{2, 4, 8, 16\}$. For each test method and dimension, 100000 gates were generated, their $\mathcal{I}^*$ calculated numerically and their behaviour categorised as either monotonic or overshooting as shown in Table 5.1.

Figures 5.8 and 5.9 display the data of these experiments by plotting histograms of the probability densities of the $\mathcal{I}^*$ for each category of gate, $\mathcal{I}^*_{mono}$ in orange and $\mathcal{I}^*_{over}$ in blue, as well as their combined distribution $\mathcal{I}^*_{total}$ in grey. The histograms were normalised such that the area under the curve of $p(\mathcal{I}^*_{total})$ was equal to 1. The red and black vertical lines



(a) $d = 100$ level density

(b) $d = 100$ spacings

(c) $d = 2$ level density

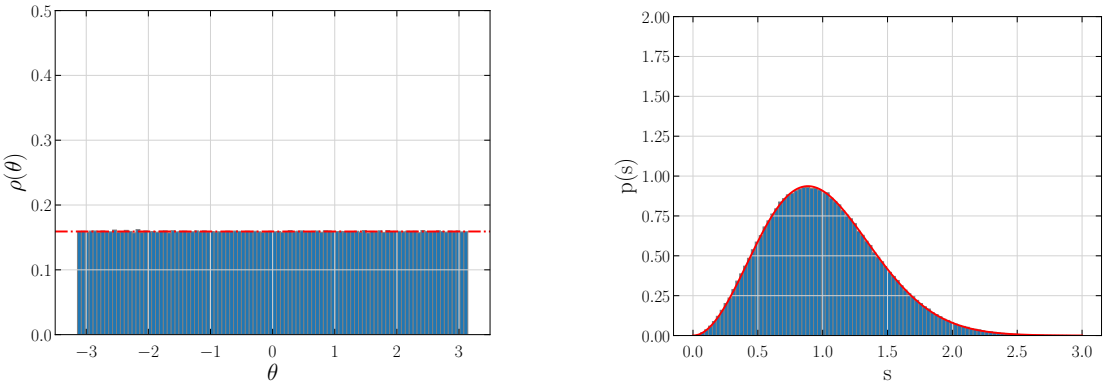
(d) $d = 2$ spacings

Figure 5.6 – Eigenvalue distributions for method Bristol.gen_cue. (a) Level density of eigenvalue phases for 10000 randomly generated $d = 100$ qudit gates. (b) Nearest-neighbour spacing distribution of eigenvalue phases for 10000 randomly generated $d = 100$ qudit gates. (c) Level density of eigenvalue phases for 500000 randomly generated $d = 2$ qubit gates. (d) Nearest-neighbour spacing distribution of eigenvalue phases for 500000 randomly generated $d = 2$ qubit gates.

show the upper and lower bounds on $\mathcal{I}^*$, respectively. The dashed blue vertical lines show the expected mean value for each dimension.

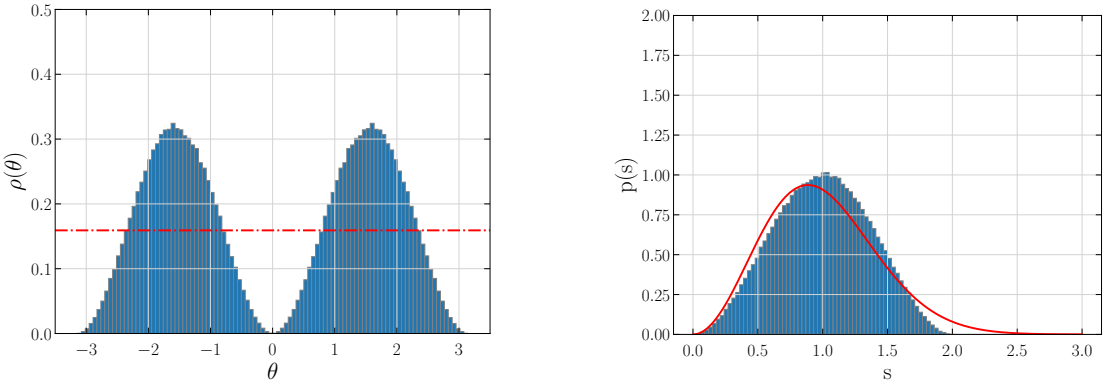
Looking closer at Fig. 5.8, the two Cirq methods in Figs. 5.8c and 5.8d appear to have distributions matching most closely with that of QuTiP.`rand_unitary_haar` in Fig. 5.9a, although the normalisation procedure for the special unitary matrices appears to generate a larger proportion of gates with overshoot. It is interesting to note that the Bristol.`gen_cue` method in Fig. 5.8a generates an increasing number of gates near the expected mean, but only below, with no gates in the range $1 - \frac{1}{d} \leq \mathcal{I}^* \leq 1 - \frac{1}{d+1}$. As mentioned in Section 5.4.3.1, QuTiP.`rand_unitary` in Fig. 5.8b generates a large number of diagonal unitary matrices, whose $\mathcal{I}^* = \mathcal{I}^*_{min} = 1 - \frac{2}{d+1}$ are equivalent to that of the identity matrix $\mathbb{1}_d$.

Figure 5.9 shows the preferred QuTiP.`rand_unitary_haar` method for different dimensions $d \in \{2, 4, 8, 16\}$. We note that at each dimension the computed mean over all sampled $\mathcal{I}^*$ is equal to (within statistical error) the expected mean shown by the dashed blue vertical line, $\bar{\mathcal{I}}^* = 1 - \frac{1}{d}$. However, most striking is the fact that for $d > 2$ the total probability density is no longer uniformly distributed between $\mathcal{I}^*_{min}$ and $\mathcal{I}^*_{max}$, but



(a) $d = 100$ level density

(b) $d = 100$ spacings



(c) $d = 2$ level density

(d) $d = 2$ spacings

Figure 5.7 – Eigenvalue distributions for method `CIRQ.rand_special_unitary`. (a) Level density of eigenvalue phases for 10000 randomly generated $d = 100$ qudit gates. (b) Nearest-neighbour spacing distribution of eigenvalue phases for 10000 randomly generated $d = 100$ qudit gates. (c) Level density of eigenvalue phases for 500000 randomly generated $d = 2$ qubit gates. (d) Nearest-neighbour spacing distribution of eigenvalue phases for 500000 randomly generated $d = 2$ qubit gates.

becomes increasingly concentrated about the mean.

We remark that this observed behaviour is due to the concentration of measure phenomenon as the dimensionality of the system increases [191, 192]. To understand this, we first demonstrate the following property of the AGI:

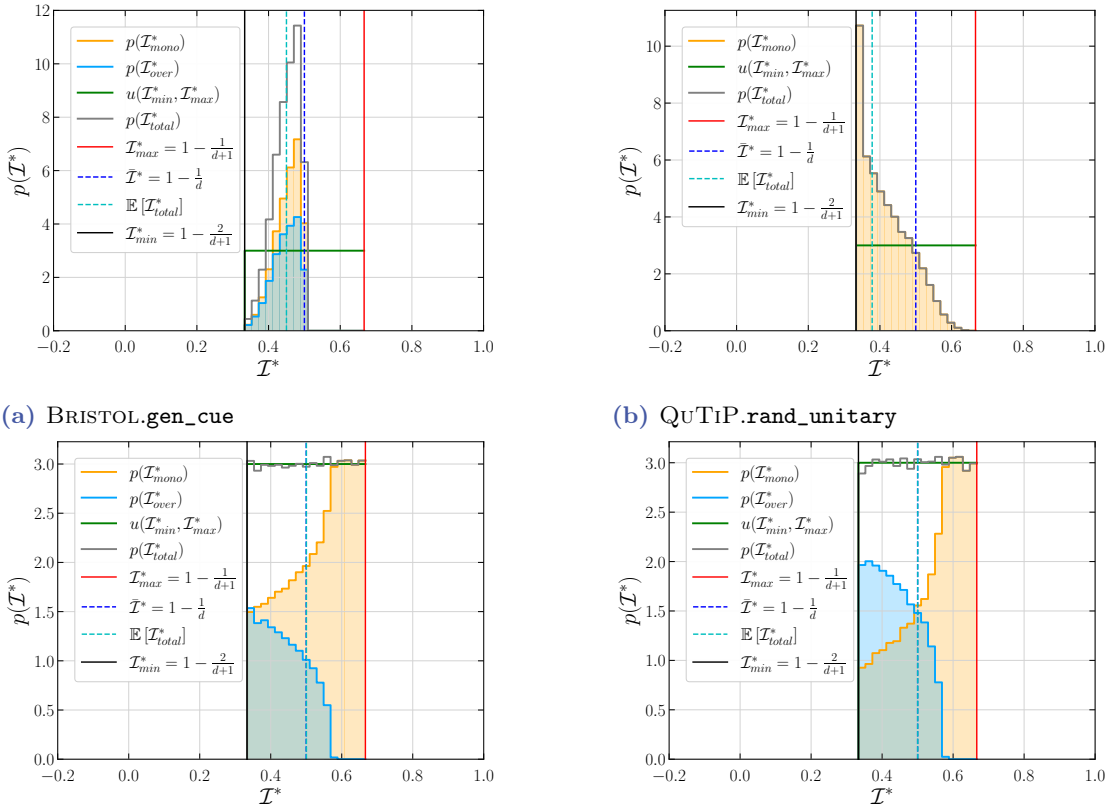
Lemma 5.4.1. *The AGI function $\mathcal{I} : \mathbf{U}(d) \to \mathbb{R}$ is L-Lipschitz continuous with respect to the Frobenius norm $\|A\|_F = \sqrt{\mathrm{Tr}\{A^\dagger A\}}$ over the unitary group $\mathbf{U}(d)$ with Lipschitz constant $L = \frac{2}{d+1}$, such that*

$$\left|\mathcal{I}(U) - \mathcal{I}(U')\right| \leq L\left\|U - U'\right\|_F \tag{5.40}$$

where $U, U' \in \mathbf{U}(d)$.

Proof. The AGF $\mathcal{F}$ can be written in terms of the process fidelity F as [193]

$$\mathcal{F} = \frac{dF + 1}{d + 1}, \tag{5.41}$$



(a) Bristol.`gen_cue` **(b)** QuTiP.`rand_unitary`

(c) Cirq.`rand_unitary` **(d)** Cirq.`rand_special`

Figure 5.8 – Probability distributions of the AGI plateaus for different gate generation methods. 100000 gates were generated for qubits using (a) Bristol.`gen_cue`, (b) QuTiP.`rand_unitary`, (c) Cirq.`rand_unitary` and (d) Cirq.`rand_special_unitary`. The $\mathcal{I}^*$ were categorised according to monotonic (orange) or overshooting (blue) AGIs. Their probability densities were plotted in the domain $[\mathcal{I}^*_{min}, \mathcal{I}^*_{max}]$ (black and red vertical lines, respectively), with the total distribution $p(\mathcal{I}^*_{total})$ in grey. The mean plateau value $\mathbb{E}(\mathcal{I}^*_{total})$ (cyan, dotted vertical line), was compared with the expected mean $\bar{\mathcal{I}}^* = 1 - \frac{1}{d}$ (blue, dashed vertical line). The green line represents the expected uniform distribution $u(\mathcal{I}^*_{min}, \mathcal{I}^*_{max})$.

where $F = \frac{1}{d^2}\left|\mathrm{Tr}\{U^\dagger V\}\right|^2$ for two unitaries $U, V \in \mathbf{U}(d)$. Then, with $\mathcal{I} = 1 - \mathcal{F}$, we have that

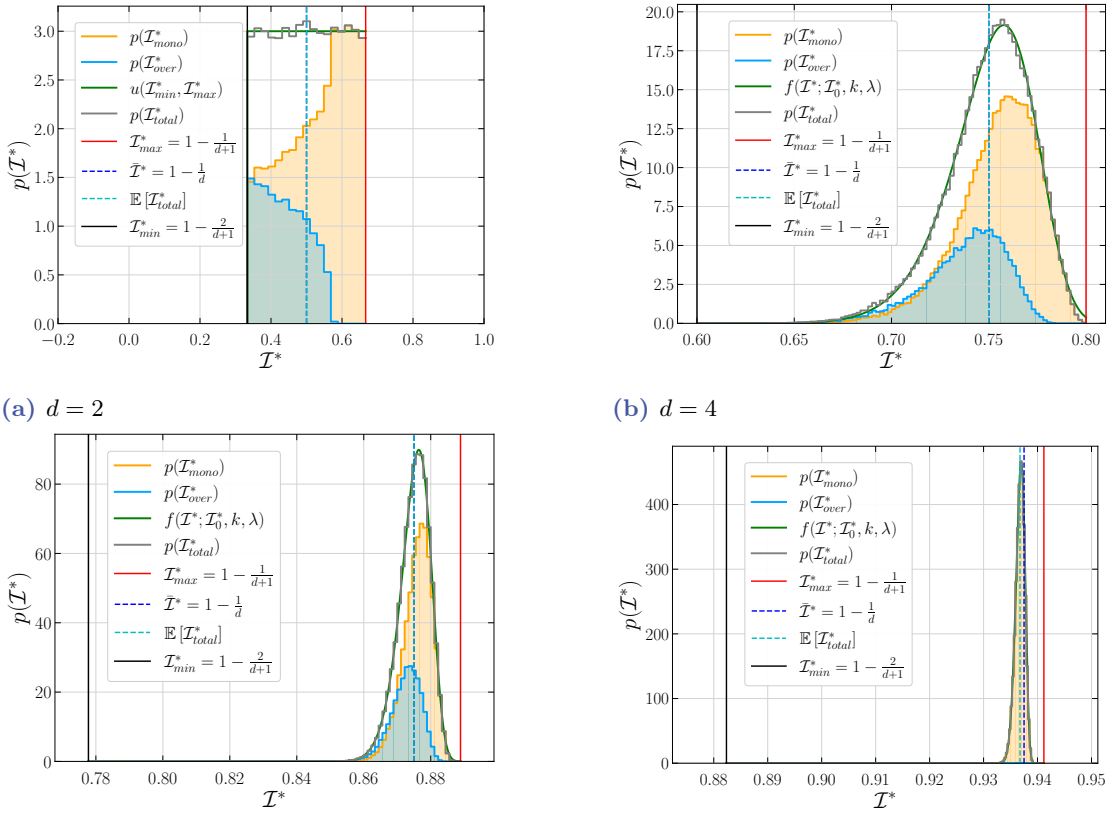
$$\mathcal{I} = \frac{d^2 - \left|\mathrm{Tr}\{U^\dagger V\}\right|^2}{d(d+1)}. \tag{5.42}$$

Considering the difference, we have that

$$\begin{aligned} \left|\mathcal{I}(U) - \mathcal{I}(U')\right| &= \frac{1}{d(d+1)}\left|\left|\mathrm{Tr}\{U^\dagger V\}\right|^2 - \left|\mathrm{Tr}\{U'^\dagger V\}\right|^2\right| \\ &= \frac{1}{d(d+1)}\left|\left|\mathrm{Tr}\{U^\dagger V\}\right| - \left|\mathrm{Tr}\{U'^\dagger V\}\right|\right| \times \\ &\times \left|\left|\mathrm{Tr}\{U^\dagger V\}\right| + \left|\mathrm{Tr}\{U'^\dagger V\}\right|\right|, \end{aligned} \tag{5.43}$$

by difference of squares. Now,

$$\begin{aligned} \left|\left|\mathrm{Tr}\{U^\dagger V\}\right| + \left|\mathrm{Tr}\{U'^\dagger V\}\right|\right| &\leq \left|\mathrm{Tr}\{U^\dagger V\}\right| + \left|\mathrm{Tr}\{U'^\dagger V\}\right| \\ &\leq 2d, \end{aligned} \tag{5.44}$$



(a) $d = 2$ **(b)** $d = 4$

(c) $d = 8$ **(d)** $d = 16$

Figure 5.9 – Probability distributions of the AGI plateaus. 100000 gates were generated using the method QuTiP.`rand_unitary_haar` of [186] at different dimensions: (a) $d = 2$, (b) $d = 4$, (c) $d = 8$, and (d) $d = 16$. The $\mathcal{I}^*$ were categorised according to monotonic (orange) or overshooting (blue) AGIs. Their probability densities were plotted in the domain $[\mathcal{I}^*_{min}, \mathcal{I}^*_{max}]$ (black and red vertical lines, respectively), with the total distribution $p(\mathcal{I}^*_{total})$ in grey. The mean plateau value $\mathbb{E}(\mathcal{I}^*_{total})$ (cyan, dotted vertical line), was plotted in comparison with the expected mean $\bar{\mathcal{I}}^* = 1 - \frac{1}{d}$ (blue, dashed vertical line). The green curve represents the fitted Weibull distributions $f(\mathcal{I}^*;\mathcal{I}^*_0,k,\lambda) = \frac{k}{\lambda}\left(\frac{\mathcal{I}^*-\mathcal{I}^*_0}{\lambda}\right)^{k-1} e^{-\left(\frac{\mathcal{I}^*-\mathcal{I}^*_0}{\lambda}\right)^k}$ in the domain.

by the Cauchy-Schwartz inequality and since the trace of a unitary is at most d. Similarly,

$$\begin{aligned}
\left|\left|\mathrm{Tr}\left\{U^\dagger V\right\}\right| - \left|\mathrm{Tr}\left\{U'^\dagger V\right\}\right|\right| &\leq \left|\mathrm{Tr}\left\{U^\dagger V\right\} - \mathrm{Tr}\left\{U'^\dagger V\right\}\right| \\
&\leq \left\|U^\dagger V - U'^\dagger V\right\|_F \qquad (5.45)\\
&\leq \left\|\left(U-U'\right)^\dagger V\right\|_F \qquad (5.46)\\
&\leq \left\|U-U'\right\|_F, \qquad (5.47)
\end{aligned}$$

and by unitary invariance of the Frobenius norm. Therefore, substituting these two expressions,

$$\left|\mathcal{I}(U) - \mathcal{I}(U')\right| \leq \frac{2}{d+1}\left\|U-U'\right\|_F, \qquad (5.48)$$

and thus $\mathcal{I}$ is Lipschitz with $L = \frac{2}{d+1}$. □

d	Method	$\mathcal{I}^*_{mono}$ (%)	$\mathcal{I}^*_{over}$ (%)	ϵ_{rel} (%)	D_{KL}
2	Bristol.`gen_cue`	59.56	40.44	0.100	0.885
2	QuTiP.`rand_unitary`	100.00	0.00	0.243	0.438
2	Cirq.`rand_unitary`	73.06	26.94	1.02×10^{-3}	5.92×10^{-5}
2	Cirq.`rand_special_unitary`	61.66	38.34	6.83×10^{-4}	1.32×10^{-4}
2	QuTiP.`rand_unitary_haar`	75.51	24.49	2.56×10^{-4}	7.15×10^{-5}
4	QuTiP.`rand_unitary_haar`	71.24	28.76	4.38×10^{-5}	2.92×10^{-3}
8	QuTiP.`rand_unitary_haar`	70.21	29.79	1.27×10^{-5}	1.21×10^{-3}
16	QuTiP.`rand_unitary_haar`	99.95	0.05	7.98×10^{-4}	1.36×10^{-3}

Table 5.1 – Proportions of random gates with and without turning points. 100000 gates were generated for each of the method and dimension pairs shown. The $\mathcal{I}^*_{mono}$ (%) and $\mathcal{I}^*_{over}$ columns show the percentages of gates falling into either of the two categories: (1) monotonic growth, and (2) overshooting behaviour. The column ϵ_{rel} gives the relative error between the measured mean of the overall data $\mathbb{E}(\mathcal{I}^*_{total})$ and the expected mean $\bar{\mathcal{I}}^* = 1 - \frac{1}{d}$ for the calculated AGI plateau values, given by $\epsilon_{rel} = \left|\frac{\mathbb{E}(\mathcal{I}^*_{total}) - \bar{\mathcal{I}}^*}{\bar{\mathcal{I}}^*}\right|$. The quantity D_{KL} is the Kullback-Leibler divergence measuring the relative entropy between the distribution $p\left(\mathcal{I}^*_{total}\right)$ and the reference distribution: $D_{KL}\left(p(\mathcal{I}^*_{total})||u\left(\mathcal{I}^*_{min}, \mathcal{I}^*_{max}\right)\right)$ for $d = 2$ uniform and $D_{KL}\left(p(\mathcal{I}^*_{total})||f\left(\mathcal{I}^*; \mathcal{I}^*_0, k, \lambda\right)\right)$ for $d > 2$ Weibull.

Now, we can apply this result for $\mathcal{I}$ in conjunction with Levy's Lemma extended to the classical compact group $\mathbf{U}(d)$ [194], which we restate here without proof:

Theorem 5.4.2. *Let $f : X \to \mathbb{R}$ be L-Lipschitz continuous with Lipschitz constant L, and let X be an element of one of the compact classical groups. Then, for each $t > 0$,*

$$\mathbb{P}\left[|f(X) - \mathbb{E}\left[f(X)\right]| \geq t\right] \leq e^{-\frac{(d-2)t^2}{24L^2}}. \tag{5.49}$$

Using our result for $\mathcal{I}$, we have that

$$\mathbb{P}\left[|\mathcal{I}(U) - \mathbb{E}\left[\mathcal{I}(U)\right]| \geq t\right] \leq e^{-\frac{(d-2)(d+1)^2t^2}{96}}. \tag{5.50}$$

This therefore confirms our observation of the concentration of measure phenomenon in Fig. 5.9; it tells us that the probability of observing a gate whose infidelity is further than t from the expectation value of the AGI decays exponentially in the distance t^2 and the dimensionality $(d-2)(d+1)^2$ of the system.

For the case $d = 2$, the exponent is zero and thus the probability is constant for all t and so we see in Fig. 5.9a that the AGI plateau values are uniformly distributed. However, as $d > 2$ for Figs. 5.9b to 5.9d, the $\mathcal{I}^*$ become exponentially concentrated about the mean $\bar{\mathcal{I}}^*$.

This could also account for the fluctuation in the ratios of $\mathcal{I}^*_{mono}/\mathcal{I}^*_{over}$ at different system sizes. However, further work is needed to elucidate the precise reasons for these observations.

5.4.4 Gate- and Noise-Dependence of the Fidelity

Having identified particular aspects of interest in the AGI behaviour in the strong coupling regime, let us investigate these characteristics in further detail.

5.4.4.1 Universal bounds on the AGI

Repeating the simulations presented in Fig. 5.3 for larger dimensions, we observed that the lower and upper bounds, $\mathcal{I}^*_{min}$ and $\mathcal{I}^*_{max}$ respectively, and the mean value, $\bar{\mathcal{I}}^*$, depend only on the dimension d of the system, and are given precisely by the following expressions, for any d:

$$\mathcal{I}^*_{max} = 1 - \frac{1}{d+1}, \tag{5.51}$$

$$\bar{\mathcal{I}}^* = 1 - \frac{1}{d}, \tag{5.52}$$

$$\mathcal{I}^*_{min} = 1 - \frac{2}{d+1}. \tag{5.53}$$

It has previously been shown [193] that, for the case of a qudit in the singlet state evolving in a noisy quantum channel, the infidelity is bounded by $1 - \frac{2}{d+1} \leq \mathcal{I}^* \leq 1 - \frac{1}{d}$. This result matches with our case of a single qudit in the large-d limit due to convergence of the mean and upper bound. However, for our single qudit system we shall use our existing framework to prove these limits for arbitrary d.

Writing the quantum channel as $\mathcal{E} = \mathcal{U} \circ M$, and substituting into the expression for the AGF in Eq. (5.8),

$$\mathcal{F} = \int_{\mathscr{H}} \mathrm{Tr}\{M\left[\rho_0\right]\rho_0\} d\rho_0 \tag{5.54}$$

$$= \frac{\mathrm{Tr}\{M\} + \mathrm{Tr}\{M\left[\mathbb{1}\right]\}}{d(d+1)}. \tag{5.55}$$

Given that the quantum channel is CPTP, and that $\mathcal{U}$ is a unitary operator, we know that the superoperator M must also be trace-preserving and thus $\mathrm{Tr}\{M\left[\mathbb{1}\right]\} = d$. Furthermore, in the strong coupling limit where the collapse operator $L = J_z$ describes pure dephasing, it is clear that the action of M on a state ρ is to transform it to a diagonal density matrix where the coherences (off-diagonal elements) have all decayed to zero. Expressing $M = \sum_{k=1}^{K} E_k^* \otimes E_k$ in the Kraus representation, the trace can be written as

$$\mathrm{Tr}\{M\} = \sum_{k=1}^{K} \sum_{i=0}^{d-1} |E_{k,ii}|^2. \tag{5.56}$$

Furthermore, it can be shown that (see Appendix D.2.4 for a detailed derivation) each of the d squared-elements are bounded by $0 \leq |E_{k,ii}|^2 \leq 1$ and hence in the large noise regime the AGI is bounded by

$$1 - \frac{2}{d+1} \leq \mathcal{I}^* \leq 1 - \frac{1}{d+1}. \tag{5.57}$$

5.4.4.2 Quantum gates

Given the significance of this result, it is now of interest to consider how the behaviour is affected by the choice of quantum gate. In other words, we want to identify any particular unitary operators U_g, or properties thereof, whose AGIs $\mathcal{I}(\mathcal{E}, U_g)$ when $(\gamma t) \gg 1$ are precisely the $\mathcal{I}^*_{min}$, $\mathcal{I}^*_{max}$ or $\bar{\mathcal{I}}^*$.

In Fig. 5.10, we present simulations of the AGI, as a function of γt, on a $d = 4$ qudit for a set of gates that do indeed reflect this behaviour when undergoing pure dephasing.

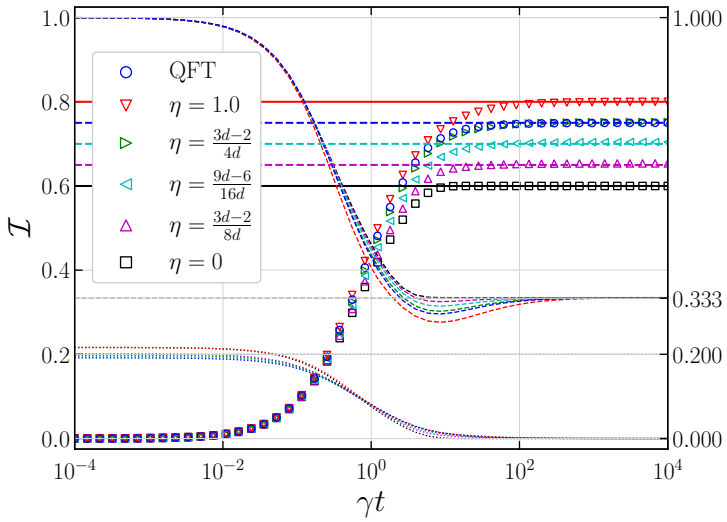


Figure 5.10 – Gate-dependence of the AGIs and qudit state evolution as functions of noise strength. Simulations of a $d = 4$ qudit under pure dephasing were time-evolved according to one in the set of 6 listed quantum gates. The blue circular points show the AGI for the QFT gate. The other points represent the interpolated X^η gate taken to the power of a d-dependent scaling factor, $\eta \in [0, 1]$. These values produce evenly spaced plateau AGI values between the upper (X, $\eta = 1$) and lower ($\mathbb{1}$, $\eta = 0$) bounds. For $\eta = \frac{3d-2}{4d}$, the interpolating X gate (for any d) converges to the same value as the QFT gate, $\mathcal{I}^* = 1 - \frac{1}{d}$. The dashed-dotted horizontal lines show the plateaus. 2400 Randomly generated pure Hermitian states were time-evolved, and the averaged final states per gate showed: (i) The purity $\left(\mathrm{Tr}\left(\rho^2\right)\right)$ (dashed) decaying from 1 to $\frac{1}{d-1}$, and (ii) the mean coherences $\left(2\frac{\sum_{i>j}|\rho_{i,j}|}{d(d-1)}\right)$ decaying towards zero due to dephasing. For small γt the coherences vary based on gate type.

The AGI values (discrete data points) are accompanied by dashed and dotted curves representing the state purity and mean coherences, while the horizontal lines show the $\mathcal{I}^*$ values of the associated gates. The purities and coherences were calculated over a set of $n = 2400$ randomly generated pure Hermitian density matrices. The purity $\mathrm{Tr}\{\rho^2\}$ decays from 1 to a constant $\frac{1}{d-1}$, while the averages of the $\frac{d(d-1)}{2}$ coherences decay to zero, confirming the dephasing action of the J_z collapse operator.

Regarding the set of gates, in addition to the QFT gate, we introduce the interpolated-X gate, X^η, where the matrix is raised to the η-th power for $\eta \in [0, 1]$. Clearly, $\eta = 1$ or 0 produces the X or $\mathbb{1}_d$ gate, respectively, while for $0 < \eta < 1$ the action interpolates between these two extremes.

We find that

$$\mathcal{I}^*(\mathcal{E}, \mathbb{1}_d) = \mathcal{I}^*_{min}, \tag{5.58}$$
$$\mathcal{I}^*(\mathcal{E}, F_d) = \bar{\mathcal{I}}^*, \tag{5.59}$$
$$\mathcal{I}^*(\mathcal{E}, X_d) = \mathcal{I}^*_{max}. \tag{5.60}$$

Specifically, the $\mathcal{I}^*$ are extremised above and below by the X and identity gates, respectively, while the mean value $\bar{\mathcal{I}}^*$ indeed corresponds to the action of the QFT gate that creates a superposition state. Furthermore, by careful choice of the values of η, we can obtain intermediate values of $\mathcal{I}^*$. For example, the η values chosen and shown in Fig. 5.10 lead to curves with plateau values that are equally spaced within the bounding

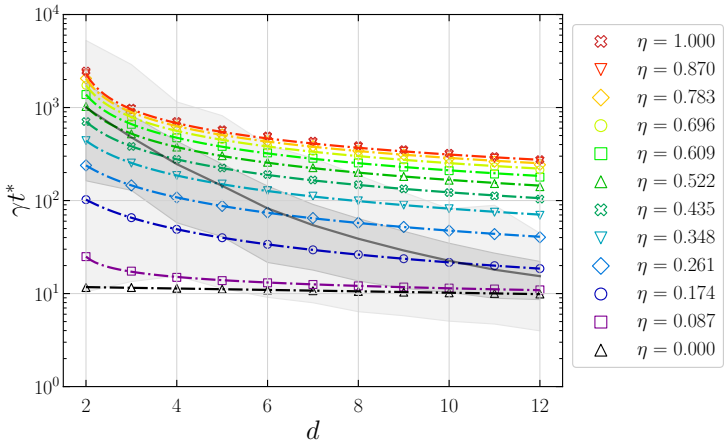


Figure 5.11 – Saturation points ($(\gamma t)^*$) of the AGIs for interpolated X^η gates as functions of qudit dimension. AGIs were calculated for a set of 12 interpolated X^η gates for $0 \leq \eta \leq 1$, at dimensions $d \in [2, 12]$. For each dimension and gate, the AGI curve over γt was interpolated by a cubic spline. The saturation points $(\gamma t)^*$ were identified by root-finding algorithm of the points at which they converged (within $\varepsilon < 10^{-8}$) to their AGI plateau values. The plotted data points, on log-linear axes, indicate these root values as functions of d for each gate, and the dashed lines represent their associated power-law fits. This analysis was repeated for a set of $n = 4800$ Haar-random gates at each dimension. The light shaded areas are bounded by the maximum and minimum saturation points found at each dimension. The darker shaded areas represent a 1σ deviation about the mean (solid gray line).

region. We observed that for the value $\eta = \frac{3d-2}{4d}$, the $\mathcal{I}^*$ matches that of the QFT gate, also converging to the mean.

The effect of these gates on the AGI can be understood by following the arguments in Appendix D.2.6 regarding the operator M and its form based on the choice of quantum gate. It is clear that for the identity gate, or more generally any diagonal unitary matrix, $\mathrm{Tr}\{M\} = d$ which minimises $\mathcal{I}^* = 1 - \frac{2}{d+1}$. Similarly, the QFT gate produces a superposition state with each of the d basis elements of ρ being $\frac{1}{d}$, thus $\mathrm{Tr}\{M\} = 1$ and $\mathcal{I}^* = 1 - \frac{1}{d}$. Finally the X gate increments all states circularly, and, having no diagonal elements, results in traceless $\mathrm{Tr}\{M\} = 0$ and thus $\mathcal{I}^* = 1 - \frac{1}{d+1}$.

5.4.4.3 Quantum gate dependence of the AGI saturation point

Let us now consider how the choice of quantum gate affects the saturation point $(\gamma t)^*$ at which the AGI attains the plateau value $\mathcal{I}^*$. Figure 5.11 presents simulations of the plateau saturation points as a function of the qudit dimension for set of X^η gates over a range of η values from 0 to 1. In addition, the calculations were repeated over a set of $n = 4800$ Haar random gates at each dimension from $d = 2$ to 12. The grey curve represents the mean value of the saturation point at each dimension, while the dark grey and light gray shaded regions indicate the standard deviations and max-min values, respectively.

For each of the simulated X^η gates, the dashed-dotted lines represent power-law fits to the discrete data points at each dimension. The power-law model is given by

$$(\gamma t)^* = \alpha(d - \beta)^\delta, \tag{5.61}$$

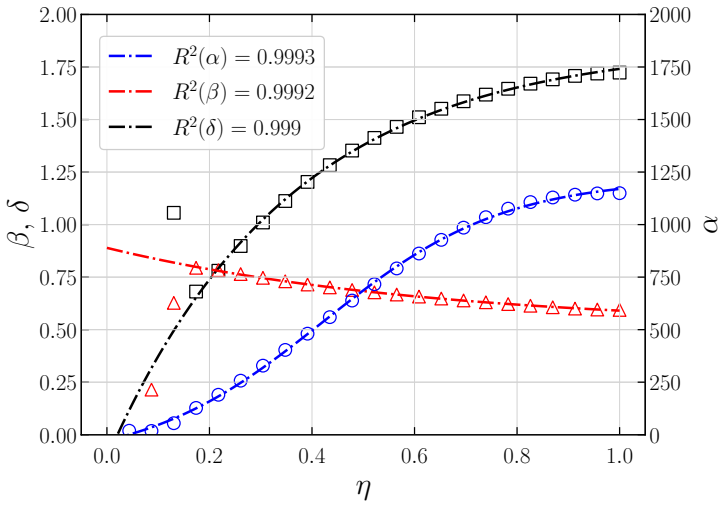


Figure 5.12 – Fitted power-law model parameters as functions of η for the saturation points $(\gamma t)^*$ of the X^η gates. AGIs for X^η with $\eta \in (0, 1]$ for $d \in [2, 12]$. Saturation points $(\gamma t)^*$ were calculated by interpolation and root-finding. A power law model was fitted with parameters $\alpha(\eta)$ (blue, circles), $\beta(\eta)$ (red, triangles), and $\delta(\eta)$ (black, squares) were then fitted to sigmoidal and exponential models (dashed lines) as functions of η.

and, fitted by nonlinear least-squares regression, resulted in $R^2 > 0.999$ for each fit. It is interesting to note that for the case of the identity gate, the saturation point remains constant independent of dimension.

Continuing the investigation, we performed regression analysis of the fitted model parameters α, β and δ across the set of η values. We observed that parameter α was best described by a sigmoid model while β and δ by exponential models,

$$\alpha(\eta) = \frac{\alpha_0}{(1 + e^{\alpha_1(\eta - \alpha_2)})} + \alpha_3, \tag{5.62}$$

$$\beta(\eta) = \beta_0 e^{\beta_1(\eta - \beta_2)} + \beta_3, \tag{5.63}$$

$$\delta(\eta) = \delta_0 e^{\delta_1(\eta - \delta_2)} + \delta_3. \tag{5.64}$$

The initial analysis was performed for each gate in a range of values $\eta = (0, 1]$ for $d \in [2, 12]$ by: (1) computing the AGIs numerically for a range of γt values in Python using QuTiP's `propagator` and `process_fidelity` methods, (2) interpolating the AGI curves using SciPy.`interpolate.CubicSpline`, and (3) finding the plateau saturation points $(\gamma t)^*$ by root-finding with SciPy.`optimize.root_scalar`.

Then, this three-parameter power law model in Eq. (5.61) was fitted on $(\gamma t)^*$ as a function of d for each η curve by nonlinear least-squares regression using the `optimize.curve_fit` method from SciPy. This produced three sets of data for the fitted parameters α, β, γ as functions of η. These three curves were then themselves fitted to their respective sigmoidal and exponential models in Eqs. (5.62) to (5.64), using the same SciPy.`optimize.curve_fit` method. The models showed good agreement with the data, with $R^2(\alpha) = 0.9992$, $R^2(\beta) = 0.9992$ and $R^2(\delta) = 0.9989$.

The fitted data points and resulting models are shown in Fig. 5.12. We note that the outliers at small values of η (including $\eta = 0$ for the identity gate with constant $(\gamma t)^*$) are due to the near-constant saturation point values of these gates over the range of d, which slowly transition towards more power-law-like behaviour as η increases. For

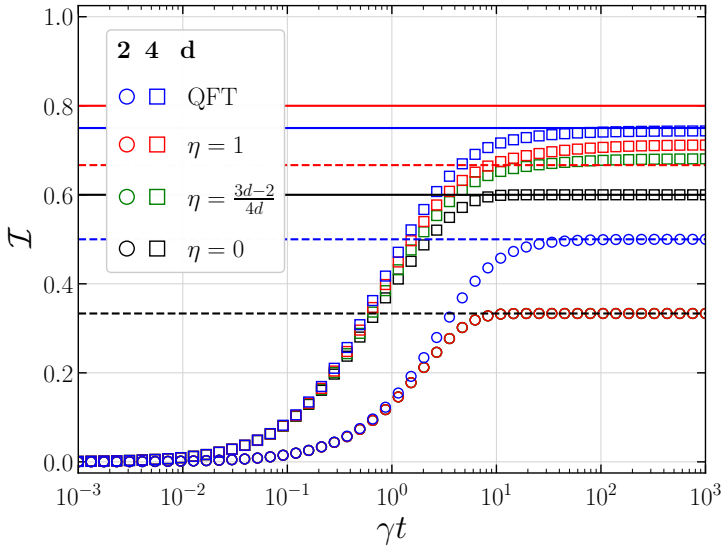


Figure 5.13 – Effect of bit-flip errors on the AGI. X^η and QFT gate simulations were repeated on qudits for $d \in \{2, 4\}$ undergoing bit-flip ($L = J_x$) errors, rather than pure dephasing noise. For $d = 2$ (circles) and $d = 4$ (squares) the following gates were simulated: $\mathbb{1} = X^0$ (black, $\eta = 0$), X^η (green, $\eta = \frac{3d-2}{4d}$), X (red, $\eta = 1$) and QFT (blue). The dashed ($d = 2$) and solid ($d = 4$) horizontal lines show the upper ($1 - \frac{1}{d+1}$, red) and lower ($1 - \frac{2}{d+1}$, black) bounds of the AGIs, as well as the mean ($1 - \frac{1}{d}$, blue). For qubits, the AGIs for all matrix powers of the X^η gate behaved exactly as the $\mathbb{1}$ gate, while for $d = 4$ the plateau AGI values for the non-zero matrix powers were observed to deviate upwards from the identity gate, but not to the same extent as for the case of pure dephasing. On the other hand, the QFT gate response was the same for both types of noise.

example, for $\eta = 0$ the saturation point is constant in d, giving a horizontal line. Fitting a power-law curve to this dataset was possible but required unrealistic fit parameters like $\alpha \sim 10^{50}$. Nevertheless, this analysis hints at a potential approach for estimating the saturation points based only on the parameter η, without requiring the explicit numerical simulation.

5.4.4.4 Effect of bit-flip errors on the AGI

Thus far in our investigation, we have restricted analysis to the effect of pure dephasing by the operator J_z on a qudit. Let us conclude this section by studying the effects of the $L = J_x$ operator, corresponding to bit-flip errors. In Fig. 5.13, we present simulations of 4 gates: the QFT gate F and 3 X^η gates for $\eta = 0, \frac{3d-2}{4d}, 1$, for qubits (circles) and $d = 4$ qudits (squares). The qubit case for the X^η gates is pathological, since for $d = 2$ the J_x operator commutes with the X^η gates and thus the AGIs plateau at the level of the identity gate. This changes for $d = 4$ where they no longer commute. However, it is interesting to observe that the behaviour is different from the J_z case, and the X^η gates plateau below the QFT gate.

5.4.5 First- and Second-Order Correction Terms to the AGI

Section 5.4.1 presented our general result for the perturbative expansion of the AGI to arbitrary order m in Eq. (5.30). Now, let us investigate in further detail the first and second-order correction terms.

5.4.5.1 First order

Beginning with the first-order correction, at $m = 1$, it can be seen that (see Appendix D.2.5) the trace over $M^{(1)}$ simplifies to

$$\mathcal{I}^{(1)} = -\frac{(\gamma t)}{d(d+1)} \operatorname{Tr}\{\mathcal{L}\}, \tag{5.65}$$

which confirms the gate-independent nature of the first-order term as the AGI depends only on the noise superoperator $\mathcal{L}$. Additionally, this trace can be expressed in terms of the regular operator L as

$$\operatorname{Tr}\{\mathcal{L}\} = |\operatorname{Tr}\{L\}|^2 - d \operatorname{Tr}\left\{L^\dagger L\right\}, \tag{5.66}$$

reproducing the results of [122]. For the case of pure dephasing, we obtain the familiar result in Eq. (5.37)

$$\mathcal{I}^{(1)} = \frac{\gamma t}{12} d(d-1), \tag{5.67}$$

using the element-wise definition of the dephasing operator in Eq. (5.19)

$$(J_z)_{ii} = \frac{d-(2i-1)}{2}. \tag{5.68}$$

Now, if we compare this analytical result with numerical simulations, we observe in Fig. 5.14 the relative error of the first-order correction to the AGI for dimensions $d = 2, 4$ over $\gamma t \in [0, 0.1]$. This relative error is expressed by

$$\varepsilon_{\mathcal{I}}^{(1)} = \frac{\mathcal{I} - \mathcal{I}^{(1)}}{\mathcal{I}}. \tag{5.69}$$

The simulations were performed for the QFT, identity, X and X^η gates for $\eta = \frac{3d-2}{4d}$. The dashed lines show the expected analytic results for each dimension. The dark and light shaded regions represent the standard deviations and max-min values taken over a sample of Haar random gates

Clearly, the gate independence of the first-order correction term matches precisely the identity gate. The remaining gates show the expected deviation from linearity, with the analytic value underestimating the AGI values. We observe that the relative error for $d = 2$ is approximately one order of magnitude smaller than for $d = 4$.

5.4.5.2 Second order

Moving on to the second-order correction term, we have from Eq. (5.30)

$$\mathcal{I}^{(2)} = \sum_{n_1,n_2=0}^{\infty} \frac{-(\gamma t)^2(-t)^{n_1+n_2} \operatorname{Tr}\{[(S)^{n_1}, \mathcal{L}][(S)^{n_2}, \mathcal{L}]\}}{d(d+1)n_1!(n_2+1)!(n_1+n_2+2)}, \tag{5.70}$$

which we reduce (see Appendix D.2.6) to a single iterated commutator using the relation $n_1 + n_2 + 2 = s$,

$$\mathcal{I}^{(2)} = -\frac{(\gamma t)^2}{d(d+1)} \sum_{s=0}^{\infty} \operatorname{Tr}\{\mathcal{L}\,[(\mathcal{S})^s, \mathcal{L}]\} \frac{(-t)^s}{(s+2)!}. \tag{5.71}$$

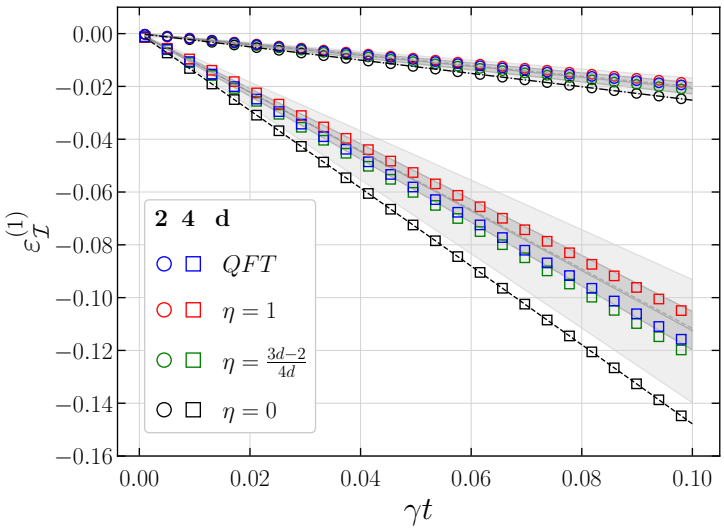


Figure 5.14 – Relative error of the first-order correction to the AGI, and gate-dependent deviation from linearity. AGIs were simulated for 4 gates acting on qubits (circles) and $d = 4$ qudits (squares) undergoing $L = J_z$ pure dephasing. The relative error $\varepsilon_{\mathcal{I}}^{(1)} = \frac{\mathcal{I}-\mathcal{I}^{(1)}}{\mathcal{I}}$ was calculated for the first-order analytical correction. The dashed-dotted and dashed lines represent the first-order term of the perturbative expansion of the AGI, for $d = 2$ and $d = 4$, respectively. These gate-independent terms correspond to the behaviour of the identity gate, $\mathbb{1} = X^0$ (black, $\eta = 0$). The X^η (green, $\eta = \frac{3d-2}{4d}$), X^1 (red, $\eta = 1$) and F (blue, QFT) gates show significant deviation from the gate-independent term, and for $d = 4$ are roughly 10 times larger than for $d = 2$. The solid and dashed grey lines represent the mean and median relative errors over a sample of $n = 4800$ Haar-random gates, with the light and dark shaded areas indicating the min-max bounds and standard deviations.

For $s = 0$, the trace term reduces further to $\mathrm{Tr}\{\mathcal{L}^2\}$ by definition of the iterated commutator. Additionally, we show (see Appendix D.2.7) that, using the property [195],

$$[(A)^s, B] = \sum_{k=0}^{s} (-1)^k \binom{s}{k} A^{s-k} B A^k, \tag{5.72}$$

the trace over the iterated commutator is zero for all odd values of s. Therefore,

$$\mathcal{I}^{(2)} = -\frac{(\gamma t)^2}{d(d+1)} \left(\frac{\mathrm{Tr}\{\mathcal{L}^2\}}{2} + \sum_{s=2}^{\infty} \frac{\mathrm{Tr}\{\mathcal{L}[(\mathcal{S})^s, \mathcal{L}]\}(-t)^s}{(s+2)!} \right). \tag{5.73}$$

This shows us that the AGI remains gate-independent at order $\gamma^2 t^2$. Indeed the first appearance of gate-dependence through the $\mathcal{S}$ operator occurs at order $\gamma^2 t^4$, when $s = 2$ and the iterated commutator term contains $\mathcal{S}$ and is non-zero.

5.4.5.3 Convergence of the iterated commutator

Since the summation of s is over all even integers, we can introduce a maximum cutoff value to render this calculation computationally tractable. Indeed, for the correction term to not be unbound, we must have that the sum is convergent, allowing us to identify such a value. We can understand this computationally by identifying the s-th order of the summation,

$$f(s) = \mathrm{Tr}\{\mathcal{L}\,[(\mathcal{S})^s, \mathcal{L}]\} \frac{(-t)^s}{(s+2)!}. \tag{5.74}$$

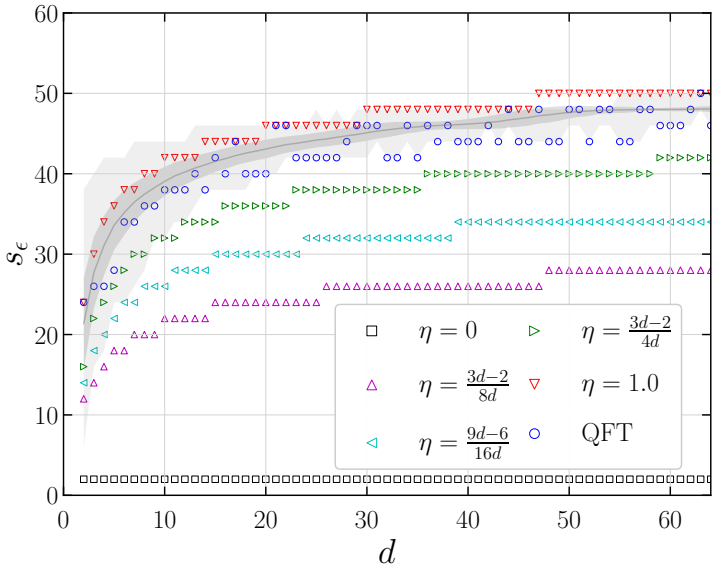


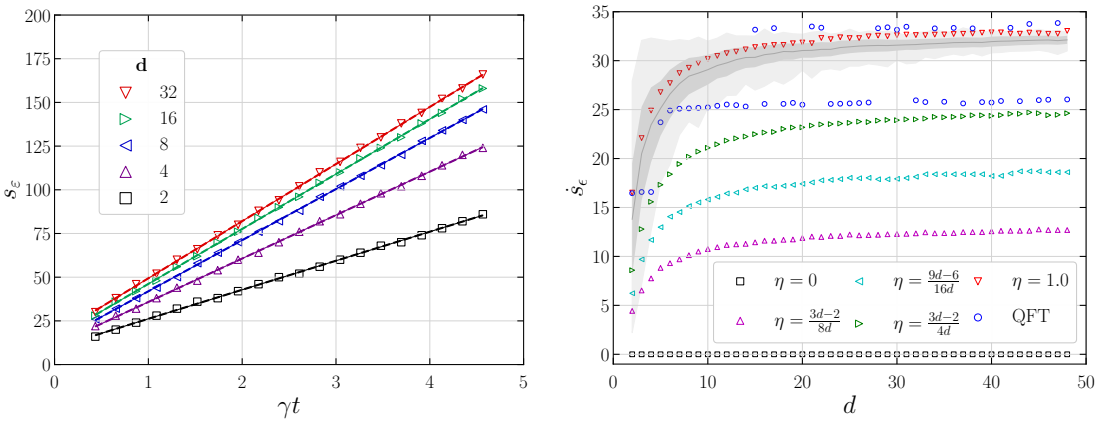
Figure 5.15 – Iteration-dependent convergence of the second-order AGI correction against qudit dimension. The critical order s_ε was calculated as the number of iterations over the summation term in the second-order AGI correction such that the absolute difference $|f_2(s_\varepsilon) - f_2(s_\varepsilon - 1)| < \varepsilon$ is less than the error threshold $\varepsilon = 1 \times 10^{-8}$. Calculations were performed for a set of interpolated X^η gates and the QFT gate, as well as $n = 2500$ Haar-random gates, over dimensions $d \in [2, 64]$. The identity gate ($\eta = 0$) only required the minimal $s = 2$ iterations, independent of dimension, since the identity commutes with the collapse operator. Of the interpolated gates, the number of iterations required scales with the interpolation parameter η, while the QFT gate shows marked variation over d, without exceeding the critical order for $\eta = 1$. The mean of the Haar-random gates (dark grey) also lies below the $\eta = 1$ curve, while the min-max interval, (light grey), shows gates at lower dimension requiring a larger number of iterations to converge.

Then, for a given error threshold ε, the cutoff order s_ε is simply the s at which the absolute difference from the preceding order $s_\varepsilon - 2$ is below this threshold,

$$|f(s_\varepsilon) - f(s_\varepsilon - 2)| < \varepsilon. \tag{5.75}$$

In Fig. 5.15 we present this iteration-dependent convergence of the second-order AGI correction term. Our set of interpolated X^η gates and the QFT gate were simulated over dimensions $d \in [2, 64]$ for a uniform gate time of $t = 1$. We calculated for each of them the cutoff order s_ε within an error threshold $\varepsilon = 1 \times 10^{-8}$. This analysis was repeated for a set of $n = 2500$ Haar random gates, and shown by the grey curve (mean value) and shaded region (bounds). It is useful to note that the number of iterations required grows approximately logarithmically with d. Furthermore we have a fairly clear range of validity on s_ε for the gates, although the X gate does not give a consistent upper bound here for smaller dimensions. On the other hand, the identity gate $\mathbb{1} = X^0$ always gives the lower bound of $s_\varepsilon = 2$, since then $[\mathbb{1}, \mathcal{L}] = \mathbb{0}$.

Next, we need to investigate the effect of the gate time parameter t on the second-order correction term, since in the summation it is raised to the power of s. We choose our set of quantum gates, $U_g \in \{X^\eta, F\}$ with $\eta \in \{0, \frac{3d-2}{8d}, \frac{9d-6}{16d}, \frac{3d-2}{4d}, 1\}$, and simulate them on qudits of dimension $d \in [2, 48]$. Instead of varying the noise parameter γ with constant gate time $t = 1$, we fix $\gamma = 1$ and then vary the gate time $t \in [0, 5]$. Note that, in order to implement the full quantum gate during this modified gate time, the amplitude of the



(a) **(b)**

Figure 5.16 – Time dependence of the convergence of the second-order AGI correction over qudit dimension. (a) The X gate ($\eta = 1$) was simulated for dimensions $d \in \{2, 4, 8, 16, 32\}$ over gate times $\gamma t \in [0.5, 4.5]$ with $\gamma = 1$ fixed. The second-order gate-dependent correction term was calculated at each t for increasing order s in the summation until convergence between successive terms was obtained at the critical value s_ε. For each d, a linear model was fitted to the data as shown by the dashed lines. (b) Linear gradients of the critical order s_ε as a function of t were fitted by linear regression for each of a set of gates at each dimension $d \in [2, 48]$. The gate set included the QFT, identity (X^0), X, and uniformly interpolated X^η gates and $n = 200$ Haar-random gates. For the identity gate this is constant at zero-gradient, while the gradients for the interpolated gates show rapid initial growth that levels off as d increases. The gradients of the QFT gates for $d > 10$ appear to populate two distinct regimes around 25 and 33. The sampled Haar-random gates exhibit behaviour similar to that of the X gate within one standard deviation of the mean, and the large variation at lower dimensions stabilises as d increases.

control-pulse Hamiltonian matrix must be modulated by the inverse of the gate time, $H_c \to \frac{1}{t} H_c$.

Then, the number of iterations s_ε required to reach convergence of two successive terms in the summation was calculated according to Eq. (5.74) and Eq. (5.75). Interestingly, we can see that in Fig. 5.16a the s_ε does indeed appear linear in t for each dimension shown for the X gate: $s_\varepsilon \propto t$. We found that this behaviour extends to other η values. Therefore, a linear least-squares regression was performed on these data points using the SciPy.`optimize.curve_fit` with model

$$s_\varepsilon = mt + c, \tag{5.76}$$

where $m = \frac{\mathrm{d}s_\varepsilon}{\mathrm{d}t}$. The resulting fitted models for the example of the X gate are shown in Fig. 5.16a alongisde the data points, indicating good agreement. The resulting gradients $m = \frac{\mathrm{d}s_\varepsilon}{\mathrm{d}t}$ for each fitted curve for each gate as a function of qudit dimension are thus the data shown in Fig. 5.16b.

This analysis is also extended to a set of $n = 200$ Haar random gates at each dimension, indicated by the grey curve and shaded regions. The interpolated gates all appear to evolve smoothly to a nearly constant value at large d. On the other hand, the QFT gate for $d > 6$ appears to oscillate randomly between two constant regimes near $\frac{\mathrm{d}s_\varepsilon}{\mathrm{d}t} \simeq 25$ and $\frac{\mathrm{d}s_\varepsilon}{\mathrm{d}t} \simeq 33$.

Based on these two analyses, we can identify a safe bound on s_ε for precise calcula-

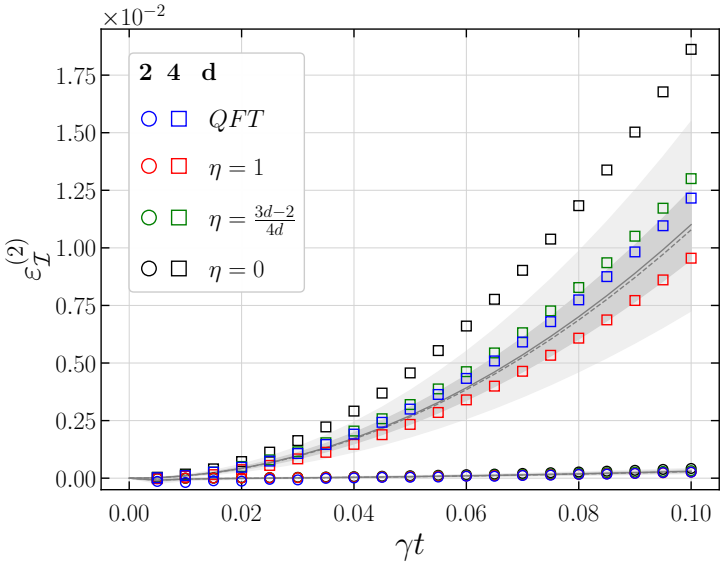


Figure 5.17 – Relative error of the AGI up to second-order. AGIs were simulated for 4 fixed gates and $n = 1000$ Haar-random gates acting on qubits (circles) and $d = 4$ qudits (squares) undergoing $L = J_z$ pure dephasing. The relative error $\varepsilon_{\mathcal{I}}^{(2)} = \frac{\mathcal{I}-\mathcal{I}^{(1)}-\mathcal{I}^{(2)}}{\mathcal{I}}$ was calculated for the second-order perturbative correction. The error for $d = 4$ is roughly 1% while for qubits this is reduced to 0.01%, two orders of magnitude lower than the relative error at first-order.

tion of the second-order correction. Recall our standard approach of normalising the Hamiltonian such that the gate time $t = 1$, varying γ only, and generally considering $d < 64$. Then, we observe that approximately 50 iterations are sufficient to calculate the second-order correction to a precision of $\varepsilon < 1 \times 10^{-8}$.

We now present in Fig. 5.17 our results for the relative error of the AGI up to second-order. The results presented follow the same approach as for those up to first-order shown in Fig. 5.14. Choosing the same set of gates, $\{X^0, X^\eta, X^1, F\}$ with $\eta = \frac{3d-2}{4d}$ and evolving over $\gamma t \in [0, 0.1]$, we show the scaling of the relative error for $d = 2, 4$,

$$\varepsilon_{\mathcal{I}}^{(2)} = \frac{\mathcal{I} - \mathcal{I}^{(1)} - \mathcal{I}^{(2)}}{\mathcal{I}}. \tag{5.77}$$

Comparing these results with those of just the first-order in Fig. 5.14, we see that the error for $d = 4$ is reduced by one order of magnitude to $\sim 1\%$, while for $d = 2$ the error of $\sim 0.01\%$ is lower by two orders of magnitude. Additionally, the sign of the relative error has changed from negative to positive, indicating that despite the increased precision, the correction up to second order will tend to understate the actual AGI value, with this error growing quadratically in γt.

5.4.5.4 Explicit operator representation

Finally, as for the first-order case, it is important to express the trace of the repeated commutator of superoperators $\mathcal{S}$ and $\mathcal{L}$ in terms of regular operators H and L. This will give a clear representation of the effect of the control Hamiltonian on the AGI, as well as its interaction with the collapse operator. Let us consider separately the two trace terms of $\mathcal{I}^{(2)}$ in Eq. (5.73): $\mathrm{Tr}\{\mathcal{L}^2\}$ and $\mathrm{Tr}\{\mathcal{L}[(\mathcal{S})^s, \mathcal{L}]\}$. We find (see Appendix D.2.5)

that the gate-independent expression can be written as

$$\mathrm{Tr}\{\mathcal{L}^2\} = \left|\mathrm{Tr}\{L^2\}\right|^2 + \frac{1}{2}\mathrm{Tr}\{L^\dagger L\}^2 + \frac{d}{2}\mathrm{Tr}\{(L^\dagger L)^2\}, \tag{5.78}$$

which, in the case of pure dephasing, $L = J_z$, reduces to

$$\mathrm{Tr}\{J_z^2\} = \frac{d^2(3 - 5d^2 + 2d^4)}{120}, \tag{5.79}$$

using the element-wise definition in Eq. (5.68). This allows us express the $\gamma^2 t^2$ correction in terms of the first-order correction term from Eq. (5.67),

$$-\frac{(\gamma t)^2}{d(d+1)}\frac{\mathrm{Tr}\{J_z^2\}}{2} = -(\gamma t)\frac{2d^2 - 3}{20}\mathcal{I}^{(1)}. \tag{5.80}$$

However, it is not necessarily the case that any m-th order expresssion can be written recursively in terms of lower orders. Equation (5.80) for the second-order appears to be a special case.

For the iterated commutator, we find that (see Appendix D.2.6)

$$\begin{aligned}
&\mathrm{Tr}\{\mathcal{L}[(\mathcal{S})^s, \mathcal{L}]\} \\
&= \sum_{k=0}^{s}\sum_{j=0}^{k}\sum_{l=0}^{s-k}\binom{s}{k}\binom{k}{j}\binom{s-k}{l}(-1)^{s+k-j-l}\times \\
&\times \mathrm{Re}\Big[\mathrm{Tr}\{LH^{k-j}LH^{s-k-l}\}^*\,\mathrm{Tr}\{LH^jLH^l\} \\
&+ \frac{1}{2}\mathrm{Tr}\{L^TL^*H^{s-j-l}\}^*\,\mathrm{Tr}\{L^TL^*H^{j+l}\} \\
&+ \frac{1}{2}\mathrm{Tr}\{L^TL^*H^{k-j}L^TL^*H^{s-k-l}\}^*\,\mathrm{Tr}\{H^{j+l}\} \\
&- \mathrm{Tr}\{LH^{k-j}L^TL^*H^{s-k-l}\}^*\,\mathrm{Tr}\{LH^{j+l}\} \\
&- \mathrm{Tr}\{L^TL^*H^{k-j}LH^{s-k-l}\}^*\,\mathrm{Tr}\{LH^{j+l}\}\Big]
\end{aligned} \tag{5.81}$$

This gives a complete description of the second-order gate-dependence in terms of the explicit Hamiltonian terms, without resorting to the superoperator representation. The superoperator and operator expressions have complexity $\mathcal{O}(sd^6)$ and $\mathcal{O}((sd)^3)$, respectively. Since we observed in Fig. 5.15 that the maximal s_ε needed to reach convergence is roughly logarithmic in d, the complexities can then be reduced to $\mathcal{O}(d^6 \log d)$ and $\mathcal{O}((d\log d)^3)$. Therefore, for $d \gg 2$, it is computationally preferred to use the operator-based expression, while for smaller qudits with $d \sim 2$, the superoperator representation is generally preferable for numerical simulations.

5.5 Discussion

5.5.1 Summary

In this work, we have performed a comprehensive analysis of the AGF for single qudit open quantum systems coupled to Markovian noise environments in the Lindblad superoperator formalism. Our primary contributions and findings are as follows:

We have expanded the AGF perturbatively in powers of the dimensionless coupling constant γt. From this we derived our main result in Eq. (5.30) for the general expressions of the correction terms to arbitrary order. The result was expressed in terms of the iterated commutators of the gate and noise superoperators, $\mathcal{S}$ and $\mathcal{L}$, respectively, based on the expansion obtained in Eq. (5.27). It is particularly significant that these corrections were expressed in a form that may be directly implemented in numerical calculations. We found that, at each order above the first, the correction term could be separated into a gate-independent term $\mathcal{O}((\gamma t)^m)$ depending only on $\mathcal{L}$, and gate-dependent terms containing $\mathcal{S}$ and higher powers of t. The first-order correction term, $\mathcal{I}^{(1)}$, is gate-independent and depends solely on the noise superoperator $\mathcal{L}$. The gate-dependence appears for the first time at $\gamma^2 t^4$, in the second-order correction term $\mathcal{I}^{(2)}$, highlighting the significant role of the interaction between the control Hamiltonian $\mathcal{S}$ and the noise operator $\mathcal{L}$. Explicit expressions for the first- and second-order correction terms in the operator representation were also derived.

Our numerical simulations under pure dephasing noise revealed a clear transition from linear to nonlinear behaviour in the AGI as the noise coupling strength γt increases. For $\gamma t \sim 1$, the AGI deviates significantly from the linear approximation and eventually reaches a plateau at a stable value. The plateau values, $\mathcal{I}^*$, as well as their corresponding saturation points, $(\gamma t)^*$, were found to be dependent not only on the qudit dimension d but also on the specific quantum gate implemented.

Indeed, utilising our theoretical framework we were able to derive in Eq. (5.57) a significant result for universal upper and lower bounds of the AGI plateau values in the strong coupling regime, depending only on the dimensionality of the system. Furthermore we were able to identify specific gates that saturate these bounds: The identity gate ($\mathbb{1}_d$) and the generalised-NOT (X) achieve the lower and upper limits, respectively, while the QFT gate (F_d) was found to plateau at the mean AGI value of the Haar measure. Additionally, we introduced the interpolated X^η gates to demonstrate the range of AGI values between these bounds. The saturation points of these interpolated gates were studied numerically, and were well-described by a power-law model of $(\gamma t)^*$ vs d.

We analysed the convergence behaviour of the second-order correction term, identifying that approximately 50 iterations are sufficient for precise calculation up to a qudit dimension of $d < 64$ within an absolute tolerance of $\varepsilon < 1 \times 10^{-8}$. The number of iterations to convergence was found to scale logarithmically with the system dimension d, and linearly with the gate time t.

Numerical simulations confirmed the analytical predictions, demonstrating that the relative error of the AGI is significantly reduced when including the second-order correction term. For $d = 4$, the error is reduced to the order of 1%, and for $d = 2$, it is reduced to 0.01%, indicating the necessity of higher-order corrections for accurate fidelity modeling, particularly as the dimension of the system increases.

5.5.2 Outlook

The detailed insights gained from this study have several important applications and implications for the field of quantum computing, particularly given the growing interest in qudits. Understanding the behaviour of the AGI and its dependence on the type of quantum gate and environmental noise facilitates the optimisation of quantum gate design. Our approach provides a methodology for identifying quantum gates that have favourable fidelity characteristics. Thus, through appropriate choice or design of basis

gates it may be possible to enhance the performance of quantum circuits. This could lead to significant improvements for optimising the robustness of quantum algorithms on near-term noisy platforms.

The results underscore the importance of incorporating higher-order corrections into error correction protocols. This is particularly relevant for qudits of higher dimensions, where noise effects are more pronounced. We envisage that the detailed perturbative expansions provided in this work could be leveraged to develop advanced error correction techniques, for example by incorporating the higher-order correction terms into the cost function of optimal control methods. In particular, our correction terms can be used to quantify and mitigate the error in logical qubit embedding protocols up to arbitrary order. Future research is needed to show how this could result in protection against such errors above first-order, and how this might incorporate the gate-dependencies identified.

The derived bounds and behaviours of AGI for different gates and dimensions also serve as benchmarks for assessing the performance of quantum systems. These benchmarks can guide experimentalists in evaluating and improving their quantum hardware and gate implementations. Indeed further study is needed to extend these results from the idealised single-pulse (time-independent) Hamiltonian to realistic pulse-based optimal control techniques for gate generation.

While this study focused primarily on pure dephasing and bit-flip errors, future research should explore further the impact of other noise models, such as amplitude damping and depolarising noise. Understanding how different types of noise affect the AGI will provide a more comprehensive framework for designing noise-resilient quantum systems.

Extending the framework to multi-qudit systems is a necessity. These introduce additional complexity due to inter-qudit interactions and correlated noise effects. Investigating these factors will be crucial for the scalability of qudit-based architectures, but could prove fruitful in reducing the circuit complexity of long range entangling operations.

Finally, it would be beneficial to have experimental verification of these predictions. Testing the derived correction terms and transition points in real quantum systems will help to validate and refine the models presented.

In conclusion, this study provides a detailed theoretical foundation for understanding the fidelity of quantum gates in noisy environments. The findings contribute to the ongoing efforts to develop robust, high-fidelity quantum operations, paving the way for practical and scalable quantum computing.

References Cited in this Chapter

[1] O. Ezratty. "Perspective on superconducting qubit quantum computing". In: *The European Physical Journal A* 59.5 (May 2, 2023), p. 94. DOI: 10.1140/epja/s10050-023-01006-7.

[16] Y. Chi, J. Huang, et al. "A programmable qudit-based quantum processor". In: *Nature Communications* 13.1 (Mar. 4, 2022), p. 1166. DOI: 10.1038/s41467-022-28767-x.

[21] E. Moreno-Pineda, C. Godfrin, et al. "Molecular Spin Qudits for Quantum Algorithms". In: *Chemical Society Reviews* 47.2 (2018), pp. 501–513. DOI: 10.1039/c5cs00933b.

[26] F. Arute, K. Arya, et al. "Quantum supremacy using a programmable superconducting processor". In: *Nature* 574.7779 (Oct. 24, 2019), pp. 505–510. DOI: 10.1038/s41586-019-1666-5.

[31] Y. Wang, Z. Hu, et al. "Qudits and High-Dimensional Quantum Computing". In: *Frontiers in Physics* 8 (Nov. 10, 2020), p. 589504. DOI: 10.3389/fphy.2020.589504.

[32] N. P. Brusentsov and J. Ramil Alvarez. "Ternary Computers: The Setun and the Setun 70". In: *Perspectives on Soviet and Russian Computing*. Ed. by J. Impagliazzo and E. Proydakov. Vol. 357. IFIP Advances in Information and Communication Technology. Berlin, Heidelberg: Springer Berlin Heidelberg, 2011, pp. 74–80. DOI: 10.1007/978-3-642-22816-2_10.

[33] A. Chiesa, F. Petiziol, et al. "Embedded quantum-error correction and controlled-phase gate for molecular spin qubits". In: *AIP Advances* 11.2 (Feb. 1, 2021), p. 025134. DOI: 10.1063/9.0000166.

[41] E. Moreno-Pineda and W. Wernsdorfer. "Measuring molecular magnets for quantum technologies". In: *Nature Reviews Physics* 3.9 (Sept. 2021), pp. 645–659. DOI: 10.1038/s42254-021-00340-3.

[42] S. Thiele, F. Balestro, et al. "Electrically driven nuclear spin resonance in single-molecule magnets". In: *Science* 344.6188 (June 6, 2014), pp. 1135–1138. DOI: 10.1126/science.1249802.

[43] C. Godfrin, A. Ferhat, et al. "Operating Quantum States in Single Magnetic Molecules: Implementation of Grover's Quantum Algorithm". In: *Physical Review Letters* 119.18 (Nov. 2, 2017), p. 187702. DOI: 10.1103/PhysRevLett.119.187702.

[56] W. Wernsdorfer and M. Ruben. "Synthetic Hilbert Space Engineering of Molecular Qu *d* its: Isotopologue Chemistry". In: *Advanced Materials* 31.26 (June 2019), p. 1806687. DOI: 10.1002/adma.201806687.

[83] V. Gorini, A. Kossakowski, et al. "Completely positive dynamical semigroups of *N* -level systems". In: *Journal of Mathematical Physics* 17.5 (May 1, 1976), pp. 821–825. DOI: 10.1063/1.522979.

[84] G. Lindblad. "On the generators of quantum dynamical semigroups". In: *Communications in Mathematical Physics* 48.2 (June 1976), pp. 119–130. DOI: 10.1007/BF01608499.

[85] D. Manzano. "A short introduction to the Lindblad master equation". In: *AIP Advances* 10.2 (Feb. 1, 2020), p. 025106. DOI: 10.1063/1.5115323.

[90] F. Petiziol, A. Chiesa, et al. "Counteracting dephasing in Molecular Nanomagnets by optimized qudit encodings". In: *npj Quantum Information* 7.1 (Aug. 26, 2021), p. 133. DOI: 10.1038/s41534-021-00466-3.

[91] A. Chiesa, E. Macaluso, et al. "Molecular Nanomagnets as Qubits with Embedded Quantum-Error Correction". In: *The Journal of Physical Chemistry Letters* 11.20 (Oct. 15, 2020), pp. 8610–8615. DOI: 10.1021/acs.jpclett.0c02213.

[122] D. Janković, J.-G. Hartmann, et al. "Noisy qudit vs multiple qubits: conditions on gate efficiency for enhancing fidelity". In: *npj Quantum Information* 10.1 (June 10, 2024), p. 59. DOI: 10.1038/s41534-024-00829-6.

[126] M. A. Nielsen. "A simple formula for the average gate fidelity of a quantum dynamical operation". In: *Physics Letters A* 303.4 (Oct. 2002), pp. 249–252. DOI: 10.1016/S0375-9601(02)01272-0.

[127] J. R. Johansson, P. D. Nation, et al. "QuTiP: An open-source Python framework for the dynamics of open quantum systems". In: *Computer Physics Communications* 183.8 (Aug. 2012), pp. 1760–1772. DOI: 10.1016/j.cpc.2012.02.021.

[128] J. R. Johansson, P. D. Nation, et al. "QuTiP 2: A Python framework for the dynamics of open quantum systems". In: *Computer Physics Communications* 184.4 (Apr. 2013), pp. 1234–1240. DOI: 10.1016/j.cpc.2012.11.019.

[129] J.-G. Hartmann, D. Janković, et al. "Nonlinearity of the Fidelity in Open Qudit Systems: Gate and Noise Dependence in High-dimensional Quantum Computing". In: *Quantum* 9 (Apr. 7, 2025), p. 1690. DOI: 10.22331/q-2025-04-07-1690.

[130] J.-G. Hartmann, D. Janković, et al. *Code and Data for "Nonlinearity of the Fidelity in Open Qudit Systems: Gate and Noise Dependence in High-dimensional Quantum Computing"*. Zenodo, Mar. 19, 2025. DOI: 10.5281/ZENODO.13618284.

[131] N. P. De Leon, K. M. Itoh, et al. "Materials challenges and opportunities for quantum computing hardware". In: *Science* 372.6539 (Apr. 16, 2021), eabb2823. DOI: 10.1126/science.abb2823.

[132] M. Ringbauer, M. Meth, et al. "A universal qudit quantum processor with trapped ions". In: *Nature Physics* 18.9 (Sept. 2022), pp. 1053–1057. DOI: 10.1038/s41567-022-01658-0.

[133] H. Miyahara, Y. Chen, et al. "Decoherence mitigation by embedding a logical qubit in a qudit". In: *Quantum Information Processing* 22.7 (July 11, 2023), p. 278. DOI: 10.1007/s11128-023-04035-9.

[134] L. G. Gunderman. "Local-dimension-invariant qudit stabilizer codes". In: *Physical Review A* 101.5 (May 28, 2020), p. 052343. DOI: 10.1103/PhysRevA.101.052343.

[135] Y. Zheng, H. Sharma, et al. "Entanglement Distribution with Minimal Memory Requirements Using Time-Bin Photonic Qudits". In: *PRX Quantum* 3.4 (Nov. 16, 2022), p. 040319. DOI: 10.1103/PRXQuantum.3.040319.

[136] F. Bouchard, R. Fickler, et al. "High-dimensional quantum cloning and applications to quantum hacking". In: *Science Advances* 3.2 (Feb. 3, 2017), e1601915. DOI: 10.1126/sciadv.1601915.

[137] S. Boixo, S. V. Isakov, et al. "Characterizing quantum supremacy in near-term devices". In: *Nature Physics* 14.6 (June 2018), pp. 595–600. DOI: 10.1038/s41567-018-0124-x.

[138] M. Otten, K. Kapoor, et al. "Impacts of noise and structure on quantum information encoded in a quantum memory". In: *Physical Review A* 104.1 (July 16, 2021), p. 012605. DOI: 10.1103/PhysRevA.104.012605.

[139] M. A. Nielsen and I. L. Chuang. *Quantum computation and quantum information*. Cambridge, NY: Cambridge University Press, 2000. 676 pp. DOI: 10.1017/CBO9780511976667.

[167] M. Suezen, C. Weber, et al. *Spectral Ergodicity In Deep Learning Architectures Via Surrogate Random Matrices*. July 3, 2017. DOI: 10.5281/zenodo.822410.

[174] H.-P. Breuer and F. Petruccione. *The Theory of Open Quantum Systems*. First. Oxford: Oxford University Press, Jan. 25, 2007. DOI: 10.1093/acprof:oso/9780199213900.001.0001.

[175] J. Watrous. *The Theory of Quantum Information*. First. Cambridge: Cambridge University Press, Apr. 26, 2018. DOI: 10.1017/9781316848142.

[176] I. Bengtsson and K. Zyczkowski. *Geometry of Quantum States: An Introduction to Quantum Entanglement*. First. Cambridge: Cambridge University Press, May 11, 2006. DOI: 10.1017/CBO9780511535048.

[177] T. F. Havel. "Robust procedures for converting among Lindblad, Kraus and matrix representations of quantum dynamical semigroups". In: *Journal of Mathematical Physics* 44.2 (Feb. 1, 2003), pp. 534–557. DOI: 10.1063/1.1518555.

[178] T. A. Loring. "Computing a logarithm of a unitary matrix with general spectrum". In: *Numerical Linear Algebra with Applications* 21.6 (Dec. 2014), pp. 744–760. DOI: 10.1002/nla.1927.

[179] M. Aifer and S. Deffner. "From quantum speed limits to energy-efficient quantum gates". In: *New Journal of Physics* 24.5 (May 1, 2022), p. 055002. DOI: 10.1088/1367-2630/ac6821.

[180] A. Vourdas. "Quantum systems with finite Hilbert space". In: *Reports on Progress in Physics* 67.3 (Mar. 1, 2004), pp. 267–320. DOI: 10.1088/0034-4885/67/3/R03.

[181] J. Martínez-Carranza, F. Soto-Eguibar, et al. "Alternative analysis to perturbation theory in quantum mechanics: Dyson series in matrix form". In: *The European Physical Journal D* 66.1 (Jan. 2012), p. 22. DOI: 10.1140/epjd/e2011-20654-5.

[182] B. M. Villegas-Martínez, F. Soto-Eguibar, et al. "Application of Perturbation Theory to a Master Equation". In: *Advances in Mathematical Physics* 2016 (2016), pp. 1–7. DOI: 10.1155/2016/9265039.

[183] J. E. Campbell. "On a Law of Combination of Operators bearing on the Theory of Continuous Transformation Groups". In: *Proceedings of the London Mathematical Society* s1-28.1 (Nov. 1896), pp. 381–390. DOI: 10.1112/plms/s1-28.1.381.

[184] B. C. Hall. *Lie groups, Lie algebras, and representations: an elementary introduction*. Second edition. Graduate texts in mathematics 222. Cambridge, NY: Springer, 2015. 449 pp. DOI: 10.1007/978-3-319-13467-3.

[185] B. Collins, S. Matsumoto, et al. "The Weingarten Calculus". In: *Notices of the American Mathematical Society* 69.5 (May 1, 2022), p. 1. DOI: 10.1090/noti2474.

[186] F. Mezzadri. "How to generate random matrices from the classical compact groups". In: *Notices of the American Mathematical Society* 54.5 (Feb. 27, 2007), pp. 592–604. DOI: 10.48550/arXiv.math-ph/0609050.

[187] F. J. Dyson. "The Threefold Way. Algebraic Structure of Symmetry Groups and Ensembles in Quantum Mechanics". In: *Journal of Mathematical Physics* 3.6 (Nov. 1, 1962), pp. 1199–1215. DOI: 10.1063/1.1703863.

[188] M. L. Mehta. *Random matrices*. Third. Pure and applied mathematics series 142. Amsterdam: Elsevier, 2004. 688 pp. DOI: 10.1016/S0079-8169(04)80088-6.

[189] E. P. Wigner. "Characteristic Vectors of Bordered Matrices With Infinite Dimensions". In: *The Annals of Mathematics* 62.3 (Nov. 1955), p. 548. DOI: 10.2307/1970079.

[190] C. Developers. *Cirq*. Google Quantum AI, Dec. 1, 2023. DOI: 10.5281/ZENODO.4062499.

[191] A. A. Giannopoulos and V. D. Milman. "Concentration Property on Probability Spaces". In: *Advances in Mathematics* 156.1 (Dec. 2000), pp. 77–106. DOI: 10.1006/aima.2000.1949.

[192] M. Ledoux. *The concentration of measure phenomenon*. Mathematical surveys and monographs Issue 89. Providence, RI: American Mathematical Society, 2001. DOI: 10.1090/surv/089.

[193] M. Horodecki, P. Horodecki, et al. "General teleportation channel, singlet fraction, and quasidistillation". In: *Physical Review A* 60.3 (Sept. 1, 1999), pp. 1888–1898. DOI: 10.1103/PhysRevA.60.1888.

[194] E. S. Meckes. *The Random Matrix Theory of the Classical Compact Groups*. First. Cambridge: Cambridge University Press, Aug. 31, 2019. DOI: 10.1017/9781108303453.

[195] H. C. Volkin, U. S. N. Aeronautics, et al. *Iterated commutators and functions of operators*. NASA technical note. National Aeronautics and Space Administration, 1968.

CHAPTER 6

QUANTUM OPTIMAL CONTROL TECHNIQUES FOR QUDIT GATE SYNTHESIS

Who controls the past controls the future. Who controls the present controls the past.

Party slogan in "1984" - George Orwell

Contents

6.1 Introduction . . . 167
6.1.1 Background . . . 167
6.1.2 Objectives and Contributions . . . 168
6.1.3 Organisation . . . 168
6.2 Theory . . . 169
6.2.1 Modelling and Control of Single-qudit Systems . . . 169
6.2.1.1 Quantum mechanics for quantum computing . . . 169
6.2.1.2 Pulse-level control of quantum systems . . . 171
6.2.1.3 Controllability and universality . . . 177
6.2.1.4 Sources of control errors . . . 177
6.2.2 Gate Generation Techniques . . . 180
6.2.2.1 Givens rotation decomposition . . . 180
6.2.2.2 GRAPE algorithm . . . 184
6.3 Methods . . . 186
6.3.1 Numerical Tools . . . 186
6.3.1.1 Standard libraries . . . 186
6.3.1.2 External libraries . . . 186
6.3.2 Simulation Framework . . . 187
6.4 Results . . . 188
6.4.1 Gate Synthesis . . . 189
6.4.1.1 Givens rotation decomposition . . . 192
6.4.1.2 GRAPE algorithm . . . 194
6.4.2 Comparison of the Different Gate Synthesis Methods . . . 196
6.4.2.1 Computational cost . . . 197
6.4.2.2 Gate times . . . 199
6.4.2.3 Effects of Markovian noise on gate fidelity . . . 203
6.4.2.4 Robustness to control errors . . . 207
6.5 Discussion . . . 210
6.5.1 Summary . . . 210
6.5.2 Outlook . . . 214
References Cited in this Chapter . . . 217

Note: The results presented in this Chapter are currently being prepared as a manuscript for publication, and will be made publicly available upon submission. All code and data used in generating the results presented will be made publicly available alongside.

6.1 Introduction

In this chapter, we investigate the problem of pulse-level control techniques for single-qudit quantum systems, focusing on implementing different methods for gate synthesis and comparing their robustness to noise and control errors. The goal is to extend the capabilities of quantum control methods developed for qubit systems to higher dimensional qudits with an emphasis on their potential for quantum information processing. Qudit systems offer advantages over qubits by allowing for more compact information encoding and potentially faster implementation of certain quantum algorithms by reducing the number of entangling operations needed. However, as we have already seen, they also present significant challenges in terms of gate control and noise management. In this introduction, we provide the necessary background, outline the motivation and objectives of this study, summarise the key contributions, and describe the organisation of this chapter.

6.1.1 Background

Quantum optimal control has emerged as a vital area of research in the quest to build scalable and fault-tolerant quantum computers. At the heart of quantum control lies the problem of synthesising quantum gates using time-dependent control fields. Much of the research to date has focused on controlling qubit systems, where gate synthesis methods like the GRAPE algorithm [97] and other pulse-shaping techniques have proven highly effective when customised for specific hardware platforms. However, with the growing interest in qudit systems, there is a need to extend these control techniques to higher dimensions and to study their performance.

Qudits have been studied extensively for their potential to provide increased computational power of quantum systems. In particular, qudit systems allow for a more efficient encoding of quantum information, reducing the complexity of certain quantum algorithms such as Grover's algorithm [31, 54, 55]. Moreover, multi-qudit systems may exhibit enhanced robustness to noise, and with appropriate encodings may provide new avenues for fault-tolerant quantum computing [33, 90, 91, 133]. However, to fully exploit the potential of qudit systems, it is essential to develop efficient and scalable methods for controlling the larger number of control channels required, especially in the face of environmental noise and hardware imperfections.

There has been considerable progress in developing qudit gate synthesis techniques, and certain methods, such as the Givens Rotation Decomposition (GRD) [96], offer an algebraic approach to generating quantum gates through sequential rotations that scales naturally to higher-dimensional systems, making them computationally efficient for specific types of gates. However, the comparison between numerical optimisation methods, such as GRAPE, and algebraic methods, like GRD, in the context of optimal control for qudit systems remains underexplored compared to qubit systems [140].

Additionally, noise and control errors remain significant obstacles to achieving high-fidelity gates. While much attention has been given to understanding the effects of

environmental noise and control errors for specific hardware on qubit-based systems, less is known about how such noise and error impacts qudit-based systems. Through Chapters 4 and 5 thus far, we have studied the effects of Markovian environments on ideal, single-pulse, qudit gates in the linear and nonlinear regimes, respectively. Investigating these effects on pulse-level controls is crucial for the future development of quantum technologies that leverage the full potential of qudits.

6.1.2 Objectives and Contributions

The aim of this study is to advance pulse-level control techniques for qudit quantum systems, focusing on gate synthesis through the GRD and the GRAPE algorithm. By comparing these methods, we investigate their respective benefits and limitations in achieving efficient qudit gate control. Furthermore, the impact of Markovian noise, including dephasing, bit-flip, and spin relaxation, as well as control errors such as amplitude and phase fluctuations and clock skew, are analysed to understand their influence on gate fidelity.

To facilitate this exploration, we develop a modular and flexible simulation framework, providing a foundation for future research on control techniques, noise models, and more realistic error scenarios, as well as scaling to multi-qudit systems. Additionally, hybrid approaches to gate synthesis are explored by combining the GRD algebraic technique with numerical optimisation via GRAPE, aiming to enhance computational efficiency and gate fidelity.

The contributions of this work include a comparative analysis of the GRD and GRAPE algorithms for single-qudit gate synthesis, offering insights into their computational and gate efficiency. We examine the robustness of these gate synthesis methods under various noise conditions and control errors, providing guidance for mitigating the effects of noise in practical qudit systems.

Our developed simulation framework is versatile, supporting the generation and fidelity analysis of qudit gates under different conditions and facilitating future comparative studies of quantum control techniques. The introduction of hybrid synthesis approaches leverages the strengths of both algebraic and numerical methods, optimising gate performance and suggesting new directions for robust quantum control protocol development.

6.1.3 Organisation

The chapter is organised as follows: In the Section 6.2, we provide a detailed description of the theoretical background underlying qudit gate synthesis, including the GRD and GRAPE algorithm. In Section 6.3 we describe the simulation framework and noise models used in this study. Section 6.4 is divided into two parts: first, a discussion of the gate synthesis methods and their performance in noise-free conditions in Section 6.4.1; second, an analysis of the effects of noise and control errors on gate fidelity in Section 6.4.2. Here, we also introduce the hybrid approaches and discuss their impact on gate efficiency. Finally, in Section 6.5, we discuss the key findings, discuss the implications of our results, and outline future research directions.

6.2 Theory

In this section, we introduce the theoretical background for modelling qudit systems and the pulse-level control techniques used to generate quantum gates.

6.2.1 Modelling and Control of Single-qudit Systems

6.2.1.1 Quantum mechanics for quantum computing

The following definitions and concepts serve as foundational elements in quantum mechanics, especially in the context of quantum computing. They provide the necessary mathematical structures and tools used in describing quantum systems and their evolution. These concepts can be found in most pedagogical references, such as [82, 85, 184, 196, 197].

Definition 6.2.1 (Hilbert Space)**.** *We consider the finite dimensional Hilbert space $\mathcal{H} = \mathbb{C}^d$ where d is the dimension of the qudit system. $\mathcal{H}$ is a complete inner product space over the complex field with the inner product $\langle\cdot|\cdot\rangle$ inducing the Frobenius norm $\|\cdot\|^2$.*

Given this finite dimensional state space, we can define the computational basis that is used extensively in quantum computing.

Definition 6.2.2 (Computational Basis)**.** *The computational basis for a d-dimensional qudit system is given by the set of orthonormal basis vectors $\{|0\rangle, \ldots, |d-1\rangle\}$ with unit vectors $|i\rangle = e_i$.*

Now, let us define quantum states in terms of the density matrix formalism in this basis.

Definition 6.2.3 (States)**.** *In the density matrix formalism, a state of a qudit system is represented by a density matrix ρ which is a positive semi-definite, Hermitian matrix with unit trace. The density matrix is given by*

$$\rho = \sum_{i=0}^{d-1}\sum_{j=0}^{d-1} \alpha_i(t)\alpha_j^*(t)\,|i\rangle\langle j|\,, \tag{6.1}$$

where the purity of a quantum state is a measure of the mixedness of the state and is given by $\frac{1}{d} \leq \mathrm{Tr}\{\rho^2\} \leq 1$.

Definition 6.2.4 (Operators)**.** *States are transformed by bounded linear operators acting on the Hilbert space $B : \mathcal{H} \to \mathcal{H}$. These operators can be represented by matrices in the computational basis, and can be unitary, Hermitian, or Lindblad operators. They form a Banach space $\mathcal{B}(\mathcal{H})$ with the operator norm $\|B\| = \sup\|B(\rho) : \|\rho\| = 1\|$.*

The transformation of these states over time is governed by such operators, and among them, unitary quantum gates are particularly important, as they are the building blocks of quantum algorithms:

Definition 6.2.5 (Quantum Gates)**.** *A quantum gate is a unitary operator of the unitary group $U \in \mathbf{U}(d)$, being a compact, connected Lie group with associated Lie algebra $\mathfrak{u}$. It is represented by a $d \times d$ matrix with the property $U^\dagger U = UU^\dagger = \mathbb{1}$.*

Quantum gates govern the evolution of quantum states, which in turn are generated by the Hamiltonian operator of the system.

Definition 6.2.6 (Hamiltonians)**.** *The Hamiltonian operator H is a Hermitian operator that generates the unitary time evolution of the quantum state $\rho(t)$. The set of skew-Hermitian matrices iH generates the Lie algebra $\mathfrak{u}(d)$ with the commutator $[A, B] = AB - BA$ defining the Lie bracket $[\cdot, \cdot] : \mathfrak{u} \times \mathfrak{u} \to \mathfrak{u}$.*

To connect the Lie algebra to the unitary group, we make use of the matrix exponential map, which facilitates the time evolution.

Definition 6.2.7 (Matrix Exponential Map)**.** *The exponential map $\exp : \mathfrak{u}(d) \to \mathbf{U}(d)$ is a surjective map from the Lie algebra to the Lie group, defined by $U(t) = \exp(-iH(t))$. This surjectivity is a consequence of global phase invariance, thus when the operators are restricted to the interval $(-\pi, \pi]$ the exponential map is bijective.*

This leads to the time evolution for closed systems:.

Definition 6.2.8 (Liouville-Von Neumann Equation)**.** *The time evolution of the density matrix of a closed quantum system is governed by the Liouville-Von Neumann equation ($\hbar = 1$)*

$$\dot{\rho}(t) = -i[H, \rho]. \tag{6.2}$$

However, when considering open quantum systems, which interact with their environment, the time evolution is described by the Gorini-Kossakowski-Sudarshan-Lindblad (GKSL) master equation.

Definition 6.2.9 (Gorini-Kossakowski-Sudarshan-Lindblad Master Equation)**.** *The time evolution of the density matrix of an open quantum system is governed by the Gorini-Kossakowski-Sudarshan-Lindblad (GKSL) master equation ($\hbar = 1$)*

$$\dot{\rho}(t) = -i[H, \rho] + \sum_k \left(L_k \rho L_k^\dagger - \frac{1}{2} \left\{ L_k^\dagger L_k, \rho \right\} \right), \tag{6.3}$$

where L_k are the Lindblad operators corresponding to the dissipative channels of the system. These operators satisfy the Lindblad condition such that the master equation generates a quantum dynamical semigroup represented by a completely positive, trace-preserving (CPTP) quantum channel $\mathcal{E}(\rho) : \mathcal{B}(\mathcal{H}) \to \mathcal{B}(\mathcal{H})$.

In the Lindblad formalism, the dissipative channels of the system are represented by the Lindblad operators L_k that describe the interaction of the system with its environment. These operators introduce decoherence and dissipation effects that drive the system towards a steady state. We recall the definitions of the d-dimensional spin operators from Section 5.2.2, J_z, J_x, J_y and $J_\pm$:

$$J_z = \sum_{j=1}^{d} \frac{1}{2}(d + 1 - 2j) \, |j\rangle\langle j| \,, \tag{6.4}$$

$$J_x = \sum_{j=1}^{d-1} \frac{1}{2} \sqrt{j(d-j)} \left(|j+1\rangle\langle j| + |j\rangle\langle j+1| \right), \tag{6.5}$$

$$J_\pm = J_x \pm i J_y. \tag{6.6}$$

In the presence of such environmental effects, we can define the fidelity of an operation in several ways as discussed in Chapter 5:

Definition 6.2.10 (State Fidelity). *The fidelity of a quantum state ρ with respect to a target state σ is given by the expression*

$$F(\rho,\sigma) = \left|\mathrm{Tr}\left\{\sqrt{\sqrt{\rho}\sigma\sqrt{\rho}}\right\}\right|^2, \tag{6.7}$$

where the fidelity is a measure of the overlap between the two states, and is bounded by $0 \leq F(\rho,\sigma) \leq 1$.

Fidelity measures are essential tools for assessing how well a quantum system performs in achieving a desired state or operation. In the case of quantum gates, we can also define the process fidelity.

Definition 6.2.11 (Process Fidelity). *The fidelity of a quantum gate U_g with respect to a target process U_t is given by the expression*

$$F(U_g,U_t) = \left|\frac{\mathrm{Tr}\left\{U_g^\dagger U_t\right\}}{d}\right|^2, \tag{6.8}$$

measuring the overlap of the two gate operations.

Lastly, we consider the average gate fidelity, which represents the fidelity of a quantum gate across all possible input states:

Definition 6.2.12 (Average Gate Fidelity). *The average gate fidelity of a quantum gate implemented over a (noisy) quantum channel $\mathcal{E}[\rho]$ is given by the expression*

$$\bar{\mathcal{F}}(\mathcal{E},\mathcal{U}) = \int_{\mathscr{H}} \exp\left\{U^\dagger \mathcal{E}[\rho_0]U\right\}_0 d\rho_0, \tag{6.9}$$

representing the average over all possible input states ρ_0. Nielsen [126] and Horodecki et. al. [193] showed separately that it can be expressed in terms of the process fidelity as

$$\bar{\mathcal{F}}(\mathcal{E},\mathcal{U}) = \frac{dF(U_g,U_t)+1}{d+1}. \tag{6.10}$$

6.2.1.2 Pulse-level control of quantum systems

In the context of quantum computing, the control of quantum systems is achieved through the application of external fields to the system. These fields are typically represented by a time-dependent Hamiltonian $H(t)$ that drives the system from an initial state to a target state. The control of quantum systems is a central problem in quantum information science, and is typically formulated as an optimal control problem. The objective is to find the optimal control fields that minimise a cost functional while satisfying the dynamics of the system. The optimal control problem can be formulated as follows.

Definition 6.2.13 (Optimal Control Problem). *In general, given a set $\mathcal{R}$ of quantum states $\rho : \mathbb{C} \to \mathbb{C}^{d\times d}$, and a set $\mathcal{U}$ of control functions $u : \mathbb{R} \to \mathbb{R}^{d\times d}$, we want to find the functions $\rho \in \mathcal{R}$ and $u \in \mathcal{U}$ that minimise a cost functional $J : \mathcal{R}\times\mathcal{U} \to \mathbb{R}$ and satisfy the system dynamics*

$$\dot{\rho}(t) = \mathcal{L}[\rho(t),u(t)] \tag{6.11}$$

$$= -i[u(t),\rho(t)] + \mathcal{D}[\rho(t)], \tag{6.12}$$

with initial condition $\rho(0) = \rho_0$ and $\mathcal{D}[\rho(t)]$ the Lindbladian dissapator term.

We can consider 2 general types of objective or cost functionals [80, 198], referred to as problems of (i) Mayer type:

$$\mathcal{J}[u] = \phi(\rho(T), T), \tag{6.13}$$

and those of (ii) Lagrange type:

$$\mathcal{J}[u] = \int_0^T \mathcal{L}[\rho(t), u(t), t]\,\mathrm{d}t\,. \tag{6.14}$$

Generally speaking, we can consider the Mayer terms to represent the cost of reaching the target state at the final time T, and the Lagrange terms to represent the cost of the control fields over the entire time interval $[0, T]$. Some examples of Mayer terms include the fidelity of the final state with respect to the target state, and the total time taken to reach the target state. Lagrange terms can introduce time-dependent constraints on the control fields, such as bounds on the amplitude, the rate of change or the total energy cost.

One can also consider hybrid cost functionals that combine both Mayer and Lagrange terms, known as problems of Bolza type,

$$\mathcal{J}[u] = \alpha\phi(\rho(T), T) + (1-\alpha)\int_0^T \mathcal{L}[\rho(t), u(t), t]\,\mathrm{d}t\,, \tag{6.15}$$

where we introduce the weighting parameter $\alpha \in [0, 1]$ in order to balance which costs are prioritised in the optimisation process. Indeed this becomes interesting when one considers that α can be varied adiabatically between optimisation iterations to better explore the optimisation landscape. For example, with ϕ a fidelity term and $\mathcal{L}$ an energy-time penalty, one can start with $\alpha = 1$ to first maximise the fidelity, and then gradually decrease α to search for more efficient control fields in the region of the (local) fidelity maximum [199].

Although the cost problem may not be completely solvable in an analytical approach, such analysis can still provide valuable insights. These insights can then be used to design more efficient numerical optimisation algorithms, potentially with fewer free parameters. A classic result in such analyses is [80]:

Definition 6.2.14 (Pontryagin's Maximum Principle (PMP))**.** *Given an optimal control field $\vec{u}^*(t)$ that minimises the cost functional, there exists a set of adjoint variables $\vec{\lambda}(t)$ and a pseudo-Hamiltonian $\mathcal{H}[\rho(t), \vec{\lambda}(t), \vec{u}(t), t]$ such that the optimal control field $\vec{u}^*(t)$ and the optimal state $\rho^*(t)$ satisfy the following system of equations:*

$$\mathcal{H}[\rho(t), \vec{\lambda}(t), \vec{u}(t), t] = \vec{\lambda}^\dagger \cdot f[\rho(t), t] + \mathcal{L}(x, \vec{u}), \tag{6.16}$$

$$\dot{\rho}(t) = \frac{\partial \mathcal{H}}{\partial \vec{\lambda}}, \tag{6.17}$$

$$\dot{\vec{\lambda}}^\dagger(t) = -\frac{\partial \mathcal{H}}{\partial \rho} = -\vec{\lambda}^\dagger \frac{\partial f}{\partial \rho} - \frac{\partial \mathcal{L}}{\partial \rho}, \tag{6.18}$$

$$\vec{0} = \frac{\partial \mathcal{H}}{\partial \vec{u}^*}. \tag{6.19}$$

By solving the third equation, the optimal control field $\vec{u}^*(t)$ may be determined, with the optimal state $\rho^*(t)$ derived from the solution of the first equation. The adjoint variables $\vec{\lambda}(t)$ play a role in calculating the optimal control field.

The optimal control problem is a well-explored area within control theory, and PMP is one of the most effective tools for addressing it. The PMP is a necessary condition for optimality in optimal control problems and provides a set of differential equations, called the Pontryagin equations, which the optimal control fields must satisfy. It is a generalisation of the Euler-Lagrange equations found in classical mechanics and forms a fundamental part of optimal control theory. While a direct application of the PMP lies beyond the scope of this study, we note that it is has shown significant potential for finding time-optimal solutions, and in hybrid approaches, improving the speed of existing optimisation algorithms.

For the purposes of the study in this chapter, we will focus on the Mayer type functional of the average gate (in)fidelity,

$$\mathcal{J}[u] = 1 - \bar{\mathcal{F}}(\mathcal{E},\mathcal{U}), \tag{6.20}$$

and will keep in mind the possibility of including a penalty term on the maximum instantaneous power of the control fields,

$$\mathcal{J}[u] = 1 - \bar{\mathcal{F}}(\mathcal{E},\mathcal{U}) + \beta \int_0^T \|u(t)\|^2 \,\mathrm{d}t\,. \tag{6.21}$$

However, as an alternative implementation in the first instance, we will instead perform direct post-processing on the control fields to ensure the amplitudes do not exceed a certain threshold Ω_{max}.

We can make the control problem more explicit by considering the dynamics of a quantum system under the influence of a time-dependent Hamiltonian in the bilinear form

$$H(t) = H_0 + \sum_k u_k(t) H_k, \tag{6.22}$$

where H_0 is the drift Hamiltonian governing the internal system dynamics, and $u_k(t)$ are the amplitudes of the external control pulses that interact with the system through the time-independent control Hamiltonians H_k. These Hamiltonians are parameterised by a set of basis elements representing a particular control field.

Definition 6.2.15 (Generalised Gell-Mann Matrices)**.** *Given a d-dimensional quantum system, the d^2-1 traceless and Hermitian generalised Gell-Mann matrices can be represented in 3 groups in the computational basis with basis vectors $\{|j\rangle, |k\rangle\}$*

$$H^x_{j,k} = |j\rangle\langle k| + |k\rangle\langle j|\,, \quad \{0 \le j,k \le d-1 \,:\, k > j\}, \tag{6.23}$$

$$H^y_{j,k} = -i(|j\rangle\langle k| - |k\rangle\langle j|), \quad \{0 \le j,k \le d-1 \,:\, k > j\}, \tag{6.24}$$

$$H^z_k = h(k,d) = \begin{cases} \sqrt{\frac{2}{d(d-1)}}\left(\mathbb{1}_{d-1} \oplus (1-d)\right), & \text{if } k = d-1, \\ h(k,d-1) \oplus (0), & \text{if } 0 < k < d-1. \end{cases} \tag{6.25}$$

Together, these Hermitian matrices form a basis on the fundamental representation of $\mathfrak{su}(d)$. As an example, for the qubit case of $d = 2$ they reduce to the familiar Pauli matrices $\sigma^x, \sigma^y, \sigma^z$. They can therefore be used to implement any special unitary operator $U \in \mathbf{SU}(d)$ through the composition

$$U = \mathcal{T}\left\{ \exp\left(-i \sum_{k=0}^{d^2-1} \int_0^t u_k(t') H_k \mathrm{d}t' \right) \right\}, \tag{6.26}$$

where $\mathcal{T}$ is the time-ordering operator that ensures the control fields are integrated in the correct order over the gate time, and $H_k \in \{H^x_{j,k}, H^y_{j,k}, H^z_k\}$.

Remark 6.2.1 (Trajectories and Rotations)**.** *Given this set of control fields generating* $\mathbf{SU}(d)$*, any unitary operator can be represented by a trajectory on the unit sphere in the space* $\mathbf{SO}(d^2-1)$ *up to a global phase. Moreover, as for the Pauli matrices, the superscripts* x, y, z *of the matrices in Eqs. (6.23) to (6.25) indicate that each control field generates a rotation about the corresponding axis in the Bloch sphere representation of the 2-dimensional subspace* $\mathcal{S} = span\{|j\rangle, |k\rangle\} \subset \mathcal{H}$ *identified by the pair of basis vectors.*

Let us now consider the parameterisation of the control fields $u_k(t)$ in the context of pulse-level control. The control fields are generally represented by piecewise-constant functions that are discretised in time and amplitude. This is a practical consideration that arises from physical limitations of the control hardware, such as Arbitrary Waveform Generators (AWGs).

Definition 6.2.16 (Control Pulse)**.** *The control fields are approximated by a set of pulses* $\{u^{(n)}_k\}$ *that are applied to the system at discrete time intervals* $\{t_n\}$*, where* $n \in [0, N]$ *and* $t_n = n\Delta t$ *such that* $t_N = T$ *the gate time. These are given by the piecewise-constant function*

$$u_k(t) = \sum_{n=1}^{N} u^{(n)}_k \Theta(t - t_n), \tag{6.27}$$

where $\Theta(t)$ *is the Heaviside step function.*

We shall address in Section 6.2.1.4 issues relating to the physical implementation of the control pulses. But first let us consider further the parameterisation of the ideal pulses $u^{(n)}_k H_k$ applied to a single qudit.

In the interaction picture, the $d(d-1)$ Hamiltonians $H^x_{j,k}$ and $H^y_{j,k}$ effect (one of) the $\binom{d}{2} = \frac{1}{2}d(d-1)$ transitions between the computational basis states $|j\rangle$ and $|k\rangle$. However, the diagonal terms H^z_k do not have an intuitive physical correspondence in their form in Eq. (6.25). Instead, we can consider the linear combinations [200]

$$H^z_{j,k} = |j\rangle\langle j| - |k\rangle\langle k|, \quad \{0 \leq j, k \leq d-1 \,:\, k > j\} \tag{6.28}$$

In this form, the $d-1$ terms $H^z_{j,k}$ can be interpreted as detunings on the transitions between the states $|j\rangle$ and $|k\rangle$. Then, we can write the general interaction Hamiltonian for a single transition between the states $|j\rangle$ and $|k\rangle$ as

$$H_{j,k}(t) = u_{j,k}(t)\left(H^x_{j,k} + H^y_{j,k} + H^z_{j,k}\right). \tag{6.29}$$

In the laboratory frame, this can be written more precisely with a (high-frequency) oscillating field $u_{j,k}(t)$ detuned from the transition frequency $\omega_{j,k}$ by an amount $\delta_{j,k} \ll \omega_{j,k}$, giving

$$H_{lab}(t) = -\frac{1}{2}\omega_{j,k}H^z_{j,k} + \Omega\cos\left((\omega_{j,k} - \delta_{j,k})t + \phi\right)H^x_{j,k}, \tag{6.30}$$

where Ω is the Rabi frequency of the transition, and ϕ is the relative phase between x and y that is introduced by combining the $H^x_{j,k}$ and $H^y_{j,k}$ terms into a single, complex pulse corresponding to (in the Bloch sphere representation) a single rotation about the axis $\vec{r} = \Omega(\cos\phi, \sin\phi, 0)$ on the (x, y)-plane.

Now, we want to move from the high-frequency control pulses in the laboratory frame to the rotating frame of the qudit. This is important since, (i) the rotating frame is the natural frame in which to consider the dynamics of the system in the contexxt of implementing quantum gates through our control pulses, and (ii) the rotating frame allows us to remove the high-frequency oscillations of the control fields, simplifying the control problem and enabling more efficient and accurate numerical simulations. This transformation is achieved through the Rotating Wave Approximation (RWA) [174], which is a common technique in quantum optics and quantum information science. For the simple case of a singly-rotating frame in a two-level system, the RWA is achieved by the transformation

$$|\psi\rangle_{rot} = e^{-\frac{1}{2}i\omega_{j,k}t\sigma^z} |\psi\rangle_{lab} \,. \tag{6.31}$$

However, for the general case of a qudit system with multiple transitions, the transformation is more complex and involves additional considerations. Following the earlier work of Einwohner, Wong and Garrison [201, 202], and the later work of Fisher [200], we can write the transformation for the general case as

$$|\psi\rangle_{rot} = e^{-iR} |\psi\rangle_{lab} \tag{6.32}$$

$$\implies H_{rot}(t) = e^{-iR} H_{lab}(t) e^{iR} - \frac{\mathrm{d}R}{\mathrm{d}t}, \tag{6.33}$$

where, recalling the bilinear Hamiltonian of Eq. (6.22),

$$H_{lab} = H_0 + u(t)H_c \tag{6.34}$$

we can make a judicious choice of R such that the terms involving the drift Hamiltonian H_0 are removed in the transformation to the rotating frame:

$$R(t) = \sum c_{j,k}(t) H^z_{j,k} \,, \tag{6.35}$$

or, equivalently,

$$R(t) = \sum \omega_k t \, |k\rangle\langle k| \,, \tag{6.36}$$

where R is diagonal, traceless and Hermitian with diagonal values equal to the eigenvalues of H_0. Substituting the expressions for H_{lab} and $R(t)$ reduces the transformation in Eq. (6.33) to

$$H_{rot}(t) = e^{-iR(t)} u(t) H_c e^{iR(t)} \,, \tag{6.37}$$

and thus the rotating frame Hamiltonian depends only on the control terms. Now, proceeding to compute this with

$$H_c = \sum_{j>k} g_{j,k} H^x_{j,k} \,, \tag{6.38}$$

leads to the interaction picture Hamiltonian, H_{int}, where, in addition to the requirement that $\Omega_{j,k} \ll \delta_{j,k} \ll \omega_{j,k}$, we also require that the fields being applied simultaneously are disjoint sets of transitions, i.e. $\{j,k\} \cap \{l,m\} = \emptyset \; \forall \; \{j,k\}, \{l,m\}$. Put another way, the transitions must be non-resonant with each other in order to prevent cross-talk where multiple transitions may be excited by a single control field. With this in mind, we

arrive at the following form for the control Hamiltonian in the multiply-rotating frame of a d-level system in the interaction picture:

$$H_{int}(t) = \sum_{j,k} \Omega_{j,k}(t) \left(\cos\left(\phi_{j,k}(t)\right) H^x_{j,k} + \sin\left(\phi_{j,k}(t)\right) H^y_{j,k} \right) \tag{6.39}$$

$$= \sum_{j,k} \theta_{j,k}(t) \left(e^{i\phi_{j,k}(t)} \left|j\right\rangle\!\left\langle k\right| + e^{-i\phi_{j,k}(t)} \left|k\right\rangle\!\left\langle j\right| \right), \tag{6.40}$$

where $\theta_{j,k}(t) = \Omega_{j,k}(t)/2$ is the Rabi frequency of the transition corresponding to a rotation of angle $\theta_{j,k}(t)$ about the axis $\vec{r}_{j,k}(t) = (\cos\phi_{j,k}(t), \sin\phi_{j,k}(t), 0)$ at an angle $\phi_{j,k}(t)$ on the (x, y)-plane of the Bloch sphere.

This is a convenient parameterisation, as it allows us to consider the control fields as a set of rotations about the Bloch sphere axes of the subspace, and the control problem is then to find the optimal sequence of angles $\theta_{j,k}(t)$ and phases $\phi_{j,k}(t)$ that generate the desired unitary operator. Moreover, each rotation can then be represented as a planar rotation of the form:

Definition 6.2.17 (Givens Rotation)**.** *A Givens rotation in the* 2*-dimensional subspace spanned by* $\{|j\rangle, |k\rangle\}$ *is a (unitary) planar rotation matrix*

$$U(\theta, \phi) = \begin{pmatrix} \cos\theta & -ie^{-i\phi}\sin\theta \\ -ie^{i\phi}\sin\theta & \cos\theta \end{pmatrix}, \tag{6.41}$$

which, when written in the full $d\times d$ *matrix representation as* $G_{j,k}(\theta, \phi)$*, is a block-diagonal matrix with matrix elements* $|j\rangle\!\langle j| = |k\rangle\!\langle k| = \cos\theta$*, and* $|j\rangle\!\langle k| = |k\rangle\!\langle j|^* = -ie^{-i\phi}\sin\theta$ *at the intersections of the* j*-th and* k*-th rows and columns in the* (j, k) *block and the identity elsewhere.*

Now, it is worth remarking that, physically speaking, the control pulses will not always be perfectly on resonance with the associated transition frequencies. Therefore, some small detuning parameter $\delta_{j,k} \ll \omega_{j,k}$ can be considered. In the rotating frame transformation, this corresponds to the $\left|\frac{\mathrm{d}R}{\mathrm{d}t} - H_0\right| > 0$ not perfectly cancelling out the drift Hamiltonian, resulting in a set of constant σ_z rotations on each subspace that can be combined into a detuning Hamiltonian H_δ, giving

$$H_{rot}(t) = \sum_{j>k} \theta^x_{j,k}(t) H^x_{j,k} + \theta^y_{j,k}(t) H^y_{j,k} + H_\delta \,, \tag{6.42}$$

in the rotating frame, and in the interaction picture corresponding to a constant shift in the axis of rotation on the (x, y)-plane given by the now time-dependent rotation angle $\phi_{j,k}(t)$ modulated by an amount δt,

$$H_{int}(t) = \sum_{j,k} \theta_{j,k} \left(e^{i(\phi_{j,k} - \delta t)} \left|j\right\rangle\!\left\langle k\right| + e^{-i(\phi_{j,k} - \delta t)} \left|k\right\rangle\!\left\langle j\right| \right) . \tag{6.43}$$

While this might seem disadvantageous to have to introduce an additional parameter δ, that may be not perfectly controlled and that increases the complexity of our control Hamiltonian, we may speculate that having access to this additional control term may actually produce improved solutions to the control problem.

6.2.1.3 Controllability and universality

If we now augment our set of $d^2 - 1$ basis matrices with the identity, referred to by $H_0^z = h(0, d) = \mathbb{1}_d$, we obtain a basis of d^2 elements generating the full Lie algebra $\mathfrak{u}(d)$, and can therefore implement any unitary operator $U \in \mathbf{U}(d)$.

This leads naturally to the concept of controllability of the dynamical system [203], which is the ability to drive the system from any initial state to an arbitrary target state through application of suitable control fields.

Definition 6.2.18 (Complete Controllability)**.** *A quantum system of dimension d and governed by Eq. (6.22) is said to be completely controllable if the Lie algebra $\mathfrak{u}(d)$ generated by the skew-Hermitian control terms $\{iH_k\}$ has dimension d^2 [204].*

This is related to the Lie Algebra Rank Condition (LARC) [80, 205]. For the case of the dynamical Lie group $\mathbf{U}(d)$, being compact and simply connected, satisfying the LARC condition is necessary and sufficient for complete controllability [206].

While this concept is applicable in the context of generic dynamical quantum systems, it becomes particularly relevant to the implementation of quantum gates in quantum computing. The ability to generate arbitrary unitary operators is a fundamental requirement for the implementation of quantum algorithms. Indeed, this is generally referred to by the term universality, being one of the fundamental (diVincenzo) criteria for universal quantum computation (UQC) [30].

In the context of gate-based models of QC, we have the following two notions:

Definition 6.2.19 (Universality)**.** *A set of quantum gates is said to be universal if it generates a dense subgroup of $\mathbf{U}(d)$, i.e. it can approximate any unitary operator to arbitrary precision [207].*

Definition 6.2.20 (Exact Universality)**.** *A set of quantum gates is said to be exactly universal if it generates the full unitary group $\mathbf{U}(d)$ [207].*

However, as argued by Brylinski in [207], exact universality is not a necessary condition for UQC, as any universal set of gates can be used to approximate any unitary operator to arbitrary precision, known as the Solovay-Kitaev theorem [82]. Furthermore, a finite set of basis gates can never be exactly universal, as it can only generate a countable set of unitary operators, while $\mathbf{U}(d)$ is uncountably infinite. As an alternative to a finite gate set, procedures involving continuous parameter gate sets have been proposed which are provably exact [96, 208].

6.2.1.4 Sources of control errors

Returning to our pulse-level control of single qudit systems with this new context of gate universality in mind, it is clear that exact universality would require perfect, infinitesimal, control of the $\{u_k\}$ as continuous control fields. Nevertheless, the concept of complete controllability is still relevant, as it ensures that the system can be driven to any target state with arbitrary precision. Moreover, given that the control fields are generally approximated by piecewise-constant functions, and implemented through finite-precision control hardware, it is sufficient to consider the relaxed universality condition for a controllable system.

To more accurately model the control pulses that might be generated, it is essential to consider the physical limitations of the control hardware. While there are many

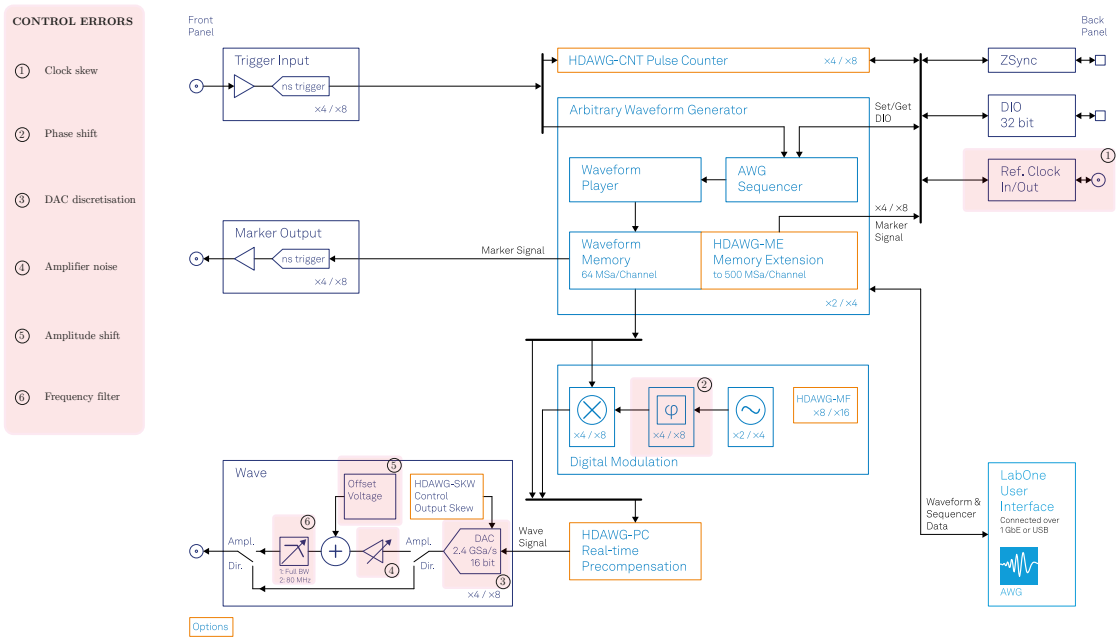


Figure 6.1 – Sources of control errors in arbitrary waveform generators. Block diagram of an Arbitrary Waveform Generator (AWG) showing the key sources of control errors in the generation of control pulses. The shaded regions highlight the stages where the error sources under consideration in this work are introduced. Adapted from the original functional overview diagram of the Zurich Instruments HDAWG [209].

potential physical sources of error based on the specific hardware, let us focus on some general categories of errors that can arise regardless of the physical platform. These errors can be broadly categorised into two types: systematic errors and random errors. Systematic errors are deterministic and arise from inaccuracies in the control hardware, while random errors are stochastic and arise from environmental factors.

To elaborate on some of these sources of error, we can consider the control process from the design of the control pulses to the application of the control fields on the qudit system. For arbitrary control over the the shape of complex, possibly multichromatic, pulse sequences with high accuracy, Arbitrary Waveform Generators (AWGs) are often the preferred hardware. To better understand the pulse generation procedure using an AWG, we can consider the block diagram in Fig. 6.1. This is a detailed diagram adapted from actual physical hardware, the Zurich Instruments HDAWG [209], but we can identify the overall stages:

① **Numerical calculation of idealised pulses**: The control pulses are designed by numerical algorithms that generate the idealised pulse shapes.

② **Arbitrary waveform generator**: The idealised pulses are then sequenced into digital waveforms, still in the RWA.

③ **Digital modulation**: The digital waveforms are modulated onto carrier signals at the frequencies of the respective physical transitions.

④ **Digital-to-analog conversion (DAC)**: The modulated signals are converted to analog signals by the DAC.

⑤ **Amplification and Transmission**: The analog signals are amplified to the nec-

essary power and shaped through filtering before being transmitted to the qudit system.

Now, some examples of generic systematic errors that may arise in this process include: numerical inaccuracies in the control algorithms, discretisation error in the waveform sequencer, clock shifts between pulse channels, phase modulation and detuning errors, finite precision and sampling limitations in the DAC, bandwidth limitations and non-linearities in amplifiers, losses and crosstalk in the transmission lines, as well as general offset and calibration errors. As for random errors, these can arise from environmental factors such as thermal noise, electronic noise, and electromagnetic interference.

Summarising the key sources highlighted (in red) in the diagram that may be have significant impact but could also be readily mitigated:

① **Clock Skew**: Timing errors between pulse channels can cause misalignment of the control pulses, and random fluctuations can be caused by timing jitter.

② **Detuning**: Inaccuracies in the frequencies of the carrier signals can lead to detuning of the control fields due to inaccurate calibration.

③ **Phase Shifts**: Errors in the phase modulation of the carrier signals can introduce phase errors in the control pulses, both between pulse channels but also between the real and imaginary components of a pulse.

④ **Quantisation Error**: The finite resolution of the DAC introduces quantisation error in the control pulses.

⑤ **Amplifier Noise**: Nonlinear responses of the amplifiers can cause distortion, and noise in the amplifiers can cause random amplitude fluctuations.

⑥ **Voltage Offset**: Offset erorrs in the voltages of the signal generators through inaccurate calibration can cause constant bias effects.

⑦ **Frequency Error**: Finite bandwidth in the signal generators can distort the signals through the Gibbs phenomenon.

⑧ **Transmission Losses**: Attenuation and dispersion in the transmission lines can distort the control pulses in a frequency dependent manner, and random fluctuations can be caused by environmental effects

Collectively, these factors affect the accuracy of the control pulses, potentially leading to deviations from the desired qudit state manipulation. Various techniques can be implemented to mitigate these errors. Calibration procedures allow systematic hardware errors to be characterised and compensated, particularly for controlling detuning and offset bias. Real-time adaptive control algorithms and compensation, as shown in the precompensation stage of the diagram, can dynamically correct deviations from the desired control, while error-correcting codes help minimse the impact of random errors. Systematic error management and noise reduction strategies are therefore essential to maintaining high-fidelity control over qudit systems.

In the context of our control problem, we can model these errors as perturbations to our ideal control fields, leading to deviations in the dynamics of the system.

An idealised pulse, as described in Eq. (6.40) and implemented by, for example, a Givens rotation of Eq. (6.41) has parameters $\theta_{j,k}(t)$ and $\phi_{j,k}(t)$ that can be subject to both systematic and random errors. Moreover, the timing of the pulses can also be subject to

such errors through clock skew or jitter, while detuning errors can arise from (constant) offsets in the frequency modulation, or (stochastically) from the presence of cross-talk or shifts in the transition frequencies through, for example, the Stark effect or temperature variations. Finally let us keep in mind the quantisation and discretisation errors due to the DACs. Summarising these for a particular set of θ, ϕ, t and δ parameters, we can write

$$\theta_{j,k}(t) \to \theta_{j,k}(t)(1+\varepsilon_\theta) + \delta_\theta, \tag{6.44}$$
$$\phi_{j,k}(t) \to \phi_{j,k}(t)(1+\varepsilon_\phi) + \delta\phi, \tag{6.45}$$
$$t \to t(1+\varepsilon_t) + \delta_t, \tag{6.46}$$

where the ε terms represent the random errors modeled by stochastic noise, and the δ terms represent the systematic errors modeled by a fixed drift. For the purposes of this initial study, we shall investigate the effects due to constant, systematic, errors only, in two cases, either absolute errors δ_θ, δ_ϕ, δ_t, or relative errors ε_θ, ε_ϕ. We note that future work will expand this modelling to include stochastic noise with different distribution kernels, as well as consider the additional error sources discussed.

6.2.2 Gate Generation Techniques

Having introduced the concept of pulse-level control of single qudit systems, we now turn our attention to the generation of quantum gates through the application of appropriate control pulses. We introduce two main techniques for gate generation: the GRD and the Gradient Ascent Pulse Engineering (GRAPE) algorithm. These techniques provide different methods for solving the optimal control problem and generating high-fidelity quantum gates.

6.2.2.1 Givens rotation decomposition

The GRD is a method for generating quantum gates by decomposing the target unitary operator into a sequence of Givens rotations as defined in Eq. (6.41). In the absence of control and environmental errors, the GRD provides an exact solution to the control problem, as it directly implements the desired unitary operator through a sequence of elementary rotations [80]. This approach may be exact with regards to fidelity, but it may not be optimal in terms of gate time or robustness to errors, which we study in Section 6.4.

The Givens rotation was introduced by (Givens, 1958) [210] in the context of solving systems of linear equations through the QR decomposition of a (unitary) matrix into an (unitary) orthogonal matrix Q and (digaonal) upper triangular matrix R. It was then applied by (Murnaghan, 1958, 1962) [211, 212] to the decomposition of the unitary group into elementary planar rotations.

Following the extensive initial work during the 90s on circuit-based models for universal quantum computation using finite gate sets (see for example [82, 213, 214]), Cybenko showed that Givens rotations could be used to implement single-qubit gates [215]. This work was generalised to qudits by Brennen, Bullock and O'Leary [216, 217], and in [96] they showed that the GRD is exactly universal for a single-qudit system, and moreover exactly universal for a multi-qudit system when combined with a carefully designed 2-qudit gate.

To implement this decomposition method universally, we note that Brennen *et. al.* proved the following necessary and sufficient requirement, which we restate without proof:

Lemma 6.2.1 (Single-qudit Universality)**.** *Given a d-node coupling graph $\mathcal{G}$ of allowed Givens rotations, then any $U \in SU(d)$ can be brought to diagonal form using $d(d-1)/2$ allowed rotations if and only if $\mathcal{G}$ is connected.*

To understand this, let us make precise the notion of a coupling graph and its connectivity properties.

Definition 6.2.21 (Coupling Graph)**.** *Given a d-dimensional quantum system with some set of allowed transitions between states, the coupling graph $\mathcal{G}(V, E)$ is a finite, simple (unweighted, undirected and loop-free) dyadic graph with vertex set $V = \{v_0, \ldots, v_{d-1}\}$ representing the states of the system, and non-empty edge set $E \subseteq V \times V$ of unordered vertex pairs (with edges $e_{i,j} := (i, j) = (v_i, v_j) = (v_j, v_i)$ connecting the i-th and j-th vertices) representing the allowed transitions between states.*

Definition 6.2.22 (Connected Graph)**.** *A graph $\mathcal{G}(V, E)$ is connected if there exists a path between any pair of vertices in V, where a path is a sequence of edges (i_1, i_2), (i_2, i_3), $\ldots$, (i_{n-1}, i_n) connecting vertices i_1 and i_n.*

Conversely, a graph is disconnected if there exists a pair of vertices for which no path exists between them. Moreover, a graph is fully connected (complete) if there exists an edge between every $\frac{d(d-1)}{2}$ pair of vertices. With this in mind, we can say that the graph size (number of edges) must be $d - 1 \leq |E| \leq \frac{d(d-1)}{2}$.

For the purposes of this study, we shall consider the minimally connected graph of a ladder system with d vertices and $d - 1$ edges, where each vertex is connected to its nearest neighbours with edge set $E = \{(0, 1), (1, 2), \ldots, (d - 2, d - 1)\}$. This graph is connected, and therefore satisfies the necessary and sufficient condition for single-qudit universality, while also minimising the number of allowed transitions, thereby preventing frequency crowding and cross-talk between transitions. Furthermore, our molecular nuclear spin qudit systems are naturally modelled by ladder systems with $\Delta m = \pm 1$ allowed transitions, as shown in the experimental work of Thiele *et. al.* [42] and Godfrin *et. al.* [43].

Now, we can finally present Brennen's constructive proof of the GRD of a target unitary operator $U = QR \in SU(d)$ applied to a single qudit ladder system, as summarised by [80]:

Theorem 6.2.2 (Givens Rotation Decomposition)**.** *For any matrix $U \in SU(d)$, there exist $n - 1$ parameters $\{\alpha_1, \ldots, \alpha_{d-1}\}$, $\frac{d(d-1)}{2}$ parameters $\{\theta_1, \ldots \theta_{\frac{d(d-1)}{2}}\}$, and $\frac{d(d-1)}{2}$*

parameters $\{\phi_1, \ldots, \phi_{\frac{d(d-1)}{2}}\}$ *such that*

$$\begin{aligned} U = & G^{(1)}_{d,d-1}(\theta_1,\phi_1)G^{(1)}_{d-1,d-2}(\theta_2,\phi_2)\cdots G^{(1)}_{2,1}(\theta_{d-1},\phi_{d-1})\times \\ & \times G^{(2)}_{d,d-1}(\theta_d,\phi_d)G^{(2)}_{d-1,d-2}(\theta_{d+1},\phi_{d+1})\cdots G^{(2)}_{3,2}(\theta_{(d-1)+(d-2)},\phi_{(d-1)+(d-2)})\times \\ & \times \cdots \\ & \times G^{(i)}_{d,d-1}(\theta_{\sum_{j=1}^{i-1}(d-j)+1},\phi_{\sum_{j=1}^{i-1}(d-j)+1})\cdots G^{(i)}_{i+1,i}(\theta_{\sum_{j=1}^{i}(d-j)},\phi_{\sum_{j=1}^{i}(d-j)})\times \\ & \times \cdots \\ & \times G^{(d-1)}_{d,d-1}(\theta_{\frac{d(d-1)}{2}},\phi_{\frac{d(d-1)}{2}})\times \\ & \times R(\alpha_1,\cdots,\alpha_{d-1}), \end{aligned} \tag{6.47}$$

where the indices of $G^{(j)}_{i+1,i}$ *effect a transition between* i*-th and* $(i+1)$*-th states of the ladder system by acting on the* i*-th and* $(i+1)$*-th row elements of the* j*-th column of the matrix, and the subscripts of the* θ *and* ϕ *parameters being the index in the rotation sequence. The* R *matrix is a diagonal matrix given by*

$$R(\alpha_1,\ldots,\alpha_{d-1}) = diag\left(e^{i\alpha_1},\cdots,e^{i\alpha_{d-1}},e^{-i\left(\frac{\sum_{j=1}^{d}\alpha_j}{d}\right)}\right) \tag{6.48}$$

Following the procedure of the QR-decomposition, since we have the property of the Givens rotations

$$[G_{j,k}(\theta,\phi)]^{-1} = G^{\dagger}_{j,k}(\theta,\phi) = G_{j,k}(-\theta,\phi), \tag{6.49}$$

the unitary U can be brought into upper triangular form by applying the givens rotations in the reverse order. In other words, $Q^{-1}U = R$ where the unitary Q is the product of the sequence of the Givens rotations. Thus, since R is upper triangular and unitary, it must be diagonal as in Eq. (6.48).

This method is thus constructive, as each Givens rotation can be implemented sequentially on the chosen unitary, the only difference being a change of sign of the rotation angle $\theta \to -\theta$. To see it more clearly, let us consider the action of the i-th Givens rotation on U as

$$Q^{-1}U = R \tag{6.50}$$

$$G^{(d-1)}_{d,d-1}(\theta_{\frac{d(d-1)}{2}},\phi_{\frac{d(d-1)}{2}})\cdots G^{(k)}_{j+1,j}(\theta_i,\phi_i)U^{(i-1)} = R, \tag{6.51}$$

where $U^{(i-1)}$ is the unitary after the first $(i-1)$ Givens rotations.

At each step, the action of the Givens rotation $G_{j,j-1}$ is to zero out the off-diagonal element of the matrix $U^{(i-1)}$ in the j-th row and k-th column, $U^{(i-1)}_{j,k} \to 0$. This is achieved through row reduction (in the 2-dimensional subspace),

$$\begin{bmatrix} \cos\theta_i & -ie^{-i\phi_i}\sin\theta_i \\ -ie^{i\phi_i}\sin\theta_i & \cos\theta_i \end{bmatrix} \begin{bmatrix} U^{(i-1)}_{j-1,k} \\ U^{(i-1)}_{j,k} \end{bmatrix} = \begin{bmatrix} U^{(i)}_{j-1,k} \\ 0 \end{bmatrix}, \tag{6.52}$$

resulting in

$$\theta_i = \arctan\left|\frac{U^{(i-1)}_{j,k}}{U^{(i-1)}_{j-1,k}}\right|, \tag{6.53}$$

$$\phi_i = \arg\left(U^{(i-1)}_{j,k}\right) - \arg\left(U^{(i-1)}_{j-1,k}\right) + \frac{\pi}{2}. \tag{6.54}$$

By zeroing out all of the lower-triangular elements of the matrix, this sequence of rotations has the effect of fixing the populations (probability amplitudes) of the density matrix when applied as evolution operators on the initial state. However, the coherences still need to be fixed, and this is achieved by the diagonal matrix R of $(d-1)$ phases. To calculate these phases in Eq. (6.48), we recall that application of the $d(d-1)/2$ Givens rotations produces the diagonal matrix

$$U^{(\frac{d(d-1)}{2})} = \mathrm{diag}\left(e^{i\alpha_1}, \cdots, e^{i\alpha_d}\right). \tag{6.55}$$

Now, in principle this matrix could be implemented through a sequence of z-rotations $H^z_{j,j+1}$ to fix the coherences of the density matrix, but we encounter the issue that the basis matrices H^z are traceless, while $U^{(\frac{d(d-1)}{2})}$ is not. To fix this, we use global phase invariance to introduce a phase factor $\phi = \frac{\sum_{j=1}^{d}\alpha_j}{d}$ to the diagonal elements of U, giving the $d-1$ independent phase parameters of R,

$$R = e^{-i\phi}U^{(\frac{d(d-1)}{2})} \tag{6.56}$$

$$= \mathrm{diag}\left(e^{i\phi}e^{i\alpha_1}, \cdots, e^{i\phi}e^{i\alpha_d}\right) \tag{6.57}$$

where, due to linear dependence the phases can all be calculated by row reduction of the following linear system:

$$\begin{bmatrix} -1 & 0 & 0 & \cdots & 0 \\ 1 & -1 & 0 & \cdots & 0 \\ 0 & 1 & -1 & \ddots & 0 \\ \vdots & \ddots & \ddots & \ddots & 0 \\ 0 & \cdots & 0 & 1 & -1 \\ 0 & \cdots & 0 & 0 & 1 \end{bmatrix} \begin{bmatrix} \theta^z_1 \\ \vdots \\ \theta^z_{d-1} \end{bmatrix} = \begin{bmatrix} \alpha_1 - \phi \\ \vdots \\ \alpha_d - \phi \end{bmatrix}. \tag{6.58}$$

Thus we can express the R matrix as the sequence of z-rotations

$$R = \prod_{j=1}^{d-1} \exp\left\{-i\theta^z_j H^z_{j,j+1}\right\}. \tag{6.59}$$

While we cannot directly implement z-rotations alone on the ladder system, we can implement them as a sequence of x-rotations and y-rotations through the Euler decomposition of each z-rotation matrix into an $x-y-x$ sequence of 3 Givens rotations:

$$\exp\left\{-i\theta^z_j H^z_{j,j+1}\right\} = G_{j,j+1}\left(\frac{-\pi}{4}, \frac{\pi}{2}\right) G_{j,j+1}\left(-\theta^z_j, 0\right) G_{j,j+1}\left(\frac{\pi}{4}, \frac{\pi}{2}\right). \tag{6.60}$$

Thus we have constructed a sequence of N elementary planar rotations for implementing any desired unitary operator, where

$$N = \frac{d(d-1)}{2} + 3(d-1), \tag{6.61}$$

scales quadratically in the qudit dimension.

6.2.2.2 GRAPE algorithm

Returning to the optimal control problem defined in Eq. (6.11), it is clear now that the GRD is only able to provide an exact solution to the case

$$J[u] = \mathcal{F}(\mathcal{E}, U) \tag{6.62}$$

$$= \frac{\left|\mathrm{Tr}\{U^\dagger \mathcal{E}(U)\}\right|^2}{d}, \tag{6.63}$$

for an optimal control problem of the Mayer type, by always returning exactly 1 for the fidelity in the absence of control or environmental errors. Moreover, it does not enable generalisation to the case of the Bolza type through addition of a Lagrange functional. Thus we cannot consider more realistic situations with constraints on the control fields, or to optimise for robustness to errors.

To address this more general and physically realistic problem, we turn to the Gradient Ascent Pulse Engineering (GRAPE) algorithm. It was named as such by Khaneja *et. al.* [97] in their seminal work on optimal control in nuclear magnetic resonance, and has since been widely used in the field of quantum control.

The GRAPE algorithm is a gradient-based numerical optimisation method that seeks to maximise the fidelity of the target unitary operator by adjusting the control fields. It is based on the gradient ascent method, which iteratively updates the control fields in the direction of the gradient of the fidelity with respect to the control parameters.

Given our bilinear Hamiltonian in Eq. (6.22), together with the piece-wise constant control fields in Eq. (6.27) discretised into N steps with $\Delta t = \frac{T}{N}$, the evolution due to the controls (drift $H_0 = \mathbb{0}$ for convenience, but without loss of generality) at each timestep n can be written as

$$H^{(n)} = \sum_{k=1}^{d} u_k^{(n)} H_k, \tag{6.64}$$

$$\implies U^{(n)} = \exp\left\{-i\Delta t \sum_{k=1}^{d} u_k^{(n)} H_k\right\}, \tag{6.65}$$

and thus the unitary propagator over the entire time interval $[0, T]$ is given by the product of the individual propagators,

$$U(T) = \prod_{n=N}^{1} U^{(n)}. \tag{6.66}$$

Now, if we consider a small perturbation to the k-th control amplitude at step n, $u_k^{(n)} \to u_k^{(n)} + \delta u_k^{(n)}$, the change in the propagator is given by

$$U^{(n)} = \exp\left\{-i\Delta t \sum_{k=1}^{d} u_k^{(n)} H_k - i\Delta t \delta u_k^{(n)} H_k\right\}. \tag{6.67}$$

$$\tag{6.68}$$

Using the property [97, 200]

$$\frac{\mathrm{d}}{\mathrm{d}x} e^{A+xB}|_{x=0} = e^A \int_0^{\Delta t} e^{A\tau} B e^{-A\tau}\, \mathrm{d}\tau\,, \tag{6.69}$$

the sensitivity of the propagator to the control perturbation is

$$\frac{\partial U^{(n)}}{\partial u_k^{(n)}} = -i\left(\int_0^{\Delta t} U^{(n)}(\tau) H_k U^{(n)}(-\tau)\mathrm{d}\tau\right) U^{(n)}, \tag{6.70}$$

where

$$U^{(n)}(\tau) = \exp\left\{-i\tau \sum_{k=1}^{d} u_k^{(n)} H_k\right\}. \tag{6.71}$$

In the limit of small timesteps,

$$\Delta t \ll \left\| \sum_{k=1}^{d} u_k^{(n)} H_k \right\|^{-1}, \tag{6.72}$$

the integral in Eq. (6.70) can be expanded in a Taylor series, which to first order in Δt results in the approximation

$$\frac{\partial U^{(n)}}{\partial u_k^{(n)}} \simeq -i\Delta t H_k U^{(n)}, \tag{6.73}$$

$$\implies \frac{\partial U(T)}{\partial u_k^{(n)}} \simeq U^{(N)} \cdots U^{(n+1)} \left(-i\Delta t H_k U^{(n)}\right) U^{(n-1)} \cdots U^{(1)} \tag{6.74}$$

Finally, we use this expression to find the gradient of the fidelity with respect to the control field,

$$\frac{\partial \mathcal{F}}{\partial u_k^{(n)}} = \frac{1}{d}\frac{\partial}{\partial u_k^{(n)}} \left|\mathrm{Tr}\left\{U_t^\dagger U(T)\right\}\right|^2 \tag{6.75}$$

$$= \frac{2}{d}\,\mathrm{Re}\left\{\mathrm{Tr}\left\{U_t^\dagger U(T)\right\}\,\mathrm{Tr}\left\{\frac{\partial U^\dagger(T)}{\partial u_k^{(n)}} U_t\right\}\right\}, \tag{6.76}$$

where the first trace term represents the feedforward (unperturbed) propagator, and the second trace term represents the back-propagated (perturbed) propagator. Therefore, if we now consider this gradient as the actual perturbation to the control field, we can update

$$u_k^{(n)} \to u_k^{(n)} + \epsilon \frac{\partial \mathcal{F}}{\partial u_k^{(n)}}, \tag{6.77}$$

with a small step size ϵ such that the fidelity is guaranteed to increase. Repeating this process over all control fields and timesteps yields the following procedure:

1. Initialise the $N \times d$ individual control amplitudes $u_k^{(n)}$ with some initial guess.
2. Calculate the unperturbed propagator $U(T)$
3. Calculate the back-propagated perturbed propagator $\frac{\partial U^\dagger(T)}{\partial u_k^{(n)}}$
4. Calculate the gradient of the fidelity with respect to the control fields $\frac{\partial \mathcal{F}}{\partial u_k^{(n)}}$ and update the control fields

5. Repeat steps 2-4 until the fidelity converges to a maximum value or the maximum number of iterations is reached.

The GRAPE algorithm is a powerful tool for solving the optimal control problem and generating high-fidelity quantum gates. It has been successfully applied to a wide range of quantum systems, including nuclear magnetic resonance, trapped ions, and superconducting qubits. By combining the power of numerical optimisation with the physical constraints of the system, the GRAPE algorithm can efficiently search the control landscape and find the control fields that (at least locally) maximise the fidelity of the target unitary operator.

Furthermore, the GRAPE algorithm can be extended to include additional constraints on the control fields, such as bounds on the amplitude or duration of the pulses. This allows for the generation of robust and experimentally feasible control pulses that are less sensitive to errors in the control hardware.

6.3 Methods

6.3.1 Numerical Tools

As discussed in detail in Section 5.3.1, all numerical simulations were conducted using Python (v3.9.5) using similar standard, external, and custom libraries. The primary numerical tools used in this study are summarised as follows.

6.3.1.1 Standard libraries

Built-in Python libraries, including `pickle` for data serialisation, `joblib` for parallel processing, and others like `os`, `time`, `math`, and `sys`, were employed for various routine tasks.

6.3.1.2 External libraries

The external libraries and their functions mirror those described in Section 5.3.1 (see Appendix D.1 for specific versions). Key libraries included:

- QuTiP (v4.7.1): For simulating quantum systems, particularly employing the `mesolve`, `propagator`, and various superoperator-related functions, as well as the fidelity calculation using `process_fidelity`.
- NumPy (v1.24.3): For array manipulation, random number generation, and matrix operations, especially within the `linalg` sub-package.
- SciPy (v1.14.0): For numerical integration, optimisation, and statistical analysis, using sub-packages like `linalg`, `interpolate`, `stats`, and `optimize`.
- Matplotlib (v3.7.1): For data visualisation, generating plots and histograms.
- StatsModels (v0.14.1) & Scikit-learn (v1.4.1): Alternative package for additional statistical modeling and testing.
- Cirq (v1.2.0): Alternative package for generating random quantum gates.

6.3.2 Simulation Framework

For the purposes of this study, we extended the tools developed in Section 5.3.2 to create an extensible simulation framework for pulse-level optimal control of qudit quantum systems. The framework is designed to be modular and flexible, allowing for easy integration of different gate generation methods, optimisation algorithms, and error models. The key components of the simulation framework are summarised as follows (for additional details about each method, see Appendix E.1).

The simulation framework for qudit quantum systems is organised into several classes and modules, each with specific responsibilities and interactions. The core of the framework revolves around the `Qudit` class, which represents the qudit system, encapsulating its dimensionality, basis states, and associated operators. This class closely interacts with `QuditGate` and `PulseSequence` classes, as well as noise and pulse sequence components such as `GRAPE` and `QR`. The `QuditGate` class is responsible for creating and manipulating quantum gates that are compatible with the dimensionality of the qudit system, ensuring proper integration with the pulse sequences generated by the `PulseSequence` class.

The `PulseSequence` class plays a pivotal role in generating sequences of pulses necessary for implementing quantum gates on the qudit system. It utilises the `QuditGate` class to access the matrix representations of the gates and interacts with various pulse generation techniques, including `GRAPE`, `QR`, `PMPINN`, and `MATRIXLOG`. These techniques are implemented as subclasses of the `Pulse` base class, each employing different algorithms for pulse optimisation. Specifically, `GRAPE` uses the Gradient Ascent Pulse Engineering method, `QR` implements the GRD, `PMPINN` combines Physics-Informed Neural Networks with the Pontryagin Maximum Principle, and `MATRIXLOG` generates pulses using an idealised matrix logarithm.

Managing multichromatic pulse sequences, the `MultiPulse` class coordinates the combination of different pulse sequences through interactions with `ComplexPulse` and `Pulse`. The `ComplexPulse` class extends the `Pulse` class by representing pulses with both real and imaginary components, while the `Pulse` class itself acts as the fundamental building block for all control pulses within the qudit system.

Noise effects are modeled through the `NoiseGenerator` class, which generates both control and environmental noise, simulating their impact on pulse sequences and ensuring consistency in noise application across qudit operations. The configuration of these simulations is handled by the `Config`, `ConfigData`, and `ConfigManager` classes. The `Config` class reads and manages settings, `ConfigData` structures the configuration for ease of access, and `ConfigManager` oversees loading, validating, and applying configurations across the framework.

Simulation results are managed by the `DatabaseManager` class, which provides an interface for interacting with the database of results. It coordinates with the `db_tables` module, which defines the database schema through various classes representing quantum gates, pulse sequences, fidelity metrics, noise types, and related data. These classes enable complex relationships, such as one-to-many and many-to-one associations, facilitating efficient storage and retrieval of simulation data.

Overall, the framework integrates qudit system modeling, gate synthesis, pulse sequence generation, noise simulation, configuration management, and result storage, enabling detailed analysis and simulation of quantum control techniques for qudit-based quantum

computing. Given this framework, we can now describe the simulation process in detail.

Algorithm 1: Qudit System Simulation

Input: Configuration file path
Output: Simulation results saved to a CSV file

Initialise:
    `cfg_filename` ← Command-line argument specifying configuration file path;
    `cfg` ← Load configuration using `ConfigManager` initialised with `cfg_filename`;
    Initialise `Qudit` object with dimension `dim`;
    `initial_state` ← Generate initial qudit state (e.g., random ket or GHZ state);
    Initialise `NoiseGenerator` object with noise configurations from `cfg`;

Function *Generate Quantum Gates*:
    `gate_type` ← Extract gate type from `cfg`;
    `num_gates` ← Extract number of gates from `cfg`;
    if *`gate_type` == 'fixed'* **then**
        Generate fixed gates (e.g., `crest`, `INC`) and store in `unitary_gates`;
    else
        if *`gate_type` == 'interpolated'* **then**
            Generate interpolated gates with varying `eta` values and store in `unitary_gates`;
        else
            Generate random gates based on `gate_type` and store in `unitary_gates`;
    Store `unitary_gates` list of `QuditGate` objects in dataframe structure `data`;

if *fidelity calculations are enabled in `cfg`* **then**
    `method` ← Extract pulse generation method from `cfg`;
    `pulse_gen_func` ← `obtain_pulses(method)`;
    Generate pulse sequences using `method` for each gate in `unitary_gates`;
    Sort `data` by gate durations in ascending order;
    if *calculate noise-free fidelity* **then**
        Perform noise-free time evolution and calculate fidelity for each gate;
        Store the noise-free fidelities in `data`;
    foreach *environmental noise type in `gamma_list['ENVT']`* **do**
        foreach *gamma value* **do**
            Calculate fidelities and coherences for the corresponding collapse operator;
            Store the results in `data`;
    foreach *control noise type in `gamma_list['CTRL']`* **do**
        foreach *channel* **do**
            foreach *gamma value* **do**
                Calculate fidelities and coherences for the corresponding noise channel;
                Store the results in `data`;

6.4 Results

Having established the theoretical framework and simulation methodology, we now present the results of our investigation into pulse-level optimal control of qudit quantum systems. We begin by examining the fidelity of quantum gates generated using our two different gate synthesis methods: the GRD, and the GRAPE algorithm. We then explore the impact of environmental and control noise on the fidelity of either specially chosen gates and algorithms, in addition to ensembles of Haar random generated gates. This is done by investigating the robustness of the gate synthesis methods to different control noise models, as well as the performance in the presence of environmental noise. Finally, we discuss the implications of our findings for the practical implementation of quantum gates in qudit systems.

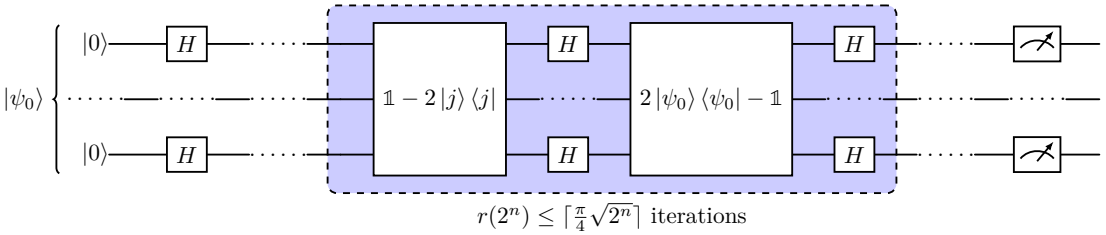


Figure 6.2 – Qubit-based circuit diagram for Grover's search algorithm. The algorithm is composed of (i) the Hadamard gate H, (ii) the oracle gate $\mathbb{1} - 2\,|j\rangle\langle j|$, and (iii) the diffusion operator $2\,|\psi_0\rangle\langle\psi_0| - \mathbb{1}$, arranged as shown. The first set of Hadamard gates prepare the uniform superposition states from the initial states $|0\rangle$. The Grover iteration, shown in blue, is the composition of the oracle and diffusion operators, and is repeated $\lceil \frac{\pi}{4}\sqrt{2^n} \rceil$ times to find the target state with maximum probability.

6.4.1 Gate Synthesis

Let us begin with some practical applications of the gate synthesis methods discussed in Section 6.2.2, with examples of their implementation.

We introduce some gates and algorithms of interest for testing the gate synthesis methods: the generalised Hadamard gate, and Grover's Search Algorithm.

Recall from Section 5.2.2, Eq. (5.18), that the Hadamard gate is generalised to higher-dimensions by the quantum Fourier transform (QFT), whose matrix elements are the d-th roots of unity,

$$F_d = \frac{1}{\sqrt{d}} \sum_{j,k=0}^{d-1} e^{i\frac{2\pi jk}{d}} |j\rangle\langle k| . \tag{6.78}$$

Regarding Grover's Search Algorithm, recall that the original qubit-based algorithm was first proposed by Lov Grover in 1996 [8]. However, it is of particular interest to us as it can be easily generalised to, and implemented on, single-qudit (nuclear spin) systems following the work of Leuenberger and Loss *et. al.* [35, 54, 55].

The algorithm is composed of 3 elementary gates: (i) the (generalised Hadamard) QFT gate, (ii) the oracle gate, and (iii) the diffusion operator, and arranged as in the qubit-based circuit diagram in Fig. 6.2. The oracle is also referred to as the phase inversion step, as the purpose is to invert the phase of the target state. This is implemented by a Householder reflection, being a diagonal matrix with -1 in the j target state and 1 elsewhere,

$$O_d^{(j)} = \mathbb{1}_d - 2\,|j\rangle\langle j| . \tag{6.79}$$

The diffusion operator, also referred to as the amplitude amplification step, is a reflection about the average amplitude of the states, and is implemented by

$$D_d^{\psi_0} = 2\,|s\rangle\langle s| - \mathbb{1}_d. \tag{6.80}$$

$$= 2F_d\,|\psi_0\rangle\langle\psi_0|\,F_d^\dagger - \mathbb{1}_d, \tag{6.81}$$

where $|s\rangle = F_d\,|\psi_0\rangle$ is the uniform superposition state.

Definition 6.4.1 (Grover Iteration)**.** *Given a qudit system of dimension d, with initial state ψ_0 and search state j, the Grover iteration is the composition of the oracle and diffusion operators,*

$$G_d = O_d^{(j)} D_d^{\psi_0}. \tag{6.82}$$

Example 6.4.1 (Grover's Algorithm in $d = 4$)**.** *Given a qudit system of dimension $d = 4$ initialised in the ground state $|\psi_0\rangle = |0\rangle$, the QFT gate is*

$$F_4 = \frac{1}{2}\begin{bmatrix} 1 & 1 & 1 & 1 \\ 1 & i & -1 & -i \\ 1 & -1 & 1 & -1 \\ 1 & -i & -1 & i \end{bmatrix}, \tag{6.83}$$

the oracle operator for the $j = 1$ search state is

$$O_4^{(1)} = \begin{bmatrix} 1 & 0 & 0 & 0 \\ 0 & -1 & 0 & 0 \\ 0 & 0 & 1 & 0 \\ 0 & 0 & 0 & 1 \end{bmatrix}, \tag{6.84}$$

and the diffusion operator is

$$D_4^{(0)} = \frac{1}{2}\begin{bmatrix} -1 & i & -1 & -i \\ -i & -1 & i & -1 \\ -1 & -i & -1 & i \\ i & -1 & -i & -1 \end{bmatrix}, \tag{6.85}$$

giving Grover iteration $G = O_4^{(1)} D_4^{(0)}$.

Now, in $d = 4$, exactly one Grover iteration is required to find the target state $j = 1$ from the initial state $|0\rangle$, as shown in the circuit diagram in Fig. 6.2,

$$|j\rangle\langle j| = GF_4 \, |0\rangle\langle 0| \, F_4^\dagger G^\dagger. \tag{6.86}$$

Remark 6.4.1 (Optimality of Grover's Algorithm)**.** *As noted in Example 6.4.1, when $d = 4$ exactly 1 Grover iteration was required to find exactly the target state $|j\rangle\langle j|$ from the initial state $|0\rangle$. However, as indicated in Fig. 6.2, for arbitrary dimensions, the near-optimal number of Grover iterations required to find the target state is given approximately by*

$$r(d) = \left\lceil \frac{\pi}{4}\sqrt{d} \right\rceil. \tag{6.87}$$

Moreover, for a choice of dimension d and number of iterations r, the probability of finding the target state is given by

$$P\big[\rho(t_f) = |j\rangle\langle j|\big] = \sin^2\left(2\left(\frac{2r+1}{2}\right)\arcsin\left(d^{-1/2}\right)\right), \tag{6.88}$$

and for the optimal number of iterations $r(d)$ as $d \gg 1$, the probability of success approaches unity. Indeed, it has been shown that Grover's algorithm is optimal in the sense that it achieves the maximum possible probability of success for unstructured search problems [218].



Figure 6.3 – Deterministic 2-parameter (D2p) Grover search algorithm on the Bloch sphere. Separating the full state space into the unmarked states $|R\rangle = \frac{1}{\sqrt{d-M}} \sum_{r=1}^{d-M} |r\rangle$ and marked (search target) states $|T\rangle = \frac{1}{\sqrt{M}} \sum_{t=1}^{M} |t\rangle$ enables representation of this two-dimensional subspace on the Bloch sphere. (a) Depicts the original Grover's algorithm with $\alpha = \beta = \pi$ approximating the target state after $r(d)$ iterations, where the rotations are about the Y-axis. (b) Depicts the D2p Grover algorithm reaching the target state after k iterations by rotating about an axis in the XY-plane. Reproduced from [220].

For situations where the target state must be found with certainty, or for near-term systems where dimensionality is not arbitrarily large, it is possible to consider generalisations of the Grover gates that are able to operate deterministically. Early work by Long [219], as initially proposed by Zalka [218] provides such a generalisation, but requires a generalisation of the oracle and diffusion operators:

$$O_d^{(j)}(\alpha) = \mathbb{1}_d - (1 - e^{i\alpha}) \, |j\rangle\langle j| \, , \tag{6.89}$$

$$D_d^{\psi_0}(\beta) = e^{i\beta} \left(\mathbb{1} - (1 - e^{-i\beta}) F_d \, |\psi_0\rangle\langle\psi_0| \, F_d^\dagger \right) . \tag{6.90}$$

Here, the parameterisation of the oracle operator produces a controlled-phase gate with phase α on the target state. Unfortunately, it has been noted that a parameteric Oracle of this form is unlikely to be physically realisable in a practical manner. Recently however, a more practical generalisation was proposed by Roy *et. al.* [220] using a so-called restricted-phase oracle to produce the deterministic 2-parameter (D2p) search algorithm, which we briefly summarise. With this parameterisation of the oracle and diffusion operators, we can see that the original Grover operators are recovered for $\alpha = \beta = \pi$. By instead using the parameters

$$\alpha = \beta = 2 \arcsin \left(\frac{1}{\sqrt{\lambda}} \sin \frac{\pi}{4k+2} \right), \tag{6.91}$$

where $\lambda = M/d$ the ratio of M marked (search) states to the dimensionality of the system, and the optimal number of Grover iterations $G(\alpha, \beta) = D(\beta)O(\alpha)$ (see Fig. 6.3 for an illustrative example) is given by

$$k = \left\lceil \frac{\pi}{4 \arcsin \sqrt{\lambda}} - \frac{1}{2} \right\rceil \tag{6.92}$$

Now, it is possible to restrict the phase of the oracle to $\alpha = \pi$ and still achieve deterministic performance by modifying the phase of the diffusion operator at each iteration as

$$|j\rangle = \begin{cases} [G(\pi, \theta_2) G(\pi, \theta_1)]^{k/2} \, F_d \, |\psi_0\rangle \quad , & \text{if } k \text{ is even} \\ G(\pi, \theta_1) \, [G(\pi, \theta_2) G(\pi, \theta_1)]^{\lfloor k/2 \rfloor} \, F_d \, |\psi_0\rangle \quad , & \text{if } k \text{ is odd,} \end{cases} \tag{6.93}$$

where θ_1 and θ_2 are solved by

$$1 + 4\lambda(1-2\lambda)\sin\left(\frac{\theta_1}{2}\right)\sin\left(\frac{\theta_2}{2}\right)\frac{\tan(k\phi)}{\sin(\phi)} = 0 \tag{6.94}$$

$$(1-4\lambda)\tan\left(\frac{\theta_1}{2}\right) + \tan\left(\frac{\theta_2}{2}\right) = 0 \tag{6.95}$$

$$\cos\left(\frac{\theta_1+\theta_2}{2}\right) + 8\lambda(1-\lambda)\sin\left(\frac{\theta_1}{2}\right)\sin\left(\frac{\theta_2}{2}\right) = \cos(\phi) \tag{6.96}$$

6.4.1.1 Givens rotation decomposition

Here is a simple example of the GRD method applied to a general unitary matrix for $d = 3$:

Example 6.4.2 (Givens Rotation Decomposition)**.** *Given a unitary matrix A,*

$$A = \begin{bmatrix} A_{11} & A_{12} & A_{13} \\ A_{21} & A_{22} & A_{23} \\ A_{31} & A_{32} & A_{33} \end{bmatrix},$$

we apply Givens rotations in the following sequence:

$$G_{3,2}(\theta_1,\phi_1)\begin{bmatrix} A_{11} & A_{12} & A_{13} \\ A_{21} & A_{22} & A_{23} \\ A_{31} & A_{32} & A_{33} \end{bmatrix} = \begin{bmatrix} A'_{11} & A'_{12} & A'_{13} \\ A'_{21} & A'_{22} & A'_{23} \\ 0 & A'_{32} & A'_{33} \end{bmatrix}$$

$$G_{2,1}(\theta_2,\phi_2)\begin{bmatrix} A'_{11} & A'_{12} & A'_{13} \\ A'_{21} & A'_{22} & A'_{23} \\ 0 & A'_{32} & A'_{33} \end{bmatrix} = \begin{bmatrix} A''_{11} & A''_{12} & A''_{13} \\ 0 & A''_{22} & A''_{23} \\ 0 & A''_{32} & A''_{33} \end{bmatrix}$$

$$G_{3,2}(\theta_3,\phi_3)\begin{bmatrix} A''_{11} & A''_{12} & A''_{13} \\ A''_{21} & A''_{22} & A''_{23} \\ 0 & A''_{32} & A''_{33} \end{bmatrix} = \begin{bmatrix} A'''_{11} & A'''_{12} & A'''_{13} \\ 0 & A'''_{22} & A'''_{23} \\ 0 & 0 & A'''_{33} \end{bmatrix},$$

resulting in the final matrix R,

$$R = G_{3,2}(\theta_3,\phi_3)G_{2,1}(\theta_2,\phi_2)G_{3,2}(\theta_1,\phi_1)A = \begin{bmatrix} A'''_{11} & 0 & 0 \\ 0 & A'''_{22} & 0 \\ 0 & 0 & A'''_{33} \end{bmatrix}$$

where the rotation angles were calculated as

$$\theta_1 = \arctan\frac{|A_{3,1}|}{|A_{2,1}|}$$

$$\phi_1 = \arg A_{3,1} - \arg A_{2,1} + \frac{\pi}{2}$$

$$\theta_2 = \arctan\frac{|A'_{2,1}|}{|A'_{1,1}|}$$

$$\phi_2 = \arg A'_{2,1} - \arg A'_{1,1} + \frac{\pi}{2}$$

$$\theta_3 = \arctan \frac{|A''_{3,2}|}{|A''_{2,2}|}$$
$$\phi_3 = \arg A''_{3,2} - \arg A''_{2,2} + \frac{\pi}{2}$$

and the final matrix R is a diagonal matrix whos elements we calculate by adding the global phase factor

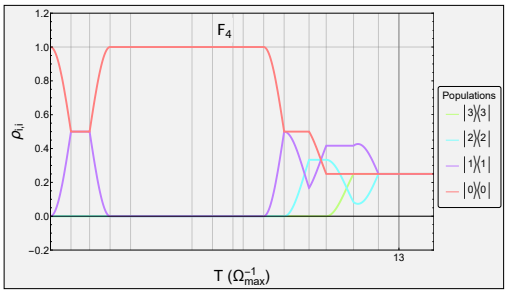
$$R \to e^{-i\phi}R = \begin{bmatrix} e^{-i\phi}A'''_{11} & 0 & 0 \\ 0 & e^{-i\phi}A'''_{22} & 0 \\ 0 & 0 & e^{-i\phi}A'''_{33} \end{bmatrix}$$
$$\implies \begin{bmatrix} 1 & 0 \\ -1 & 1 \\ 0 & -1 \end{bmatrix} \begin{bmatrix} \theta_1^z \\ \theta_2^z \end{bmatrix} = \begin{bmatrix} \arg A'''_{1,1} - \phi \\ \arg A'''_{2,2} - \phi \\ \arg A'''_{3,3} - \phi \end{bmatrix}$$
$$\implies R = G_{2,1}\left(\frac{-\pi}{4}, \frac{\pi}{2}\right) G_{2,1}\left(-\theta_1^z, 0\right) G_{2,1}\left(\frac{\pi}{4}, \frac{\pi}{2}\right) \times$$
$$\times G_{3,2}\left(\frac{-\pi}{4}, \frac{\pi}{2}\right) G_{3,2}\left(-\theta_2^z, 0\right) G_{3,2}\left(\frac{\pi}{4}, \frac{\pi}{2}\right)$$

Using this linear algebraic method, we developed a Mathematica implementation that provides an interactive notebook environment that generates and displays the Givens pulses and time evolution of the state density matrix for a choice of quantum gate or algorithm of gates for a single qudit system. The system can be configured by dimension, initial state, gate sequence and Markovian noise type, as well as providing pulse normalisation options in post-processing.

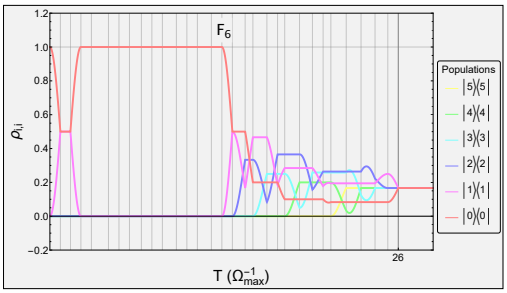
Figures 6.4 and 6.5 show the results of applying the GRD to generate the QFT gate for $d \in \{4, 6\}$ and the probabilistic and deterministic Grover's Algorithms for $d = 6$ qudit systems, respectively. In Fig. 6.4, the populations shown in Figs. 6.4a and 6.4b demonstrate the evolution of the state density matrix from the ground state $|0\rangle\langle 0|$ to the pure superposition final state due to the pulses shown in Figs. 6.4c and 6.4d.

In Fig. 6.5, a qudit of $d = 6$ was initialised in the ground state and then evolved by either the probabilistic (Fig. 6.5a) or deterministic (Fig. 6.5b) Grover's Algorithm pulse sequences generated by the GRD. In each case, the Oracle was applied to the marked search state $|2\rangle\langle 2|$. It is clear that the deterministic algorithm achieves the target state exactly, while one iteration of the probabilistic algorithm only approaches approximately. Note that for $d = 6$, Eq. (6.87) gives $r(6) = 1$ iteration as optimal with probability of success $P \simeq 0.91$, compared with $P \simeq 0.74$ for two iterations (as indicated by the population of the $|2\rangle\langle 2|$ state in Fig. 6.5a).

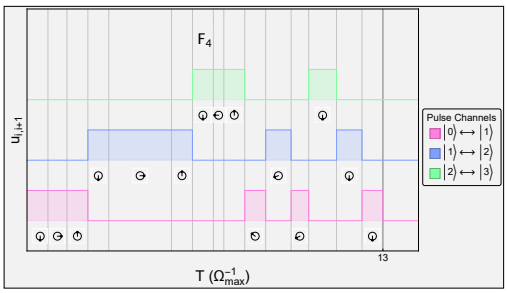
Despite the benefits of the deterministic search algorithm, the increased complexity leads to longer total gate time and subsequent numbers of pulses. The required four Grover iterations, as opposed to one for the probabilistic search, results in a gate time of $161\Omega_{max}^{-1}$ rather than $68\Omega_{max}^{-1}$, and requires three times the number of pulses. This is a significant drawback for practical implementations, and highlights the need for further research into more efficient gate synthesis methods, as the longer gate times increase the likelihood of errors due to environmental interactions, and the increased number of pulses means more susceptibility to control errors.



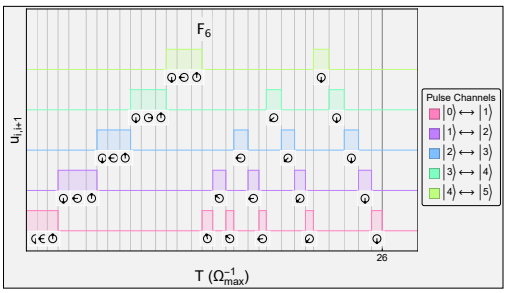
(a) Populations $\rho_{i,i}$ for $d = 4$.



(b) Populations $\rho_{i,i}$ for $d = 6$.



(c) Pulses $u_{i,i+1}(t)$ for $d = 4$.



(d) Pulses $u_{i,i+1}(t)$ for $d = 6$.

Figure 6.4 – Givens rotation pulses and populations for the QFT gate. The GRD was applied to a qudit system of dimension $d = 4$ (a, c) and $d = 6$ (b, d) to generate the QFT gate F_d. For each simulation, the state density matrices $\rho(t)$ shown in (a) and (b) were initialised in the ground state $\rho_{0,0}$ and evolved by the pulse sequences generated by the GRD as shown in (c) and (d). The final states $\rho(T)$ were obtained after the gate time T as measured in units of inverse Rabi frequency Ω^{-1}, with the monochromatic pulse amplitudes normalised to $\Omega_{max} = 1$ by the condition $\Omega(t) = \sqrt{\sum_{k=1}^{d-1} |u_k(t)|^2}$. The clock symbols below each pulse indicate the phases of the pulses. Note that the gate time of ~ 26 for $d = 6$ is approximately twice as long as the ~ 13 for $d = 4$, with 30 pulses required instead of 15.

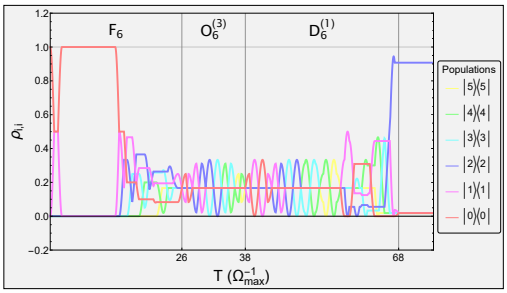
6.4.1.2 GRAPE algorithm

Based on the scalability issues of the GRD, we now turn to the GRAPE algorithm for generating quantum gates, and show some applications to the QFT gate and Grover's Algorithm.

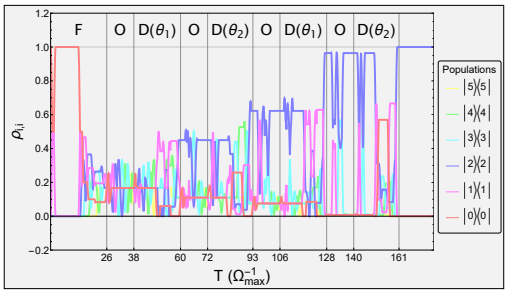
In Fig. 6.6, the GRAPE algorithm was applied to the QFT gate for a $d = 4$ qudit system initialised in the ground state $|0\rangle\langle 0|$. The populations shown in Fig. 6.6a demonstrate the evolution of the state density matrix to the pure superposition final state due to the pulse sequences shown in Fig. 6.6b. For this simulation, the GRAPE algorithm was configured with a total gate time of $T = 1$ discretised into 40 timesteps. The real and imaginary components of each pulse channel were initialised by sinusoidal functions:

$$u^{(0)}(t_n) = 2\pi T \sin(2\pi T t_n) \tag{6.97}$$

The optimisation algorithm was run over 5000 iterations to produce the final multichromatic pulse sequences $u^{(f)}$ in $t \in [0, 1]$, as shown in the upper panel of Fig. 6.6b. The pulses were then normalised by the maximum amplitude,



(a) Populations $\rho_{i,i}$ for the probabilistic Grover's algorithm.



(b) Populations $\rho_{i,i}$ for the deterministic Grover's algorithm.

Figure 6.5 – GRD of the probabilistic and deterministic Grover's algorithms. The GRD was applied to each gate generating the different Grover's algorithms in $d = 6$ with $\rho_{2,2}$ the marked search state. The probabilistic Grover's algorithm (a) was implemented with the oracle operator $O_6^{(2)}$ and diffusion operator $D_6^{(\rho_0)}$, while the deterministic (D2p) Grover's Algorithm (b) was implemented with the restricted-phase oracle operator $O_6^{(2)}(\pi)$ and alternating generalised amplitude amplification operators $G_6(\theta_1)$ and $G_6(\theta_2)$. The state density matrices $\rho(t)$ were initialised in the ground state $\rho_{0,0}$ and the monochromatic pulse amplitudes normalised to $\Omega_{max} = 1$.

$$\Omega_{max} = \max \sqrt{\sum_{k=1}^{d-1} |u_k(t)|^2} \tag{6.98}$$

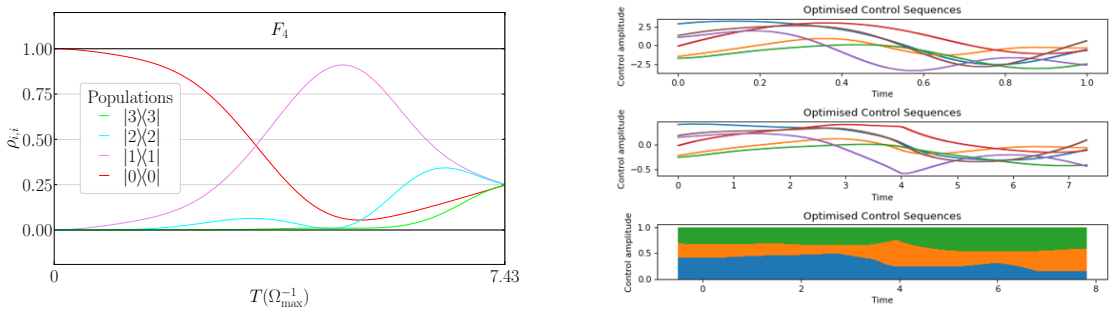
$$u_{i,i+1}^{(f)}(t) \to \frac{u_{i,i+1}^{(f)}(t)}{\Omega_{max}}, \tag{6.99}$$

$$T \to T\Omega_{max}, \tag{6.100}$$

as shown in the central panel of Fig. 6.6b. The lower panel shows the variation in the relative amplitudes between each channel, and how the total amplitude over all channels is now normalised to 1 at all timesteps.

Making a brief comparison between this GRAPE implementation of the QFT gate, and the GRD method in Figs. 6.4a and 6.4c, the first thing to note is regarding the gate times (see Section 6.4.2) where the GRAPE QFT gate is nearly twice as fast as that of the GRD, with a gate time of ~ 7.5 vs ~ 13 in units of Ω_{max}^{-1}. Moreover,the shorter gate times and smooth variation in populations (and coherences) indicates less susceptibility to errors due to environmental interactions, such as dephasing, bit-flip or relaxation processes (see Section 6.4.2.3). The pulses also vary smoothly in time, which may be: (i) more practical to implement experimentally due to constraints on the control electronics, and (ii) possibly less sensitive to control errors. On the other hand, it should be noted that the numerical optimisation approach of GRAPE is significantly more computationally expensive than the linear algebraic method of the GRD, and scalability to higher dimensions could become infeasible rapidly, while also incurring the risk of becoming trapped in local minima or failing to converge to an acceptable solution (see Section 6.4.2.1).

Before studying these issues in detail in Section 6.4.2, we demonstrate a hybrid implementation of the probabilistic Grover's Algorithm using the GRAPE algorithm to generate the QFT and diffusion gates, and Givens rotations to implement the Oracle phase inversion. The resulting simulation is shown in Fig. 6.7. The reason for this hybrid approach



(a) Populations $\rho_{i,i}$.

(b) Pulses $u_{i,i+1}(t)$.

Figure 6.6 – GRAPE algorithm implementation of the qu-4-it QFT gate. The GRAPE algorithm was applied to a qudit system of dimension $d = 4$ to generate the QFT gate F_d. The state density matrix was initialised in the ground state $\rho(0) = |0\rangle\langle 0|$. The states $\rho_{i,i}$ shown in (a) were evolved by the pulse sequences generated by the GRAPE algorithm as shown in (b). In (b), the GRAPE algorithm was initially configured with a total gate time of $T = 1$, with the initial pulse guess evolved over 5000 iterations, resulting in the real and imaginary pulses of each channel as shown in the upper panel. The pulse amplitudes were then normalised to by the condition $\Omega(t) = \sqrt{\sum_{k=1}^{d-1} |u_k(t)|^2}$, resulting in the central panel. The lower panel shows the variation in the relative amplitudes between each channel.

is that our initial configurations of the GRAPE algorithm were not well-suited to generating the Oracle operator, possibly due to the fact that the phase inversion process involves no evolution of the populations, leading to the optimiser failing to converge to an acceptable solution.

In this case it was straightforward to run the individual algorithms separately on their respective gates, and then concatenate the resulting pulse sequences as shown in Fig. 6.7b, provided that the final pulses were normalised by the maximum amplitude as before. The populations shown in Fig. 6.7a demonstrate the evolution of the state density matrix, successfully producing the marked search state $|2\rangle\langle 2|$ after one Grover iteration.

Regarding the optimisation of the GRAPE pulses, the real and imaginary components of each pulse channel were initialised with uniformly distributed random values at each timestep, and smoothed by convolution:

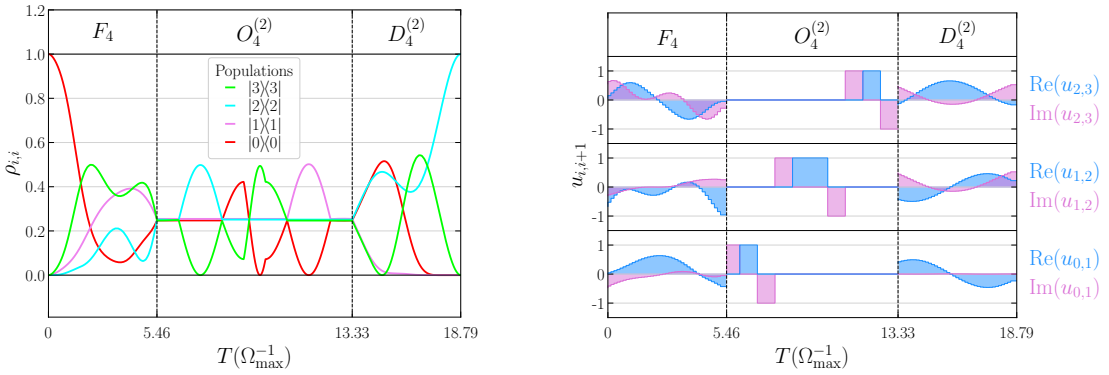
$$u^{(0)}(t_n) = \frac{2\pi}{100T}\mathbb{U}[0,1] \tag{6.101}$$

$$u^{(0)}(t_n) \to \sum_{m=0}^{9} \frac{1}{10} u^{(0)}(t_{n-m}). \tag{6.102}$$

This change in the initial guess is interesting as it produces a much faster gate, reducing the $\sim 7.5\Omega_{max}^{-1}$ gate time of the sinusoidal guess to $\sim 5.5\Omega_{max}^{-1}$.

6.4.2 Comparison of the Different Gate Synthesis Methods

We are now in a position to compare the performance of the different gate generation methods in terms of gate times, gate fidelity, robustness to noise and computational cost.



(a) Populations $\rho_{i,i}$. **(b)** Pulses $u_{i,i+1}(t)$.

Figure 6.7 – Hybrid GRD-GRAPE algorithm implementation of the probabilistic Grover's algorithm. The GRAPE algorithm was applied to a qudit system of dimension $d = 4$ to generate the QFT and diffusion gates, while the Oracle phase inversion was implemented by Givens rotations. The qudit was initialised in the ground state $\rho(0) = |0\rangle\langle 0|$ and the state $|2\rangle\langle 2|$ marked as the search state. The states $\rho_{i,i}$ shown in (a) were evolved by the normalised complex pulse sequences as shown in (b), resulting in the final state after one Grover iteration.

6.4.2.1 Computational cost

The primary concern for simulating high-dimensional quantum systems is the memory demand due to the exponential growth of the Hilbert space, and consequent scaling of the data required to store the state and operator matrices. This becomes exacerbated when simulating the time evolution of open quantum system in the superoperator formalism. Moreover, this scaling of the matrix dimensions directly affects the processing times due to the increased number of matrix operations required.

In Fig. 6.8, we show the memory usage and processing times for the time evolution of a single qudit system using the `mesolve` function in QuTiP. This is a simplified example of the computational cost of simulating qudit systems, and is not directly related to the gate synthesis methods discussed thus far. However, it provides a useful benchmark for the cost of the time evolution solver, which is a key component in studying the gate synthesis techniques.

The test was configured as follows: a single qudit was initialised for $d \in [2, 512]$ with one random unitary gate for a single timestep $t = 1$. Markovian dephasing noise with $L = J_z$ and $\gamma = 0.01$ was introduced to prevent the `mesolve` function from defaulting to the simpler `sesolve` method for closed quantum systems. This ensured use of the full backward-differentiation formula (bdf) ODE solver in the dense superoperator representation. The following solver parameters were used:

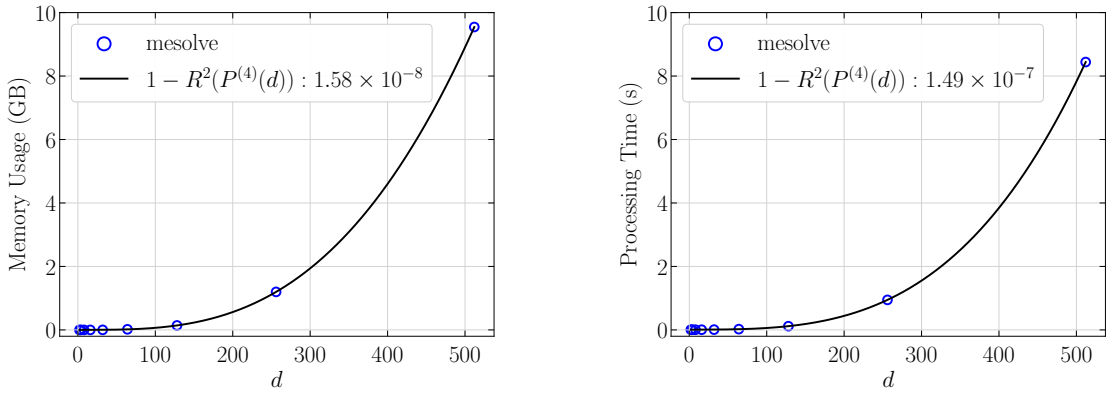
① Relative Tolerance: $r_{tol} = 1 \times 10^{-16}$,

② Absolute Tolerance: $a_{tol} = 1 \times 10^{-16}$,

③ Maximum Steps: $\mathrm{steps}_{\max} = 1 \times 10^{6}$, and

④ Maximum Step Size: $t_{\max} = 1 \times 10^{-3}$.

In this test, the calculations were performed in a separate thread process using the Threading library to isolate the `mesolve` function from the main process. The psutil and time libraries were used to measure the memory usage and processing times, respec-



(a) Memory usage.

(b) Processing times.

Figure 6.8 – Memory usage and processing times for simulating single-qudits with `mesolve`. The (a) memory usage, and (b) processing times of the `mesolve` function in QuTiP were tested for simulating the time evolution of a single qudit system for $d \in [2, 512]$ by one random unitary gate for a single timestep $t = 1$ subject to Markovian dephasing noise with $L = J_z$ and $\gamma = 0.01$. The solver was configured with: $r_{tol} = a_{tol} = 1 \times 10^{-16}$, $\max(n_{\text{steps}}) = 1 \times 10^6$ and $\max(t_{\text{step}}) = 1 \times 10^{-3}$ for the backward-differentiation formula (bdf) ODE solver. The fourth-order polynomial ($P^{(4)}(d)$) fits indicate both memory usage and processing times scaling as d^4.

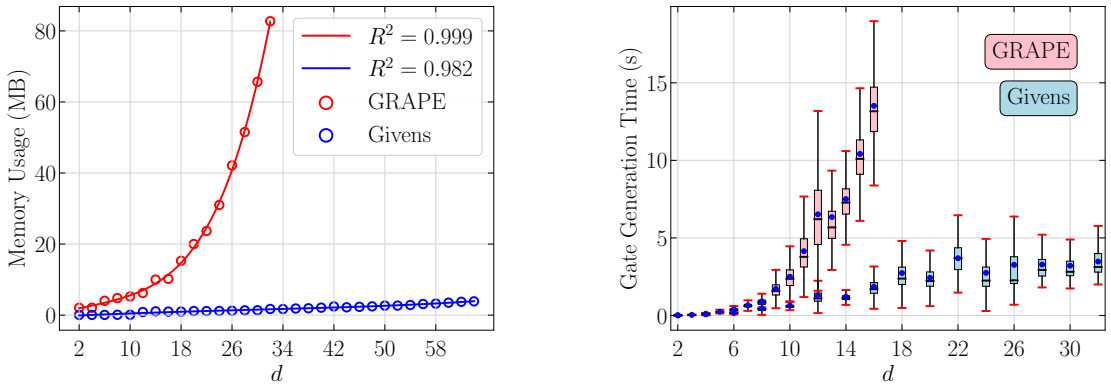
tively. It is worth noting that the test was only run up to $d = 512$ due to the memory limitations of the test machine hardware.

The results in Fig. 6.8 strongly suggest that both the memory usage and processing times scale as d^4, as indicated by the fourth-order polynomial fits with $R^2 \sim 1$ close to unity in both cases. This is consistent with the fundamental factor being the expected scaling of the Hilbert space dimension, as the superoperators scale as $(d \times d) \times (d \times d) = d^4$.

In Fig. 6.9, we compare the memory usage and processing times for the GRD and GRAPE algorithm for generating quantum gates over a range of qudit dimensions. Note that the GRAPE algorithm was only run up to half the dimensions of the GRD method due to the strong scaling demands.

In Fig. 6.9a, the memory usage of the GRAPE and GRD methods was tested on synthesising a single QFT gate at each dimension. In this more complex computation it was not feasible to measure the memory using PSUTILS as in Fig. 6.8a. Instead, the MEMORY_PROFILER library was used to measure the memory usage of the gate generation functions directly. Fourth-order polynomial fits were applied to both sets of data, with the GRAPE method showing stronger agreement than the GRD method, with R^2 values of 0.999 and 0.982 respectively. This suggests that the memory usage of the GRAPE algorithm scales as d^4 as expected, while the GRD method may have additional factors contributing to the memory usage.

To understand this behaviour, let us consider first the GRAPE algorithm: QuTiP's `optimize_pulse_unitary` method in the `control.pulseoptim` library was used to generate the control pulses. This method is a wrapper for SciPy's `optimize.fmin_l_bfgs_b` function, which is an implementation of the Limited-memory Bounded Broyden-Fletcher-Goldfarb-Shanno (L-BFGS-B) second-order quasi-Newton method [221, 222], which approximates the Hessian matrix of the cost function by storing only the most recent m updates to the gradient. Now, the memory requirement of this method is well-known to



(a) Memory usage for the QFT gate.

(b) Processing times for Haar random gates.

Figure 6.9 – Memory usage and processing times for the GRAPE and GRD methods. In (a), the memory usage of the GRAPE (red) and GRD (blue) methods were measured for generating the QFT gate for $d \in [2, 64]$. Both sets of data were fitted with fourth-order polynomials with R^2 values as shown. In (b), the processing times (in s) of the GRD (blue) and GRAPE algorithm (pink) were measured for generating pulses for 1000 Haar random unitary gates in $d \in [2, 32]$. The box and whisker markers show the mean (blue circle), median (black line), quartiles (box) and range (red) at each dimension.

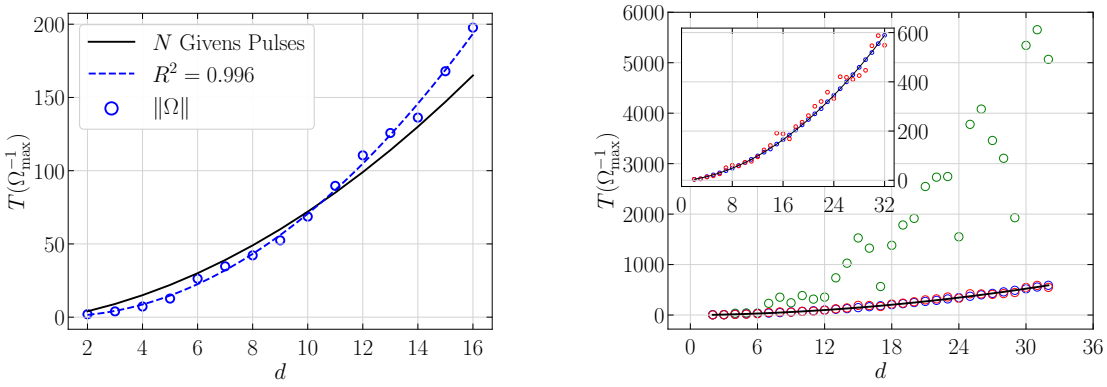
scale approximately as $(12 + 2m)N$, where $m = 10$ by default in the SciPy implementation and used by QuTiP, and N is the size of the model space. In our case this should be $N = 2(d+1) \times (d-1) \times (d \times d) \sim d^4$ since the model must store a $(d \times d)$ matrix for each $(d-1)$ control pulse at each of the $2(d+1)$ timesteps. Now, while we do not necessarily observe the precise $(12+2m)$ prefactor, the scaling of the memory usage with d^4 is consistent with this expected behaviour.

Regarding the GRD, we first remark that unlike the GRAPE function, this is not a built-in function of QuTiP, and was implemented directly in Python in a custom class. Therefore it is not as well-optimised, and may have additional unecessary memory overheads. Nevertheless, it shows significantly lower memory requirements due to the linear-algebraic approach. While a fourth-order polynomial provided the best fit (compared to tests from first- to fifth-order in terms of coefficient of determination), the results are not conclusive enough to definitively state this scaling behaviour. On the other hand, if we consider in principle the memory requirements, we remark that the method generates $\frac{1}{2}d(d-1) + 3(d-1)$ discrete ideal control pulses, each of which is a $(d \times d)$ matrix, and so the total memory requirement should scale roughly as d^4.

Turning now to the processing times in Fig. 6.9b, the GRD and GRAPE algorithm were compared for generating the pulses for each gate in the set of 1000 Haar random unitary gates used in Figs. 6.11a and 6.11b for $d \in [2, 32]$. Again, we observe very similar scaling behaviour in the processing times for each method as for their respective memory requirements. The increased variability is likely due to the sensitivity of the processing times to fluctuations in background CPU load that is difficult to isolate.

6.4.2.2 Gate times

The gate time is a key metric for evaluating the efficiency of a gate synthesis method, as it directly affects the likelihood of errors due to environmental interactions. As discussed in Chapter 4, an important generalisation in this case is to define the figure-of-merit as



(a) GRAPE algorithm **(b)** GRD

Figure 6.10 – Gate times of the GRD and GRAPE algorithms for the QFT gate. The GRD and GRAPE algorithm were compared for generating the QFT gate for single qudits with dimension $d \in [2, 32]$ and $d \in [2, 16]$, respectively. The times were compared to the scaling of the number of pulses required per dimension for the GRD, $\frac{1}{2}d(d-1) + 3(d-1)$. In (a), the GRAPE algorithm shows approximate quadratic scaling in d, with a second-order polynomial fit and $R^2 = 0.996$. In (b), the GRD shows the time-normalised pulses following the theoretical scaling almost exactly, while the amplitude-normalised pulses show variation but still reasonably follow the scaling of pulse number. The two-stage time-and-amplitude normalised pulses are shown in green. The inset shows a zoomed-in view of the amplitude and time normalised pulses.

the ratio of the total gate time T to the decoherence time T_2 of the system,

$$\tau = \frac{T}{T_2}, \tag{6.103}$$

as it provides a measure of the relative performance of different physical platforms. For clarity, here we will make the distinction between the total time T taken for an operation or algorithm, and the gate time t_g of a single quantum gate (as seen in Chapter 5 and later sections).

For the case of a single qudit subject only to dephasing noise, the decoherence time is given by the inverse of the coupling strength γ of the dephasing operator $L = J_z$ in the Lindblad master equation. In this case, the decoherence time is simply $T_2 = 1/\gamma$. For the purposes of this study, however, we are interested in comparing the two gate generation methods directly, and so we will focus only on the total gate time T as the primary metric, as including the decoherence time is not relevant when we are comparing the two methods in isolation.

In Fig. 6.10, we show the gate times for the GRD and GRAPE algorithm for generating the QFT gate up to $d = 32$ and $d = 16$, respectively. In both cases, the gate times were compared to the theoretical scaling of the number of pulses required per dimension, $\frac{1}{2}d(d-1)+3(d-1)$, as discussed in Section 6.4.1.1, which provided a practical benchmark for comparison.

For the GRAPE method shown in Fig. 6.10a, the gate times show approximate quadratic scaling in d, as shown by the second-order polynomial fit with $R^2 = 0.996$. It tends to track closely with the theoretical scaling of the number of pulses for the GRD, although interestingly the gate times for $d < 10$ are shorter while for $d > 10$ they are longer. This is likely due to the scaling of the search space for the optimisation algorithm (discussed in Section 6.4.2.1). However, due to the numerical nature of the search algorithm, it is

Norm		1	2	3	4	5	6	T_{gate}
N/A	θ_{Givens}	$\frac{\pi}{4}$	$\frac{\pi}{2}$	$\frac{\pi}{4}$	$\frac{\pi}{4}$	0.955	$\frac{\pi}{4}$	5.43
$\|\|\Omega\|\|$	t_{pulse}	$\frac{\pi}{4}$	$\frac{\pi}{2}$	$\frac{\pi}{4}$	$\frac{\pi}{4}$	0.955	$\frac{\pi}{4}$	5.43
	Ω_{pulse}	1	1	1	1	1	1	
$\|\|T\|\|$	t_{pulse}	1	1	1	1	1	1	6
	Ω_{pulse}	$\frac{\pi}{4}$	$\frac{\pi}{2}$	$\frac{\pi}{4}$	$\frac{\pi}{4}$	0.955	$\frac{\pi}{4}$	
$\|\|T\|\|_{\Omega_{\max}=1}$	t_{pulse}	$\frac{\pi}{2}$	$\frac{\pi}{2}$	$\frac{\pi}{2}$	$\frac{\pi}{2}$	$\frac{\pi}{2}$	$\frac{\pi}{2}$	9.42
	Ω_{pulse}	$\frac{1}{2}$	1	$\frac{1}{2}$	$\frac{1}{2}$	0.608	$\frac{1}{2}$	

Table 6.1 – Table of results for the GRD of the qutrit QFT gate. The GRD was applied to the QFT gate, producing 6 Givens rotations with angles θ_{Givens} and corresponding pulses numbered in columns 1−6 for each of the three normalisation methods shown in Fig. 6.10b. The total gate time T_{gate} was calculated for each normalisation method, with the final gate times highlighted according to the corresponding red, blue and green. Pulse two was also highlighted in red for the time normalisation method as it exceeded the maximum Rabi frequency, and in green for the amplitude normalisation method as it was the only pulse operating at $\Omega_{\max}$ after rescaling.

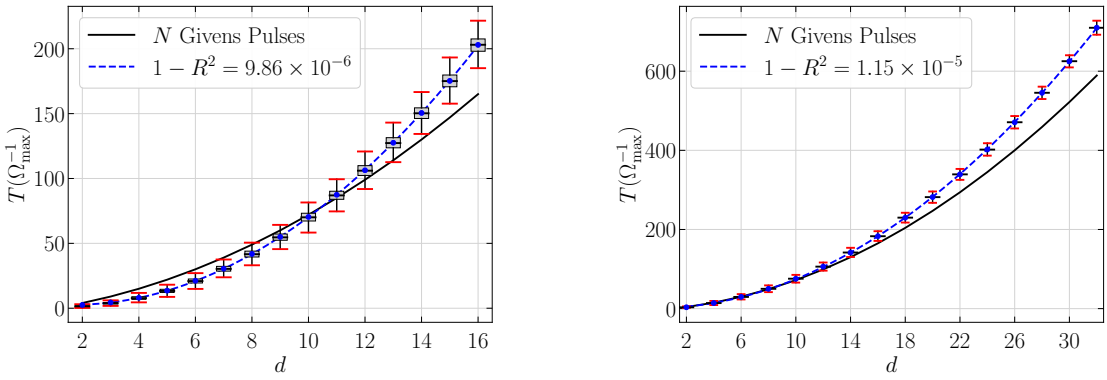
necessary to repeat this test over a larger number of random unitary gates to obtain a more statistically significant result.

For the GRD method in Fig. 6.10b, the pulses were generated and then initially normalised either by time (in blue), with all pulses having unit duration but varying amplitude, or by amplitude (in red) where all pulses have unit amplitude but varying duration.

It is clear that the time normalised pulses following the theoretical scaling almost exactly, although there are situations where, depending on the gate, the matrix reduction technique calculates a zero-angle Givens rotation $\theta = 0$ and thus a pulse is not generated. This applies too for the amplitude normalised pulses, but by fixing all pulses to $\Omega_{max} = 1$ the varying pulse times lead to variation while still reasonably following the scaling of pulse number.

Furthermore, we remark that the the time normalisation of the blue data points is not physically realistic, as it generates pulses with varying amplitudes that can exceed the maximum Rabi frequency. On the other hand, the amplitude normalisation approach fixes all pulses to a constant, maximal Rabi frequency. If we instead rescale the time-normalised pulses to the maximum Rabi frequency in a second step, we obtain the green data points, which show an order-of-magnitude increase in the gate times, since now only the (initially) maximal amplitude pulse operates at Ω_{max}, while the remaining pulses are all scaled down relative to this. Table 6.1 summarises the results of the GRD for the qutrit QFT gate, showing the angles θ of the Givens rotations and the corresponding pulse parameters $\theta_{\text{Givens}} = \Omega_{\text{pulse}} t_{\text{pulse}}$. The rescaling of the time-normalised pulses by the maximum Rabi frequency shows the significant increase in gate time due to the reduced pulse amplitudes.

In Fig. 6.11, we show the gate times for the GRD and GRAPE algorithms applied to the set of 1000 Haar random unitary gates referred to in Section 6.4.2.1. In both cases, the gate times were compared to the number of pulses generated by the GRD, $\frac{1}{2}d(d-1) + 3(d-1)$, and second-order polynomials were fitted to the means of each dataset. Each dataset was displayed as a box-and-whisker plot, showing the means,



(a) GRAPE algorithm **(b)** GRD

Figure 6.11 – Gate times of the GRD and GRAPE algorithms for Haar-random gates. The GRAPE (a) and GRD (b) methods were used used to generate pulses for a set of 1000 Haar random unitary gates for single qudits over dimensions $d \in [2, 16]$ and $d \in [2, 32]$, respectively. The gate times were compared to the scaling of the number of pulses required per dimension for the GRD, $\frac{1}{2}d(d-1) + 3(d-1)$. The data for each dimension is represented in box-and-whisker plots, showing the mean (blue circle), median (black line), quartiles (gray box) and range (red lines). Second-order polynomial fits were applied to the means of each dataset.

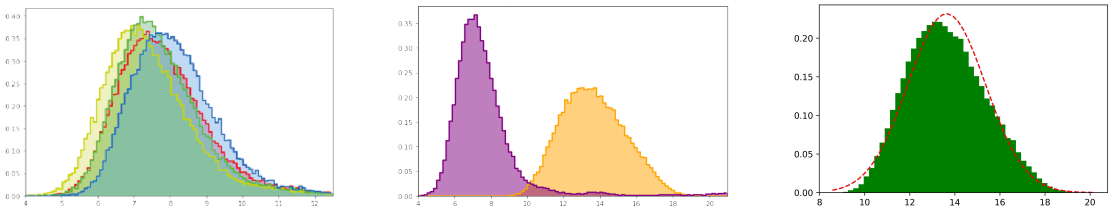
medians, quartiles and ranges of the gate times at each dimension. Note that for the GRD in Fig. 6.11b, the inter-quartile ranges were too small to be effectively displayed.

Comparing these two methods, we see that they demonstrate very similar scaling behaviour, indeed, the coefficients of determination for both second order fits are both very close to unity as noted in the figure. It should be noted that GRAPE was only run up to $d = 16$ due to the strong scaling demands, but extrapolating the fit suggests that the GRAPE algorithm would generate gates for $d = 32$ with a time of approximately $T \sim 1000$ compared to approximately $T \sim 700$ for the GRD.

This suggests that in the current implementations the GRD may produce faster gates for larger dimensions, whereas the GRAPE algorithm may be more efficient for smaller dimensions. Again, this is likely due to the scaling of the search space for the optimisation algorithm, as well as to the particular configuration of the GRAPE algorithm used in this study. Further study on optimisation of the hyperparameters configuring the GRAPE algorithm could be beneficial in elucidating more efficient solutions for higher-dimensional qudit systems.

Finally, in Fig. 6.12, we compare the gate times for the GRAPE algorithm and GRD for implementing Haar random unitary gates specifically for qudits with $d = 4$. In each configuration, the pulse amplitudes were normalised by Ω_{max}, as previously discussed, and the results displayed as probability densities over the range of recorded total gate times.

In Fig. 6.12a, we investigated the effect of different initial pulse guesses on the gate times for the GRAPE algorithm, as an initial step towards understanding the sensitivity of the optimisation algorithm to the hyperparameters. In this case, 1000 Haar random gates were generated and repeatedly simulated by the GRAPE algorithm for 4 different initial pulse guesses: a sinusoidal pulse (red), zero amplitude (yellow), zero-mean random (green) and a square pulse (blue). The results show that the initial guess has a marked effect on the gate time, with the zero amplitude (empty, null) pulse guesses generally



(a) GRAPE initial guesses for 1000 gates.

(b) GRAPE vs GRD for 50000 gates.

(c) GRD for 50000 gates.

Figure 6.12 – Comparison of gate times between the GRAPE and GRD algorithms for $d = 4$. The GRAPE algorithm was compared to the GRD for implementing Haar random unitary gates for single qudits with dimension $d = 4$. In each configuration, the pulse amplitudes were normalised by Ω_{max} and the results displayed as probability densities over the range of recorded total gate times. In (a), 1000 Haar random gates were generated and simulated by the GRAPE algorithm, repeated for 4 different initial pulse guesses: a sinusoidal pulse (red), zero amplitude (yellow), zero-mean random (green) and a square pulse (blue). In (b), the GRAPE algorithm was compared to the GRD over a set of 50000 Haar random gates. In (c), the asymmetry in the distribution of the total gate times for the GRD is shown by fitting a Gaussian distribution.

producing the fastest gates and with smaller variance, while the square pulse guesses produced the slowest pulses with the largest variance.

In Fig. 6.12b, we compared the GRAPE algorithm to the GRD over a set of 50000 Haar random gates. The results show that the GRAPE algorithm produced gates with a mean time of $T \sim 7$, while the GRD produced gates with a mean time of $T \sim 13.5$. Thus, as observed in Fig. 6.11, the GRAPE pulses are generally faster than the Givens pulses for $d = 4$, and with a smaller variance. However, it is worth noting that, due to the numerical nature of the optimisation algorithm, the GRAPE algorithm may produce suboptimal solutions for certain gates, as evidenced by the longer tail in the distribution of gate times, whereas the GRD method is guaranteed to produce gates below a threshold time of $T_{max} = 2\pi N_{\text{pulses}}$ in the amplitude normalisation scheme due to the 2π rotational symmetry of the Givens rotations.

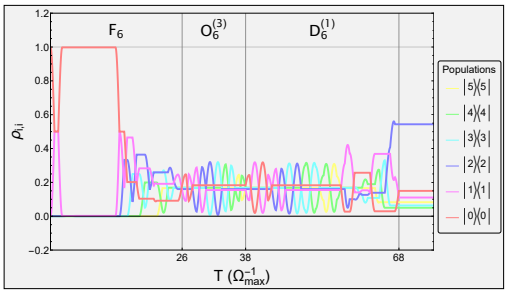
In the third panel, Fig. 6.12c, a Gaussian distribution was fitted to the distribution of gate times for the GRD, showing a clear asymmetry. The nature of this asymmetry is not immediately clear, but it does suggest that the GRD may have a bias towards producing slower gates, as the distribution is skewed towards longer gate times. However, this may not be specific to the GRD, as it appears that the GRAPE distributions also present a certain amount of asymmetry.

6.4.2.3 Effects of Markovian noise on gate fidelity

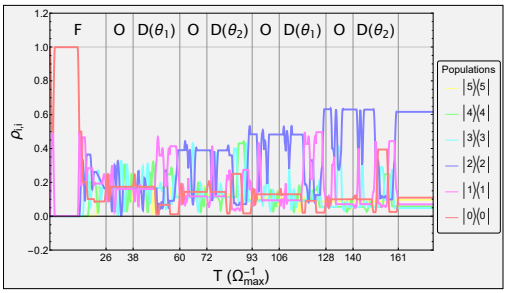
In this section, we investigate the effects of Markovian noise in the Lindblad formalism on the average gate (in)fidelity (AGF/AGI) for qudit quantum gates synthesised by pulse sequences generated by the GRAPE algorithm and GRD methods.

We consider three types of Markovian noise: dephasing noise, bit-flip error and spin relaxation, each characterised by a different collapse operator $L \in \{J_z, J_x, J_-\}$ in the Lindblad master equation and defined by the spin angular momentum operators Eqs. (6.4) to (6.6), respectively.

We begin in Figs. 6.13 and 6.14 with some examples of the effects of environmental

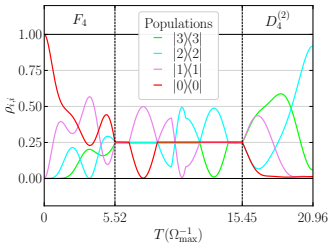


(a) Populations $\rho_{i,i}$ for the probabilistic Grover's Algorithm.

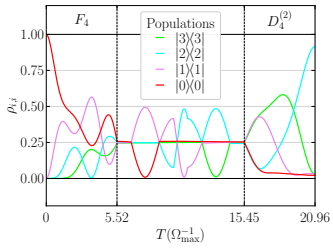


(b) Populations $\rho_{i,i}$ for the deterministic Grover's Algorithm.

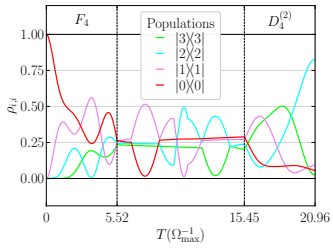
Figure 6.13 – GRD of the probabilistic and deterministic Grover's algorithms under Markovian dephasing noise. Based on the configured noise-free simulations in Fig. 6.5, the GRD was applied to each gate generating the different Grover's algorithms in $d = 6$ with $\rho_{2,2}$ the marked search state. In this case, the state density matrices $\rho(t)$ were evolved under the influence of Markovian dephasing noise through the collapse operator $L = J_z$ with dimensionless coupling strength-time $\gamma T = 0.1$ normalised by the total running time of each algorithm. The resulting state fidelities were (a) ~ 0.56 and (b) ~ 0.62.



(a) $L = J_z$ dephasing.



(b) $L = J_x$ bit-flip.



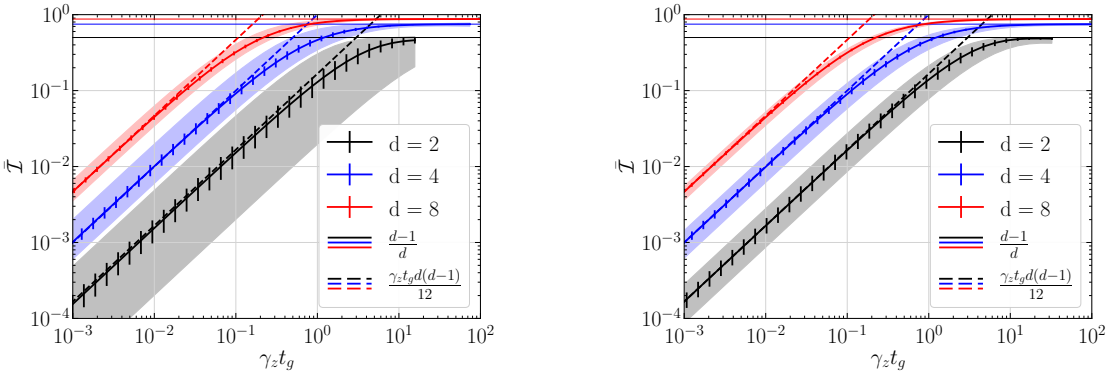
(c) $L = J_-$ relaxation.

Figure 6.14 – Comparison of Markovian error types on Grover's algorithm with GRAPE. Grover's Algorithm was implemented for a qudit with $d = 4$ using the GRAPE algorithm, and the state density matrices $\rho(t)$ were evolved under the influence of Markovian noise through the collapse operators: (a) $L = J_z$ dephasing, (b) $L = J_x$ bit-flip and (c) $L = J_-$ spin relaxation each with coupling strength $\gamma = \frac{0.1}{T}$ normalised by time. The state fidelities were found to be (a) ~ 0.92, (b) ~ 0.91 and (c) ~ 0.82, respectively.

noise on Grover's algorithm. Figure 6.13 shows the effects of pure dephasing on the probabilistic (left panel) and deterministic (right panel) Grover's algorithms for a qudit with $d = 6$. Here, the GRD was applied to each gate in the algorithm and the evolution of the state density matrix presented using our custom Mathematica notebook. For both examples, the coupling strength of the dephasing noise was fixed to a relatively large value of $\gamma = \frac{0.1}{T}$, to exaggerate the effects of the dephasing for visualisation. The normalisation by total running time T is important to remove the dependence on the gate time, and allows for a direct comparison of the effects of noise on the algorithms.

The state fidelities were calculated using the definition of the state fidelity Eq. (6.7). Comparing the results in Figs. 6.13a and 6.13b with their noise-free counterparts in Fig. 6.5, the state fidelities were found to be ~ 0.56 and ~ 0.62, respectively, showing that the deterministic algorithm is more robust to dephasing noise than the probabilistic algorithm after removing the effects of the different overall running times.

Figure 6.14 shows the effects of different Markovian noise types on the probabilistic Grover's Algorithm for a qudit with $d = 4$ using the hybrid Givens-GRAPE algorithm.



(a) GRAPE algorithm.

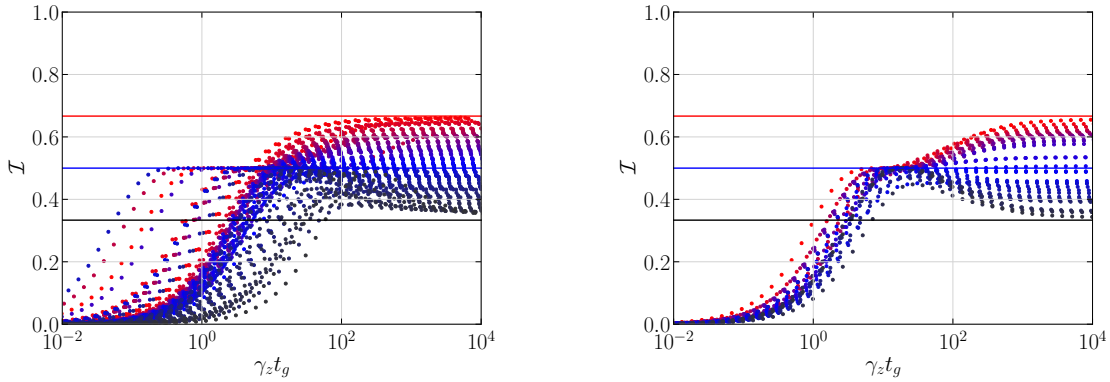
(b) GRD

Figure 6.15 – AGIs of the GRAPE and GRD for Haar random gates under pure dephasing. A set of Haar random gates were synthesised by the (a) GRAPE algorithm and (b) GRD methods for dimensions 2 (black), 4 (blue) and 8 (red). Their AGIs were calculated under the influence of Markovian dephasing noise for $L = J_z$ with coupling strengths γ_z, and plotted against the dimensionless coupling strength/ gate time $\gamma_z t_g$. The solid lines show the mean AGI for each coupling strength, with solid vertical lines indicating the standard deviation and the shaded areas showing the full range of AGIs. The solid horizontal line indicates the mean theoretical value of the AGI at each dimension, and the dashed line shows the theoretical value of the AGI in the linear regime. In (a), 6550, 6550 and 4400 gates were generated for $d = 2$, 4 and 8, respectively. In (b), 50000, 37000 and 5000 gates were generated for $d = 2$, 4 and 8, respectively.

These simulations can be contrasted with the noise free example shown in Fig. 6.7. In each case, the state density matrices $\rho(t)$ were evolved under the influence of Markovian noise through the collapse operators $L = J_z$ dephasing, $L = J_x$ bit-flip and $L = J_-$ spin relaxation, each with a fixed coupling strength of $\gamma = \frac{0.1}{T}$. The results show that the algorithm is most robust to dephasing noise and similarly to bit-flip errors, with state fidelities of ~ 0.92 and ~ 0.91 respectively. Spin relaxation noise had the largest effect on the algorithm, with a state fidelity of ~ 0.82.

Now, recall that in Fig. 5.2 in Chapter 5 the calculations of the AGIs were performed for the quantum gates synthesised by a single pulse generated by the idealised matrix logarithm operation. In analogy, we present the statistical behaviour of the AGIs for the GRAPE and GRD algorithms for Haar random unitary gates under pure dephasing noise. For each gate generation method, a set of Haar random gates was generated for dimensions $d \in \{2, 4, 8\}$ (black, blue and red), for a total of 6550, 6550 and 4400 gates respectively for the GRAPE algorithm, and 50000, 37000 and 5000 gates respectively for the GRD. The shaded regions show the full range between the maximum and minimum AGI values at each coupling strength, while the solid lines show the mean AGI values, with error bars of one standard deviation. Alongside, the dashed and solid lines show the linear and large coupling limit behaviour of the AGI at each dimension, respectively.

This result complements well the idealised result in Chapter 5, as it shows that even for the more realistic case of pulse sequences generated by the GRAPE algorithm and GRD, the AGIs of the gates still agree with the theoretical predictions both in the linear, weak coupling regime and in the plateau-like large coupling limit. This suggests that the AGI is a robust metric for characterising the performance of quantum gates under the influence of Markovian noise, and that the theoretical predictions for the AGI are valid for a wide range of gate synthesis methods.



(a) GRAPE algorithm **(b)** GRD

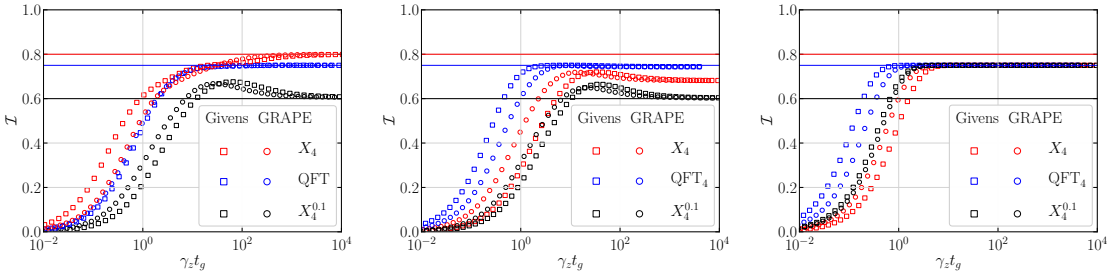
Figure 6.16 – AGIs of the GRAPE and GRD for qubits under pure dephasing. A set of 100 Haar random qubit gates were synthesised by the (a) GRAPE and (b) GRD algorithms under pure dephasing noise. The AGIs were calculated for each gate and plotted as a function of the dimensionless coupling strength $\gamma_z t_g$. The solid horizontal lines show the following AGI values: the minimum, $1-\frac{2}{d+1}$ (black), maximum, $1-\frac{1}{d+1}$ (red), and mean, $1-\frac{1}{d}$ (blue) theoretical values. The colormap gradient from black to red through blue was applied to the AGI curves based on their final plateau value in the large $\gamma_z t_g$ limit.

Furthermore, in comparing these two methods, we see that after normalising by the gate times, the AGIs of the gates generated by the GRAPE algorithm and GRD are very similar, with the GRAPE algorithm showing slightly lower AGIs at each dimension. On the other hand, the GRAPE-generated gates also have a much larger variance in the AGIs, as evidenced by the larger shaded regions in Fig. 6.15a. Nevertheless, both methods also appear to follow the concentration of measure phenomenon for increasing dimension, as studied in Chapter 5.

We continue our study of the gate generation methods in Fig. 6.16 in analogy to Fig. 5.3 of Chapter 5. There, we showed the AGIs of single-pulse matrix logarithm gates for qubits under pure dephasing noise. Here, we extend the analysis to GRAPE (left panel) and GRD (right panel) for 100 Haar random gates. Each AGI curve for each gate was plotted with a colorscale gradient from black to red through blue, based on the final plateau value in the large $\gamma_z t_g$ limit.

This figure shows an interesting differentiation between the two methods, that was hinted at in the large spread of values observed for GRAPE in Fig. 6.15. Whereas the GRD gates have their AGIs clustered together in the linear regime, the GRAPE gates show immediate variation in the weak coupling limit. Furthermore, based on the colorscale grading, it appears that the gates with the largest infidelities in the plateau regime (red) show the greatest sensitivity to the noise strength in the weaker coupling regime, while the gates with the smallest pleateau infidelities (black) show the least sensitivity. In Fig. 6.16b, the AGI curves all appear to converge to the mean theoretical value of $1-\frac{1}{d}$ after transitioning away from the linear regime, and then as the noise continues to increase in strength the curves begin to diverge uniformly.

Finally, in Fig. 6.17, we compare the AGIs of the GRAPE and GRD algorithms for different Markovian noise types for a qudit with $d=4$. This is in similarity with Figs. 5.10 and 5.13 in Chapter 5. Based on our choice of three specific gates: the QFT, generalised-X and interpolated-X with $\eta = 0.1$, the pulses were generated by either method and



(a) $L = J_z$ dephasing. **(b)** $L = J_x$ bit-flip. **(c)** $L = J_-$ relaxation.

Figure 6.17 – Comparison of the AGIs of the GRAPE and GRD algorithms for different Markovian noise types. A qudit of $d = 4$ was evolved by either the QFT (blue), generalised-X (red) and interpolated-X with $\eta = 0.1$ (black) gates. The interpolated gate was chosen to approximate the action of the identity gate, $X_4^{0.1} \sim \mathbb{1}_4$. The gates were synthesised by pulses generated by either the GRAPE algorithm (circles) or the GRD (squares). The AGIs were calculated under the influence of Markovian noise through the collapse operators: (a) $L = J_z$ dephasing, (b) $L = J_x$ bit-flip and (c) $L = J_-$ spin relaxation. The horizontal lines show the theoretical AGI plateau values for each gate type under pure dephasing: the QFT gate, $1 - \frac{1}{d}$, the generalised-X gate, $1 - \frac{1}{d+1}$, and the identity gate, $1 - \frac{2}{d+1}$.

plotted side-by-side for comparison. Note that the interpolated gate was chosen to approximate the action of the identity gate, $X_4^{0.1} \sim \mathbb{1}_4$, while still being able to be synthesised by non-zero pulse sequences. In Fig. 6.17a, the AGIs were calculated under the influence of Markovian dephasing noise, in Fig. 6.17b under bit-flip error and in Fig. 6.17c under spin relaxation.

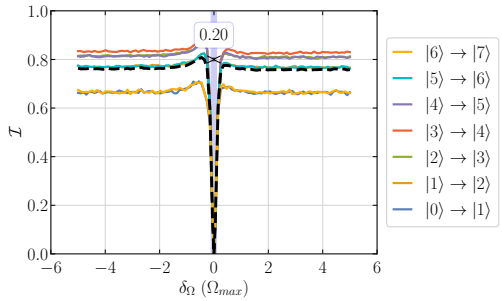
For the case of pure dephasing noise, the AGIs show the gates behaving very similarly to their idealised counterparts in Fig. 5.10, each plateauing towards their theoretical values. The differences between the curves for each method are minor; indeed, for the QFT gates they are almost indistinguishable.

For the bit-flip error, the AGIs again reflected the behaviour of the idealised gates studied in Fig. 5.13, with the QFT gates showing the largest infidelities, followed by the generalised-X gates and then the identity gates. Both methods converged towards the same values, while transitioning through the linear regime in a similar manner.

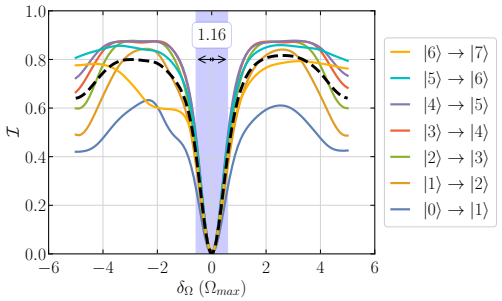
The spin relaxation noise showed the interesting behaviour of having the least differences between the two methods, with the AGI curves showing some overlap and all reaching the same plateau value, regardless of gate. This suggests that the spin relaxation noise has a more uniform effect on the gates, and that the differences between the two methods are less pronounced in this case. Indeed, it is interesting to note that all the gates plateaued towards the mean theoretical value of $1 - \frac{1}{d}$, which is the expected value for the QFT gate.

6.4.2.4 Robustness to control errors

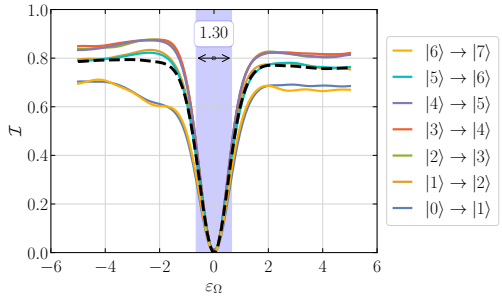
In this section, we investigate the effects of control errors on the performance of quantum gates synthesised by pulse sequences generated by the GRAPE algorithm and GRD methods. Based on the discussion in Section 6.2.1.4 regarding the sources of control errors in a simplified model signal generator or arbitrary waveform generator (AWG) as shown in Fig. 6.1, we shall consider in this section the following types of control errors on a pulse channel:



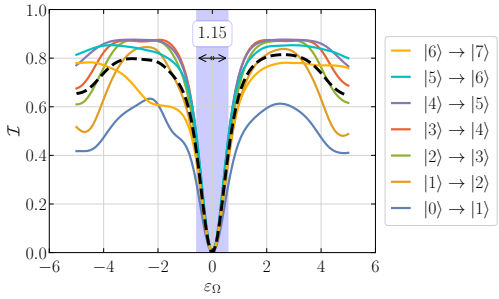
(a) GRAPE - Absolute amplitude offset.



(b) GRD - Absolute amplitude offset.



(c) GRAPE - Relative amplitude offset.



(d) GRD - Relative amplitude offset.

Figure 6.18 – AGIs vs amplitude offset errors for qu-8-its. 100 Haar random gates were synthesised for a qudit with $d = 8$ by the GRAPE algorithm (a, c) and GRD (b, d). The normalised ($\Omega_{max} = 1$) pulse sequences were modulated by absolute (a, b) and relative (c, d) amplitude offset errors through $\Omega \to \delta_\Omega + (1 + \varepsilon_\Omega)\Omega$. The errors were applied separately to each pulse channel of each gate, with the per-channel average for each transition shown. The dashed line shows the average over all transitions and all gates. The blue shaded region indicates the FWHM of the mean.

1. Absolute amplitude offset errors: $\Omega \to \delta_\Omega + \Omega$.
2. Relative amplitude offset errors: $\Omega \to (1 + \varepsilon_\Omega)\Omega$.
3. Absolute phase shift errors: $\phi \to \delta_\phi + \phi$.
4. Relative phase shift errors: $\phi \to (1 + \varepsilon_\phi)\phi$.
5. Clock skew errors: $t \to \delta_t T_g + t$.

For the study of each type of control error, we proceeded in the following fashion: We generate a set of 100 Haar random gates for a qudit, where in this case we have selected $d = 8$ to represent a higher-dimensional system with more pulse channels and greater complexity than for $d = 2$ or $d = 4$. For each gate, the noise-free pulse sequence is generated by either of our two gate synthesis methods, where the pulses are normalised by $\Omega_{max} = 1$ as previously discussed. For each of the $d - 1$ control channels, we then apply independently the chosen control error type over a range of error strengths. For each error strength value (varying symmetrically about 0), the system was time-evolved and the AGI calculated. This therefore produces a dataset of $n_{gates} \times (d - 1) \times n_{errors}$ AGI values per error type per method.

In order to present this data visually in Figs. 6.18 to 6.20, we averaged the AGI values for each control channel, corresponding to the qudit transitions, over all gates, producing $d-1$ averaged AGI curves as a function of the error strength. Going further, these curves were then averaged over all control channels, producing a single (dashed, black) curve

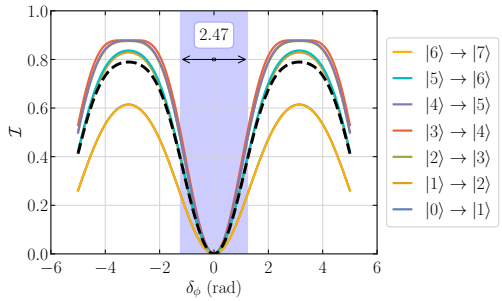
for each error type. This enabled us to compare the average AGI behaviour for each method under the influence of the different control errors by the width of their respective valleys about the zero-noise condition. This value is quantified by the full width at half maximum (FWHM) of the mean AGI curve, as shown by the blue shaded region. The FWHM provides a measure of the robustness of the AGIs to the strength of each error type, as the larger the FWHM, the less sensitive the gates are to the error.

In Fig. 6.18, we show the effects of amplitude offset errors on the AGIs of the gates for each method, for the cases of absolute and relative amplitude offset errors. This corresponds to a constant voltage offset error modulating a single channel of the signal generator. Keeping the offset error range of $\pm 5\Omega_{max}$ constant between the two methods, we see that the GRAPE algorithm is more sensitive to absolute amplitude offset errors, with a FWHM of ~ 0.2, compared to ~ 1.16 for the GRD. This large difference in behaviour is due to the fact that the GRAPE pulses are multichromatic, with the sum of the amplitudes across all channels normalised to $\Omega_{max} = 1$, and thus the absolute error being larger relative to the amplitude of a single pulse. On the other hand, the GRD pulses are monochromatic, with the amplitude of each pulse normalised to $\Omega_{max} = 1$, leading to a smaller relative shift. This effect is negated for the relative amplitude offset errors shown in Figs. 6.18c and 6.18d, where the GRAPE algorithm shows a FWHM of ~ 1.3, compared to ~ 1.15 for the GRD. The greater robustness of GRAPE is reasonably explained by the more gradual variation in the piecewise-constant amplitudes over time.

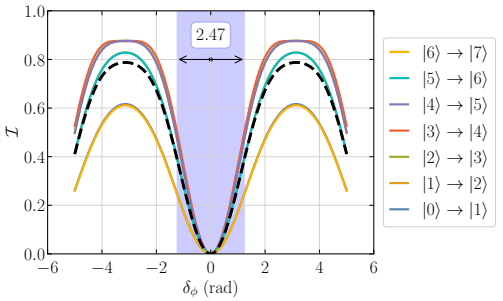
Looking now at the individual pulse channels, the following observations are noteworthy: the AGI curves show (i) a distinct asymmetry between the positive and negative error values, and (ii) a dependence on the choice of transition being modulated. Indeed, for both gate generation methods, we can see that the edge cases for the transitions involving the ground state or most excited state, $|0\rangle \leftrightarrow |1\rangle$ and $|d-1\rangle \leftrightarrow |d\rangle$ respectively, show lower sensitivity to the amplitude offset errors, whereas the inner transitions result in larger infidelities away from the zero-noise condition. A possible explanation for this behaviour is that the $|0\rangle$ and $|d\rangle$ states are only affected by a single transition, whereas the inner states are affected by two transitions to their neighbouring states.

Turning now towards the effect of phase shift errors in Fig. 6.19, we see in Figs. 6.19a and 6.19b that an absolute phase shift has an almost identical effect on the AGIs of the gates for both methods, with a FWHM of ~ 2.47. Moreover, the AGI curves are both symmetric about zero and show 2π-periodicity, as expected from the definition of the phase shift error. The relative phase shift errors in Figs. 6.19c and 6.19d also show similar behaviour between methods, with FWHMs of ~ 0.94 and ~ 0.78 for GRAPE and GRD, respectively. Note the stronger symmetry about zero for the GRD as compared with GRAPE. As remarked for the amplitude offset errors, the greater robustness of the GRAPE method is likely due to the gradual variation in the pulse amplitudes over time leading to less abrupt effects than for the GRD. Furthermore, we see that the same dependence on the choice of control channel shown for amplitude shift is repeated for the phase shift errors.

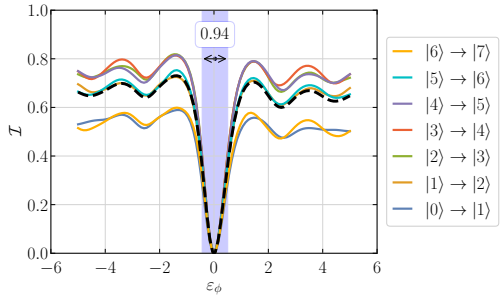
Figure 6.20 presents the effects of absolute clock skew errors, where the pulse timings are shifted by $\pm 0.5T_g$ for GRAPE and $\pm 0.1T_g$ for Givens. In each configuration, this corresponds to the chosen pulse being advanced or delayed by a constant proportion of the total gate duration T_g. In this case, we again see the differences in behaviour due to the multichromatic, piecewise-constant, nature of the GRAPE pulses, with a FWHM of ~ 0.19, compared to ~ 0.05 for the monochromatic, bang-bang, GRD pulses. The



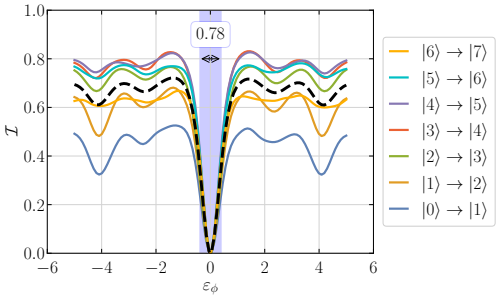
(a) GRAPE - Absolute phase shift.



(b) GRD - Absolute phase shift.



(c) GRAPE - Relative phase shift.



(d) GRD - Relative phase shift.

Figure 6.19 – AGIs vs phase shift errors for qu-8-its. 100 Haar random gates were synthesised for a qudit with $d = 8$ by the GRAPE algorithm (a, c) and GRD (b, d). The pulses were modulated by absolute (a, b) and relative (c, d) phase shift errors through $\phi \to \delta_\phi + (1+\varepsilon_\phi)\phi$. The errors were applied separately to each pulse channel of each gate, with the per-channel average for each transition shown. The dashed line shows the average over all transitions and all gates. The blue shaded region indicates the FWHM of the mean.

GRAPE pulses are significantly more robust to the shifts in timing, and also show a more symmetric behaviour about zero, whereas the GRD pulses exhibit a stronger asymmetry, particular for the ground state transition $|0\rangle \leftrightarrow |1\rangle$.

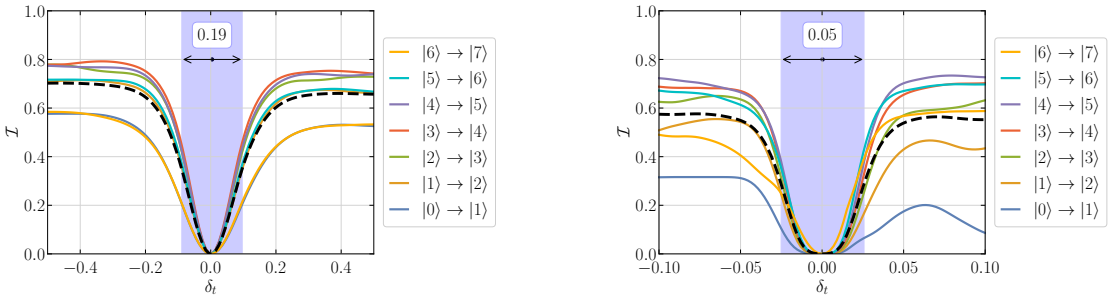
6.5 Discussion

6.5.1 Summary

In this chapter, we presented a detailed study of methods for pulse-level synthesis of single-qudit quantum gates. Having established in Section 6.2 the theoretical foundation for modelling such systems, our primary contributions and results are as follows:

Section 6.2 discussed the conditions of controllability and gate universality in single-qudit systems of arbitrary dimensionality. Given a set of control Hamiltonians, the system is said to be controllable if the Lie algebra of skew-Hermitian control Hamiltonians generates the full Lie group of unitary operators in the system Hilbert space. Indeed, it was sufficient to show that the system exhibits universality if the transition graph of the system is connected. In other words that there exists a sequence of control Hamiltonians (path) that can drive the system from any initial state to any final state. With this in mind, we chose to restrict our study to the minimal case of qudit ladder systems, with only xy-control pulses (in the interaction picture) between adjacent states.

The GRD method was introduced as a linear algebraic approach to generating quantum



(a) GRAPE algorithm **(b)** GRD

Figure 6.20 – AGIs vs absolute clock skew for qu-8-its. 100 Haar random gates were synthesised for a qudit with $d = 8$ by the GRAPE algorithm (a) and GRD (b). The pulses were modulated by absolute clock skew errors as a function of the gate duration through $t \to \delta_t T_g + t$. The errors were applied separately to each pulse channel of each gate, with the per-channel average for each transition shown. The dashed line shows the average over all transitions and all gates. The blue shaded region indicates the FWHM of the mean. The pulse timings were shifted by (a) $-0.5T_g \leq \delta_t \leq 0.5T_g$, and (b) $-0.1T_g \leq \delta_t \leq 0.1T_g$, respectively.

gates by decomposing unitary operations into a sequence of simpler Givens rotations, each acting on a 2-dimensional subspace of the full Hilbert space. This method is convenient both conceptually and in implementation, as each rotation can be analytically derived and, in the case of ideal pulses in a closed quantum system, is exact. Additionally, the rotations can be applied to the system as a single bang-bang pulse using our set of control Hamiltonians, and are easy to visualise as rotations about an axis on the xy-plane of the subspace's Bloch sphere.

The GRAPE algorithm was introduced as a numerical optimisation-based method for generating quantum gates through a sequence of multichromatic piecewise-constant pulses. Beginning with an initial guess for the pulse sequence, the algorithm iteratively optimises the pulse parameters to minimise a cost functional to achieve the target unitary operation. This method is highly flexible, and can be configured with a variety of cost functionals of Mayer, Lagrange or Bolza types, as well as constraints to optimise the pulse sequence for different scenarios. In this work we considered the standard fidelity-based cost functional, which minimises the infidelity between the target and achieved unitary operations.

In Section 6.3 we discussed our development of an extensible simulation framework designed for simulating pulse-level control of qudit quantum systems. The codebase is based on the QuTiP library in Python, and extends the functionality of the library to include classes for simulating quantum gates on qudit systems in noisy environments. Using this framework, our results in Section 6.4 were separated into two parts: in Section 6.4.1 we showed some examples of applying the different gate generation methods for different quantum gates, and in Section 6.4.2 we performed a detailed comparison of the performance of the GRAPE and GRD algorithms.

We tested the gate generation methods on the QFT gate and Grover's search algorithm, and found that both methods were able to synthesise the gates precisely in the noise-free case. The only exception was for the Oracle operator in Grover's algorithm, for which the GRAPE algorithm failed to find an acceptable solution, likely due to the phase inversion operation being a diagonal gate that does not affect the populations dynamics. In this case, we were able to use our framework to simulate the algorithm by a hybrid GRAPE-GRD approach where the Oracle was implemented by Givens rotations and the

QFT and Diffusion operators by GRAPE. This was a novel approach, highlighting the flexibility of our framework in combining different gate generation methods to achieve a desired result. On the other hand, we showed that the GRD was able to synthesise all the Grover operators sufficiently well. Using a custom-built interactive Mathematica notebook for visualising qudit gate simulations, we extended the simulations from the probabilistic version to a more recent, deterministic 2-parameter protocol that is able to locate the target state with certainty. This deterministic variant is very promising in principle, but does come at the cost of increased complexity and number of iterations leading to substantially longer the gate times for the full algorithm.

In Section 6.4.2 we compared the GRAPE algorithm and GRD in terms of: (i) computational cost, (ii) gate duration, (iii) gate fidelity under Markovian noise, and (iv) robustness to control errors.

In terms of computational cost, we found that the memory usage of both methods scales approximately as d^4. However, the GRD requires significantly less memory than GRAPE due to a much smaller prefactor, making it more suitable for higher-dimensional systems. GRAPE also has a higher processing cost due to the iterative nature of the L-BFGS-B optimisation routine, while the GRD offers faster processing due to its linear-algebraic approach, with the processing time scaling similarly to the memory usage for both gates due to the growth in the number of matrix calculations scaling with the dimensionality of the system. This makes the GRD more suitable for larger systems where computational resources and generation time are critical, while GRAPE is competitive for lower dimensions.

Gate time is a critical performance metric in noisy quantum systems, and in order to accurately analyse the gate times across the two methods, the pulse amplitudes of each method were normalised to $\Omega_{max} = 1$, and tests performed over large ensembles of Haar random gates. Simulations were performed over qudit dimensions from $d = 2$ up to $d = 32$ for the GRD and up to $d = 16$ for GRAPE due to computational constraints. In both cases, the gate times were found to scale most appropriately as d^2 by least-squares analysis.

Looking closer, we found that the GRAPE algorithm produced significantly faster and more optimised pulses in lower dimensions below $d \leq 12$, but due to steeper scaling produced longer gate times than GRD for higher dimensions above $d \geq 12$. Looking at the box-and-whisker plots for each method, it is reasonable that this poorer scaling of GRAPE is due to the increased complexity of the search space for higher dimensions, leading to longer times and potentially suboptimal solutions. This is contrasted by the GRD, which shows a more predictable scaling with dimensionality, and is able to maintain a consistent performance across all dimensions.

The impact of Markovian noise through dephasing, bit-flip, and relaxation noise on the average gate fidelity (AGF) was studied for both methods. The tests were performed analogously to those in Section 5.4, where the AGIs were calculated over ensembles of Haar random gates for a range of qudit dimensions, as well as for the QFT and generalised-X gates for $d = 4$. One difference from the results presented in Chapter 5 was that it was necessary to account for the variation in gate times in the dimensionless coupling strength parameter $\gamma_z t_g$ in order to consistently compare the performance across the different gates, generation methods and dimensions.

Overall, there was little statistically significant difference between the GRAPE and GRD

algorithms when accounting for the variation in gate times and averaging over an ensemble of Haar random gates. Indeed, the mean AGIs of both methods were found to be consistent with the theoretical predictions of the ideal AGI behaviour in the linear, weak coupling, regime as identified in Chapter 4. Again in the nonlinear, strong coupling, regime, both methods demonstrated the same plateau-like behaviour within the universal bounds identified in Chapter 5, as well as the expected concentration phenomenon for increasing dimensionality.

A noteworthy difference between the two methods was the variance in the AGIs, with GRAPE exhibiting a larger range of values than GRD at each noise strength. This was most evident in the weak coupling limit for lower dimensions. This suggests that, while GRAPE may perform better for some gates, the GRD provides a more reliable and consistent performance across different noise conditions. This may be of particular importance for practical applications where gate fidelity is critical, and where the environmental conditions are not precisely known.

Finally, we investigated the effects of control errors on the performance of gates synthesised by the GRAPE algorithm and GRD. In this investigative study, we considered constant errors in amplitude offset, phase shift, and clock skew errors on the control pulses, and studied the robustness of the gates to these errors through the full-width at half maximum (FWHM) of the mean AGI curve about the zero-noise condition. For the amplitude offsets and phase shifts, we considered two cases of absolute and relative errors, while for the clock skew errors only the absolute shifts in the pulse timings were considered physically relevant. The methods were compared over a set of Haar random gates, with errors introduced individually to each pulse channel for each gate.

The results showed that the GRD is more resilient than GRAPE to absolute amplitude offset errors due to the effects of amplitude normalisation on the monochromatic vs multichromatic pulse sequences, respectively. On the other hand, GRAPE is more robust to relative amplitude errors due to its smoother pulse profiles over the bang-bang GRD rotations. This same effect was reflected in the relative phase errors, where GRAPE has a slight edge due to its continuous pulse structure. GRAPE also exhibits greater robustness to timing errors (clock skew), while GRD suffers severely due to its reliance on precise pulse timings in the monochromatic sequence.

As an additional remark, it was interesting to observe the dependence of the AGI curves on the choice of transition being modulated, as well as the asymmetry between positive and negative error values. This suggests that the robustness of the gates to control errors is not uniform across the Hilbert space, and that the pulse channels controlling the transitions of the central states are significantly more sensitive to all control errors than the edge (ground- and most excited-) states.

Overall, this chapter offers a comprehensive analysis of two known gate synthesis techniques for qudit systems: the GRD and the GRAPE algorithms. Each method presents strengths and weaknesses depending on the system's dimensionality, computational constraints, and the nature of noise and control errors. The GRD is computationally efficient, making it ideal for large qudit systems where scalability is critical. It also performs well in scenarios with limited resources and offers consistent performance across various noise conditions and system sizes. The GRAPE algorithm, while computationally expensive, excels in small-to-medium systems requiring precise, optimised control, especially where fast gates times and robust controls are essential.

6.5.2 Outlook

The results presented in this chapter offer a comprehensive framework for understanding and implementing pulse-level optimal control of qudit quantum systems. The comparison between the GRD and GRAPE algorithms in gate synthesis provides valuable insights into their practical applications and limitations. Moving forward, there are several potential applications, extensions, and areas for improvement that can be explored based on these findings. Additionally, there are important gaps in our knowledge that future research can address to advance the practical implementation of quantum gates in qudit-based systems.

The GRAPE algorithm has proven highly effective for small-to-medium dimensional systems but suffers from scalability issues and the risk of getting trapped in local minima. A first step would be to explore in more detail the optimisation of the GRAPE algorithm hyperparameters, such as the number of iterations, the choice of cost functional, and the initial pulse guess. Additionally, the algorithm could be parallelised to take advantage of modern high-performance computing resources, enabling faster convergence and more robust solutions for larger qudit systems.

Future work could explore alternative gradient-based numerical optimisation algorithms or gradient-free optimisation techniques like particle swarm optimisation and genetic algorithms. These methods may offer better convergence properties and gate times, improved scalability for high-dimensional qudit systems or improved noise robustness. As an important note in this regard, we have already begun exploratory work on machine learning-based approaches [223]: The blank slate approach of deep Reinforcement Learning (RL) is conceptually interesting but was found to be challenging to train on complex quantum systems, while we have found the Physics-Informed Neural Network (PINN) approach to be a powerful technique for generating high-fidelity gates with very fast gate times. Furthermore, the neural networks can be easily trained on noisy data and with arbitrary constraints and cost functions, making them a potentially powerful tool for generating pulses that are robust to different noise sources and control errors.

This study also introduced a hybrid approach, using GRAPE for complex gate synthesis and the GRD for other operations like phase inversions in the Grover Oracle operator. Expanding on this concept, future work could investigate more sophisticated hybrid methods that leverage the strengths of each technique. For instance, the GRD could be used to generate a rough approximation of a gate, which is then refined by GRAPE or by a machine learning model trained on the GRD pulses. This hybrid strategy could improve computational efficiency and performance for large-scale or noisy qudit systems.

This study primarily focused on Markovian noise models, where the environment's effects on the quantum system are memoryless. However, many realistic quantum systems, particularly in solid-state and molecular platforms, exhibit non-Markovian behaviour, where environmental correlations persist over time. Extending the framework to include non-Markovian noise would provide a more accurate model for qudit systems, improving the robustness of pulse sequences against real-world noise sources. Techniques such as time-convolutionless master equations or stochastic Hamiltonian models could be incorporated to simulate such dynamics.

The control errors studied in this work were limited to constant amplitude and phase offset errors and clock skew errors. Future research could explore additional more physically realistic control errors, including stochastic noise due to thermal and environmental

noise on the control hardware, crosstalk between pulse channels, pulse shape distortions due to finite bandwidth limitations in the filters, timing jitter, and the interaction between signal frequency and amplitude in the pulse generators. These errors are common in experimental quantum systems and can significantly impact gate fidelity. By incorporating these errors into our simulation framework, we could develop more robust pulse sequences that are resilient to a wider range of experimental imperfections.

Despite the advancements made in this study, several gaps remain that future research must address to bring qudit-based quantum computing closer to practical implementation. In practical quantum computing, gate errors and decoherence are inevitable. While this study analyses the effects of noise and control errors on gate fidelity, it will become necessary to explore real-time error mitigation strategies. This includes techniques such as dynamical decoupling, real-time feedback control, and quantum error correction, which could be integrated into the pulse-level control framework. These methods would help maintain high gate fidelity in the presence of environmental noise and imperfect controls.

This study focused exclusively on synthesising gates for single-qudit systems. However, to progress towards practical qudit-based quantum computing, multi-qudit systems must be addressed, where interactions between qudits introduce additional complexities. It is essential as a forthcoming step to extend the simulation framework to include multi-qudit entangling gates, such as generalisations of the CNOT, SWAP or controlled-increment (CINC) gates to higher-dimensional systems. Indeed, here we have begun investigating the further work of Brennen *et. al.* that generalises the linear-algebraic approach of the QR decomposition using Householder reflections to synthesise the CINC entangling gate on 2-qudit systems, requiring only a dipolar-interaction coupling term to be implemented. Being able to simulate entangling operations would enable the design of more complex quantum circuits and algorithms in qudit-based architectures, and would facilitate a much deeper study on the performance differences between multi-qudit and muti-qubit systems.

Finally, while the theoretical and simulation results presented here provide valuable insights into qudit gate synthesis, experimental validation is necessary to confirm these findings. Here, we are planning collaboration with an experimental group in the Faculty of Chemistry at the University of Strasbourg who are specialists on pulsed-EPR (Electron paramagnetic resonance) techniques for SMMs. This would allow us as a first step to test the implementation of the generated pulse sequences on real quantum systems related to our lanthanide-organic molecular complexes. This would provide crucial feedback on the practical challenges of qudit gate implementation, such as system-specific noise sources and control limitations.

As quantum hardware continues to develop, there is a growing need to tailor pulse-level control methods to specific platforms, such as trapped ions, superconducting circuits, or photonic systems. Each hardware platform has unique constraints, such as bandwidth limitations, qudit coherence times, and control resolution. Future work could involve optimising the gate synthesis methods presented here for specific hardware architectures, ensuring that the theoretical benefits translate effectively into experimental realisations.

This study provides a critical step towards the practical realisation of qudit-based quantum computing, offering insights into pulse-level control, gate synthesis, and the effects of noise and control errors. By building on this foundation, future research can extend and improve the methods presented here, bringing us closer to scalable, high-dimensional quantum systems capable of outperforming classical computers. The challenges ahead —

scalability, noise resilience, and hardware optimisation — are significant, but the potential rewards, particularly in areas such as quantum information processing, cryptography, and simulation, make this a promising and exciting field of research.

References Cited in this Chapter

[8] L. K. Grover. "A fast quantum mechanical algorithm for database search". In: *Proceedings of the twenty-eighth annual ACM symposium on Theory of computing - STOC '96*. Philadelphia, Pennsylvania, United States: ACM Press, 1996, pp. 212–219. DOI: 10.1145/237814.237866.

[30] D. P. DiVincenzo. "The Physical Implementation of Quantum Computation". In: *Fortschritte der Physik* 48.9 (Sept. 2000), pp. 771–783. DOI: 10.1002/1521-3978(200009)48:9/11<771::AID-PROP771>3.0.CO;2-E.

[31] Y. Wang, Z. Hu, et al. "Qudits and High-Dimensional Quantum Computing". In: *Frontiers in Physics* 8 (Nov. 10, 2020), p. 589504. DOI: 10.3389/fphy.2020.589504.

[33] A. Chiesa, F. Petiziol, et al. "Embedded quantum-error correction and controlled-phase gate for molecular spin qubits". In: *AIP Advances* 11.2 (Feb. 1, 2021), p. 025134. DOI: 10.1063/9.0000166.

[35] M. N. Leuenberger and D. Loss. "Grover algorithm for large nuclear spins in semiconductors". In: *Physical Review B* 68.16 (Oct. 16, 2003), p. 165317. DOI: 10.1103/PhysRevB.68.165317.

[42] S. Thiele, F. Balestro, et al. "Electrically driven nuclear spin resonance in single-molecule magnets". In: *Science* 344.6188 (June 6, 2014), pp. 1135–1138. DOI: 10.1126/science.1249802.

[43] C. Godfrin, A. Ferhat, et al. "Operating Quantum States in Single Magnetic Molecules: Implementation of Grover's Quantum Algorithm". In: *Physical Review Letters* 119.18 (Nov. 2, 2017), p. 187702. DOI: 10.1103/PhysRevLett.119.187702.

[54] M. N. Leuenberger and D. Loss. "Quantum computing in molecular magnets". In: *Nature* 410.6830 (Apr. 2001), pp. 789–793. DOI: 10.1038/35071024.

[55] M. N. Leuenberger, D. Loss, et al. "Quantum Information Processing with Large Nuclear Spins in GaAs Semiconductors". In: *Physical Review Letters* 89.20 (Oct. 28, 2002), p. 207601. DOI: 10.1103/PhysRevLett.89.207601.

[80] D. D'Alessandro. *Introduction to quantum control and dynamics*. 2nd edition. Advances in mathematics series. Boca Raton: CRC Press, 2021.

[82] M. A. Nielsen and I. L. Chuang. *Quantum Computation and Quantum Information: 10th Anniversary Edition*. Cambridge: Cambridge University Press, 2010. DOI: 10.1017/CBO9780511976667.

[85] D. Manzano. "A short introduction to the Lindblad master equation". In: *AIP Advances* 10.2 (Feb. 1, 2020), p. 025106. DOI: 10.1063/1.5115323.

[90] F. Petiziol, A. Chiesa, et al. "Counteracting dephasing in Molecular Nanomagnets by optimized qudit encodings". In: *npj Quantum Information* 7.1 (Aug. 26, 2021), p. 133. DOI: 10.1038/s41534-021-00466-3.

[91] A. Chiesa, E. Macaluso, et al. "Molecular Nanomagnets as Qubits with Embedded Quantum-Error Correction". In: *The Journal of Physical Chemistry Letters* 11.20 (Oct. 15, 2020), pp. 8610–8615. DOI: 10.1021/acs.jpclett.0c02213.

[96] G. Brennen, D. O'Leary, et al. "Criteria for exact qudit universality". In: *Physical Review A* 71.5 (May 16, 2005), p. 052318. DOI: 10.1103/PhysRevA.71.052318.

[97] N. Khaneja, T. Reiss, et al. "Optimal control of coupled spin dynamics: design of NMR pulse sequences by gradient ascent algorithms". In: *Journal of Magnetic Resonance* 172.2 (Feb. 2005), pp. 296–305. DOI: 10.1016/j.jmr.2004.11.004.

[126] M. A. Nielsen. "A simple formula for the average gate fidelity of a quantum dynamical operation". In: *Physics Letters A* 303.4 (Oct. 2002), pp. 249–252. DOI: 10.1016/S0375-9601(02)01272-0.

[133] H. Miyahara, Y. Chen, et al. "Decoherence mitigation by embedding a logical qubit in a qudit". In: *Quantum Information Processing* 22.7 (July 11, 2023), p. 278. DOI: 10.1007/s11128-023-04035-9.

[140] S. Machnes, U. Sander, et al. "Comparing, optimizing, and benchmarking quantum-control algorithms in a unifying programming framework". In: *Physical Review A* 84.2 (Aug. 3, 2011), p. 022305. DOI: 10.1103/PhysRevA.84.022305.

[174] H.-P. Breuer and F. Petruccione. *The Theory of Open Quantum Systems*. First. Oxford: Oxford University Press, Jan. 25, 2007. DOI: 10.1093/acprof:oso/9780199213900.001.0001.

[184] B. C. Hall. *Lie groups, Lie algebras, and representations: an elementary introduction*. Second edition. Graduate texts in mathematics 222. Cambridge, NY: Springer, 2015. 449 pp. DOI: 10.1007/978-3-319-13467-3.

[193] M. Horodecki, P. Horodecki, et al. "General teleportation channel, singlet fraction, and quasidistillation". In: *Physical Review A* 60.3 (Sept. 1, 1999), pp. 1888–1898. DOI: 10.1103/PhysRevA.60.1888.

[196] M. Le Bellac. *A short introduction to quantum information and quantum computation*. OCLC: ocm65203239. Cambridge, UK ; New York: Cambridge University Press, 2006. 167 pp.

[197] B. C. Hall. *Quantum theory for mathematicians*. Graduate texts in mathematics 267. OCLC: ocn828487961. New York: Springer, 2013. 554 pp.

[198] S. Shapiro. "Lagrange and Mayer problems in optimal control". In: *Automatica* 3.3 (Jan. 1966), pp. 219–230. DOI: 10.1016/0005-1098(66)90014-8.

[199] K. Lutz and Y. Privat. "Decoherence control for quantum information". In: (2023).

[200] R. Fisher and R. Fisher. *Optimal control of multi-level quantum systems*. KS Omniscriptum Publishing, 2010.

[201] T. H. Einwohner, J. Wong, et al. "Analytical solutions for laser excitation of multilevel systems in the rotating-wave approximation". In: *Physical Review A* 14.4 (Oct. 1, 1976), pp. 1452–1456. DOI: 10.1103/PhysRevA.14.1452.

[202] J. Wong, J. C. Garrison, et al. "Multiple-time-scale perturbation theory applied to laser excitation of atoms and molecules". In: *Physical Review A* 13.2 (Feb. 1, 1976), pp. 674–687. DOI: 10.1103/PhysRevA.13.674.

[203] S. G. Schirmer, H. Fu, et al. "Complete controllability of quantum systems". In: *Physical Review A* 63.6 (May 15, 2001). Publisher: American Physical Society, p. 063410. DOI: 10.1103/PhysRevA.63.063410.

[204] V. Ramakrishna, M. V. Salapaka, et al. "Controllability of molecular systems". In: *Physical Review A* 51.2 (Feb. 1, 1995), pp. 960–966. DOI: 10.1103/PhysRevA.51.960.

[205] T. M. Cavalheiro, A. J. Santana, et al. *An accessibility condition for discrete-time linear systems on Lie groups*. June 23, 2024. DOI: https://doi.org/10.48550/arXiv.2406.16237.

[206] V. Ayala and L. A. B. S. Martin. "Controllability properties of a class of control systems on lie groups". In: *Nonlinear control in the Year 2000*. Ed. by A. Isidori, F. Lamnabhi-Lagarrigue, et al. Vol. 258. London: Springer London, 2000, pp. 83–92. DOI: 10.1007/BFb0110209.

[207] J.-L. Brylinski and R. Brylinski. "Universal quantum gates". In: (Aug. 13, 2001). DOI: https://doi.org/10.48550/arXiv.quant-ph/0108062.

[208] A. Muthukrishnan and C. R. Stroud. "Multivalued logic gates for quantum computation". In: *Physical Review A* 62.5 (Oct. 16, 2000), p. 052309. DOI: 10.1103/PhysRevA.62.052309.

[209] Zurich Instruments. *Functional Overview - HDAWG User Manual*. URL: https://docs.zhinst.com/hdawg_user_manual/functional_overview.html (visited on 09/08/2024).

[210] W. Givens. "Computation of Plain Unitary Rotations Transforming a General Matrix to Triangular Form". In: *Journal of the Society for Industrial and Applied Mathematics* 6.1 (Mar. 1958), pp. 26–50. DOI: 10.1137/0106004.

[211] F. D. Murnaghan. "The orthogonal and symplectic groups". In: *Commun. Dublin Inst. Adv. Stud.* A 13 (1958), p. 156.

[212] F. D. Murnaghan. *The Unitary and Rotation Groups*. Vol. 3. Lecture Notes in Applied Mathematics. Washington, D.C.: Spartan Books, 1962.

[213] A. Barenco, C. H. Bennett, et al. "Elementary gates for quantum computation". In: *Physical Review A* 52.5 (Nov. 1, 1995), pp. 3457–3467. DOI: 10.1103/PhysRevA.52.3457.

[214] D. P. DiVincenzo. "Two-bit gates are universal for quantum computation". In: *Physical Review A* 51.2 (Feb. 1, 1995), pp. 1015–1022. DOI: 10.1103/PhysRevA.51.1015.

[215] G. Cybenko. "Reducing quantum computations to elementary unitary operations". In: *Computing in Science and Eng.* 3.2 (Mar. 1996), pp. 27–32. DOI: 10.1109/5992.908999.

[216] D. P. O'Leary and S. S. Bullock. "QR factorizations using a restricted set of rotations". In: *Electronic Transactions on Numerical Analysis* 21 (2005), pp. 20–27.

[217] S. S. Bullock and I. L. Markov. "Asymptotically optimal circuits for arbitrary n-qubit diagonal comutations". In: *Quantum Info. Comput.* 4.1 (Jan. 2004), pp. 27–47. DOI: 10.5555/2011572.2011575.

[218] C. Zalka. "Grover's quantum searching algorithm is optimal". In: *Physical Review A* 60.4 (Oct. 1, 1999), pp. 2746–2751. DOI: 10.1103/PhysRevA.60.2746.

[219] G. L. Long. "Grover algorithm with zero theoretical failure rate". In: *Physical Review A* 64.2 (July 11, 2001), p. 022307. DOI: 10.1103/PhysRevA.64.022307.

[220] T. Roy, L. Jiang, et al. "Deterministic Grover search with a restricted oracle". In: *Physical Review Research* 4.2 (Apr. 21, 2022), p. L022013. DOI: 10.1103/PhysRevResearch.4.L022013.

[221] R. H. Byrd, P. Lu, et al. "A Limited Memory Algorithm for Bound Constrained Optimization". In: *SIAM Journal on Scientific Computing* 16.5 (Sept. 1995), pp. 1190–1208. DOI: 10.1137/0916069.

[222] C. Zhu, R. H. Byrd, et al. "Algorithm 778: L-BFGS-B: Fortran subroutines for large-scale bound-constrained optimization". In: *ACM Transactions on Mathematical Software* 23.4 (Dec. 1997), pp. 550–560. DOI: 10.1145/279232.279236.

[223] Initiated by Julian Mayr (University of Heidelberg) during his MSc. Physics internship on this project.

CONCLUSIONS

CHAPTER 7

SUMMARY AND PERSPECTIVES

At last, after our long journey, we have reached the beginning.

ancient Mentat conundrum in "Hunters of Dune" - Brian Herbert and Kevin Anderson

7.1 Thesis Summary

This thesis has undertaken a multidisciplinary exploration bridging quantum information science and nuclear structure theory, aiming to advance our understanding of hyperfine interactions in lanthanide-molecular complexes and the fidelity of quantum operations in high-dimensional qudit systems. Organised into two main parts, the research traversed the domains of nuclear structure modelling and quantum information processing with qudits, converging on the overarching theme of leveraging nuclear spin properties for advancements in quantum computing.

In Part I, we focused on the nuclear structure and hyperfine anomalies of lanthanide ions, establishing a theoretical foundation for nuclear spin-based qudit systems.

In Chapter 2, we employed the Skyrme-Hartree-Fock-Bardeen-Cooper-Schrieffer (HFBCS) model to elucidate the nuclear structure of the lanthanide isotopes $^{159}_{65}$Tb, $^{161}_{66}$Dy, $^{163}_{66}$Dy, and $^{165}_{67}$Ho. The HFBCS approach, integrating effective interactions and self-consistent blocking, enabled the identification of pronounced deformations in nucleon distributions, particularly for the dysprosium and holmium nuclei. These deformations had significant implications for their magnetic dipole and electric quadrupole moments. While the quadrupole moments were accurately predicted with relative errors below 5% across all isotopes, the magnetic dipole moments showed larger deviations, particularly for ^{161}Dy, highlighting areas where the model could be refined. These results validated the model's applicability to highly deformed nuclear structures, and also emphasised the importance of incorporating relativistic and mesonic corrections to improve the predictive accuracy of calculating the hyperfine splittings in nuclear spin systems, particularly relevant to qudit applications.

In Chapter 3, the hyperfine structure of hydrogen-like dysprosium ions was further investigated, with a focus on the Breit-Rosenthal (BR) and Bohr-Weisskopf (BW) corrections, representing finite nuclear size and magnetisation effects on hyperfine interactions. Detailed comparisons between nuclear models, including point-like, spherical, Fermi, and HFBCS distributions, demonstrated the improved accuracy of the *ab initio* approach. The study of electronic versus muonic ions revealed the heightened sensitivity of muonic systems to nuclear structure, with BR corrections reaching up to 90% in muonic atoms compared to around 5% in electronic systems. Similarly, the BW corrections showed a marked impact on muonic hyperfine splitting, being around 80%, providing a unique window into nuclear magnetism. The calculated hyperfine anomalies between isotopes ^{161}Dy and ^{163}Dy provided key insights into the interplay between nuclear and atomic physics, revealing differences that were orders of magnitude larger in muonic ions than in electronic ones. These findings underscored the potential of muonic spectroscopy to probe nuclear properties with unprecedented precision, suggesting that muonic ions could serve as critical tools for refining nuclear models and exploring hyperfine anomalies experimentally, particularly in the context of quantum information processing.

Part II transitioned into the domain of qudit-based quantum computing, exploring the theory and practical applications of high-dimensional systems.

In Chapter 4, we examined the gate efficiency and fidelity of noisy single-qudit systems in comparison to multi-qubit systems of equivalent Hilbert space dimensions. By deriving a fluctuation-dissipation-like relation for gate infidelity and evaluating the operational efficiency of qudits against qubits, we established a critical curve delineating the necessary efficiency for qudit gates, specifically $d^2-1)/3\log_2(d)$. This critical curve provides a

benchmark for assessing conditions under which qudits can maintain fidelity advantages as dimensionality increases.The study demonstrated that qudit systems can extend up to dimensions of approximately $d \approx 40$ in nuclear spin platforms while retaining operational advantages.These analytical expressions offer essential criteria for optimizing qudit platforms in terms of fidelity, indicating when qudits outperform qubits and providing practical guidelines for qudit-based quantum computing architectures.

In Chapter 5, we extended the fidelity analysis to the nonlinear regime, focusing on the Average Gate Fidelity (AGF) in open quantum systems coupled to Markovian noise. Theoretical perturbative expansions of the AGF in terms of the dimensionless coupling constant γt provided universal bounds and explicit correction terms for arbitrary collapse operators, extending the scope of qudit noise analysis. Numerical simulations confirmed a transition from linear to nonlinear behavior in the AGF as noise strength increased, with plateaus indicating stable infidelity values dependent on both gate type and qudit dimension. The derived bounds established that specific gates saturated these bounds: the identity gate achieving lower limits and the generalized-NOT gate reaching the upper bounds, with the Quantum Fourier Transform (QFT) gate plateauing at mean AGI values as defined by the Haar measure. The ability to separate gate-dependent and gate-independent terms in higher-order corrections enabled a more nuanced understanding of noise impacts across different gates and dimensions. This comprehensive analysis emphasised the necessity of including higher-order corrections in modelling fidelity for high-dimensional qudits and suggested that noise-dependent gate design could further enhance qudit performance.

In Chapter 6, we examined pulse-level synthesis of qudit gates through the Givens Rotation Decomposition (GRD) and the Gradient Ascent Pulse Engineering (GRAPE) algorithm. The development of a modular simulation framework using Python and QuTiP facilitated comparisons of these methods under noise and control errors. Simulations revealed that GRAPE excelled in generating precise, optimised pulses for lower-dimensional systems ($d \leq 12$), while the GRD offered a computationally efficient, consistent approach across larger dimensions ($d \geq 12$). The GRD approach, being linear algebraic, offered scalability and consistent performance across dimensions, particularly for high-dimensional systems. The study of these methods highlighted key trade-offs: GRAPE exhibited faster gates for lower dimensions but encountered computational scalability issues in higher dimensions, while the GRD, despite its reduced flexibility, demonstrated predictable scaling with system size. A hybrid approach combining the efficiency of Givens with the precision of GRAPE was found to be advantageous, particularly in complex scenarios like synthesising the QFT and Grover's search algorithm. The noise analysis confirmed the consistency of both methods with the universal bounds derived in Chapter 5, and highlighted the distinct variances in gate fidelity, offering key insights for pulse-level control in practical qudit-based quantum computing.

7.2 Future Directions

The comprehensive modelling of lanthanide nuclear structure in Chapter 2 lays a strong theoretical foundation for understanding hyperfine interactions in potential qudit platforms. However, further refinement of the HFBCS model is essential to capture the full complexity of nucleon interactions, particularly for magnetic dipole moments. Incorporating relativistic corrections and mesonic contributions to account for neutron-proton dynamics could significantly improve the accuracy of hyperfine splitting predictions. Ex-

tending the model to self-consistent Hartree-Fock-Bogoliubov (HFB) treatments and exploring higher-order multipole moments, such as octupole or hexadecapole, would capture finer details of nuclear shape and collective excitations, particularly in highly deformed nuclei. These developments would not only advance nuclear structure theory but also provide a robust basis for qudit platforms where nuclear spin states play a pivotal role.

Chapter 3's exploration of BR and BW corrections in hydrogen-like dysprosium ions underscores the potential of muonic systems as precise probes of nuclear structure. Future work should focus on leveraging this enhanced sensitivity to refine nuclear models, correlating theoretical predictions with experimental data from muonic and electronic spectroscopy. The substantial hyperfine anomalies in muonic systems present an opportunity for direct experimental measurements, which would offer stringent tests of nuclear models and provide crucial insights into the interplay between nuclear magnetisation and hyperfine interactions, directly impacting qudit-based quantum information applications.

The derived critical curve in Chapter 4 offers a framework for assessing when qudits can outperform qubits in noisy environments. Extending this analysis to multi-qudit systems, accounting for inter-qudit interactions and correlated noise effects, is crucial for determining the scalability and robustness of qudit architectures. The study of Hamiltonian-dependent effects on Average Gate Infidelity (AGI), alongside logical qudit embeddings that are resilient to noise, will reveal whether the fidelity advantages of qudits persist as systems scale, and inform the design of noise-robust qudit operations, particularly for fault-tolerant quantum computing beyond the NISQ era.

In Chapter 5, the detailed perturbative expansions of the AGF set the groundwork for advanced noise analysis and gate optimisation. Future research should incorporate these higher-order correction terms into error mitigation strategies, optimal control protocols, and logical qudit embeddings, extending the scope of gate synthesis to multi-qudit entangling operations. Exploring different noise models beyond pure dephasing, such as amplitude damping and depolarising noise, will enhance the framework's applicability across varied quantum platforms and further refine our understanding of noise impacts on high-dimensional systems.

The comparison of gate synthesis techniques in Chapter 6 highlights the trade-offs between Givens decomposition and GRAPE in qudit control. To further refine these methods, future work should explore optimising GRAPE's hyperparameters and investigate alternative optimisation techniques, including gradient-free approaches like particle swarm optimisation or machine learning-based strategies such as Physics-Informed Neural Networks (PINNs). A significant extension would involve integrating these techniques with error correction protocols, real-time feedback control, and noise-adaptive pulse design. The potential for hybrid control strategies, combining the efficiency of Givens with the precision of GRAPE, offers a promising direction for large-scale quantum systems, where balancing computational efficiency and control precision is critical. Extending the framework to account for non-Markovian noise, complex control errors, and inter-qudit interactions will be essential for developing scalable, robust, qudit-based quantum circuits.

Recent advances have demonstrated that qudit systems can be manipulated using Raman-assisted two-photon interactions, allowing for the precise control of high-dimensional states in superconducting circuits. These circuits act as nonlinear harmonic oscillators, enabling the encoding of multiple states within a single qudit and allowing for the creation of complex quantum states like squeezed states and Schrödinger cat states. Such high-dimensional control not only provides a platform for scaling quantum devices but

also increases resilience to noise—a critical factor for fault-tolerant quantum computing. Developments in programmable qudit processors, such as the implementation of two-ququart ($d = 4$) processing units based on integrated photonics, highlight the rapid progress being made in this field and open new opportunities for realising practical and scalable qudit-based quantum circuits.

Overall, this thesis makes significant contributions to the understanding and development of qudit-based quantum computing, providing theoretical foundations for nuclear structure in hyperfine interactions, detailed noise analysis for fidelity optimisation, and practical guidelines for gate synthesis. The multidisciplinary approach, bridging nuclear physics and quantum information science, not only advances the theory of hyperfine interactions and noise analysis but also provides a robust foundation for developing scalable, high-fidelity quantum operations. Future experimental work, particularly in nuclear spin-based qudit platforms and their associated control techniques, will be instrumental in validating and expanding upon the theoretical insights gained here, guiding the way towards practical, high-dimensional quantum computing systems.

APPENDICES

APPENDIX A

APPENDICES TO CHAPTER 2

A.1 Lanthanide Isotopes

Here we list the lanthanide isotopes considered in the calculations discussed in the main text. The isotope data is obtained from Stone [112]. We show the three elements: dysprosium (Dy), terbium (Tb), and holmium (Ho), with their respective isotopes and nuclear properties.

A	$T_{1/2}$	NA (%)	K^{π}	μ (nm)	Q (b)
147	1.7 h	0	1/2+	+1.70(5)	
148	60 m	0	2-	-1.75(2)	-0.3(2)
149	4.12 h	0	1/2+	+1.35(2)	
150	3.48 h	0	2(-)	-0.90(2)	0.00(13)
151	17.6 h	0	1/2(+)	+0.919(6)	
152	17.5 h	0	2-	-0.58(2)	0.34(13)
153	2.34 d	0	5/2+	+3.44(2)	1.08(14)
154	9.4 h	0	3-	+1.6(2)	2.4(13)
155	5.32 d	0	3/2+	+2.01(2)	1.41(6)
156	5.35 d	0	3-	+1.7(2)	2.3(8)
157	99 y	0	3/2+	+2.01(2)	1.40(8)
158	150 y	0	3-	+1.758(7)	2.7(5)
159	Stable	100	3/2+	+2.014(4)	1.432(8)
160	72.1 d	0	3-	+1.790(7)	3.85(5)
161	6.9 d	0	3/2+	+2.2(1)	1.3(6)

Table A.1 – Table listing the isotopes of terbium ($_{65}$Tb) with experimentally observed ground-states and non-zero spin-parities. The table, adapted from Stone [112], lists the isotopes, half-lives, natural abundances, spin-parities, magnetic moments (in nm) and quadrupole moments (in b).

A	$T_{1/2}$	NA (%)	K^{π}	μ (nm)	Q (b)
147	1.3 m	0	1/2+	-0.915(9)	+0.67(10)
149	4.23 m	0	7/2-	-0.119(7)	-0.62(5)
151	17 m	0	7/2-	-0.945(7)	-0.30(5)
153	6.3 h	0	7/2-	-0.782(6)	-0.02(5)
155	10.0 h	0	3/2-	-0.385(4)	+1.04(3)
157	8.1 h	0	3/2-	-0.301(2)	+1.30(2)
159	144 d	0	3/2-	-0.354(3)	+1.37(2)
161	Stable	18.9	5/2+	-0.480(3)	+2.51(2)
163	Stable	24.9	5/2-	+0.673(4)	2.318(6)
165	2.33 h	0	7/2+	-0.520(5)	-3.48(7)

Table A.2 – Table listing the isotopes of dysprosium ($_{66}$Dy) with experimentally observed ground-states and non-zero spin-parities. The table, adapted from Stone [112], lists the isotopes, half-lives, natural abundances, spin-parities, magnetic moments (in nm) and quadrupole moments (in b).

A	$T_{1/2}$	NA (%)	K^{π}	μ (nm)	Q (b)
152	161.8 s	0	2-	-1.02(2)	+0.1(2)
153	2.0 m	0	11/2-	+6.81(5)	-1.1(5)
154	11.76 m	0	2-	-0.643(6)	+0.19(10)
155	48 m	0	5/2+	+3.51(3)	+1.56(10)
156	56 m	0	4+	+2.99(3)	+2.40(18)
157	12.6 m	0	7/2-	+4.35(3)	+3.05(13)
158	11.3 m	0	5+	+3.77(3)	+4.2(4)
159	35.05 m	0	7/2-	+4.28(3)	+3.27(13)
160	25.6 m	0	5+	+3.71(3)	+4.0(2)
161	2.48 h	0	7/2-	+4.25(3)	+3.30(11)
163	4570 y	0	7/2-	+4.23(4)	+3.7(6)
165	Stable	100	7/2-	+4.17(3)	3.58(2)

Table A.3 – Table listing the isotopes of holmium ($_{67}$Ho) with experimentally observed ground-states and non-zero spin-parities. The table, adapted from Stone [112], lists the isotopes, half-lives, natural abundances, spin-parities, magnetic moments (in nm) and quadrupole moments (in b).

A.2 Numerical Methods

Here we list more detailed functional definitions of the numerical methods used in the calculations discussed in the main text.

A.2.1 Dipole Moments

This section summarises the structure and key computations in the Fortran subroutines designed to compute magnetic dipole moments and potentials for both protons and neutrons based on nuclear data. The following integration routines were implemented:

- **This subroutine computes spherical averages over the mesh points, using spherical harmonics and interpolation.**
- **Inputs:**
  - `zin`, `rhin`: Arrays representing spatial coordinates and radii.
  - `fin`: The function data to be averaged.
  - `conv`: A scaling factor for unit conversion.
  - `Ck`, `Cl`: Parameters that define the spherical harmonics to be used.
- **Outputs:**
  - `fout`: The computed spherical averages.
- **Key Computations:**
  - Uses the `qshep2` interpolation function for 2D data.
  - Integrates using the `integrate_trapz_7` function over mesh points.
- **This function performs trapezoidal integration over the input data, using weights optimised for high accuracy.**
- **Inputs:**
  - `Rp`: The radial coordinates.
  - `f`: The function values to be integrated.
- **Outputs:**
  - `s`: The result of the integration.
- **Key Computations:**
  - Applies a weighted trapezoidal rule using specific coefficients for a 7-point integration method.

The module contains the physical constants used in the computations, including the g-factors for protons and neutrons:

$$g_{p_l} = +1.0, \quad g_{p_s} = +5.5856946893$$
$$g_{n_l} = +0.0, \quad g_{n_s} = -3.82608545$$

It also defines conversion factors such as:

$$\texttt{fm2au} = 1.8897261339213 \times 10^{-5} \text{ a.u./fm}$$

Next, the `m_dipole` subroutine computes the magnetic dipole moments by calling the `mu_component` subroutine for each relevant component (orbital and spin for protons and neutrons).

- `m_dipole`
- **Inputs:**
  - `n_data`: Number of data points.
  - `n_mesh`: Number of mesh points.
  - `z_data`, `rho_data`: Arrays representing the spatial coordinates and proton density data.
  - `j_l_phi_p_data`, `j_s_phi_p_data`, `j_s_phi_n_data`: Arrays containing current components for protons (orbital and spin) and neutrons (spin).
- **Outputs:**
  - Magnetic dipole moments for internal (`mu_in`) and external (`mu_ex`) contributions:

    `mu_l_z_p_in`, `mu_s_z_p_in`, `mu_s_z_n_in`(internal proton/neutron contributions)
    `mu_l_z_p_ex`, `mu_s_z_p_ex`, `mu_s_z_n_ex`(external proton/neutron contributions)

- **Key Computations:**
  - Calls the subroutine `mu_component` to compute each component of the magnetic moment using appropriate coupling constants:

$$\begin{aligned} \texttt{conv\_p\_l} &= 2.0 \cdot g_{p\_l}, \\ \texttt{conv\_p\_s} &= 0.5 \cdot g_{p\_s}, \\ \texttt{conv\_n\_s} &= 0.5 \cdot g_{n\_s}. \end{aligned}$$

The `mu_component` subroutine computes both the internal and external components of the magnetic moment by integrating over the spatial mesh.

- `mu_component`
- **Inputs:**
  - `n_data`: Number of data points.
  - `n_mesh`: Number of mesh points.
  - `z_data`, `rho_data`: Arrays containing spatial and density data.
  - `j_component_data`: Array of current density for the component being calculated (orbital or spin).
  - `g`: Coupling constant for the specific component.
- **Outputs:**
  - `mu_in_comp`, `mu_ex_comp`: Internal and external magnetic moment contributions for the specific component.

- **Key Computations:**
  - Computes spherical averages for the current component using `spherical_av`.
  - Integrates using the mesh to compute internal and external contributions:

$$\texttt{mu\_in\_comp}(r_i) = 0.5 \cdot g \cdot \int_0^{r_i} \rho_{\text{mesh}}^3 \cdot j_{\text{component\_mesh}} \, \mathrm{d}r,$$
$$\texttt{mu\_ex\_comp}(r_i) = 0.5 \cdot g \cdot \int_{r_i}^{R} j_{\text{component\_mesh}} \, \mathrm{d}r.$$

The `m_dipole_potential` subroutine computes the magnetic dipole potentials (`A_wp` and `A_np`) by integrating over the mesh, considering both internal and external contributions.

- `m_dipole_potential`
- **Inputs:**
  - `n_mesh`: Number of mesh points.
  - `rho_mesh`, `rhop_mesh`: Arrays for spatial coordinates and densities.
  - `mu_in`, `mu_ex`: Arrays of internal and external magnetic moment contributions.
  - `P`, `Q`: Auxiliary functions for the potential computation.
- **Outputs:**
  - `A_wp`, `A_np`: Computed magnetic dipole potentials for protons and neutrons.
- **Key Computations:**
  - Integrates over the mesh to compute potentials:

$$\texttt{A\_wp} = \int \left(P \cdot Q \cdot \left(\rho_{\text{mesh}}^{-2} \cdot \mu_{\text{in}} + \rho_{\text{mesh}} \cdot \mu_{\text{ex}} \right) \right) \, \mathrm{d}r,$$
$$\texttt{A\_np} = \int \left(P \cdot Q \cdot \left(\rho_{\text{mesh}}^{-2} \cdot \mu_{\text{in}}(n\_mesh) \right) \right) \, \mathrm{d}r.$$

A.2.2 Quadrupole Moments

Repeating now for the quadrupole calculations, This section summarises the structure and key computations in the Fortran subroutines designed to compute them. The main routines include `e_quadrupole` and `e_quadrupole_potential`.

The `e_quadrupole` subroutine calculates the intrinsic and spectroscopic quadrupole moments for a nucleus using the density data.

- `e_quadrupole`
- **Inputs:**
  - `n_mesh`: Number of mesh points.
  - `I_nuc`: Nuclear spin.
  - `rp`, `r`: Arrays representing spatial mesh and radial coordinates.
  - `rho_C20`: Array representing the quadrupole charge density.

- **Outputs:**
  - `e_quad_intr`, `e_quad_spec`: Intrinsic and spectroscopic quadrupole moments.
- **Key Computations:**
  - Uses the conversion factor `conv_Q_int_to_spec` to compute the spectroscopic quadrupole moment:

$$\texttt{e\_quad\_spec} = \texttt{in2spec} \cdot \texttt{e\_quad\_intr}$$

  - Computes the intrinsic quadrupole moment by integrating the radial density function:

$$\texttt{e\_quad\_intr} = \texttt{au2barn} \cdot \int r^4 \cdot \rho_{C20}\, dr$$

The `e_quadrupole_potential` subroutine computes the quadrupole potential for both the electric field and charge density, by integrating over the mesh points.

- `e_quadrupole_potential`
- **Inputs:**
  - `n_mesh`: Number of mesh points.
  - `rp_mesh`, `r_mesh`: Mesh points and radial coordinates.
  - `rho_C20`: Quadrupole charge density array.
- **Outputs:**
  - `e_quad_phi`: Quadrupole potential for the electric field.
  - `e_quad_rho`: Quadrupole potential for the charge density.
- **Key Computations:**
  - Integrates internal and external contributions using:

$$Q_{\text{in}} = \int r^4 \cdot \rho_{C20}\, dr, \quad Q_{\text{ex}} = \int \frac{\rho_{C20}}{r}\, dr$$

  - Combines internal and external components to compute the quadrupole potential:

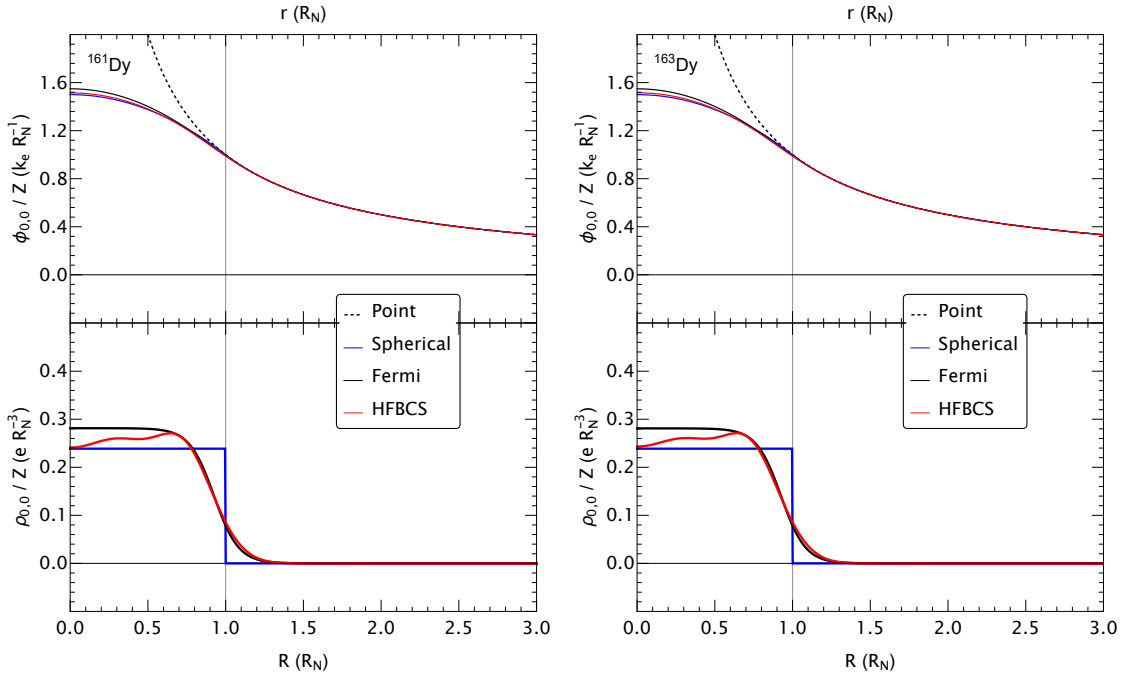
$$e\_quad\_phi = \texttt{au2barn} \cdot \left(\frac{Q_{\text{in}}}{r^3} + Q_{\text{ex}} \cdot r^2 \right)$$

  - Computes the charge density potential as:

$$e\_quad\_rho = \frac{e\_quad\_intr}{r^3}$$

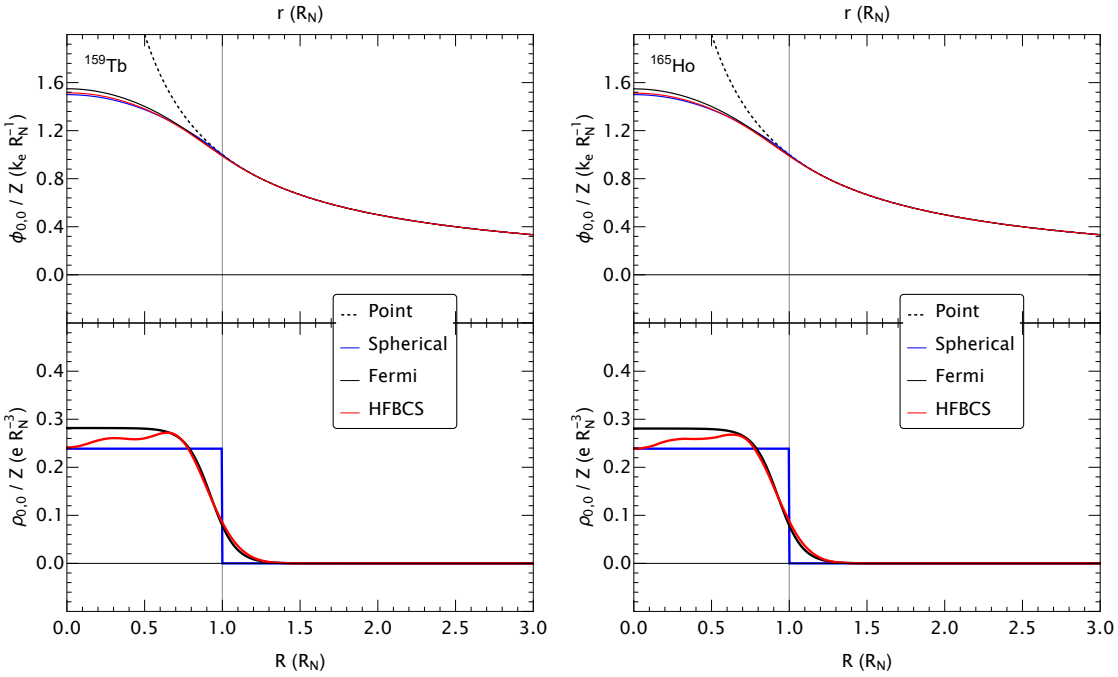
A.3 Additional Results

Here we collect auxiliary results and figures that complement the main text.



(a) ^{161}Dy **(b)** ^{163}Dy

Figure A.1 – Monopole potentials and densities of ^{161}Dy, ^{163}Dy. Z-normalized proton monopole density (lower panels) obtained for the (a) ^{161}Dy and (b) ^{163}Dy nuclei from a uniform sharp-edge (blue), a Fermi-function type (black) and the distribution resulting from the HFBCS type (red) calculation with self-consistent blocking and the Z-normalized monopole potential experienced by the electron resulting from the different approaches for the density (upper panels). The Coulomb potential generated by a nuclear point-charge densities is shown by the dotted line. $k_e \equiv \frac{e}{4\pi\epsilon_0}$ is the Coulomb constant.



(a) ^{159}Tb (b) ^{165}Ho

Figure A.2 – Monopole potentials and densities of ^{159}Tb and ^{165}Ho. Z-normalised proton monopole density (lower panels) obtained for the (a) ^{159}Tb, and (b) ^{165}Ho nuclei from a uniform sharp-edge (blue), a Fermi-function type (black) and the distribution resulting from the HFBCS type (red) calculation with self-consistent blocking and the Z-normalised monopole potential experienced by the electron resulting from the different approaches for the density (upper panels). The Coulomb potential generated by a nuclear point-charge densities is shown by the dotted line. $k_e \equiv \frac{e}{4\pi\epsilon_0}$ is the Coulomb constant.

References Cited in this Appendix

[112] N. Stone. "Table of nuclear magnetic dipole and electric quadrupole moments". In: *Atomic Data and Nuclear Data Tables* 90.1 (May 2005), pp. 75–176. DOI: 10.1016/j.adt.2005.04.001.

APPENDIX B

APPENDICES TO CHAPTER 3

B.1 Additional Results

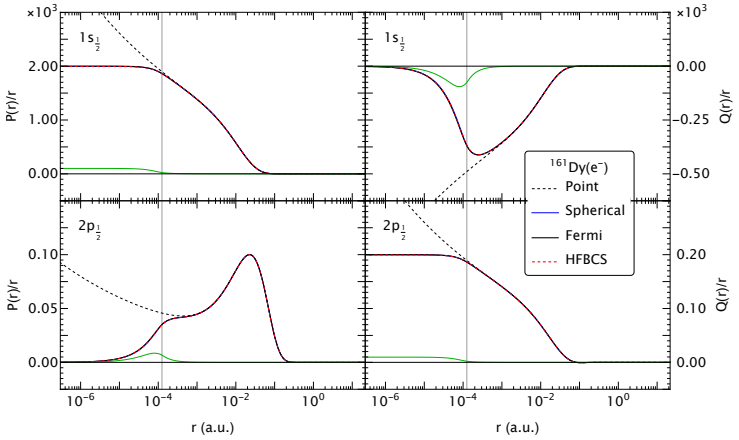


Figure B.1 – Electronic wavefunctions of hydrogen-like ^{161}Dy. The large ($P_{n\kappa}$, left panels) and small components ($Q_{n\kappa}$, right panels) of the radial wave functions for the $1s_{1/2}$ (upper panels) and $2p_{1/2}$ orbitals (lower panels) of $^{161}Dy^{65+}$ are shown. The dashed black and red curves represent the point and HFBCS models respectively, while the solid black and blue curves represent the Fermi and spherical models respectively. The solid green line represents the difference between the Fermi and HFBCS models multiplied by 20. Vertical lines indicate the position of the nuclear radius R_N. Atomic units are used.

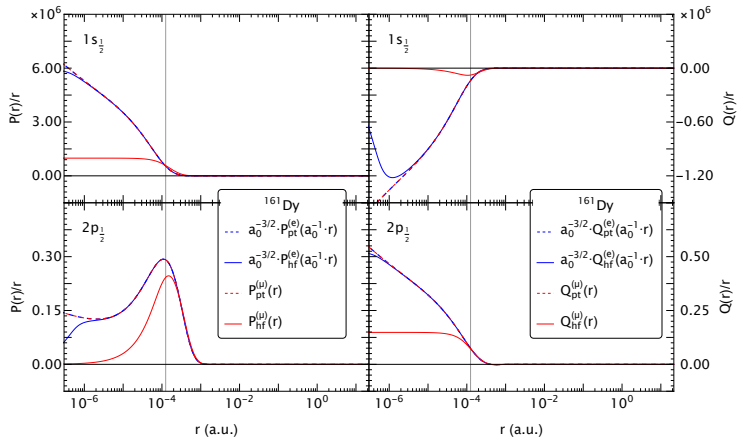


Figure B.2 – Muonic wavefunctions of hydrogen-like ^{161}Dy. Same as Fig. B.1 but for a muonic hydrogen-like atom.

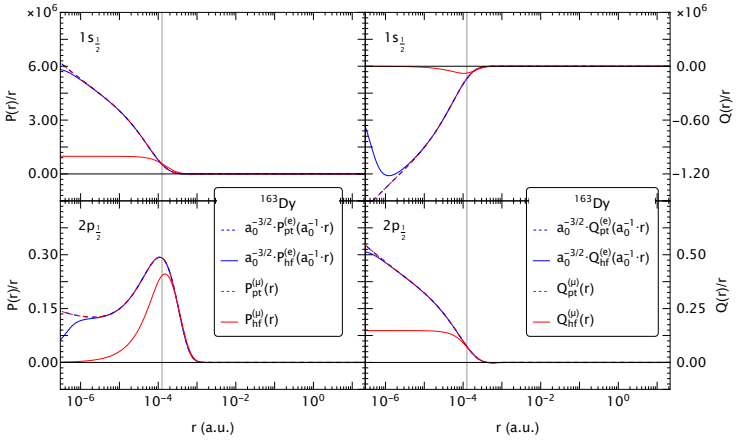
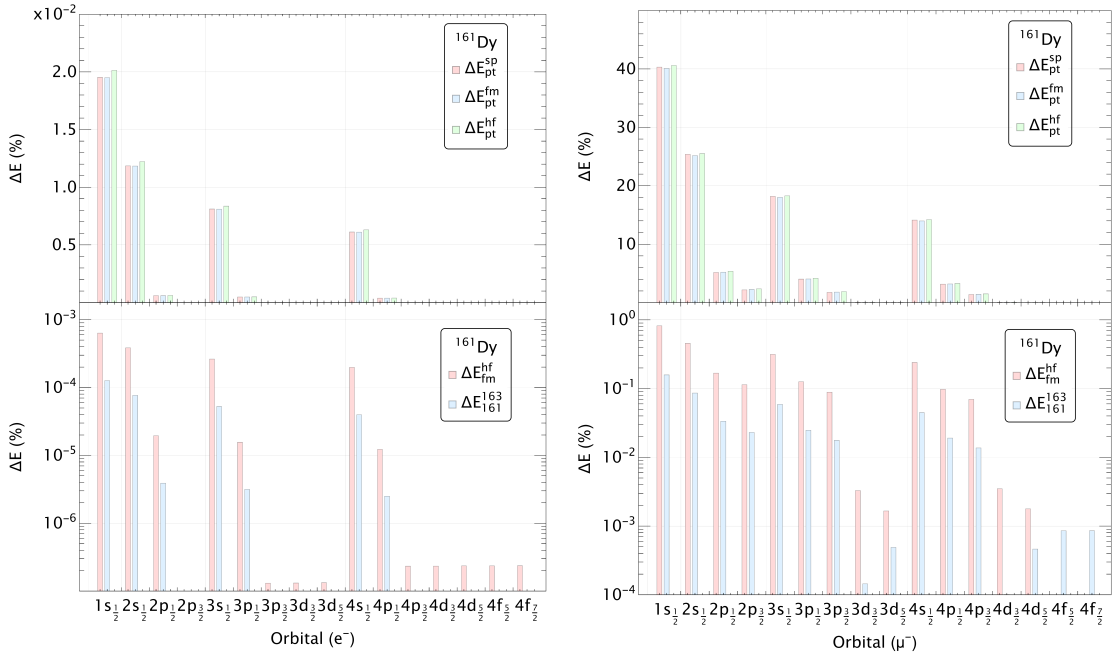
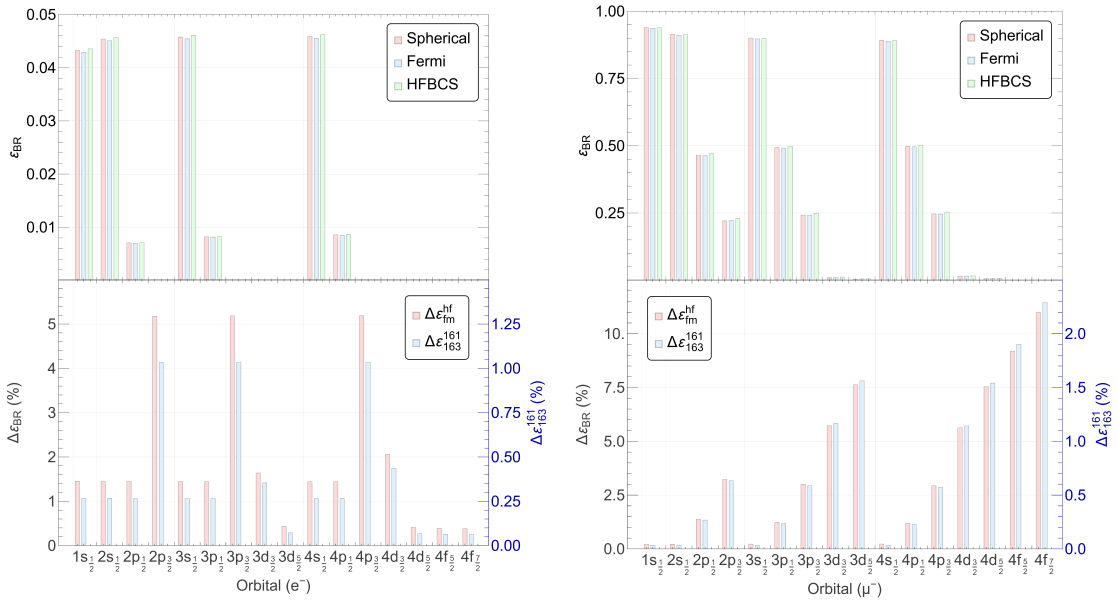


Figure B.3 – Rescaled wavefunctions of the electronic and muonic hydrogen-like ^{161}Dy. The rescaled large ($P_{n\kappa}$, left panels) and small components ($Q_{n\kappa}$, right panels) of the radial wave functions for the $1s_{1/2}$ (upper panels) and $2p_{1/2}$ (lower panels) orbitals of $^{161}Dy^{65+}$ are shown in atomic units. The figures show the comparison between the electronic (blue) and muonic (red) states for point (dashed lines) and HFBCS (solid lines) models. The results for the electron are rescaled using the Bohr radius for the muon ($a_0 = 1/207$ a.u). The vertical lines indicate the position of the nuclear radius R_N. For the point model, we note that $a_0^{-3/2} P_{\mathrm{pt}}^{(e)}(a_0^{-1} r)$ and $P_{\mathrm{pt}}^{(\mu)}(r)$ are identical. The same is true for $a_0^{-3/2} Q_{\mathrm{pt}}^{(e)}(a_0^{-1} r)$ and $Q_{\mathrm{pt}}^{(\mu)}(r)$.



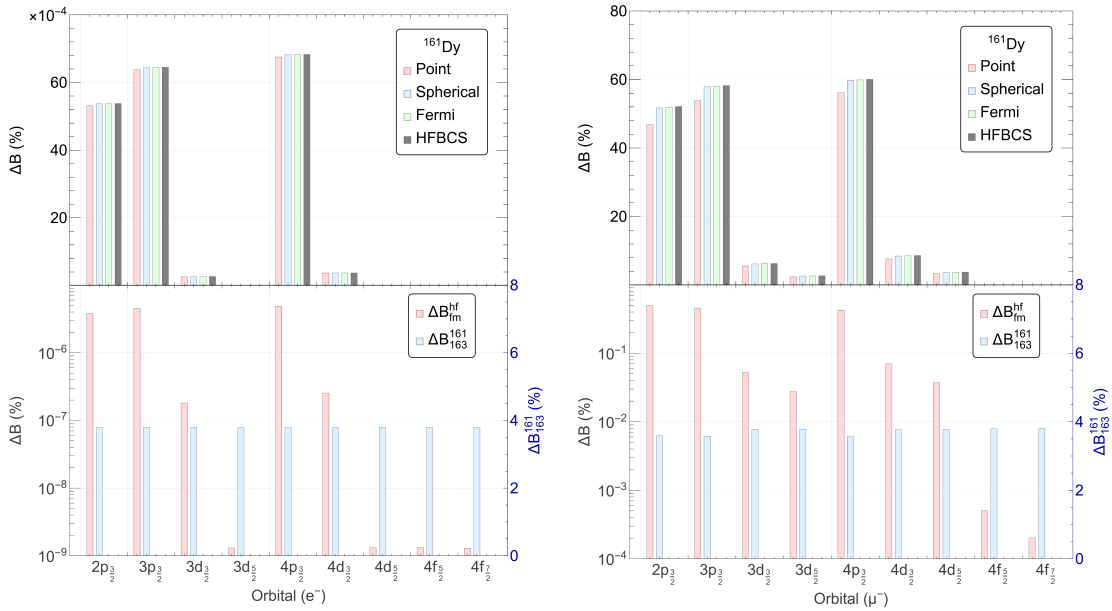
(a) Electronic **(b)** Muonic

Figure B.4 – Monopolar shifts in the energy levels of orbitals of ^{161}Dy^{65+}. Shown are the relative shifts in energy of the (a) electronic and (b) muonic states from $1s_{1/2}$ to $4f_{7/2}$ for different nuclear models: point (pt), spherical (sp), Fermi (fm) and HFBCS (hf). We have defined, $\Delta E^{m_2}_{m_1,i} \equiv \frac{E^{m_2}_i - E^{m_1}_i}{E^{m_1}_i}$ with $m_2 = sp, fm, hf$ and $m_1 = pt, fm$ and $\Delta E^{163}_{161,i} \equiv \frac{E^{163}_i - E^{161}_i}{E^{161}_i}$ with i running from $1s_{1/2}$ to $4f_{7/2}$.



(a) Electronic **(b)** Muonic

Figure B.5 – Breit-Rosenthal correction ε_{BR} for ^{161}Dy^{65+}. Shown are the BR effects for the (a) electronic and (b) muonic states for the different nuclear models: spherical, Fermi and HFBCS. We have defined $\Delta\varepsilon^{hf}_{fm} \equiv \frac{\varepsilon^{hf}_{BR} - \varepsilon^{fm}_{BR}}{\varepsilon^{fm}_{BR}}$ (left axis) and $\Delta\varepsilon^{163}_{161} \equiv \frac{\varepsilon^{hf}_{BR}(163) - \varepsilon^{hf}_{BR}(161)}{\varepsilon^{hf}_{BR}(161)}$ (right axis).



(a) Electronic **(b)** Muonic

Figure B.6 – Quadrupole corrections for $^{161}Dy^{65+}$. The relative shifts in the quadrupole moment of the (a) electronic and (b) muonic states from $1s_{1/2}$ to $4f_{7/2}$ for different nuclear models: point (pt), spherical (sp), Fermi (fm) and HFBCS (hf). We have defined (upper panels) $\Delta B^{\mathrm{m}} \equiv \frac{b^{\mathrm{pt}}_{\mathrm{np}} - b^{\mathrm{m}}_{\mathrm{wp}}}{b^{\mathrm{pt}}_{\mathrm{np}}}$ with $\mathrm{m} \in \{\mathrm{pt}, \mathrm{sp}, \mathrm{fm}, \mathrm{hf}\}$. The lower indices np and wp represent no penetration and with penetration respectively (see text for explanation). In the lower panels, the two quantities are depicted $\Delta B \equiv \frac{b^{\mathrm{fm}}_{\mathrm{wp}} - b^{\mathrm{hf}}_{\mathrm{wp}}}{B^{\mathrm{fm}}_{\mathrm{wp}}}$ for $^{163}Dy^{65+}$ (in red and reading on the left axis) and $\Delta B^{163}_{161} \equiv \frac{b^{\mathrm{hf}}_{\mathrm{wp}}(163) - b^{\mathrm{hf}}_{\mathrm{wp}}(161)}{b^{\mathrm{hf}}_{\mathrm{wp}}(161)}$ (in blue and reading on the right axis).

APPENDIX C

APPENDICES TO CHAPTER 4

C.1 Published Article

npj | quantum information

Article

Published in partnership with The University of New South Wales

https://doi.org/10.1038/s41534-024-00829-6

Noisy qudit vs multiple qubits: conditions on gate efficiency for enhancing fidelity

Check for updates

Denis Janković [1,2] ✉, Jean-Gabriel Hartmann [1], Mario Ruben [2,3,4] & Paul-Antoine Hervieux[1]

As qubit-based platforms face near-term technical challenges in terms of scalability, qudits, d-level bases of quantum information, are being implemented in multiple platforms as an alternative for Quantum Information Processing (QIP). We compare the infidelity scalings of single qudit and multiqubit systems within identical Hilbert space dimensions and noisy environments in the Lindblad formalism. We find them to be gate-independent to first-order and present an analytically-derived critical curve $(d^2-1)/3\log_2(d)$ that benchmarks the operational time efficiency of qudits and qubits relative to their decoherence times. This comparison reveals conditions under which qudits offer competitive gate efficiencies compared to leading qubit platforms. Our findings, supported by numerical simulations testing the applicability and limits of the linear response formalism, highlight the relevance of qudits in near-term QIP. This provides a benchmark for evaluating qudit platforms, specifically those with lower dimensionality, in terms of their operational efficiency relative to the qubit state-of-the-art.

The paradigmatic bases of information in Quantum Information Processing (QIP) are qubits: two-level individually addressable quantum systems. However, several QIP platforms have recently been proposed that instead make use of d-level systems, referred to as qudits[1–6]. In its infancy, classical computing did experiment with ternary, quaternary, or higher-dimensional, bases of information, before eventually settling on the simplest (bits), when near-zero error rates and easy scalability were attained[7]. Analogously, it could be argued that quantum computing is likely to follow a similar trend in the long-term; as fault-tolerant platforms emerge and technologies mature, the industry could indeed fully settle on multiqubit systems. However, QIP research is currently not in the noise-free regime but near it, and in order to reach significant quantum supremacy[8], increasing the total Hilbert space dimension of the physical platform is a primordial requirement. As such, there is a current race to increase the number n of coupled qubits ($d=2$) with superconducting platforms leading the way with $n=51$[9] or $n=433$[10]. While in general the Hilbert space dimension increases exponentially in the number of sites, the relatively slow 2^n scaling of qubits, compared to d^n for qudits, is proving challenging, necessitating ever-more robust systems and complex control mechanisms.

Given these current technical challenges, most qudit-based platforms that have been physically implemented argue for near-term advantages over equivalent multiqubit implementations. Thus, the principal motivations of qudit platforms over qubits include: (i) the underlying physical systems having lower decoherence rates[11], (ii) using the redundancy in additional levels for quantum error correction[12,13], (iii) the higher density of information per physical system (site)[14], (iv) the reduced number of nonlocal, hence more decoherence-sensitive, operations[15] or (v) more robust flying quantum memories[16,17]. Furthermore, qudits present fundamental theoretical advantages, enabling QIP capabilities offered by $\bigotimes SU(d)$ vs. $\bigotimes SU(2)$ of qubits[18] such as simplifying some quantum algorithms[19], and therefore a fault-tolerant qudit quantum computer indeed remains conceivable. Hence, qudits provide an alternative scaling solution by linearly increasing d, instead of scaling up n, the number of sites, as well as increasing efficiency through single qudit gates operating on larger computational subspaces[4,9,20,21]. However, one of the disadvantages raised for qudits is the larger number of error channels compared to multiple qubits[22]. In this context, a study of the near-term viability of qudits is needed to investigate the interplay between computational efficiency and noise error rates in higher dimensions.

In this work, we consider one single qudit versus multiqubit systems, in the context of near noise-free implementations. We undertake an inquiry to determine under what conditions on the applied gates a single qudit system does not lose more computational information than an equivalent multiqubit system, even when the qudit system initially presents more potential error channels. For this purpose, a standard measure to quantify the loss of computational information, that we study, is the Average Gate Infidelities (AGI), as defined by Nielsen[23] where the average is over the Haar measure.

[1]Institut de Physique et Chimie des Matériaux de Strasbourg (IPCMS), UMR 7504, Université de Strasbourg, CNRS, 23, Rue du Loess, 67000 Strasbourg, France. [2]Institute of Nanotechnology (INT), Karlsruhe Institute of Technology, P.O. Box 3640, 76021 Karlsruhe, Germany. [3]Institute for Quantum Materials and Technologies (IQMT), Karlsruhe Institute of Technology, P.O. Box 3640, 76021 Karlsruhe, Germany. [4]Centre Européen de Sciences Quantiques (CESQ), Institut de Science et d'Ingénierie Supramoléculaires (ISIS), Université de Strasbourg, 8, Allée Gaspard Monge, 67000 Strasbourg, France. ✉e-mail: denis.jankovic@ipcms.unistra.fr

https://doi.org/10.1038/s41534-024-00829-6 **Article**

The choice of the AGI ensures the calculated fidelity is not dependent on the input state and therefore remains relevant even if the gate is applied in later stages of a quantum algorithm. We conduct an in-depth analysis in which we compare the computational fidelity of a single qudit and n-qubit systems, both with identical dimensions of Hilbert space, undergoing arbitrary unitary transformations, and evolving under the influence of comparable noisy conditions. Our benchmark for successful analysis is defined by a lower first-order response of the AGI to the environmental noise, providing a measure of computational fidelity independent of initial states. We investigate, for increasing values of d, the respective growth rates of the AGIs with respect to error rates γ and dimensionless gate time γt. The latter quantifies the gate efficiency by indicating how time-efficient operations on these systems are relative to decoherence timescales, therefore this paper presents a study of the first-order connection between the AGI and this time-efficiency γt.

In other words, this study aims to investigate how the AGI scales proportionally with both the error rate and the speed at which gate operations are performed, as well as the dimension d of the qudit. Additionally, this study aims to provide a benchmarking tool to decide if a qudit platform, for a given (γ,t,d) specification, can compensate for its greater number of error channels by leveraging advantageous decoherence times and gate speeds. Both of those quantities depend intrinsically on the physical platform implementing the single qudit or multiqubit system, in particular their coupling to the environment, the mathematical form of the control pulses' Hamiltonian, and the addressing speed. In particular, given a single qudit platform and a multiqubit platform with equivalent Hilbert space dimensionality, and specifying a fixed pair of parameters (γ,t), one could conduct a comparative analysis to determine if the qudit platform exhibits sufficiently low decoherence and sufficiently rapid gate time to achieve computational fidelities that are competitive with the multiqubit platform. Or, similarly, since increasing d on a single site in a given qudit platform is a prevailing goal for some platforms[14], assuming γt remains of the same order of magnitude, this study would also allow setting theoretical upper limits on the value of d in order to remain advantageous.

In the first part, a gate-independent formula is presented for the first-order response in γt of the AGI to Markovian noise in the Lindblad formalism. The first-order formalism corresponds to the quasi-errorless regime of near-term QIP systems. Expressions for the linear dependency of the AGI on γt for a single qudit, multiqubits and also multiqudits are derived for an arbitrary collapse operator. A comparison is then made between the rate of increase of the AGI of a single qudit vs. equivalent multiple qubits.

This is then followed by numerical simulations, performed with the `Python` package `QuTiP`[24], that complement and illustrate the analytical results. Discussions of the applicability and limits of the linear response formalism for AGI are given and the following aspects are studied: (i) the applicable range of γt and its dependency on the dimension of the qudit; (ii) the extent of the gate-independence of the result; (iii) the applicability to noise models other than pure dephasing; and finally (iv) the conditions on gate times for which either qudits or multiple qubits are advantageous. This latter aspect is then examined in more detail with respect to existing platforms by taking into account their respective decoherence rate and gate operation time.

Results and Discussion

Fluctuation-dissipation relation for a perturbed pure state

Consider a qudit, a d-level quantum system whose dynamics are governed by the Lindblad master equation[25]:

$$\frac{\mathrm{d}\rho}{\mathrm{d}t} = -\mathrm{i}\big[H,\rho\big] + \sum_{k=1}^{K}\gamma_k\left(L_k\rho L_k^\dagger - \frac{1}{2}\left\{L_k^\dagger L_k,\rho\right\}\right), \tag{1}$$

where $\rho(t)$ is the density matrix of the system at time t, H the Hamiltonian of the system, L_k the so-called collapse operators characterizing the Markovian noise, and γ_k the decay parameters for each of the K noise processes. $H = H_0 + H_c(t)$ where H_0 models the free evolution of the physical system and encompassing its internal interactions, and $H_c(t)$ is a time-dependent pulse Hamiltonian allowing the controlled evolution. Moreover, the interactions of H with the collapse operators determine relevant timescales such as the gate-time t and the decoherence time T_2 that are thus inherent to the physical realization under consideration.

The aim is to study the effect of a single collapse operator $\sqrt{\gamma_1}L_1 = \sqrt{\gamma}L$ on short timescales and under small-amplitude noise, i.e., $\gamma t \ll 1$. Under these assumptions, one can consider an *ansatz* of the form:

$$\rho(t) = \rho^* - \gamma t M + \mathcal{O}((\gamma t)^2), \tag{2}$$

with ρ^* the noiseless target state, which is the solution of $\dot{\rho} = -\mathrm{i}\big[H,\rho\big]$ after time t, and M the perturbation matrix resulting from the presence of a small-amplitude noise. Terms in $\mathcal{O}((\gamma t)^2)$ include terms whose prefactor is of the form $\left(\gamma^l t^k\right)_{l+k\geq 3}$, a more in-depth discussion is available in Supplementary Notes 2b.

One can easily see that the use of (2) in (1) leads to

$$M = \frac{1}{2}\left\{L^\dagger L,\rho^*\right\} - L\rho^* L^\dagger. \tag{3}$$

Consider now a quantum operation bringing the initial state ρ_0 to a final state $\rho(t)$ at time t. One define the fidelity $\mathcal{F}$ of this final state relative to some target state ρ^*[26] as

$$\mathcal{F}(\rho(t),\rho^*) \equiv \left[\mathrm{Tr}\left(\sqrt{\sqrt{\rho(t)}\rho^*\sqrt{\rho(t)}}\right)\right]^2. \tag{4}$$

Subsequently, the infidelity, is then defined as

$$\mathscr{E} \equiv 1 - \mathcal{F}. \tag{5}$$

Since ρ^* is a pure state ($\rho^* = |\varphi^*\rangle\langle\varphi^*|$) Eq. (4) simplifies to[26]

$$\mathcal{F}(\rho(t),\rho^*) = \mathrm{Tr}\big(\rho(t)\rho^*\big). \tag{6}$$

Finally, substituting Eq. (2) into Eq. (6) leads to (see Supplementary Notes 1a)

$$\mathscr{E}(\rho^*) = \gamma t\Delta_* L + \mathcal{O}((\gamma t)^2). \tag{7}$$

where $\Delta_* L = \langle L^\dagger L\rangle_* - \langle L^\dagger\rangle_*\langle L\rangle_*$ with $\langle L^\dagger L\rangle_* \equiv \mathrm{Tr}\big(\rho^* L^\dagger L\big)$.

Average Gate Fidelity of a single qudit

Only $\mathscr{E}(\rho^*)$ for a specific ρ^* was obtained in the previous subsection. However, is there a state-independent approach to obtaining the infidelity of a quantum gate under small-amplitude noise? One defines the quantum gate U applied during a time duration t, whose resulting operation brings all initial states ρ_0 to all corresponding $\rho^* = U\rho_0 U^\dagger$. There is then a definition of the average gate fidelity of a quantum channel $\mathcal{E}$, attempting to carry the unitary operation U despite a noisy environment, which reads as follows[23]

$$\begin{aligned}\bar{\mathcal{F}}(\mathcal{E},U) &= \int d\rho_0\,\mathcal{F}(\rho(t),\rho^*)\\ &= \int d\rho_0\,\langle U^\dagger\mathcal{E}[\rho_0]U\rangle_0 = \int d\rho_0\left\langle\left(\mathcal{U}^\dagger\circ\mathcal{E}\right)[\rho_0]\right\rangle_0,\end{aligned} \tag{8}$$

where the normalized integral is over the Fubini-Study measure on pure states (sometimes called the Haar measure)[27], $\mathcal{U}^\dagger[\rho] \equiv U^\dagger\rho U$ and $\mathcal{E}[\rho_0] = \rho(t)$.

Introducting $\tilde{E}_k = E_k U$ the Kraus operators such that

$$\rho(t) = \left(\mathcal{U}^\dagger\circ\mathcal{E}\right)[\rho_0] = \sum_k \tilde{E}_k\rho_0\tilde{E}_k^\dagger = \sum_k E_k\rho^* E_k^\dagger, \tag{9}$$

https://doi.org/10.1038/s41534-024-00829-6

the Average Gate Fidelity $\bar{\mathcal{F}}$ given in (8) can be rewritten as[28]

$$\bar{\mathcal{F}}(\mathcal{E},U)=\frac{d+\sum_k|\mathrm{Tr}(\tilde{E}_kU^\dagger)|^2}{d(d+1)}=\frac{d+\sum_k|\mathrm{Tr}(E_k)|^2}{d(d+1)}\,. \tag{10}$$

Using Eq. (3), one seeks the sets of Kraus operators $\{\tilde{E}_k\}$ or $\{E_k\}$ such that, to $\mathcal{O}((\gamma t)^2)$, $\forall\,\rho_0,\rho^*$,

$$\begin{aligned}\sum_k\tilde{E}_k\rho_0\tilde{E}_k^\dagger &= U\rho_0U^\dagger-\gamma t\tfrac{1}{2}\{L^\dagger L,U\rho_0U^\dagger\}+\gamma tLU\rho_0U^\dagger L^\dagger\\ \sum_k E_k\rho^*E_k^\dagger &= \rho^*-\gamma t\tfrac{1}{2}\{L^\dagger L,\rho^*\}+\gamma tL\rho^*L^\dagger.\end{aligned} \tag{11}$$

One can see that the following two sets would work up to the first order in γt

$$\begin{aligned}\tilde{E}_0&=(\mathbb{1}_d-\tfrac{\gamma t}{2}L^\dagger L)U,\quad \tilde{E}_1=\sqrt{\gamma t}LU,\\ E_0&=\mathbb{1}_d-\tfrac{\gamma t}{2}L^\dagger L,\qquad E_1=\sqrt{\gamma t}L.\end{aligned} \tag{12}$$

In order to use Eq. (12) in Eq. (8), it is necessary to calculate the traces of the operators. Let us consider a pure dephasing channel of a qudit coupled to a thermal environment through the operator J_z (In general the coupling of a qudit, or qubit, to a thermal environment can be represented by a linear combination, or mixture, of collapse operators, though a pure dephasing channel will typically be present and can be represented by the operator J_z. As a toy model, let us consider a coupling term dominated by a pure dephasing channel.) i.e. $\mathcal{E}_z$ with $L=J_z$[29]. One obtains a *gate-* (and Hamiltonian-) independent result for the Average Gate Fidelity which reads as (see Supplementary Notes 1b)

$$\bar{\mathcal{F}}(\mathcal{E}_z)=1-\frac{\gamma t}{12}d(d-1)+\mathcal{O}((\gamma t)^2). \tag{13}$$

In other words the Average Gate Infidelity (AGI) is given by

$$\bar{\mathscr{E}}(\mathcal{E}_z)=\frac{\gamma t}{12}d(d-1)+\mathcal{O}((\gamma t)^2), \tag{14}$$

or more generally for an arbitrary quantum channel $\mathcal{X}$ with collapse operator L

$$\bar{\mathscr{E}}(\mathcal{X})=\frac{\gamma t}{d+1}\left(\mathrm{Tr}(L^\dagger L)-\frac{1}{d}|\mathrm{Tr}(L)|^2\right)+\mathcal{O}((\gamma t)^2). \tag{15}$$

Note that it is always possible to find a traceless collapse operator L emulating $\mathcal{X}$[25], so the previous expression can be, in this case, simplified as follows

$$\bar{\mathscr{E}}(\mathcal{X})=\frac{\gamma t}{d+1}\mathrm{Tr}(L^\dagger L)+\mathcal{O}((\gamma t)^2). \tag{16}$$

It follows from (16) that, if L were independent of d, increasing the dimension d of the Hilbert space would also increase the *robustness* of qudit gates to a dimension-independent quantum channel.

AGI of qudits vs. qubits

Now let us apply the same technique as described above to another system: an ensemble of n identical dephasing qubits (Hilbert space of dimension $d=2^n$). In order to compare it with the qudit analysis in the previous subsection, each individual qubit decoheres with the same rate (has the same type, and strength, of environmental coupling) through its spin operator S_z in the same way as the individual qudit (with $d=2$). Considering any additional coupling mechanism to the environment arising from inter-qubit interactions would only further disadvantage the multi-qubit implementation. Our considerations then provide a best-case scenario for comparable qubits. This yields the master equation

$$\frac{\mathrm{d}\rho}{\mathrm{d}t}=-\mathrm{i}[H,\rho]+\sum_{k=1}^n L_k\rho L_k^\dagger-\frac{1}{2}\sum_{k=1}^n\left\{L_k^\dagger L_k,\rho\right\}, \tag{17}$$

with

$$L_k=\underbrace{\mathbb{1}_2^{(1)}\otimes\cdots\otimes\mathbb{1}_2^{(k-1)}}_{k-1}\otimes S_z^{(k)}\otimes\underbrace{\mathbb{1}_2^{(k+1)}\otimes\cdots\otimes\mathbb{1}_2^{(n)}}_{n-k} \tag{18}$$

for $k\in[\![1,n]\!]$.

Using the same reasoning as for dephasing qudits one obtains $n+1$ Kraus operators to first order in γt

$$E_0=\mathbb{1}_{2^n}-\sum_{k=1}^n\frac{\gamma t}{2}L_k^\dagger L_k,\quad E_k=\sqrt{\gamma t}L_k. \tag{19}$$

In this case (see Supplementary Notes 1c),

$$\bar{\mathscr{E}}(\mathcal{E}_z)=\frac{\gamma t}{4}\frac{n2^n}{2^n+1}+\mathcal{O}((\gamma t)^2)=\frac{\gamma t}{4}\frac{\log_2(d)d}{d+1}+\mathcal{O}((\gamma t)^2)\,. \tag{20}$$

Let us stress that (20) yields the same result as Abad et al.[30] in the case of identically dephasing qubits with no energy relaxation.

The analytical expressions (16) and (20) are one of the main results of this work.

Following those last two results, two expressions for the AGI have been found: for a single qudit, one finds an infidelity that scales as d^2: $\bar{\mathscr{E}}_d(\mathcal{E}_z)=c_d\gamma t$ in (14) and for an ensemble of n qubits one finds an infidelity that scales as $\log_2(d)$: $\bar{\mathscr{E}}_{\mathrm{b},n}(\mathcal{E}_z)=c_{\mathrm{b},n}\gamma t$ in (20). Moreover, in the case of pure dephasing, one can define the $T_{2,d}$ dephasing time between two energy-adjacent levels for a qudit. It then shares the same expression (in terms of γ) as the typical $T_{2,\mathrm{b}}$ dephasing time of a single qubit, namely $\frac{1}{T_2}=\frac{\gamma}{2}$.

The ratio between two average gate infidelities, of duration t_d and $t_{\mathrm{b},n}$ for qudit and n qubits, respectively, becomes

$$\frac{\bar{\mathscr{E}}_d(\mathcal{E}_z)}{\bar{\mathscr{E}}_{\mathrm{b},n}(\mathcal{E}_z)}=\frac{c_dt_d/T_{2,d}}{c_{\mathrm{b},n}t_{\mathrm{b},n}/T_{2,\mathrm{b}}}. \tag{21}$$

Therefore, in order for a *single* qudit ($d=2^n$) to outperform *an ensemble* of n qubits in noise-robustness, i.e., to have a smaller AGI, the following inequality must hold true

$$\frac{t_{\mathrm{b},n}/T_{2,\mathrm{b}}}{t_d/T_{2,d}}>\frac{c_d}{c_{\mathrm{b},n}}=\frac{d^2-1}{3\log_2(d)}=\frac{4^n-1}{3n}. \tag{22}$$

This expression quantifies the requirements on the figure of merit which is the gate time in units of decoherence time $\tau_d=t_d/T_{2,d}$ relative to $\tau_{\mathrm{b},n}=t_{\mathrm{b},n}/T_{2,\mathrm{b}}$ in order for the qudit to yield higher-fidelity gates. Moreover, it confirms that the infidelity of an ensemble of n identical qubits and the infidelity of a single qudit will generally not have the same linear behaviour in γt even if they have the same T_2, thus simply having $\tau_d<\tau_{\mathrm{b},n}$ is not sufficient to guarantee a more noise-resilient qudit. Moreover, Eq. (22) provides a more precise condition on the ratio of figure of merits than a simple qualitative result such as $\frac{d^2}{\log_2(d)}$, while maintaining the expected $O(d^2/\log_2(d))$ behaviour as $d\to\infty$. In particular, see Supplementary Notes 1b for the full analytical calculations, including the derivation of the non-trivial factor $\frac{1}{3}$.

On a side note, the previous calculations could also be applied to an ensemble of N qudits under identical pure dephasing, in which case we have

$$\bar{\mathscr{E}}_{d,N}(\mathcal{E}_z)=\frac{\gamma t}{12}\frac{Nd^N}{d^N+1}(d^2-1)+\mathcal{O}((\gamma t)^2), \tag{23}$$

https://doi.org/10.1038/s41534-024-00829-6 **Article**

and for $2^n = d^N$ one obtains

$$\frac{t_{\mathrm{b},n}/T_{2,\mathrm{b}}}{t_{d,N}/T_{2,d}} > \frac{c_{d,N}}{c_{\mathrm{b},n}} = \frac{d^2-1}{3\log_2(d)}. \tag{24}$$

Let us also note that for L arbitrary (23) yields

$$\overline{\mathscr{E}_{d,N}}(\mathcal{X}) = \gamma t N \frac{d^{N-1}}{d^N+1}\left(\mathrm{Tr}(L^\dagger L) - \frac{1}{d}|\mathrm{Tr}(L)|^2\right) + \mathcal{O}((\gamma t)^2). \tag{25}$$

This equation encompasses both scenarios under investigation in this paper until this point. We recall that we construct two systems of equivalent Hilbert Space dimension: a single qudit of dimension d and a system of N qubits. (25) reflects two different scalings of the AGI in N and d respectively. In N, it is linear, and, in d, it scales as $\left(\mathrm{Tr}(L^\dagger L) - \frac{1}{d}|\mathrm{Tr}(L)|^2\right)$ since the dimension affects the definition of L. In Supplementary Notes 1b we computed that spin-based L lead to a quadratic scaling in d. Therefore, in the qudit subsection, for a single qudit, we study this quantity for fixed $N = 1$ and varying d, while in the multiqubits subsection, it is for fixed $d = 2$, but varying N. The subtlety in the latter case being that, by construction $N := \log_2(d)$, with d being that of the single qudit, hence the different scalings in d in (14) and (20). See Fig. 1 for a visual summary of the results.

And if each qudit k has a different set of noise parameters (γ_k, L_k), an even more general formula arises :

$$\overline{\mathscr{E}_{d,N}}(\mathcal{X}) = \frac{d^{N-1}}{d^N+1}\sum_{k=1}^{N}\gamma_k t\left(\mathrm{Tr}(L_k^\dagger L_k) - \frac{1}{d}|\mathrm{Tr}(L_k)|^2\right) + \mathcal{O}((\gamma_k t)^2). \tag{26}$$

This formula through its general form, can be applied to any qudits whose physical implementation implies different collapse operators from the ones considered in this paper.

Process fidelity & averaged fluctuation-dissipation relation

One may link the fluctuation-dissipation relation obtained in (7) with the results regarding average gate infidelities from Eq. (15),

$$\overline{\mathscr{E}}(\mathcal{X}) = \gamma t \int d\rho^* \mathscr{E}(\rho^*) = \gamma t \int d\rho^* \Delta_* L + \mathcal{O}((\gamma t)^2). \tag{27}$$

This integral over the Fubini-Study measure can formally be computed using Weingarten calculus methods[31] (see Supplementary Notes 1d) which can be expressed as

$$\int d\rho \Delta L = \frac{1}{d+1}\mathrm{Tr}(L^\dagger L) - \frac{1}{d(d+1)}|\mathrm{Tr}(L)|^2, \tag{28}$$

leading to (15).

In contrast to this formal approach, a more physically-informed approach to obtain the same result was proposed in the previous subsections.

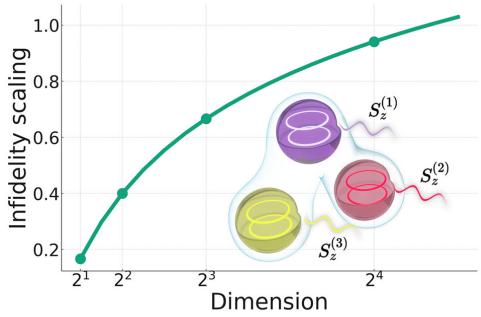
Furthermore, it is possible to express all the computed average gate infidelities as process/entanglement infidelities $\mathscr{E}^{(\mathrm{p})}$ making use of the relation $D\mathscr{E}^{(\mathrm{p})} = (D+1)\overline{\mathscr{E}}$, with $D = d$, 2^n or d^N, the dimension of the Hilbert space[32]. This yields the expression

$$\mathscr{E}^{(\mathrm{p})}_{d,n}(\mathcal{X}) = \gamma t \frac{n}{d}\left(\mathrm{Tr}(L^\dagger L) - \frac{1}{d}|\mathrm{Tr}(L)|^2\right) + \mathcal{O}((\gamma t)^2), \tag{29}$$

which is linear in the number of subsystems n. Likewise we have

$$\mathscr{E}^{(\mathrm{p})}_{d}(\mathcal{E}_z) = \frac{\gamma t}{12}(d^2-1) + \mathcal{O}((\gamma t)^2), \tag{30}$$

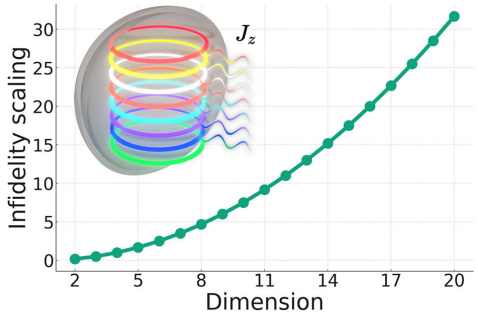
$$\mathscr{E}^{(\mathrm{p})}_{\mathrm{b},n}(\mathcal{E}_z) = \frac{\gamma t}{4} n + \mathcal{O}((\gamma t)^2). \tag{31}$$



$$L_1 = S_z^{(1)} \otimes \begin{pmatrix} 1 & 0 \\ 0 & 1 \end{pmatrix} \otimes \begin{pmatrix} 1 & 0 \\ 0 & 1 \end{pmatrix}$$

$$L_2 = \begin{pmatrix} 1 & 0 \\ 0 & 1 \end{pmatrix} \otimes S_z^{(2)} \otimes \begin{pmatrix} 1 & 0 \\ 0 & 1 \end{pmatrix}$$

$$L_3 = \begin{pmatrix} 1 & 0 \\ 0 & 1 \end{pmatrix} \otimes \begin{pmatrix} 1 & 0 \\ 0 & 1 \end{pmatrix} \otimes S_z^{(3)}$$



$$L = J_z = \begin{pmatrix} \frac{d-1}{2} & \cdots & 0 \\ 0 & \ddots & 0 \\ 0 & \cdots & -\frac{d-1}{2} \end{pmatrix}$$

Fig. 1 | Visual synthesis of the infidelity scaling in multiple qubits and a single qudit. Summary diagram illustrating the selected collapse operators and the associated analytically derived expected infidelity scalings as functions of the Hilbert Space dimension, as derived from (20) and (14). This is depicted for two distinct systems: multiple qubits (left) and a single qudit (right). The term 'infidelity scaling' here refers to the slopes of the first-order-in-γt AGIs, denoted as c in (21).

https://doi.org/10.1038/s41534-024-00829-6 **Article**

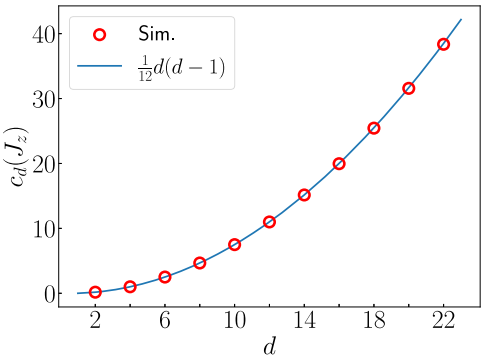


Fig. 2 | Rate of increase of $\overline{\delta_d}(\mathcal{E}_z) = c_d(J_z)\gamma t$ as a function of qudit dimension. The data shown was generated for $H = \mathbb{0}_d$ and $\gamma t \in [0, 10^{-4}]$. The circled dots show the numerical results. The solid curve presents the expected analytical result given by (14).

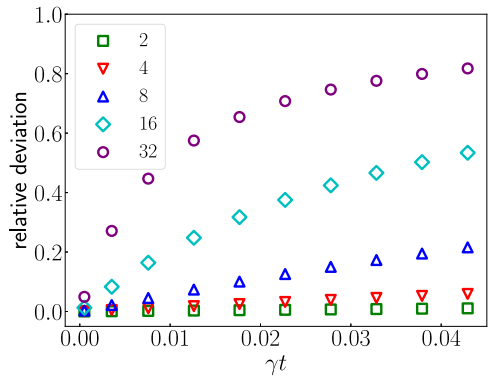


Fig. 4 | Relative deviation $1 - \frac{\overline{\delta_d}^{\text{sim}}}{\overline{\delta_d}^{\text{th}}}$ as a function of γt for $H = \mathbb{0}_d$. The quantities $\overline{\delta_d}^{\text{sim}}$ and $\overline{\delta_d}^{\text{th}}$ were obtained from numerical computations and (14) respectively. Each marker corresponds to a different value of d.

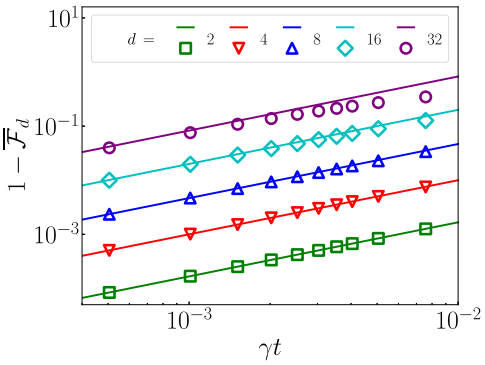


Fig. 3 | Average gate infidelities as a function of γt for $H = \mathbb{0}_d$. The data points show the computed values. The solid lines represent the linear theoretical behaviour from (13). Each colour/marker pair corresponds to a different value of d.

Note that (31) has been verified experimentally, for example by Ozaeta and McMahon[33].

Fit and deviation from the linear behaviour

Using the procedures described in the Methods section, we simulated single qudits of dimension d under pure dephasing, with $H = \mathbb{0}_d$ and small $\gamma t \in [0, 10^{-4}]$ ($\gamma \sim 10^{-4}$ in some nuclear spins in molecular magnets such as in the experiments of Godfrin et al.[20]). For example, the simulations were performed for even dimensions $d \in [\![2, 22]\!]$. Fitting the AGIs $\overline{\delta_d}(\mathcal{E}_z) = c_d\gamma t$ as a function of γt yielded the slopes c_d that are shown in Fig. 2, along with their analytical expression as a function of d predicted in (14).

The same simulations were repeated for larger values of $\gamma t \in [5 \times 10^{-4}, 1 \times 10^{-2}]$ and $H = \mathbb{0}_d$. The AGIs were then computed and are shown in Fig. 3 alongside the linear infidelity predicted in (14).

For more insight, Fig. 4 shows the relative deviation of the computed infidelities from the expected first-order linear behaviour for a broader range of γt up to 5×10^{-2}.

Average gate infidelities linear in γt with gradients $\frac{d(d-1)}{12}$ were expected in the case of a single qudit under pure dephasing, according to (14). Figure 2 supports this for small values of γt: a least-squares fit of the computed gradients yields the expected relationship with $1 - R^2 < 10^{-5}$. Simulations for larger values of γt (Fig. 3) highlight deviations from this linear behaviour. These originate from $\mathcal{O}((\gamma t)^2)$ terms of the form $(\gamma t)^{k>1}$ (see Supplementary Notes 2b). Moreover, for fixed values of γt, as d increases, the amplitude of this deviation is observed to increase (Fig. 4). This implies that the range of γt values for which the AGI can be treated linearly diminishes with increasing qudit dimension. Assuming a prefactor of the order d^4 for the $(\gamma t)^2$ term in the AGI series expansion (as Supplementary Notes 2b hints), this provides an estimate of the range for which the deviation from linearity is negligible: $\gamma t \ll 1$ and $\frac{1}{d^2}$.

Gate dependence

While the linearity of the AGI does not scale well with d, Eq. (14) has another important characteristic that deserves to be studied: the gate independence of the AGI. This was investigated over a large number of random gates for a given dimension d. Random unitary quantum gates in $U(d)$ were sampled from the circular unitary ensemble, which represents a uniform distribution over the unitary square matrices of dimension d, also known as the Haar measure on the unitary group $U(d)$, and implemented on a qudit through a Hamiltonian obtained by gradient-ascent methods. We decided to model qudits as ladder systems, with one pulse per transition between adjacent levels as considered for example in the experiments of Godfrin et al.[20], for a single-molecule magnet ($TbPc_2$, qudit with $d = 4$), the $d - 1$ pulses are then each represented by a control Hamiltonian in the interaction picture. More details are discussed in the Methods section. There are a large number of parameters that can influence the results under consideration, such as the free-evolution Hamiltonian or the matrix form of the control pulses, both of which are inherent to the physical realization. Therefore other physical implementations and reference frames for the pulses can be considered, and the deviation from linearity they cause needs to be studied in more detail. The AGIs were then computed for $\gamma t \in [10^{-5}, 10^{-3}]$, which lie in the typical ranges observed in current platforms as seen in Table 2, and their rate of increase as a function of γt was fitted. Figure 5 shows the statistical distributions of the relative deviations from the linear behaviour of the obtained rates.

Considering Fig. 5, the relative deviation from the linear behaviour for different random gates seems to exceed 1‰ rarely and was not observed outside the < 1% range. Moreover, the range of deviations decreases as the dimension d increases. The inset highlights a noticeable irregularity for $d = 2$, a single qubit, where the relative deviation is of the order of 1%. Note that for the $H = \mathbb{0}_d$ case simulated in Fig. 2, this shift remained < 1‱, coinciding with the dashed line in Fig. 5, including the case $d = 2$. Beginning at $d = 2$, the gradient distributions appear broad and off-centred from the $H = \mathbb{0}_d$ case. As d increases further, the distributions become progressively concentrated around 0. The gate-dependence also arises from $\mathcal{O}((\gamma t)^2)$

https://doi.org/10.1038/s41534-024-00829-6 **Article**

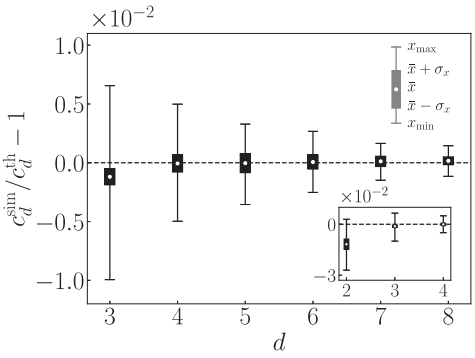


Fig. 5 | Hamiltonian-induced deviation of infidelity gradients from linear behavior. Statistical distributions of the relative deviation from the linear behaviour in (14) of the numerically obtained infidelity gradients c_d for $N_g = 5000$ gates for $\gamma t \in [10^{-5}, 10^{-3}]$, as a function of the dimension $d \in [\![3, 8]\!]$. The candlestick bar chart should be interpreted as indicated in the upper right, with σ denoting the standard deviation, and the error bars denoting the extremal values. The lower right inset shows the same results for $d \in [\![2, 4]\!]$.

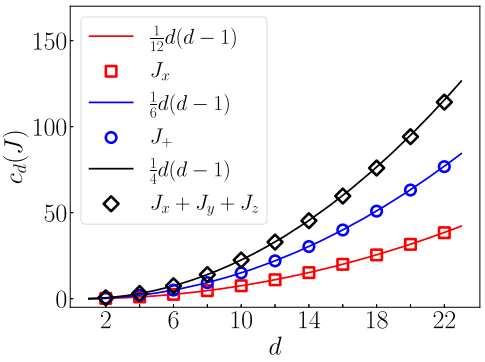


Fig. 6 | Rate of increase of $\overline{\mathscr{E}_d}(\mathcal{X}) = c_d(J)\gamma t$ as a function of qudit dimension. The data shown was generated for $H = \mathbb{0}_d$ and $\gamma t \in [0, 10^{-4}]$. The markers show the numerical results. The solid curves represent the expected linear responses according to (16). Each marker/colour pair corresponds to a different error channel $\mathcal{X}$, with collapse operators J specified in the legend.

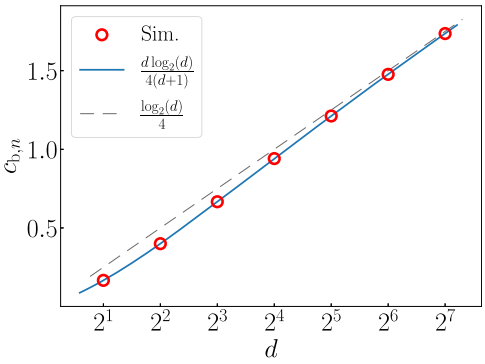


Fig. 7 | Rate of increase of $\overline{\mathscr{E}_{b,n}}(\mathcal{E}_z) = c_{b,n}(\{L_k\})\gamma t$ as a function of Hilbert Space dimension $d = 2^n$. The data shown was generated for $H = \mathbb{0}_{2^n}$ and $\gamma t \in [0, 10^{-4}]$. The $\{L_k\}$ collapse operators are the ones defined in (18). The circled dots show the numerical results. The solid curve presents the expected theoretical result according to (20). The dashed line shows $\mathscr{E}^{(p)}_{b,n}(\mathcal{E}_z)$ given in (31) which is linear in $n = \log_2(d)$.

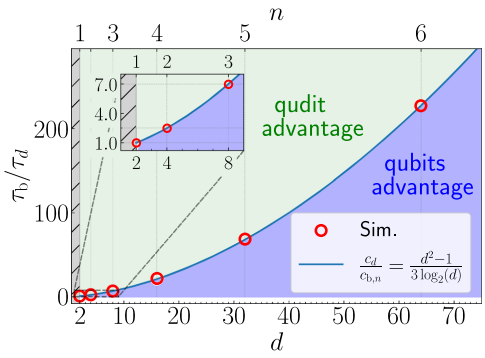


Fig. 8 | Potential range for the ratio of figure of merits τ_b/τ_d. The rounded circles show the numerical values obtained for $c_d/c_{b,n}$. The solid curve comes from (22) and highlights the theoretical critical values of $T_{2,d}/T_{2,b}$.

terms, with γt^2 being dominant in the $\gamma t^2||H|| \gtrsim 1$ regime (see Supplementary Notes 2b). Therefore, the AGI can only be considered gate-independent when $\gamma t \ll 1$ and $\gamma t \ll \frac{1}{||H||}$. An informative figure showing the deviation from linearity and gate-dependence at higher values of γt is available in Supplementary Notes 2a.

Other cases than pure dephasing

Figure 6 shows AGI rates of increase for channels different from pure dephasing namely: $\overline{\mathscr{E}_d}(\mathcal{E}_x)$, $\overline{\mathscr{E}_d}(\mathcal{E}_+)$, and $\overline{\mathscr{E}_d}(\mathcal{E}_{x,y,z})$ corresponding to bit-flip, amplitude damping and depolarizing channels respectively. The simulations were performed again with $H = \mathbb{0}_d$, small $\gamma t \in [0, 10^{-4}]$ and for even dimensions $d \in [\![2, 22]\!]$.

Consider $\mathcal{R}$, the unitary transformation representing a change of basis, such as a 3D real-space rotation. The average gate fidelity defined in (8) is invariant under the transformation $\rho \to \mathcal{R}^\dagger \rho \mathcal{R}$. This is supported by a comparison of the results for $L = J_z$ and $L = J_x$ in Figs. 2 and 6, respectively, since the two gradients appear to share the same dependency in d. Moreover, let $\{l_k\}$ be an ensemble of traceless collapse operators with corresponding error channels $\{e_k\}$, then define $L = \sum_k l_k$ and associated error channel $\mathcal{E}$. From (10) and (12), as long as $\mathrm{Tr}(l_k^\dagger l_j) = 0,\ \forall j \neq k$ then $\overline{\mathscr{E}}(\mathcal{E}) = \sum_k \overline{\mathscr{E}}(e_k)$. Figure 6 again supports such behaviour since simulations with the collapse operator $L = J_+ \equiv J_x + iJ_y$ yield gradients twice as large as, and $L = J_x + J_y + J_z$ yield gradients three times as large as, the $L = J_z$ case.

A single qudit vs an ensemble of qubits

An ensemble of n qubits were simulated under identical pure dephasing, with $H = \mathbb{0}_{2^n}$ and small $\gamma t \in [0, 10^{-4}]$. The simulations were performed for $n \in [\![1, 7]\!]$. Fitting the AGI $\overline{\mathscr{E}_{b,n}}(\mathcal{E}_z) = c_{b,n}\gamma t$ as a function of γt yielded the slopes $c_{b,n}$ that are shown in Fig. 7, along with their analytical expression as a function of d given in (20).

The same simulations were performed on a single qudit with dimension $d = 2^n$ and Fig. 8 shows the ratios $\frac{c_d}{c_{b,n}}$ for $n \in [\![1, 6]\!]$ as well as the theoretical curve provided by Eq. (22) on which the points should be falling. According to the same Eq. (22), this curve also highlights the critical values of τ_b/τ_d, denoting the figure of merit $\tau_k = t_k/T_{2,k} = \gamma_k t_k/2$, with respect to qudit/qubits advantage in terms of the rate of increase of the AGI.

https://doi.org/10.1038/s41534-024-00829-6

The AGI gradients obtained for an ensemble of n qubits under identical pure dephasing were expected to follow a $\frac{d\log_2(d)}{4(d+1)}$ relationship as a function of d(20). Figure 7 justifies this for small values of γt with the least-square fit now yielding $1 - R^2 < 10^{-7}$. Finally, Fig. 8 provides quantitative data for the ratio of the decoherence times of a single qudit vs an ensemble of qubits. Some values of interest are summarised in Table 1. For example, in order for a qu-8-it (qudit with $d = 8$) to present a computational fidelity advantage over 3 qubits for a fixed gate time, the qudit platform needs a coherence time at least 7 times longer than the multiqubit platform. Note that an intuitive scaling such as $\frac{d^2}{\log_2(d)}$ would indicate a much more demanding constraint of 21.5.

From Table 2, state-of-the-art single qudit platforms, such as trapped ions[4], present coherence times of the order of 100 ms for a single qu-7-it, orders of magnitude longer than superconducting qubits[33–36]. Trapped ions present $\gamma t \approx 10^{-3}$, while $\gamma t \approx 10^{-2}$ for superconducting qubits; this ratio of 10 would allow qudits with $d \lesssim 10$ to still be advantageous i.e., according to (22), the single qu-7-it would still maintain a higher average gate fidelity over one gate acting on the whole Hilbert Space than the multiqubit platform. Another comparison with superconducting qubits could be molecular nuclear spin qudits, where some proposals put $\gamma t \approx 10^{-4}$ (see Moreno-Pineda et al.[1]), and whose coherence times are $\sim 6 - 7$ times larger than the superconducting qubit case. With figure of merits $\tau \sim 100$ larger than superconduction platforms, single molecular nuclear spin qudits with $d \lesssim 40$ are still advantageous over equivalent superconducting qubits, i.e. $n \sim 5$. Such high-d qudit platforms can still be conceivable, given that some specific quantum operations on $d = 52$ have already successfully been implemented on, for example, Rydberg atoms[37]. However, it remains to be seen if universal quantum gate generation will become easily achievable in practice with such high d.

Finally, one can compare (22) and (24) to discuss conditions on N qudits outperforming $N\log_2(d)$ qubits. From this, if a single qudit outperforms $\log_2(d)$ qubits, the advantage remains conserved as long as the multiqudit gate time scales slower from 1 qudit to N qudits than the multiqubit from $\log_2(d)$ to $N\log_2(d)$ qubits.

Table 1 | Ratios of gate times in units of decoherence times between qubits and qudits for specific values of n and d (τ_b/τ_d needs to be larger than the critical values in order for a single qudit to be advantageous vs an equivalent ensemble of n qubits)

Number n of qubits	Dimension d of the qudit	Critical τ_b/τ_d
1	2	1
2	4	2.5
3	8	7
6	64	227.5

Perspectives on scalability and pathways beyond the first order

Given the rapid development of quantum computing platforms with very different physical properties, such as decoherence time or Hilbert space dimension (see Table 2), there is a growing need for detailed elaboration of the tradeoffs between their information density and noise error rates. By combining analytical results and numerical simulations, we have performed a comparative study of gate efficiency for systems composed of sets of qubits or qudits. A fluctuation-dissipation-like relation for the gate infidelity of an operation on a pure state was derived. We then put forward a physically-informed method to obtain the first-order effect of Markovian noise on the average gate infidelity (AGI). A connection was made between the latter and the first gate-independent result. The rate of increase of the AGI of a single qudit vs equivalent multiple qubits under pure dephasing was compared. This yielded a critical curve of the ratio of their respective gate times in units of decoherence time, a quantity indicating how time-efficient operations on a particular system are. Values on either side of the curve specify which of the two systems had a higher rate of increase of the AGI. To compete in terms of gate fidelity, as the dimension increases, the efficiency of qudit gates must not simply always be larger than the multiqubit one by a factor $O(d^2/\log_2(d))$, but precisely by a factor $\frac{d^2-1}{3\log_2(d)}$, which makes a significant difference for lower values of d for which it provides less demanding constraints. Additionally, analytical expressions of linear response for arbitrary collapse operators and a general multiqudit system were presented (see (16) and (25)). They may be useful to those working in the field of quantum computing e.g., to, as mentioned in the introduction, benchmark qudit platforms either in terms of maximal practical d or in terms of conditions on the figure of merit to compensate for the greater noise scaling, in comparison with current state-of-the-art multiqubit platforms.

Numerical simulations contributed to the discussion on the validity and limits of the linear response assumption. This further restricted the ranges of possible $\gamma t \ll 1$ accounting for qudit dimension, gate, and noise type. For example, the larger the dimension, the lower the relative gate-dependent response. Finally, after simulations supported the analytical critical curve, different current platforms were studied with respect to this condition on gate time efficiency. Given equivalent Hilbert space dimensions, viable qudit platforms (leveraging advantageous decoherence times and gate speeds to compensate for the higher rate of increase in AGI) capable of outperforming equivalent state-of-the-art multiqubit ones in gate fidelity have been found for pure dephasing. Moreover, this performance could be extended to qudits with d as large as ~ 40 in the case of nuclear spins in molecular magnets, for example. Some multiqubit platforms still outperform any existing qudit platform regarding scalability in

Table 2 | Decoherence times (T_2) and gate times (t_n) of different qubit/qudit platforms

	d	n	T_2	t_n	τ_n	ref.	platform
qubits	2	2	~ 10 μs	60 ns	~ 10^{-2}	[41] (2020)	superconducting qubits
	2	2	~ 2 μs	51 ns	~ 10^{-2}	[42] (2020)	Rydberg atoms
	2	17	~ 30 μs	~ 100 ns	~ 10^{-3}	[43] (2022)	superconducting qubits
	2	24	~ 100 ms	~ 200 μs	~ 10^{-3}	[44] (2021)	trapped ions
	2	1	~ 1 ms	~ 1 μs	~ 10^{-3}	[5] (2023)	electronic spins in molecular magnets
qudits	4	1	0.32 ms	~ 100 ns	~ 10^{-4}	[1] (2018)	nuclear spins in molecular magnets
	4	1	~ 100 μs	~ 150 ns	~ 10^{-3}	[6,45] ('20,'23)	superconducting qubits
	3	2	~ 100 ms	~ 100 μs	~ 10^{-3}	[4] (2022)	trapped ions
	4	2	∞[(1)]	–	0	[3] (2022)	photonic qudits
	52	1	–	~ 100 ns[(2)]	–	[37] (2020)	Rydberg atoms

d and n are the maximum dimension and number of qudits an operation was applied to, while $\tau_n = t_n/T_2$ is the figure of merit.
[(1)]considered unlimited by the source authors.
[(2)]no universal gates for the moment, only specific quantum operations implemented.

https://doi.org/10.1038/s41534-024-00829-6 **Article**

the number of subsystems. However, it is conceivable that some scalable qudit platforms continue to outperform equivalent multiqubit systems in terms of attainable fidelity. Further study of how multiqudit and multiqubit gate times scale with the number of subsystems is needed. Moreover, this study was limited to first-order noise responses. However, using the notation "qu-j-it" for a qudit of dimension $d = j$, through carefully chosen quantum error correction schemes, it was recently demonstrated it is possible to entirely remove the first-order response of logical qu-k-its embedded in physical qu-d-its ($k < d$) through carefully chosen encodings[12,13]. Of particular interest in the authors' future work is the study of the Hamiltonian-dependent response of the dimension-dependent AGI. More generally, an additional study of higher-order responses of logical qudits vs. physical qubits would therefore also be required to assess the viability of these logical error-resilient qudits. This could elucidate if the presence of single qudit advantage, as quantified by this paper, is robust to system scaling and if qudits will remain useful beyond the NISQ era.

Methods

Numerical noisy qudit/multiqubit simulation

The data and source code used for generating the results shown in this paper are publicly available on the RADAR4KIT Repository[38]. All simulations were done using the `Python` package `QuTiP24` version 4.7, `SciPy` version 1.7.3, and `NumPy` version 1.21.5. This subsection aims to present the *modus operandi* for obtaining the "numerical results" referenced in the different figures: the AGIs ($\overline{\delta}$) for Figs. 3 and 4 and the slope of the AGIs (c) in the other figures.

Standard packages. Essential functions for simulating quantum dynamics and fitting curves to data are provided by the `QuTiP` library, including functions for propagator calculation in superoperator form (`qt.propagator`) and gate fidelity evaluation (`average_gate_fidelity` from `qutip.metrics`), along with the `curve_fit` function from `scipy.optimize`.

Parameters. We define the system's dimension d, the decay parameter γ, and the collapse operators $\{L_k\}$ under consideration. The collapse operators are `QObj` instances characterized by their matrix form in the canonical basis. Additionally, we generate a list of time points for simulating the system's evolution. Considering the quantity of interest in this study is γt, γ is chosen as fixed, and the range of γt is then given by the range of the time points.

Time evolution. The simulation of the quantum system's time evolution is facilitated by computing the propagator using the system's Hamiltonian, the list of time points, and the collapse operators multiplied by $\sqrt{\gamma}$. This generates a time-dependent propagator in the form of a list of `QObj` superoperators for different values of γt. The system's Hamiltonian will be discussed in further detail in the following subsection. However, apart from Fig. 5 studying the gate/Hamiltonian-dependence, the other figures report simulations done with a vanishing Hamiltonian $H = \mathbb{0}_d$ since the quantities under consideration are considered Hamiltonian-independent.

Fidelity calculation. At each γt the average gate fidelity is computed relative to a target gate, in the case of $H = \mathbb{0}_d$: the identity matrix. This is the quantity displayed in Figs. 3 and 4.

Curve fitting. A curve is fitted to the calculated fidelities over the range of γt using the `curve_fit` function. This process involves fitting the function $1 - c\gamma t$ for the parameter c. The obtained slopes $c(\{L_k\})$ are then the ones displayed in the Figs. 2, 5, 6, 7 and 8. Moreover the least-square fit parameter R given by the fitting functions is the one reported in this study.

Random gate and pulse Hamiltonian generation

Gate generation. In the study of the gate-dependent deviation from the analytical results of this manuscript, for each dimension d under consideration, a set of $N_g = 5000$ gates have been randomly generated with the `Bristol39` package in `Python`. The gates have been drawn from the circular unitary ensemble, and are thus considered to be uniformly distributed over the Haar measure. Subsequently, to generate an associated set of pulses for each gate, we have used the `optimize_pulse_unitary` function from the pulse optimization module (`control.pulse_optim`) of `QuTiP`.

Pulse generation. The pulse generation is done through gradient-ascent methods using the `GRAPE` algorithm[40] and was run in parallel for each gate using a high-performance cluster. The numerical optimizer used by default is the L-BFGS-B method. Assuming the control Hamiltonian, as discussed after (1), takes the form

$$Hc(t) = \sum_{k=0}^{N} u_k(t) H_k, \tag{32}$$

with H_k being a basis set of controls and $u_k(t)$ representing the time-dependent control amplitudes, the optimization process involves finding the set of $u_k(t)$ that best approximates the target gate.

Choice of Hamiltonian. For the simulations reported in this paper, we decided to model qudits as ladder systems, with one pulse per transition between adjacent levels as considered for example in the experiments of Godfrin et al.[20], for a single-molecule magnet ($TbPc_2$, qudit with $d = 4$), the $d - 1$ pulses are then each represented by two control Hamiltonians in the interaction picture. More explicitly, the basis set of controls is chosen to be the ensemble of pairs $|k\rangle\langle k+1| + |k+1\rangle\langle k|$ and $\mathrm{i}(|k\rangle\langle k+1| - |k+1\rangle\langle k|)$, with k running from 1 to $d - 1$. Moreover, H_0, the free-evolution, is chosen to be vanishing since we consider the interaction reference frame.

Data availability

The numerical data presented in this study are available on the RADAR4KIT Repository[38]: https://doi.org/10.35097/1953.

Code availability

The code for numerical simulations performed in this study is available on the RADAR4KIT Repository[38]: https://doi.org/10.35097/1953. The code generating the data used for Fig. 5 is available from the authors upon reasonable request.

Received: 22 November 2023; Accepted: 15 March 2024;
Published online: 10 June 2024

References

1. Moreno-Pineda, E., Godfrin, C., Balestro, F., Wernsdorfer, W. & Ruben, M. Molecular Spin Qudits for Quantum Algorithms. *Chem. Soc. Rev.* **47**, 501–513 (2018).
2. Jenkins, M. D. et al. Coherent manipulation of three-qubit states in a molecular single-ion magnet. *Phys. Rev. B* **95**, 064423 (2017).
3. Chi, Y. et al. A programmable qudit-based quantum processor. *Nat. Commun.* **13**, 1166 (2022).
4. Ringbauer, M. et al. A universal qudit quantum processor with trapped ions. *Nat. Phys.* **18**, 1053–1057 (2022).
5. Chiesa, A. et al. Blueprint for a molecular-spin quantum processor. *Phys. Rev. Appl.* **19**, 064060 (2023).
6. Cao, S. et al. Emulating two qubits with a four-level transmon qudit for variational quantum algorithms. https://arxiv.org/abs/2303.04796. (2023).

7. Brusentsov, N. P. & Ramil Alvarez, J.*Ternary Computers: The Setun and the Setun 70*, 74–80. IFIP Advances in Information and Communication Technology (Springer, Berlin, Heidelberg, 2011).
8. Boixo, S. et al. Characterizing quantum supremacy in near-term devices. *Nat. Phys.* **14**, 595–600 (2018).
9. Arute, F. et al. Quantum supremacy using a programmable superconducting processor. *Nature* **574**, 505–510 (2019).
10. IBM Unveils 400 Qubit-Plus Quantum Processor and Next-Generation IBM Quantum System Two. https://newsroom.ibm.com/2022-11-09-IBM-Unveils-400-Qubit-Plus-Quantum-Processor-and-Next-Generation-IBM-Quantum-System-Two (2022).
11. Wang, Y., Hu, Z., Sanders, B. C. & Kais, S. Qudits and High-Dimensional Quantum Computing. *Front. Phys.* **8**, 589504 (2020).
12. Chiesa, A. et al. Embedded quantum-error correction and controlled-phase gate for molecular spin qubits. *AIP Adv.* **11**, 025134 (2021).
13. Petiziol, F., Chiesa, A., Wimberger, S., Santini, P. & Carretta, S. Counteracting dephasing in Molecular Nanomagnets by optimized qudit encodings. *npj Quantum Inf.* **7**, 1–10 (2021).
14. Wernsdorfer, W. & Ruben, M. Synthetic Hilbert Space Engineering of Molecular Qudits: Isotopologue Chemistry. *Adv. Mater.* **31**, 1806687 (2019).
15. Luis, F. et al. A dissymmetric [gd2] coordination molecular dimer hosting six addressable spin qubits. *Commun. Chem.* **3**, 176 (2020).
16. Zheng, Y., Sharma, H. & Borregaard, J. Entanglement Distribution with Minimal Memory Requirements Using Time-Bin Photonic Qudits. *PRX Quantum* **3**, 040319 (2022).
17. Bouchard, F., Fickler, R., Boyd, R. W. & Karimi, E. High-dimensional quantum cloning and applications to quantum hacking. *Sci. Adv.* **3**, e1601915 (2017).
18. Campbell, E. T., Anwar, H. & Browne, D. E. Magic-State Distillation in All Prime Dimensions Using Quantum Reed-Muller Codes. *Phys. Rev. X* **2**, 041021 (2012).
19. Lanyon, B. P. et al. Simplifying quantum logic using higher-dimensional hilbert spaces. *Nat. Phys.* **5**, 134–140 (2008).
20. Godfrin, C. et al. Operating Quantum States in Single Magnetic Molecules: Implementation of Grover's Quantum Algorithm. *Phys. Rev. Lett.* **119**, 187702 (2017).
21. Thiele, S. et al. Electrically driven nuclear spin resonance in single-molecule magnets. *Science* **344**, 1135–1138 (2014).
22. Otten, M. et al. Impacts of noise and structure on quantum information encoded in a quantum memory. *Phys. Rev. A* **104**, 012605 (2021).
23. Nielsen, M. A. A simple formula for the average gate fidelity of a quantum dynamical operation. *Phys. Lett. A* **303**, 249–252 (2002).
24. Johansson, J., Nation, P. & Nori, F. QuTiP: An open-source Python framework for the dynamics of open quantum systems. *Computer Phys. Commun.* **183**, 1760–1772 (2012).
25. Manzano, D. A short introduction to the Lindblad master equation. *AIP Adv.* **10**, 025106 (2020).
26. Jozsa, R. Fidelity for Mixed Quantum States. *J. Mod. Opt.* **41**, 2315–2323 (1994).
27. Qi, J. & Ng, H. K. Comparing the randomized benchmarking figure with the average infidelity of a quantum gate-set. *Int. J. Quantum Inf.* **17**, 1950031 (2019).
28. Johnston, N. & Kribs, D. W. Quantum gate fidelity in terms of Choi matrices. *J. Phys. A: Math. Theor.* **44**, 495303 (2011).
29. Zhong, W., Sun, Z., Ma, J., Wang, X. & Nori, F. Fisher information under decoherence in Bloch representation. *Phys. Rev. A* **87**, 022337 (2013).
30. Abad, T., Fernández-Pendás, J., Frisk Kockum, A. & Johansson, G. Universal Fidelity Reduction of Quantum Operations from Weak Dissipation. *Phys. Rev. Lett.* **129**, 150504 (2022).
31. Collins, B., Matsumoto, S. & Novak, J. The Weingarten Calculus. https://arxiv.org/abs/2109.14890 (2021).
32. Horodecki, M., Horodecki, P. & Horodecki, R. General teleportation channel, singlet fraction, and quasidistillation. *Phys. Rev. A* **60**, 1888–1898 (1999).
33. Ozaeta, A. & McMahon, P. L. Decoherence of up to 8-qubit entangled states in a 16-qubit superconducting quantum processor. *Quantum Sci. Technol.* **4**, 025015 (2019).
34. Chen, Y. et al. Qubit Architecture with High Coherence and Fast Tunable Coupling. *Phys. Rev. Lett.* **113**, 220502 (2014).
35. Kjaergaard, M. et al. Superconducting Qubits: Current State of Play. *Annu. Rev. Condens. Matter Phys.* **11**, 369–395 (2020).
36. Rosenblum, S. et al. A CNOT gate between multiphoton qubits encoded in two cavities. *Nat. Commun.* **9**, 652 (2018).
37. Larrouy, A. et al. Fast Navigation in a Large Hilbert Space Using Quantum Optimal Control. *Phys. Rev. X* **10**, 021058 (2020).
38. Janković, D. Source Code for data generation and pulses data for Noisy Qudit vs Multiple Qubits. https://doi.org/10.35097/1953 (2024).
39. Suezen, M. Bristol: A Python Package for Random Matrix Ensembles. https://zenodo.org/record/579642 (2017).
40. Khaneja, N., Reiss, T., Kehlet, C., Schulte-Herbrüggen, T. & Glaser, S. J. Optimal control of coupled spin dynamics: design of NMR pulse sequences by gradient ascent algorithms. *J. Magn. Reson.* **172**, 296–305 (2005).
41. Kjaergaard, M. et al. Programming a quantum computer with quantum instructions. https://arxiv.org/abs/2001.08838 (2020).
42. Madjarov, I. S. et al. High-fidelity entanglement and detection of alkaline-earth Rydberg atoms. *Nat. Phys.* **16**, 857–861 (2020).
43. Krinner, S. et al. Realizing repeated quantum error correction in a distance-three surface code. *Nature* **605**, 669–674 (2022).
44. Pogorelov, I. et al. Compact Ion-Trap Quantum Computing Demonstrator. *PRX Quantum* **2**, 020343 (2021).
45. Wu, X. et al. High-fidelity software-defined quantum logic on a superconducting qudit. *Phys. Rev. Lett.* **125**, 170502 (2020).

Acknowledgements

This work was funded by the French National Research Agency (ANR) through the Programme d'Investissement d'Avenir under contract ANR-11-LABX-0058_NIE and ANR-17-EURE-0024 within the Investissement d'Avenir program ANR-10-IDEX-0002-02. D.J. and M.R. gratefully acknowledge financial support from the Deutsche Forschungsgemeinschaft (DFG, German Research Foundation) through the Collaborative Research Centre "4f for Future" (CRC 1573, project number 471424360) project B3. J-G.H. also acknowledges QUSTEC funding from the European Union's Horizon 2020 research and innovation program under the Marie Skłodowska-Curie Grant Agreement No. 847471. The authors would like to acknowledge the High Performance Computing Center of the University of Strasbourg for supporting this work by providing scientific support and access to computing resources. Part of the computing resources were funded by the Equipex Equip@Meso project (Programme Investissements d'Avenir) and the CPER Alsacalcul/Big Data.

Author contributions

D.J. conceptualized the study, derived analytical results, and drafted the manuscript with subsequent input of all the authors. D.J. and J-G.H. designed the methodology of the study with the input of P-A.H. D.J. and J-G.H. wrote the computational code and performed numerical simulations. D.J. generated and prepared the figures. P-A.H. and M.R. supervised and conceptualized the project and advised on the manuscript's drafting. All authors participated in the proofreading and the preparation of the manuscript.

Competing interests

The authors declare no competing interests.

https://doi.org/10.1038/s41534-024-00829-6 **Article**

Additional information

Supplementary information The online version contains supplementary material available at https://doi.org/10.1038/s41534-024-00829-6.

Correspondence and requests for materials should be addressed to Denis Janković.

Reprints and permissions information is available at http://www.nature.com/reprints

Publisher's note Springer Nature remains neutral with regard to jurisdictional claims in published maps and institutional affiliations.

Open Access This article is licensed under a Creative Commons Attribution 4.0 International License, which permits use, sharing, adaptation, distribution and reproduction in any medium or format, as long as you give appropriate credit to the original author(s) and the source, provide a link to the Creative Commons licence, and indicate if changes were made. The images or other third party material in this article are included in the article's Creative Commons licence, unless indicated otherwise in a credit line to the material. If material is not included in the article's Creative Commons licence and your intended use is not permitted by statutory regulation or exceeds the permitted use, you will need to obtain permission directly from the copyright holder. To view a copy of this licence, visit http://creativecommons.org/licenses/by/4.0/.

© The Author(s) 2024

C.2 Supplementary Information

Supplementary Notes

Noisy Qudit vs Multiple Qubits: Conditions on Gate Efficiency for Enhancing Fidelity

Denis Janković[1,2*], Jean-Gabriel Hartmann[1], Mario Ruben[2,3,4], Paul-Antoine Hervieux[1]

[1]Institut de Physique et Chimie des Matériaux de Strasbourg (IPCMS), UMR 7504, Université de Strasbourg, CNRS, 23, Rue du Loess, 67000 Strasbourg, France.
[2]Institute of Nanotechnology (INT), Karlsruhe Institute of Technology, P.O. Box 3640, 76021 Karlsruhe, Germany.
[3]Institute for Quantum Materials and Technologies (IQMT), Karlsruhe Institute of Technology, P.O. Box 3640, 76021 Karlsruhe, Germany.
[4]Centre Européen de Sciences Quantiques (CESQ), Institut de Science et d'Ingénierie Supramoléculaires (ISIS), Université de Strasbourg, 8, Allée Gaspard Monge, 67000 Strasbourg, France.

*Corresponding author(s). E-mail(s): denis.jankovic@ipcms.unistra.fr;
Contributing authors: jean-gabriel.hartmann@ipcms.unistra.fr;
mario.ruben@kit.edu; hervieux@unistra.fr;

Supplementary Notes 1 : Complementary Derivations

Supplementary Notes 1a : Fluctuation-dissipation relation

Substituting, from the article, (3) and (2) into (6) and (5) leads to

$$\mathscr{E}(\rho^*) = \gamma t \left(\frac{1}{2} \mathrm{Tr}\left(\rho^* \left\{L^\dagger L, \rho^*\right\}\right) - \mathrm{Tr}\left(\rho^* L \rho^* L^\dagger\right)\right) + \mathscr{O}((\gamma t)^2). \tag{1}$$

The trace being invariant by cyclic permutations and $\rho^{*2} = \rho^*$ leads to the simplification

$$\frac{1}{2} \mathrm{Tr}\left(\rho^* \left\{L^\dagger L, \rho^*\right\}\right) = \mathrm{Tr}\left(\rho^* L^\dagger L\right) \equiv \langle L^\dagger L \rangle_* \,. \tag{2}$$

Moreover

$$\mathrm{Tr}\left(\rho^* L \rho^* L^\dagger\right) = \mathrm{Tr}\left(|\varphi^*\rangle \langle\varphi^*|L|\varphi^*\rangle \langle\varphi^*| L^\dagger\right) \tag{3}$$
$$= \langle L\rangle_* \mathrm{Tr}\left(\rho^* L^\dagger\right) \tag{4}$$
$$= \langle L^\dagger\rangle_* \langle L\rangle_* \,. \tag{5}$$

Accounting for the above results, one finally obtains

$$\mathscr{E}(\rho^*) = \gamma t \left(\langle L^\dagger L\rangle_* - \langle L^\dagger\rangle_* \langle L\rangle_*\right) + \mathscr{O}((\gamma t)^2), \tag{6}$$

which can be rewritten as (7) from the article.

Supplementary Notes 1b : Average Gate Infidelity for the Pure Dephasing Channel of one qudit

In a trivial way we have $\mathrm{Tr}(E_1) \propto \mathrm{Tr}(J_z) = 0$, and

$$\begin{aligned}
\mathrm{Tr}(E_0) &= d - \frac{\gamma t}{2}\mathrm{Tr}\left(J_z^2\right) \\
&= d - \frac{\gamma t}{2}\sum_{k=0}^{d-1}\left(\frac{d-1-2k}{2}\right)^2 \\
&= d - \frac{\gamma t}{8}\left[d(d-1)^2 - 4(d-1)\sum_{k=0}^{d-1} k + 4\sum_{k=0}^{d-1} k^2\right] \\
&= d - \frac{\gamma t}{8}\left[d(d-1)^2 - 2d(d-1)^2 + 4\frac{d(d-1)(2d-1)}{6}\right] \\
&= d - \frac{\gamma t}{24} d(d^2-1),
\end{aligned}$$

which results in

$$|\mathrm{Tr}(E_0)|^2 = d^2 - \frac{\gamma t}{12} d^2(d^2-1) + \mathscr{O}((\gamma t)^2)\,. \tag{7}$$

Therefore

$$\overline{\mathscr{F}}(\mathscr{E}_z) = \frac{d + d^2 - \frac{\gamma t}{12} d^2(d^2-1)}{d(d+1)} + \mathscr{O}((\gamma t)^2) = 1 - \frac{\gamma t}{12} d(d-1) + \mathscr{O}((\gamma t)^2)\,, \tag{8}$$

which leads to the simplified expression (13) from the article.

Moreover, this is the origin of the factor $\frac{1}{12}$ in (14) from the article whose ratio with the $\frac{1}{4}$ obtained in (20) from the article and (10) leads to the non-trivial factor $\frac{1}{3}$ in (22) from the article.

Supplementary Notes 1c : Average Gate Infidelity for the pure dephasing channel of n qubits

Since $\mathrm{Tr}(E_k) = 0\ \forall k \neq 0$, only $\mathrm{Tr}(E_0)$ is left and is given by

$$\begin{aligned}\mathrm{Tr}(E_0) &= 2^n - \frac{\gamma t}{2}\sum_{k=1}^{n}\left[\mathrm{Tr}\left(S_z^{2\,(k)}\right)\prod_{j\neq k}\mathrm{Tr}\left(\mathbb{1}_2^{2\,(j)}\right)\right] \\ &= 2^n - n\frac{\gamma t}{8}2^n,\end{aligned} \tag{9}$$

leading to

$$|\mathrm{Tr}(E_0)|^2 = 2^{2n} - \frac{\gamma t}{4}n2^{2n} + \mathscr{O}((\gamma t)^2)\,, \tag{10}$$

which allows to obtain (20) from the article using (10) from the article.

Supplementary Notes 1d : Average over the Fubini-Study measure of the uncertainty of L

First, rewriting $\int \mathrm{d}\rho\,\mathrm{Tr}\left(\rho M^\dagger M\right)$ yields

$$\int dU\ \mathrm{Tr}\left(U\rho U^\dagger M^\dagger M\right) = \mathrm{Tr}\left[\left(\int dU\, U\rho U^\dagger\right)M^\dagger M\right]$$

, where the integration is performed over the uniform Haar measure in the space of unitaries. Using the identity

$$\int dU\, UXU^\dagger = \frac{\mathrm{Tr}(X)I}{d}$$

valid for any linear operator X, for the special case of ρ pure one obtains

$$\int d\rho\ \mathrm{Tr}(\rho M^\dagger M) = \frac{1}{d}\mathrm{Tr}(M^\dagger M). \tag{11}$$

Now, rewriting $\int \mathrm{d}\rho\,\mathrm{Tr}\left(\rho M^\dagger M\right)$ yields

$$\begin{aligned}&\int\ dU\,\mathrm{Tr}\left(U\rho U^\dagger M\right)^2 = \\ &\sum_{\substack{i,j,k,l\\m,n,p,q}}\int\ dU\,U_{ij}U_{k\ell}\bar{U}_{mn}\bar{U}_{pq}\rho_{jn}\rho_{\ell q}M_{mi}M_{pk}.\end{aligned}$$

Collins, Matsumoto, and Novak[1] provide formulae to integrate polynomials of unitary matrices

$$\begin{aligned}&\int_{U_d} dU U_{ij}U_{k\ell}\bar{U}_{mn}\bar{U}_{pq} = \\ &\frac{1}{d^2-1}\Big[(\delta_{im}\delta_{jn}\delta_{kp}\delta_{\ell q} + \delta_{ip}\delta_{jq}\delta_{km}\delta_{\ell n})\end{aligned}$$

$$- \frac{1}{d}(\delta_{im}\delta_{jq}\delta_{kp}\delta_{\ell n} + \delta_{ip}\delta_{jn}\delta_{km}\delta_{\ell q})\Big] \,, \tag{12}$$

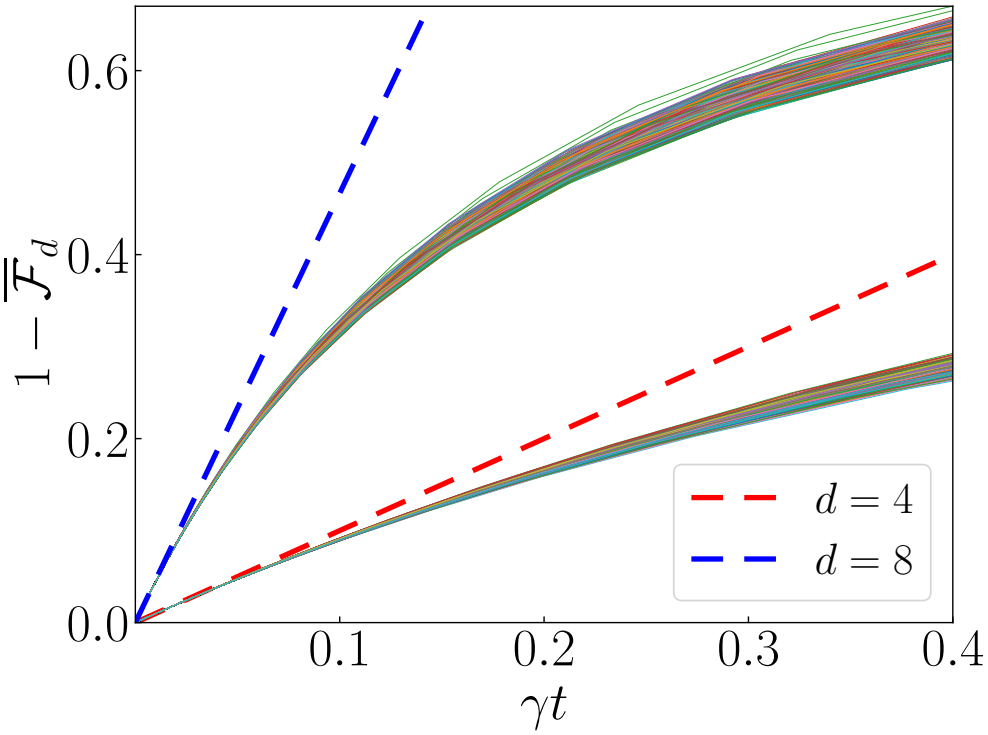
which contracting the indices gives

$$\int d\rho \; |\mathrm{Tr}(\rho M)|^2 = \frac{1}{d(d+1)} \left(\mathrm{Tr}(M^\dagger M) + |\mathrm{Tr}(M)|^2\right).$$

Finally subtracting (12) from (11) leads to (28) from the article.

Supplementary Notes 2 : Higher-order effects of the collapse operators

Supplementary Notes 2a : Complementary figure : deviation from linearity and gate dependence



Supplementary Figure 1 Simulated AGIs of $N_g = 4400$ gates for $d = 4, 8$ in solid lines. The dashed lines correspond to the expected linear behaviour at small γt.

Fig.1 allows for observation of (i) the deviation from linear behaviour as γt increases, (ii) for higher d, this deviation becomes noticeable for smaller values of γt and, (iii) the infidelity becomes increasingly gate-dependent as γt increases.

Supplementary Notes 2b : Full expansion of the density matrix

The density matrix $\rho(t)$ can be decomposed as

$$\rho(t) = \rho^* + \sum_{l=1}\sum_{k=1} \rho_{lk} \gamma^l t^k \,. \tag{13}$$

Substituting (13) in (1) from the article yields the following results:

- $\rho_{11} = \mathscr{D}[\rho^*] := \sum_k L_k \rho^* L_k^\dagger - \frac{1}{2}\{L_k^\dagger L_k, \rho^*\}$.
- for $l \geq 2$, $k = 1$, $\rho_{l,1} = 0$.
- for $l = 1$, $k \geq 2$,
$$k\rho_{1k} = -\mathrm{i}[H, \rho_{1(k-1)}] - \dot{\rho}_{1(k-1)} \,. \tag{14}$$
- $\forall l, k \geq 2$,
$$k\rho_{lk} = -\mathrm{i}[H, \rho_{l(k-1)}] - \dot{\rho}_{l(k-1)} + \mathscr{D}[\rho_{(l-1)(k-1)}] \,. \tag{15}$$

It can be linked to (3) from the article by noticing that $M = -\rho_{11}$.

Moreover, for $k = l = 2$ we obtain

$$\rho_{22} = \mathscr{D}[\rho_{11}] = \mathscr{D}\left[\mathscr{D}[\rho^*]\right] \,. \tag{16}$$

Finally we have

$$\rho_{12} = \frac{\mathrm{i}}{2}\left(\mathscr{D}\left[[H, \rho^*]\right] - [H, \rho^*]\right), \tag{17}$$

and

$$\rho_{13} = -\frac{\mathrm{i}}{3}[H, \rho_{12}] - \frac{\dot{\rho}_{12}}{3}. \tag{18}$$

This gives us the following expansion

$$\rho(t) = \rho^* + \gamma t \rho_{11} + \gamma t^2 \rho_{12} + \gamma t^3 \rho_{13} + (\gamma t)^2 \rho_{22} + \varepsilon, \tag{19}$$

with $\varepsilon = O\left(\gamma^l t^k\right)_{l+k\geq 5}$.

Interestingly, it can be proven by induction that if $H = \mathbb{0}_d$ then,

$$\rho(t) = \rho^* + \sum_k (\gamma t)^k \rho_{kk}, \tag{20}$$

with $\rho_{kk} = \frac{1}{k!}\mathscr{D}^{(k)}[\rho^*]$.

References

[1] Collins, B., Matsumoto, S. & Novak, J. The Weingarten Calculus. Preprint at https://arxiv.org/abs/2109.14890 (2021).

APPENDIX D

APPENDICES TO CHAPTER 5

D.1 Numerical Packages

The numerical simulations in this work were performed using the following software packages in Python version 3.9.5:

Package	Version	Package	Version
bristol	0.2.14	cirq	1.2.0
cirq_core	1.2.0	cvxpy	1.5.2
Cython	0.29.35	functorch	2.0.0
joblib	1.3.2	loguru	0.7.0
matplotlib	3.7.1	networkx	2.8.8
numpy	1.24.3	pandarallel	1.6.5
pandas	2.0.2	qutip	4.7.1
scikit_learn	1.4.1.post1	scipy	1.14.0
setuptools	45.2.0	SQLAlchemy	2.0.20
statsmodels	0.14.1	torch	2.0.1
tqdm	4.65.0		

D.2 Complementary Derivations

Here, we present the detailed derivations of the analytical results in the main text.

D.2.1 Integration of the m-th Order Solution to the Master Equation

Theorem D.2.1. *Consider an open quantum system of a single qudit of dimension d, initiated in a pure state $\mathrm{Tr}\{\rho_0^2\} = 1$, under the influence of a time-independent noise superoperator $\mathcal{L}$ with coupling constant γ, and evolving via a time-independent unitary superoperator $\mathcal{S}$ over time t. Then, the solution to the master equation evolving by a CPTP quantum channel can be expressed in a perturbative expansion in γ, where the m-th order correction term is given by (5.23) in the main text. Then, the nested integral can be evaluated, by induction, and results in the following expression in (5.26) in the main text:*

$$\tilde{M}^{(m)}(t) = \int_0^t \cdots \int_0^{t_{m-1}} \left(\prod_{i=1}^{m} e^{-\mathcal{S}t_i} \mathcal{L} e^{\mathcal{S}t_i} \right) dt_m \cdots dt_1 \tag{D.1}$$

$$= t^m \sum_{n_1,\cdots,n_m=0}^{\infty} \left(\prod_{i=1}^{m} \frac{(-t)^{n_i} [(\mathcal{S})^{n_i}, \mathcal{L}]}{n_i! \sum_{j=i}^{m} (n_j + 1)} \right). \tag{D.2}$$

Proof. In the calculations that follow, we make use of Campbell's lemma, based on the Baker-Campbell-Hausdorff Formula [183, 184], as stated in (5.24) in the main text,

$$e^X Y e^{-X} = \sum_{n=0}^{\infty} \frac{[(X)^n, Y]}{n!}, \tag{D.3}$$

with $[(X)^n, Y] = \big[X, \big[(X)^{n-1}, Y\big]\big]$ and $\big[(X)^0, Y\big] = Y$, and proceed with proof by

induction. *Base Case:* To first-order, $m = 1$,

$$\begin{aligned}\int_0^t e^{-\mathcal{S}t_1}\mathcal{L}e^{\mathcal{S}t_1}dt_1 &= \int_0^t \sum_{n_1=0}^{\infty}\frac{[(-\mathcal{S}t_1)^{n_1},\mathcal{L}]}{n_1!}dt_1 \\ &= \sum_{n_1=0}^{\infty}\frac{(-1)^{n_1}}{n_1!}[(\mathcal{S})^{n_1},\mathcal{L}]\int_0^t t_1^{n_1}dt_1 \\ &= t\sum_{n_1=0}^{\infty}\frac{(-t)^{n_1}[(\mathcal{S})^{n_1},\mathcal{L}]}{n_1!(n_1+1)} \\ &= \tilde{M}^{(1)}(t).\end{aligned}$$

Induction Step: Assume that the result in Eq. (D.2) holds at m-th order, and relabel indices $t, t_1, \cdots, t_{m-1} \to t_1, t_2, \cdots, t_m$ and $t \to t_1$:

$$\begin{aligned}\tilde{M}^{(m)}(t_1) &= \int_0^{t_1}\cdots\int_0^{t_m}\left(\prod_{2=1}^{m+1}e^{-\mathcal{S}t_i}\mathcal{L}e^{\mathcal{S}t_i}\right)dt_{m+1}\cdots dt_2 \\ &= t_1^m\sum_{n_2=0}^{\infty}\cdots\sum_{n_{m+1}=0}^{\infty}\left(\prod_{i=2}^{m+1}\frac{(-t_1)^{n_i}[(\mathcal{S})^{n_i},\mathcal{L}]}{n_i!\sum_{j=i}^{m+1}(n_j+1)}\right).\end{aligned}$$

Then, to order $m+1$,

$$\begin{aligned}&\int_0^t \tilde{M}^{(m)}(t_1)\left(e^{-\mathcal{S}t_1}\mathcal{L}e^{\mathcal{S}t_1}\right)dt_1 \\ &= \int_0^t\left(t_1^m\sum_{n_2=0}^{\infty}\cdots\sum_{n_{m+1}=0}^{\infty}\prod_{i=2}^{m+1}\frac{(-t_1)^{n_i}[(\mathcal{S})^{n_i},\mathcal{L}]}{n_i!\sum_{j=i}^{m+1}(n_j+1)}\right)\left(\sum_{n_1=0}^{\infty}\frac{(-t_1)^{n_1}[(\mathcal{S})^{n_1},\mathcal{L}]}{n_1!}\right)dt_1 \\ &= \sum_{n_2=0}^{\infty}\cdots\sum_{n_{m+1}=0}^{\infty}\frac{(-1)^{n_1}[(\mathcal{S})^{n_1},\mathcal{L}]}{n_1!}\prod_{i=2}^{m+1}\left(\frac{(-1)^{n_i}[(\mathcal{S})^{n_i},\mathcal{L}]}{n_i!\sum_{j=i}^{m+1}(n_j+1)}\right)\int_0^t t_1^m t_1^{n_1}\prod_{i=2}^{m+1}t_1^{n_i}dt_1 \\ &= \sum_{n_2=0}^{\infty}\cdots\sum_{n_{m+1}=0}^{\infty}\frac{(-1)^{n_1}[(\mathcal{S})^{n_1},\mathcal{L}]}{n_1!}\prod_{i=2}^{m+1}\left(\frac{(-1)^{n_i}[(\mathcal{S})^{n_i},\mathcal{L}]}{n_i!\sum_{j=i}^{m+1}(n_j+1)}\right)\frac{t^{m+1+\sum_{i=1}^{m+1}n_i}}{m+1+\sum_{j=1}^{m+1}n_j} \\ &= t^{m+1}\sum_{n_2=0}^{\infty}\cdots\sum_{n_{m+1}=0}^{\infty}\frac{(-t)^{n_1}[(\mathcal{S})^{n_1},\mathcal{L}]}{n_1!\sum_{j=1}^{m+1}(n_j+1)}\prod_{i=2}^{m+1}\frac{(-t)^{n_i}[(\mathcal{S})^{n_i},\mathcal{L}]}{n_i!\sum_{j=i}^{m+1}(n_j+1)} \\ &= t^{m+1}\sum_{n_2=0}^{\infty}\cdots\sum_{n_{m+1}=0}^{\infty}\prod_{i=1}^{m+1}\frac{(-t)^{n_i}[(\mathcal{S})^{n_i},\mathcal{L}]}{n_i!\sum_{j=i}^{m+1}(n_j+1)} \\ &= \tilde{M}^{(m+1)}(t),\end{aligned}$$

hence completing the proof by induction. □

D.2.2 Perturbative Expansion of the AGI

We define the Average Gate Infidelity (AGI) as

$$\mathcal{I}(\mathcal{E},\mathcal{U}) = 1 - \mathcal{F}(\mathcal{E},\mathcal{U}) \tag{D.4}$$

$$= 1 - \left(1 - \sum_{m=1}^{\infty}\gamma^m F^{(m)}\right), \tag{D.5}$$

where the quantum channel is given by

$$\mathcal{E} = \mathcal{U} + \sum_{m=1}^{\infty} \gamma^m \mathcal{E}^{(m)} \tag{D.6}$$

$$= \mathcal{U} + \sum_{m=1}^{\infty} \gamma^m \mathcal{U}\tilde{M}^{(m)}. \tag{D.7}$$

Then, from (5.8) in the main text,

$$\begin{aligned}
&\mathcal{F}(\mathcal{E},\mathcal{U}) \\
&= \int_{\mathscr{H}} \left\langle \left(\mathcal{U}^\dagger \circ \mathcal{E}\right)[\rho_0] \right\rangle_0 d\rho_0 \\
&= \int_{\mathscr{H}} \left\langle \left(\mathcal{U}^\dagger \circ \left(\mathcal{U} + \sum_{m=1}^{\infty} \gamma^m \mathcal{U}\tilde{M}^{(m)} \right) \right)[\rho_0] \right\rangle_0 d\rho_0 \\
&= \int_{\mathscr{H}} \left\langle \rho_0 + \sum_{m=1}^{\infty} \gamma^m \tilde{M}^{(m)}[\rho_0] \right\rangle_0 d\rho_0,
\end{aligned}$$

and evaluating the expectation value over ρ_0 of initial states with $\langle \mathcal{A} \rangle_0 = \mathrm{Tr}\{\mathcal{A}\rho_0\}$,

$$\begin{aligned}
1 - \sum_{m=1}^{\infty} \gamma^m F^{(m)} &= \int_{\mathscr{H}} \mathrm{Tr}\left\{ \rho_0^2 + \sum_{m=1}^{\infty} \gamma^m \tilde{M}^{(m)}[\rho_0]\rho_0 \right\} d\rho_0 \\
&= 1 + \sum_{m=1}^{\infty} \gamma^m \int_{\mathscr{H}} \mathrm{Tr}\left\{ \tilde{M}^{(m)}[\rho_0]\rho_0 \right\} d\rho_0,
\end{aligned}$$

since $\mathrm{Tr}\{\rho_0^2\} = 1$ and $\int_{\mathscr{H}} d\rho_0 = 1$, and using (5.21) from the main text. The m-th order term of the AGF is therefore

$$F^{(m)} = -\int_{\mathscr{H}} \mathrm{Tr}\left\{ \tilde{M}^{(m)}[\rho_0]\rho_0 \right\} d\rho_0, \tag{D.8}$$

and we may write the AGI in terms of $t^m M^{(m)} = \tilde{M}^{(m)}$,

$$\mathcal{I}(\mathcal{E},\mathcal{U}) = -\sum_{m=1}^{\infty} (\gamma t)^m \int_{\mathscr{H}} \mathrm{Tr}\left\{ M^{(m)}[\rho_0]\rho_0 \right\} d\rho_0. \tag{D.9}$$

D.2.3 Integral over the Fubini-Study Measure

We can evaluate Eq. (D.9) to arrive at the result in (5.30) in the main text. The integral over the Fubini-Study measure is calculated using methods from [185] relating to Weingarten calculus. Specifically, we make use of the following result,

$$\begin{aligned}
&\int_{\mathscr{H}} U_{ka} U_{ic} \bar{U}_{jb} \bar{U}_{rd} dU \\
&= \frac{1}{(d^2-1)} \left[(\delta_{kj}\delta_{ab}\delta_{ir}\delta_{cd} + \delta_{kr}\delta_{ad}\delta_{ij}\delta_{cb}) \right] - \\
&- \frac{1}{d(d^2-1)} \left[(\delta_{kj}\delta_{ad}\delta_{ir}\delta_{cb} + \delta_{kr}\delta_{ab}\delta_{ij}\delta_{cd}) \right],
\end{aligned} \tag{D.10}$$

where, and for the remainder of this section, the indices represent the matrix elements using Einstein sum notation.

Now, beginning with the element-wise definition of the superoperator term,

$$\left(M[\rho]\right)_{pi} = M_{kj,pi}\rho_{kj}, \tag{D.11}$$

where we identify ρ and ρ_0 for convenient usage of the element-wise sum notation, this extends to

$$\begin{aligned}\left(M[\rho]\rho\right)_{pq} &= \left(M[\rho]\right)_{pi}\rho_{iq} \\ &= M_{kj,pi}\rho_{kj}\rho_{iq}.\end{aligned} \tag{D.12}$$

Taking the trace of this term corresponds to

$$\begin{aligned}\mathrm{Tr}\{M[\rho]\rho\} &= \delta_{pq}\left(M[\rho]\rho\right)_{pq} \\ &= M_{kj,ri}\rho_{kj}\rho_{ir},\end{aligned} \tag{D.13}$$

where we define $r := p = q$. Rewriting the integral of this expression in terms of the associated unitary operator U leads to

$$\begin{aligned}&\int_{\mathscr{H}} \mathrm{Tr}\left\{M\left[U\rho U^\dagger\right]U\rho U^\dagger\right\}dU \\ &= \int_{\mathscr{H}} M_{kj,ri}\left(U_{ka}\rho_{ab}\bar{U}_{jb}\right)\left(U_{ic}\rho_{cd}\bar{U}_{rd}\right)dU \\ &= \rho_{ab}M_{kj,ri}\rho_{cd}\int_{\mathscr{H}}\left(U_{ka}\bar{U}_{jb}U_{ic}\bar{U}_{rd}\right)dU.\end{aligned} \tag{D.14}$$

If we now substitute the result of this integral from Eq. (D.10), and evaluate all of the delta function terms, we arrive at

$$\begin{aligned}&\int_{\mathscr{H}} \mathrm{Tr}\{M[\rho]\rho\}d\rho \\ &= \frac{1}{(d^2-1)}\left[\rho_{aa}\rho_{cc}M_{jj,ii} + \rho_{ac}\rho_{ac}M_{ki,ki}\right] - \\ &- \frac{1}{d(d^2-1)}\left[\rho_{ac}\rho_{ac}M_{jj,ii} + \rho_{aa}\rho_{cc}M_{ki,ki}\right] \\ &= \frac{1}{(d^2-1)}\left[\left(\mathrm{Tr}\{\rho\}\right)^2\mathrm{Tr}\{M\left[\mathbb{1}\right]\} + \mathrm{Tr}\left\{\rho^2\right\}\mathrm{Tr}\{M\}\right] - \\ &- \frac{1}{d(d^2-1)}\left[\mathrm{Tr}\left\{\rho^2\right\}\mathrm{Tr}\{M\left[\mathbb{1}\right]\} + \left(\mathrm{Tr}\{\rho\}\right)^2\mathrm{Tr}\{M\}\right].\end{aligned} \tag{D.15}$$

Returning to the matrix forms from the Einstein sum notation, it can be seen that:

$$\rho_{aa}\rho_{cc} = \left(\mathrm{Tr}\{\rho\}\right)^2, \tag{D.16}$$

$$\rho_{ac}\rho_{ac} = \mathrm{Tr}\left\{\rho^2\right\}, \tag{D.17}$$

$$M_{jj,ii} = \mathrm{Tr}\{M\left[\mathbb{1}\right]\}, \tag{D.18}$$

$$M_{ki,ki} = \mathrm{Tr}\{M\}, \tag{D.19}$$

which results in

$$\begin{aligned}&\int_{\mathscr{H}} \mathrm{Tr}\{M[\rho]\rho\}d\rho \\ &= \frac{1}{(d^2-1)}\left[(\mathrm{Tr}\{\rho\})^2\,\mathrm{Tr}\{M\,[\mathbb{1}]\} + \mathrm{Tr}\{\rho^2\}\,\mathrm{Tr}\{M\}\right] - \\ &- \frac{1}{d(d^2-1)}\left[\mathrm{Tr}\{\rho^2\}\,\mathrm{Tr}\{M\,[\mathbb{1}]\} + (\mathrm{Tr}\{\rho\})^2\,\mathrm{Tr}\{M\}\right]. \end{aligned} \tag{D.20}$$

Finally, noting that $\mathrm{Tr}\{\rho\} = 1$, $\mathrm{Tr}\{\rho^2\} = 1$ and $\rho^2 = \rho$, we arrive at

$$\int_{\mathscr{H}} \mathrm{Tr}\{M[\rho]\rho\}d\rho = \frac{\mathrm{Tr}\{M\} + \mathrm{Tr}\{M\,[\mathbb{1}]\}}{d(d+1)} \tag{D.21}$$

$$= \frac{\mathrm{Tr}\{M\}}{d(d+1)}, \tag{D.22}$$

since for the cases where M is composed of a traceless Lindbladian operator $\mathcal{L}$, $\mathrm{Tr}\{M[\mathbb{1}]\} = 0$, and we obtain (5.30) in the main text.

D.2.4 Boundedness of the AGI

We make use of the relation in Eq. (D.21) to prove that, in the limit of strong dephasing, the AGI of a single qudit is bounded above and below, with the bounds depending only on the dimension of the system.

Theorem D.2.2. *Consider an open quantum system of a single qudit of dimension d, initiated in a pure state $\mathrm{Tr}\{\rho_0^2\} = 1$, under the influence of a time-independent noise superoperator $\mathcal{L}$ with coupling constant γ and pure dephasing collapse operator $L = J_z$, and evolving via an arbitrary time-independent unitary superoperator $\mathcal{S}$ over time t. Then, in the limit of strong coupling where $(\gamma t) \gg 1$, the AGI $\mathcal{I}$ is bounded in the region*

$$1 - \frac{2}{d+1} \leq \mathcal{I} \leq 1 - \frac{1}{d+1}. \tag{D.23}$$

Proof. In superoperator form, the quantum channel can be written as $\mathcal{E} = \mathcal{U} \circ M$. Now, since the channel is completely positive and trace-preserving (CPTP) and $\mathcal{U}$ is a unitary operator, M must also be CPTP. Substituting this into the integral equation for the AGF in (5.8) from the main text and using Eq. (D.21), we have

$$\mathcal{F} = \frac{\mathrm{Tr}\{M\} + \mathrm{Tr}\{M\,[\mathbb{1}]\}}{d(d+1)}. \tag{D.24}$$

Therefore, proving the bound on $\mathcal{I}$ is equivalent to proving that

$$1 \leq (d+1)\mathcal{F} \leq 2, \tag{D.25}$$

$$d \leq \mathrm{Tr}\{M\} + \mathrm{Tr}\{M\,[\mathbb{1}]\} \leq 2d, \tag{D.26}$$

$$0 \leq \mathrm{Tr}\{M\} \leq d, \tag{D.27}$$

since $\mathrm{Tr}\{M\,[\mathbb{1}]\} = \mathrm{Tr}\{\mathbb{1}\} = d$ due to the trace-preservation of M.

Now, to show this, consider the action of M on the state ρ. The collapse operator $L = J_z$ of pure dephasing is a diagonal matrix which preserves the populations of ρ while causing

the coherences to decay to zero. Thus,

$$M \ : \ \rho \to \sum_{i=0}^{d-1} \rho'_{ii} \, |i\rangle\langle i| \tag{D.28}$$

$$\forall \rho \ , \ M_{ij}^{kl} \rho_{kl} \propto \delta_{ij} \tag{D.29}$$

$$M_{ij}^{kl} = \lambda_i^{kl} \delta_{ij}. \tag{D.30}$$

In the Kraus representation, using $M = \sum_{k=1}^{K} E_k^* \otimes E_k$, the matrix elements are given, trivially, by

$$M_{ij}^{nm} = \sum_{k=1}^{K} E_{k,jm}^* E_{k,in}, \tag{D.31}$$

and, since M is trace-preserving,

$$\forall n, m, \ \sum_{i=0}^{d-1} M_{ii}^{nm} = \sum_{k=1}^{K} \sum_{i=0}^{d-1} E_{k,im}^* E_{k,in} \tag{D.32}$$

$$= \delta_{nm}. \tag{D.33}$$

Furthermore,

$$\mathrm{Tr}\{M\rho\} = \mathrm{Tr}\{\rho\} \tag{D.34}$$

$$\mathrm{vec}(\mathbb{1})^{\mathrm{T}} \cdot M \cdot \mathrm{vec}(\rho) = \mathrm{vec}(\mathbb{1})^{\mathrm{T}} \cdot \mathrm{vec}(\rho) \tag{D.35}$$

$$\therefore \sum_{n=0}^{d-1} M_{ij}^{nn} = \delta_{ij}. \tag{D.36}$$

Thus, in particular, if $n = m$:

$$\sum_{k=1}^{K} \sum_{i=0}^{d-1} |E_{k,in}|^2 = 1 \tag{D.37}$$

$$\iff \sum_{k, \, i=n} |E_{k,in}|^2 + \sum_{k, \, i \neq n} |E_{k,in}|^2 = 1 \tag{D.38}$$

$$\therefore \forall n \ , \ 0 \leq \sum_{k=1}^{K} |E_{k,nn}|^2 \leq 1 \tag{D.39}$$

Moreover, since

$$\mathrm{Tr}\{M\} = \sum_{k, \, ij} E_{k, \, jj}^* E_{k, \, ii} \tag{D.40}$$

$$= \sum_{k} |\mathrm{Tr}\{E_k\}|^2, \tag{D.41}$$

the trace of M can be equivalently expressed by

$$\mathrm{Tr}\{M\} = \sum_{i=0}^{d-1} \sum_{j=0}^{d-1} M_{ij}^{ij} \tag{D.42}$$

$$= \sum_{i=0}^{d-1} M_{ii}^{ii} \tag{D.43}$$

$$= \sum_{k=1}^{K} \sum_{i=0}^{d-1} |E_{k, \, ii}|^2. \tag{D.44}$$

Therefore, combining this last expression with Eq. (D.39) where each of the d elements $|E_{k,ii}|^2$ are bounded above by 1, it is clear that the sum of all d of them, and thus $\mathrm{Tr}\{M\}$, must be bounded by d,

$$0 \leq \sum_{k}^{K} \sum_{i=0}^{d-1} |E_{k,ii}|^2 \leq d, \tag{D.45}$$

proving the boundedness of $\mathcal{F}$ and $\mathcal{I}$. □

D.2.5 Gate-Independent Correction Terms

We found in (5.31) in Section 5.4.1 that the m-th order AGI correction always contains a gate-independent term proportional to the trace of the m-th power of the collapse operator $\mathcal{L}$ in superoperator form. Moreover, in (5.65) and (5.73) in Section 5.4.5 in the main text we presented the first- and second-order gate-independent AGI correction terms.

Since we have from (5.12) in the main text an expression for $\mathcal{L}$ in terms of the (regular) collapse operators L, we can use this to express the correction terms in terms of L instead. To first-order,

$$\begin{aligned}
\mathrm{Tr}\{\mathcal{L}\} &= \mathrm{Tr}\Big\{L^* \otimes L - \frac{1}{2}\Big(L^\dagger L \otimes \mathbb{1}_d + \big(\mathbb{1}_d \otimes L^\dagger L\big)^T\Big)\Big\} \\
&= \mathrm{Tr}\{L^* \otimes L\} - \frac{1}{2}\mathrm{Tr}\Big\{L^\dagger L \otimes \mathbb{1}_d + \mathbb{1}_d \otimes \big(L^\dagger L\big)^T\Big\} \\
&= \mathrm{Tr}\{L^*\}\,\mathrm{Tr}\{L\} - \frac{d}{2}\Big(\mathrm{Tr}\Big\{L^\dagger L\Big\} + \mathrm{Tr}\Big\{\big(L^\dagger L\big)^T\Big\}\Big) \\
&= |\mathrm{Tr}\{L\}|^2 - d\,\mathrm{Tr}\Big\{L^\dagger L\Big\},
\end{aligned} \tag{D.46}$$

giving the result of (5.66) in the main text.

By the same procedure, it is trivial to see that the second-order term in (5.78) of the main text is given by,

$$\mathrm{Tr}\{\mathcal{L}^2\} = \big|\mathrm{Tr}\{L^2\}\big|^2 + \frac{1}{2}\Big|\mathrm{Tr}\Big\{L^\dagger L\Big\}\Big|^2 + \frac{d}{2}\,\mathrm{Tr}\Big\{(L^\dagger L)^2\Big\}. \tag{D.47}$$

Furthermore, it is possible to make use of the multinomial expansion to find the m-th power trace to arbitrary order. In general this produces a non-trivial sum over all L-words of length m. In the specific case of real and symmetric collapse operators $L = L^* = L^T = L^\dagger$, these words can be factorised, resulting in the triangular sum

$$\begin{aligned}
&\mathrm{Tr}\{\mathcal{L}^m\} \\
&= \mathrm{Tr}\Big\{\Big(L^* \otimes L - \frac{1}{2}\Big(L^\dagger L \otimes \mathbb{1}_d + \big(\mathbb{1}_d \otimes L^\dagger L\big)^T\Big)\Big)^m\Big\} \\
&= \sum_{k_1+k_2+k_3=m} \frac{m!\,\mathrm{Tr}\Big\{(L^*)^{k_1}(L^\dagger L)^{k_2} \otimes L^{k_1}((L^\dagger L)^T)^{k_3}\Big\}}{(-2)^{k_2+k_3}k_1!k_2!k_3!} \\
&= m! \sum_{k_1+k_2+k_3=m} \frac{\mathrm{Tr}\Big\{L^{k_1+2k_2}\Big\}\,\mathrm{Tr}\Big\{L^{k_1+2k_3}\Big\}}{(-2)^{k_2+k_3}k_1!k_2!k_3!}. \\
&= m! \sum_{k_1=0}^{m} \sum_{k_2=0}^{m-k_1} \frac{\mathrm{Tr}\Big\{L^{k_1+2k_2}\Big\}\,\mathrm{Tr}\Big\{L^{2m-k_1-2k_2}\Big\}}{(-2)^{m-k_1-1}k_1!k_2!(m-k_1-k_2)!}.
\end{aligned} \tag{D.48}$$

D.2.6 Second-order Gate-Dependent Correction Term

Beginning with the general expression for the second-order term in the AGI expansion in (5.30) of the main text, and combining with the $m = 2$ term $M^{(2)}(t)$ in (5.27) of the main text, we obtain the result of (5.70) in the main text,

$$\mathcal{I}^{(2)} = \frac{-(\gamma t)^2}{d(d+1)} \operatorname{Tr}\left\{M^{(2)}(t)\right\} \tag{D.49}$$

$$= \frac{-(\gamma t)^2}{d(d+1)} \operatorname{Tr}\left\{ \frac{\mathcal{L}^2}{2!} + \sum_{n_1=1}^{\infty}\sum_{n_2=1}^{\infty} \left(\prod_{i=1}^{2} \frac{(-t)^{n_i}[(\mathcal{S})^{n_i}, \mathcal{L}]}{n_i! \sum_{j=i}^{2}(n_j+1)} \right) \right\} \tag{D.50}$$

$$= \frac{-(\gamma t)^2}{d(d+1)} \left(\operatorname{Tr}\left\{\frac{\mathcal{L}^2}{2!}\right\} + \sum_{n_1=1}^{\infty}\sum_{n_2=1}^{\infty} \frac{(-t)^{n_1+n_2} \operatorname{Tr}\{[(\mathcal{S})^{n_1}, \mathcal{L}][(\mathcal{S})^{n_2}, \mathcal{L}]\}}{n_1! n_2! (n_1+n_2+2)(n_2+1)} \right). \tag{D.51}$$

Focusing now on the gate-dependent terms only, we can express the double summation of the trace term using the relation $n_1 + n_2 + 2 = s$

$$\sum_{n_1=1}^{\infty}\sum_{n_2=1}^{\infty} \frac{(-t)^{n_1+n_2} \operatorname{Tr}\{[(\mathcal{S})^{n_1}, \mathcal{L}][(\mathcal{S})^{n_2}, \mathcal{L}]\}}{n_1! n_2! (n_1+n_2+2)(n_2+1)} \tag{D.52}$$

$$= \sum_{s=0}^{\infty}\sum_{n=0}^{s-2} \frac{(-t)^{s-2} \operatorname{Tr}\{[(\mathcal{S})^{n}, \mathcal{L}]\big[(\mathcal{S})^{s-2-n}, \mathcal{L}\big]\}}{n! s (s-1-n)!} \tag{D.53}$$

$$= \sum_{s=0}^{\infty} \frac{(-t)^{s-2}}{s(s-1)!} \sum_{n=0}^{s-2} \binom{s-1}{n} \operatorname{Tr}\{[(\mathcal{S})^{n}, \mathcal{L}]\big[(\mathcal{S})^{s-2-n}, \mathcal{L}\big]\}. \tag{D.54}$$

Lemma D.2.3. *Given operators A and B the following binomial sum of the product of iterated commutators at order n and $j-n$ is traceless,*

$$\sum_{n=1}^{j} \binom{j+1}{n} \operatorname{Tr}\{[(A)^n, B]\big[(A)^{j-n}, B\big]\} = 0. \tag{D.55}$$

Proof. Using $\binom{j+1}{n} = \binom{j+1-1}{n-1} + \binom{j+1-1}{n}$, we have

$$\sum_{n=1}^{j} \binom{j+1}{n} \operatorname{Tr}\{[(A)^n, B]\big[(A)^{j-n}, B\big]\}$$

$$= \sum_{n=1}^{j} \binom{j}{n-1} \operatorname{Tr}\{[(A)^n, B]\big[(A)^{j-n}, B\big]\} +$$

$$+ \sum_{n=1}^{j} \binom{j}{n} \operatorname{Tr}\{[(A)^n, B]\big[(A)^{j-n}, B\big]\}. \tag{D.56}$$

Now, for the first term with binomial $\binom{j+1-1}{n-1}$ and using the change of index $n = n+1$,

$$\begin{aligned}
&\sum_{n=1}^{j}\binom{j}{n-1}\mathrm{Tr}\big\{\big[(A)^n,B\big]\big[(A)^{j-n},B\big]\big\}\\
&=\sum_{n=0}^{j-1}\binom{j}{n}\mathrm{Tr}\big\{\big[(A)^{n+1},B\big]\big[(A)^{j-n-1},B\big]\big\}\\
&=\sum_{n=0}^{j-1}\binom{j}{n}\mathrm{Tr}\big\{\big[A,\big[(A)^n,B\big]\big]\big[(A)^{j-n-1},B\big]\big\}\\
&=-\sum_{n=0}^{j-1}\binom{j}{n}\mathrm{Tr}\big\{\big[(A)^n,B\big]\big[(A)^{j-n},B\big]\big\},
\end{aligned}\tag{D.57}$$

by cyclic permutation of the trace. This summation is the negation of the second binomial term $\binom{j+1-1}{n}$ for all terms $1 \leq n \leq j-1$. Therefore only the $n=0$ and $n=j$ terms remain. Moreover since $\binom{j}{j} = \binom{j}{0} = 1$, we have that

$$\begin{aligned}
&\sum_{n=1}^{j}\binom{j+1}{n}\mathrm{Tr}\big\{\big[(A)^n,B\big]\big[(A)^{j-n},B\big]\big\}\\
&=\mathrm{Tr}\big\{\big[(A)^j,B\big]B\big\}-\mathrm{Tr}\big\{B\big[(A)^j,B\big]\big\}\\
&=0.
\end{aligned}\tag{D.58}$$

□

Now, applying this result to the summation in Eq. (D.54), where we identify $j = s-2$, we have that all terms for $n \geq 1$ are zero, and therefore only the $n=0$ term survives giving the following relation

$$\sum_{n=0}^{s-2}\binom{s-1}{n}\mathrm{Tr}\big\{\big[(\mathcal{S})^n,\mathcal{L}\big]\big[(\mathcal{S})^{s-2-n},\mathcal{L}\big]\big\}=\mathrm{Tr}\big\{\mathcal{L}\big[(\mathcal{S})^{s-2},\mathcal{L}\big]\big\}.\tag{D.59}$$

From this, with a change of index $s-2=s$, we can rewrite the full second-order correction as

$$\mathcal{I}^{(2)}=\frac{-(\gamma t)^2}{d(d+1)}\left(\frac{\mathrm{Tr}\{\mathcal{L}^2\}}{2}+\sum_{s=2}^{\infty}\frac{(-t)^s\,\mathrm{Tr}\{\mathcal{L}[(\mathcal{S})^s,\mathcal{L}]\}}{(s+2)!}\right),\tag{D.60}$$

giving the result in (5.73) in the main text.

Now, as for the gate-independent terms, we wish to express this gate-dependent trace of superoperators explicitly in terms of the operators H and L.

Beginning with the binomial expansion of the trace of the iterated commutator [195],

$$\begin{aligned}
&\mathrm{Tr}\{\mathcal{L}[(\mathcal{S})^s,\mathcal{L}]\}\\
&=\sum_{k=0}^{s}(-1)^k\binom{s}{k}\mathrm{Tr}\big\{\mathcal{L}\mathcal{S}^k\mathcal{L}\mathcal{S}^{s-k}\big\}\\
&=i^s\sum_{k=0}^{s}\sum_{j=0}^{k}\sum_{l=0}^{s-k}\binom{s}{k}\binom{k}{j}\binom{s-k}{l}(-1)^{s+k-j-l}\times\\
&\times\mathrm{Tr}\Big\{\mathcal{L}\left((H^*)^{k-j}\otimes H^j\right)\mathcal{L}\left((H^*)^{s-k-l}\otimes H^l\right)\Big\},
\end{aligned}\tag{D.61}$$

where we used the binomial expansion of the expression for $\mathcal{S}$ in terms of H in (5.11) from the main text,

$$\mathcal{S}^k = i^k \sum_{j=0}^{k} (-1)^{k-j} \binom{k}{j} (H^*)^{k-j} \otimes H^j. \tag{D.62}$$

Substituting now the expression for $\mathcal{L}$ in terms of L in (5.12) from the main text, and expanding algebraically the products of the operator terms in the trace, we obtain the following nine expressions, the sum of which is equivalent to the superoperator trace (omitting the prefactors and summations for convenience):

$$\operatorname{Tr}\left\{LH^{k-j}LH^{s-k-l}\right\}^* \operatorname{Tr}\left\{LH^jLH^l\right\}, \tag{D.63}$$

$$-\frac{1}{2}\operatorname{Tr}\left\{LH^{k-j}L^TL^*H^{s-k-l}\right\}^* \operatorname{Tr}\left\{LH^{j+l}\right\}, \tag{D.64}$$

$$-\frac{1}{2}\operatorname{Tr}\left\{LH^{s-j-l}\right\}^* \operatorname{Tr}\left\{LH^jL^TL^*H^l\right\}, \tag{D.65}$$

$$-\frac{1}{2}\operatorname{Tr}\left\{L^TL^*H^{k-j}LH^{s-k-l}\right\}^* \operatorname{Tr}\left\{LH^{j+l}\right\}, \tag{D.66}$$

$$\frac{1}{4}\operatorname{Tr}\left\{L^TL^*H^{k-j}L^TL^*H^{s-k-l}\right\}^* \operatorname{Tr}\left\{H^{j+l}\right\}, \tag{D.67}$$

$$\frac{1}{4}\operatorname{Tr}\left\{L^TL^*H^{s-j-l}\right\}^* \operatorname{Tr}\left\{L^TL^*H^{j+l}\right\}, \tag{D.68}$$

$$-\frac{1}{2}\operatorname{Tr}\left\{LH^{s-j-l}\right\}^* \operatorname{Tr}\left\{L^\dagger LH^jLH^l\right\}, \tag{D.69}$$

$$\frac{1}{4}\operatorname{Tr}\left\{L^TL^*H^{s-j-l}\right\}^* \operatorname{Tr}\left\{L^\dagger LH^{j+l}\right\}, \tag{D.70}$$

$$\frac{1}{4}\operatorname{Tr}\left\{H^{s-j-l}\right\}^* \operatorname{Tr}\left\{L^\dagger LH^jL^TL^*H^l\right\}. \tag{D.71}$$

Now, we can simplify these expressions by making the following observations: Firstly, s must be even since (i) heuristically, the trace must be real since we are calculating the fidelity (a real quantity) and therefore the prefactor i^s in Eq. (D.61) cannot be imaginary, and (ii) formally we prove this in Appendix D.2.7. Secondly, by symmetry of the binomial expansions, we are free to make the following change of variables:

$$\begin{aligned} j &\to k - j, \\ l &\to s - k - l. \end{aligned}$$

For clarity, note that this change of variables does not affect the prefactor

$$(-1)^{s+k-j-l} \to (-1)^{j+k+l},$$

since, with s even, the ratio of these two terms is always a power of 2 and therefore equal to 1.

As an example to illustrate the effect of this change of variables, for the first term Eq. (D.63), the forward and backwards sums are complex conjugates and therefore only

the real part can remain (omitting prefactors of the full expression):

$$\begin{aligned}
&\sum_{j=0}^{k}\sum_{l=0}^{s-k}\mathrm{Tr}\left\{LH^{k-j}LH^{s-k-l}\right\}^{*}\mathrm{Tr}\left\{LH^{j}LH^{l}\right\} \\
\rightarrow&\sum_{j=0}^{k}\sum_{l=0}^{s-k}\mathrm{Tr}\left\{LH^{j}LH^{l}\right\}^{*}\mathrm{Tr}\left\{LH^{k-j}LH^{s-k-l}\right\} \qquad \text{(D.72)}\\
\Longrightarrow&\sum_{j=0}^{k}\sum_{l=0}^{s-k}\mathrm{Tr}\left\{LH^{k-j}LH^{s-k-l}\right\}^{*}\mathrm{Tr}\left\{LH^{j}LH^{l}\right\} \\
=&\sum_{j=0}^{k}\sum_{l=0}^{s-k}\mathrm{Re}\left\{\mathrm{Tr}\left\{LH^{k-j}LH^{s-k-l}\right\}^{*}\mathrm{Tr}\left\{LH^{j}LH^{l}\right\}\right\}. \qquad \text{(D.73)}
\end{aligned}$$

Similarly, by comparing the remaining terms in Eqs. (D.64) to (D.71) with their counterparts following the change of variables, it is possible to identify the following sums as complex conjugates of one another:

$$\begin{aligned}
\sum_{j=0}^{k}\sum_{l=0}^{s-k}(D.64+D.65)&=\sum_{j=0}^{k}\sum_{l=0}^{s-k}2\,\mathrm{Re}\{D.64\},\\
\sum_{j=0}^{k}\sum_{l=0}^{s-k}(D.66+D.69)&=\sum_{j=0}^{k}\sum_{l=0}^{s-k}2\,\mathrm{Re}\{D.66\},\\
\sum_{j=0}^{k}\sum_{l=0}^{s-k}(D.68+D.70)&=\sum_{j=0}^{k}\sum_{l=0}^{s-k}2\,\mathrm{Re}\{D.68\},\\
\sum_{j=0}^{k}\sum_{l=0}^{s-k}(D.67+D.71)&=\sum_{j=0}^{k}\sum_{l=0}^{s-k}2\,\mathrm{Re}\{D.67\}.
\end{aligned}$$

Hence, by combining all of these terms into the full expression for $\mathrm{Tr}\{\mathcal{L}[(\mathcal{S})^{s},\mathcal{L}]\}$ in Eq. (D.61), we obtain the following result of (5.81) in the main text:

$$\begin{aligned}
&\mathrm{Tr}\{\mathcal{L}[(\mathcal{S})^{s},\mathcal{L}]\}\\
&=\sum_{k=0}^{s}\sum_{j=0}^{k}\sum_{l=0}^{s-k}\binom{s}{k}\binom{k}{j}\binom{s-k}{l}(-1)^{s+k-j-l}\times\\
&\times\mathrm{Re}\Bigg[\mathrm{Tr}\left\{LH^{k-j}LH^{s-k-l}\right\}^{*}\mathrm{Tr}\left\{LH^{j}LH^{l}\right\}\\
&+\frac{1}{2}\mathrm{Tr}\left\{L^{T}L^{*}H^{s-j-l}\right\}^{*}\mathrm{Tr}\left\{L^{T}L^{*}H^{j+l}\right\}\\
&+\frac{1}{2}\mathrm{Tr}\left\{L^{T}L^{*}H^{k-j}L^{T}L^{*}H^{s-k-l}\right\}^{*}\mathrm{Tr}\left\{H^{j+l}\right\}\\
&-\mathrm{Tr}\left\{LH^{k-j}L^{T}L^{*}H^{s-k-l}\right\}^{*}\mathrm{Tr}\left\{LH^{j+l}\right\}\\
&-\mathrm{Tr}\left\{L^{T}L^{*}H^{k-j}LH^{s-k-l}\right\}^{*}\mathrm{Tr}\left\{LH^{j+l}\right\}\Bigg].
\end{aligned}\qquad \text{(D.74)}$$

D.2.7 Tracelessness of the Odd-Order Iterated Commutator

Theorem D.2.4. *Given two operators A and B, the product of B with the iterated commutator of order s, $B[(A)^s, B]$, is traceless for all odd s,*

$$\forall\, s = 2k+1\,,\; k \in \mathbb{Z}\,,\; \mathrm{Tr}\{B[(A)^s, B]\} = 0. \tag{D.75}$$

Proof. We begin with the trace of the binomial expansion of the iterated commutator [195],

$$B[(A)^s, B] = \sum_{k=0}^{s} (-1)^k \binom{s}{k} BA^{s-k}BA^k \tag{D.76}$$

$$\therefore \mathrm{Tr}\{B[(A)^s, B]\} = \sum_{k=0}^{s} (-1)^k \binom{s}{k} \mathrm{Tr}\left\{BA^{s-k}BA^k\right\}. \tag{D.77}$$

By symmetry of the binomial expansion $\binom{s}{k} = \binom{s}{s-k}$, and considering s odd $(-1)^{s-k} = -(-1)^k$, we can write the equivalent expansion

$$B[(A)^s, B] = -\sum_{k=0}^{s} (-1)^k \binom{s}{k} BA^kBA^{s-k} \tag{D.78}$$

$$\therefore \mathrm{Tr}\{B[(A)^s, B]\} = -\sum_{k=0}^{s} (-1)^k \binom{s}{k} \mathrm{Tr}\left\{BA^kBA^{s-k}\right\} \tag{D.79}$$

$$= -\sum_{k=0}^{s} (-1)^k \binom{s}{k} \mathrm{Tr}\left\{BA^{s-k}BA^k\right\}, \tag{D.80}$$

by cyclic permutation of the trace, $\mathrm{Tr}\{CD\} = \mathrm{Tr}\{DC\} \implies \mathrm{Tr}\{[C, D]\} = 0$. Hence, we have the result for odd s that

$$\mathrm{Tr}\{B[(A)^s, B]\} = -\,\mathrm{Tr}\{B[(A)^s, B]\} \tag{D.81}$$

$$\implies \mathrm{Tr}\{B[(A)^s, B]\} = 0, \tag{D.82}$$

thus completing the proof. □

References Cited in this Appendix

[183] J. E. Campbell. "On a Law of Combination of Operators bearing on the Theory of Continuous Transformation Groups". In: *Proceedings of the London Mathematical Society* s1-28.1 (Nov. 1896), pp. 381–390. DOI: 10.1112/plms/s1-28.1.381.

[184] B. C. Hall. *Lie groups, Lie algebras, and representations: an elementary introduction*. Second edition. Graduate texts in mathematics 222. Cambridge, NY: Springer, 2015. 449 pp. DOI: 10.1007/978-3-319-13467-3.

[185] B. Collins, S. Matsumoto, et al. "The Weingarten Calculus". In: *Notices of the American Mathematical Society* 69.5 (May 1, 2022), p. 1. DOI: 10.1090/noti2474.

[195] H. C. Volkin, U. S. N. Aeronautics, et al. *Iterated commutators and functions of operators*. NASA technical note. National Aeronautics and Space Administration, 1968.

APPENDIX E

APPENDICES TO CHAPTER 6

E.1 Numerical Methods

Here we list more detailed functional definitions of the numerical methods used in the calculations discussed in the main text.

1. **Qudit**
   (a) The `Qudit` class represents the qudit system, including its dimensions, basis states, and corresponding operators.
   (b) Relationships:
      i. It interacts with other classes such as `QuditGate`, `NoiseGenerator`, and pulse sequence classes like `GRAPE`, `QR`, etc.
2. **QuditGate**
   (a) The `QuditGate` class is used to create and manipulate quantum gates applicable to qudit systems.
   (b) Relationships:
      i. It is utilized within the `PulseSequence` class to generate the necessary gate operations.
      ii. It interacts with the `Qudit` class to ensure gate operations are compatible with the qudit system's dimensionality.
3. **PulseSequence**
   (a) The `PulseSequence` class generates the pulse sequences required to implement the quantum gates on the qudit system.
   (b) Relationships:
      i. It uses the `QuditGate` class to obtain the matrix representation of the gate.
      ii. It interacts with different pulse generation methods such as `GRAPE`, `QR`, `PMPINN`, and `MATRIXLOG`.
4. **MultiPulse**
   (a) The `MultiPulse` class manages multichromatic pulse sequences for qudit systems.
   (b) Relationships:
      i. It interacts with the `ComplexPulse` and `Pulse` classes to represent the combination of different pulse sequences.
5. **ComplexPulse**
   (a) The `ComplexPulse` class represents a pulse with both real and imaginary components.
   (b) Relationships:
      i. It is used by the `MultiPulse` class to manage pulses with complex amplitudes.

6. **Pulse**
   (a) The `Pulse` class represents a single control pulse for the qudit system.
   (b) Relationships:
      i. It serves as a base class for more complex pulse types, such as `ComplexPulse`.
      ii. It is managed by the `MultiPulse` class to create sequences of pulses.
7. **GRAPE**
   (a) The `GRAPE` class implements the Gradient Ascent Pulse Engineering algorithm for generating pulse sequences.
   (b) Relationships:
      i. Child class inheriting from the `Pulse` base class, used by the `PulseSequence` class.
8. **QR**
   (a) The `QR` class implements the Givens Rotation Decomposition algorithm for generating pulse sequences.
   (b) Relationships:
      i. Child class inheriting from the `Pulse` base class, used by the `PulseSequence` class.
9. **PMPINN**
   (a) The `PMPINN` class uses Physics-Informed Neural Networks (PINNs) and the Pontryagin Maximum Principle (PMP) to generate pulse sequences.
   (b) Relationships:
      i. Child class inheriting from the `Pulse` base class, used by the `PulseSequence` class.
10. **MATRIXLOG**
   (a) The `MATRIXLOG` class generates pulse sequences using the simple and idealised matrix logarithm.
   (b) Relationships:
      i. Child class inheriting from the `Pulse` base class, used by the `PulseSequence` class.
11. **NoiseGenerator**
   (a) The `NoiseGenerator` class generates noise values for control and environment noise types.
   (b) Relationships:
      i. It interacts with the `PulseSequence` class to simulate the effect of noise on the generated pulse sequences.
      ii. It also works with the `Qudit` class to ensure noise is applied consistently across all qudit operations.

12. **Config**
    (a) The `Config` class reads and manages the configuration settings for the simulation.
    (b) Relationships:
        i. It interacts with all other classes to provide the necessary configuration settings.
13. **ConfigData**
    (a) The `ConfigData` class structures the configuration data for easy access and modification.
    (b) Relationships:
        i. It is used by the `ConfigManager` class to load and validate the configuration data.
14. **ConfigManager**
    (a) The `ConfigManager` class manages the entire configuration process, including loading, validating, and applying the configuration settings.
    (b) Relationships:
        i. It interacts with the `Config` and `ConfigData` classes to manage the configuration.
15. **DatabaseManager**
    (a) The `DatabaseManager` class provides an interface for creating, adding, deleting, and querying the database of simulation results.
    (b) Relationships:
        i. It interacts with the classes in `db_tables` to manage database records for simulations of quantum gates, pulse sequences, metrics, and other related data.
16. **db_tables**
    (a) The `db_tables` module defines several classes representing the database schema, including `QuantumGate`, `PulseSequence`, `Metrics`, `Fidelity`, `DissipatorType`, `DissipatorCoupling`, `HamiltonianCoupling`, `ControlNoiseType`, and `ControlNoise`.
    (b) Relationships:
        i. These classes are used by the `DatabaseManager` class to perform database operations.
        ii. They define relationships such as one-to-many and many-to-one between quantum gates, pulse sequences, and their associated metrics and noise types.

Bibliography

[1] O. Ezratty. "Perspective on superconducting qubit quantum computing". In: *The European Physical Journal A* 59.5 (May 2, 2023), p. 94. DOI: 10.1140/epja/s10050-023-01006-7.

[2] R. P. Feynman. "Simulating physics with computers". In: *International Journal of Theoretical Physics* 21.6 (June 1982), pp. 467–488. DOI: 10.1007/BF02650179.

[3] "40 years of quantum computing". In: *Nature Reviews Physics* 4.1 (Jan. 10, 2022), pp. 1–1. DOI: 10.1038/s42254-021-00410-6.

[4] J. I. Manin. "Mathematics as Metaphor: Selected Essays of Yuri I. Manin". In: *Philosophia Mathematica* 17.1 (Apr. 1, 2008), pp. 122–123. DOI: 10.1093/philmat/nkn013.

[5] P. Benioff. "The computer as a physical system: A microscopic quantum mechanical Hamiltonian model of computers as represented by Turing machines". In: *Journal of Statistical Physics* 22.5 (May 1980), pp. 563–591. DOI: 10.1007/BF01011339.

[6] D. Deutsch. "Quantum theory, the Church–Turing principle and the universal quantum computer". In: *Proceedings of the Royal Society of London. A. Mathematical and Physical Sciences* 400.1818 (July 8, 1985), pp. 97–117. DOI: 10.1098/rspa.1985.0070.

[7] P. W. Shor. "Polynomial-Time Algorithms for Prime Factorization and Discrete Logarithms on a Quantum Computer". In: *SIAM Journal on Computing* 26.5 (Oct. 1997), pp. 1484–1509. DOI: 10.1137/S0097539795293172.

[8] L. K. Grover. "A fast quantum mechanical algorithm for database search". In: *Proceedings of the twenty-eighth annual ACM symposium on Theory of computing - STOC '96*. Philadelphia, Pennsylvania, United States: ACM Press, 1996, pp. 212–219. DOI: 10.1145/237814.237866.

[9] S. Lloyd. "Universal Quantum Simulators". In: *Science* 273.5278 (Aug. 23, 1996), pp. 1073–1078. DOI: 10.1126/science.273.5278.1073.

[10] M. Veldhorst, H. G. J. Eenink, et al. "Silicon CMOS architecture for a spin-based quantum computer". In: *Nature Communications* 8.1 (Dec. 15, 2017), p. 1766. DOI: 10.1038/s41467-017-01905-6.

[11] M. F. Gonzalez-Zalba, S. De Franceschi, et al. "Scaling silicon-based quantum computing using CMOS technology". In: *Nature Electronics* 4.12 (Dec. 20, 2021), pp. 872–884. DOI: 10.1038/s41928-021-00681-y.

[12] D. Spicer. "The First Computers: History and Architectures (review)". In: *Technology and Culture* 42.3 (July 2001), pp. 615–617. DOI: 10.1353/tech.2001.0140.

[13] M. Kjaergaard, M. E. Schwartz, et al. *Programming a quantum computer with quantum instructions*. Dec. 28, 2020. DOI: https://doi.org/10.48550/arXiv.2001.08838.

[14] I. Pogorelov et al. "Compact Ion-Trap Quantum Computing Demonstrator". In: *PRX Quantum* 2.2 (June 2021), p. 020343. DOI: 10.1103/PRXQuantum.2.020343.

[15] C. D. Bruzewicz, J. Chiaverini, et al. "Trapped-ion quantum computing: Progress and challenges". In: *Applied Physics Reviews* 6.2 (June 1, 2019), p. 021314. DOI: 10.1063/1.5088164.

[16] Y. Chi, J. Huang, et al. "A programmable qudit-based quantum processor". In: *Nature Communications* 13.1 (Mar. 4, 2022), p. 1166. DOI: 10.1038/s41467-022-28767-x.

[17] S. Slussarenko and G. J. Pryde. "Photonic quantum information processing: A concise review". In: *Applied Physics Reviews* 6.4 (Dec. 1, 2019), p. 041303. DOI: 10.1063/1.5115814.

[18] M. Morgado and S. Whitlock. "Quantum simulation and computing with Rydberg-interacting qubits". In: *AVS Quantum Science* 3.2 (June 1, 2021), p. 023501. DOI: 10.1116/5.0036562.

[19] I. S. Madjarov et al. "High-fidelity entanglement and detection of alkaline-earth Rydberg atoms". In: *Nature Physics* 16.8 (Aug. 2020), pp. 857–861. DOI: 10.1038/s41567-020-0903-z.

[20] A. Chiesa et al. "Blueprint for a molecular-spin quantum processor". In: *Physical Review Applied* 19 (June 2023). Publisher: American Physical Society, p. 064060. DOI: 10.1103/PhysRevApplied.19.064060.

[21] E. Moreno-Pineda, C. Godfrin, et al. "Molecular Spin Qudits for Quantum Algorithms". In: *Chemical Society Reviews* 47.2 (2018), pp. 501–513. DOI: 10.1039/c5cs00933b.

[22] Alejandro Gaita-Ariño, Fernando Luis, et al. "Molecular spins for quantum computation." In: *Nature Chemistry* 11.4 (Apr. 1, 2019). MAG ID: 2924254540, pp. 301–309. DOI: 10.1038/s41557-019-0232-y.

[23] G. Burkard, T. D. Ladd, et al. "Semiconductor spin qubits". In: *Reviews of Modern Physics* 95.2 (June 14, 2023), p. 025003. DOI: 10.1103/RevModPhys.95.025003.

[24] X. Zhang, H.-O. Li, et al. "Semiconductor quantum computation". In: *National Science Review* 6.1 (Jan. 1, 2019), pp. 32–54. DOI: 10.1093/nsr/nwy153.

[25] F. Flamini, N. Spagnolo, et al. "Photonic quantum information processing: a review". In: *Reports on Progress in Physics* 82.1 (Jan. 1, 2019), p. 016001. DOI: 10.1088/1361-6633/aad5b2.

[26] F. Arute, K. Arya, et al. "Quantum supremacy using a programmable superconducting processor". In: *Nature* 574.7779 (Oct. 24, 2019), pp. 505–510. DOI: 10.1038/s41586-019-1666-5.

[27] *First IBM Quantum Data Center in Europe Opens; Will Include IBM's Most Performant Quantum Systems*. IBM Newsroom. URL: https://newsroom.ibm.com/2024-10-01-first-ibm-quantum-data-center-in-europe-opens-will-include-ibms-most-performant-quantum-systems (visited on 10/02/2024).

[28] D. Castelvecchi. "Quantum computers ready to leap out of the lab in 2017". In: *Nature* 541.7635 (Jan. 2017), pp. 9–10. DOI: 10.1038/541009a.

[29] S. Krinner et al. "Realizing repeated quantum error correction in a distance-three surface code". In: *Nature* 605.7911 (May 2022), pp. 669–674. DOI: 10.1038/s41586-022-04566-8.

[30] D. P. DiVincenzo. "The Physical Implementation of Quantum Computation". In: *Fortschritte der Physik* 48.9 (Sept. 2000), pp. 771–783. DOI: 10.1002/1521-3978(200009)48:9/11<771::AID-PROP771>3.0.CO;2-E.

[31] Y. Wang, Z. Hu, et al. "Qudits and High-Dimensional Quantum Computing". In: *Frontiers in Physics* 8 (Nov. 10, 2020), p. 589504. DOI: 10.3389/fphy.2020.589504.

[32] N. P. Brusentsov and J. Ramil Alvarez. "Ternary Computers: The Setun and the Setun 70". In: *Perspectives on Soviet and Russian Computing*. Ed. by J. Impagliazzo and E. Proydakov. Vol. 357. IFIP Advances in Information and Communication Technology. Berlin, Heidelberg: Springer Berlin Heidelberg, 2011, pp. 74–80. DOI: 10.1007/978-3-642-22816-2_10.

[33] A. Chiesa, F. Petiziol, et al. "Embedded quantum-error correction and controlled-phase gate for molecular spin qubits". In: *AIP Advances* 11.2 (Feb. 1, 2021), p. 025134. DOI: 10.1063/9.0000166.

[34] N. P. D. Sawaya, T. Menke, et al. "Resource-efficient digital quantum simulation of d-level systems for photonic, vibrational, and spin-s Hamiltonians". In: *npj Quantum Information* 6.1 (June 2, 2020), p. 49. DOI: 10.1038/s41534-020-0278-0.

[35] M. N. Leuenberger and D. Loss. "Grover algorithm for large nuclear spins in semiconductors". In: *Physical Review B* 68.16 (Oct. 16, 2003), p. 165317. DOI: 10.1103/PhysRevB.68.165317.

[36] A. Mair, A. Vaziri, et al. "Entanglement of the orbital angular momentum states of photons". In: *Nature* 412.6844 (July 2001), pp. 313–316. DOI: 10.1038/35085529.

[37] F. A. An, A. Ransford, et al. "High Fidelity State Preparation and Measurement of Ion Hyperfine Qubits with I $>$ 1 2". In: *Physical Review Letters* 129.13 (Sept. 19, 2022), p. 130501. DOI: 10.1103/PhysRevLett.129.130501.

[38] C. Adambukulam, B. C. Johnson, et al. "Hyperfine Spectroscopy and Fast, All-Optical Arbitrary State Initialization and Readout of a Single, Ten-Level Ge 73 Vacancy Nuclear Spin Qudit in Diamond". In: *Physical Review Letters* 132.6 (Feb. 9, 2024), p. 060603. DOI: 10.1103/PhysRevLett.132.060603.

[39] B. L. Brock, S. Singh, et al. *Quantum Error Correction of Qudits Beyond Break-even*. Sept. 23, 2024. DOI: https://doi.org/10.48550/arXiv.2409.15065.

[40] L. E. Fischer, D. Miller, et al. "Ancilla-free implementation of generalized measurements for qubits embedded in a qudit space". In: *Physical Review Research* 4.3 (July 11, 2022), p. 033027. DOI: 10.1103/PhysRevResearch.4.033027.

[41] E. Moreno-Pineda and W. Wernsdorfer. "Measuring molecular magnets for quantum technologies". In: *Nature Reviews Physics* 3.9 (Sept. 2021), pp. 645–659. DOI: 10.1038/s42254-021-00340-3.

[42] S. Thiele, F. Balestro, et al. "Electrically driven nuclear spin resonance in single-molecule magnets". In: *Science* 344.6188 (June 6, 2014), pp. 1135–1138. DOI: 10.1126/science.1249802.

[43] C. Godfrin, A. Ferhat, et al. "Operating Quantum States in Single Magnetic Molecules: Implementation of Grover's Quantum Algorithm". In: *Physical Review Letters* 119.18 (Nov. 2, 2017), p. 187702. DOI: 10.1103/PhysRevLett.119.187702.

[44] A. L. Thomas. *Phthalocyanine Research and Applications*. 1st ed. Boca Raton: CRC Press, Sept. 25, 2024. DOI: 10.1201/9781003574231.

[45] P. Gregory. "Industrial applications of phthalocyanines". In: *Journal of Porphyrins and Phthalocyanines* 04.4 (June 2000). Publisher: World Scientific Publishing Co., pp. 432–437. DOI: 10.1002/(SICI)1099-1409(200006/07)4:4<432::AID-JPP254>3.0.CO;2-N.

[46] B. E. Williamson, T. C. VanCott, et al. "Determination of the ground state of manganese phthalocyanine in an argon matrix using magnetic circular dichroism and absorption spectroscopy". In: *Journal of the American Chemical Society* 114.7 (Mar. 1992), pp. 2412–2419. DOI: 10.1021/ja00033a016.

[47] Naoto Ishikawa, Miki Sugita, et al. "Lanthanide Double-Decker Complexes Functioning as Magnets at the Single-Molecular Level". In: *Journal of the American Chemical Society* 125.29 (June 25, 2003), pp. 8694–8695. DOI: 10.1021/ja029629n.

[48] N. Ishikawa, M. Sugita, et al. "Quantum Tunneling of Magnetization in Lanthanide Single-Molecule Magnets". In: *Angewandte Chemie International Edition* 44.19 (May 6, 2005), pp. 2931–2935. DOI: 10.1002/anie.200462638.

[49] L. Thomas, F. Lionti, et al. "Macroscopic quantum tunnelling of magnetization in a single crystal of nanomagnets". In: *Nature* 383.6596 (Sept. 1996), pp. 145–147. DOI: 10.1038/383145a0.

[50] H. Biard, E. Moreno-Pineda, et al. "Increasing the Hilbert space dimension using a single coupled molecular spin". In: *Nature Communications* 12.1 (Dec. 2021), p. 4443. DOI: 10.1038/s41467-021-24693-6.

[51] W. Wernsdorfer. "From micro- to nano-SQUIDs: applications to nanomagnetism". In: *Superconductor Science and Technology* 22.6 (June 1, 2009), p. 064013. DOI: 10.1088/0953-2048/22/6/064013.

[52] Romain Vincent, Svetlana Klyatskaya, et al. "Electronic read-out of a single nuclear spin using a molecular spin transistor". In: *Nature* 488.7411 (Aug. 16, 2012), pp. 357–360. DOI: 10.1038/nature11341.

[53] J. Angel and P. Sandars. "The hyperfine structure Stark effect I. Theory". In: *Proceedings of the Royal Society of London. Series A. Mathematical and Physical Sciences* 305.1480 (May 21, 1968), pp. 125–138. DOI: 10.1098/rspa.1968.0109.

[54] M. N. Leuenberger and D. Loss. "Quantum computing in molecular magnets". In: *Nature* 410.6830 (Apr. 2001), pp. 789–793. DOI: 10.1038/35071024.

[55] M. N. Leuenberger, D. Loss, et al. "Quantum Information Processing with Large Nuclear Spins in GaAs Semiconductors". In: *Physical Review Letters* 89.20 (Oct. 28, 2002), p. 207601. DOI: 10.1103/PhysRevLett.89.207601.

[56] W. Wernsdorfer and M. Ruben. "Synthetic Hilbert Space Engineering of Molecular Qu *d* its: Isotopologue Chemistry". In: *Advanced Materials* 31.26 (June 2019), p. 1806687. DOI: 10.1002/adma.201806687.

[57] K. Najafi, A. L. Wysocki, et al. "Toward Long-Range Entanglement between Electrically Driven Single-Molecule Magnets". In: *The Journal of Physical Chemistry Letters* 10.23 (Dec. 5, 2019), pp. 7347–7355. DOI: 10.1021/acs.jpclett.9b03131.

[58] E. Moreno-Pineda, S. Klyatskaya, et al. "Observation of Cooperative Electronic Quantum Tunneling: Increasing Accessible Nuclear States in a Molecular Qudit". In: *Inorganic Chemistry* 57.16 (Aug. 20, 2018), pp. 9873–9879. DOI: 10.1021/acs.inorgchem.8b00823.

[59] W. Gerlach and O. Stern. "Der experimentelle Nachweis der Richtungsquantelung im Magnetfeld". In: *Zeitschrift für Physik* 9.1 (Dec. 1, 1922), pp. 349–352. DOI: 10.1007/BF01326983.

[60] E. M. Purcell, H. C. Torrey, et al. "Resonance Absorption by Nuclear Magnetic Moments in a Solid". In: *Physical Review* 69.1 (Jan. 1, 1946), pp. 37–38. DOI: 10.1103/PhysRev.69.37.

[61] A. Caneschi, D. Gatteschi, et al. "Toward molecular magnets: the metal-radical approach". In: *Accounts of Chemical Research* 22.11 (Nov. 1, 1989), pp. 392–398. DOI: 10.1021/ar00167a004.

[62] G. Christou, D. Gatteschi, et al. "Single-Molecule Magnets". In: *MRS Bulletin* 25.11 (Nov. 2000), pp. 66–71. DOI: 10.1557/mrs2000.226.

[63] D. Gatteschi, R. Sessoli, et al. *Molecular Nanomagnets*. Oxford University Press, Mar. 2, 2006. DOI: 10.1093/acprof:oso/9780198567530.001.0001.

[64] J. E. Rosenthal and G. Breit. "The Isotope Shift in Hyperfine Structure". In: *Physical Review* 41.4 (Aug. 15, 1932), pp. 459–470. DOI: 10.1103/PhysRev.41.459.

[65] A. Bohr and V. F. Weisskopf. "The Influence of Nuclear Structure on the Hyperfine Structure of Heavy Elements". In: *Physical Review* 77.1 (Jan. 1, 1950), pp. 94–98. DOI: 10.1103/PhysRev.77.94.

[66] C. D. Anderson and S. H. Neddermeyer. "Cloud Chamber Observations of Cosmic Rays at 4300 Meters Elevation and Near Sea-Level". In: *Physical Review* 50.4 (Aug. 15, 1936), pp. 263–271. DOI: 10.1103/PhysRev.50.263.

[67] V. W. Hughes, D. W. McColm, et al. "Formation of Muonium and Observation of its Larmor Precession". In: *Physical Review Letters* 5.2 (July 15, 1960), pp. 63–65. DOI: 10.1103/PhysRevLett.5.63.

[68] K. P. Jungmann. "Past, Present and Future of Muonium". In: *In Memory of Vernon Willard Hughes*. Proceedings of the Memorial Symposium in Honor of Vernon Willard Hughes. Yale University, USA: World Scientific, Dec. 2004, pp. 134–153. DOI: 10.1142/9789812702425_0009.

[69] G. Lospalluto, A. Antognini, et al. "Towards muon cooling at the Paul Scherrer Institute". In: *Proceedings of Muon4Future Workshop — PoS(Muon4Future2023)*. Muon4Future Workshop. Istituto Veneto di Lettere, Scienze ed Arti - Palazzo Franchetti, Venezia, Italy: Sissa Medialab, Mar. 15, 2024, p. 009. DOI: 10.22323/1.452.0009.

[70] K. Shimomura, A. Koda, et al. "Pulsed muon facility of J-PARC MUSE". In: *Interactions* 245.1 (Mar. 5, 2024), p. 31. DOI: 10.1007/s10751-024-01863-8.

[71] E. L. Hahn. "Spin Echoes". In: *Physical Review* 80.4 (Nov. 15, 1950), pp. 580–594. DOI: 10.1103/PhysRev.80.580.

[72] M. H. Levitt. "Composite pulses". In: *Progress in Nuclear Magnetic Resonance Spectroscopy* 18.2 (Jan. 1986), pp. 61–122. DOI: 10.1016/0079-6565(86)80005-X.

[73] A. P. Peirce, M. A. Dahleh, et al. "Optimal control of quantum-mechanical systems: Existence, numerical approximation, and applications". In: *Physical Review A* 37.12 (June 1, 1988), pp. 4950–4964. DOI: 10.1103/PhysRevA.37.4950.

[74] C. Brif, R. Chakrabarti, et al. "Control of quantum phenomena: past, present and future". In: *New Journal of Physics* 12.7 (July 1, 2010), p. 075008. DOI: 10.1088/1367-2630/12/7/075008.

[75] J. Preskill. "Quantum Computing in the NISQ era and beyond". In: *Quantum* 2 (Aug. 6, 2018), p. 79. DOI: 10.22331/q-2018-08-06-79.

[76] J. P. Dowling and G. J. Milburn. "Quantum technology: the second quantum revolution". In: *Philosophical Transactions of the Royal Society of London. Series A: Mathematical, Physical and Engineering Sciences* 361.1809 (Aug. 15, 2003). Ed. by A. G. J. MacFarlane, pp. 1655–1674. DOI: 10.1098/rsta.2003.1227.

[77] Clément Godfrin, Stefan Thiele, et al. "Electrical Read-Out of a Single Spin Using an Exchange-Coupled Quantum Dot". In: *ACS Nano* 11.4 (Apr. 14, 2017). MAG ID: 2606235355, pp. 3984–3989. DOI: 10.1021/acsnano.7b00451.

[78] C. Godfrin, R. Ballou, et al. "Generalized Ramsey interferometry explored with a single nuclear spin qudit". In: *npj Quantum Information* 4.1 (Dec. 2018), p. 53. DOI: 10.1038/s41534-018-0101-3.

[79] M. James. "Optimal Quantum Control Theory". In: *Annual Review of Control, Robotics, and Autonomous Systems* 4.1 (May 3, 2021), pp. 343–367. DOI: 10.1146/annurev-control-061520-010444.

[80] D. D'Alessandro. *Introduction to quantum control and dynamics*. 2nd edition. Advances in mathematics series. Boca Raton: CRC Press, 2021.

[81] I. R. Sola, B. Y. Chang, et al. "Quantum Control in Multilevel Systems". In: *Advances In Atomic, Molecular, and Optical Physics*. Vol. 67. Elsevier, 2018, pp. 151–256. DOI: 10.1016/bs.aamop.2018.02.003.

[82] M. A. Nielsen and I. L. Chuang. *Quantum Computation and Quantum Information: 10th Anniversary Edition*. Cambridge: Cambridge University Press, 2010. DOI: 10.1017/CBO9780511976667.

[83] V. Gorini, A. Kossakowski, et al. "Completely positive dynamical semigroups of N -level systems". In: *Journal of Mathematical Physics* 17.5 (May 1, 1976), pp. 821–825. DOI: 10.1063/1.522979.

[84] G. Lindblad. "On the generators of quantum dynamical semigroups". In: *Communications in Mathematical Physics* 48.2 (June 1976), pp. 119–130. DOI: 10.1007/BF01608499.

[85] D. Manzano. "A short introduction to the Lindblad master equation". In: *AIP Advances* 10.2 (Feb. 1, 2020), p. 025106. DOI: 10.1063/1.5115323.

[86] H.-P. Breuer, E.-M. Laine, et al. "*Colloquium* : Non-Markovian dynamics in open quantum systems". In: *Reviews of Modern Physics* 88.2 (Apr. 19, 2016), p. 021002. DOI: 10.1103/RevModPhys.88.021002.

[87] C. G. Almudever, L. Lao, et al. "The engineering challenges in quantum computing". In: *Design, Automation & Test in Europe Conference & Exhibition (DATE), 2017*. 2017 Design, Automation & Test in Europe Conference & Exhibition (DATE). Lausanne, Switzerland: IEEE, Mar. 2017, pp. 836–845. DOI: 10.23919/DATE.2017.7927104.

[88] C. G. Almudever and E. Alarcon. "Structured Optimized Architecting of Full-Stack Quantum Systems in the NISQ era". In: *2021 Design, Automation & Test in Europe Conference & Exhibition (DATE)*. 2021 Design, Automation & Test in Europe Conference & Exhibition (DATE). Grenoble, France: IEEE, Feb. 1, 2021, pp. 762–767. DOI: 10.23919/DATE51398.2021.9474197.

[89] M. Grassl, L. Kong, et al. "Quantum Error-Correcting Codes for Qudit Amplitude Damping". In: *IEEE Transactions on Information Theory* 64.6 (June 2018), pp. 4674–4685. DOI: 10.1109/TIT.2018.2790423.

[90] F. Petiziol, A. Chiesa, et al. "Counteracting dephasing in Molecular Nanomagnets by optimized qudit encodings". In: *npj Quantum Information* 7.1 (Aug. 26, 2021), p. 133. DOI: 10.1038/s41534-021-00466-3.

[91] A. Chiesa, E. Macaluso, et al. "Molecular Nanomagnets as Qubits with Embedded Quantum-Error Correction". In: *The Journal of Physical Chemistry Letters* 11.20 (Oct. 15, 2020), pp. 8610–8615. DOI: 10.1021/acs.jpclett.0c02213.

[92] R. F. Uy and D. A. Gangloff. *Qudit-based quantum error-correcting codes from irreducible representations of SU(d)*. Oct. 3, 2024. DOI: 10.48550/arXiv.2410.02407.

[93] E. D. Sontag. *Mathematical Control Theory*. Red. by J. E. Marsden, L. Sirovich, et al. Vol. 6. Texts in Applied Mathematics. New York, NY: Springer New York, 1998. DOI: 10.1007/978-1-4612-0577-7.

[94] C. P. Koch, U. Boscain, et al. "Quantum optimal control in quantum technologies. Strategic report on current status, visions and goals for research in Europe". In: *EPJ Quantum Technology* 9.1 (Dec. 2022), p. 19. DOI: 10.1140/epjqt/s40507-022-00138-x.

[95] S. J. Glaser, U. Boscain, et al. "Training Schrödinger's cat: quantum optimal control: Strategic report on current status, visions and goals for research in Europe". In: *The European Physical Journal D* 69.12 (Dec. 2015), p. 279. DOI: 10.1140/epjd/e2015-60464-1.

[96] G. Brennen, D. O'Leary, et al. "Criteria for exact qudit universality". In: *Physical Review A* 71.5 (May 16, 2005), p. 052318. DOI: 10.1103/PhysRevA.71.052318.

[97] N. Khaneja, T. Reiss, et al. "Optimal control of coupled spin dynamics: design of NMR pulse sequences by gradient ascent algorithms". In: *Journal of Magnetic Resonance* 172.2 (Feb. 2005), pp. 296–305. DOI: 10.1016/j.jmr.2004.11.004.

[98] G. E. Karniadakis, I. G. Kevrekidis, et al. "Physics-informed machine learning". In: *Nature Reviews Physics* 3.6 (May 24, 2021), pp. 422–440. DOI: 10.1038/s42254-021-00314-5.

[99] M. Raissi, P. Perdikaris, et al. "Physics-informed neural networks: A deep learning framework for solving forward and inverse problems involving nonlinear partial differential equations". In: *Journal of Computational Physics* 378 (Feb. 2019), pp. 686–707. DOI: 10.1016/j.jcp.2018.10.045.

[100] S. Mowlavi and S. Nabi. "Optimal control of PDEs using physics-informed neural networks". In: *Journal of Computational Physics* 473 (Jan. 2023), p. 111731. DOI: 10.1016/j.jcp.2022.111731.

[101] A. D. Jagtap, K. Kawaguchi, et al. "Adaptive activation functions accelerate convergence in deep and physics-informed neural networks". In: *Journal of Computational Physics* 404 (Mar. 2020), p. 109136. DOI: 10.1016/j.jcp.2019.109136.

[102] A. Norambuena, M. Mattheakis, et al. "Physics-Informed Neural Networks for Quantum Control". In: *Physical Review Letters* 132.1 (Jan. 3, 2024), p. 010801. DOI: 10.1103/PhysRevLett.132.010801.

[103] N. B. Dehaghani and A. P. Aguiar. *An Application of Pontryagin Neural Networks to Solve Optimal Quantum Control Problems*. Feb. 1, 2023. DOI: https://doi.org/10.48550/arXiv.2302.09143.

[104] P. Ring and P. Schuck. *The nuclear many body problem*. 1. ed., 3. print., study ed. Texts and monographs in physics. Berlin Heidelberg: Springer, 2004. 716 pp.

[105] J. Stone and P.-G. Reinhard. "The Skyrme interaction in finite nuclei and nuclear matter". In: *Progress in Particle and Nuclear Physics* 58.2 (Apr. 2007), pp. 587–657. DOI: 10.1016/j.ppnp.2006.07.001.

[106] M. Bender, P.-H. Heenen, et al. "Self-consistent mean-field models for nuclear structure". In: *Reviews of Modern Physics* 75.1 (Jan. 23, 2003), pp. 121–180. DOI: 10.1103/RevModPhys.75.121.

[107] L. Bonneau, N. Minkov, et al. "Effect of core polarization on magnetic dipole moments in deformed odd-mass nuclei". In: *Physical Review C* 91.5 (May 11, 2015), p. 054307. DOI: 10.1103/PhysRevC.91.054307.

[108] N. Minkov, A. Pálffy, et al. "Skyrme-Hartree-Fock-BCS approach to Th 229 m and neighboring nuclei". In: *Physical Review C* 110.3 (Sept. 26, 2024), p. 034327. DOI: 10.1103/PhysRevC.110.034327.

[109] G. Tessitore, G. A. Mandl, et al. "The role of lanthanide luminescence in advancing technology". In: *RSC Advances* 13.26 (2023), pp. 17787–17811. DOI: 10.1039/D3RA00991B.

[110] H. Carvajal Gallego, J. Deprince, et al. "Overview of the contributions from all lanthanide elements to kilonova opacity in the temperature range from 25 000 to 40 000 K". In: *Astronomy & Astrophysics* 685 (May 2024), A91. DOI: 10.1051/0004-6361/202347723.

[111] D. Serrano, S. K. Kuppusamy, et al. "Ultra-narrow optical linewidths in rare-earth molecular crystals". In: *Nature* 603.7900 (Mar. 10, 2022), pp. 241–246. DOI: 10.1038/s41586-021-04316-2.

[112] N. Stone. "Table of nuclear magnetic dipole and electric quadrupole moments". In: *Atomic Data and Nuclear Data Tables* 90.1 (May 2005), pp. 75–176. DOI: 10.1016/j.adt.2005.04.001.

[113] C. Schwartz. "Theory of Hyperfine Structure". In: *Physical Review* 97.2 (Jan. 15, 1955), pp. 380–395. DOI: 10.1103/PhysRev.97.380.

[114] J. Persson. *Muonic Hyperfine Structure and the Bohr-Weisskopf Effect*. Aug. 11, 2023. DOI: 10.20944/preprints202308.0903.v1.

[115] B. M. Roberts and J. S. M. Ginges. "Hyperfine anomaly in heavy atoms and its role in precision atomic searches for new physics". In: *Physical Review A* 104.2 (Aug. 27, 2021), p. 022823. DOI: 10.1103/PhysRevA.104.022823.

[116] A. Knecht, A. Skawran, et al. "Study of nuclear properties with muonic atoms". In: *The European Physical Journal Plus* 135.10 (Oct. 2020), p. 777. DOI: 10.1140/epjp/s13360-020-00777-y.

[117] A. Skawran, A. Adamczak, et al. "Towards nuclear structure with radioactive muonic atoms". In: *Il Nuovo Cimento C* 42.203 (Sept. 20, 2019), pp. 1–4. DOI: 10.1393/ncc/i2019-19125-7.

[118] P. Strasser, A. Taniguchi, et al. "Muon spectroscopy with trace alkaline-earth and rare-earth isotopes implanted in solid D2". In: *Hyperfine Interactions* 193.1 (Sept. 2009), pp. 121–127. DOI: 10.1007/s10751-009-0055-0.

[119] T. Y. Saito, M. Niikura, et al. *Muonic X-Ray Measurement for the Nuclear Charge Distribution: the Case of Stable Palladium Isotopes*. Apr. 7, 2022.

[120] A. Antognini, N. Berger, et al. "Measurement of the quadrupole moment of Re 185 and Re 187 from the hyperfine structure of muonic X rays". In: *Physical Review C* 101.5 (May 22, 2020), p. 054313. DOI: 10.1103/PhysRevC.101.054313.

[121] T. Okumura, T. Azuma, et al. *Few-electron highly charged muonic Ar atoms verified by electronic K x rays*. July 10, 2024.

[122] D. Janković, J.-G. Hartmann, et al. "Noisy qudit vs multiple qubits: conditions on gate efficiency for enhancing fidelity". In: *npj Quantum Information* 10.1 (June 10, 2024), p. 59. DOI: 10.1038/s41534-024-00829-6.

[123] D. Jankovic. *Source Code for data generation and pulses data for Noisy Qudit vs Multiple Qubits*. In collab. with D. Jankovic. 2024. DOI: 10.35097/1953.

[124] A. S. Nikolaeva, E. O. Kiktenko, et al. "Efficient realization of quantum algorithms with qudits". In: *EPJ Quantum Technology* 11.1 (Dec. 2024), p. 43. DOI: 10.1140/epjqt/s40507-024-00250-0.

[125] N. Cao, J. Lin, et al. "NISQ: Error Correction, Mitigation, and Noise Simulation". In: (Nov. 3, 2021). DOI: 10.48550/arXiv.2111.02345.

[126] M. A. Nielsen. "A simple formula for the average gate fidelity of a quantum dynamical operation". In: *Physics Letters A* 303.4 (Oct. 2002), pp. 249–252. DOI: 10.1016/S0375-9601(02)01272-0.

[127] J. R. Johansson, P. D. Nation, et al. "QuTiP: An open-source Python framework for the dynamics of open quantum systems". In: *Computer Physics Communications* 183.8 (Aug. 2012), pp. 1760–1772. DOI: 10.1016/j.cpc.2012.02.021.

[128] J. R. Johansson, P. D. Nation, et al. "QuTiP 2: A Python framework for the dynamics of open quantum systems". In: *Computer Physics Communications* 184.4 (Apr. 2013), pp. 1234–1240. DOI: 10.1016/j.cpc.2012.11.019.

[129] J.-G. Hartmann, D. Janković, et al. "Nonlinearity of the Fidelity in Open Qudit Systems: Gate and Noise Dependence in High-dimensional Quantum Computing". In: *Quantum* 9 (Apr. 7, 2025), p. 1690. DOI: 10.22331/q-2025-04-07-1690.

[130] J.-G. Hartmann, D. Janković, et al. *Code and Data for "Nonlinearity of the Fidelity in Open Qudit Systems: Gate and Noise Dependence in High-dimensional Quantum Computing"*. Zenodo, Mar. 19, 2025. DOI: 10.5281/ZENODO.13618284.

[131] N. P. De Leon, K. M. Itoh, et al. "Materials challenges and opportunities for quantum computing hardware". In: *Science* 372.6539 (Apr. 16, 2021), eabb2823. DOI: 10.1126/science.abb2823.

[132] M. Ringbauer, M. Meth, et al. "A universal qudit quantum processor with trapped ions". In: *Nature Physics* 18.9 (Sept. 2022), pp. 1053–1057. DOI: 10.1038/s41567-022-01658-0.

[133] H. Miyahara, Y. Chen, et al. "Decoherence mitigation by embedding a logical qubit in a qudit". In: *Quantum Information Processing* 22.7 (July 11, 2023), p. 278. DOI: 10.1007/s11128-023-04035-9.

[134] L. G. Gunderman. "Local-dimension-invariant qudit stabilizer codes". In: *Physical Review A* 101.5 (May 28, 2020), p. 052343. DOI: 10.1103/PhysRevA.101.052343.

[135] Y. Zheng, H. Sharma, et al. "Entanglement Distribution with Minimal Memory Requirements Using Time-Bin Photonic Qudits". In: *PRX Quantum* 3.4 (Nov. 16, 2022), p. 040319. DOI: 10.1103/PRXQuantum.3.040319.

[136] F. Bouchard, R. Fickler, et al. "High-dimensional quantum cloning and applications to quantum hacking". In: *Science Advances* 3.2 (Feb. 3, 2017), e1601915. DOI: 10.1126/sciadv.1601915.

[137] S. Boixo, S. V. Isakov, et al. "Characterizing quantum supremacy in near-term devices". In: *Nature Physics* 14.6 (June 2018), pp. 595–600. DOI: 10.1038/s41567-018-0124-x.

[138] M. Otten, K. Kapoor, et al. "Impacts of noise and structure on quantum information encoded in a quantum memory". In: *Physical Review A* 104.1 (July 16, 2021), p. 012605. DOI: 10.1103/PhysRevA.104.012605.

[139] M. A. Nielsen and I. L. Chuang. *Quantum computation and quantum information*. Cambridge, NY: Cambridge University Press, 2000. 676 pp. DOI: 10.1017/CBO9780511976667.

[140] S. Machnes, U. Sander, et al. "Comparing, optimizing, and benchmarking quantum-control algorithms in a unifying programming framework". In: *Physical Review A* 84.2 (Aug. 3, 2011), p. 022305. DOI: 10.1103/PhysRevA.84.022305.

[141] Initié par Julian Mayr (Université de Heidelberg) pendant son stage de MSc. Physique sur ce projet.

[142] In this discussion of the effective mean-field model used in this work, we must acknowledge the work of our collaborators on this project, Johann Bartel and Hervé Molique. They provided the necessary nuclear charge distribution data and helped to refine our understanding of the techniques used in the effective model. Further information on the computational techniques and theoretical framework can be found in the publication resulting from our collaboration.

[143] T. Skyrme. "The effective nuclear potential". In: *Nuclear Physics* 9.4 (Jan. 1958), pp. 615–634. DOI: 10.1016/0029-5582(58)90345-6.

[144] D. Vautherin and D. M. Brink. "Hartree-Fock Calculations with Skyrme's Interaction. I. Spherical Nuclei". In: *Physical Review C* 5.3 (Mar. 1, 1972), pp. 626–647. DOI: 10.1103/PhysRevC.5.626.

[145] M. Beiner, H. Flocard, et al. "Nuclear ground-state properties and self-consistent calculations with the skyrme interaction". In: *Nuclear Physics A* 238.1 (Jan. 1975), pp. 29–69. DOI: 10.1016/0375-9474(75)90338-3.

[146] J. Damgaard, H. Pauli, et al. "A method for solving the independent-particle Schrödinger equation with a deformed average field". In: *Nuclear Physics A* 135.2 (Oct. 1969), pp. 432–444. DOI: 10.1016/0375-9474(69)90174-2.

[147] D. Vautherin. "Hartree-Fock Calculations with Skyrme's Interaction. II. Axially Deformed Nuclei". In: *Physical Review C* 7.1 (Jan. 1, 1973), pp. 296–316. DOI: 10.1103/PhysRevC.7.296.

[148] *Hartree-Fock-Bogoliubov results based on the Gogny force*. URL: https://www-phynu.cea.fr/science_en_ligne/carte_potentiels_microscopiques/carte_potentiel_nucleaire_eng.htm (visited on 09/24/2024).

[149] H. Flocard, P. Quentin, et al. "Nuclear deformation energy curves with the constrained Hartree-Fock method". In: *Nuclear Physics A* 203.3 (Mar. 1973), pp. 433–472. DOI: 10.1016/0375-9474(73)90357-6.

[150] J. Dechargé and D. Gogny. "Hartree-Fock-Bogolyubov calculations with the D 1 effective interaction on spherical nuclei". In: *Physical Review C* 21.4 (Apr. 1, 1980), pp. 1568–1593. DOI: 10.1103/PhysRevC.21.1568.

[151] V. Magnasco. *Methods of molecular quantum mechanics: an introduction to electronic molecular structure*. OCLC: 501193479. Chichester, U.K.: Wiley, 2009.

[152] J. Bardeen, L. N. Cooper, et al. "Theory of Superconductivity". In: *Physical Review* 108.5 (Dec. 1, 1957), pp. 1175–1204. DOI: 10.1103/PhysRev.108.1175.

[153] J. W. Negele. "The mean-field theory of nuclear structure and dynamics". In: *Reviews of Modern Physics* 54.4 (Oct. 1, 1982), pp. 913–1015. DOI: 10.1103/RevModPhys.54.913.

[154] J. D. Jackson. *Classical electrodynamics*. 3. ed., [Nachdr.] Hoboken, NY: Wiley, 2009. 808 pp.

[155] A. Pálffy. "Nuclear effects in atomic transitions". In: *Contemporary Physics* 51.6 (Nov. 2010), pp. 471–496. DOI: 10.1080/00107514.2010.493325.

[156] R. P. de Groote and G. Neyens. "Spins and electromagnetic moments of nuclei". In: *Handbook of nuclear physics*. Ed. by I. Tanihata, H. Toki, et al. Singapore: Springer Nature, 2020, pp. 1–36. DOI: 10.1007/978-981-15-8818-1_42-1.

[157] G. Fricke and H. Schopper, eds. *Numerical data and functional relationships in science and technology. Bd. 20: Gruppe 1: Kern- und Teilchenphysik = Group 1: @Nuclear and particle physics Nuclear charge radii / ed.: H. Schopper. Authors: G. Fricke*. Vol. 20. Berlin Heidelberg: Springer, 2004. 385 pp.

[158] M. Chemtob. "Two-body interaction currents and nuclear magnetic moments". In: *Nuclear Physics A* 123.2 (Jan. 1969), pp. 449–470. DOI: 10.1016/0375-9474(69)90513-2.

[159] P. Strange. *Relativistic quantum mechanics: With applications in condensed matter and atomic physics*. Cambridge: Cambridge University Press, 1998. DOI: 10.1017/CBO9780511622755.

[160] W. R. Johnson. *Atomic structure theory*. Berlin, Heidelberg: Springer, 2007. DOI: 10.1007/978-3-540-68013-0.

[161] S. Büttgenbach. "Magnetic hyperfine anomalies". In: *Hyperfine Interactions* 20.1 (July 1984), pp. 1–64. DOI: 10.1007/BF02043319.

[162] S. Boucard. "Calcul de haute precision d'energies de transitions dans les atomes exotiques et les lithiumoides : corrections relativistes, corrections radiatives, structure hyperfine et interaction avec le cortege electronique residuel". These de doctorat. Paris 6, Jan. 1, 1998.

[163] J. Persson. "Table of hyperfine anomaly in atomic systems — 2023". In: *Atomic Data and Nuclear Data Tables* 154 (Nov. 2023), p. 101589. DOI: 10.1016/j.adt.2023.101589.

[164] J. Persson. "Table of hyperfine anomaly in atomic systems". In: *Atomic Data and Nuclear Data Tables* 99.1 (Jan. 2013), pp. 62–68. DOI: 10.1016/j.adt.2012.04.002.

[165] R. Jozsa. "Fidelity for Mixed Quantum States". In: *Journal of Modern Optics* 41.12 (Dec. 1994), pp. 2315–2323. DOI: 10.1080/09500349414552171.

[166] N. Johnston and D. W. Kribs. "Quantum gate fidelity in terms of Choi matrices". In: *Journal of Physics A: Mathematical and Theoretical* 44.49 (Dec. 9, 2011), p. 495303. DOI: 10.1088/1751-8113/44/49/495303.

[167] M. Suezen, C. Weber, et al. *Spectral Ergodicity In Deep Learning Architectures Via Surrogate Random Matrices*. July 3, 2017. DOI: 10.5281/zenodo.822410.

[168] T. Abad, J. Fernández-Pendás, et al. "Universal Fidelity Reduction of Quantum Operations from Weak Dissipation". In: *Physical Review Letters* 129.15 (Oct. 7, 2022), p. 150504. DOI: 10.1103/PhysRevLett.129.150504.

[169] S. Cao, M. Bakr, et al. "Emulating two qubits with a four-level transmon qudit for variational quantum algorithms". In: *Quantum Science and Technology* 9.3 (July 1, 2024), p. 035003. DOI: 10.1088/2058-9565/ad37d4.

[170] A. Larrouy et al. "Fast Navigation in a Large Hilbert Space Using Quantum Optimal Control". In: *Physical Review X* 10.2 (June 2020), p. 021058. DOI: 10.1103/PhysRevX.10.021058.

[171] A. Ozaeta and P. L. McMahon. "Decoherence of up to 8-qubit entangled states in a 16-qubit superconducting quantum processor". In: *Quantum Science and Technology* 4.2 (Apr. 2019), p. 025015. DOI: 10.1088/2058-9565/ab13e5.

[172] Y. Chen et al. "Qubit Architecture with High Coherence and Fast Tunable Coupling". In: *Physical Review Letters* 113.22 (Nov. 2014), p. 220502. DOI: 10.1103/PhysRevLett.113.220502.

[173] S. Rosenblum et al. "A CNOT gate between multiphoton qubits encoded in two cavities". In: *Nature Communications* 9.1 (Feb. 2018), p. 652. DOI: 10.1038/s41467-018-03059-5.

[174] H.-P. Breuer and F. Petruccione. *The Theory of Open Quantum Systems*. First. Oxford: Oxford University Press, Jan. 25, 2007. DOI: 10.1093/acprof:oso/9780199213900.001.0001.

[175] J. Watrous. *The Theory of Quantum Information*. First. Cambridge: Cambridge University Press, Apr. 26, 2018. DOI: 10.1017/9781316848142.

[176] I. Bengtsson and K. Zyczkowski. *Geometry of Quantum States: An Introduction to Quantum Entanglement*. First. Cambridge: Cambridge University Press, May 11, 2006. DOI: 10.1017/CBO9780511535048.

[177] T. F. Havel. "Robust procedures for converting among Lindblad, Kraus and matrix representations of quantum dynamical semigroups". In: *Journal of Mathematical Physics* 44.2 (Feb. 1, 2003), pp. 534–557. DOI: 10.1063/1.1518555.

[178] T. A. Loring. "Computing a logarithm of a unitary matrix with general spectrum". In: *Numerical Linear Algebra with Applications* 21.6 (Dec. 2014), pp. 744–760. DOI: 10.1002/nla.1927.

[179] M. Aifer and S. Deffner. "From quantum speed limits to energy-efficient quantum gates". In: *New Journal of Physics* 24.5 (May 1, 2022), p. 055002. DOI: 10.1088/1367-2630/ac6821.

[180] A. Vourdas. "Quantum systems with finite Hilbert space". In: *Reports on Progress in Physics* 67.3 (Mar. 1, 2004), pp. 267–320. DOI: 10.1088/0034-4885/67/3/R03.

[181] J. Martínez-Carranza, F. Soto-Eguibar, et al. "Alternative analysis to perturbation theory in quantum mechanics: Dyson series in matrix form". In: *The European Physical Journal D* 66.1 (Jan. 2012), p. 22. DOI: 10.1140/epjd/e2011-20654-5.

[182] B. M. Villegas-Martínez, F. Soto-Eguibar, et al. "Application of Perturbation Theory to a Master Equation". In: *Advances in Mathematical Physics* 2016 (2016), pp. 1–7. DOI: 10.1155/2016/9265039.

[183] J. E. Campbell. "On a Law of Combination of Operators bearing on the Theory of Continuous Transformation Groups". In: *Proceedings of the London Mathematical Society* s1-28.1 (Nov. 1896), pp. 381–390. DOI: 10.1112/plms/s1-28.1.381.

[184] B. C. Hall. *Lie groups, Lie algebras, and representations: an elementary introduction*. Second edition. Graduate texts in mathematics 222. Cambridge, NY: Springer, 2015. 449 pp. DOI: 10.1007/978-3-319-13467-3.

[185] B. Collins, S. Matsumoto, et al. "The Weingarten Calculus". In: *Notices of the American Mathematical Society* 69.5 (May 1, 2022), p. 1. DOI: 10.1090/noti2474.

[186] F. Mezzadri. "How to generate random matrices from the classical compact groups". In: *Notices of the American Mathematical Society* 54.5 (Feb. 27, 2007), pp. 592–604. DOI: 10.48550/arXiv.math-ph/0609050.

[187] F. J. Dyson. "The Threefold Way. Algebraic Structure of Symmetry Groups and Ensembles in Quantum Mechanics". In: *Journal of Mathematical Physics* 3.6 (Nov. 1, 1962), pp. 1199–1215. DOI: 10.1063/1.1703863.

[188] M. L. Mehta. *Random matrices*. Third. Pure and applied mathematics series 142. Amsterdam: Elsevier, 2004. 688 pp. DOI: 10.1016/S0079-8169(04)80088-6.

[189] E. P. Wigner. "Characteristic Vectors of Bordered Matrices With Infinite Dimensions". In: *The Annals of Mathematics* 62.3 (Nov. 1955), p. 548. DOI: 10.2307/1970079.

[190] C. Developers. *Cirq*. Google Quantum AI, Dec. 1, 2023. DOI: 10.5281/ZENODO.4062499.

[191] A. A. Giannopoulos and V. D. Milman. "Concentration Property on Probability Spaces". In: *Advances in Mathematics* 156.1 (Dec. 2000), pp. 77–106. DOI: 10.1006/aima.2000.1949.

[192] M. Ledoux. *The concentration of measure phenomenon*. Mathematical surveys and monographs Issue 89. Providence, RI: American Mathematical Society, 2001. DOI: 10.1090/surv/089.

[193] M. Horodecki, P. Horodecki, et al. "General teleportation channel, singlet fraction, and quasidistillation". In: *Physical Review A* 60.3 (Sept. 1, 1999), pp. 1888–1898. DOI: 10.1103/PhysRevA.60.1888.

[194] E. S. Meckes. *The Random Matrix Theory of the Classical Compact Groups*. First. Cambridge: Cambridge University Press, Aug. 31, 2019. DOI: 10.1017/9781108303453.

[195] H. C. Volkin, U. S. N. Aeronautics, et al. *Iterated commutators and functions of operators*. NASA technical note. National Aeronautics and Space Administration, 1968.

[196] M. Le Bellac. *A short introduction to quantum information and quantum computation*. OCLC: ocm65203239. Cambridge, UK ; New York: Cambridge University Press, 2006. 167 pp.

[197] B. C. Hall. *Quantum theory for mathematicians*. Graduate texts in mathematics 267. OCLC: ocn828487961. New York: Springer, 2013. 554 pp.

[198] S. Shapiro. "Lagrange and Mayer problems in optimal control". In: *Automatica* 3.3 (Jan. 1966), pp. 219–230. DOI: 10.1016/0005-1098(66)90014-8.

[199] K. Lutz and Y. Privat. "Decoherence control for quantum information". In: (2023).
[200] R. Fisher and R. Fisher. *Optimal control of multi-level quantum systems*. KS Omniscriptum Publishing, 2010.
[201] T. H. Einwohner, J. Wong, et al. "Analytical solutions for laser excitation of multilevel systems in the rotating-wave approximation". In: *Physical Review A* 14.4 (Oct. 1, 1976), pp. 1452–1456. DOI: 10.1103/PhysRevA.14.1452.
[202] J. Wong, J. C. Garrison, et al. "Multiple-time-scale perturbation theory applied to laser excitation of atoms and molecules". In: *Physical Review A* 13.2 (Feb. 1, 1976), pp. 674–687. DOI: 10.1103/PhysRevA.13.674.
[203] S. G. Schirmer, H. Fu, et al. "Complete controllability of quantum systems". In: *Physical Review A* 63.6 (May 15, 2001). Publisher: American Physical Society, p. 063410. DOI: 10.1103/PhysRevA.63.063410.
[204] V. Ramakrishna, M. V. Salapaka, et al. "Controllability of molecular systems". In: *Physical Review A* 51.2 (Feb. 1, 1995), pp. 960–966. DOI: 10.1103/PhysRevA.51.960.
[205] T. M. Cavalheiro, A. J. Santana, et al. *An accessibility condition for discrete-time linear systems on Lie groups*. June 23, 2024. DOI: https://doi.org/10.48550/arXiv.2406.16237.
[206] V. Ayala and L. A. B. S. Martin. "Controllability properties of a class of control systems on lie groups". In: *Nonlinear control in the Year 2000*. Ed. by A. Isidori, F. Lamnabhi-Lagarrigue, et al. Vol. 258. London: Springer London, 2000, pp. 83–92. DOI: 10.1007/BFb0110209.
[207] J.-L. Brylinski and R. Brylinski. "Universal quantum gates". In: (Aug. 13, 2001). DOI: https://doi.org/10.48550/arXiv.quant-ph/0108062.
[208] A. Muthukrishnan and C. R. Stroud. "Multivalued logic gates for quantum computation". In: *Physical Review A* 62.5 (Oct. 16, 2000), p. 052309. DOI: 10.1103/PhysRevA.62.052309.
[209] Zurich Instruments. *Functional Overview - HDAWG User Manual*. URL: https://docs.zhinst.com/hdawg_user_manual/functional_overview.html (visited on 09/08/2024).
[210] W. Givens. "Computation of Plain Unitary Rotations Transforming a General Matrix to Triangular Form". In: *Journal of the Society for Industrial and Applied Mathematics* 6.1 (Mar. 1958), pp. 26–50. DOI: 10.1137/0106004.
[211] F. D. Murnaghan. "The orthogonal and symplectic groups". In: *Commun. Dublin Inst. Adv. Stud.* A 13 (1958), p. 156.
[212] F. D. Murnaghan. *The Unitary and Rotation Groups*. Vol. 3. Lecture Notes in Applied Mathematics. Washington, D.C.: Spartan Books, 1962.
[213] A. Barenco, C. H. Bennett, et al. "Elementary gates for quantum computation". In: *Physical Review A* 52.5 (Nov. 1, 1995), pp. 3457–3467. DOI: 10.1103/PhysRevA.52.3457.
[214] D. P. DiVincenzo. "Two-bit gates are universal for quantum computation". In: *Physical Review A* 51.2 (Feb. 1, 1995), pp. 1015–1022. DOI: 10.1103/PhysRevA.51.1015.
[215] G. Cybenko. "Reducing quantum computations to elementary unitary operations". In: *Computing in Science and Eng.* 3.2 (Mar. 1996), pp. 27–32. DOI: 10.1109/5992.908999.
[216] D. P. O'Leary and S. S. Bullock. "QR factorizations using a restricted set of rotations". In: *Electronic Transactions on Numerical Analysis* 21 (2005), pp. 20–27.

[217] S. S. Bullock and I. L. Markov. "Asymptotically optimal circuits for arbitrary n-qubit diagonal comutations". In: *Quantum Info. Comput.* 4.1 (Jan. 2004), pp. 27–47. DOI: 10.5555/2011572.2011575.

[218] C. Zalka. "Grover's quantum searching algorithm is optimal". In: *Physical Review A* 60.4 (Oct. 1, 1999), pp. 2746–2751. DOI: 10.1103/PhysRevA.60.2746.

[219] G. L. Long. "Grover algorithm with zero theoretical failure rate". In: *Physical Review A* 64.2 (July 11, 2001), p. 022307. DOI: 10.1103/PhysRevA.64.022307.

[220] T. Roy, L. Jiang, et al. "Deterministic Grover search with a restricted oracle". In: *Physical Review Research* 4.2 (Apr. 21, 2022), p. L022013. DOI: 10.1103/PhysRevResearch.4.L022013.

[221] R. H. Byrd, P. Lu, et al. "A Limited Memory Algorithm for Bound Constrained Optimization". In: *SIAM Journal on Scientific Computing* 16.5 (Sept. 1995), pp. 1190–1208. DOI: 10.1137/0916069.

[222] C. Zhu, R. H. Byrd, et al. "Algorithm 778: L-BFGS-B: Fortran subroutines for large-scale bound-constrained optimization". In: *ACM Transactions on Mathematical Software* 23.4 (Dec. 1997), pp. 550–560. DOI: 10.1145/279232.279236.

[223] Initiated by Julian Mayr (University of Heidelberg) during his MSc. Physics internship on this project.

Roads Go Ever On

Roads go ever ever on,
Over rock and under tree,
By caves where never sun has shone,
By streams that never find the sea;
Over snow by winter sown,
And through the merry flowers of June,
Over grass and over stone,
And under mountains in the moon.

Roads go ever ever on,
Under cloud and under star.
Yet feet that wandering have gone
Turn at last to home afar.
Eyes that fire and sword have seen,
And horror in the halls of stone
Look at last on meadows green,
And trees and hills they long have known.

The Road goes ever on and on
Down from the door where it began.
Now far ahead the Road has gone,
And I must follow, if I can,
Pursuing it with eager feet,
Until it joins some larger way,
Where many paths and errands meet.

The Road goes ever on and on
Down from the door where it began.
Now far ahead the Road has gone,
And I must follow, if I can,
Pursuing it with eager feet,
Until it joins some larger way,
Where many paths and errands meet.
And whither then? I cannot say.

Frodo Baggins in “The Lord of the Rings” - J.R.R. Tolkien

Université de Strasbourg

Jean-Gabriel HARTMANN

École doctorale Physique, chimie-physique ED 182 Université de Strasbourg

Hilbert space engineering and optimal control for quantum computing with applications for rare-earth single molecule magnets

Résumé: L'objectif de cette thèse est d'étudier et de développer les capacités de calcul quantique (QC) des états qudit de haute dimension dans les spins nucléaires d'ions de terres rares (RE) intégrés dans des aimants à molécule unique (SMM). Notre travail est structuré en trois parties principales, chacune abordant des aspects critiques de ce développement : Premièrement, du point de vue de la physique nucléaire et atomique, nous avons utilisé les codes numériques HTDA-Skyrme-HFBCS pour simuler de grands noyaux complexes d'éléments de terres rares tels que le terbium (Tb), le dysprosium (Dy) et le holmium (Ho). Nous calculons les moments dipolaires magnétiques et quadripolaires électriques de ces noyaux de lanthanides à partir de simulations de la charge des nucléons et des distributions de densité de courant pour des isotopes choisis. L'utilisation de ces distributions réalistes nous permet d'étudier l'interaction hyperfine dans des configurations atomiques hydrogénoïdes électroniques et muoniques libres, ainsi que les contributions dues à la pénétration des fonctions d'onde leptoniques dans le noyau. Plus précisément, nous menons une étude détaillée sur ^{161}Dy et ^{163}Dy pour examiner l'anomalie hyperfine entre ces isotopes par le calcul des corrections de Bohr-Weisskopf (BW) et de Breit-Rosenthal (BR) dues aux effets de taille finie. Nous constatons que, pour les configurations muoniques, ces effets sont suffisamment importants pour être mesurés physiquement, proposant ainsi un moyen de validation expérimentale. Deuxièmement, nous effectuons une analyse fondamentale des interactions des systèmes qudit généraux avec un environnement markovien, suivant le formalisme de Lindblad. Nous étudions l'infidélité moyenne des portes (AGI) en tant que mesure de l'interaction d'un système avec son environnement, indépendante de la plateforme. Une première étude se concentre sur les effets de premier ordre dans la limite d'un bruit faible, avec une analyse comparative des systèmes multiqubit et qudit. Nous dérivons une relation pour la figure de mérite entre les temps de porte et de décohérence, en comparant les plateformes QC actuelles basées sur les qudits et les qubits. Nous étendons ensuite ce travail au régime de couplage fort pour les systèmes qudit bruyants par le biais d'une expansion perturbative formelle de l'AGI. Ce cadre complet fournit une méthode constructive pour calculer les termes de correction à n'importe quel ordre. Grâce à lui, nous fixons des limites universelles à l'AGI dans la limite d'un fort déphasage et nous montrons comment les termes d'ordre supérieur introduisent du bruit et des effets dépendant de la porte. Ces résultats permettent d'optimiser les opérations de portes logiques quditiques et d'améliorer les protocoles de correction d'erreur. Enfin, nous étudions les techniques de contrôle optimal pour la mise en œuvre de portes quantiques quditiques universelles. Nous utilisons des méthodes de génération d'impulsions, notamment la décomposition de la rotation de Givens (GRD) et un algorithme de gradient ascendant (GRAPE), dans le cadre du développement d'un cadre numérique extensible, permettant d'étudier plus profondément les approches avancées de *machine learning*. En développant un flux de travail numérique robuste, nous étudions leur efficacité dans l'optimisation des performances des portes quantiques dans des conditions de bruit réalistes. Grâce à cette étude comparative détaillée, nous établissons des points de référence et des limites pour la performance des systèmes quantiques bruyants de dimension arbitraire, offrant ainsi des perspectives précieuses pour le développement futur de l'informatique quantique de haute dimension.

Mots clés: Calcul quantique, terres rares, qudits, SMM, anomalie hyperfine, théorie du contrôle optimal quantique, infidélité moyenne des portes logiques

Abstract: The aim of this thesis is to study and develop the quantum computing (QC) capabilities of the high-dimensional qudit states in the nuclear spins of rare-earth (RE) ions embedded in single molecule magnets (SMMs). Our work is structured into three main parts, each addressing critical aspects of this development: First, from a nuclear and atomic physics perspective, we used state-of-the-art HTDA-Skyrme-HFBCS numerical codes to simulate the large complex nuclei of rare-earth elements such as terbium (Tb), dysprosium (Dy) and holmium (Ho). We compute the magnetic dipole and electric quadrupole moments of these lanthanide nuclei from simulations of nucleon charge and current density distributions for selected isotopes. Using these realistic distributions allows us to study the hyperfine interaction in free hydrogen-like electronic and muonic atomic configurations, as well as the contributions due to the penetration of the leptonic wavefunctions within the nucleus. Specifically, we conduct a detailed investigation of ^{161}Dy and ^{163}Dy to examine the hyperfine anomaly between these isotopes through the calculation of the Bohr-Weisskopf (BW) and Breit-Rosenthal (BR) corrections due to finite size effects. We find that, for the muonic configurations, these effects are large enough to be measured physically, proposing a means for experimental validation. Second, we conduct a fundamental analysis of the interactions of general qudit systems with a Markovian environment, in the Lindblad formalism. We investigate the Average Gate Infidelity (AGI) as a platform-agnostic measure of a system's interaction with its environment. An initial study focuses on the first-order effects in the limit of weak noise with a comparative analysis of multi-qubit and qudit systems. We derive a relationship in the figure-of-merit relating gate and decoherence times, benchmarking current qudit- and qubit-based QC platforms. We then extend this work to the strong-coupling regime for noisy qudit systems through a formal perturbative expansion of the AGI. This comprehensive framework provides a constructive method for calculating correction terms to any order. With it, we set universal bounds on the AGI in the limit of strong dephasing and show how higher-order terms introduce noise and gate-dependent effects. These results enable optimisation of qudit gate operations and enhanced error-correction protocols. Finally, we study optimal control techniques for implementing universal quantum gates in qudits. We employ pulse generation methods, including the Givens Rotation Decomposition (GRD) and the gradient-based (GRAPE) algorithm, within development of an extensible numerical framework, enabling further study of advanced machine learning approaches. By developing a robust numerical workflow, we study their effectiveness in optimising quantum gate performance under realistic noise conditions. Through this detailed comparative study, we set benchmarks and establish limits for the performance of noisy quantum systems of arbitrary dimension, offering valuable insights for the future development of high-dimensional quantum computing.

Keywords: Quantum computing, rare-earths, qudits, SMM, hyperfine anomaly, quantum optimal control theory, average gate infidelity